UNIVERSITY OF SOUTHAMPTON

Faculty of Engineering and Physical Sciences

Aeronautics, Astronautics and Computational Engineering

High-Temperature Resistojets for All-Electric Spacecraft

DOI: 10.5258/SOTON/D0903

By

Federico Romei

ORCID ID https://orcid.org/0000-0003-2283-4658

A thesis submitted for the degree of

Doctor of Philosophy

May 2019

University of Southampton

Abstract

Faculty of Engineering and Physical Sciences
Aeronautics, Astronautics and Computational Engineering

Thesis for the degree of Doctor of Philosophy

High-Temperature Resistojets for All-Electric Spacecraft

by

Federico Romei

Electrothermal propulsion systems for spacecraft consist of an electrically powered heat exchanger, which increases the enthalpy of a propellant. Enthalpy is traded for kinetic energy through a gas dynamic expansion process to produce a high-velocity exhaust jet via a converging-diverging nozzle producing thrust. The performance is quantified by the specific impulse (I_{sp}), which increases proportionally to the square root of the stagnation gas temperature. By increasing the stagnation temperature, the amount of propellant required on board of the spacecraft to accomplish a specific mission decreases or greater total impulse is provided for a fixed quantity of propellant. Surrey Satellite Technology Limited (SSTL) has used a low power hot gas system, known as a resistojet, since 2002, which uses either butane or xenon as propellant. This system has flown on 21 spacecraft including the European GPS Galileo Testbed GIOVE-A validation satellite. A collaborative development programme between the University of Southampton and SSTL is currently proceeding to develop a high-temperature resistojet which nearly doubles current ISP performance. Selective Laser Melting (SLM) manufacturing is being utilised to build a novel complex thin-wall concentric cylindrical heat exchanger (HE) as a single component, for this reason, this thruster has been named Super-high Temperature Additive Resistojet (STAR). High-resolution micro-Computed Tomography (CT) is used as a tool for non-destructive inspection since the HE of the thruster is closed preventing visual inspection. The CT volume data is used to determine a surface mesh to perform coordinate measurements, nominal/actual comparison and wall thickness analysis. STAR is

designed to increase the stagnation temperature of the propellant to approximately 2,500K with a resulting I_{sp} for xenon propellant above 80 s. Presently, the driver of the high-temperature resistojet technology is a requirement for the all-electric propulsion spacecraft bus. Geostationary telecommunication satellites typically use chemical propulsion for attitude control as well as orbit–raising and station-keeping. The benefit of using STAR is in fuel mass savings, cost savings in launch vehicle option for lighter spacecraft and further reduction of costs by eliminating the use of hazardous propellants. This research presents the design, construction and performance evaluation of the first proof of concept thruster, STAR-0, through vacuum testing with Ar propellant at the University of Southampton facility. The prototypes are made of stainless steel, which limits the maximum gas temperature to approximately 1,000 K. A set of multiphysics simulations is validated against the experimental results and the numerical investigation is extended to high-temperature refractory metals, which will enable the construction of an engineering model.

Table of Contents

Table of Contents ..... **iii**

List of Tables ..... **ix**

List of Figures ..... **xiii**

Definitions and Abbreviations ..... **xxiii**

Declaration of Authorship ..... **xxviii**

Acknowledgement ..... **xxxi**

Introduction **1**

1

1.1 Motivation and Objectives of the Research 1

1.2 Methodology 2

1.3 Overview of the Thesis 3

1.4 Review of Resistojet Technology 4

1.4.1 Introduction to Resistojets 4

1.4.2 Resistojet Investigation 15

1.4.3 Materials Applied to Resistojets 30

1.4.4 Review of High-Temperature Materials 35

1.4.5 Summary 42

1.5 High-Temperature Resistojet: Investigation and Design Concept 43

1.5.1 Definition and Applications 43

2

1.5.2 Development of the Thruster Concept 53

1.5.3 Summary 66

Metal Additive Manufacturing Investigation **67**

2.1 Background 67

2.1.1 Introduction to Metal Additive Manufacturing 67

2.1.2 Selection of Stainless Steel 316L for Prototype 72

2.1.3 Potential Defects 75

2.1.4 Inspection 77

2.2 SLM Manufacturing Verification 78

2.2.1 Printing Strategy 78

2.2.2 Dimensional Accuracy 80

2.2.3 Surface Characterisation 91

2.2.4 Welding Tests 103
2.3 Heat Exchanger Design 104
2.3.1 Baseline Design 105
2.3.2 HE Design Iteration 1 119
2.3.3 HE Design Iteration 2 122
2.3.4 HE Design Iteration 3 127
2.3.5 Summary of the HE Iterations 131
2.4 Summary 133

Design, Manufacturing and Testing of the Prototype Model 137

3.1 Preliminary Considerations 137
3 3.1.1 Preliminary Dimensioning of the Heat Exchanger 138
3.1.2 Nozzle Calculations 139
3.1.3 Voltage-Current Range 142
3.1.4 Power Electronics Discussion 143
3.2 STAR-0 Preliminary Assembly Design 144
3.2.1 Assembly Design Process 144
3.2.2 Selection of Ceramics 146
3.2.3 Modal Analysis of the STAR-0 Assembly 148
3.3 Detailed Assembly Design and Manufacturing 148
3.3.1 Detailed Design 149
3.3.2 Manufacturing of the Parts 150
3.3.3 Fit Assembly Notes 155
3.3.4 Construction of the Proof of Concept Thrusters 157
3.4 Test Setup and Computational Models 157
3.4.1 Facility 159
3.4.2 Test Instrumentation 162
3.4.3 Software Selection 166
3.4.4 Summary of the Validation Studies 167
3.4.5 Computational Models 168
3.5 Preliminary Tests on STAR-0-A 169
3.5.1 Test Setup 170
3.5.2 Methodology 171
3.5.3 Results and Discussion 172
3.6 Final Tests on STAR-0-A and STAR-0-B 174
3.6.1 Test Methodology 174

3.6.2 Wet-firing Test Results 176
3.6.3 Dry-firing Performance 178
3.6.4 Wet-firing Performance 180
3.7 Summary 185

Numerical Study of the Super-high Temperature Additive Resistojet Concept 187

4.1 Preliminary Considerations 187
4.1.1 Broad Mission Requirements 187
4 4.1.2 Methodology 188
4.2 Nozzle Study 189
4.2.1 Nozzle Dimensioning 189
4.2.2 CFD Optimisation Method 191
4.2.3 Grid Independent Study 192
4.2.4 Results 194
4.2.5 Examples of CFD optimisation 196
4.3 Multi-physics Study of the STAR Thruster 198
4.3.1 Geometry and Assumptions 198
4.3.2 Grid Independent Study 200
4.3.3 Stationary Analysis of the STAR Configurations 202
4.3.4 Time-dependent Analysis 204
4.3.5 Results of the Numerical Study on the Three Test Cases 206
5 4.4 Summary 210

Conclusions 213

5.1 Novelty of Research 213
5.2 Summary of the Thesis 215
5.3 Highlights of the Thesis 217
5.4 Impact of the Work 219
5.5 Future Work and Outlook 221

Appendix A Electric Propulsion Overview 223

A.1 Electric Propulsion Overview 223
A.1.1 General Applications for Electric Propulsion 226
A.2 Electric Propulsion Technologies 227
A.2.1 Electrothermal Thrusters 231
A.2.2 Electrostatic Thrusters 233
A.2.3 Electromagnetic Thrusters 234

Appendix B Multiphysics Modelling with COMSOL 235

B.1 Overview 235

B.2 Modelling Equations 236

B.2.1 Energy Balance 237

B.2.2 Fluid Flow and Heat Transfer 238

B.2.2.1 High Mach Number Flow (HMNF) Interface 240

B.2.2.2 Radiation 241

B.2.3 Electric Current (EC) Interface 243

B.2.4 Optimisation 244

B.2.4.1 Objective Function 245

B.2.4.2 Optimisation Algorithm 246

B.3 Computing on the Iridis Cluster 246

Appendix C Multiphysics Simulations – Validation Studies 249

C.1 Nozzle Study 249

C.1.1 Low-Reynolds-number Nozzle 249

C.1.2 SSTL T50 Nozzle Study 252

C.1.2.1 Nozzle Geometry 253

C.1.2.2 Multi-physics Model 254

C.1.2.3 Mesh Optimisation 254

C.1.2.4 Boundary Conditions 255

C.1.2.5 Optimisation Solver 257

C.1.2.6 Results and Discussion 257

C.2 3 kW Hydrogen Resistojet 262

C.2.1 Nozzle Evaluation 263

C.2.1.1 Computational grid convergence study 263

C.2.1.2 Parametric sweep of stagnation conditions 265

C.2.1.3 Vacuum chamber effect 267

C.2.1.4 Error analysis 269

C.2.1.5 Result and Discussion 271

C.2.2 Complete thruster model 272

C.2.2.1 Materials and Geometry 273

C.2.2.2 Problem Definitions and Mesh 274

C.2.3 Results and Discussion 275

Appendix D Technical Drawings 279

Appendix E Dataset Description 281

References 283

List of Tables

Table 1.1. List of propellant gases applicable to resistojets with properties and specific impulse evaluation. . 10

Table 1.2. Handling properties of cold-gas propellants [17]. 12

Table 1.3. Comparison of properties between xenon and other monopropellants [16,17] 12

Table 1.4. Terms involved in the power balance and the efficiency calculations. Negligible terms are marked with the symbol ≪. 14

Table 1.5. Resistojet flight history [20,21] 17

Table 1.6. Resistojets found in literature and available in the market. 18

Table 1.7 .PACT resistojet characteristics. 21

Table 1.8. MR-502A schematisc [36]. 22

Table 1.9. The variants of SSTL's low-cost resistojet [5]. 26

Table 1.10. SSTL resistojets' missions with the number of thruster employed [44]. 27

Table 1.11. Heater and heat exchanger materials for resistojets (references as from Table 1.6). 32

Table 1.12. Electric insulation materials for resistojets (references as Table 1.6). 33

Table 1.13. Thermal insulation materials for resistojets (references as from Table 1.6). 34

Table 1.14. Radiative shielding materials for resistojets (references as from Table 1.6). 35

Table 1.15. Melting point and electrical resistivity at 20°C (* at 0°C) of refractory metals [47]. Materials in the 3,000 K operating range are highlighted. 38

Table 1.16. Properties of some UHTCs [48]. 39

Table 1.17. Electrical, thermal and mechanical properties of ZrB_2 and HfB_2 [48]. 40

Table 1.18. Characteristics of Dynaquartz, Dynaflex and Sapphire Wool insulators [49]. 41

Table 1.19. HTR performance requirements for a LEO mission as primary propulsion on small satellites and for All-Electric GEO spacecraft as secondary propulsion [53]. 45

Table 1.20. Details of main missions utilising EP for orbit raising and station-keeping. 49

Table 1.21. Performance requirements for the LEO mission for primary propulsion on small satellites using xenon as propellant. 51

Table 1.22. Performance requirements for A-E GEO spacecraft for de-spin and momentum dumping (based on SSTL GMP-T Platform) [53]. 52

Table 1.23. Summary of nozzle dimensioning results in terms of stagnation and performance parameters. .. 61

Table 1.24. Comparison between candidate materials for the STAR heat exchanger and attainable performance. 64

Table 2.1. Maximum Operating Temperature (MOT) for SLM materials. 71

Table 2.2. M2 Cusing performance data [85]. 73

Table 2.3. Full list of designed and manufactured AM components, including brief descriptions. 79

Table 2.4. Area location (X, Y) and Z direction range for the 3-D image reconstruction. 98

Table 2.5. Surface texture measurement of the 3-D form-removed datasets. 99

Table 2.6. Profile roughness measurements of the 3-D form-removed dataset. 99

Table 2.7. Main properties of the test CT scan performed on the AM-25 component 107

Table 2.8. Deviation of the actual radius of each cylinder element with respect to the nominal radius. 114

Table 2.9. Cylinder wall thickness of HE_v2 variations for failure analysis 123

Table 2.10. Main dimensions corresponding to each heat exchanger iteration with dimensions in mm (f.c. states for fluidic channels). 133

Table 3.1. Nozzle performance of STAR-0 at MOT calculated at increasing thrust levels for Xe (top) and Ar (bottom). 140

Table 3.2. Expected current-voltage characteristics of STAR-0 up to the MOT 142

Table 3.3. Expected voltage-current characteristic of the STAR-0 prototype for the calculated electrical power at the MOT in the assumption of η_{ts} = 0.6. 143

Table 3.4. Main properties of the selected ceramics for the prototype assembly [92]. 148

Table 3.5. Main components of the STAR-0 resistojet (* only one version used per assembly). 152

Table 3.6. Pumping speed breakdown of the test facility. 160

Table 3.7. Summary of instrumentation used for the tests with measurement accuracy. 163

Table 3.8. Simulation over experimental error with different assumptions. 169

Table 3.9. Performance data of STAR-0-A in vacuum with starting pressure of 1.8E-6 mbar and T_{BG} = 20 K. 173

Table 3.10. Summary of M1 and M2 tests with quantities evaluated at the maximum measured thrust. 179

Table 3.11. Dry-test model results at t = 2,500 s: maximum structural temperature, T_m, and maximum temperature in the connectors regions. 181

Table 3.12. Main simulation results for M1-4 at t_b = 118.4 s. 184

Table 4.1. Resistojet requirements for two selected missions with the Xe propellant. 188

Table 4.2. Nozzle optimisation results for the three thrusters in analysis. 195

Table 4.3. Power balance of the optimal solution of the HTR nozzle (units in W). 198

Table 4.4. Summary of the thermal insulation and radiation shielding parametrisation study. “ 203

Table 4.5. Summary of main thruster parameters in the stationary case when T_m = MOT. 204

Table 4.6. Comparison of performance immediately after ignition and the maximum performance achievable corresponding to the stationary solution. 206

Table A.1. General classification of electric propulsion technologies. 226

Table A.2. Characteristic velocity increments for planetary transfer mission [8]. 227

Table A.3. Summary for qualitative comparison of electrical propulsion systems [7]. 230

Table A.4. Typical performance, power requirements and specific weights of various types of operational electrical propulsion technologies 231

Table C.5. Reynolds numbers calculated at the nozzle throat for the 24 analysed cases. 254

Table C.6. Example of optimisation solver iterations (65 W, 1 bar). 259

Table C.7. Mass flow rate relative error, average inlet static temperature and estimated nozzle radiation-to-ambient loss, calculated for the 24 cases 259

Table C.8. Effect of different boundary conditions of Cases (1-5) as thrust relative error with respect to the experimental value F = 32.7 mN (Test-14). 268

Table C.9. List of partial derivatives of thrust with respect to selected variables for the sensitivity analysis (example with Test-14). 271

Table C.10. Relative error of the solution with respect to experimental values of Test-14. 276

Table C.11. Relative error of the solution with respect to experimental values at design point (I = 208 A). 276

List of Figures

Fig. 1.1. Schematic of resistojet with direct heating of propellant gas: (a) heater coil, (b) heater coils in series, (c) packed particle heat exchanger and (d) cylindrical heater [8]. 5

Fig. 1.2. Schematic of the nozzle with relevant parameters [8]. 7

Fig. 1.3. Resistojet energy flow process [18]. 13

Fig. 1.4. Number of EP-based satellites launched in the years 1981-2018 (3-year moving average), divided into electric thruster subclasses: GEO (top) and LEO (bottom) satellites [19]. 16

Fig. 1.5. Typical resistojet augmented by hot gas from catalytically decomposed hydrazine; two main assemblies are present: catalyst bed (left) and resistojet stage (right) [7]. 19

Fig. 1.6. HiPEHT thruster overview: detail of the resistojet schematic (left) and whole thruster schematic (right) [30]. 20

Fig. 1.7. PACT thruster overview. 21

Fig. 1.8. MR-501B thruster overview: MR-501B thruster (left) and MR-502 thruster (right) [28]. 22

Fig. 1.9. Multi-propellant resistojet cross-section [29]. 24

Fig. 1.10. MBB thruster overview [21]. 24

Fig. 1.11. Schematics of the Mark-III [25]. 25

Fig. 1.12. T50 Resistojet (left) and Rapid Eye Constellation Satellites 1-5 (right). 26

Fig. 1.13. Sitael XR-150 EM thrsuter [45]. 28

Fig. 1.14. A schematic of teh J3 thruster [31]. 29

Fig. 1.15. EHT-15 thruster (top) and Fakel thruster (bottom) overviews [21]. 30

Fig. 1.16. Back temperature tests for fibrous zirconia and silica samples (hot face T = 1,473-1,673 K) [50]. 42

Fig. 1.17. SSTL xenon propulsion system schematic [16]. 44

Fig. 1.18. Concentric tubular resistojet concept [63]. 55

Fig. 1.19. Rhenium J3 resitojet parts made by CVD [46]. 55

Fig. 1.20. Schematics of the radiation shielding (rs) located in the vacuum jacket to limit the heat transfer by radiation between the core and the external wall of the vacuum jacket (in). 57

Fig. 1.21. Plot of the improvement achieved using radiation shielding placed between the RJ core and the insulation package. 57

Fig. 1.22. Efficiency curve of a conical nozzle with 15° half-conical angle (solid line) and experimental data gathered from [68]. 60

Fig. 1.23. Nozzle efficiency colour-map with overlaid nozzle performance in terms of thrust (dashed line) and specific impulse (solid line) iso-contours as a function of the mass flow rate and propellant stagnation temperature T_0. 62

Fig. 1.24. Stagnation pressure p_0 colour-map with overlaid nozzle performance in terms of thrust (dashed line) and specific impulse (solid line) iso-contours as a function of the mass flow rate and propellant stagnation temperature T_0. 63

Fig. 1.25. Specific impulse gain with increasing stagnation temperature. The materials in analysis are highlighted in orange. 64

Fig. 1.26. Electrical resistivity of selected materials for the STAR resistojet heater. The materials in analysis are highlighted in orange. 65

Fig. 2.1. Generic illustration of an AM powder bed system (a), an AM wire feed system (b) and an AM powder feed system (c) [75]. 69

Fig. 2.2. Relevant process parameter for selective laser melting [78]. 70

Fig. 2.3. Two powder bed laser melting parts manufactured by Smit Röntgen for X-ray computed tomography applications [84]. 72

Fig. 2.4. Photo taken during the second printing session. 74

Fig. 2.5. Particle size distribution (y-axis, left: cumulative distribution, y-axis, right: distribution density, x-axis: particle diameter) [88]. 75

Fig. 2.6. Images of the Stainless Steel 316L powder taken with SEM. 76

Fig. 2.7. A Ti6A14V strut (A) directly as printed and (B) after chemical etching [87]. 77

Fig. 2.8. One-piece injector as printed (a), cut from the base plate and polished (b) and computed tomography scan to ensure that the part was printed accordingly with the design [90]. 78

Fig. 2.9. First printing session: CAD (top) and real (bottom) overview. 81

Fig. 2.10. AM-00 top view (left) and bottom view (right) with respect to the printer base plate (Wild Microscope M420). 82

Fig. 2.11. Microscope image of the AM-00 heat exchanger element after manual polishing (left) and the design dimensions of the wall gaps and thicknesses in mm (right) 82

Fig. 2.12. AM-26 component front overview (a) and detailed view (b) of the top part. Hypothetical holes are circled in red (Alicona InfiniteFocus). 83

Fig. 2.13. Build angle (α) and overhang angle (β). The sum of the two angles is 90°. 84

Fig. 2.14. AM-01 (half 2) overview, the printing direction in the SLM process was from bottom (B) to the top (T). 84

Fig. 2.15. BL area between the nozzle wall and the next one (Olympus BX51 microscope). 85

Fig. 2.16. B-L area between the outer wall and the middle wall. 86

Fig. 2.17. B-L area, particularly of the extra-material added to support the suspended walls of the AM-01 part. 87

Fig. 2.18. View of the nozzle area and the inner channel with measurements (top) and drawing detail (bottom). 88

Fig. 2.19. Central detail of the AM01 heat exchanger walls with measurements. 88

Fig. 2.20. Detailed inner channel of AM-24, with measurement of the spot's surface area 89

Fig. 2.21. Set of printed heat exchanger elbows AM-03- to AM-10 90

Fig. 2.22. Throat profile measurement setup with Olympus BX51 (left) and one of the nozzles analysed (AM-21, right) 91

Fig. 2.23. Nozzle throat as-printed morphology with measurements, half-angle of the diverging section in parenthesis 92

Fig. 2.24. Relative surface error of a spherical particle observed from the top as a function of the penetration *h* 93

Fig. 2.25. 3-D surface scan of an AM-26 inner cylinder sector (Alicona – Infinite Focus). 94

Fig. 2.26. Form-removed 3-D surface scan of an AM-26 inner cylinder sector showing the surface height in microns (Alicona InfiniteFocus, 10x objective). 95

Fig. 2.27. 3-D surface scan of the throat sector of AM-22 showing the surface height in microns (Alicona InfiniteFocus). 95

Fig. 2.28. Photo of AM-22 after-polishing (left) and overview of the AM-24 areas of study for surface roughness characterisation (right). 96

Fig. 2.29. Images of three different areas on the AM-24 external wall to show different depths of polishing. 97

Fig. 2.30. AM24 positioned under the 10x objective of Alicona 97

Fig. 2.31. Example of profile surface roughness measurement with Alicona. 99

Fig. 2.32. AM-26 production part overview 100

Fig. 2.33. AM-26 component design overview. The part has been printed in the vertical direction. 100

Fig. 2.34. TOPO-SEM of the AM-26 component showing the surface morphology. 101

Fig. 2.35. Detail of the surface morphology of the inner half-tubular channel of AM-26. 102

Fig. 2.36. Detail of a wall defect located on the 200 μm wall of AM-26. 102

Fig. 2.37. SEM image on a wall edge of the AM-00 component. 103

Fig. 2.38. As printed AM-13 (left) and AM-14 (right). 104

Fig. 2.39. TIG weld tests on two sets of AM-11-12. Weld with added material (left) and pure weld (right). 104

Fig. 2.40. CAD model top half-section of HE_v0.1 (top) and HE_v0.2 (bottom) 105

Fig. 2.41. Detailed views of the two wall-connection concepts belonging to HE_v0.1 and HE_v0.2, dimensions in mm. 107

Fig. 2.42. Automatic surface determination example: automatically selected values of background, iso-surface and material in grey (left) and resulting surface in yellow (right). 108

Fig. 2.43. Radiograms of central axis section of the components AM23 (left) and AM25 (right). 108

Fig. 2.44. Radiogram of AM-25 (a) and 3-D reconstruction of the geometry (b). The origin of the axes is coincident with the corner of the three grey surfaces. 109

Fig. 2.45. Total volume evaluation by filtering the voxels' greyscale. 109

Fig. 2.46. 3-D reconstruction of AM-25. Section parallel to the right plane at X = 8.45 mm. 110

Fig. 2.47. Bottom view of the component showing the supporting grid of about 100 μm thick walls. Y = 22.86 mm. 110

Fig. 2.48. Visual comparison of the section corresponding to the bottom flow passages (elbow end). 110

Fig. 2.49. Visual comparison of the section corresponding to the top flow passages (nozzle end). 111

Fig. 2.50. Magnification of a CT section, Y = 13.10 mm, showing the nozzle throat hole (nominal diameter = 420 μm). 111

Fig. 2.51. Some images of the CT 3-D reconstruction of the component AM-25. 112

Fig. 2.52. AM-25 nominal-to-actual comparison overview, with highlighted connecting channels. 113

Fig. 2.53. Nominal-to-actual geometry comparison of the heat exchanger wall region. 114

Fig. 2.54. CAD overview of the main parts of the component analysed. The print direction is shown. 115

Fig. 2.55. Surface comparison of the main parts of component AM-25. The print direction is shown for each part. 116

Fig. 2.56. Longitudinal-section comparison showing the short circuit created by connecting material in the nozzle region. 117

Fig. 2.57. Detailed view of the section comparison in the nozzle region. Unwanted material connects cylinder 1 and cylinder 3 to create a short circuit of the heat exchanger electrical resistance. 118

Fig. 2.58. Detailed view of the section comparison in the region of the concentric cones. 118

Fig. 2.59. CAD model top section-view of HE_v1. 119

Fig. 2.60. Double-cut section of cylinder 1 showing the parameters used for connector thickening. 120

Fig. 2.61. New design concept of AM-29/30 showing the thickening of the mini-channel sections. 121

Fig. 2.62. Section nominal-to-actual comparison in the nozzle region of HE_v1. 122

Fig. 2.63. CAD model top section-view of HE_v2.1 (top) and HE_v2.2 (bottom) 123

Fig. 2.64. Detail of the extend mini-channels of HE_v2.2 between cylinders 2-3. 124

Fig. 2.65. Overview of the HE_v2 radiograms highlighting two different failures at the top and bottom of the heat exchanger. 126

Fig. 2.66. Differences between mini-channels on cylinder 2 for HE_v2.1 (left) and HE_v2.2 (right). 126

Fig. 2.67. Overview of the HE_v2 sectioned components. 127

Fig. 2.68. CAD model top section-view of HE_v3.1 (top) and HE_v3.2 (bottom) 128

Fig. 2.69. Fluidic mini-channels in the elbow region for HE_v3.1 (left) and HE_v3.2 (right). 128

Fig. 2.70. Half-section view of the CT volume of HE v3.2, showing a successful build of the heat exchanger. 129

Fig. 2.71. HE_v3.1 inside the furnace at about 850°C (left) and resistance vs temperature with experimental and numerical values. 130

Fig. 2.72. Micro-porosity semi-logarithmic histogram of HE_v3.1 obtained from the CT volume analysis. 131

Fig. 2.73. Views of the micro-pores distribution of the HE_v3.1 {1} 131

Fig. 2.74. Flow chart of the heat exchanger design iterations. The red cross indicates the discarded variations. Iteration v3.1 was successful. 132

Fig. 3.1. Axial-symmetric schematics of the monolithic STAR heat exchanger concept. The propellant flow path (purple) and the electrical interface are shown. 138

Fig. 3.2. Nozzle stagnation pressure (left) and nozzle efficiency (right) colormaps with overlaid thrust (dashed lines) and specific impulse (solid lines) iso-contours for Xe propellant. 141

Fig. 3.3. Nozzle stagnation pressure (left) and nozzle efficiency (right) colormaps with overlaid thrust (dashed lines) and specific impulse (solid lines) iso-contours for Ar propellant. 141

Fig. 3.4. Design iteration that led to the STAR-0 detailed design shown in figure (d). Ceramic components are in purple and blue. 146

Fig. 3.5. Modal analysis results on STAR-0 assembly: modes 1–2 (left), mode 3 (centre) and mode 4–6 (right). 149

Fig. 3.6. Half-section exploded view of STAR-0 (left) and scatter-free radiograph of the STAR-0-B assembly with thermocouples and ring terminal positions (right). 151

Fig. 3.7. Thruster and thruster inflow as-printed components (print no.3) on the Concept Laser M2 Cusing base plate (left) and as-printed HE_v2 (right). 152

Fig. 3.8. Ultrasonic cleaning of the HE components (left) and removed powder (right). 153

Fig. 3.9. Jig for post-manufacturing of the heat exchanger (left), machined HE_v1_part1 (AM-29, centre) and machined thruster inflow (AM-28, right). 154

Fig. 3.10. Technicians at EDMC while drilling the AM-01 throat (left) and with the Thruster Casing on the CNC lathe (right). 154

Fig. 3.11. Machined components at the EDMC: Thruster Casing (left) and Thruster Support (right). 154

Fig. 3.12. STAR-0-A fit assembly steps to establish tolerances before EB welding. 155

Fig. 3.13. Fit-assembly adjustments. 156

Fig. 3.14. CAD view and results of EB Weld 1 (a) and EB Weld 2 (d), with intermediate assembly passages. 158

Fig. 3.15. STAR-0-A for the preliminary tests (left), STAR-0-A for the dry-firing tests (centre) and STAR-0-B for the wet-firing tests (right). 158

Fig. 3.16. University of Southampton David Fearn Electric Propulsion Laboratory. 159

Fig. 3.17. STAR-0-B test rig located into the main test chamber via the transfer system. 161

Fig. 3.18. Gallium electrical terminal overview: intact gallium shots at ambient temperature (left), melted gallium (centre) and resistojet terminals submerged into the liquid metal (right). 162

Fig. 3.19. Schematics of the test setup. 164

Fig. 3.20. Overview of the test equipment. 165

Fig. 3.21. Internal view of the rack system: cDAQ-9188XT (a), Ga terminal power switches (b), FGSE (c) and green terminal block of the thrust balance (d). 165

Fig. 3.22. Photo showing a crack that developed in the ceramic collar. 170

Fig. 3.23. Preliminary tests setup for the STAR-0-A wet-firing tests. 171

Fig. 3.24. Effect of the gas heating to the thrust profile and the operating voltage at a flow rate of 0.678 ln/min with 20 A and 25 A of constant current. Test 3 (left) and Test 4 (right) are shown. 174

Fig. 3.25. Thrust transient of the M1 and M2 test series. Each start front of the same test currents is separated by 20 seconds for presentation clarity. 177

Fig. 3.26. Dry tests: experimental temperatures (solid lines) and 3-D sector-symmetric simulation results (markers). 180

Fig. 3.27. Time-dependant model prediction of the maximum structural temperature and temperature of the connectors in the four test cases. 181

Fig. 3.28. Thrust exerted by the STAR-0-B prototype in cold gas mode at increasing mass flow rate of Ar. 182

Fig. 3.29. Iso-thermal plot of the test case M1-4 at t_b = 60 s and 120 s highlighting the maximum gas (650° C) and structural (850°C) temperatures (left) and iso-Mach plot of the nozzle at t_b = 120 s (right). 184

Fig. 4.1. Study steps performed on the three cases under examination. 190

Fig. 4.2. Flow regime estimation with the design box (in blue) in the (Isp, F) plane for the two missions M1 (left) and M2 (right). 191

Fig. 4.3. Relative error of variables measured at the exit plane of the nozzle as a function of the mesh refinement parameter. 193

Fig. 4.4. Mesh grid of the nozzle domain for f = 1, 5 and 10 (left to right). 193

Fig. 4.5. Specific impulse optimisation for the three cases in analysis as a function of the diverging angle of the nozzle. 194

Fig. 4.6. Comparison between experimental data on low Reynolds number nozzles (Fig. 1.22) and current CFD analysis. 195

Fig. 4.7. Mach number contours for initial (α = 14°) and optimised (α = 27.4°) nozzles. 197

Fig. 4.8. Nozzle boundary conditions and throat section highlighted (left), static temperature solution with optimised diverging section half-angle (centre) and Mach number colour map (right). 198

Fig. 4.9. 2-D axial-symmetric geometry of the STAR thruster. 199

Fig. 4.10. Relative error calculated at the inlet (left) and the outlet (right) of the heat exchanger..... 201

Fig. 4.11. Full thruster 2D axisymmetric domain (top) and particular of the mesh grid in the nozzle region for f = 1, 5 and 10 (left to right). 201

Fig. 4.12. Temperature stationary solution of STAR-Ta, at a test current of 77 A, showing the increase of maximum temperature when including both thermal insulation and radiation shielding located in the vacuum jacket. 202

Fig. 4.13. Ignition of STAR-Inc from the cold-gas stationary solution. 208

Fig. 4.14. Ignition of STAR-Ta (top) and STAR-Re (bottom) from the cold-gas stationary solution. 209

Fig. 4.15. Pulse-width heating cycle of STAR-Inc with two current levels corresponding to approximately 25 W and 50 W of electrical power. 210

Fig. 5.1. Operating principles and schematics of (a) resistojets, (b) arcjets, (c) Hall thrusters, (d) ion engines, (e) pulsed plasma thrusters, (f) field-effect electrostatic propulsion thrusters, and (g) self-field magneto-plasma-dynamic thrusters [20]. 229

Fig. 5.2. Energy balance diagram (COMSOL, 2015b)..... 238

Fig. 5.3. Arriving irradiation (left) and leaving radiosity (right) [119]. 243

Fig. 5.4. Rothe nozzle geometry build in COMSOL (left) and computational grid according to Kim. 250

Fig. 5.5. Mach number contour: original study (left) and simulation results (right). 251

Fig. 5.6. Axial variation of centreline density: original study (left) and simulation results (right). 251

Fig. 5.7. Density profile near the exit of the Rothe nozzle..... 251

Fig. 5.8. Knudsen number variation along the centreline. 252

Fig. 5.9. SSTL-T50 resistojet mounted vertically on a thrust balance (left) and test setup for performance measurement (right) at the European Space Agency Electric Propulsion Laboratory. 253

Fig. 5.10. Xenon dynamic viscosity, μPa. 255

Fig. 5.11. Computational grid for the T50 nozzle (left) and mesh solution accuracy (right)..... 255

Fig. 5.12. T50 nozzle boundary conditions highlighted..... 256

Fig. 5.13. Relation between nozzle temperature T_n (experimental) and inlet gas temperature T_0 (simulation output) for the 24 test cases and supply pressures of the T50 thruster with xenon propellant. 260

Fig. 5.14. Axial variations of centreline Mach number (left) and Mach number profiles at the nozzle exit plane in the 30 W operative condition at a range of inlet pressures between 1 and 4 bar (right). 261

Fig. 5.15. Axial variations of centreline static temperature (left) and exit static temperature profiles at the nozzle exit plane in the 30 W operative condition at a range of inlet pressures between 1 and 4 bar (right). 261

Fig. 5.16. Static temperature in K (for the converging section) and Mach number iso-surface profiles (for the diverging section) for the 30 W case at 1 bar inlet pressure. 262

Fig. 5.17. Computational grid of the nozzle geometry as function of the refinement parameter *f*: nozzle overview (left) and throat detail (right). 264

Fig. 5.18. Relative error of mass flow rate (left) and of the average values of *T*, *p*, *w* and *u* calculated at the nozzle exit (right) as function of the refinement parameter *f*. 265

Fig. 5.19. Experimental thrust (left) and mass flow rate (right) compared with simulations results at three different test cases 267

Fig. 5.20. Reynolds number evaluated as at the inlet, throat and exit sections for the 14 experimental points. 267

Fig. 5.21. Vacuum chamber geometry with outlet boundaries highlighted (left) and Mach number isocontour near the nozzle: Test-1 (center) and Test-14 (right). 269

Fig. 5.22. Pressure isocontour for Test-1 (left) and Test-14 (right). 270

Fig. 5.23. Computed and experimental thrust for the fourteen tests in analysis, with error bars of measurement (from thrust balance measurement accuracy) and model (from sensitivity analysis). 272

Fig. 5.24. J3 resistojet drawings with direct experimental measurement in purple, inlet and outlet boundary conditions highlighted and numbered concentric tubular heat exchanger annular passages. 274

Fig. 5.25. Computational grid of J3 thruster: nozzle region (left) and elbow region (right) (axis units in mm). 275

Fig. 5.26. Simulation results on Test-14: heater electric potential in V (left) and thermal solution in K (right) (axis units in mm). 276

Fig. 5.27. Temperature distribution at the center lines of the heat exchanger passages (numbered): Test-14 (left) and J3 at design point (right). 277

Definitions and Abbreviations

Acronyms

AC	Alternate Current
AE	All-Electric Spacecraft
AM	Additive Manufacturing
ASD	Average Storage Density of propellant
BC	Boundary Condition
BOL	Beginning of Life
CFD	Computational Fluid Dynamics
CT	Computed Tomography
CVD	Chemical Vapor Deposition
DC	Direct Current
EB	Electron Beam
EC	Electrical Current interface in COMSOL
EP	Electric Propulsion
EDM	Electrical Discharge Machining
EDMC	Engineering Design and Manufacturing Centre
EHT	Electrothermal Hydrazine Thruster
EOL	End of Life
GEO	Geostationary Equatorial Orbit
HE	Heat Exchanger
HET	Hall Effect Thruster
HMNF	High Mach Number Flow interface in COMSOL
HTR	High-Temperature Resistojet
HT	Heat Transfer interface in COMSOL
IC	Initial Condition
LEO	Low Earth Orbit
MEO	Medium Earth Orbit

MFC	Mass Flow Controller
MOT	Maximum Operational Temperature
NDT	Non-destructive Testing
NSSK	North South Station Keeping
NSTP	National Space Technology Programme, funded by the UK Space Agency
PC	Pressure Controller
PDE	Partial Derivative Equation
PPT	Pulsed Plasma Thruster
PPU	Power Processing Unit
RANS	Reynolds-Averaged Navier-Stokes equations
SC	Spacecraft
SEM	Surface Electron Microscope
SLM	Selective Laser Melting
SLS	Selective Laser Sintering
SM	Solid Mechanics interface in COMSOL
SSTL	Surrey Satellite Technology Ltd
TC	Thruster Casing
TI	Thruster Inflow
VSI	Volumetric Specific Impulse

Symbols (vectors, matrixes and tensors are bold)

A	Section area [m^2]
a	Speed of Sound [m/s]
c	Effective jet speed [m/s]
C	Set of constraints
c_p	Specific heat at constant pressure per unit mass [J/(kg·K)]
C_p	Specific heat at constant pressure [J/K]
c_v	Specific heat at constant volume per unit mass [J/(kg·K)]
E	Internal energy [J/kg]
F	Thrust [N]

F	Volume force vector [N]
$\mathbf{F_g}$	Local gravitational force [N]
G	Surface irradiation [W/m^2]
g_0	Sea-level acceleration of gravity [m/s^2]
h or H	Enthalpy per unit mass [J/kg]
I	Impulse[Ns] or terminal current [A]
I_{sp}	Specific impulse [s]
I_T	Turbulence intensity [-]
J	Surface radiosity [W/m^2] or current density (volume) [A/m^2]
k	Thermal conductivity [W/(m·K)]
Kn	Knudsen number [-]
L	Length scale [m]
L_c	Cut-off wavelength in roughness measurements [m]
L_T	Turbulence length scale [m]
m	Mass [kg]
M	Mach number [-]
M	Molecular mass [kg/kmol]
$\dot{m}$	Mass flow rate of propellant [kg/s]
n	Number of moles [-]
$\mathbf{n}$	Unit vector normal [-]
p	Pressure [Pa]
P	Power [W]
Q	Heat source [W/m^3] or objective function of the optimisation solver
Q_{vh}	Viscous heat [W/m^3]
r	Radial space component [m]
R_s	Specific gas constant per unit mass [J/(kg·K)]
R	Molar ideal gas constant [J/(K·mol)]
R_a	Average-profile roughness [m]
R_q	Root-mean-square profile roughness [m]

Re	Reynolds number [-]
S	Stain-rate tensor [-]
S_a	Average surface roughness [m]
S_q	Root-mean-square surface roughness [m]
T	Temperature [K]
u	Velocity vector [m/s]
u	Radial component of velocity [m/s] or solution of the PDE problem
U	Velocity scale [m/s]
v	Volume [m^3]
V	Terminal voltage [V]
w	Axial component of velocity [m/s]
W	Work [W/m^3]
z	Axial space component [m]

Subscripts

0	Stagnation (or total)/ initial
a	Ambient
BG	Background, quantity referred to the vacuum chamber (experimental)
e	exit plane of the nozzle/ exhaust/ electric
f	final
global	global quantity in COMSOL
h	heater/heat exchanger/heating
in	Inlet
int	Integral quantity
k	Kinetic
m	Molar or per unit mole/ maximum
n	Nozzle
out	Outlet
opt	Optimised
p	Propellant

p/l	Payload
probe	Expression defined in a geometric entity in COMSOL
r	Radial component
rad	Radiating heat
s	Propellant supply quantity (experimental)/ shields
SC	Spacecraft
t	Thruster/throat of the nozzle
T	Total
th	Theoretical
Ts	Thruster

Superscripts

$\dot{x}$	Single dot: derivative with respect to time
x^*	Asterisk: chocked flow, section of the nozzle in which the flow is sonic

Greek Symbols

α	Nozzle divergent half-angle [°] /surface absorptivity [-]
γ	Ratio of specific heats [-]
ε	Surface emissivity, nozzle area ratio [-]
η	Efficiency [-]
λ	Mean free path [m]
μ	Dynamic viscosity [Pa·s]
ξ	Control variables
ρ	Density [kg/m^3]/ reflectivity of a surface [-]/ electrical resistivity [Ω·m]
σ	Stefan-Boltzmann constant [W/(m^2·K^4)]
$\boldsymbol{\tau}$	Viscous stress tensor [Pa]
τ	Surface transmissivity [-]
Ω	Domain

Declaration of Authorship

I, Federico Romei, declare that this thesis and the work presented in it is my own and has been generated by me as the result of my own original research.

I confirm that:

1. This work was done wholly or mainly while in candidature for a research degree at this University;
2. Where any part of this thesis has previously been submitted for a degree or any other qualification at this University or any other institution, this has been clearly stated;
3. Where I have consulted the published work of others, this is always clearly attributed;
4. Where I have quoted from the work of others, the source is always given. With the exception of such quotations, this thesis is entirely my own work;
5. I have acknowledged all main sources of help;
6. Where the thesis is based on work done by myself jointly with others, I have made clear exactly what was done by others and what I have contributed myself;

Parts of this work have been published as follows:

Journal papers:

- Romei, F. and Grubišić, A.N. Validation of an additively manufactured resistojet through experimental and computational analysis. *Acta Astronautica*, Volume 167, February 2020, Pages 14-22. DOI 10.1016/j.actaastro.2019.10.046.
- Robinson, M., Grubišić, A.N., Rempelos, G., Romei, F., Ogunlesi, C., Ahmed, S. Endurance testing of the additively manufactured STAR resistojet. *Materials & Design*, Volume 180, October 2019, 107907. DOI 10.1016/j.matdes.2019.107907.
- Romei, F. and Grubišić, A.N. Numerical Study of a Novel Monolithic Heat Exchanger for Electrothermal Space Propulsion. *Acta Astronautica*, Volume 159, June 2019, Pages 8 – 16. DOI 10.1016/j.actaastro.2019.03.025.
- Romei, F., Grubišić, A. and Gibbon, D. Manufacturing of a High-Temperature Resistojet Heat Exchanger by Selective Laser Melting. *Acta Astronautica*, Volume 138, September 2017, Pages 356 – 368. DOI 10.1016/j.actaastro.2017.05.020.

Patent:

I am co-inventor with Dr Angelo Grubisic of the patent currently protected by a Provisional Patent Application in respect of a "High-Temperature Electrothermal Propulsion System," submitted by HC Starck (HCS) and received by the US Patent Office on 12 May 2017, being allocated EFS ID 29189858 and Application Number 62505169.

Conference proceedings:

- Romei, F., Grubišić, A., Gibbon, D., Aimone, P., Dary, F., High Performance Resistojet Thruster: STAR Status Update. *Space Propulsion Conference*, Seville, Spain, 14 - 18 May 2018.
- Robinson, M., Grubišić, A., Romei, F., Ogunlesi, C., Ahmed, S., Aimone, P., Dary, F., Gibbon, D. Environmental Testing and Non-Destructive Inspection of the STAR Additively Manufactured Resistojet. *Space Propulsion Conference*, Seville, Spain, 14 - 18 May 2018.
- Ogunlesi, C., Grubisic, A., Romei, F., Robinson, M., Ahmed, S., Aimone, P., Dary, F., Gibbon, D. Novel Non-Destructive Inspection of the STAR Additively Manufactured Resistojet. *Space Propulsion Conference*, Seville, Spain, 14 - 18 May 2018.
- Romei, F., Grubišić, A. and Gibbon, D. Performance Testing and Evaluation of a High Temperature Xenon Resistojet Prototype Manufactured by Selective Laser Melting, *35th International Electric Propulsion Conference*, Atlanta, Georgia, 8 – 12 October 2017.
- Romei, F., Grubišić, A., Lasagna, D., and Gibbon, D. Multiphysics Model Validation of Resistojets with Concentric Tubular Heat Exchanger. *7th European Conference for Astronautics and Space Science*, Milan, Italy, 3-6 July 2017, DOI:10.13009/EUCASS2017-378.
- Romei, F., Grubišić, A., Gibbon, D. and Lane, O. Selective Laser Melting for Production of a Novel High Temperature Electrothermal Propulsion System. *67th International Astronautical Congress*, Guadalajara, Mexico, 26 - 30 Sep 2016.
- Romei, F., Grubišić, A., Gibbon, D., Lane, O., Hertford, R. and Roberts, G. A Thermo-Fluidic Model for a Low Power Xenon Resistojet. *Joint Conference of 30th ISTS, 34th IEPC and 6th NSAT*, Hyogo, Kobe, Japan, 4 - 10 July 2015.

Signed: Date: 29/05/2019

Acknowledgement

This project was funded by the Doctoral Training Partnership through the Engineering and Physical Sciences Research Council (EPSRC), grant no. EP/M50662X/1. This work was also supported by the National Space Technology Programme (NSTP-2) with fast track project named "High Performance Xenon Resistojet", in partnership with Surrey Satellite Technology Limited as an end-user of the technology. The project was funded by the UK Space Agency and the Centre for Earth Observation Instrumentation and Space Technology (CEOI-ST).

I would like to start by thanking my supervisor Dr Angelo N Grubisic for initiating this project and for the discussions, advice and support throughout this experience. I would like to thank the people of the μVIS lab and the EDMC workshop of the University of Southampton for the technical support. Special thanks to all my colleagues who made this journey interesting and amusing, Ahmed, Mirko, Gian Luigi, Gennaro, David, Clemens, Francesca and Alek. And to the non-astronautics people who made this journey even more interesting, Davide, Stefano, Vanesa, Stefania, Simone, Laura and Bernat.

I dedicate this work the person who made this possible, Otti, my love, and to Liam, our love.

Introduction

1

This chapter introduces the main motivations and objectives of the research, with an overview of the methodology and tools employed and a section describing the structure of the thesis. This chapter also includes the background material on the resistojet technology, with a section focusing on the motivations and applications of high-temperature resistojets.

1.1 Motivation and Objectives of the Research

The current research aims to develop a next-generation resistojet that can increase the capability of small spacecraft often reliant on warm-gas technology while also enabling fully all-electric propulsion system architectures on larger spacecraft, which utilises a primary electric propulsion system. In the first instance for small spacecraft, the thruster would form the primary propulsion system while, in the latter, the thruster would constitute one of many attitude control thrusters functioning as a secondary reaction control system [1]. All-electric (A-E) geostationary telecom spacecraft will host only an electric propulsion system to perform orbit raising and station-keeping in place of the traditional chemical system, representing a significant change in the market [2]. This presents competitive cost savings, from the absence of hazardous propellants, mass saving due to greater propellant efficiency and further cost savings in launch vehicle options for lighter spacecraft. However, a new type of thruster is required to fulfil the attitude control role of the absent chemical system. One logical solution is a set of high-performance resistojets that operate from a common xenon propellant in the electric propulsions system [3,4].

The project has collaborated with Surrey Satellite Technology Ltd (SSTL) as an end-user of the technology to define the requirements of such a system. SSTL has flown a low-power resistojet thruster (T-15 and T-30) since 2002 [5]. Among the many applications, there is the European GPS Galileo Testbed (GSTB) GIOVE validation satellite [6]. Although the SSTL resistojet represents a low-cost solution, it significantly improves the performance of traditional cold-gas propulsion systems. The high-temperature resistojet concept, objective of this research, is developed as a bolt-

on addition to existing SSTL busses as a means to extend the capability of SSTL spacecraft. This also gives the benefit of a route to qualification and market adoption.

To make resistojets attractive for these purposes, it is necessary to develop a unique resistojet able to deliver a high-temperature performance comparable to the maximum operating temperature of the highest temperature refractory materials. The aim of the present research is, therefore, to enable the design, development and operation of a high-temperature xenon resistojet prototype through a combination of design and simulations, manufacturing verification and validation, post-manufacturing analysis and performance testing. Fundamentally, the driver of performance is the operating temperature of the thruster since this drives the operating propellant temperature and thus the attainable specific impulse of the device. Currently, resistojets are not capable of such performance or temperatures due to material limitations and technical challenges in high-performance designs.

In 2015, the project was awarded funding by the UK Space Agency in a National Space Technology Programme (NSTP). The participation of the PhD research in the NSTP project included access to important experimental validation data provided by SSTL and funding for the work. Although the NSTP project has commercial aims, its novelty and challenges perfectly suit the general research-centred objective of the PhD.

1.2 Methodology

The research began with a detailed review of the past applications and on the status of resistojet technology, with particular attention to its applications using xenon as propellant and those with the highest operating temperatures. A second review was performed on high-temperature materials used in high-temperature resistojet applications and possible design candidates for the high-temperature resistojet. A detailed review on metal additive manufacturing, in particular on SLM, provided the basis to develop the novel resistojet design.

The multiphysics simulations developed in the COMSOL Multiphysics software represent a significant part of the research. It required specific training through the “Introduction to COMSOL Multiphysics” workshop attended at the beginning of the research and numerous webinars illustrating the capabilities of this software. Several training sessions enabled to understand gradually the capabilities of this multiphysics tool, while specific components useful for the research were

identified and deepened through the study of the software manuals and a review on CFD and heat transfer theory and optimisation algorithms.

Additional review and training were necessary to develop the skills to understand and use the analysis tools necessary for the characterisation of the SLM components. The analysis tools involved in the research are the following: an optical microscope to accurately measure the dimensions and evaluate the features of the components produced during the manufacturing verification stage; Scanning Electron Microscope (SEM) to understand the nature of the surface resulting from the SLM process; Alicona 3D optical surface profilometer for contactless surface metrology characterisation, in particular, to measure the surface roughness parameters; and X-ray CT to non-destructively measure the dimension accuracy of the complex design of some SLM components.

Part of the work involved the construction of the test setup for the proof of concept thruster characterisation, including the fluidic system, the mechanical and electrical interfaces and the LabVIEW interface. The test equipment produced is now available to the Astronautics research group for testing several EP devices.

1.3 Overview of the Thesis

The layout of the thesis is structured in the following way. Chapter 1 outlines the key principles of the resistojet technology and provides a comprehensive literature review on the past resistojet applications. Additionally, it focuses on the possible propellants choices available and the materials implemented in past high-temperature thrusters. Moreover, it defines the high-temperature resistojet in terms of design goals and explains the two main mission scenarios where this technology can be successfully implemented. The design concept of the Super-high Additive Resistojet (STAR) is here defined and justified. The nozzle performance is here discussed in detail highlighting how a high-efficiency nozzle should be dimensioned. Finally, the materials to enable the high-temperature resistojet are discussed. In Chapter 2, a comprehensive manufacturing verification process for the SLM production of the proof of concept thruster is provided. This investigation includes an iterative design process of the heater and heat exchanger component, enabled by NDT techniques. Chapter 3, describes the detailed design and manufacturing of the proof of concept STAR-0 thrusters. The results of dry and wet-firing tests are reported, and multiphysics models are validated against the experiments, also providing further insight into the electrothermal and fluidic behaviours of the novel resistojet. Chapter 4 presents multiphysics modelling results on the STAR design applied to high-

temperature refractory metals, demonstrating that the project goals are achievable. Finally, in Chapter 5, the main results obtained in the thesis are summarised and conclusions are drawn.

1.4 Review of Resistojet Technology

In this section, resistojet technology is analysed in detail through a review of past applications. In the first section, the physics and components of resistojets are described, and the possible configurations are discussed. A subsection is dedicated to the propellant choices and the main factors influencing its selection. Both the performance parameters and thruster efficiency breakdown are derived. The second section summarises the main resistojet applications found in literature, while the third section focuses on the materials used for the fabrication of these thrusters. Finally, the fourth section discusses the materials suitable for the high-temperature resistojet development.

1.4.1 Introduction to Resistojets

Chemical propulsion is limited in performance by the propellant, which can deliver a limited enthalpy change as a result of the chemical combustion process [7]. Electrical propulsion negates this limitation by instead relying on the electrical heating and/or direct electromagnetic acceleration of the propellant, and is therefore said to be limited by the electrical power that can be delivered to the system by the spacecraft (SC). An overview of electric propulsion is summarised in Appendix A.1.

The resistojet concept revolves around the electrical heating of the propellant rather than acceleration of plasma by electric or magnetic body forces. It is usually considered a simple device and has amongst the highest total thruster efficiency of the Electric Propulsion (EP) technologies [8]. Also, the auxiliary electronics necessary to run a resistojet is generally simple because the load consists of a heater, which is purely resistive. The main components of a resistojet are as follows:

1) **Heater**: one or more electrical resistances converting electrical input power into thermal power through the process of Joule heating. The heater can transfer energy to the propellant in two different ways:
   a) Direct heating: the propellant is in direct contact with the heater;
   b) Indirect heating: the heater is encapsulated into the chamber body and transfers heat to the heat exchanger by either conduction or radiation;
2) **Heat Exchanger (HE)**: the volume where heat is transferred to the working fluid prior to entry to the nozzle inlet;

3) **Nozzle**: a converging-diverging nozzle for thermodynamic expansion to the space vacuum;
4) **Insulation Package (IP)**: components made of low thermal conductivity materials to decrease the temperature of the outer regions of the thruster. It is used to both limit the outer casing temperature, therefore mitigating the radiation loss, and to decrease the amount of heat transferred to the SC support by conduction. The main purpose of these components is to improve the thermal efficiency of the thruster.
5) **Radiation Shielding (RS)**: thin metal foils of low emissivity placed close to the highest temperature regions of the HE to limit the heat radiation outwards the thruster and improve thermal efficiency;
6) **Thermal Spacers**: they limit the conduction of heat from the hot resistojet to the spacecraft.

Direct heating allows the propellant to directly contact the heated surface and thus relies on direct convective heat transfer to heat the gas. Therefore, for a given propellant, the primary advantage of the direct heating is to offer potentially higher performance since the gas can achieve a closer temperature to the heater. Fig. 1.1 shows some possible configurations of direct heating, where the heater consists of one or more coils (a, b), a packed particle heat exchanger is heated by an external heater (c) and the heater consists of a cylindrical element.

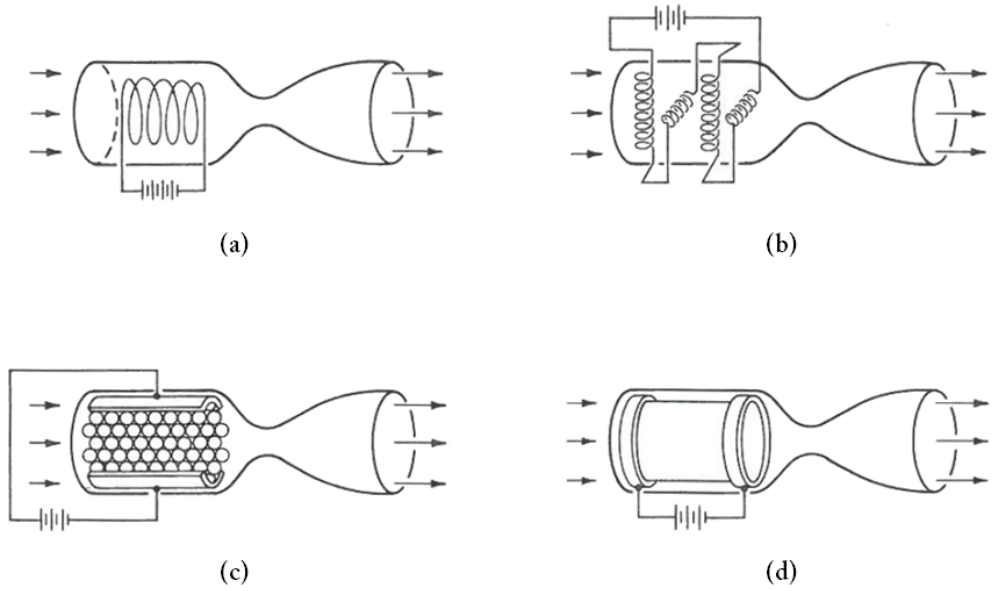

Fig. 1.1. Schematic of resistojet with direct heating of propellant gas: (a) heater coil, (b) heater coils in series, (c) packed particle heat exchanger and (d) cylindrical heater [8].

The indirect heating method, on the other hand, relies on heat transfer from the heater element to an intermediate chamber or shroud. The gas is thereby heated by direct contact with the hot surface of the intermediate boundary of the HE rather than the heater itself [9]. With this configuration, the heater has a longer lifetime because it is not exposed, if relevant, to the oxidation or corrosion of the high-temperature propellant. In fact, in this configuration, the heater is typically located in vacuum and transfers heat either by conduction or radiation to the HE body, which ultimately heats the propellant.

The nozzle of the resistojet is responsible for converting the thermal energy cumulated in the hot gas into axial kinetic energy, which produces thrust. The nozzle efficiency combined with thermal efficiency gives the total thruster efficiency. Higher thermal efficiency is achieved by limiting the heat radiation to space, using a thermal insulation package and a radiation shielding, while the heat loss by conduction to the spacecraft is limited using appropriate thermal spacers.

1.4.1.1 Performance Parameters

The general equations describing a rocket are derived in Appendix A.1. In this section, a set of equations describes the basic thermodynamics process of exhaust acceleration through the converging-diverging nozzle, which produces thrust. The thrust equation is derived in the assumption of an isentropic process (adiabatic and reversible), therefore describing an ideal nozzle, also called the de Laval nozzle. The assumptions made are

1. steady and one-dimensional flow: no radial flow components;
2. adiabatic: no shock in the nozzle;
3. frictionless: no heat loss through nozzle walls and no thermal boundary layer;
4. ideal gas: thermally and calorically perfect gas.

The gas stream is accelerated through the nozzle, where the static temperature decreases to T_e at the nozzle exit. It can be assumed that stagnation conditions exist in the chamber such that $h_c = h_0$. If the total enthalpy h_0 is conserved along the thruster axis (adiabatic process), then the total enthalpy is given by Eq.(1.1), where for an ideal gas $h = c_p T$. The specific heat per unit mass at constant pressure, c_p, represents the heat required to change one kilogramme of mass by one degree (either Celsius or Kelvin). Therefore, the total enthalpy is conserved from the thruster chamber (c) to the nozzle exit plane (e) [8]. With the further assumption of $u_c \ll u_e$ and $T_c \gg T_e$, we obtain the relation given by Eq.(1.2) [8]. In Eq.(1.1) and Eq.(1.2), the units are energy per unit mass (J/kg). Assuming a perfect

gas with constant specific heats, that is, not a function of the temperature, the exit velocity in m/s is given by Eq.(1.3).

$$h_0 = h_c + \frac{u_c^2}{2} = h_e + \frac{u_e^2}{2} \tag{1.1}$$

$$\frac{u_e^2}{2} = \frac{u_c^2}{2} + c_p(T_c - T_e) \approx c_p T_c \tag{1.2}$$

$$u_e = \sqrt{2c_p T_0 \left(1 - \frac{T_e}{T_0}\right)} \tag{1.3}$$

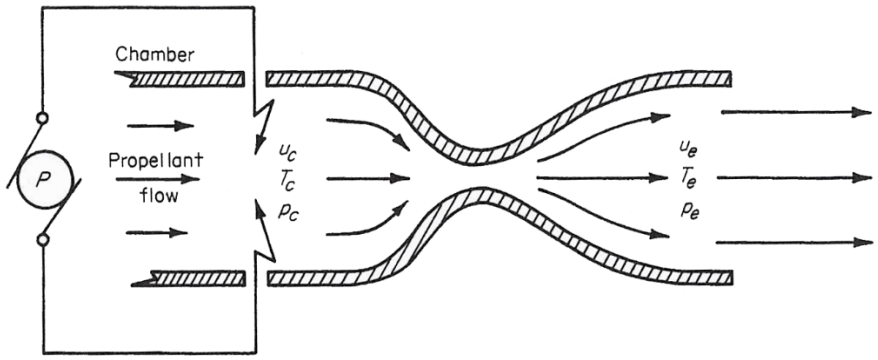

Fig. 1.2. Schematic of the nozzle with relevant parameters [8].

Now, with the further assumption of an isentropic flow process, and expressing c_p as a function of the gas constant, R, and of the specific heat ratio, $\gamma = c_p/c_v$, Eq.(1.3) can be rewritten to Eq.(1.5). From the isentropic flow relations, it is possible to determine the temperature, pressure and density relations from Eq.(1.6), where $M = u/u_s$ is the Mach number and u_s the speed of sound calculated with Eq.(1.4) for an ideal gas.

$$u_s = \sqrt{\gamma R T} \tag{1.4}$$

$$u_e = \sqrt{2\frac{\gamma R}{\gamma - 1} T_0 \left[1 - \left(\frac{p_e}{p_0}\right)^{\frac{\gamma-1}{\gamma}}\right]} \tag{1.5}$$

$$\frac{T_0}{T_e} = 1 + \frac{\gamma - 1}{2} M^2 = \left(\frac{p_0}{p_e}\right)^{\frac{\gamma-1}{\gamma}} = \left(\frac{\rho_0}{\rho_e}\right)^{\gamma-1} \tag{1.6}$$

For the conservation of mass, the mass flow rate of the propellant is constant through the nozzle. The mass flow rate is defined as $\rho u A$, where A is the considered area and u the flow velocity normal to A. The mass flow rate can be therefore determined in the isentropic flow assumption using Eq.(1.7), where A_t is the throat section area where the sonic condition $M = 1$ is achieved. Rocket performance is usually defined in terms of thrust, F, and specific impulse, I_{sp}, which are defined in Eq.(A.2) and Eq.(A.5), respectively. In the specific case of the resistojet relying on a thermodynamic acceleration of the exhaust, thrust is expressed by Eq.(1.8), where p_a is the ambient pressure and $p_a = 0$ in space, and c is the effective jet velocity.

$$\dot{m} = p_0 \gamma A_t \sqrt{\frac{1}{\gamma R T_0}\left(\frac{2}{\gamma+1}\right)^{\frac{\gamma+1}{\gamma-1}}} \tag{1.7}$$

$$F = \dot{m} u_e + A_e(p_e - p_a) = \dot{m} c \tag{1.8}$$

1.4.1.2 Propellants

In a resistojet, the propellant in gas form is heated using a resistance element, and the hot gas is expanded and accelerated through a supersonic nozzle. One of the principal advantages of the resistojet is that it is compatible with nearly any propellant. Propellants used in operational thrusters include ammonia (NH_3), nitrogen (N_2), butane (C_4H_{10}) and xenon (Xe). Besides, resistojets have been successfully used to develop the power-augmented electro-thermal stage in Electrothermal Hydrazine Thrusters (EHT). For this reason, an EHT represents a hybrid between a chemical and an electrical thruster. In addition, other propellants have been investigated in several studies during the last 50 years, including hydrogen (H_2), helium (He), water (H_2O), carbon dioxide (CO_2), methane (CH_4), nitrous oxide (N_2O) and air.

To demonstrate how the propellant properties affect performance, let consider the molar heat capacities for an ideal gas, where v is the volume, n is the number of moles, $\boldsymbol{R} = c_{p,m} - c_{v,m} = 8.3144621(75)\ \mathrm{Jmol^{-1}K^{-1}}$ is the gas constant, m is the mass and $R_s = R/M\ \mathrm{Jkg^{-1}K^{-1}}$ is the specific gas constant. The specific heat per unit mass is then given by the molar specific heat divided by the molar mass of the propellant gas molecule, $c_p = c_{p,m}/M$. Because the specific impulse is proportional to c and therefore to u_e defined in Eq.(1.5), the higher the propellant stagnation temperature T_0, the higher

the specific impulse as described by Eq.(1.9). For instance, the lighter the propellant molecule, the higher the specific impulse.

$$I_{sp} \approx \frac{1}{g_0}\sqrt{\frac{2c_{p,m}T_0}{M}} \tag{1.9}$$

Table 1.1 lists the most relevant propellants for resistojets with respective thermodynamics properties and calculated I_{sp} at a propellant stagnation temperature of 2,400 K with a nozzle efficiency of 90%. The selected temperature is a representative value that the HTR design aims to achieve. The following selection parameters are also listed: the Average Storage Density (ASD) corresponding to a particular storage phase and the Volumetric Specific Impulse (VSI). VSI is a critical parameter, especially for small satellites with strict volume requirements, which estimates the total impulse that the propulsion system can deliver per unit volume expressed by Eq.(1.10).

$$VSI = g_0 I_{sp} ASD \tag{1.10}$$

In terms of molecular mass, the best propellant is H_2 since it is the lightest element with the highest specific heat, being $c_p(H_2)$ in the range 14-20 $kJkg^{-1}K^{-1}$ depending on the gas temperature. Above 1,500 K, dissociation of the hydrogen diatomic molecule becomes appreciable, and pressure becomes a significant variable of c_p. In the assumptions of Table 1.1, a resistojet using the H_2 propellant can deliver a specific impulse of 848 s, the maximum amongst all propellants. Even though H_2 is the most abundant element in the universe and is the lightest propellant possible, its ASD is the lowest, and it requires cryogenic temperatures to maintain a liquid form. While it is used extensively for launchers, it is considered impracticable for SC applications.

Table 1.1. List of propellant gases applicable to resistojets with properties and specific impulse evaluation. I_{sp} is calculated using Eq.(1.2) divided by a conservative nozzle efficiency η_n = 0.9. The assumed propellant stagnation temperature is 2,400 K.

Propellant	M [kgkmol^{-1}]	$c_{p,m}$ [J kg^{-1} K^{-1}]	c_p [J kg^{-1}K^{-1}]	I_{sp} [s]	Storage Phase	ASD [kgm^{-3}]	VSI [kNsm^{-3}]
H_2	2.02	35.88	17,800	848	liquid	71	589
NH_3	17.02	35.15	2,065	289	liquid	600	1,700
H_2O	18.02	25.42	1,411	239	liquid	1,000	2,342
N_2	28.01	29.19	1,042	205	gas	272	547
Ar	39.95	20.77	520	145	gas	387	550
CO_2	44.01	37.06	842	185	gas	427	773
N_2O	44.01	38.51	875	188	gas	427	788
Kr	83.80	20.78	248	100	SFS	996	978
Xe	131.30	20.75	158	80	SFS	1,700	1,332
I_2	253.81	36.90	145	77	solid	4,940	3,714

SFS: Supercritical Fluid State

In terms of ASD, a well-performing propellant is iodine (I_2), with a value of 4,940 kg/m^3. It can be stored in solid phase at room temperature, which is commonly achieved in an SC using thermal control. In [10], the authors suggest that I_2 is a viable propellant for electric propulsion and, for some missions, results are superior to Xe. In particular, the authors tested this propellant with a Hall thruster. The main advantage is the drastic reduction in the system size, mass and cost. For this reason, I_2 is particularly interesting for CubeSat applications [10–13]. However, I_2 has materials compatibility issues [14] and no cathode technology has been found that works with this propellant yet. Therefore it is unlikely that I_2 will completely substitute Xe, but it could partially do so in some near future All-Electric (A-E) SC applications and, therefore, it should be considered for resistojet thrusters as well. Kr has also a good ASD and is compatible with all EP systems. It is currently used in the Hall Effect thruster on the Starlink constellation [15]. In terms of VSI, Xe comes fourth after I_2, H_2O and NH_3. However, amongst these propellants, only Xe, Kr and I_2 have been considered for electromagnetic EP and therefore are interesting for the All-Electric platform application.

Another consideration is the storage phase of the propellant. A propellant in a liquid or supercritical fluid state can cause tank sloshing. Tank sloshing is not permitted in SC having an image platform, where this disturbance could cause image jitter and degrade image quality. All atomic propellants, such as Ar, Xe and Kr, are stored in a supercritical fluid state, which necessitates storage pressures between 200 and 300 bar, determining a particularly heavy tank vessel. Xenon can be stored in a supercritical state at normal room temperature (20°C to 25°C). However, if the temperature drops below 16.7°C, the propellant state changes into both liquid and vapour phases. This is sufficient to potentially cause sloshing [16]. For this reason, Xe requires precise and redundant thermal control.

Other important parameters in the selection of the propellant are toxicity, storage feasibility and the resulting complexity of flow control and injection of the propellant. Table 1.2 shows the handling properties of some possible propellants for resistojet, while Table 1.3 shows the main storage properties of four selected propellants. N_2O is suitable for small SC because it has a relatively high storage density, being stored in liquid phase. In addition, it is not toxic; many other monopropellants, applicable for cold gas thrusters or resistojets, can be either toxic or flammable. With reference to Table 1.5, it is evident that the preferred propellant for this technology has been either N_2H_4 and NH_3, mainly for their higher specific impulse as compared to other propellants. However, both N_2H_4 and NH_3 are toxic and highly reactive chemicals. Combined with air, NH_3 may also present an explosion hazard. In addition, NH_3, which is also an exhaust product of hydrazine decomposition, is incompatible with copper, tin, zinc and their alloys [17].

Table 1.2. Handling properties of cold-gas propellants [17].

Name	Chemical Formula	Toxicity	Flammability	Remarks
Ammonia	NH_3	T	N	Highly reactive
Butane	C_4H_{10}	N	F	Non-corrosive
Carbon Dioxide	CO_2	N	N	Not chemically active
Ethylene	C_2H_4	N	F	Non-corrosive
Helium	He	N	N	Inert
Hydrogen	H_2	N	F	Non-corrosive
Methane	CH_4	N	F	Non-corrosive
Nitrogen	N_2	N	N	Inert
Xenon	Xe	N	N	Inert
Nitrous Oxide	N_2O	N	N	Supports combustion
Propane	C_3H_3	N	F	Non-corrosive

Table 1.3. Comparison of properties between xenon and other monopropellants [16,17]

Propellant	Xenon	Nitrous Oxide	Hydrogen Peroxide	Hydrazine
Chemical formula	Xe	N_2O	H_2O_2	N_2H_4
Storability	Storable	Storable	Storable (decompress)	Storable
Storage density	1,700	745 @ 21°C, 4 bar	1,347	1,004
Vapour pressure	69 bar	50.8 bar	0.00345 bar	0.0214 bar
	@ 20°C	@ 20°C	@ 20°C	@ 26.7°C
Storage temperature range, °C	16.7 to 25	-34 to 60	-7 to 38	-9 to 40
Toxicity	Non-toxic	Non-toxic	Burns skin	Very toxic
Flammability	Non-flammable	Non-flammable	Non-flammable	Flammable
Flight heritage	Flown	Feed system of UoSAT-12	Flown	Flown

1.4.1.3 Thruster Efficiency Breakdown

The main drivers for a resistojet to maximise the thruster efficiency, η_{ts}, are:

- to maximise the heat transfer from the heater element to the gas stream;
- to minimise radiation losses to space losses and the conductive losses to the spacecraft;
- to maximise the exhaust velocity through the gas dynamic expansion processes.

In the resistojet, electrical energy is converted into thermal energy via Joule heating. The conversion from the thermal energy of the gas into kinetic energy, hence thrust, is accomplished by a converging-diverging nozzle. Fig. 1.3 shows the overall energy flow process including the magnitude and the loss mechanisms measured in the 3 kW concentric tubular resistojet [18]. It is important to notice that, under some circumstances, the overall thruster efficiency can be dominated by nozzle processes. The losses involved in the expansion process through the nozzle can be divided into divergence losses, hence thrust reduction because of the divergence of the exhaust plume representing a cosine loss; incomplete expansion losses; frozen flow and frictional losses; or recombination losses of polyatomic propellants and viscous dissipation. The majority of the loss in the case depicted by Fig. 1.3 is due to thermal radiation from the thruster casing. Radiation is proportional to the fourth power of the surface temperature, which is challenging to keep low for a high-temperature resistojet aiming to maximise gas temperature.

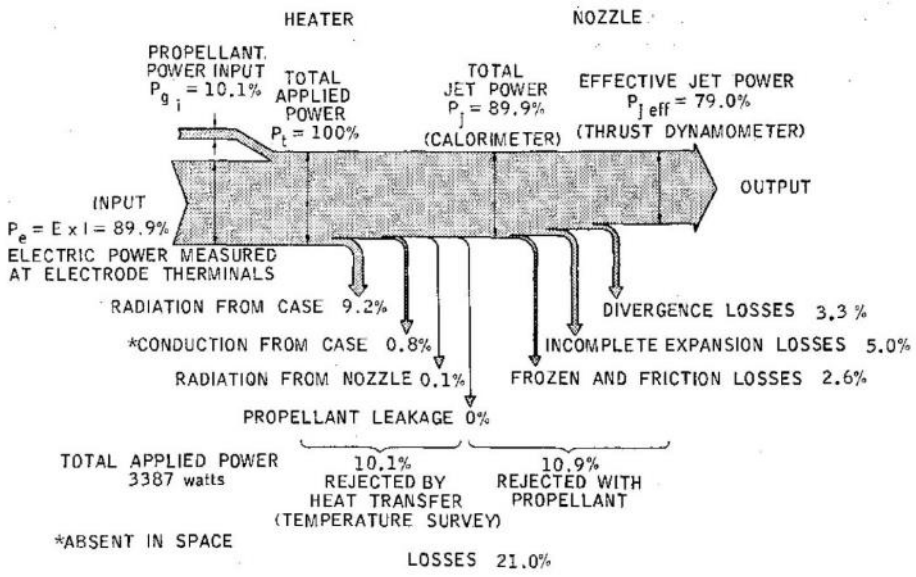

Fig. 1.3. Resistojet energy flow process [18].

Total thruster efficiency, Eq. (1.11), is expressed as the product of heater efficiency, η_h, and nozzle efficiency, η_n. The power balance $P_{in} = P_{out}$ is broken down in Eq.(1.14), where each term is described in Table 1.4. The total power input is the sum of cold-gas thermal power and electrical power, $P_{ts} = P_{0,in} + P_e$, where electrical power is calculated as the sum of the voltage-current products of each resistance. The axial and radial components of the jet velocity are w and u, respectively. The axial kinetic term P_k is the only one contributing to thrust while the radial kinetic term $P_{k,r}$ and all other

terms contribute either to nozzle or thermal losses. The incomplete expansion term P_{ie} corresponds to the component of the outlet stagnation power not converted into kinetic power. The radiation to space is expressed by the Stefan-Boltzmann law applied to the thruster's surfaces radiating heat to space, where ε is the emissivity coefficient of the surface, σ = 5.6703×10^{-8} Wm^{-2}K^{-4} is the Stefan-Boltzmann constant and A is the radiating surface area, and $T_{space} \approx 4$ K. The thermal loss due to heat conduction to the spacecraft is expressed by P_{SC}, where A is the section area of the resistojet supports on the SC. In Table 1.4, the terms that can be neglected at a first calculation are marked with a $\ll$ symbol.

$$\eta_{ts} = \eta_h \eta_n \tag{1.11}$$

$$\eta_h = P_0 \,/\, P_{ts} \tag{1.12}$$

$$\eta_n = P_k \,/\, P_0 \tag{1.13}$$

$$\overbrace{P_{0,in} + P_e}^{\text{input}} = \overbrace{P_k + \underbrace{P_{k,r} + P_{ie}}_{\substack{\text{nozzle}\\\text{loss}}} + \underbrace{P_{rad} + P_{SC}}_{\substack{\text{thermal}\\\text{loss}}}}^{\text{output}} \tag{1.14}$$

Table 1.4. Terms involved in the power balance and the efficiency calculations. Negligible terms are marked with the symbol $\ll$.

Description	Equation
Stagnation power at resistojet inlet:	$P_{0,in} = \dot{m} c_p T_{in} + \overbrace{0.5\dot{m}u_{in}^2}^{\ll}$
Electric power:	$P_e = \Sigma(VI)$
Stagnation power at nozzle inlet:	$P_0 = \dot{m} c_p T + \overbrace{0.5\dot{m}u^2}^{\ll}$
Stagnation power at nozzle outlet:	$P_{0,out} = P_{ie} + P_k = \overbrace{\dot{m} c_p T_e}^{\ll} + 0.5\dot{m}w^2$
Radiation to space:	$P_{rad} = \varepsilon\sigma A(T^4 - \overbrace{T_{space}^4}^{\ll})$
Conduction to SC:	$P_{SC} = kA(T - T_{SC})$
Radial kinetic power:	$P_{k,r} = 0.5\dot{m}u^2$

1.4.2 Resistojet Investigation

To date, a total of 587 spacecraft has been launched with EP systems [19][*]. In the first two decades, all the 48 satellites employing EP were government missions and primarily demonstrating the propulsion technologies, including resistojets, pulsed plasma thrusters, ion thruster and hall effect thrusters [19]. Table 1.5 lists the main satellites launched with resistojets aboard from the first flight of the military Navy satellite launched by USA in 1965. The EP commercialisation begins in 1980 with Intelsat V. Resistojet using hydrazine competed with high-performance chemical bipropellant propulsion at an equal or lower cost. For this reason, Electrothermal Hydrazine Thrusters (EHT) were increasingly used at increasing power, hence thrust, levels. They are still used today on the original Iridium constellation (77 spacecraft), more than 20 in LEO satellites and over 20 in GEO satellites [19]. In recent years, with the growing sector of small satellites, resistojets with high ASD, such as H_2O, N_2O and Xe, have been launched in several missions, with a greater effort by SSTL.

Table 1.6 is a comprehensive list of both operational and laboratory resistojets found in literature. Electrical power ranges between a few watts and hundreds of watts for operational thrusters while laboratory resistojets have been tested in the kW range. Each thruster is provided with literature reference and maximum propellant stagnation temperature, T_0, which illustrates a relatively small number of thrusters exceeding 2,000 K. It has to be noted that the Aerojet Rocketdyne MR-502 and 501B resistojets are the dominant models for GEO platforms with 70/85 satellites equipped with either device [19]. Fig. 1.4 shows how the resistojet technology has been dominant in the early EP years and how in recent years has been replaced by higher specific impulse technologies. In LEO satellites, the number of resistojets received a boost with the Iridium constellation employing high power EHTs, while from 2008 almost the entire number of resistojet thrusters has been released by SSTL in the Rapid Eye constellation and the Disaster Monitoring Constellation (DMC-3) using Xe propellant in both cases. The most relevant resistojets are analysed in detail in the next sections.

[*] This reference was published in January 2019, and therefore does not account of later missions, for example of the injection of 62 satellites of the Starlink constellation, which are equipped with Krypton HETs.

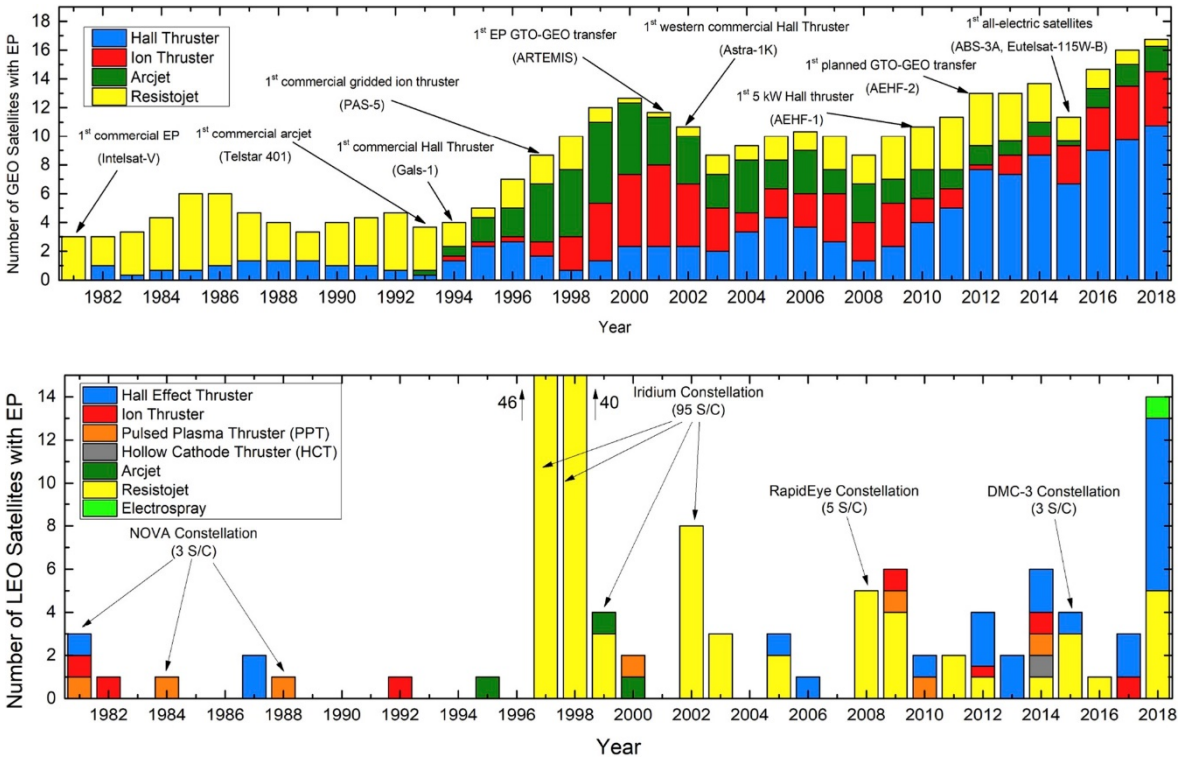

Fig. 1.4. Number of EP-based satellites launched in the years 1981-2018 (3-year moving average), divided into electric thruster subclasses: GEO (top) and LEO (bottom) satellites [19].

Table 1.5. Resistojet flight history [20,21]

Satellite name	First Flight	Flights	Prop.	Power [W]	Country	Sat. Manufacturer	Application
Navy Satellite	1965	5	NH_3	30	USA	Navy/GE	Attitude control, orbit control
ATS-A, C	1966	2	NH_3	<10	USA	AVCO	Experiment
Advanced Vela	1967	6	N_2	30	USA	AF/TRW	Phase and spin adjustment
ATS D, E	1968	2	NH_3	<30	USA	AVCO	Attitude control
Meteor, Resurs	1970	×	NH_3	×	USSR	×	Attitude control
Navy Satellite	1971	4	NH_3	10	USA	Navy/AVCO	Orbit adjustment
Navy Satellite	1971	1	N_2H_4	×	USA	AVCO	Experiment
Sol Rad-10	1971	×	N_2H_4	×	USA	AVCO	×
Intelsat V	1980	13	N_2H_4	350	USA	Ford/TRW	N/S station keeping
Meteor 3-1, etc.	1981	10	NH_3	450	USSR	NIIEM	Orbit adjustment
Satcom-1R, etc.	1983	32	N_2H_4	600	USA	RCA/RRC	N/S station keeping
Gstar-3	1988	1	N_2H_4	600	USA	RCA/RRC	Orbit transfer
COMS (Electro)	1994	1	NH_3	450	RU	NIIEM	E/W station keeping, attitude control
Iridium	1997	72	N_2H_4	500	USA	Iridium/OAC	Orbit adjustment
UOSAT-12	1997	1	H_2O - N_2O	200	GB	SSTL	Experiment
RapidEye, etc.	2005-today	25	Xe - C_4H_{10}	50	GB	SSTL	Orbit adjustment
Hawk A-C	2018	3	H_2O	×	USA	Deep Space Ind.	Formation flight

Table 1.6. Resistojets found in literature and available in the market.

Satellite/ Thruster	Prop.	Producer	T_0 [K]	Ref.
XR-50,100,150	Xe	Alta	900	[22]
T15/T30/T50	Xe - C_4H_{10}	SSTL	820	[6,16,23]
Xenon Resistojet	Xe	Moog, Inc.	650	[24]
Nitrous Oxide Resistojet	H_2O - N_2O	University of Surrey	1,000	[17,25]
FAKEL K10L	N_2 – Xe	FAKEL Enterprise	×	[1]
Fakel	NH_3	Fakel Enterprise	2,500	[21]
Multi-propellant	CO_2	MBB-ERNO*/ESA	×	[26]
PACT	NH_3	MBB-ERNO/ESA	2,000	[21]
Water Resistojet	H_2O	NASA	1,000	[27]
MR-502	N_2H_4	Aerojet Rocketdyne	×	[28]
NASA Multi-prop.[a]	H_2 – He – CH_4 - air	NASA	1,280	[29]
MR-501B	N_2H_4	Aerojet Rocketdyne	×	[28]
HiPEHT	N_2H_4	TRW	2,200	[30]
J3 Oxford	H_2	RPE, Westcott	2,530	[31]
Biowaste Resistojet[b]	CH_4 - CO_2 - H_2O - H_2	The Marquardt Corporation	1,700	[32]
ATS-III	NH_3	NASA	×	[33]
Ten-millipound	H_2 - NH_3	The Marquardt Corp.	2,200	[34]
Pulsed Resistojet	NH_3	NASA	1,180	[35]
3 kW Con.Tub.	H_2	The Marquardt Corp.	2,400	[18]

* find more detail in the related thruster sections below

a,b same resistojet project

× unknown

* Messerschmitt-Bölkow-Blohm, MBB, became part of European Aeronautic Defence and Space Company, EADS, in 2010. In January 2014, EADS was reorganized as Airbus Group combining the divisions for development and marketing of civil and military aircraft, as well as communications systems, missiles, space rockets, helicopters, satellites and related systems.

1.4.2.1 Electrothermal Hydrazine Thrusters (EHT)

Since the late 1960s, resistojets have played an important role in station-keeping of geosynchronous satellites. Most resistojet concepts until the late 1990s used hydrazine decomposition products obtained through a first-stage decomposition gas generator producing ammonia, nitrogen and hydrogen [20]. This type of resistojet, depicted in Fig. 1.5 and termed EHT, is capable of delivering a specific impulse of about 300 s, increasing the I_{sp} of standard catalytic hydrazine thrusters by approximately 35%. EHTs have been and are currently used in GEO communication satellites for station-keeping and on-orbit manoeuvring. In general, EHTs have been used for both attitude and orbit control, including phase and spin adjustment, N/S and E/W station-keeping and Δv manoeuvres. In this section, more technical details of the most relevant EHTs are presented and discussed.

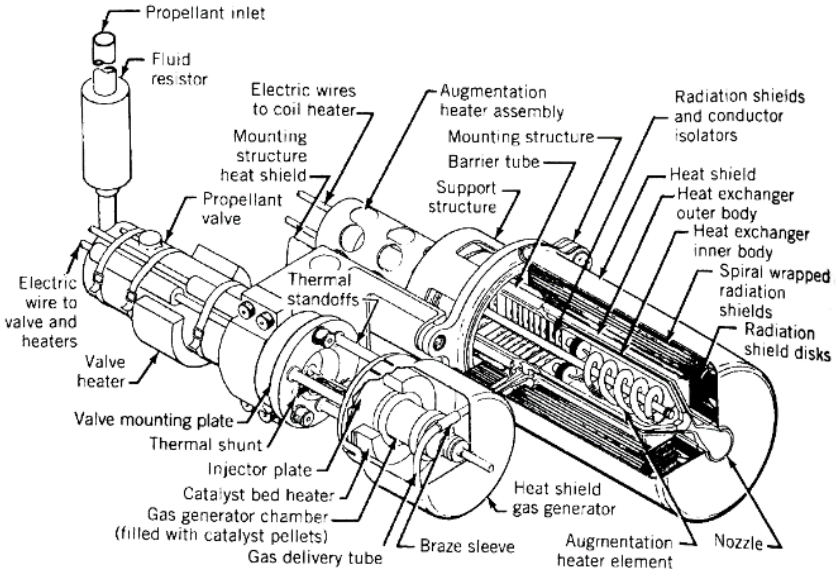

Fig. 1.5. Typical resistojet augmented by hot gas from catalytically decomposed hydrazine; two main assemblies are present: catalyst bed (left) and resistojet stage (right) [7].

High-Performance Electrothermal Hydrazine Thruster (HiPEHT)

The HiPEHT electrothermal hydrazine thruster by TRW Defence and Space Systems Group was the first utilised commercial resistojet, firstly launched in 1980 aboard of the Intelsat V satellite. The HiPEHT schematics are shown in Fig. 1.6. This design used a double-helix heater with a vortex heat exchanger and produced a specific impulse of 300 s with hydrazine. This thruster has also been

tested with nitrogen, ammonia, and hydrogen at varying mass flow rates whilst holding the input power to 500 W [25].

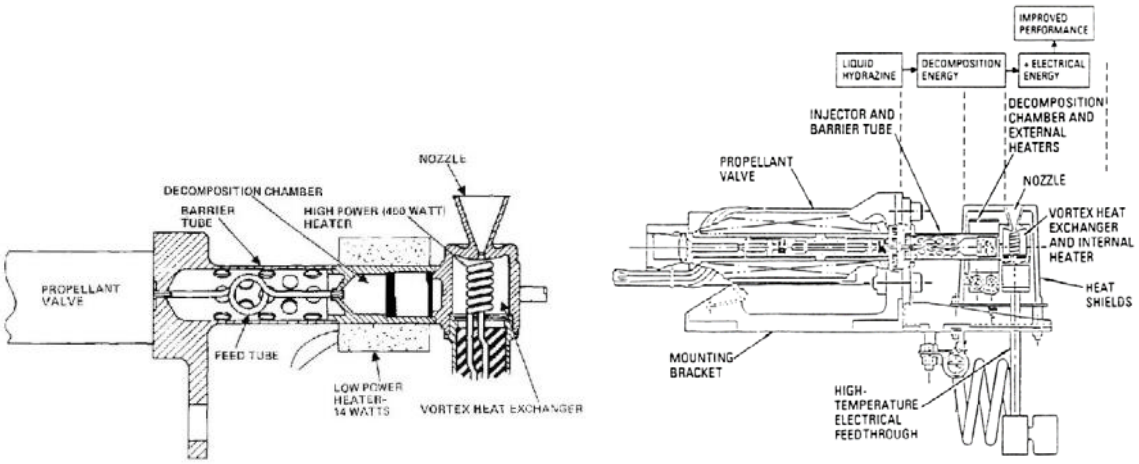

Fig. 1.6. HiPEHT thruster overview: detail of the resistojet schematic (left) and whole thruster schematic (right) [30].

Power-Augmented Catalytic Thruster

In Europe, MBB-ERNO Bremen, on behalf of ESA, has developed two types of EHTs. The first design started in 1978 and was known as the power-augmented catalytic thruster (PACT), a catalytic hydrazine thruster enhanced using a Tungsten-26 Rhenium heater element, which increases the temperature of the propellant to about 2,000 K. The hydrazine temperature peaks at approximately 866 K if the ammonia is fully decomposed before heating. The specific impulse improvement of the PACT thruster using the resistojet is approximately 35%, increasing it from 235 s to approximately 300 s. Fig. 1.7 gives an overview of the thruster while the technical data is summarised in Table 1.7.

Table 1.7 .PACT resistojet characteristics.

Technical Data	Unit	Value
Thrust Range	mN	150-500
Specific Impulse	s	306
Heater Element Power	W	500
Bed Heater Power	W	10
Operational Pressure Range	bar	5.5-22
Minimum Impulse Bit	Ns	0.006-0.02
Proof Pressure	bar	33/54
Burst Pressure	bar	88/144
Mass	G	360
Valve Power	W	5

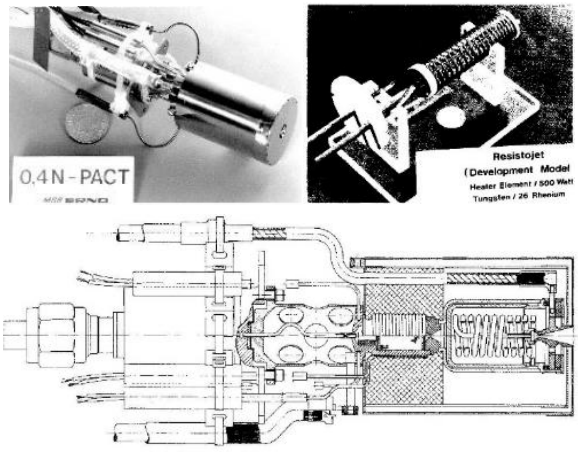

Fig. 1.7. PACT thruster overview.

Aerojet Rocketdyne MR-501 and 502 Resistojets

The MR-501B resistojet uses hydrazine propellant at a flow rate of 45-122.5 mg/s. It is formed by two main parts: a small catalyst bed with heaters to prevent propellant freezing and an electrical spiral-shaped resistance element surrounded by thin radiation shields made from tungsten and high-temperature electrical insulators to support the power leads (Fig. 1.8). The power input peaks at 500 W supplied by 25 V with a thruster mass of approximately 0.9 kg. Aerojet Rocketdyne also provides an 800 W MR-502 EHT. The 501 models' characteristics are summarised in Table 1.8. By comparison, MR-502A can provide a higher flow rate, thus thrust level, whilst maintaining the same specific impulse. This improvement is achieved by increasing the heater element power. Furthermore, the supply pressure has the same range, meaning that the nozzle throat section of the higher-power thruster (MR-502A) has been increased for this purpose.

Table 1.8. MR-502A schematisc [36].

Technical Data	Unit	MR-501B	MR-502A
Thrust Range	mN	182 - 369	360 - 800
Specific Impulse	s	294 - 303	294 - 303
Flow Rate	mg/s	45 - 123	120 - 280
Valve Voltage	V-DC	28	28
Heater Element Power	W	467 – 493*	610-885**
Bed Heater Power	W	4	3.93
Operational Pressure Range	bar	6.9-24.1	6.2-26.5
Minimum Impulse Bit	Ns	0.0022	×
Mass	g	889	870
Valve Power	W	8	8.25

* With an Augmentation Heater Power Voltage of 24.4 V DC

** With an Augmentation Heater Power Voltage of 24.5-29.5 V DC

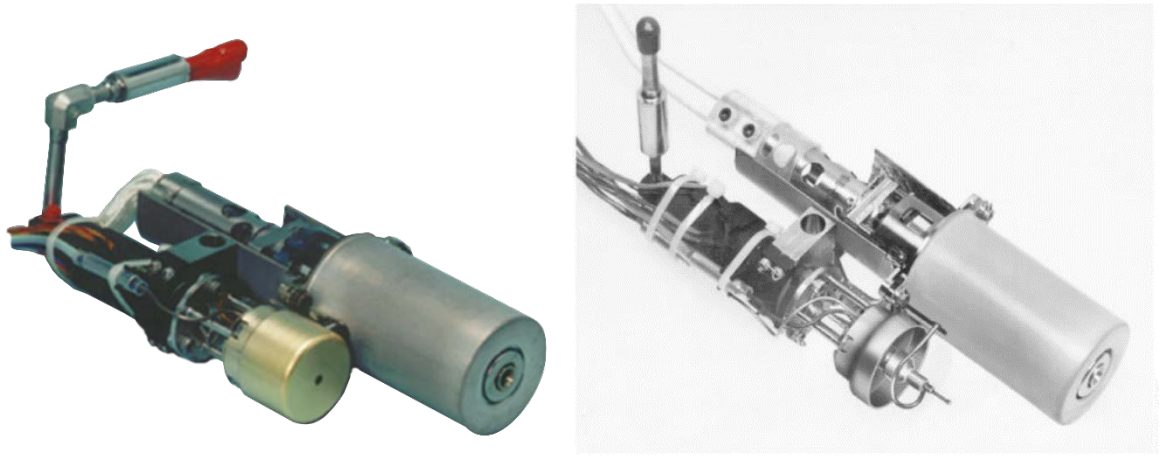

Fig. 1.8. MR-501B thruster overview: MR-501B thruster (left) and MR-502 thruster (right) [28].

1.4.2.2 Multi-propellant Thrusters

The two main multi-propellant resistojets developed by NASA and ESA are here discussed.

NASA Multi-propellant Resistojet

NASA started to develop a multi-propellant resistojet in 1968 with a 10-millipound thruster design [34]. In 1971, a bio-waste resistojet designed for the International Space Station is reported in [32], which further evolved in 1986 into the NASA Multi-propellant Resistojet described in [29].

Extensive work has been performed on the materials because the main issue in using such a variety of propellants is the corrosion of the flow channel walls [37]. A schematic of the thruster is shown in Fig. 1.9. The heating is indirect and consists of a radiative heater tube located in an evacuated cavity within an annular heat exchanger body. The choice to separate the heating element from the propellant flow lies in the lifetime optimisation of the element. The heat exchanger consists of two concentric tubes hermetically sealed together, creating an annular section through which the propellant flows. The cold gas inlet (on the left in the schematics) is passed through the radial outer channel to minimise heat loss from the hot heat exchanger to the rear of the thruster. The flow is directed axially towards the hot region by means of 16 channels and finally accelerated through the nozzle.

The dimensions of the heater tube and other components are given. The platinum thruster components are joined by Electron Beam (EB) welds. To minimise radiation loss from the outer surface of the heat exchanger, the thruster is overwrapped with radiation shielding consisting of two layers of platinum foil followed by 13 layers of stainless steel foil. The layers of the radiation shield are separated by small-diameter wires.

MBB-ERNO Multi-propellant Resistojet

The MBB-ERNO Multi-propellant Resistojet is the second thruster developed by MBB-ERNO Bremen on behalf of ESA/ESTEC in 1987. Its propellant capability includes nitrogen, hydrogen, carbon dioxide and ammonia. From this point of view, it could be compared with the NASA multi-propellant resistojet. This engine was designed for the European Columbus module of the International Space Station. The launch was delayed until 2008 and, for this reason, the engine never passed the development model stage [21]. This thruster had also the goal of providing a reasonably low-cost propulsion system for the station keeping and orbit adjustment of a 350 kg SC. Its performance with CO_2 as a test propellant was F = 300 mN, I_{sp} < 138 s, supply pressure < 10 bar, inlet temperature of 293 ± 5 K, electrical power P_e = 350 W and 3,000 hr of operation time. Fig. 1.10 shows a schematic of the resistojet.

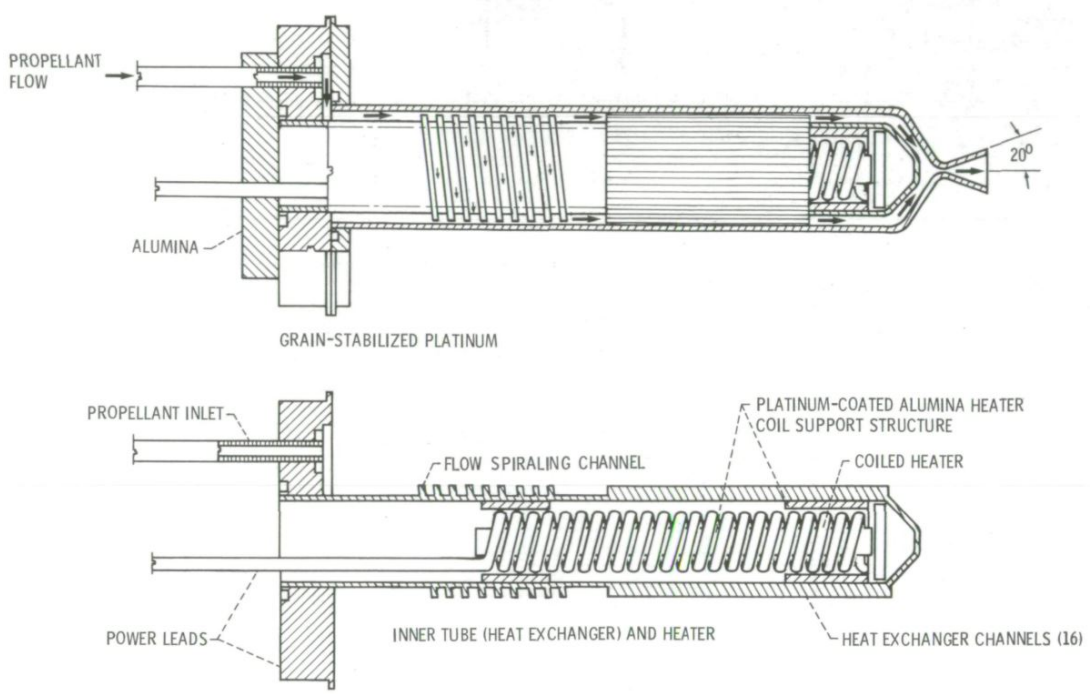

Fig. 1.9. Multi-propellant resistojet cross-section [29].

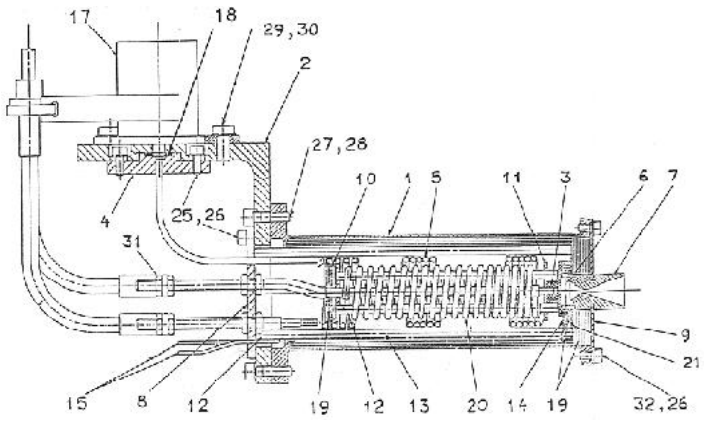

Fig. 1.10. MBB thruster overview [21].

1.4.2.3 Nitrous Oxide Resistojet

The University of Surrey developed a nitrous oxide resistojet, which uses a packet of SiC particles in the form of pellets for the heat exchanger bed. As the resistojet research progressed, the design converged on two systems, both using the same heating element and silicon carbide heat transfer bed but with different working fluids: H_2O and N_2O. The H_2O and N_2O resistojet designs each consume 100 watts of electrical power providing an I_{sp} of 125 s (N_2O) and 152 s (H_2O). The N_2O thruster has been flown in 1997 on the UoSat-12 experimental satellite. It was the first satellite to use nitrous

oxide as a propellant in an experimental resistojet thruster. It developed a thrust of 50 mN while the Δv afforded to the UoSat-12 was 10.4 m/s provided by a two-litre tank of self-pressurised nitrous oxide [38,39].

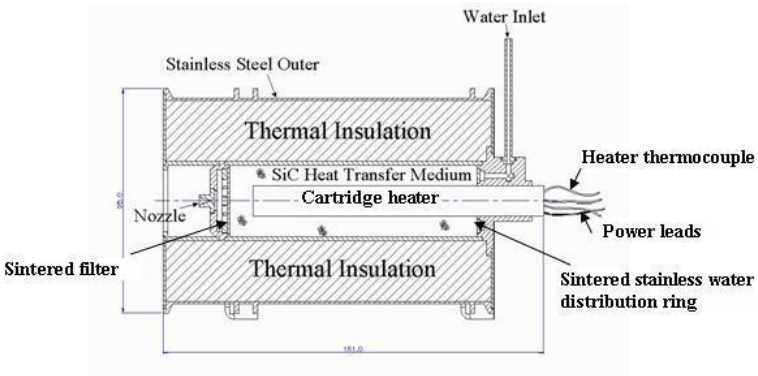

Fig. 1.11. Schematics of the Mark-III [25].

1.4.2.4 Current Xenon Resistojets

Currently, only Surrey Satellite Technology Ltd (SSTL) has heritage on Xe resistojets for medium to large platforms [16,40,41], while some manufactures produced resistojet for CubeSats but using other propellants [13]. Also, NanoSpace MEMS produced a Xe (in addition to He and N_2) resistojet with flight heritage with the satellite PRISMA [42], but little information is found on this thruster. Sitael is leading the development of a Xe resistojet having obtained an EM model, while Mars Space is developing a Very-High Temperature Resistojet with Nammo (formerly Moog) with an objective specific impulse of > 80 s with Xe of which no specific documentation is available.

Resistojet by SSTL

SSTL first developed its resistojet in 1999, and the same design has been used to date with only minor changes. The T50 resistojet has two redundant heaters and can operate reliably up to a power of 50 W. This thruster was not subjected to a severe optimisation process, but it has been designed following the 80:20 rule, that is, 80% of the performance at 20% of the cost [43]. The SSTL T-50 resistojet thruster shown in Fig. 1.12 has been the basis of SSTL hot-gas propulsion systems since 2002. There are 29 resistojet systems (15 using Xe, 10 using C_4H_{10}, 2 using H_2O and 1 using N_2O) in orbit on 20 spacecraft, with a further 6 thrusters awaiting launch [5,44]. The initial application was with butane propellant on Alsat-1 and, since then, it has been used in a further 11 butane systems

including ESAs Giove-A (Table 1.10). The thruster is also used as part of xenon propulsion systems, including ESAs Proba-2, RapidEye constellation (Fig. 1.12) and DMC3. The variants of the thruster are detailed in Table 1.9. The full list of resistojet models used by SSTL is composed by the T15 for C_4H_{10}, T30 for Xe, a 100W resistojet for N_2O (Section 1.4.2.3) and a micro-resistojet for H_2O. The T15 and T30 variants are physically identical, with the only difference being thruster operating power. The T50 is 60 mm long by 20 mm in diameter, weighs 50 g and is manufactured using two Inconel coaxial sheathed heaters wound on a central bobbin. Propellant enters the back of the thruster and is forced to spiral around the heater, hence increasing the dwell time within the heat exchanger. The heater power is rated at an input voltage of 28 V DC, and the thruster is designed to run directly off the spacecraft's 28 V DC bus; hence, no additional control electronics is required for operation.

Fig. 1.12. T50 Resistojet (left) and Rapid Eye Constellation Satellites 1-5 (right).

Table 1.9. The variants of SSTL's low-cost resistojet [5]**.**

Variant	Redundant heater power	Propellant	Thrusters	Typical operation temperature [°C]	I_{sp} [s]
T50	50 W	Xe - N_2 - C_4H_{10}	Qualification model only	< 650	< 57
T30	30 W	Xe	15 launched on 15 SCs	530	48
T15	15 W	C_4H_{10}	21 launched on 12 SCs	250 - 350	> 100

Table 1.10. SSTL resistojets' missions with the number of thruster employed [44].

Mission	Launch	Propellant	No. of thrusters
UoSAT-12	1999	N_2O	1
AISAT-1	2002	C_4H_{10}	1
UK-DMC-1	2003	C_4H_{10} - H_2O	2
NigeriaSat-1	2003	C_4H_{10}	1
BILSAT-1	2003	C_4H_{10}	1
Beijing-1	2005	Xe	1
Giove-A	2005	C_4H_{10}	10
Rapideye (constellation of 5)	2008	Xe	5
UK-DMC-2	2009	C_4H_{10}	1
Deimos-1	2009	C_4H_{10}	1
SumbandilaSat	2009	C_4H_{10}	1
Proba 2	2009	Xe	1
NigeriaSat-X	2011	C_4H_{10}	1
NigeriaSat-2	2011	Xe	1
Exactview-1	2012	C_4H_{10}	1
KazEOSat-2	2014	Xe	1
TechDemoSat-1	2014	Xe	1
DMC-3 (constellation of 5)	2015	Xe	3
Alsat-1b	2016	C_4H_{10}	1
India S1	2018	Xe	1
NovaSAR-1	2018	Xe	1
KazSTSAT	2018	C_4H_{10}	1

Sitael XR resistojets

Sitael, formerly Alta, development a family of resistojet thrusters [22] which eventually converged in the XR-150 EM depicted in Fig. 1.13. The heater consists of a standard two tungsten coils, which can be operated at the satellite bus unregulated voltage. The power ranges from 50 W to 100 W with a nominal thrust of 50 mN and an effective I_{sp} in Xe around 50-55 s and around 75 s in Ar.

Fig. 1.13. Sitael XR-150 EM thrsuter [45].

1.4.2.5 Previous High-Temperature Resistojets

Among the thruster list shown in Table 2.5, we can label as high-temperature resistojets those reporting a maximum operating temperature above 2,000 K. This definition is supported by the fact that, above this limit, the heater and heat exchanger components have to be made of refractory metals or their alloys. For this class of metals (Nb, Mo, Ta, W and Re), the melting point is above 2,300 K. EHTs are not included in this section, as they also rely on chemical reaction and are therefore a substantially different technology from a purely resistojet thruster. Therefore, thrusters of interest are the 10-millipound, the J3 Oxford and the Fakel resistojets (as named in Table 1.6)

J3 Oxford Resistojet

The Rocket Propulsion Establishment, RPE, Westcott, England, developed the J3 resistojet in the 1970s. The 3 kW thruster was successfully tested at Oxford University in 1973, obtaining an effective exhaust velocity of 7.57 km/s with an overall efficiency of 68.1%. Its design consists of a concentric tube heat exchanger terminating in a conical nozzle, both manufactured from Rhenium. A schematic of the thruster is shown in Fig. 1.14. The figure at the bottom shows the particular jointing methods adopted. To reduce heat loss in the radial direction, a vacuum jacket filled with radiation shields is placed around the concentric tube HE. In turn, this produces a steep radial temperature gradient, which causes thermal expansion of the tubes along their axis. Therefore, stainless steel bellows are incorporated to manage this expansion. The fabrication and assembly procedure of this thruster is described in [46]. In general, thin-walled rhenium tubes were made by Chemical Vapour Deposition (CVD) and then joined by EB welding. This thruster has been studied through a multi-physics simulation as a model validation process (Appendix **C.2**).

Russian Thrusters

Since 1960, different resistojet thrusters have been developed in Russia [21]. The two main thrusters illustrated here use indirect propellant heating (Fig. 1.15, top) and direct propellant heating (Fig. 1.15, bottom). The first engine, developed by Fakel Enterprise, uses an inner graphite heater, which radiatively heats the incoming propellant and the outer concentric channels walls through which the propellant flows. The propellant is usually NH_3 with a power range of 80-600 W. The main performance parameters are F = 20-200 mN, T_0 = 2,500 K and I_{sp} = 250 s. Today, Russian satellites are equipped with engines of the type EHT-15. This thruster was developed by NIIEM-ELKOS. The heating element is a porous medium, located into the inner chamber (7) while (2) is the inflow and (6) is the chamber. The propellant used is NH_3, with a power range of 100-450 W, a performance of F = 30-50 mN, I_{sp} = 296 s, a power-to-thrust ratio of 3,300 W/N and a total impulse of 500,000 Ns.

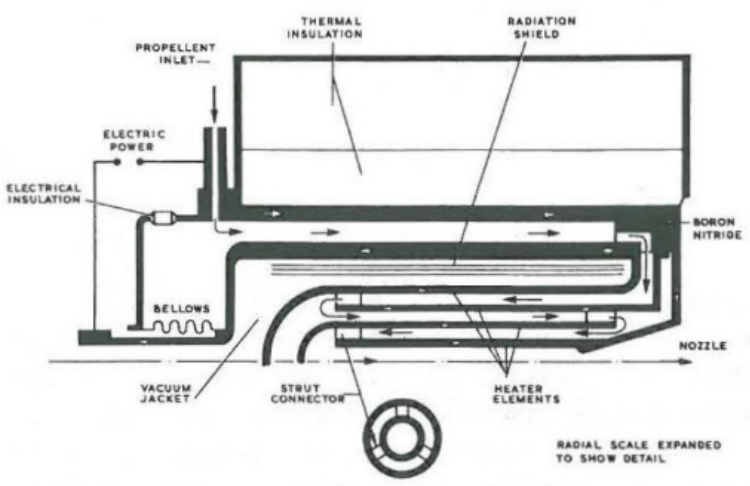

Fig. 1.14. A schematic of teh J3 thruster [31].

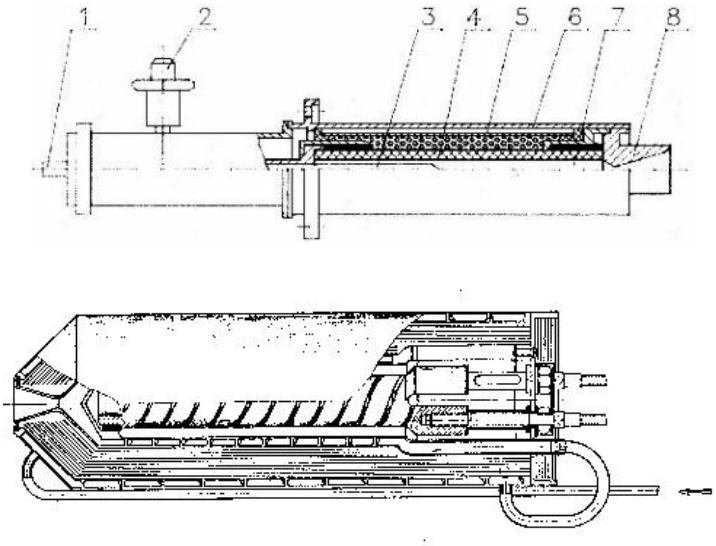

Fig. 1.15. EHT-15 thruster (top) and Fakel thruster (bottom) overviews [21].

1.4.3 Materials Applied to Resistojets

The selection of the materials used for the heater element and the heat exchanger sets a limit to the operating temperature, hence performance. Suitable materials already used in commercial resistojets and various phases of resistojet research are generally refractory metals and ceramics. However, depending on the propellant used, to meet the lifetime requirement for the specific mission, a suitable design of the heater element and the heat exchanger are necessary, as well as the selection of appropriate materials that can reliably withstand high-temperature operation with possibly oxidising or generally reactive propellants. In the following sections, the materials used in past applications are summarised and discussed. The purpose of this examination is to become familiar with suitable designs and materials that have been used for different propellants and operating temperature ranges.

1.4.3.1 Heater and Heat Exchanger

In the 1970s, NASA and the Marquardt Company* worked together to develop a multi-propellant resistojet suitable for space station auxiliary propulsion systems, which required both long life and multi-propellant capability. The authors in [32] investigated platinum-iridium (20%) as a heater material and the related issues of carbon deposition using propellant mixtures containing methane

* By 1970, Marquardt was known primarily as the company for small rocket engines and thrusters. Practically all U.S. space vehicles and satellites used their designs, eventually including a major win for the Space Shuttle program. The company developed and provided the 25 and 870 *lb*. trusters for the Space Shuttle [Wikipedia].

and carbonyl corrosion by CO_2. This study focused on selecting the best materials that could meet the requirements. Earl Morren et al. [29] at NASA Lewis Research Center (LeRC) performed endurance tests on a multi-propellant resistojet for space station auxiliary propulsion. Experiments were performed to evaluate the capability of grain-stabilised platinum tubes at a temperature of 1,700 K in environments of CO_2, CH_4, NH_3, H_2O and H_2. The thruster was tested with various propellants including hydrogen, helium, methane, air, nitrogen, argon and carbon dioxide. The measured performance was 90-420 mN, over a specific impulse range of 100-400 s, at power levels between 140 and 240 W. Rhenium or tungsten were used when the highest operating temperatures were required. Graphite is used in the Fakel resistojet as an indirect heating element to heat the NH_3 propellant to 2,500 K. Table 1.11 shows materials used in the heater or heat exchangers of resistojets found in the literature.

The 3-kW Concentric Tubular thruster employed pure W for the heater, but it was found to provide insufficient fatigue performance due to its brittleness. Re has been used in place of W to avoid the fatigue issues and has been implemented with the same design in the ATS-III and J3 thrusters. Despite the development of these thrusters was successful, the high-power concentric tubular design concept was abandoned. Multi-propellant thruster needed a huge effort in materials development to minimise corrosion and oxidation issues. In addition, these thrusters relied on indirect heating through an intermediate heat exchanger to limit the heater degradation. In conclusions, for high-temperature applications, refractory metals should be selected for the heater. If the propellant is non-corrosive and non-oxidising, like in the case of Xe, direct heating should be used to provide the highest temperature, hence performance. Thermal cycling of the heater directly influences the device lifetime, which is also strongly dependant on the design.

Table 1.11. Heater and heat exchanger materials for resistojets (references as from Table 1.6).

Satellite/Thruster	Material	Notes
3-kW Concentric Tubular	Tungsten	Nine-concentric-tube heat exchanger
ATS-III	Rhenium	CVD, single tube
	Nioro (Gold 82/Nickel 18 alloy)	The nozzle has been Nioro* brazed and supported by stainless-steel mount
	Platinum	Platinum leads provide electrical continuity from the heater to the shroud
Biowaste Resistojet	Platinum - 30 Iridium	Evacuated-concentric tubular configuration
Fakel Resistojet	Graphite	Coiled heater
J3	Pure rhenium	CVD, concentric tubular heat exchanger
Mark-II	SiC	Packed bed of SiC particles in form of pallets for the heat exchanger
NASA Multi-propellant	Grain-stabilised platinum	Coiled tube heater
	Zirconia grain-stabilised platinum	Concentric tube heat exchanger
PACT	Tungsten - 26 rhenium	Coiled tube heater
Pulsed Resistojet	Platinum, Magnesia, Hastelloy	Platinum filament wrapped on a Magnesia core, fitted into a Hastelloy X sheath
Ten-Millipound	Pure rhenium	Evacuated concentric tubular configuration
Xenon Resistojet	Nichrome	Swagged heating element wrapped around a spoon
XR-150	Tungsten	Single-coil wire
Water Propellant	Platinum - 10 Rhenium	Centre conductor of the heater coil
	Grain-stabilised platinum	Heater coil sheath and 36-channel heat exchanger

* Nioro® is a Gold 82/Nickel 18 alloy.

1.4.3.2 Electrical Insulation

The principal part of the resistojet is the resistive heating element. Electrical potential is applied across the terminals of the heater; hence, electrical insulation between this component and the surroundings is necessary. Ceramic materials accomplish both electrical insulation and mechanical support between components at high temperature. Table 1.12 summarises their application to various resistojet thrusters. Any thermal stresses due to the different thermal expansion coefficients of the insulator and the surrounding components should be carefully evaluated in the design process.

High-temperature resistojets employed principally BN or Al_2O_3 for the electrical insulators. The first one has lower mechanical performance but higher operational temperature. The second one should if within its temperature capabilities because of superior mechanical properties. For prototyping, also less performing machinable ceramics could be used.

Table 1.12. Electric insulation materials for resistojets (references as Table 1.6).

Thruster/Satellite	Material	Notes
3-kW Concentric Tubular	Boron nitride	Heat exchanger support, electrical insulators
ATS-III	Alumina	Ring separating the shroud and the thruster mounting flange
J3	Boron nitride	Heater electrical insulator
NASA Multi-propellant	Alumina/Nickel	Seal
	Alumina	SC interface
	Platinum-coated alumina	Heater coil support structure
Water Resistojet	Magnesia	Electrical insulator tube separating the Pt-10 Rh wire conductor from the grain-stabilised Pt sheath

1.4.3.3 Thermal Insulation

A few thrusters in the literature have been found to use a solid thermal insulator rather than, or in addition to, a radiative shielding. In general, high-temperature thrusters use a thermal insulation, that is, the 3 kW concentric tubular, the 10-millipound and the biowaste resistojet thrusters (as named in Table 1.6). Moreover, both the J3 and the Mark-III thrusters use a thermal insulator (Table 1.2). Table 1.13 shows the materials used for the highest operating temperature resistojets; for more details about these materials, see Section 1.4.4.3.

Thermal insulation can improve significantly the thermal efficiency of a high-temperature resistojet. Microporous ceramics materials are found particularly effective to limit the thermal radiation loss to space. However, the implementation of an insulation package could be avoided if the thrusting time of the device is relatively short, resulting in a relatively low external surface temperature. The size of the insulation is also dependant on the spacecraft volumetric requirements. A numerical analysis on

the benefit of employing a thermal insulation package in the context of this research is discussed in Chapter 4.

Table 1.13. Thermal insulation materials for resistojets (references as from Table 1.6).

Thruster/Satellite	Material	Notes
3-kW Concentric Tubular	Dynaquartz	Inner high-temperature thermal insulation.
	Min-K-2000	Outer lower-temperature thermal insulation.
	Tungsten	Three regeneratively cooled tube shields.
J3 Oxford	Dynaquartz	Inner high-temperature thermal insulation.
	Min-K-2000	Outer lower-temperature thermal insulation.

1.4.3.4 Radiation Shielding

The higher the resistojet operational temperature, the higher the power that could be lost by radiation from the thruster's envelope. When the maximum thruster temperature exceeds a threshold of about 1,500 K, a thermal insulator cannot be directly applied to the hot surface because it exceeds its maximum service temperature. In these cases, it is necessary to apply radiation shielding that reflects a part of the power coming from the inner and hotter heat exchanger, hence lowering the outer thruster temperature. The materials found in the literature that have been used in previous resistojets are listed in Table 1.14. In general, radiation shielding consists of a series of thin foils with very low emissivity. These are wrapped around the hottest part of the resistojet several times to lower as much as possible the heat radiation loss. In a concentric tubular heat exchanger configuration, the HE thin walls also operate as a radiation shield. In several resistojet designs, the high-temperature heat exchanger is confined via a radiation heat shield constructed from very thin foils (< 30 μm) wrapped concentrically, with a small separation between each layer. The gap can be created using small diameter wires to separate the foils acting as a spacer or creating a series of dimples on the foils' surface to minimise the contact area while providing separation. It is necessary to minimise the contact area between the layers to diminish heat transfer from the inner to the outer and colder layers.

The use of a radiation shielding is effective only if the hot radiating surface has a sufficiently high-temperature. A numerical analysis on the benefit of employing a radiation shielding in the context of this research is discussed in Chapter 4.

Table 1.14. Radiative shielding materials for resistojets (references as from Table 1.6).

Thruster/Satellite	Material	Notes
3-kW Concentric Tubular	Tungsten	Nozzle radiation shield
	321 stainless steel	External thruster case
Aerojet MR-501B	Tungsten	Foils
NASA Multi-propellant	Platinum/stainless steel	Two layers of 0.025 mm platinum foils followed by 13 layers of 0.127 mm stainless steel foils.
Pulsed Resistojet	Nichrome V	Shielding. Chosen for its low emissivity, heat conductivity, lightweight, ease of fabrication and non-reaction with the NH_3 propellant.
SSTL Resistojets	Aluminium	Heat shielding
	Pure nickel	Electroformed nozzle
	Inconel 600	The heat shielding should be polished previous to being gold plated, ensuring a very low emissivity.
XR-150	Stainless steel	Thruster body
Water Resistojet	Platinum	Five-layer, 0.025 mm thick shields
	Nickel	Five-layer, 0.1 mm thick shields
	Inconel	Outer case

1.4.4 Review of High-Temperature Materials

In general, the resistojet material selection should be based on appropriate testing of a particular geometry in a relevant environment. Each part of the resistojet must satisfy a set of requirements depending on the temperature range of the particular component and on its function. In particular, the efficiency requirements for the materials could be broken down in the following two categories.

1. **Temperature requirements:** to be reliable at the temperature working point.

   Hot propellant gas is heated through the heat exchanger by an electrical heater, which could have several configurations as described in Section 1.4.1. The maximum structural temperature of the resistojet is therefore withstood by the heating element. This one maintains its position through electrical insulator elements such as collars, shoulders and others. To maximise heat exchanger efficiency, a radiation shield could be used to reflect

some of the radiated heat from the heat exchanger. Finally, a thermal insulation package could further lower the thruster casing temperature. The maximum temperature of each of the above-described components has the following hierarchy: heater, heat exchanger, electrical insulator, propellant, radiation shield, thermal insulation, casing and support.

2. **Functional requirements:** each of these components have functional requirements to satisfy in their temperature range, in particular:
   - Heater: to generate electrical heating for a lifetime on the order of thousands of heating cycles;
   - Heat exchanger: to avoid leakage of the pressurised propellant;
   - Electrical insulator: to provide electric insulation either in direct contact with the propellant or in vacuum;
   - Radiation shield: to minimise the radial radiative heat from the inner core of the thruster;
   - Thermal insulation: to minimise heat conduction from the hot core to both the thruster support and the casing;
   - Casing: to minimise the heat radiation to space;
   - Mechanical interface: to provide support satisfying the mechanical environment requirements and minimise heat conduction back to the SC.

In the following sections, the candidate high-temperature materials suitable for the HTR application are discussed.

1.4.4.1 Refractory Metals

Refractory metals are the only materials capable of both reaching the objective temperature of the HTR (in the region of 3,000 K) and having good resistivity to be used as an electrical heater. By definition, refractory metals have a melting point of over 2,000˚C and high hardness at room temperature [47]. Commonly, the strict set of refractory metals is composed of niobium (Nb), molybdenum (Mo), tantalum (Ta), tungsten (W) and rhenium (Re). A wider definition of this particular category of metals enlarges to titanium (Ti), vanadium (V), chromium (Cr), zirconium (Zr), ruthenium (Ru), rhodium (Rh), hafnium (Hf), osmium (Os) and iridium (Ir).

Table 1.15 lists these materials' melting range and electrical resistivity at ambient temperature. As can be seen, the only materials able to work in the region of 3,000 K are Ta, W, Re and Os. Ta has excellent resistance to corrosion and heat. Its main commercial use is in the compact, high-performance capacitors of electronics. W has been used with H_2 propellant by for the 3 kW thruster

in the concentric tubular heater element [18]. At that time, CVD was a new manufacturing technique allowing high-density thin tubes to be built. Tungsten metal possesses outstanding mechanical damping capability, has extremely high resistance to corrosion, good mechanical properties and excellent creep resistance. Re has been used in several resistojets, particularly using CVD to build thin-wall elements [18,31,33]. Os oxide is volatile and extremely toxic; therefore, it is rarely used in its pure state and is instead often alloyed with other metals. Refractory metals are also a good candidate for high-temperature radiation shielding. In particular, W has already been used in past high-temperature resistojets (Table 1.11).

1.4.4.2 Ultra High-Temperature Ceramics

Ultra-High Temperature Ceramics, UHTCs, are ideal for extreme applications: thermal protection for hypersonic aerospace vehicles, atmospheric re-entry vehicles, specific components for propulsion, furnace elements, and others. This family of ceramic compounds is composed of borides, carbides and nitrides of transition elements such as hafnium (Hf), zirconium (Zi), tantalum (Ta) and titanium (Ti). They have some of the highest known melting points (Table 1.16), high hardness, good chemical inertness and good resistance to oxidation in severe environments.

Table 1.15. Melting point and electrical resistivity at 20°C (* at 0°C) of refractory metals [47]**. Materials in the 3,000 K operating range are highlighted.**

Atomic Number	Symbol	Melting Point [°C]	Electrical Resistivity [μΩ·cm]
22	Ti	1,668	42.0
23	V	1,910	19.7
24	Cr	1,907	12.5
40	Zr	1,855	42.1
41	Nb	2,477	15.2*
42	Mo	2,662	5.34
44	Ru	2,334	7.1*
45	Rh	1,964	4.33*
72	Hf	2,233	33.08
73	Ta	3,017	13.15
74	W	3,422	5.28
75	Re	3,186	19.3
76	Os	3,033	8.12*
77	Ir	2,466	4.71

Historically, Russian and U.S. laboratories first investigated UHTCs between the 1950s and 1970s. Recently, there is a new interest for their application in hypersonic flight vehicles with sharp aero-surfaces, in which thermal range requirements are of 2,000–2,400°C in air with the requirement of reusability. At present, the structural materials for oxidising environments are limited to SiC- and Si_3N_4-based materials, oxide ceramics and carbon/carbon composite with thermal protection. These materials have good oxidation resistance but can only sustain temperatures up to 1,600°C, with modest lifetimes. UHTCs are a good candidate for these applications. In early studies, diborides are the most resistant to oxidation, and the first one in this particular ranking is HfB_2 followed by ZrB_2. However, the use of single-phase materials was not sufficient for high-temperature structural applications. To overcome this, many additives were evaluated to improve the resistance to oxidation, such as Nb, V, C , disilicides and SiC.

Table 1.16. Properties of some UHTCs [48].

Material	Crystal structure	Density g/cm^3	Melting temperature °C
HfC	Face-centred cubic	12.76	3,900
TaC	Cubic	14.50	3,800
ZrC	Face-centred cubic	6.56	3,400
HfN	Face-centred cubic	13.9	3,385
HfB_2	Hexagonal	11.2	3,380
ZrB_2	Hexagonal	6.1	3,245
TiB_2	Hexagonal	4.52	3,225
TiC	Cubic	4.94	3,100
TaB_2	Hexagonal	12.54	3,040
ZrN	Face-centred cubic	7.29	2,950
TiN	Face-centred cubic	5.39	2,950
TaN	Cubic	14.30	2,700
SiC	Polymorph	3.21	Dissociates at 2,545

Compared with carbides and nitrides, diborides also have higher thermal conductivity, which also gives them good thermal shock resistance and makes them ideal for some high-temperature applications. An example is the leading edge of a hypersonic wing; the high thermal conductivity lowers the thermal stress inside the component, lowering the magnitude of the thermal gradient. Furthermore, it allows the conduction of heat away from the very hot tip to other parts from which the heat is re-radiated. Finally, diboride-based UHTCs exhibit high electrical conductivity (Table 1.17), which makes Electrical Discharge Machining (EDM) manufacturing a possibility.

Borides, carbides and silicides are hard and brittle, thus requiring difficult and expensive machining. However, their very low electrical resistivity (thus high electrical conductivity) also makes EDM possible ($\rho(ZrB_2)$ = 6 to 10 μΩcm, $\rho(HfB_2)$ = 10 to 16 μΩcm, ρ(SiC) ≈ 105 μΩcm and $\rho(TaSi_2)$ = 8 to 46 μΩcm). This represents a significant advantage because EDM allows the manufacture of precise and complex shapes [48].

Table 1.17. Electrical, thermal and mechanical properties of ZrB_2 and HfB_2 [48].

Property	ZrB_2	HfB_2	Units
Young's modulus	489	480	GPa
Hardness	23	28	GPa
Coefficient of thermal expansion	5.9×10^{-6}	6.3×10^{-6}	1/K
Heat capacity at 25°C	48.2	49.5	J/(molK)
Thermal conductivity	60	104	W/(mK)
Electrical conductivity	1.0×10^{7}	9.1×10^{6}	S/m

1.4.4.3 Highly Porous Fibrous Ceramics

Fibrous ceramics with high porosity are of interest as thermal insulation because of a weaved structure that gives very low density, low thermal conductivity and reasonably high mechanical strength. Heat transfer through the porous material involves both conduction through solid and gas phases and heat radiation. Rigid silica fibrous thermal insulation has been extensively studied and used successfully on the Space Shuttle. This kind of material has been also used in 1966 on a 3 kW concentric tubular resistojet developed and tested by Marquardt Corporation and later for the J3 Oxford resistojet [18]. These thrusters are the highest-power and highest-temperature resistojets found in the literature. Its design includes a fibrous ceramic insulator made of Dynaquartz, directly in contact with the external case of the heat exchanger, followed externally by a Min-K-2000 assembly, a microporous ceramic insulator suited to lower temperatures. In [49], the authors show an experimental investigation on some fibrous ceramics, the details of which are reported in Table 1.18.

In [50], the authors showed the thermal and mechanical properties of fibrous zirconia ceramics, ZrO_2, comparing it with silica, SiO_2, which is the basic composition of Dynaquartz (Section 1.4.4.2). The particular high-porosity fibrous zirconia ceramic of this work was made by mixing a fibre slurry, followed by vacuum moulding and sintering. An additional unspecified inorganic blinder was chosen to bond the fibre together. Tests on rectangular samples (150 × 150 × 20 mm^3) showed the improved performance of the zirconia samples (with a density of ρ = 0.68 g/cm^3) compared to silica samples (ρ = 0.31 g/cm^3) with the same porosity of 89%. When the hot surface temperature was 1,200°C for 30 min, the cold-face temperatures of the 20-mm-thick zirconia and silica samples were 785°C and 850°C, respectively. Moreover, when the hot-face temperature was 1,400°C for 30 min, the cold-face temperature of the same zirconia sample was only 960°C while the silica sample cannot

practically work at this temperature (Fig. 1.16). The same authors show the beneficial effect of binder content, porosity and aerogel impregnation on the material's microstructure, on alumina and silica fibres, with a diameter range of 5–10 μm. In particular, the higher the porosity, the lower the thermal conductivity. Finally, using aerogel impregnation, in the same test reported in Fig. 1.16, the fibrous silica ceramics gained at least 100°C on the cold face, going from 870°C to 750°C. This was the result of further lowering the insulator's thermal conductivity, which at room temperature decreased from 0.049 to 0.040 W/(mK). A commercially available microporous insulation is Microtherm PROMALIGHT®-1000R. This product is typically used in industrial furnaces, glass and the ceramics industry and generally as high-temperature protection board. Its maximum operating temperature is 1,000°C and has a thermal conductivity from 0.022 W/(mK) at 200°C to 0.034 W/(mK) at 800°C [51].

Table 1.18. Characteristics of Dynaquartz, Dynaflex and Sapphire Wool insulators [49].

Property	Dynaquartz	Dynaflex	Sapphire Wool	Units
Maximum Rated Temperature	1,783	1,811	2,311	K
Density	0.1	0.13 - 0.16	0.02	gc/m^3
Fibre diameter	0.03	0.09	0.03	μm
Unidimensional shrinkage after 2 hr	1% (1,700 K)	2.9% (1,700 K)	--	-
Chemical composition	SiO_2 (99%)	SiO_2 (56.9%)	Al_2O_3 (99.5%)	-
λ(T=810 K)	0.0288	0.0346	--	W/(mK)
λ(T=1366 K)	(ΔT = 450 K)	(ΔT = 444 K)	--	W/(mK)

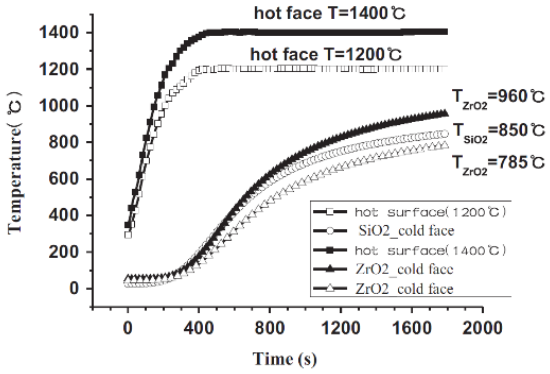

Fig. 1.16. Back temperature tests for fibrous zirconia and silica samples (hot face T = 1,473-1,673 K) [50].

1.4.5 Summary

Background material regarding the resistojet thruster performance parameters, propellant choices and efficiency breakdown has been presented. Also, this chapter provided a comprehensive literature review regarding previous research efforts on HTRs and a focus on the high-temperature materials suitable for the HTR design. The list below summarises the key points resulting from the background material analysis:

- the specific impulse of resistojets is proportional to the square root of the stagnation gas temperature;
- resistojets are compatible with almost any propellant;
- propellants with high volumetric specific impulse are the most attractive for small spacecraft;
- resistojet thruster efficiency is the product of thermal efficiency and nozzle efficiency;
- the main components of a resistojet are the heater, heat exchanger, nozzle, radiation shielding, thermal insulation and thermal spacers;
- EHT thrusters dominated the EP systems and are being today gradually substituted by higher specific impulse EP technologies;
- current Xe resistojets provide a specific impulse of 48 s;
- past high-temperature resistojets demonstrated successfully heating of the propellant to a stagnation temperature in the region of 2,500 K;
- refractory metals and ceramics are suitable materials for the construction of an HTR.

The following chapter provides the initial development of the high-temperature resistojet concept.

1.5 High-Temperature Resistojet: Investigation and Design Concept

A preliminary investigation on the design of the High-Temperature Resistojet (HTR) is here reported. In Section 1.5.1, a definition for the HTR is given, the choice of Xe as propellant is justified and the main applications are discussed. Section 1.5.2 outlines the design concept of the HTR and discusses the motivations of using metal additive manufacturing.

1.5.1 Definition and Applications

A broad definition of the HTR is given here in the context of the present research.

Definition of HTR: *a resistojet capable of raising the stagnation temperature of the propellant gas in the region of 2,500 K, with a total thruster* > 60% *and a nozzle efficiency* > 90%.

The temperature range in the definition is compatible with the maximum operating temperature of the highest-melting-point refractory metals described in Section 1.4.4. In addition, past resistojet applications showed that this temperature range is possible (see summary Table 1.6). For these reasons, it is set as a minimum objective for the HTR. The requirement on the total thruster efficiency is based on the values found in literature based on the previous high-temperature resistojet. A requirement for the nozzle efficiency is also set because a less efficient nozzle would frustrate the purpose of the high propellant stagnation temperature. This last manner is discussed in detail in Section 1.5.2.3.

1.5.1.1 Motivations of Xe as Propellant

In Section 1.4.1.2, the possible and current propellants for EP were discussed. With respect to Xe, Kr is much lighter and can produce higher specific impulse, but it has a lower ionisation degree and lower storage density. I_2 leads to a thrust efficiency similar to that of Xe and has three times its storage density. However, the main disadvantage of I_2 is that it is a reactive compound, and compatibility with the spacecraft (SC) must be guaranteed. Bismuth (Bi) is a low-cost potential propellant, which is comparable to I_2 in terms of performance and which also has a higher thrust-to-power ratio due to its higher molecular mass and high ionisation efficiency, and it is storable in solid phase like I_2. The main disadvantage of Bi, however, is that a high temperature is required to prevent condensation [52].

For the reasons mentioned above, today Xe is the main choice for EP thrusters and is particularly the most preferred propellant for Hall thrusters and ion engines. Despite the fact that I_2 may be a

real candidate for future applications [52], it is still under development. In the context of all-electric (AE) platforms, the primary EP technology drives the propellant choice of Xe, while for small platforms the high VSI of Xe makes it an attractive propellant. The latter is the main motivation of SSTL's choice to use this propellant for small platforms (Table 1.10). For these reasons, Xe is the selected propellant for the HTR development. Fig. 1.17 shows the schematic of the SSTL xenon system employed for one single resistojet. The system consists of a high-pressure solenoid valve, a flow control orifice and a plenum volume. The regulation is of the bang-bang type, which is achieved using an embedded microcontroller to operate the valves on the basis of the feedback information on the current plenum pressure measured with a pressure transducer. The HTR may use this kind of propellant feed system. It has to be noted that the prototype thruster will be tested in a laboratory environment using Ar propellant. The main reason is the excessive cost of Xe is not justifiable to conduct performance tests on a prototype model.

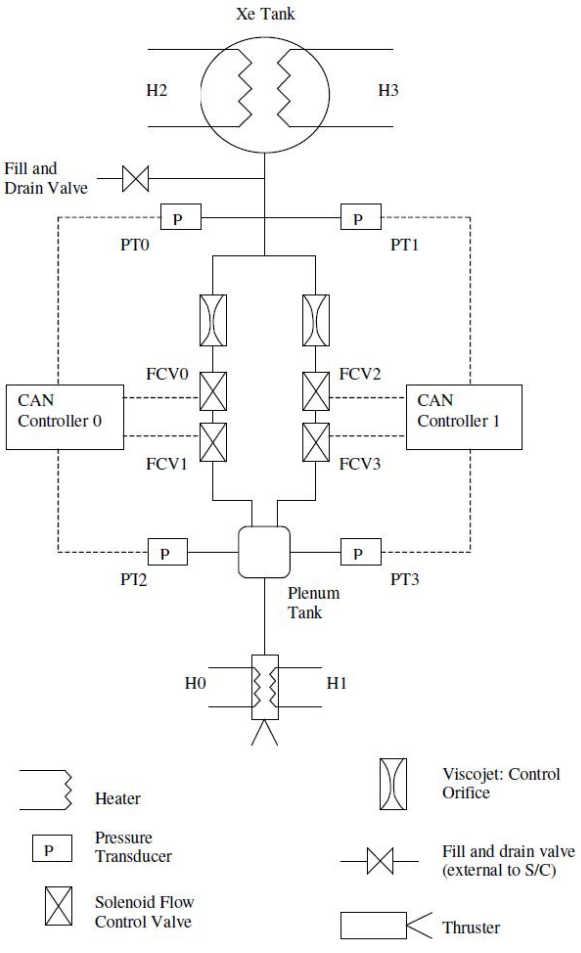

Fig. 1.17. SSTL xenon propulsion system schematic [16].

1.5.1.2 Mission Applications

Two missions would benefit from the HTR thruster. The requirements were produced within the NTSP-2 project "High Performance Xenon Resistojet" and were particularly produced by SSTL in the work package "system requirements and architecture analysis". The two applications are a LEO mission, where one HTR forms the primary propulsion system and uses the existing SSTL Xe propellant system, while the second one is a GEO mission, where a number of HTRs are used as RCS with a common Xe propellant with a primary EP system. A general overview of the requirements of the two mission scenarios is shown in Table 1.19. The listed requirements are the result of a market investigation conducted within the NSTP-2 project and no further details can be disclosed. The requirement on the specific impulse derives from the definition of the HTR. With a target I_{sp} > 80, the HTR brings important advantages, which are analysed in the following sections.

Table 1.19. HTR performance requirements for a LEO mission as primary propulsion on small satellites and for All-Electric GEO spacecraft as secondary propulsion [53].

Requirement	LEO Mission (M1)	GEO Mission (M2)
Mission	Δv manoeuvres – no pulse mode	De-spin and momentum dumping
Propellant	xenon	
Specific Impulse	> 80 s (target 100 s)	
Thrust	Single point within the range 20-50 mN	Single point within the range 50-500 mN
Total Impulse	> 23.5 kNs (target 30kNs)	> 50 kNs
Design Life	10 years in orbit life	15 years in orbit life
Average Power	< 50 W	< 150 W

Scenario 1 – LEO Mission

The advantages of using Xe propellant in small platforms come from the high VSI of this propellant (Section 1.4.1.2), which particularly suits the tight volumetric constraints of satellite with a mass on the order of 200 kg. In addition, the inert nature of Xe lowers the costs of Assembly Integration and Test (AIT) due to the elimination of hazardous mono-methyl-hydrazine (MMH) and unsymmetrical dimethyl-hydrazine (UDMH), which are commonly used for in-space chemical propulsion systems. SSTL built a long heritage on warm gas Xe resistojet as discussed in Section 1.4.2.4. The advantage of using an HTR resistojet in place of the current state-of-the-art resistojet,

for instance, the T-15 and T-30 resistojets by SSTL, is immediately clear by comparing their respective attainable increments of velocities with the same mass of propellant. Let consider as an example the DMC-3 SSTL's platform, which has a dry mass of 350 kg, a payload (p/l) mass of 100 kg and 29 kg of Xe propellant. The quantities referred to the HTR are indicated with a prime symbol. Assuming that the HTR can achieve I_{sp} = 80 s, Eq.(1.15) determines $\Delta v'$ = 49.0 m/s, compared to the original 29.4 m/s. This corresponds to a Δv increment of 67%.

$$\Delta v = g_0 I_{sp} \ln\left(\frac{m_0}{m_f}\right) \tag{1.15}$$

Alternatively, at the original Δv requirement, the HTR would introduce a propellant mass saving of 41%, where the mass of propellant needed with the HTR is reduced to 17.2 kg, as calculated from Eq.(1.16). Assuming a launch cost of about 10,000 USD per kg delivered in LEO, the saving reaches 118,000 USD. Additional savings not shown in the calculations are the reduction of tank mass, which results in further launch cost reduction, and the cost reduction of Xe propellant.

$$m_p' = (m_{dry} + m_{p/l})\left[e^{\Delta v/(g_0 I_{sp}')} - 1\right] \tag{1.16}$$

In addition, since the HTR provides a higher specific impulse, its specific power (P_{ts}/m) is higher with respect to the current SSTL resistojet. However, the total required power for the thrust range of 20–50 mN results in the region of 13.1-32.7 W in the assumption of a total thruster efficiency η_{ts} = 60%. Either the increment of Δv or the decrease in m_p are believed by SSTL to be more important than the higher specific power required. In particular, even at the higher thrust level of 50 mN, the power requirement of < 50 W is satisfied when η_{ts} > 40%, which can be easily satisfied.

Scenario 2 – All-Electric Geostationary Spacecraft

EP is increasingly substituting the on-board traditional propulsion systems, such as chemical and cold gas thrusters, in the direction of an A-E platform. The levels of EP integration are listed below:

- Level 1: station keeping
- Level 2: station keeping + orbit raising

- Level 3: station keeping + orbit raising + reaction control system = A-E spacecraft

By definition, an A-E spacecraft has a Level 3 integration of EP systems to perform all on-orbit manoeuvres, such as station-keeping (SK), orbit raising (OR) and trajectory corrections and attitude control through an EP reaction control system (RCS). The main advantages of an A-E spacecraft are:

1. A common xenon propellant, which introduces mass saving in the propellant management system and reduces complexity by using a common architecture. In addition, the risk of not using part of the mass of propellant of either the primary propulsion system or the RCS is eliminated;
2. The absence of hydrazine, which reduces the costs of Assembly Integration and Testing (AIT) and lowers the risk of regulatory changes. For instance, the current EU REACH regulation makes provision for a ban on hydrazine and chromates (an anti-corrosion substance);

The full-electric spacecraft concept was proposed by NASA in 1997 [1], who evaluated the performance of a Fakel K10K resistojet with Xe propellant to give insight to its applicability. Nowadays, ESA is also interested in developing a full electric spacecraft [54], while CNES forecasts that by 2020 more than half of all satellites will be either all-electric or combining EP with chemical propulsion [55]. Nicolini et al. proposed the use of high-temperature Xe resistojets, performing 70 s of specific impulse, for all-electric interplanetary missions, in which the HTRs performs attitude and orbital control [23]. The use of hollow cathodes to form a RCS in an all-electric platform has also been proposed [4].

Table 1.20 shows a list of the main commercial platforms employing EP for either station keeping, orbit raising or attitude control. OHB System AG provides the SmallGEO platform in two configurations, characterised by hybrid (FAST) and full-electric propulsion (FLEX), which allows for potential mission lifetime extension. In FAST, used in HAG1 mission for the first time in 2015, a bi-propellant system on-board provides the injection into geosynchronous orbit in 1-2 weeks. Final orbit transition and placement is however performed with EP. Electric propulsion is then used for all nominal station-keeping and momentum management for the entire lifetime of 15 years [56]. FLEX, also called Electra, is the first OHB all-EP platform and its first mission is planned for 2022 [57]. All propulsive tasks, station keeping and momentum management will be performed with two thrusters, with two redundant pairs mounted on two articulated EP booms [58]. Airbus uses high-

power HETs in the SpaceBus NEO platform to perform transfer and station keeping operations, enabled by a deployable thruster module assembly [59]. Thales Alenia Space (TAS) Spacebus uses a xenon propulsion module to both raise the satellite to its operational orbital position and keep it in place during its 15 years of operational lifetime [60]. Astrium and TAS developed the AlphaBus, which utilises HETs for NSSK [55]. Boeing provided the first platform using xenon ion thrusters to perform both orbit raising and NSSK manoeuvres in 2015 [54]. In particular, this is achieved with the 702SP platform and was firstly demonstrated with the ABS-3A telecommunication satellite. Lockheed Martin's used high-power HET for orbit raising for the first time with the Advanced EHF spacecraft, and is now used on the LM2100 platform [36,61].

The first single Xe propellant spacecraft was the satellite STRV 1A, which was launched in 1994 and implemented three Xe cold gas thrusters, two for spin-up and one as a backup for precession control in case of momentum wheels' failure. Also, the mission Nuclear Electric Propulsion Space Test Program (NEPSTP) was considering to implement cold gas and resistojet thruster for small attitude control of the nuclear-powered platform [1]. Resistojets are currently proposed to enable all-electric platforms, in particular, Sitael placed their XR-150 resistojet in the full electric spacecraft context [45] and Mars Space is developing a Very High Temperature Resistojet for this purpose [62]. Finally, the use of both Xe cold gas and resistojet thrusters has been tested numerically to perform fine attitude control on a GEO communication mission [3].

In summary, an A-E spacecraft uses a primary EP propulsion, such as HETs or ion engines, while a secondary EP system performs small Δv manoeuvres, such as momentum wheel desaturation, attitude control and de-spin. While the resistojet has, typically, a lower specific impulse with respect to other EP technologies (e.g. HETs), the simpler architecture and associated electronics, and the lower cost of this technology could open to new A-E solutions. Possible new solutions include using 8 to 10 HTRs to form a RCS in place of big and expensive reaction wheels. In addition, the resistojet heater failure is usually a benign failure mode, which does not prevent the thruster to operate in cold gas mode. For this reason, it can operate in cold gas redundancy for safe mode and de-spin operations.

Table 1.20. Details of main missions utilising EP for orbit raising and station-keeping.

Name	Prime	Launch mass [kg]	SC Power [kW]	Payload Mass [kg]	Duration of orbit injection	Lifetime [years]	Thruster type	No. of thrusters	F [mN]	I_{sp} [s]	P_e [kW]	Application
Hispasat AG1 - SmallGEO Fast	OHB System	3,200	>6 kW EOL	400	1-2 weeks	15	SPT-100 (HET)	8	75	1,500 s	1.6	Station keeping and momentum management
Electra - SmallGEO Flex	OHB System	3,000	10 (BOL) 8 (EOL)	600	6 months	15	SPT-140 (HET)	2 x 2	330 – 550	1,700 – 3,500	9	Orbit raising, station keeping and momentum management
Eurostar NEO	Airbus	3,000 – 7,500	7 - 25	-	-	-	(HET)	-	-	-	5	Orbit raising
SpaceBus NEO	TAS	-	16	1,400	-	-	-	-	-	-	-	-
AlphaBus Extension	Astrium/TAS	-	22	-	-	-	PPS-1350G (HET)	2x4	80 – 90	1,510 – 1,670	1.5	NSSK
702SP	Boeing	1,900 – 2,200	8	200 – 680	7-9 months	16	XIPS (GIT)	4	79	3,400	2.2	Station Keeping
									165	3,500	4.4	Orbit Transfer
Advanced EHF/LM2100	Aerojet/Lockheed Martin	2,300	20	-	-	-	BPT-4000 (HET)	-	-	-	4.5	Orbit raising

Numerical Examples of EP integration

The benefits of a Level 1 EP integration are shown in the following example. Let us consider a typical GEO satellite with a 15-year lifetime and a wet mass of 2,600 kg. Assuming a required increment of velocity for North-South Station Keeping (NSSK) of Δv =50 m/s per year, the total increment for this mission is estimated of Δv =750 m/s. Using Eq.(1.16), this would require about 585 kg of chemical propellant, which represents 23% of the spacecraft mass. Using an electric propulsion system with a specific impulse of 2,800 s (ion engine), compared to the 300 s delivered by the chemical propulsion, this would require only 70 kg of propellant. It should also be considered the mass difference by adding the EP subsystem weight and subtracting the mass of the chemical system. With an estimated launch cost of 30,000 USD/kg delivered in GEO, the potential saving in developing a Level 1 is of several USD millions [7].

Let us consider the GEO mission requirements on the HTR described in Table 1.19, where de-spin and momentum dumping manoeuvres are required in addition to RCS manoeuvres for a total impulse of I > 50 kNs. The propellant mass can be estimated from the total impulse requirement as shown by Eq.(1.17). Putting in comparison the performance of the current Xe resistojet with 48 s ISP with the 80 s ISP of the HTR, at the abovementioned launch cost estimated per kg to be delivered in GEO, with a propellant mass reduction of 43 kg the cost-saving is of about 1,300,000 USD. For this reason, the primary driver of the HTR technology is now the A-E propulsion bus.

$$m_p = \frac{I}{g_0 I_{sp}} \tag{1.17}$$

Detailed Requirements of the Two Mission Scenarios

The requirements summarised in Table 1.19 are defined in detail for the two missions in Table 1.21 and Table 1.22. For both missions, the propellant used is Xe, and the objective I_{sp} for the HTR is set to > 80 s. The requirements include the start-up duration, which is < 60 in both cases, and a maximum expected operating pressure of 4 bar, which is based on the current SSTL xenon system [16]. Present requirements are also set on the basis that ideally the HTR should be directly connected to the spacecraft bus voltage. Finally, SSTL's requirements for the two missions on which the HTR applies are based on existing platforms.

Table 1.21. Performance requirements for the LEO mission for primary propulsion on small satellites using xenon as propellant. Propulsion is used only for Δv manoeuvres – no pulse mode (based on SSTL-DMC 3 Platform) [53].

#	Sec.	Requirement	Requirement Text
1.1	Cold Gas Performance With Xe	Thrust	Single point within the range 20-50 mN
1.2		Thrust Accuracy	+/-2%
1.3		Thrust Resolution	+/-1%
1.4		Specific Impulse	> 25 s
1.5		Total Impulse	7.5 kNs
1.6		Start-up Duration	No requirement
2.1	Resistojet Performance With Xe	Thrust	Single point within the range 20-50 mN
2.2		Thrust Accuracy	+/-2%
2.3		Thrust Resolution	+/-1%
2.4		Specific Impulse	> 80 s (target 100 s)
		Minimum I-bit	No requirement
2.5		Total Impulse	> 23.5 kNs (target 30 kNs)
2.6		Start-up Duration	< 60 s
3.1	General Requirements	Operating Media	Primarily GXe, backup GKr, GAr, GN2
3.2		Heater Cycle Life	4,200
3.3		Design Life	10 years in orbit life
3.4		MEOP	4 bar
3.5		Proof Pressure	1.5 × MEOP
3.6		Burst Pressure	4 × MEOP
3.7		External Leakage (Plugged Nozzle)	< 1.0×10^{-6} sccm/s He
3.8		Mass (Excluding Valve)	< 250 g Target < 100 g
3.9		Non-operating Temperature Range	-30°C to +65°C
3.10		Thermal Dissipation (Conductive)	< 10 W (500 W/(km^2)) TBC
3.11		Average Power	< 50 W
3.12		Bus Supply Voltage	28V–33.5 V range
3.13		Peak Current Draw	< 4 A TBC
3.14		Normal Current Draw	< 2 A
3.15		Electrical Interface	-
3.16		Propellant Interface	1/8" AN (37° flare) screwed mechanical joint
3.17		Storage	Under atmospheric conditions without special precautions

Table 1.22. Performance requirements for A-E GEO spacecraft for de-spin and momentum dumping (based on SSTL GMP-T Platform) [53].

#	Sec.	Requirement	Requirement Text
1.1	Cold Gas Performance	Thrust	Single point within the range 50–500 mN
1.2		Thrust Accuracy	+/-2%
1.3		Thrust Resolution	+/-1%
1.4		Specific Impulse	> 25s, target 30 s
1.5		Total Impulse	~10 kNs
1.6		Start-up Duration	< 50 ms
2.1	Resistojet Performance	Thrust	Single point within the range 50–500 mN
2.2		Thrust Accuracy	+/-2% TBC
2.3		Thrust Resolution	+/-1% TBC
2.4		Specific Impulse	> 80 s (target 100 s)
		Minimum I-bit	0.1 mNs
2.5		Total Impulse	> 50 kNs
2.6		Start-up Duration (to full working temperature)	< 60 s
3.1	General Requirements	Operating Media	Primarily GXe, but also GKr, GAr, GN2
3.2		Heater Cycle Life	> 5,500
3.3		Design Life	15 years in orbit life
3.4		MEOP	4 bar
3.5		Proof Pressure	1.5 × MEOP
3.6		Burst Pressure	4 × MEOP
3.7		External Leakage (Plugged Nozzle)	< 1.0×10^{-6} scc/s He
3.8		Mass (Excluding Valve)	< 250 g (target < 100 g)
3.9		Non-operating Temperature Range	-30°C to +65°C
3.10		Thermal Dissipation (Conductive)	< 10 W (500 W/(km^2)) TBC
3.11		Average Power	< 150 W
3.12		Bus Supply Voltage	50 V regulated bus
3.13		Peak Current Draw	< 10 A
3.14		Normal Current Draw	< 5 A
3.15		Electrical Interface	-
3.16		Propellant Interface	Welded tube or screwed mechanical joint (AN-fitting)
3.17		Storage	Under atmospheric conditions without special precautions

1.5.2 Development of the Thruster Concept

In Section 1.5.1, the motivations of developing an HTR thruster have been explained. In this section, the HTR concept is defined and the design choices justified.

1.5.2.1 Design Objectives

The literature review on the past resistojet thrusters (Section 1.4.2), on the material used for their construction (Section 1.4.3) and on the high-temperature materials relevant for HTR development (Section 1.4.4) converge into the design of the HTR concept. For the motivations reported in Section 1.5.1.1, the HTR uses Xe as propellant. The main design drivers are:

R1. To maximise the propellant stagnation temperature that reaches the inlet of the nozzle. By definition of the thruster, T_0 must be in the region of 2,500 K;

R2. To maximise the efficiency of the nozzle to efficiently convert the propellant thermal energy into axial kinetic energy. By definition of the HTR, the requirement is $\eta_n > 90\%$;

R3. To minimise the thermal losses deriving from the radiation to space and conduction to the spacecraft through the supports;

R4. To satisfy the start-up duration requirement, t_b, which is defined as the maximum allowable time in which the thruster shall reach steady-state operation in full working temperature. In both mission scenarios, the requirement is $t_b < 60$ s;

R5. To satisfy the mission lifetime requirement, which is defined in terms of heater cycles as 4,200 for the LEO mission and > 5,500 for the GEO mission (assuming one propulsive manoeuvre per day).

As discussed in Section 1.4.1.3 the sources of inefficiency in a resistojet can be grouped into thermal losses and flow losses, defining the heat exchanger efficiency η_h and the nozzle efficiency η_n, respectively. The first group includes the radiation from the thruster casing to the space ambient and the conduction of heat back to the SC through the thruster support. The flow losses include incomplete expansion, radial flow and frozen flow losses. The latter mechanism does not apply to Xe, which is monoatomic and therefore does not present dissociation/recombination losses at high-temperature. Several methods to both maximise the propellant stagnation temperature and the total thruster efficiency have been utilised. Besides, the pressure drop across the heat exchanger is desired as little as possible. The pressure drop depends on the heat exchanger configuration and is influenced by surface roughness only if the flow is turbulent. Generally, pressure drop depends on flow regime,

flow path length, bends, bellow and all cases where the flow path encounters a change in section. Because of the high temperature and relatively low pressure at the inlet of the resistojets nozzle, it is usually characterized by a high viscous effect, which in most of the applications leads to the use of a simple conical nozzle with an angle of 15°-30°.

1.5.2.2 Super-high Temperature Additive Resistojet Concept

In this section, the design baseline and the manufacturing strategy of a HTR novel concept is given.

Additive Manufacturing to Enable a Novel Design

In the literature (Section 1.4.2), the resistojet heat exchanger design shown to provide the highest propellant temperature is the concentric regenerative type, such as the 3-kW concentric tubular, the ten-millipound and the J3 resistojets, all producing propellant temperature in the region of 2,500 K. Also the Fakel ammonia resistojet performed at high-temperature and used recirculating channels, but used a graphite heater to indirectly heat the ammonia propellant through radiative heat transfer to the flow recirculation walls. Since the objective propellant for the HTR is Xe, the best method to reach the highest propellant temperature is direct heating. With the concentric regenerative heat exchanger type, the maximum propellant temperature is the closest to the maximum structural temperature of the thruster amongst all designs. For the J3 thruster with hydrogen propellant the design offered an overall efficiency of 68.1% with an electrical power of 3 kW, reaching a gas temperature of 2,400–2,500 K. In particular, the heat exchanger efficiency was $\eta_h \approx 97.6\%$ while the main loss was due to the nozzle, with $\eta_n \approx 69.8\%$. This type of configuration has also been termed low-thermal inertia tubular resistojet for the reason that the heater, which coincides with the concentric regenerative heat exchanger, has a typically low mass. This aspect is in favour of a low star-up time as in the HTR requirements.

The concentric regenerative HE depicted in Fig. 1.18 is typically made of a heater assembly, which is attached to the outer assembly by stainless steel bellows. These ones serve to maintain pressure and also permit differential thermal expansion. These heater tubes, either in W or Re were manufactured by Chemical Vapour Deposition (CVD) (Fig. 1.19), and their assembly through strut connectors was performed with a high number of EB welds requiring close tolerances [46].

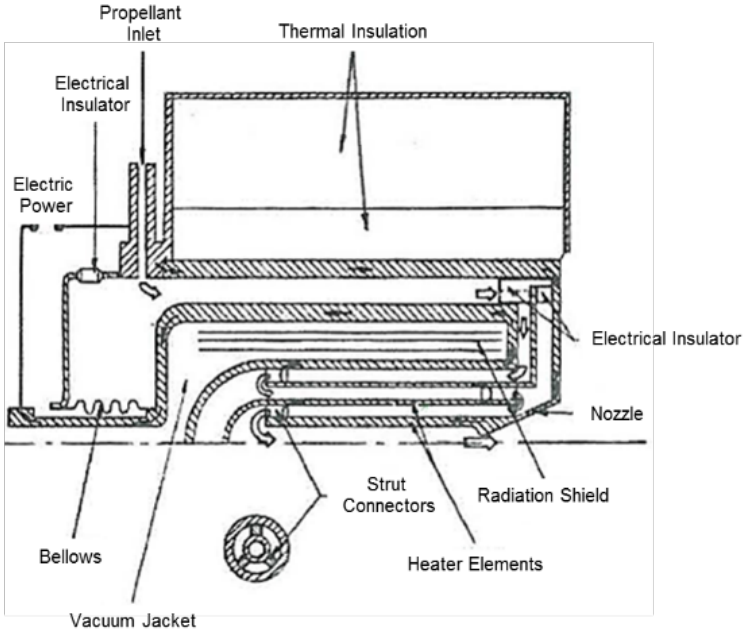

Fig. 1.18. Concentric tubular resistojet concept [63].

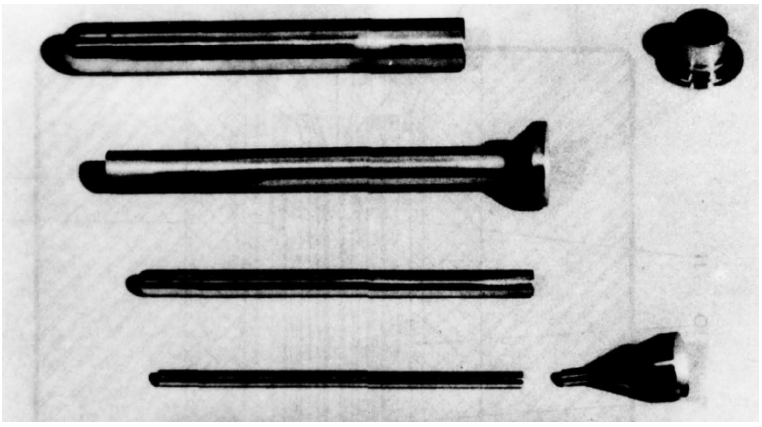

Fig. 1.19. Rhenium J3 resitojet parts made by CVD [46].

In this thesis, a novel monolithic concentric regenerative HE manufactured via metal additive manufacturing is proposed. The reason of suing AM is to enable a one components monolithic HE, which also integrates the nozzle. The main advantages of this strategy are to reduce dramatically the assembly complexity and also the cost of producing such a design. In addition, AM allows for much greater design freedom with respect to the previously adopted CVD + EB method. A specific AM manufacturing verification process was conducted to investigate the feasibility of this idea and it is presented in Chapter 2. The novel design concept is named Super-high Temperature Additive Resistojet (STAR).

STAR Assembly Preliminary Concept

The STAR assembly draft is based on the research work done with the 3-kW concentric tubular, the ten-millipound and the J3 resistojets (see Section 1.5.2), with the introduced novelty of a monolithic HE manufactured via AM. To maximise the heat exchanger efficiency, it is necessary to minimise the heat transfer from the very hot inner heater core to the outer shell of the thruster that ultimately radiates heat to space. To do so, and with reference to Fig. 1.18, a vacuum jacket is typically used to insulate the very hot walls with the cooler walls of the propellant inflow. Furthermore, a radiation heat shield (RS) is placed in it to minimise as much as possible the radiative heat transfer from the inner to the outer part of the heat exchanger. The RS is generally a third body located between two bodies exchanging heat by radiation and it usually consists of a series of thin foils wrapped around the inner core of the resistojet. A thermal insulation package (IP) further confines the heat in the interior of the thruster, of which the exterior is enfolded with a low emissivity foil (4) to reduce the radiation to space to a minimum. The propellant inlet can be either radial or axial. Finally, the support to the SC is made usually with thermal spacers consisting of ceramics sleeves. For high-temperature resistojets, the use of a RS has been found effective. The core transfers heat by radiation to the RS, which in time gains energy and rises in temperature, further radiating energy to the vacuum jacket external wall. The radiation shield confines the energy coming from the hot core and lowers the temperature of the outer part of the HE.

To evaluate the effectiveness of the RS, let assume that the surfaces behave like a grey body, such as they emit diffusely. With reference to Fig. 1.20, the components would have the following temperatures $T_{core} > T_{RS} > T_{in}$. In the assumption of infinite parallel plates, the heat flux exchange between these components, measured in W/m^2, is expressed by the Eq.(1.18) [64]. Applying it to the two cases with and without radiation shield, combining the equations, eliminating the variable T_{RS}, and considering that $q_{core \to in} = q_{core \to RS} + q_{RS \to in}$, the heat flux ratio from the core to the insulation package interior wall is derived in Eq.(1.19). In the assumptions of $\varepsilon_{core} = \varepsilon_{In} = 0.6$, Fig. 1.21 shows the trend of this relationship as function of ε_{RS}. For a refractory RS operating at 2,500 K, a surface emissivity of 0.3 can be expected in a worst-case scenario. In this case, the RS reduces the radiated heat from the core to the IP interior wall of about 70%. Finally, it has to be noted that the RS might not be relevant in a lower temperature resistojet, where the conduction of heat through the resistojet body can be a dominant heat transfer mode.

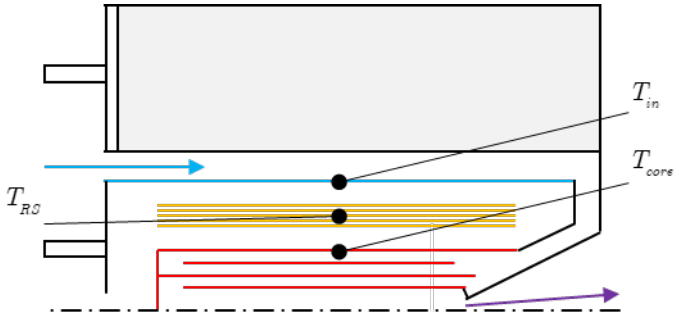

Fig. 1.20. Schematics of the radiation shielding (rs) located in the vacuum jacket to limit the heat transfer by radiation between the core and the external wall of the vacuum jacket (in).

$$q_{1\to 2} = \frac{\sigma(T_1^4 - T_2^4)}{\frac{1}{\varepsilon_1} + \frac{1}{\varepsilon_2} - 1} \tag{1.18}$$

$$\frac{q_{core\to IP}\,(\text{with shield})}{q_{core\to IP}\,(\text{without shield})} = \frac{\frac{1}{\varepsilon_{core}} + \frac{1}{\varepsilon_{IP}} - 1}{\frac{1}{\varepsilon_{core}} + \frac{2}{\varepsilon_{RS}} + \frac{1}{\varepsilon_{IP}} - 2} \tag{1.19}$$

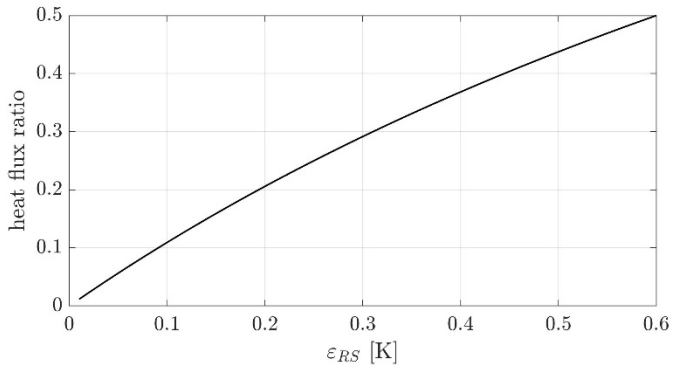

Fig. 1.21. Plot of the improvement achieved using radiation shielding placed between the RJ core and the insulation package.

1.5.2.3 Nozzle Considerations

Literature Review

Resistojets usually generate a relatively low thrust level compared to chemical rockets. In addition, they are designed to operate at low chamber pressures and have small throat dimensions. For these reasons, the Reynold numbers are low, and the viscous losses can be significant. While this effect can be lowered by shortening the nozzle and keeping the same exit area, the divergence of the exhaust

also increases, leading to divergence losses [65]. It is now well-known that for conventional resistojet high-Reynolds number conical nozzles, the optimum diverging half-angle is about 15°. However, for low Reynolds numbers, the viscous effect becomes relevant and significantly lowers the exit Mach number [66]. For these reasons, it is reasonable to increase the half-angle of the diverging section to optimise the nozzle ability to convert the thermal energy of the gas into axial kinetic energy. As confirmed from the review on the past resistojets (Section 1.4.2), the nozzle is commonly conical and has a half-angle in the range 10°-30°. This result is a trade-off between the viscosity effect of the propellant on the nozzle wall and the divergence of the outgoing flow.

There are two main parameters to take into account in the analysis, the Reynolds number and the Knudsen number. The first determines whether the flow is laminar or turbulent while the second states whether the flow can be assumed to be a continuum or it should be modelled as a rarefied gas. The Reynolds number definition is given by Eq.(1.20). where U [m/s] represents a velocity scale while L [m] a length scale. Laminar flow exists at low Reynolds numbers, where the viscous forces dominate inertial forces, damping out disturbances. Alternatively, high Reynolds numbers correspond to a flow where viscous damping is very weak, thus allowing small disturbances to grow and develop with non-linear interactions. If this number is particularly high, the flow is fully turbulent. In the pipe flow case, which can be applied to the nozzle, a flow regime is considered laminar when Re < 2,300 and turbulent when Re > 4,000. In the range between 2,100 and 4,000, the flow can be either laminar or turbulent (transition flows), depending on factors such as surface roughness and flow uniformity.

$$\mathrm{Re} = \frac{\text{inertial forces}}{\text{viscous forces}} = \frac{\rho U L}{\mu} = \frac{4\dot{m}}{\pi \mu d_t} \tag{1.20}$$

The Knudsen number definition is given by Eq.(1.21) where λ [m] is the mean free path and L [m] is the characteristic length scale. The Knudsen number can be also rewritten as a function of Re (right-hand side of the equation) and Mach number. For a low Knudsen number, the continuum mechanics can be used, but when it reaches 0.1, this assumption is no longer valid.

$$Kn = \frac{\lambda}{L} = \frac{M}{\mathrm{Re}} \sqrt{\frac{\gamma \pi}{2}} \tag{1.21}$$

In 1973, Donovan et al. [67] conducted an experimental campaign on the J3 resistojet. A nozzle efficiency of 79% was expected, but the tests determine a considerably lower efficiency of 68.1%, with a throat Reynolds number of about 2,100. In 1987, Whalen [68] investigated experimentally the performance of 15°, 20° and 25° conical nozzles, bell nozzles and trumpet nozzles using hydrogen and nitrogen at low Reynolds numbers. Although it was shown that the trumpet and 25° nozzles had a slightly higher performance at lower Reynolds numbers, it was not clear which nozzle was superior because the measurements fell into the experimental error band. In 1994, Zelesnik et al. [69] used the direct simulation Monte Carlo method on low-Reynolds-number nozzles showing that a trumpet-shaped diverging section increases the efficiency compared to a conical nozzle with stagnation temperature of about 300 K. In 1996, Hussaini and Korte [70] developed a CFD-based optimisation procedure using parabolised Navier-Stokes equations to design optimum conical and contoured axisymmetric nozzles. It was found that for a contoured nozzle, the optimum condition was with a negative nozzle angle, that is, a trumpet shape. More recently, in 2005, Ketsdever et al. [66] performed an experimental and numerical investigation on nozzle performance for very low Reynolds numbers of nozzles with a throat diameter of 1 mm. They compared Direct Simulation of Monte Carlo with experiments, finding the viscous effect dominated with throat Reynolds numbers as low as 60 and a Knudsen number of 0.1.

Calculations on the Xe HTR Case

Xe is amongst the most viscous propellants, with a viscosity at 20°C of 22.8 μPa·s compared to the 0.99 μPa·s of NH_3 or o the 0.88 μPa·s of H_2. Therefore, the low-Reynolds nozzle efficiency issue found in literature is particularly relevant to this propellant. The viscosity of Xe in μPa·s is calculated using the polynomial function Eq.(1.22) from the COMSOL material library (*Xenon [gas]*) (c_0 = -2.35601, c_1 = 9.510836, c_2 = -3.583807, c_3 = 9.891332, c_4 = -1.081838).

$$\mu_{Xe}(T) = c_0 10^{-6} + c_1 10^{-8} T^1 + c_2 10^{-11} T^2 + c_3 10^{-15} T^3 + c_4 10^{-18} T^4 \qquad (1.22)$$

The nozzle efficiency can be extrapolated from the low Reynolds nozzle experimental data produced by Whalen [68]. A logarithmic approximation of $\eta_n(\mathrm{Re}_t)$ has been derived in Eq.(1.23) from the experimental data in the cases of 15° conical half-angle, with an expansion ratio of 200:1 and with

unheated N_2 and H_2 propellants. Fig. 1.22 shows the interpolating function with a solid line and the experimental data with markers. The data points have been obtained using the free tool WebPlotDigitizer [71].

$$\eta_n = 0.063754\log(\mathrm{Re}_t) + 0.36894 \tag{1.23}$$

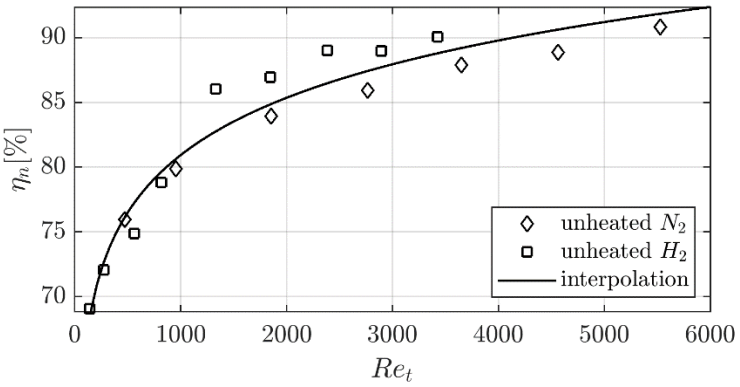

Fig. 1.22. Efficiency curve of a conical nozzle with 15° half-conical angle (solid line) and experimental data gathered from [68].

Fig. 1.23 shows the nozzle efficiency colour-map with overlaid thrust and specific impulse iso-contours calculated for nozzles with four selected throat sizes for Xe propellant at a range of stagnation temperature and mass flow rates. For each nozzle stagnation temperature and mass flow rate couple, the throat Reynolds number R_t is calculated with Eq.(1.20) (right-hand side), using the temperature-dependant viscosity expressed by Eq.(1.22). The specific impulse is then calculated using Eq.(1.9) multiplied by the nozzle efficiency, while the thrust is finally derived using Eq.(A.5). The specific impulse iso-contours would be horizontal lines if the efficiency of the nozzle was constant with Re_t. In practice instead, these lines are bended upwards at low flow rates and high temperatures. The thrust iso-contours show that, at a fixed thrust, an increase in T_0 determines a higher specific impulse and a lower required mass flow rate, as expected. However, since the Reynolds number decreases, the efficiency of the nozzle also decreases. In addition, the specific impulse iso-contours are pulled up at bigger throat sizes, as a result of a lower Re_t, hence efficiency.

The nozzle stagnation pressure p_0 can be evaluated using the choked flow Eq.(1.7). Fig. 1.24 shows the colour-map of the stagnation pressure of the nozzle with overlaid thrust and specific impulse iso-

contours. Because Xe propellant is stored in a pressurised tank, the lower the resistojet operating pressure, the better. As an example, the SSTL xenon feed system has a maximum operating thruster feed pressure of 5 bar, with a nominal feed pressure of 1 bar [16]. Depending on the requirement of the thruster pressure, the throat must be opportunely sized. Assuming the SSTL Xe system limitations, the yellow region in Fig. 1.24 corresponding to p_0 > 5 bar, represents forbidden areas for the thruster operation. The SSTL T-30 pressure diagram shows the area of its operation, ranging from 20 mN to about 50 mN of thrust, at a maximum I_{sp} of 48 s.

This analysis on the nozzle highlighted that the low-Reynolds number effect is particularly relevant for the HTR using Xe propellant. Based on the feed pressure limitations of the propellant system, the throat diameter should be selected as the lowest to maximise the pressure. In fact, a higher pressure goes towards a higher nozzle efficiency and, as a result, higher specific impulses are possible at lower stagnation temperatures. Fig. 1.21 summarises the main results of this analysis, showing the possible regions of operation of each thruster. The throat diameter necessary to maximise the operating specific impulse of HTR-M1 is of about 0.3 mm. On the other hand, for HTR-M2 to operate at the objective I_{sp} > 80 s and F = 50 mN to 500 mN, a bigger throat diameter of about 0.92 mm is required. In the HTR-M1 case, the achievable specific impulse at the same temperature of HTR-M2 thruster is lower. Similarly, HTR-M2 performs worse at the low thrust range, with a nozzle efficiency drop of 13.7%.

Table 1.23. Summary of nozzle dimensioning results in terms of stagnation and performance parameters.

Thruster	p_0 [bar]	T_0 [K]	$\dot{m}$ [mg/s]	I_{sp} [s]	F [mN]	η_n [%]
SSTL-T30	2.42	840	105.8	48.3	50	91.9
HTR-M1	2.49	2,234	33.94	70.6	20	82.4
	4.83	2,234	65.86	75.8	50	86.6
HTR-M2	4.93	2,234	632.4	80.5	500	93.9
	0.58	2,234	73.8	68.7	50	80.2
	0.64	2,727	73.84	75.1	50	79.3

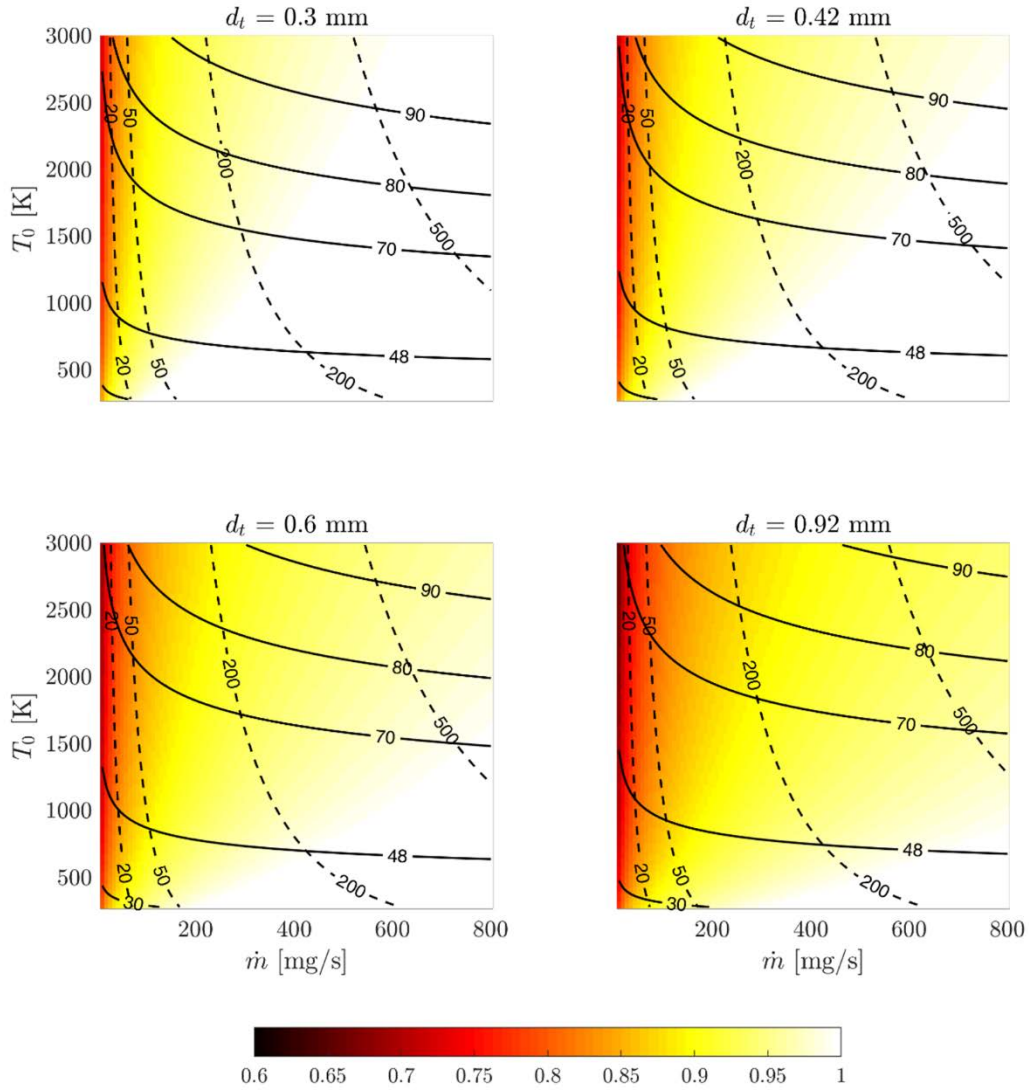

Fig. 1.23. Nozzle efficiency colour-map with overlaid nozzle performance in terms of thrust (dashed line) and specific impulse (solid line) iso-contours as a function of the mass flow rate and propellant stagnation temperature T_0. Calculations are made on four selected throat diameters d_t.

1.5.2.4 Materials for the Heat Exchanger

In Section 1.4.4.1, it was discussed that the only materials suitable for the heat exchanger were Ta, W and Re. Table 1.24 shows a comparison between these materials with the addition of a nickel-based alloy with the possibility of using it for improving the performance of existing Xe resistojets and also because they are compatible with I_2. The candidate materials for the STAR thruster are therefore Inconel 718 and pure Ta, Re and W. Parameters for comparison are the melting range of the materials, T_{melt}; the maximum operating temperature, MOT; the attainable specific impulse, I_{sp}; and the hot-to-cold specific impulse gain, $\hat{I}_{sp}$. The specific impulse is calculated using Eq.(1.9) with the assumptions of T_0 = MOT and η_n = 90%. Fig. 1.25 depicts $\hat{I}_{sp}$ as a function of the stagnation

temperature calculated using Eq.(1.24), which can be obtained with the ratio of specific impulse calculated in the cold gas (300 K) and hot gas cases. In addition, stainless steel is displayed because it is the material for the production of the thruster prototype.

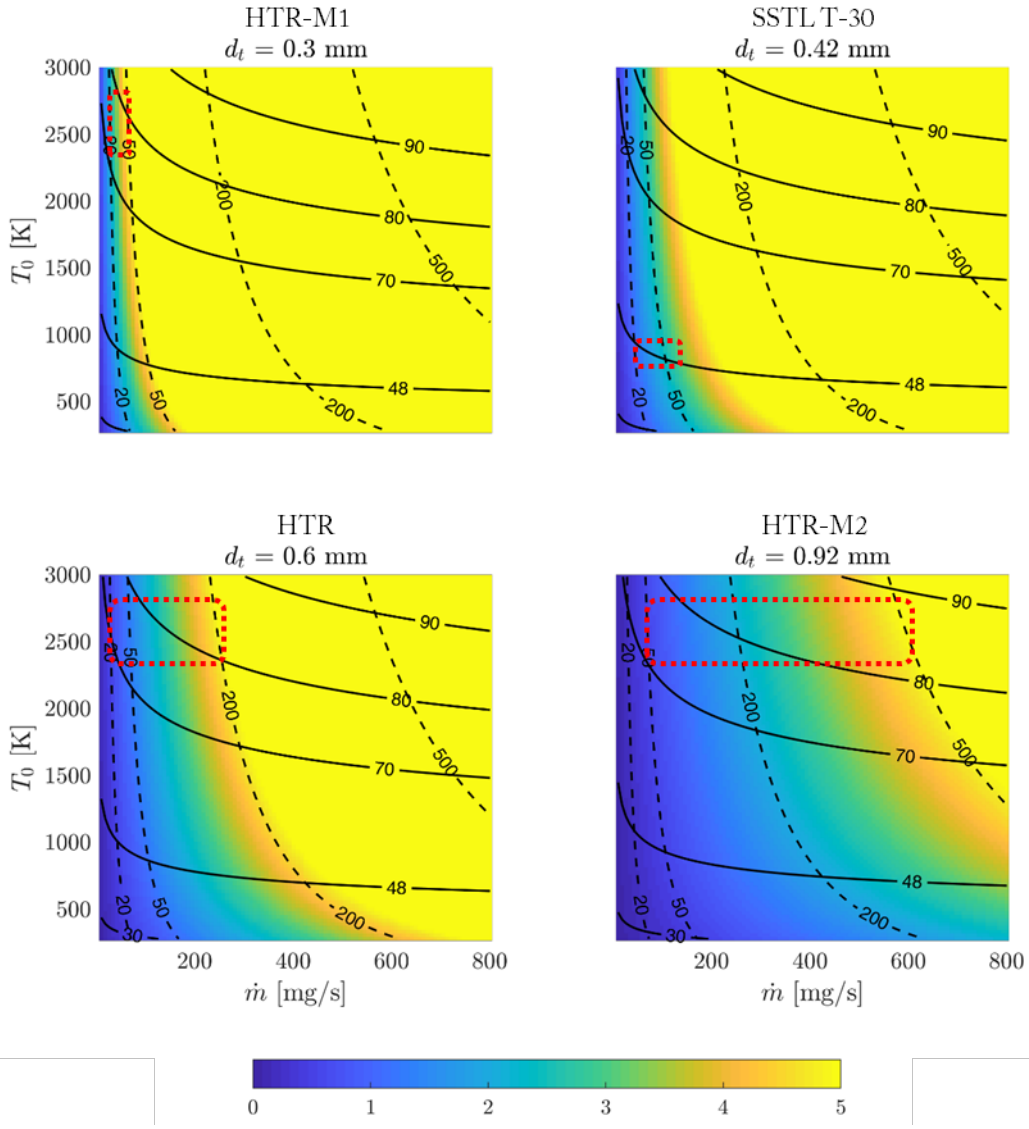

Fig. 1.24. Stagnation pressure p_0 colour-map with overlaid nozzle performance in terms of thrust (dashed line) and specific impulse (solid line) iso-contours as a function of the mass flow rate and propellant stagnation temperature T_0. Calculations are made on four selected throat diameters d_t. The area of operation of each thruster is highlighted with a dotted red box.

Table 1.24. Comparison between candidate materials for the STAR heat exchanger and attainable performance.

Parameter	Units	Inconel 718	Tantalum	Rhenium	Tungsten
T_{melt}	K	1,533 – 1,609	3,290	3,459	3,700
MOT	K	1,350	2,640	2,800	2,960
I_{sp}	s	60	84	86	89
$\hat{I}_{sp}$	%	+53	+66	+67	+68

$$\hat{I}_{sp} = 1 - \frac{\sqrt{300K}}{\sqrt{T_0}} \tag{1.24}$$

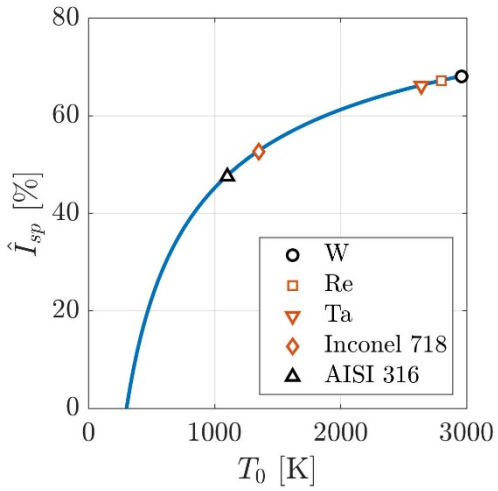

Fig. 1.25. Specific impulse gain with increasing stagnation temperature. The materials in analysis are highlighted in orange.

Fig. 1.26 shows the electrical resistance of Inconel 718 [72], Stainless Steel 316 [73], Rhenium [solid, annealed] (from COMSOL material library), tantalum and tungsten with purity above 99.9% and 99.99%, respectively [74]. Inconel alloys are high-strength and corrosion-resistant nickel-chromium materials used commonly up to 1,000 K. However, they can operate at temperatures as high as 1,350 K depending on the ambient and load conditions. Whilst this material can only develop up to 60 s specific impulse with the above assumptions, the increased electrical resistivity is attractive for the development of high-performance thruster LEO applications. In particular, a higher resistance would result in a reasonable supply voltage for a given power, which is more convenient from a power supply perspective. In addition, the resistivity of Inconel is quasi-constant with a cold-to-hot ratio

of 93%, while for Re, Ta and W, it is 16%, 13% and 6%, respectively. The high ratio avoids a current peak load at cold thruster ignition if operating at a constant voltage. Finally, Inconel is compatible with iodine propellant [14], which is a promising alternative propellant to Xe for the future of electric propulsion [11,52].

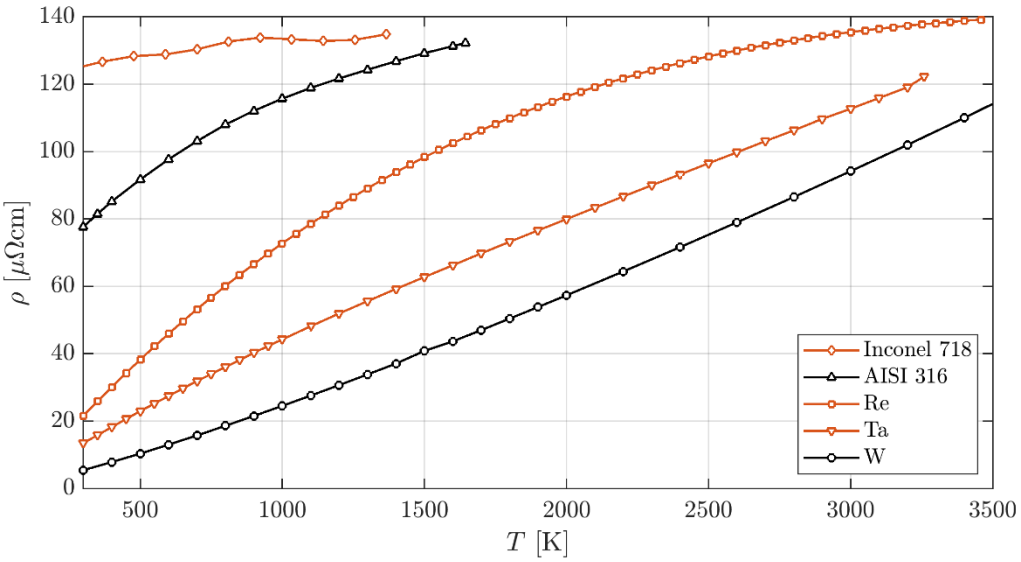

Fig. 1.26. Electrical resistivity of selected materials for the STAR resistojet heater. The materials in analysis are highlighted in orange.

Pure Ta, Re and W are the highest-melting-point refractory metals available and are therefore attractive for the STAR application. Whilst W has the highest melting point among the others, it also has a high ductile-brittle transition temperature, particularly after heating above 2,270 K, and also tends to crack during welding [46]. For this reason, pure W is eliminated as a heat exchanger material choice. Pure Re does not present these issues and has been successfully demonstrated at 2,500 K with hydrogen propellant [31,67]. Ta is another suitable material with similar operational temperature, which has excellent resistance to corrosion and heat.

For W, which is accessible at a relatively low price, Ta is an order of magnitude more costly whilst the cost of Re is one further order of magnitude. While the current numerical study considers pure Ta and Re, ultimately the STAR heat exchanger material will be in an alloy of refractory metals. In particular, commercially available alloys of interest are TaW, TaNb, MoRe and WRe. The latter is of significant interest, as Re transfers its higher electrical resistivity in alloys of W (Fig. 1.26), which is more suitable for the STAR.

In general, resistojet materials selection is also based on appropriate testing in a relevant environment. It should be noted that the maximum structural temperature of any material depends on the mechanical load and the ambient conditions. The resistojet is exposed to the vacuum space environment or pressurised inert monoatomic xenon. Xe used in electric propulsion has typically a purity of 99.9995%, with a maximum impurity of 0.1 PPM. Finally, the only load during operation is determined by the degree of thermal stress that the heating generates. For these reasons, the maximum structural temperatures selected are only an initial approximation to serve as a base of the numerical investigation conducted in the following chapter.

1.5.3 Summary

The list below summarises the key points resulting from the HTR investigation:

- a general broad definition of HTR is given;
- the advantages of Xe propellant for both LEO and GEO platforms are discussed;
- the main driver of the HTR technology is the all-electric spacecraft mission, where several HTRs perform small Δv manoeuvres;
- two real applicable mission scenarios are given as a result of the collaboration with SSTL;
- a new concentric regenerative HE design with an integrated nozzle is proposed to be built via metal additive manufacturing in a monolithic component;
- the nozzle loss mechanism at low Reynold number is highlighted and the background on this topic is discussed;
- the nozzle throat diameter dimensioning is the starting point of the HTR development;
- three materials are further investigated for their applicability to the STAR design, such as Ta, W and Re. Also, Inconel 718 is discussed because of advantageous electrical characteristics.

Metal Additive Manufacturing Investigation

2

Part of this work was published in:

Romei, F., Grubišić, A.N. and Gibbon, D. Manufacturing of a high-temperature resistojet heat exchanger by selective laser melting. Acta Astronautica, Volume 138, September 2017, Pages 356-368.

Metal Additive Manufacturing (AM) has been proposed as a manufacturing technology that enables the STAR heat exchanger concept. AM could substantially reduce assembly complexity and cost while allowing greater freedom of design. In this chapter, the first section will be dedicated to an overview of state-of-the-art metal additive manufacturing technologies, with a particular focus on Selective Laser Melting. The second section is dedicated to the Selective Laser Melting (SLM) manufacturing verification process, performed through the design, manufacturing and inspection of a series of AM components, including an iterative design process to produce the novel Super-high Temperature Additive Resistojet (STAR) heat exchanger.

2.1 Background

2.1.1 Introduction to Metal Additive Manufacturing

Additive Manufacturing (AM), also known as direct digital manufacturing, free-form manufacturing and 3-D printing, is capable of using a wide range of materials, including metals. This technology has the potential to revolutionise the manufacturing and logistics landscape. It enables the production of parts on-demand starting from a 3-D model and, at the same time, guarantees cost, energy and carbon footprint reduction. The international community is working on several aspects towards the standardisation and improvement of metal AM: machine-to-machine variability understanding and controlling, physics-based models for microstructure, properties and performance, in-situ process

monitoring techniques and the standardisation of the 3-D model data file format [75]. Fig. 2.1 shows the three main metal AM methods categorised by material feedstock: (a) powder bed system, (b) powder feed system and (c) wire feed system. In method (a), the powder bed is created by raking powder across the work area. Then, the energy source (laser or electron beam) delivers energy to the surface of the bed sintering or melting the powder into the desired layer shape. The process is repeated to create a three-dimensional shape. In method (b), the powder is conveyed through a nozzle on the surface where a laser is used to melt it locally. The work piece can be stationary while the deposition head moves or vice versa. The main advantages of this system are the ability to build larger volumes and to refurbish worn or damaged components. Finally, in method (c) the feedstock can consist of a wire, which is fused by the energy source (electron beam, laser beam or plasma arc). The main advantage of this method is the high deposition rate for large volumes. However, the wire feed system–fabricated products require more extensive post-manufacturing machining because of the lower manufacturing precision.

Compared with the powder feed and the wire feed systems, the powder bed system is the only one capable of manufacturing small components and high-resolution features (up to 100 microns) whilst maintaining dimensional control. Within the powder bed systems, a metal printer uses one of the following processes: Electron Beam Melting (EBM), Selective Laser Melting (SLM) or Direct Metal Laser Sintering (DMLS). Both EBM and SLM fully melt the powder layer into a homogeneous part using an electron beam or a laser source, respectively. On the other hand, DMLS does not heat the powder to its melting point, but it fuses the powder to a molecular level. The latter process is also used for plastic, glass and ceramic materials.

The National Institute of Standards and Technology (NIST) discussed the need for real-time monitoring and control for powder bed fusion processes [76]. Today, for high-value or mission-critical applications, such as for space, this technology is still not accepted because of the variability of quality, dimensional tolerances, surface roughness and defects. A lack of process measurement methods is highlighted, while the process control is currently based on heuristic and experimental data, which limits the improvement of the technology. For these reasons, in-process measurement and real-time control are suggested to enable closed-loop control of metal AM. Now, there is a correlation between the laser power and the melt-pool surface geometry and surface temperature. It is important to notice that researchers have found that residual stress increases for smaller build platforms.

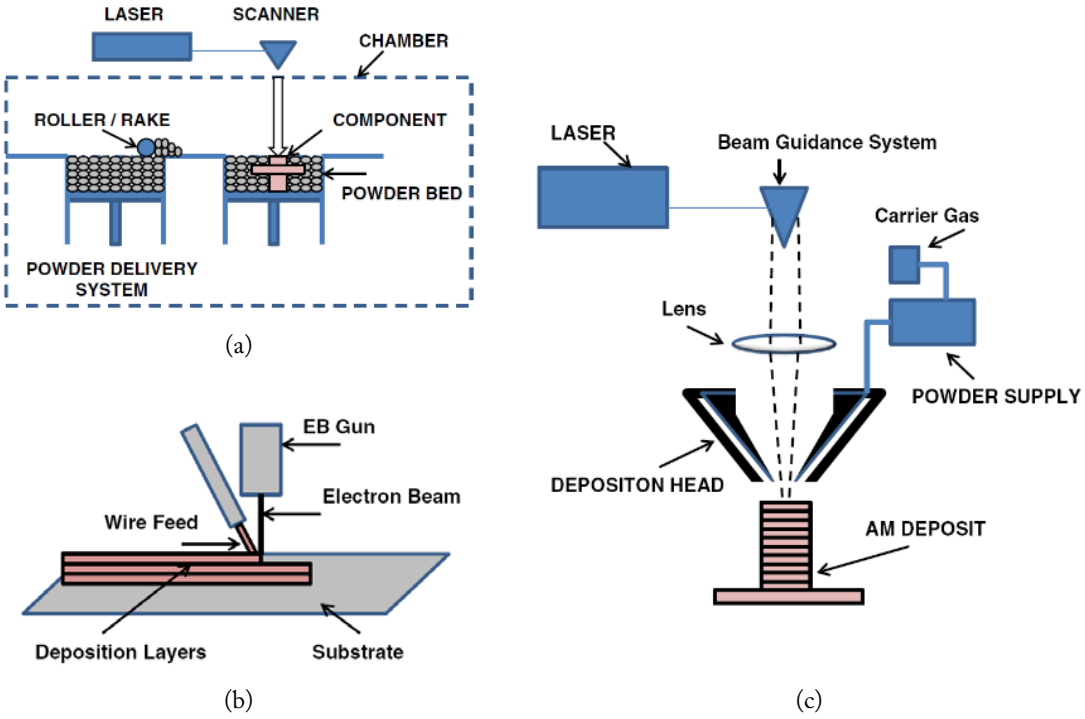

Fig. 2.1. Generic illustration of an AM powder bed system (a), an AM wire feed system (b) and an AM powder feed system (c) [75].

2.1.1.1 Selective Laser Melting

SLM machines are composed of three main units: (1) laser and scanner system (2) controller system and (3) build chamber. Fig. 2.2 shows a schematic of the main parameters involved in the SLM process: laser power, focus diameter, scan speed, hatching distance and layer thickness. Laser scanning is carried out in an inert/protective controlled atmosphere using mostly N_2 or Ar gas circulation. Unlike Selective Laser Sintering (SLS), SLM can produce very high-density parts, reaching 98%–99% of the bulk material. However, for some applications, the remaining porosity may be a significant problem. In [77] the authors illustrate how re-melting of each layer during the manufacturing process can almost eliminate the porosity, reaching a residual porosity of < 0.032% for AISI 316L, depending on the re-melting strategy adopted. The same concept is used to improve the specimen surface quality, lowering the initial surface roughness of 90%. The possibility of reducing the stair effect (when the layer marks become distinctly visible on the surface of the parts, giving the perception of a staircase) is also demonstrated.

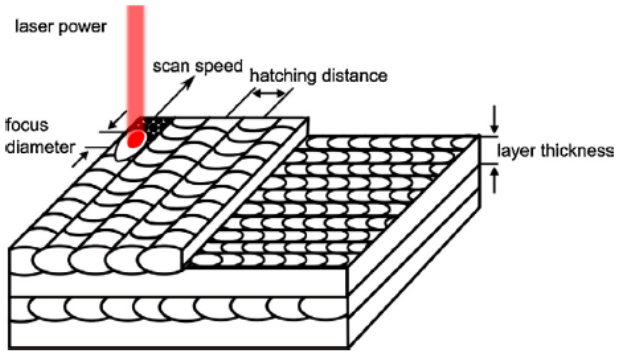

Fig. 2.2. Relevant process parameter for selective laser melting [78].

Among the metal additive manufacturing technologies, the powder bed system with the SLM process allows high-resolution features, complex and net-shaped parts, and also maintains dimensional control over the component. For this reason, it is the most suitable for the STAR fabrication because it can enable the complex thruster geometries illustrated in Section 1.5.2.2 to be produced in a single process and with the required accuracy.

2.1.1.2 Materials Available and in Development

Table 2.1 shows the Maximum Operating Temperature (MOT) of the available metal powder for powder bed systems. The following references are used: Building Success Layer by Layer [79] and EOS GmbH Electro Optical Systems [80]. The MOT for the 316L powder is not available; therefore the value from AK Steel [81] is used. It has to be considered that the reported MOT corresponds to particular conditions, such as mechanical stress (pressurised shells, vibration) or corrosive environments. For this reason, the reported MOT has a degree of uncertainty when applied to the STAR case. In particular, the STAR design has the favourable condition of operating either in vacuum (warm-up of the thruster) or with an inert and high-purity propellant gas such as Xe or Ar (during operation), which avoids any corrosion or oxidation. In addition, the heat exchanger operates at 4 bar with a low-pressure gradient across it, determining a negligible pressure load between the concentric cylinders. On the other hand, the high thermal gradient between the concentric cylinders can be subjected to significant thermal stress.

Table 2.1. Maximum Operating Temperature (MOT) for SLM materials.

Material	MOT, ˚C	Reference
Cobalt Chrome Alloy Co28Cr6Mo	1,150	BSLL
Nickel Alloy Inconel 718	980	BSLL
316L Stainless Steel	871	AK Steel
DirectSteel 20	800	EOS
15-5PH Stainless Steel	550	BSLL
Maraging Steel 1.2709	400	BSLL
DirectMetal 20	400	EOS
Titanium Alloy Ti6Al4V	350	BSLL
Commercially Pure Titanium TiCP	n/a	BSLL
Aluminium AlSi10Mg	n/a	BSLL

EOS suggests the use of Co28Cr6Mo for components with very small features such as thin walls, which require particularly high strength and/or stiffness, for instance, turbines and parts of engines. Concept Laser (CL) mentions the application of Inconel 718 for an exhaust probe, where the gas reaches a maximum temperature of 2,150˚C. CL also suggests using it for turbine applications where components are exposed at high thermal stress of up to 1,000˚C. The energy density of the laser in SLM is high enough to melt refractory materials such as Ta and produce fully dense and strong parts. The nature of the AM process, especially for melting by tracks and layers and large directional cooling rates, provides unique solidification conditions. For Ta, this results in large columnar grains formation across layers [82]. Finally, Smit Röntgen, a Philips brand, is a leading manufacturer capable of controlled pure tungsten processing via the additive manufacturing technique powder bed laser melting. In 2014 they collaborated with EOS GmbH to develop extensive know-how on pure tungsten SLM [83]. The main driver of investment in this research is healthcare, specifically to build more efficient 2-D Computed-Tomography (CT) collimators for X-ray tomography. This company currently claims the following capabilities: minimum feature size of 100 μm, minimum wall thickness of 100 μm, minimum tolerance of 25 μm, aspect ratio of 1:700 and maximum product size of 230 mm × 230 mm × 200 mm. In conclusion, both commercial and research efforts are ongoing to

standardise and generally improve SLM. For the STAR concept, the introduction of pure refractory metals (such as Ta and W) is particularly important.

Fig. 2.3. Two powder bed laser melting parts manufactured by Smit Röntgen for X-ray computed tomography applications [84].

2.1.2 Selection of Stainless Steel 316L for Prototype

The selection of a material for the prototype construction is necessary as to validate the STAR concept at moderate temperatures, while the SLM technology is moving in the direction of high-quality refractory metals, which will allow the development of an engineering model for the STAR thruster. Even though the most attractive available materials in terms of MOT are Co28Cr6Mo and Inconel 718, the only currently available metal powder at EDMC is Stainless Steel – Grade 316L. Besides, being a cheaper material compared with the former ones and having a sufficiently high MOT, 316L has been selected to manufacture a functional STAR prototype. Stainless Steel – Grade 316L represents a good choice of powder material in terms of cost, and it allows a functional prototype to be manufactured, STAR-0. Therefore, a characterisation of this AM material within the SLM appears substantial for both what concerns the microstructure and the properties because the resistojet is designed to operate at the material MOTs. This study will constitute the basis for a similar investigation on other AM materials, which will be used in the future to develop a STAR in the range of 2,500 K. Because the required materials to develop the STAR, particularly refractory metals, are currently difficult to find for SLM and are also mainly in research phase (see Section 2.1.1.2), it was natural to develop the STAR concept using stainless steel-grade 316L. This material has a nominal MOT of 871°C, it is easily machinable with conventional tools available at EDMC

and has been also used for the low-power T50 resistojet by SSTL. For this reason, the selected nozzle has same throat diameter (0.42 mm) and diverging section half-angle (14°) with the additional objective of comparing the performance of this STAR prototypal thruster with an existing T50 conventional resistojet. The name given to this prototypal thruster is STAR-0.

2.1.2.1 Metal Printer Facility

At the University of Southampton, an AM metal printer has been available since May 2015. The Concept Laser M2 Cusing uses the powder bed system with the SLM process. This technology allows high-resolution features, complex and net-shaped parts, and the maintenance of dimensional control over the component. Table 2.2 shows the main features of the machine, which has a build volume (x,y,z) = 250 mm × 250 mm × 280 mm. Fig. 2.4 shows the machine in operation while building some components for this current research project (see Fig. 2.3 for components reference) with other ones from other projects. A specialised technician (Richard Dooler, CNC programmer at EDMC) performs the disposition and arrangement of the job.

Table 2.2. M2 Cusing performance data [85].

Property	Value	Comment
Build rate [cm^3/h]	2-20	Job specific
Laser Power [W]	200	Rated
	177	Effective
	132	For support structure
Laser beam diameter [μm]	50	30 μm of beam compensation
Layer thickness [μm]	30	Read from screen during process
Scan speed [m/s]	0.8	Plane
	1	Support structure
	1.6	Inside and outside contour
	7	Max.
Hatch [mm]	5	Square islands
Gas	N_2	At 6 bars

2.1.2.2 316L Metal Powder

Stainless steel 316L represents a good choice of powder material in terms of cost, and it allows the manufacture of a functional prototype, STAR-0. Therefore, a characterisation of this AM material within SLM appears substantial for both microstructure and thermal property concerns since the resistojet is designed to operate at the material MOTs. Specifically, the material used at the Engineering Design and Manufacturing Centre (EDMC) for the Concept Laser Cusing M2 is 1.4404/316L stainless steel metal powder. The powder used has a diameter range that goes from a minimum of 9 μm to a maximum of 73 μm with an average size of 30.98 μm. Fig. 2.5 shows the volume cumulative distribution (Q_3) and distribution density (q_3) of the material used. The surface quality of the printed material is strongly dependent on the size, shape and purity of the pre-sintered powder particles, or raw material, on their direction and the packing density. Fig. 2.6 shows typical shapes captured with the JSM 6500 Scanning Electron Microscope (SEM) machine of the nCATS group at the University of Southampton. A small amount of powder was stuck on tape and positioned in the small vacuum chamber of the SEM to be scanned. Although the majority of the particle is spherical, it was possible to identify several non-perfect-shaped metal particles of an oval shape or irregular conglomerates of more particles. These can result in unideal packing of the particles and therefore affect the powder bed smoothness and flowability, generating defects, including porosity and cracks [86].

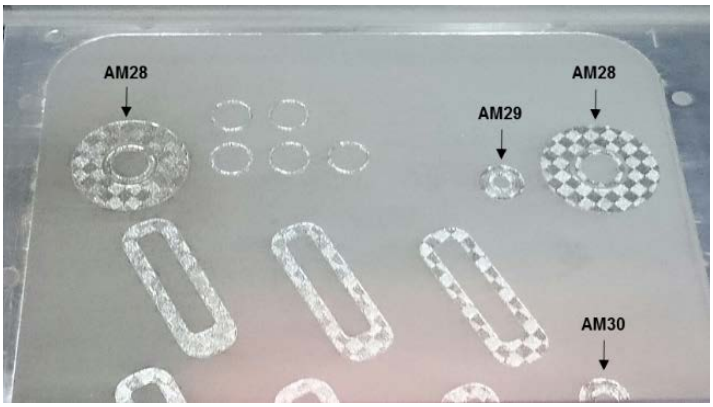

Fig. 2.4. Photo taken during the second printing session.

2.1.3 Potential Defects

The main potential defects resulting from the SLM process are material porosity, balling, residual stress and cracks. The University of Leuven (KU Leuven) is doing extensive work on SLM characterisation and has a wide range of SLM machines, including an in-house-developed printer. Kruth et al. provide a summary of the developments in SLM materials including Ta [87]. During the SLM process, porosity forms because external pressure is not applied; at the same time, only temperature gradient, capillarity forces and gravity exist. Resulting pores can be large and irregular because of the lack of complete melting, lack of powder feeding within small created passages and even spherical pores generated by trapped gas. However, by optimising the laser processing parameters (Fig. 2.2), material density can be above 99%, and for Ti6Al4V (currently the most studied material), density is well above 99.9%. Balling is a process that occurs because the molten material fails to wet the underlying substrate because of the surface tension. Balling results in irregular scan tracks with the effect of increasing the surface roughness and increasing the porosity. This process depends on wettability, which in turn depends on material properties and processing variables. Avoiding oxidation and contamination during printing limits this phenomenon.

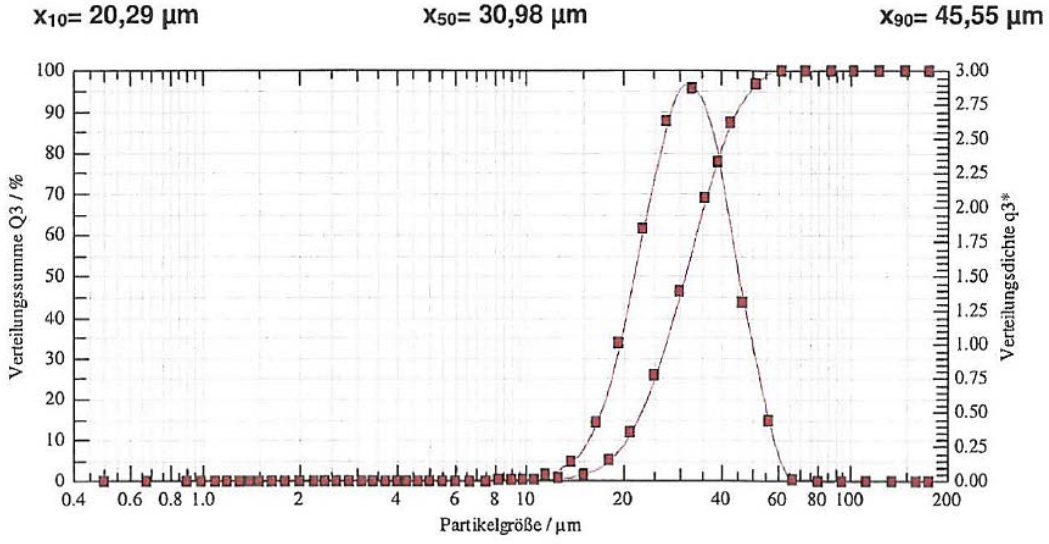

Fig. 2.5. Particle size distribution (y-axis, left: cumulative distribution, y-axis, right: distribution density, x-axis: particle diameter) [88].

All laser-based processes, including SLM, introduce a large amount of residual stress because of the high and directional thermal gradients. After cutting the printed component from the base plate, the

residual stress is partially relieved, resulting in component deformation. Generally, tensile stress accumulates on the top and the bottom of the component while compressive stress is in the centre.

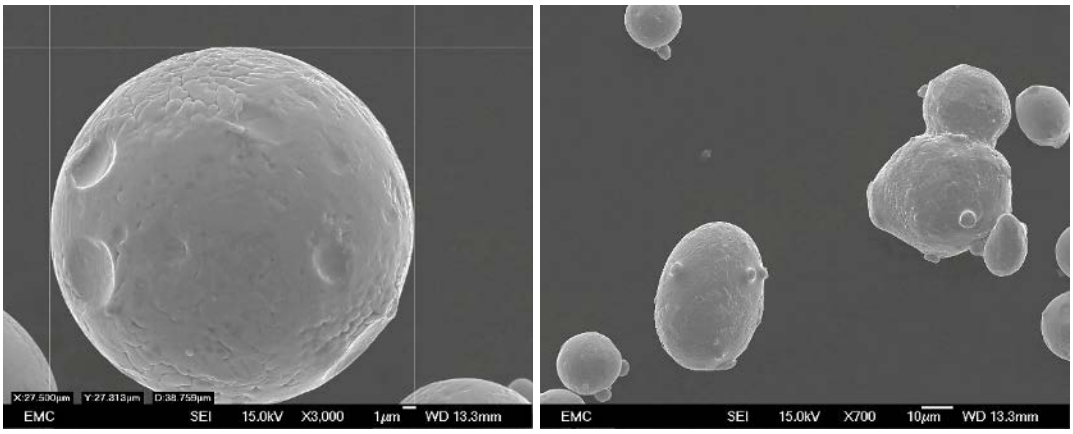

Fig. 2.6. Images of the Stainless Steel 316L powder taken with SEM. Most of the particles are spherical, but a small percentage of them are oval-shaped or a conglomerate of smaller particles.

Excessive thermal stress can cause cracks in the component. In general, alloys prone to hot cracking and solidification cracking will not be found in the SLM materials list. In addition, SLM suffers from low-quality down-facing surfaces with greater upper-surface roughness. As an example, microstructures with open porosity are used for biomedical scaffolds. The numerous powder grains are heterogeneously attached to the SLM as-printed surface and can harm the living body when released. Fig. 2.7 shows the successful removal of non-melted powder grains attached to the strut surface by a specific chemical etching.

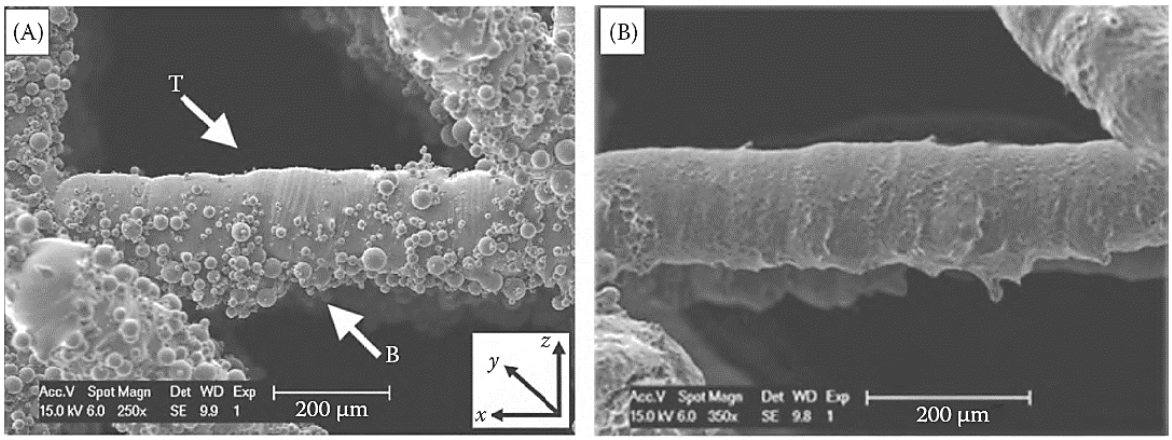

Fig. 2.7. A Ti6A14V strut (A) directly as printed and (B) after chemical etching [87].

In the last two years, three main publications treat the study of SLM parts using X-ray CT. Slotwinski et al. studied an ultrasonic in situ instrument to perform real-time measurement of the porosity during the SLM process [89]. In their paper, they used three different methods to measure the porosity of CoCr disk specimens: mass/volume, Archimedes and CT techniques. The results show good agreement, highlighting a possible application of the CT in measuring very small pores on the order of 1 μm and below. Abele et al. found correlations between the SLM manufacturing parameters, which allow for the control of the porosity of thin-wall structures [78]. They suggest that future research extend a similar analysis in a broader domain as well as study different materials. Finally, CT measurements are suggested in particular to give information about pore shape and distribution.

2.1.4 Inspection

The main objective of the PhD project is to design, build and test an HTR for an all-electric spacecraft. Within the project, X-ray computed tomography has an important role in the component and material process of characterisation. In particular, it is possible to perform non-destructive inspection of the complex geometry of STAR to access whether the printed component meets the design. NASA shows a similar process used for DMLS-manufactured subscale rocket injectors (Fig. 2.8) [90]. The same kind of process is adopted for the STAR HE iterative design process, where, through micro-CT scanning, both the component's integrity and manufacturing accuracy will be evaluated.

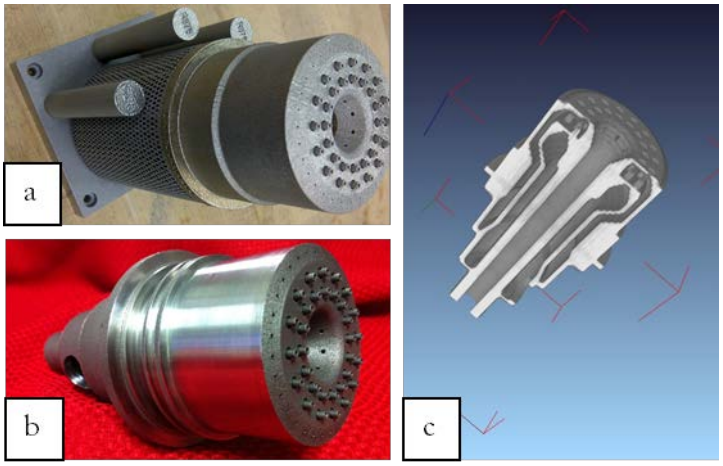

Fig. 2.8. One-piece injector as printed (a), cut from the base plate and polished (b) and computed tomography scan to ensure that the part was printed accordingly with the design [90].

2.2 SLM Manufacturing Verification

The nature of the novel HE design of the STAR concept necessitates a specific manufacturing verification process. In this section, the sub-features of the STAR design are printed and analysed for dimensional accuracy and surface characteristics. The results of this investigation are used to build up the baseline heat exchanger design.

2.2.1 Printing Strategy

The main objectives for the SLM manufacturing verification process are as follows:

1. To characterise the surface morphology and roughness of the 316L SLM components;
2. Non-destructive analysis of the printed component to achieve iteratively the desired level of accuracy for the STAR HE, determining:
    a) the dimensions' accuracy with respect to the CAD model;
    b) the optimal detail design, for example, connectors and other features;
    c) the nozzle level of accuracy;
    d) the EB welding of the SLM material;

Fig. 2.3 summarises the AM components that have been designed and produced for the SLM manufacturing verification and it also includes the HE components discussed in the next section. Fig. 2.9 shows an overview of the first print session where the 3-D printer software has automatically discarded some parts without advising the operator. The parts not printed had a minimal thickness below or equal to 100 μm. This is assumed to be the technical limit set for the CONCEPT Laser M2 machine. A total of 87 AM parts have been printed for the manufacturing verification and the HE design iterations. Technical drawings of each part, with tile corresponding to the Solidworks filename, can be found in Appendix D.

Table 2.3. Full list of designed and manufactured AM components, including brief descriptions.

Printing session	AM #	SolidWorks .SDRT {items}*	Description and Purpose
0	00	full_heat_exchanger (only HE section)	A 1.5 mm slice of the first thruster design (AM01). It was printed during the training process held by the CONCEPT Laser company at the University of Southampton.
1	01	full_heat_exchanger (half) {2}	First model of the thruster including both the heat exchanger and the nozzle to be printed. It has been EDM wire-cut at the EDMC to obtain two halves for visual inspection.
	02	full_heat_exchanger (whole)	Same as AM-01 but the whole part.
	03	elbows_150u_4	A series of elbows with different geometries. This test aims to assess which is the most suitable elbow geometry to close the bottom of each heat exchanger channel.
	04	elbows_200u_4	
	05	elbows_250u_4	
	06	elbows_300u_1	
	07	elbows_300u_2	
	08	elbows_300u_3	
	09	elbows_300u_4	
	10	elbows_300u_5	
	11	join_1_bottom {2}	Components designed to test the welding process described in Step 2-03 of the assembly process for the HPXR_V01 model.
	12	join_1_top {2}	
	13	joint_2_disk {2}	Components designed to test the welding process described in Step 4-03 of the assembly process for the HPXR_V01 model.
	14	joint_2_nozzle {2}	
	15	nozzle_10deg	A series of nozzles with all the same throat size of 0.42 mm diameter and the same inflow cylinder element size. Some nozzles have the throat hole filled with some material (ending with "full"). These nozzles will be drilled and compared with the ones printed with the throat hole in the first place. The purpose of this test is to evaluate whether the throat dimension and finish quality depend on the nozzle-diverging angle and/or on the drilling process.
	16	nozzle_14deg_full {3}	
	17	nozzle_14deg	
	18	nozzle_20deg	
	19	nozzle_30deg	
	20	nozzle_T50_full	
	21	nozzle_T50	

* When unspecified, the total number of copy printed is one.

	22	HE_v0.1_half	These are two prototypes of heat exchanger (v0.1 and v0.2) aiming to look for the best type of physical connection between the wall elements of the heat exchanger. For each one, a section has also been printed for a preliminary look at the printing result.
	23	HE_v0.1	
	24	HE_v0.2_half	
	25	HE_v0.2	
	26	walls_and_connectors_200u	These parts have been designed to establish the minimum wall thickness that the 3-D printer can reliably build. Also, another design of connectors between the heat exchanger cylinders is tested.
	27	walls_and_connectors_300u	
2	28	HE_holder_v02 {2}	This component is one of two AM components designed for STAR-0 assembly.
	29	HE_v1_part1	This component is the evolution of *HE_v0.1* in the previous printing session.
	30	HE_v1_part5	
3*	31	HE_v2.2_1	This component is one of two AM components designed for STAR-0 assembly. It is the evolution of *HE_v1* in the previous printing session. These components aim to solve the problems encountered in the previous version of the thruster, which have been highlighted by a CT scan inspection.
	32	HE_v2.2_2	
	33	HE_v2.2_3	
	34	HE_v2.1_1	
	35	HE_v2.1_2	
	36	HE_v2.1_3	
	37	HE_holder_v02 {3}	Re-printing because of deposition blade failure.
4	38	HE_v3.1 {3}	Last iteration of HE design, successfully printed.
	39	HE_v3.1_half {3}	Last iteration of HE design in half section.
	40	HE_v3.2 {3}	Last iteration of the HE design, successfully printed.
	41	HE_v3.2_half {3}	Last iteration of HE design in half section.

2.2.2 Dimensional Accuracy

In this section, the general features of the printed components are inspected with an optical microscope. The main optical microscope used for this measurement is the Olympus BX51 with 5 to 100 times magnification. On a few occasions, Wild Microscope M420 was used because it allows

* This printing session is going to be completed the first week of July 2016.

for larger images even if it does not provide a digital measurement. Both the optical units are located at the nCATS research group. When not specified in the images, the microscope used is the BX51.

Fig. 2.9. First printing session: CAD (top) and real (bottom) overview.

2.2.2.1 Wall Thickness Tests

AM-00 is one of the first parts that have been printed with the Concept Laser M2 Cusing at the EDMC. It has been printed by the university technical staff during their first training held by the company. AM-00 is a sliced volume of about 4 mm of the first AM-01 design of the heat exchanger. The technical staff decided to print only a portion of AM-01 because it was unclear whether the machine would have been able to print the thin walls and connectors properly. The minimum wall thickness has been designed to be 300 μm. Fig. 2.10 shows the top (left) and bottom (right) views of the base plate plane. The top surface has been manually polished while the other side shows the

required patterned extra-material to build the part a few millimetres above the printer base plate to allow post-production separation through EDM wire-cut (right).

Fig. 2.10. AM-00 top view (left) and bottom view (right) with respect to the printer base plate (Wild Microscope M420).

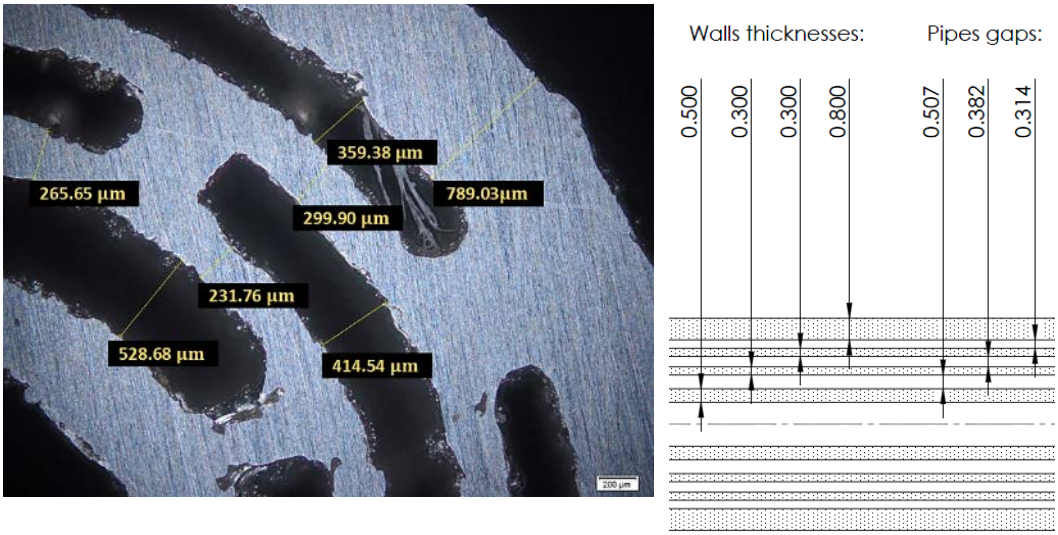

Fig. 2.11. Microscope image of the AM-00 heat exchanger element after manual polishing (left) and the design dimensions of the wall gaps and thicknesses in mm (right) (Olympus BX51).

Fig. 2.11-a shows the measurement of the wall thickness of AM-00 (left) and the design values (right). These early measurements showed that the M2 Cusing can build a section of the STAR heat exchanger design using 316L with a certain degree of accuracy. Fig. 2.12 shows the flat polished surface of the wall-thickness-test component AM-26, having a nominal wall thickness of 200 µm. A closer look (see Fig. 2.12-b) highlights zones where the walls show possible holes interconnecting either sides. However, it became apparent that those features are, most probably, not holes. In fact, this and other AM components have been printed as a half section and then have been polished.

Because in SLM a net surface is usually relatively rough and irregular, the manual polishing was not sufficient to show an actual cross-section of the component. Nevertheless, the vertically printed wall surface is quite irregular.

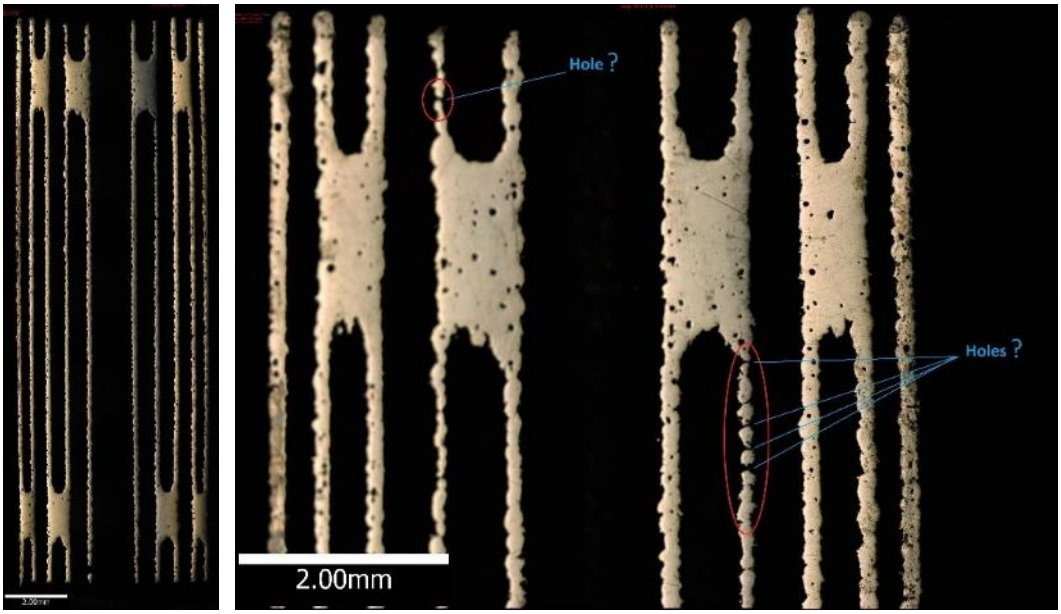

(a) (b)

Fig. 2.12. AM-26 component front overview (a) and detailed view (b) of the top part. Hypothetical holes are circled in red (Alicona InfiniteFocus).

2.2.2.2 Microscope Measurements on AM-01

The first trial of the additively manufactured concentric tubular design has been printed in two copies: AM-01 and AM-02. Although they are supposed to be identical, a difference in throat size is noticeable by eye, since one of the two looked blocked. In this section, one of the two halves, resulting from the EDM wire cut on AM-01, is analysed (Fig. 2.14). Fig. 2.13 shows the print direction and the build angle, β, and the overhang angle, α.

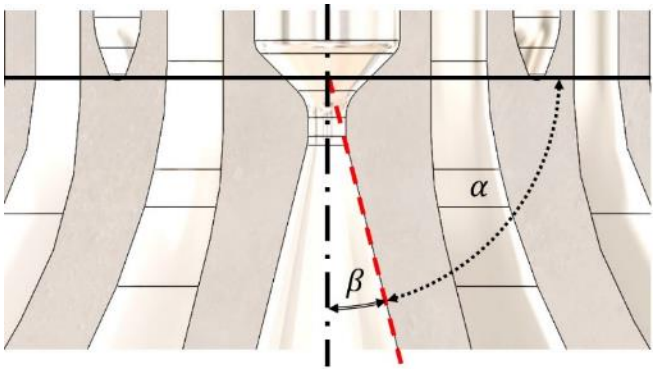

Fig. 2.13. Build angle (α) and overhang angle (β). The sum of the two angles is 90°.

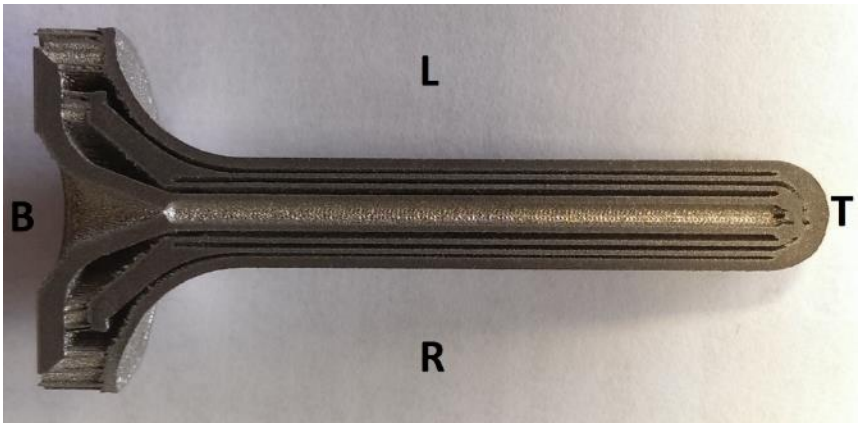

Fig. 2.14. AM-01 (half 2) overview, the printing direction in the SLM process was from bottom (B) to the top (T). At the bottom part, it is possible to see the extra-material necessary to sustain the flat walls, which are suspended in the CAD design.

Fig. 2.15 shows a microscope image of the B-L area of AM-01. The design angle between the two walls, highlighted in green in the picture, is 22.76°. Microscope measurements indicate a slightly larger divergence angle (+1.07°). However, it is difficult to take a precise measurement with such heavy wall roughness. In this case, a series of protrusions exist along the upper wall of the image. For the printing direction, this wall has a design angle of 42.76° (where the total conic angle is 85.52°). With this printing angle and this particular geometry, the resulting flatness of the upper surface is particularly poor. The material conglomerates have an orthogonal direction from the reference wall (green line) of nearly 400 μm. In this specific part of the heat exchanger, these protrusions could present a problem in terms of short circuit contact between the walls, and these manufacturing features resulting from the SLM process have to be considered when the wall gap is relatively small.

Fig. 2.16 shows the same features appearing on the outer wall of the B-L area. It is clear that these protrusions only arise on the bottom surface of an inclined wall whereas the upper surface of the same wall appears much smoother, or at least without these irregular features. The wall pictured in this figure is a revolved circular arc forming a trumpet shape. Its design thickness is 800 μm. The angle to the printing direction is approximately 60°. However, the protrusions' average length is similar to the previous case where the manufacturing angle was 40°. This fact suggests that these features start to form from a particular printing angle. Once again, it is difficult to take measurements when these features occur. The wall thickness is nearly the design thickness; however, there are locations where, because of the bottom surface irregularity, the local thickness reaches approximately 660 μm, which is about 83% of the design value.

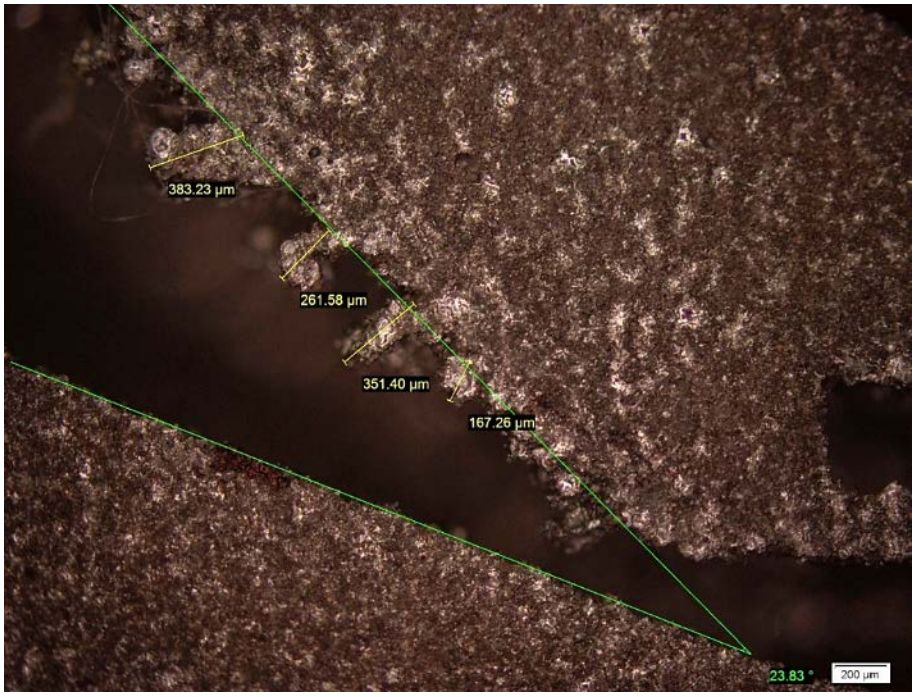

Fig. 2.15. BL area between the nozzle wall and the next one (Olympus BX51 microscope).

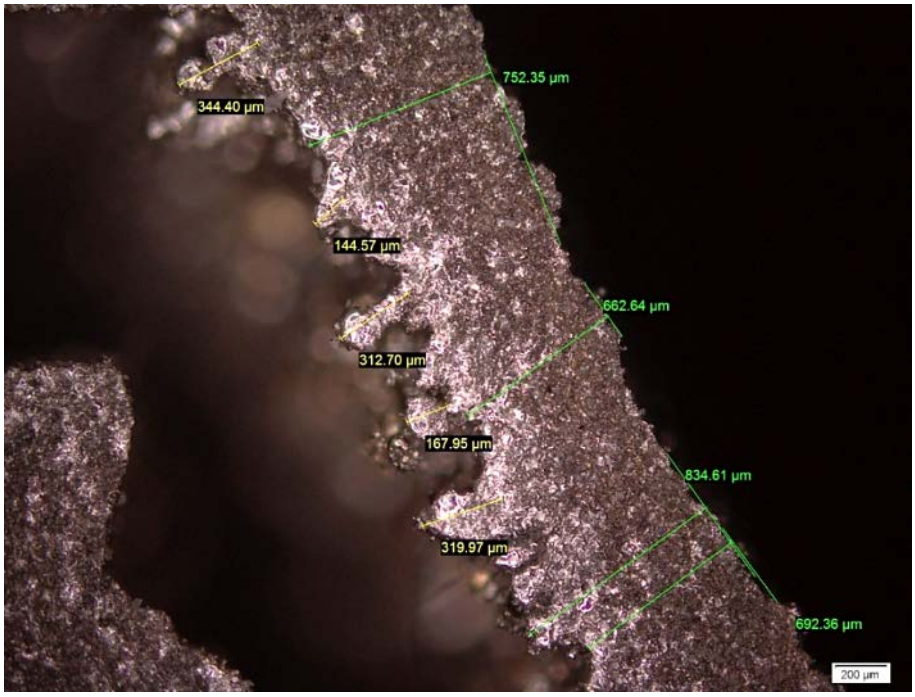

Fig. 2.16. B-L area between the outer wall and the middle wall.

Fig. 2.17 shows the structure of the extra support column material added in the manufacturing process to build suspended parts of the component. This supporting material design is implemented in the CAD design preparation process of the AM by the printer build software. The user selects this within a range of possible geometries, which typically consist of a regular polygon honeycomb-pattern extruded vertically. The figure shows that these structures have a wall thickness between 100 and 300 microns. This shows the ability of the printer to produce 100-micron standing wall thicknesses although it does not allow for reaching such thickness for the component features. The nozzle area is shown with relevant measurements in Fig. 2.18. The inner cylinder design diameter is 1.626 mm; the conical half-angle of the inlet is 60° while the divergent section half-angle is 20°. From the measurements, the divergent angle of the component is within 1° of the design value, while the inlet section angle (measuring approximately 127.5°) is approximately 7.5° wider. The throat is excessively irregular to be measured and may have been worsened by the throat design, which did not consider a cylindrical throat section.

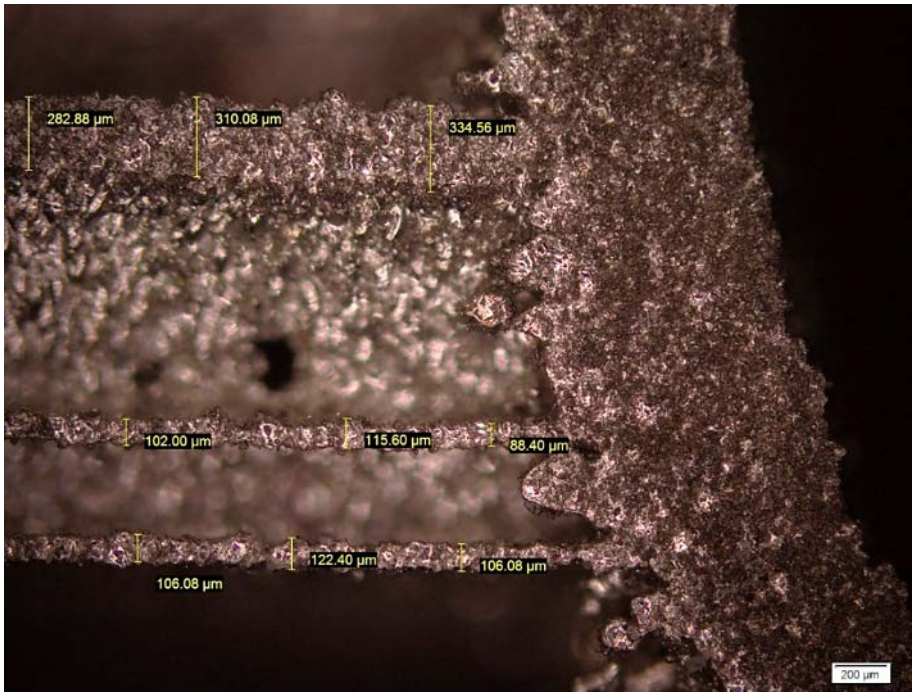

Fig. 2.17. B-L area, particularly of the extra-material added to support the suspended walls of the AM-01 part.

Fig. 2.19 shows the wall's thickness (yellow) and gap (green) measurements on an AM-01 heat exchanger section. The dimensions can be compared with the design drawing (Fig. 2.11). The accuracy of the measurements is proportional to the focus of the microscope image. Moreover, the AM-01 sections have been obtained by wire-cutting the whole component; therefore, the central axis of the component could be slightly off the cutting plane. The surface roughness is of particular interest for what concerns both the heat exchanger and the diverging nozzle. Fig. 2.20 shows that a 316L-SLM surface is typically composed of scattered circular elements of differing radius. This structure is analysed more in detail in the next section using an SEM and optical surface metrology. It will be shown that these circular elements are fused powder particles.

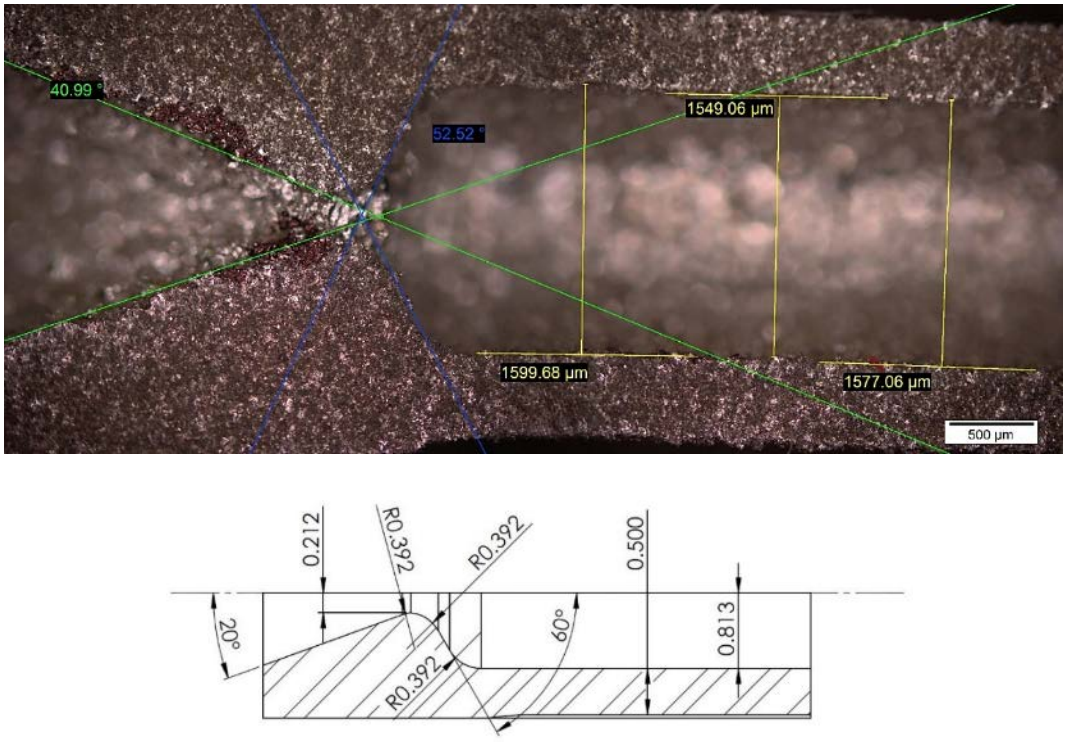

Fig. 2.18. View of the nozzle area and the inner channel with measurements (top) and drawing detail (bottom).

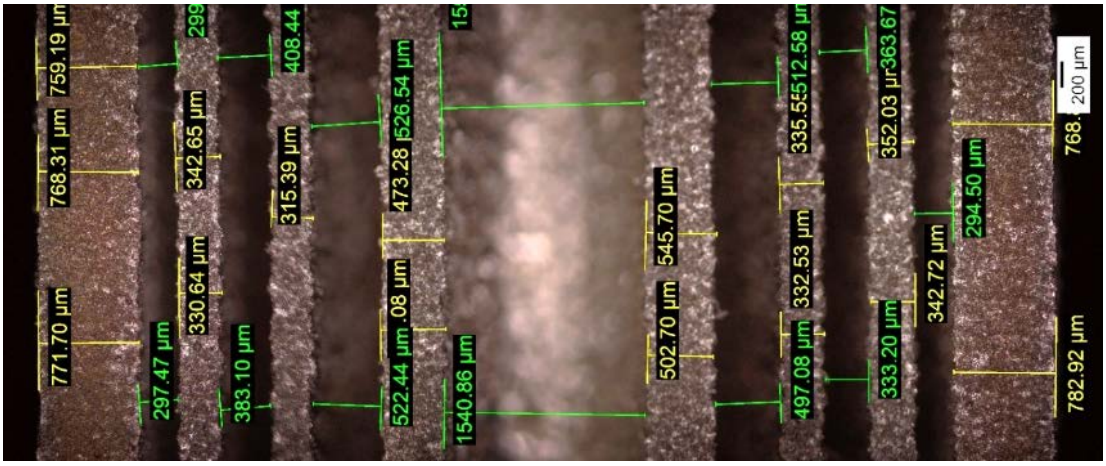

Fig. 2.19. Central detail of the AM01 heat exchanger walls with measurements.

In conclusion, this first version of the heat exchanger was an attempt to build a single-piece component to gain specific know-how of STAR design and manufacture. The primary finding of the initial test was that the build angle is critical in maintaining a good-quality surface. Any manufacturing of features in the plane of the printing process is compromised unless the features' build angle is shallow. Based on the lessons learned from this exercise, the build angles have been

optimised in the next iteration of the heat exchanger design (AM22-25) to allow for a higher-quality production.

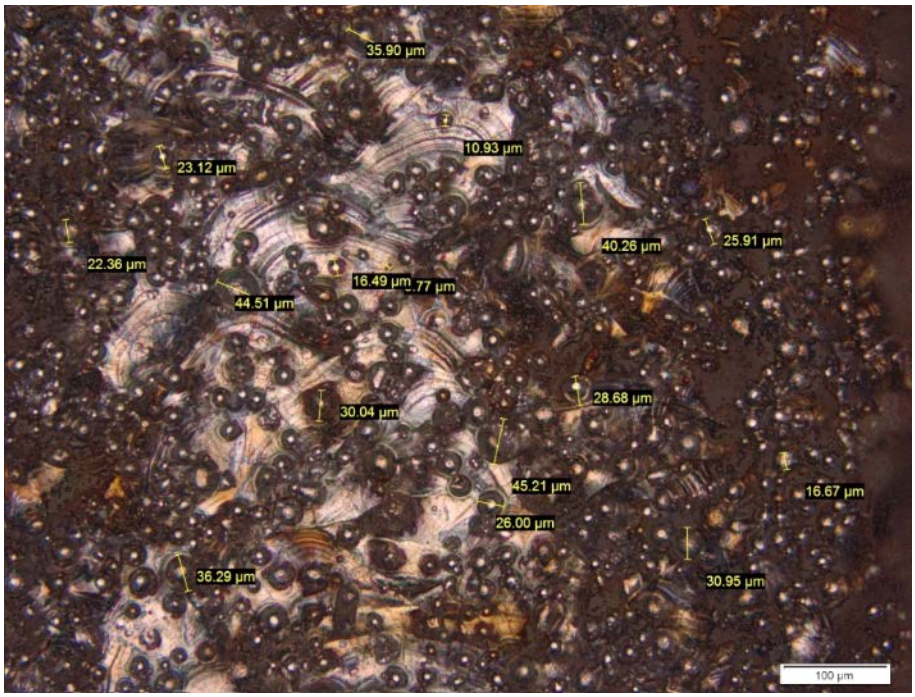

Fig. 2.20. Detailed inner channel of AM-24, with measurement of the spot's surface area.

2.2.2.3 Elbows

The elbows refer to the region at the rear of the heat exchanger, which forms a near hemisphere as the cylindrical flow paths form a closed-end. This test served to compare the AM manufacturing result on different elbow geometries, particularly to envisage the possible range of angles applicable to different wall thicknesses. Through qualitative inspection, it was assessed that going from a sharp and long cone to a hemispherical elbow, the bottom surface (see the print direction from Fig. 2.9) becomes more irregular and rougher.

Fig. 2.21. Set of printed heat exchanger elbows AM-03- to AM-10.

2.2.2.4 Nozzle

It is known that it is not possible to print a perfect small hole positioned orthogonally to the print area. The printer is much more accurate in printing holes when in-plane with the printing area. However, in the nozzle case, the throat hole is built on a cone with a particular angle. This implies that the throat and cone diameter may be less controlled for larger cone angles. To validate this, it is necessary to print several nozzles with different angles and find a correlation between throat precision and this angle. The EDMC M2 Cusing machine has been previously used to manufacture a nozzle with a throat diameter of 0.6 mm (a project supervised by Dr Graham Roberts). The subsequent measurements gave an effective diameter of 0.8 mm. In addition, the surface roughness was considered to be unacceptable. One way to obtain a precise throat diameter is to drill out a plugged or partially plugged nozzle. Therefore, it was necessary to discover the best ways to achieve this, using either a CNC machine or other manufacturing processes. The objective of these tests is to find the limits of AM manufacturing in terms of throat size accuracy and diverging section surface roughness. From a first iteration, it was clear that it was not possible to produce an AM resistojet prototype directly with both the required throat size and an acceptable surface finish on the diverging section. The following discussion is made on the seven nozzles designed with a throat hole. Fig. 2.22 shows the typical nozzle to microscope setup used for the inspection.

All nozzles have a throat diameter of 0.42 mm. Therefore, the design throat area is 138,544 μm^2. Fig. 2.23 shows a collection of images of the studied nozzle throat. These images show no strong correlation between throat dimension regularity and nozzle diverging angle (in the figures caption, it is indicated the half-angle). The nozzle area is always less than the designed one. Moreover, the throat perimeter is very irregular, which if operated could cause flow asymmetries and thus a performance drop. The protrusions do not seem to be directly correlated with either the nozzle

geometry or the half-angle of the diverging section. As a consequence, it is necessary to machine the throat to obtain a more accurate circular section and a good surface finish on the diverging section. In conclusion, as-printed nozzles do not provide the required accuracy both in the morphology and dimensions and in terms of surface roughness (visibly rough). For these reasons, the nozzle will be drilled and the diverging section polished manually.

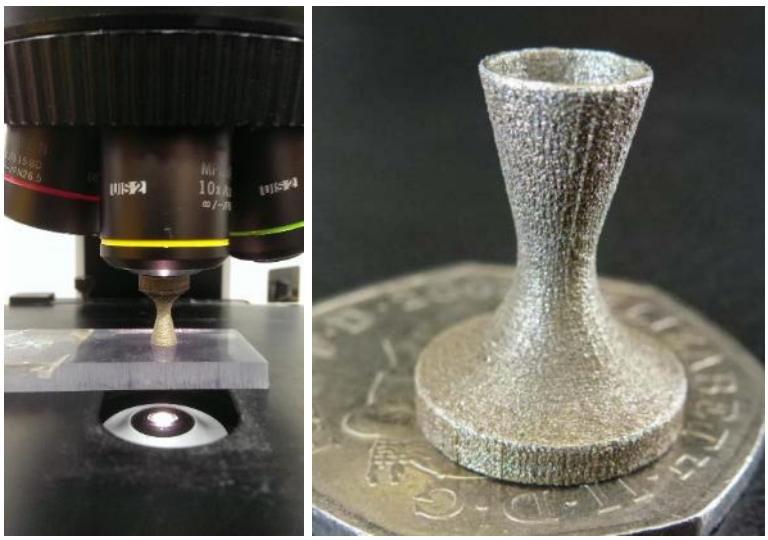

Fig. 2.22. Throat profile measurement setup with Olympus BX51 (left) and one of the nozzles analysed (AM-21, right).

2.2.3 Surface Characterisation

As part of component characterisation, surface roughness represents an important parameter for potentially both heat transfer and pressure drop evaluations. Higher surface roughness of the heat exchanger walls implies a higher wet surface area. This may increase the heat transfer effectiveness in both laminar and turbulent flow regimes. In addition, for turbulent flow, the friction factor increases with the surface roughness, resulting in a larger pressure drop. Alicona Infinite Focus is used for 3-D surface profilometry, which is obtained by applying a vertical interferometer technique to acquire both surface roughness and 3-D topography characterisation. Moreover, the JSM 6500 Scanning Electron Microscope (SEM) is used to investigate the surface morphology. Both instruments belong to the nCATS research group.

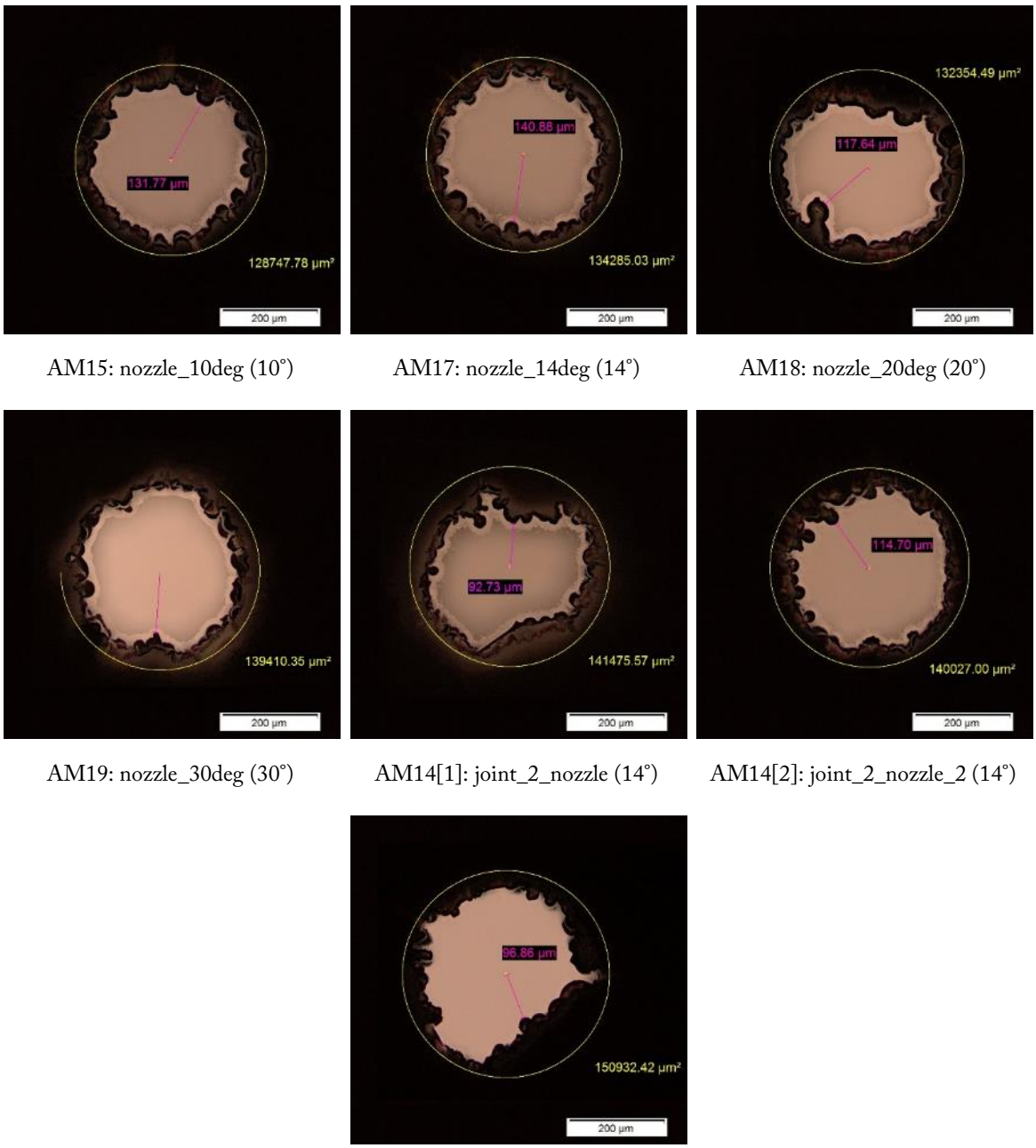

AM15: nozzle_10deg (10°) AM17: nozzle_14deg (14°) AM18: nozzle_20deg (20°)

AM19: nozzle_30deg (30°) AM14[1]: joint_2_nozzle (14°) AM14[2]: joint_2_nozzle_2 (14°)

AM21: nozzle_T50 (14°)

Fig. 2.23. Nozzle throat as-printed morphology with measurements, half-angle of the diverging section in parenthesis. Yellow: circle area, purple: minimal distance from centre to bigger protrusion (Olympus BX51).

2.2.3.1 Preliminary Surface Roughness Characterisation

Alicona InfiniteFocus uses a focus-variation technique to obtain 3-D images of surfaces. For the 3-D scanning of the images shown below, the settings used are 1 µm for the vertical resolution (depth), and 3 µm for the lateral resolution. Fig. 2.25 shows a 3-D image of an AM-26 surface section taken in the centre. As the SEM analysis will show in Section 2.2.3.3, it is possible to detect the macro-features either having spherical-cap or dune shapes. Then, the surface is scattered with smaller dots,

which will be demonstrated to be powder particles partially fused on the solid surface. It is possible to use 3-D surface profilometry (Alicona Infinite Focus) applying a vertical interferometer technique to obtain both surface roughness and 3-D topography characterisation.

Nevertheless, this scanning technique cannot visualise the true geometry of the 3-D surface because it is performed from the top, without the ability to see the shadowed areas. Assuming a spherical particle of radius *R*, with a penetration *h* into the surface and a radius of the contact area *a*, the maximum relative error of the measured to the real area, given by Eq.(2.1), is of -1.37%. The error is null both when the particle is half-melted and when it is in contact on a single point with the surface. This estimate does not take into account a particle observed on an inclined plane.

$$e = \frac{4R^2}{4R^2 - (a^2 + h^2) + 2ah} \tag{2.1}$$

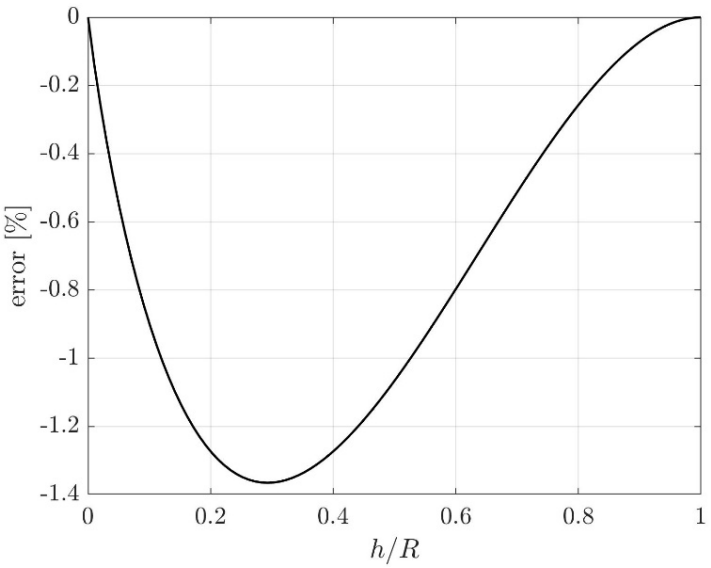

Fig. 2.24. Relative surface error of a spherical particle observed from the top as a function of the penetration *h*.

The surface roughness measurement is done the following way:

1. Measuring the 3-D data;
2. Removing the form of the 3-D data to get the surface average roughness S_a;
3. Calculating the parameters from the roughness data.

When the sample is taken from a cylinder element, the form to remove is cylindrical, while in the case of a nozzle, it is conical. The software automatically calculates the form that best fits the sampled area. In this phase, it is necessary to ensure that the calculated cylindrical or conical surface has the expected dimensions. Fig. 2.26 shows the form-removed result in Fig. 2.25's 3-D data. The surface roughness of the inner cylinder element of AM-26 results in about S_a = 15 µm, which is equivalent to ISO Grade N10. The roughness increases to about 20 µm in the diverging section of the nozzle, which has a conical angle of 28°. The real surface, compared to the ideal smooth cylinder surface, is about 70% larger in surface area, which may have a significant increase in heat exchange effectiveness between walls and propellant and could result in a lower required heat exchanger length. As previously discussed, this also increases potentially the pressure drop. Finally, Fig. 2.27 shows a 3-D data set of the AM-22 throat region. The flat surface of the section has not been polished and is not considered for this discussion. Instead, it is clear from the image that the throat accuracy is extremely poor and not sufficient. This fact was already visible by the previously shown microscope nozzle sections.

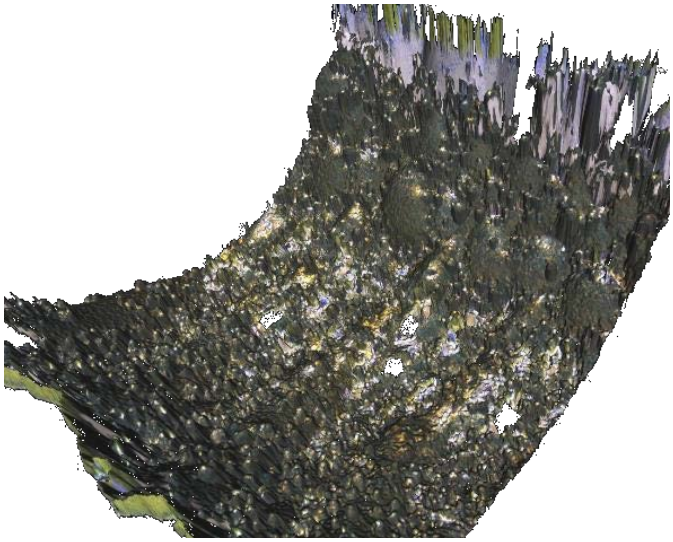

Fig. 2.25. 3-D surface scan of an AM-26 inner cylinder sector (Alicona – Infinite Focus).

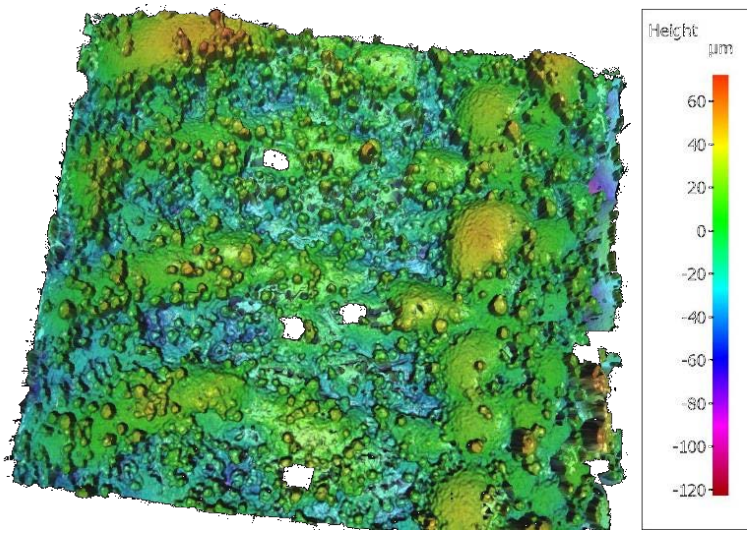

Fig. 2.26. Form-removed 3-D surface scan of an AM-26 inner cylinder sector showing the surface height in microns (Alicona InfiniteFocus, 10x objective).

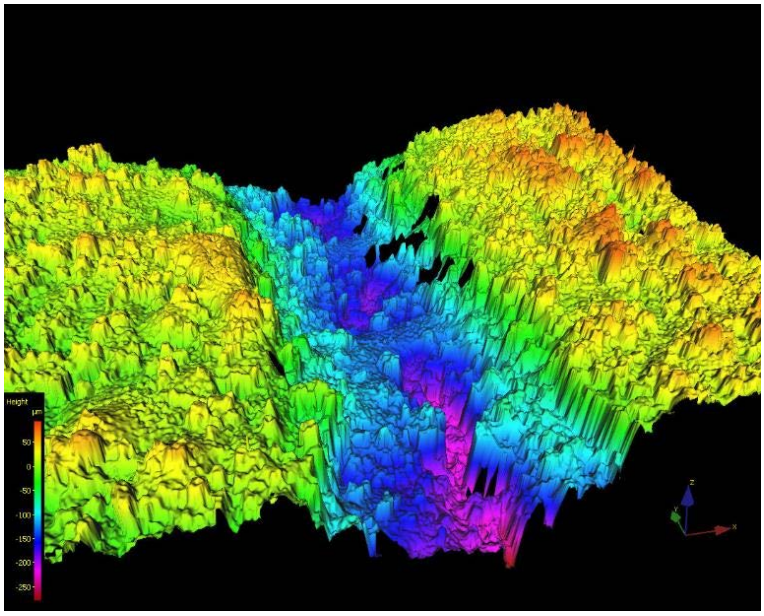

Fig. 2.27. 3-D surface scan of the throat sector of AM-22 showing the surface height in microns (Alicona InfiniteFocus).

2.2.3.2 Roughness Characterisation

From the preliminary surface characterisation, it is evident that the surface roughness may be considerably higher than expected. Hence, it is necessary to evaluate its magnitude and to characterise it in different sections of the AM components, that is, on cylindrical walls and the nozzle wall. In this section, AM-24 is subjected to a systematic surface and profile roughness analysis, while its non-sectioned geometry counterpart, AM-25, will be subject to a nominal-to-actual surface comparison

through X-ray CT inspection (Section 2.3.1). AM-22/23 and AM-24/25 have the same geometry except for the way the thin walls are connected. To build a valuable data set, the measurements have been performed three times for both the inner heat exchanger cylinder and the nozzle regions as explained in Fig. 2.28. Fig. 2.30 shows AM-24 in position for the Alicona profilometer measurements with 10x magnification. AM22 was manually polished with 1 µm diamond paste to achieve a flat section as shown in Fig. 2.29. The polishing was probably performed by pressing slightly more on the elbow region (region a). The result is similar to that one discussed in Section 2.2.2.1, where the sample was not polished to a sufficient depth to show the actual cross-section area. The progression from area (a) to area (c) is of particular interest because it gives an idea of the typical morphology of vertically printed thin walls.

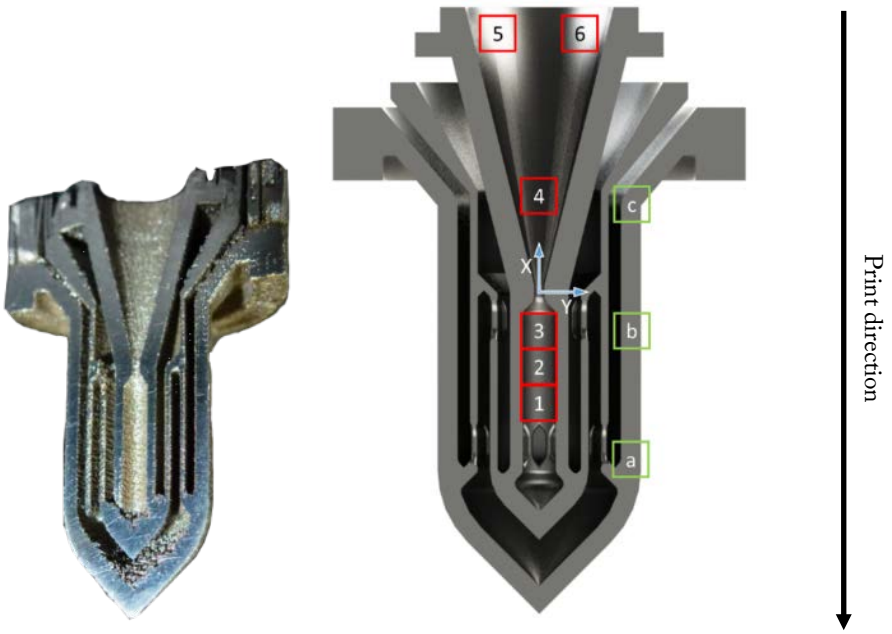

Fig. 2.28. Photo of AM-22 after-polishing (left) and overview of the AM-24 areas of study for surface roughness characterisation (right).

As described in the AM component summary AM-23 and AM-25 are prototypes of the heat exchanger using two different ways to connect the concentric thin walls and ensure both electrical continuity and flow circulation. AM-22 and AM-24 are respectively their counterparts directly printed as half-sections. The latter two components were designed to allow for optical inspection without having to cut apart a full component with the risk of not perfectly matching the central axis.

This allowed a parallel study of the surface roughness of the component using the Alicona profilometer while, at the same time, conducting a CT analysis on AM-23 and AM-25 (Section 2.3.1.2).

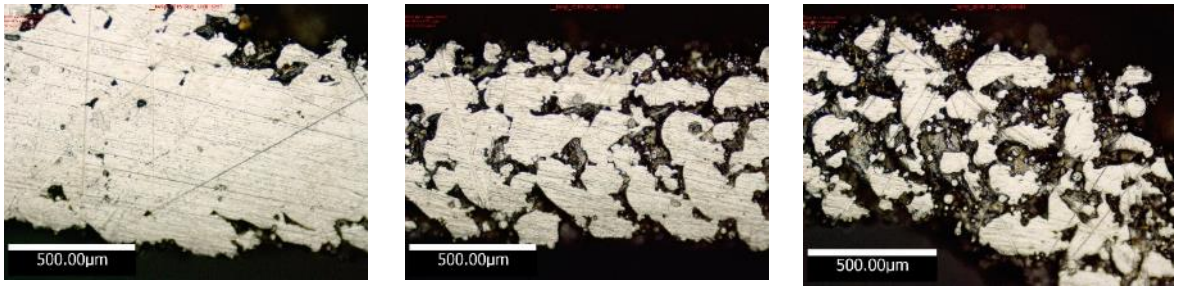

Area (a) Area (b) Area (c)

Fig. 2.29. Images of three different areas on the AM-24 external wall to show different depths of polishing.

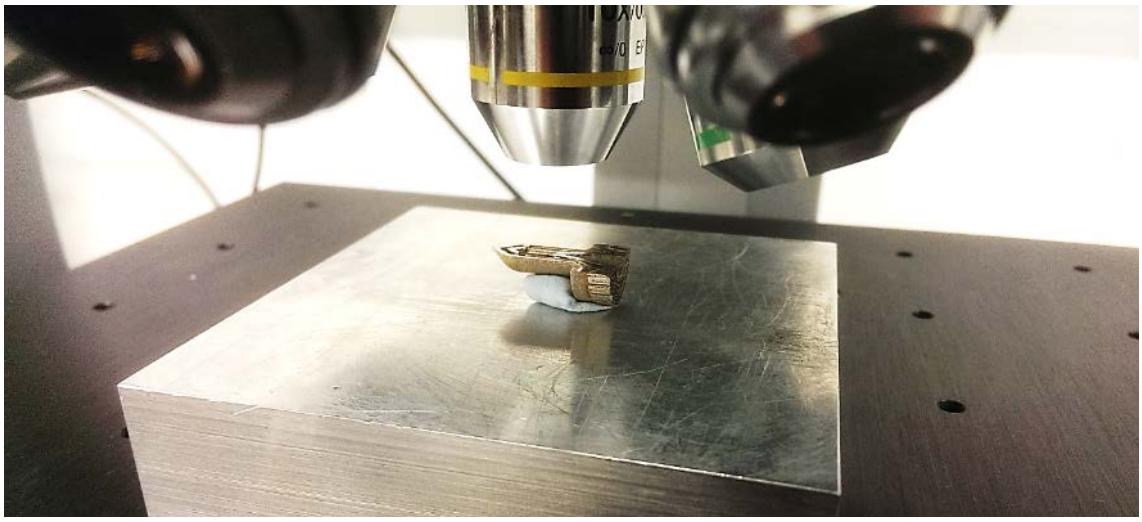

Fig. 2.30. AM24 positioned under the 10x objective of Alicona

Table 2.4 shows the spatial location of the sampled areas, as shown in Fig. 2.28. $\bar{Z}$ and $\underline{Z}$ are respectively the upper and the lower values of vertical focus for the 3-D surface evaluation. For the 3-D scanning, the settings used are 1 µm for the vertical resolution (depth) and 3 µm for the lateral resolution. Table 2.5 shows the surface texture measurement, while the waviness (or long-wave component) of the surface is removed using a short-wave Gaussian profile filter with a cut-off wavelength L_c. This one is selected to meet ISO standards and therefore needs to give a measurement

of roughness comparable to those achieved with tactile instruments. Table 2.6 shows the profile roughness measurements, both calculated from the form-removed 3-D datasets.

The surface texture measurement highlights the area ratio between the measured and the corresponding ideal form, cylindrical for regions 1–3 and conical for regions 4–6. This figure is higher for higher average surface roughness S_a, which also corresponds to higher root-mean-square surface roughness S_q, reaching a maximum of 223% in the initial part of the diverging section of the nozzle (area 4). The waviness, or the long-wave component, of the surface is removed using a short-wave Gaussian profile filter with a cut-off wavelength L_c. This one is selected to meet ISO standards and therefore provides a roughness measurement comparable to those achieved with tactile instruments. To a range of value of R_a corresponds a particular L_c and a particular profile length necessary to provide a reliable roughness measurement. Fig. 2.31 shows an example of the profile path used in the sample area to meet the ISO standards.

Table 2.4. Area location (X, Y) and Z direction range for the 3-D image reconstruction.

Area	X	Y	$\overline{Z}$	$\underline{Z}$
	mm	μm	μm	μm
1	-4.7624	103.5	-252.4650	-666.2300
2	-2.7585	32.5	-241.0400	-650.0900
3	-2.0035	46.0	-229.6300	-647.0300
4	3.0975	13	-289.3600	-1043.9
5	10.205	-837.5	-2130.5	-2934.2
6	10.245	658.5	-2149.4	-2934.2

Table 2.5. Surface texture measurement of the 3-D form-removed datasets.

Area	Area Ratio	Projected Area [mm^2]	S_a	S_q
1	1.80	1.45	1.45	10.29
2	1.82	1.5	1.50	10.63
3	1.85	1.5	1.50	10.23
4	2.23	1.53	11.71	15.32
5	1.98	1.54	9.87	12.75
6	2.11	1.53	10.69	13.64

Table 2.6. Profile roughness measurements of the 3-D form-removed dataset.

Area	L_c [μm]	ISO	R_a	R_q
1	2500	4287/4288	8.77	11.16
2	2500	4287	11.83	16.10
3	2500	4287/4288	9.69	12.31
4	8000	4287/4288	18.01	23.01
5	2500	4287	14.22	17.71
6	2500	4287	14.81	18.45

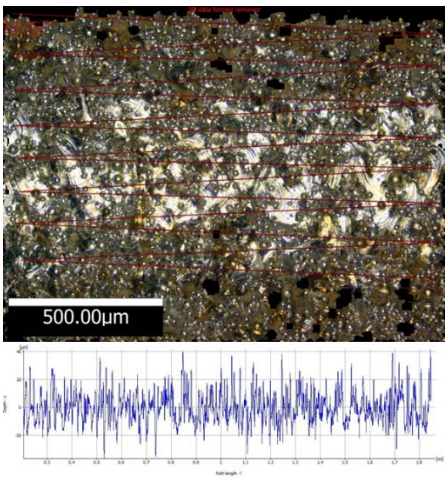

Fig. 2.31. Example of profile surface roughness measurement with Alicona. The top shows the manually sketched red path where the surface roughness measurement has been performed. The bottom figure shows the vertical position of the surface versus the path length.

2.2.3.3 Scanning Electron Microscopy Imaging

Fig. 2.32 shows the flat polished surface of the wall-thickness-test component AM-26, having a wall thickness of 200 μm. In the previous section, the surface roughness of the inner cylinder and nozzle of the component AM-24 has been measured. In this section, the nature of the surface roughness is investigated using SEM technology.

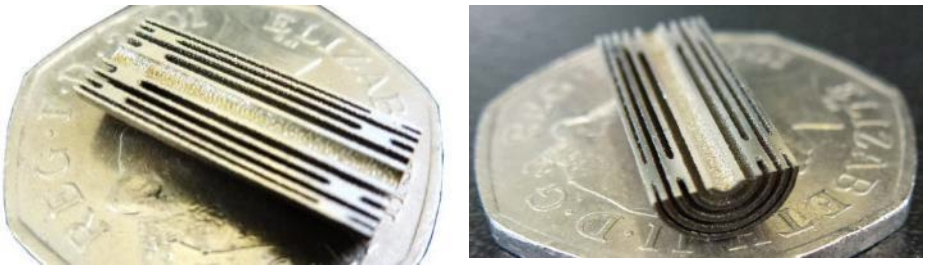

Fig. 2.32. AM-26 production part overview.

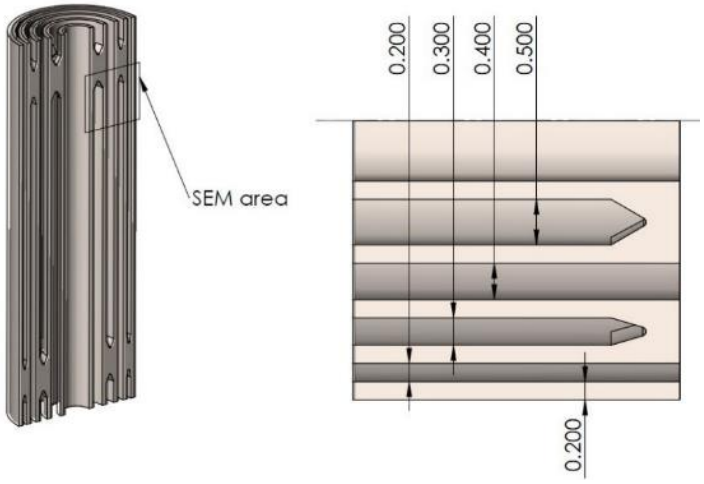

Fig. 2.33. AM-26 component design overview. The part has been printed in the vertical direction.

Fig. 2.33 shows the AM-26 design, highlighting the zone on which the SEM has been performed. To get a finely smooth cross-section of the component, the sample was carefully polished by hand down to 1 μm diamond paste. Fig. 2.34 shows the morphology of the area in analysis. The apparent pores on the wall section are the result of non-complete polishing of the section-printed component (as discussed in Section 2.2.2.1). A closer look at the central half-cylinder shows a more detailed morphology of the vertical walls (Fig. 2.35). In general, the vertical walls are characterised by a relatively smooth dune-like landscape, on which many powder particles are attached as partially fused

on the surface. This scenario leads to the macroscopic surface roughness of the 316L Stainless Steel SLM components. In several cases, apparent holes appear on the 200 μm thick wall. A gap about 200 μm wide is shown in Fig. 2.36. On that small portion of the thickness section, it is still possible to see the same features as for the bigger tubular areas. The maximum powder particle diameter is 73 μm and the particle size distribution is shown in Fig. 2.5. The conglomerate showed in Fig. 2.37 has a diameter of about 220 μm. This feature is one of the macro-structures comprising the smooth dune-like landscape, which occasionally has semi-spherical geometries as well (as in Fig. 2.35, bottom right). It is also possible to see many powder particles attached to this body. The microstructure of the surface is going to constitute the macroscopic roughness of the heat exchanger wall. It was shown in the previous section that the actual wet surface of the HE cylinders is bigger than that one which assumes a cylindrical surface. This might increase the convective heat exchange between wall and propellant. This should be considered in thruster modelling and dimensioning. If the surface roughness represents a major problem, chemical etching specific to the SLM material can be used to almost entirely eliminate the half-melted powder particles (as shown in Fig. 2.7 for a Ti6A14V strut).

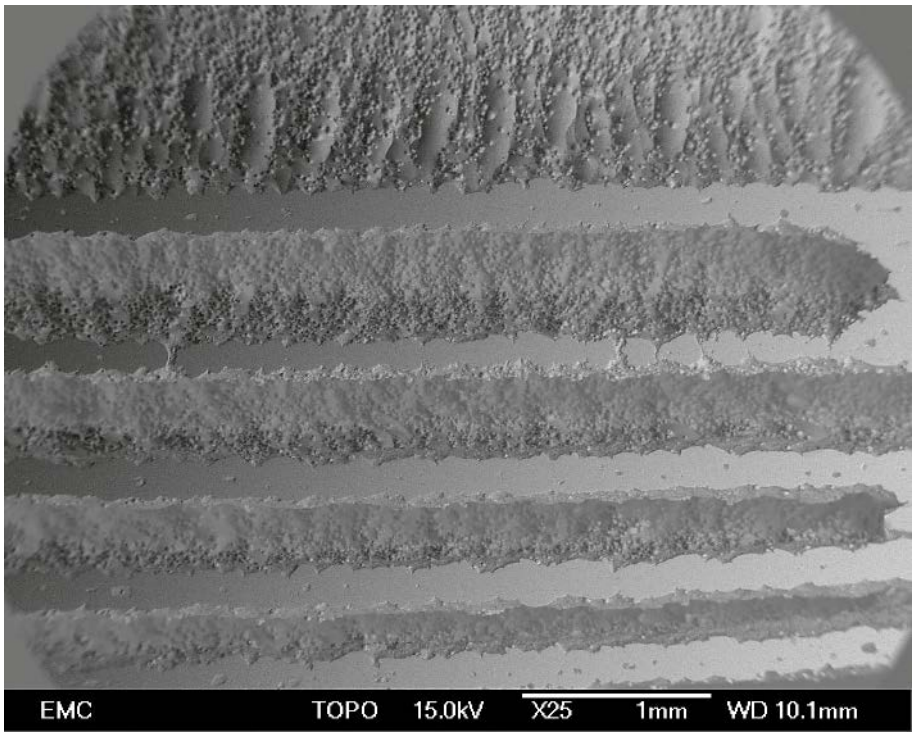

Fig. 2.34. TOPO-SEM of the AM-26 component showing the surface morphology.

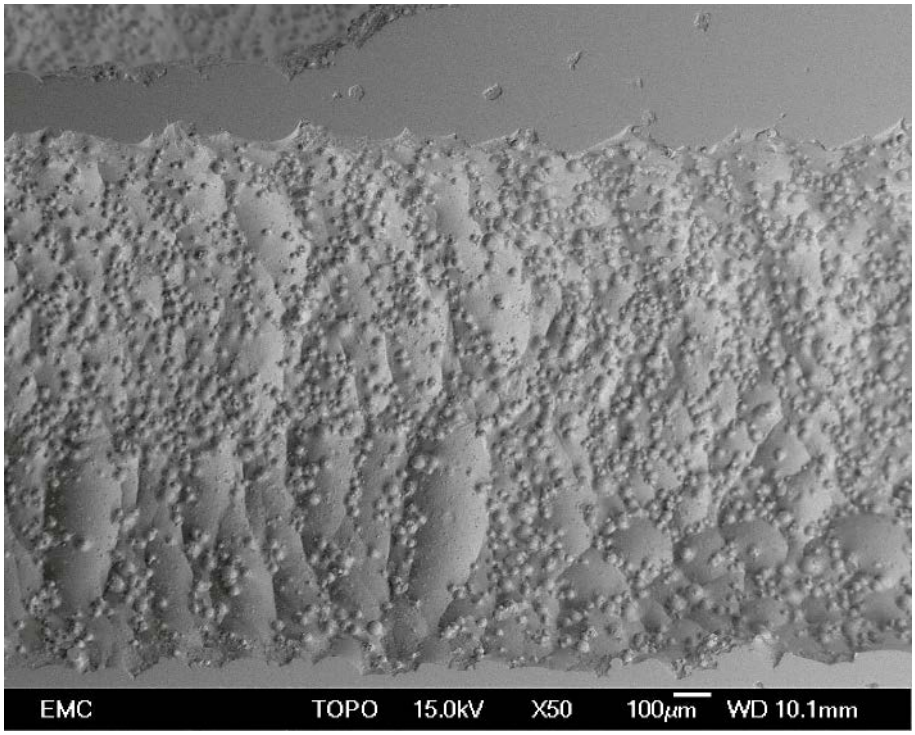

Fig. 2.35. Detail of the surface morphology of the inner half-tubular channel of AM-26.

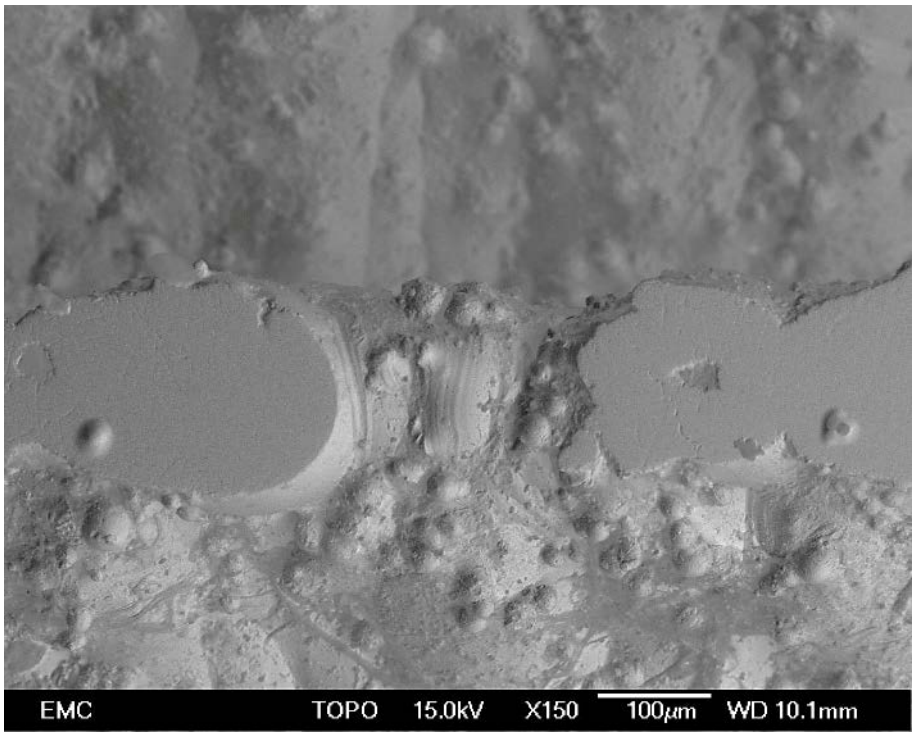

Fig. 2.36. Detail of a wall defect located on the 200 μm wall of AM-26.

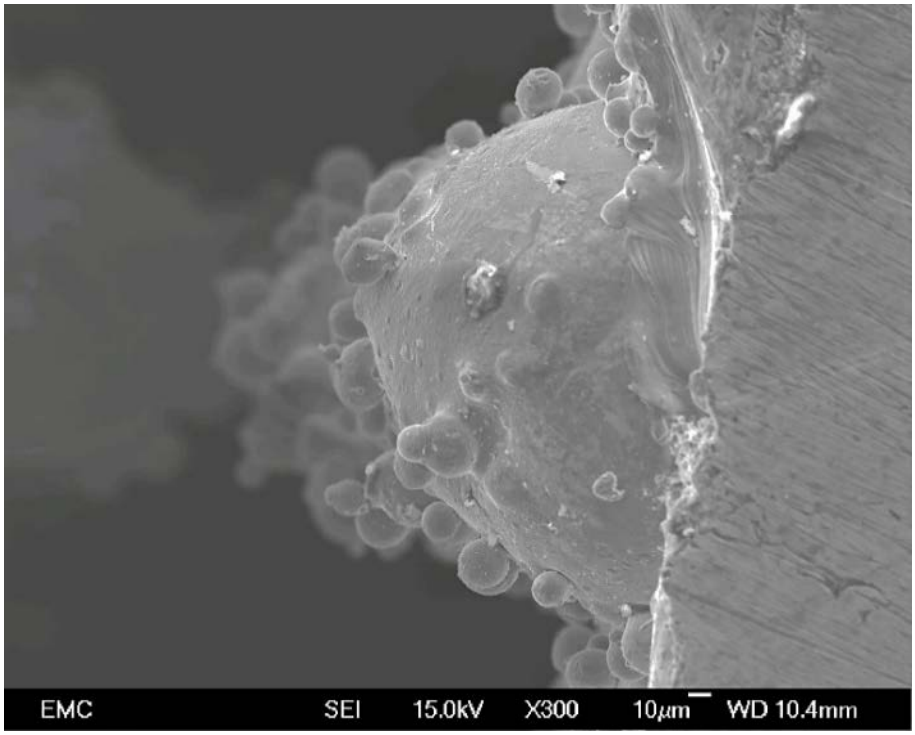

Fig. 2.37. SEM image on a wall edge of the AM-00 component.

2.2.4 Welding Tests

Two EB welds tests were performed on components AM-11-12 and AM-13-14 (Fig. 2.38), reproducing two-cylinders and a nozzle-disk joints. The EB welding tests were commissioned to TWI, who determined the optimised welding conditions. The EB welding process was performed in the 1G position with the following procedures:

- The EB weld on AM-11-12 was made using a 60kV EB machine with 11 mA beam current and a surface speed of 1,900 mm/min; the beam power was ramped up/down at a rate of ~10 mA/s and the total welding time was 1.8 seconds;
- The EB weld on AM-13-14 was made using 60kV accelerating potential, 11 mA beam current and a surface speed of 1,900 mm/min; the beam power was ramped up/down at a rate of ~12.9 mA/s and the total welding time was 0.9 seconds. This weld was cosmetically treated (by a low power pass of the welding beam) after completion to remove surface irregularities.

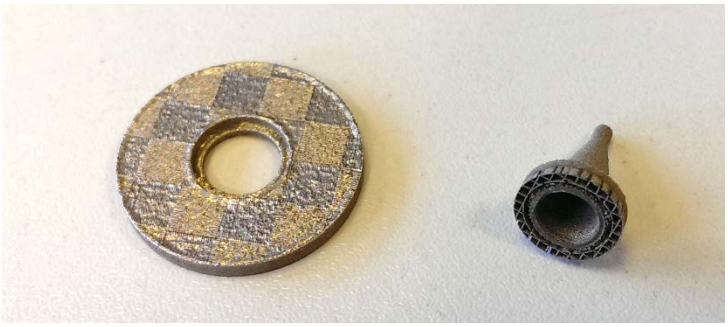

Fig. 2.38. As printed AM-13 (left) and AM-14 (right).

In addition, a TIG weld test was conducted with and without filler on two sets of AM-11-12 respectively. The welds were performed at the EDMC workshop with a Murex Transtig AC/DC 352 machine, with a 1.2 mm dia. tungsten wire at 75 A of current regulated with a pedal by the technician. Fig. 2.39 shows the results of the tests. The weld with filler presented penetration of some material inside the cylinder, therefore it is not suitable if this compromises the heater circuit.

Fig. 2.39. TIG weld tests on two sets of AM-11-12. Weld with added material (left) and pure weld (right).

2.3 Heat Exchanger Design

The nature of the novel HE design of the STAR concept necessitates an iterative verification design approach. In this section, the baseline design and the following three iterations that led to the final HE design are described in detail. At each iteration, the HE was analysed through either simple radiographs or full CT scan to produce the necessary information to move to a next iteration for improvement. X-ray CT is successfully used to perform non-destructive inspection of complex components as well as nominal-to-actual geometry comparison to account for the displacement of

the manufactured component from the actual CAD design. The scans are performed at the μ-VIS X-ray Imaging Centre and data post-processing is done using the software package VG Studio MAX. The software is used to handle the full 3-D dataset from which a first visual inspection can highlight possible failures. Then, a surface extraction tool allows a 3-D surface mesh to be exported and then imported in GOM Inspector V8 for nominal-to-actual comparison.

2.3.1 Baseline Design

The initial exploratory test AM-00 showed that it was possible to produce 300 μm walls with the M2 Cusing laser printer in 316L. The first full prototype, AM-01, showed that a high aspect ratio is possible while maintaining the dimensional accuracy. However, the elbow region was not manufactured correctly, and this was confirmed by visual inspection of the separate elbows (Section 2.2.2.3). For this reason, one change introduced with HE v0 is the elbow region. These are redesigned to form a build angle of 45° and to build a cone rather than a dome. Fig. 2.40 shows the top half-section of the CAD model of HE_v0.1. The thickness of the cylinders from the innermost is of 0.5 mm, 0.3 mm, 0.3 mm, and 0.5 mm. The three gaps between the cylinders are all set to 0.5 mm.

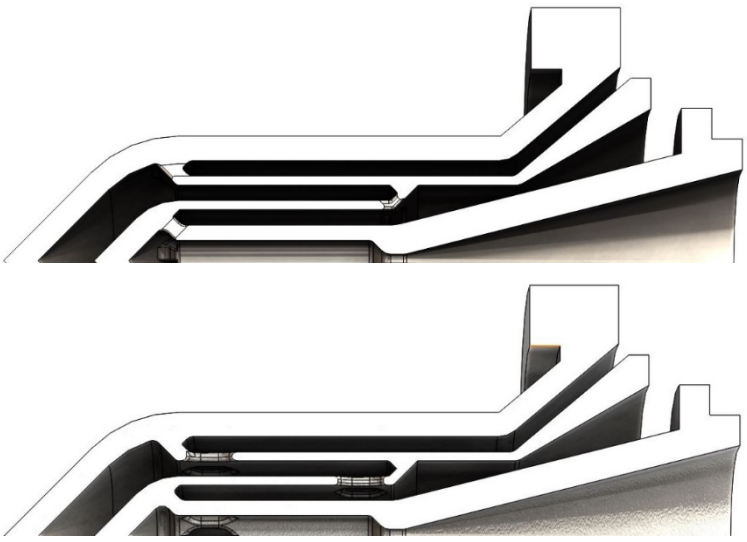

Fig. 2.40. CAD model top half-section of HE_v0.1 (top) and HE_v0.2 (bottom).

2.3.1.1 Variations: Connection Method between Concentric Cylinders

AM-22/23 (HE_v0.1) and AM-24/25 (HE_v0.2) have the same geometry except for how the thin cylindrical walls are connected to ensure electrical continuity and form a resistance. These test aims to establish the best design of connectors. Fig. 2.41 shows in detail how the heat exchanger thin walls are connected on the elbow end of the thruster. The figure shows the HE_v0.1 concept (AM22/AM23) on the left and the HE_v0.2 concept (AM24/AM25) on the right. The first one adds small connectors from a wall end to the next one with a 45° angle with respect to the printing direction. The second one instead fully joins wall ends while permitting the propellant gas to flow through mini-channels or passages. The same design applies to the top of the HE between cylinder 2 and 3.

2.3.1.2 Visual Inspection of CT 3-D Volume

The CT scan is used as a non-destructive inspection of the complex geometry of the thruster. In this section, AM-25 is analysed in detail through a preliminary visual inspection of the CT 3D dataset. A total radiograms count of 587 is obtained by rotating the component about its centreline with an angular step of about 0.61°. Table 2.7 shows the main properties of the CT scan performed on the AM-25 component. The spatial resolution used for this first demonstrative scan was about 21.7 μm. The scanning systems at the μ-VIS Centre allow for resolutions up to about 3 μm for components of 10 mm maximum size and up to 200 nm for small samples of maximum 2 mm size. The volume is obtained from the assembled images by removing the background voxels, which is performed through automatic surface determination on the volume dataset. Fig. 2.42 shows an example of this process in VG Studio MAX, where the central red bar represents the grey used for the isosurface. The surface determination process is resolved in less than one minute. Fig. 2.43 depicts the reconstructed longitudinal sections of AM-23/25, where for AM-23 a major failure is found. In particular, the inner and second outer cylindrical elements are shorted. This represents a failure for both the recirculating flow path and electrical continuity. As a result, AM-23 has been excluded while AM-25 has been taken for further investigation.

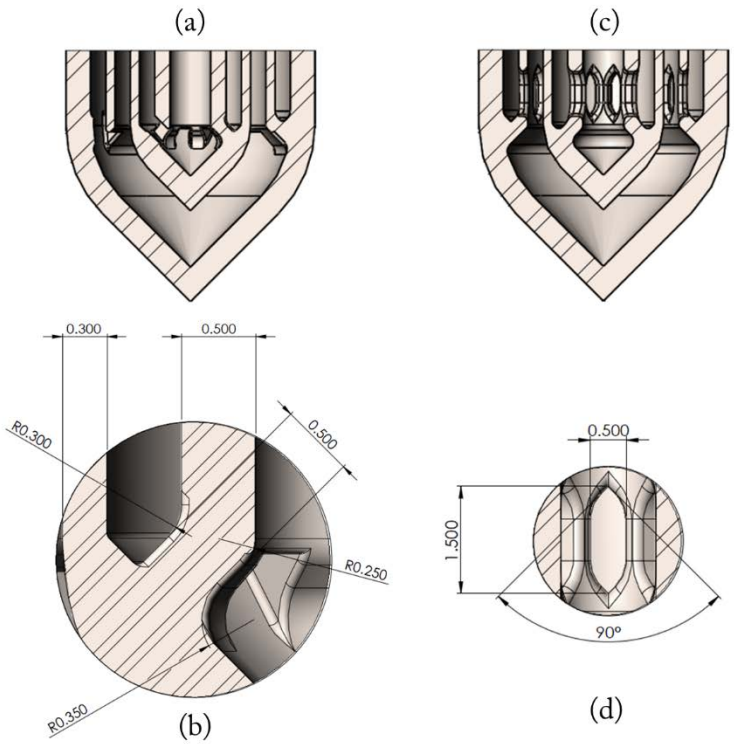

Fig. 2.41. Detailed views of the two wall-connection concepts belonging to HE_v0.1 and HE_v0.2, dimensions in mm. An overview of the connectors and their details are shown in (a-b) and (c-d), respectively.

Table 2.7. Main properties of the test CT scan performed on the AM-25 component

Image dimension	775 × 775 × 1,235 = 741,771,875 voxels
Resolution of x, y and z axes	0.021703 mm
Angular step	0.613°
Total dimensions	16.82 × 16.82 × 26.80 = 7,582 mm^3

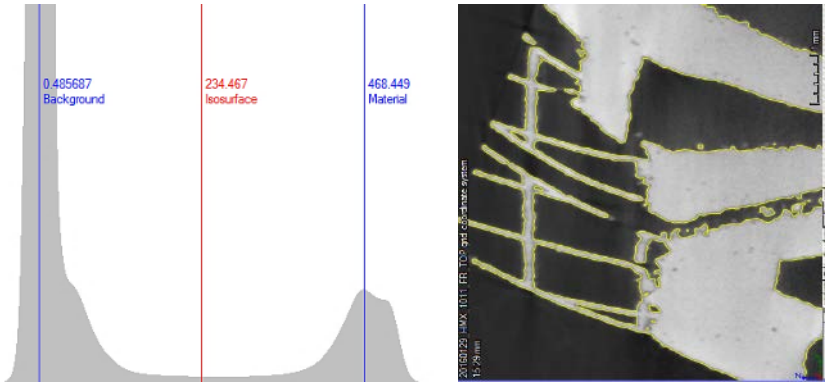

Fig. 2.42. Automatic surface determination example: automatically selected values of background, iso-surface and material in grey (left) and resulting surface in yellow (right).

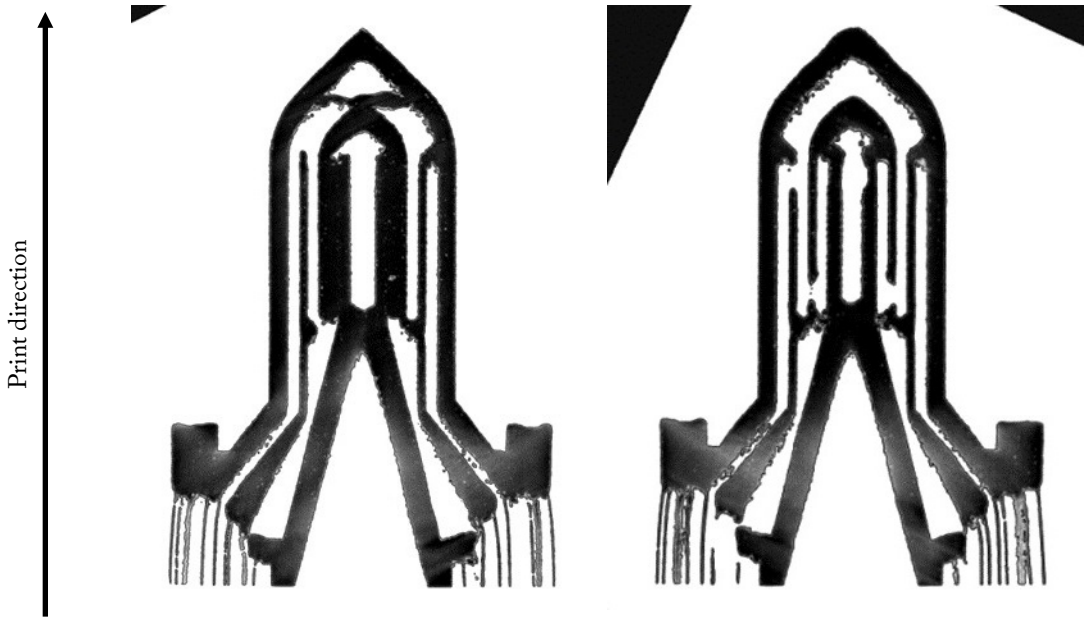

Fig. 2.43. Radiograms of central axis section of the components AM23 (left) and AM25 (right).

The total volume of the scanned component can be evaluated starting from the 3-D dataset. However, a region of uncertainty exists in terms of voxel colour. Fig. 2.45-a shows that, including the total number of voxels but the black ones (which are air by definition), the total volume is 1,268.63 mm^3. Fig. 2.45-b shows instead the volume calculation having cut out the voxels with grey less and equal to 50, which results in the lower value of 1,165.17 mm^3. This value was determined by trying to eliminate the yellow dots in the nozzle diverging section in (a), which are non-existent in reality. From the CAD model of AM-25, the total volume is 1,066.42 mm^3, but this does not account for the supporting material.

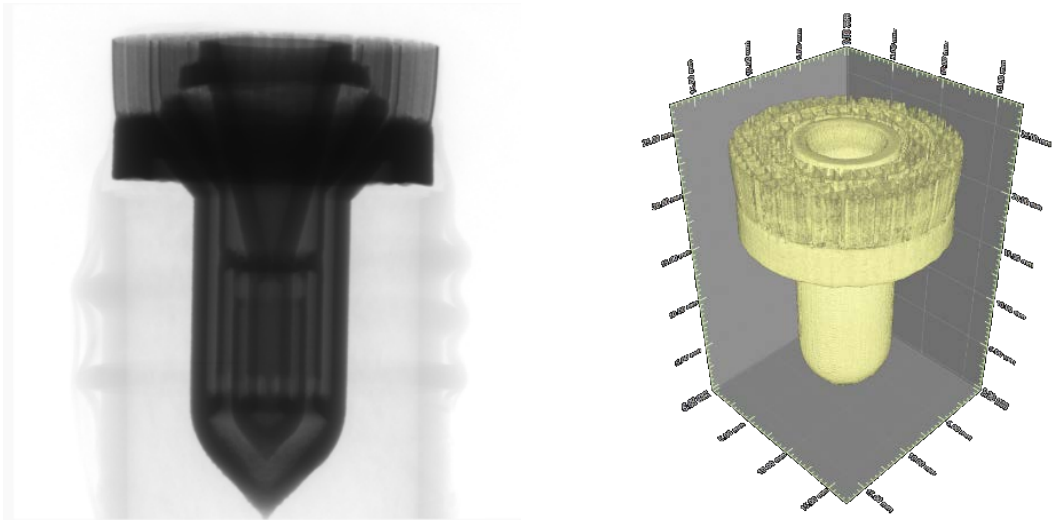

Fig. 2.44. Radiogram of AM-25 (a) and 3-D reconstruction of the geometry (b). The origin of the axes is coincident with the corner of the three grey surfaces. The vertical direction is represented by the *y*-axis.

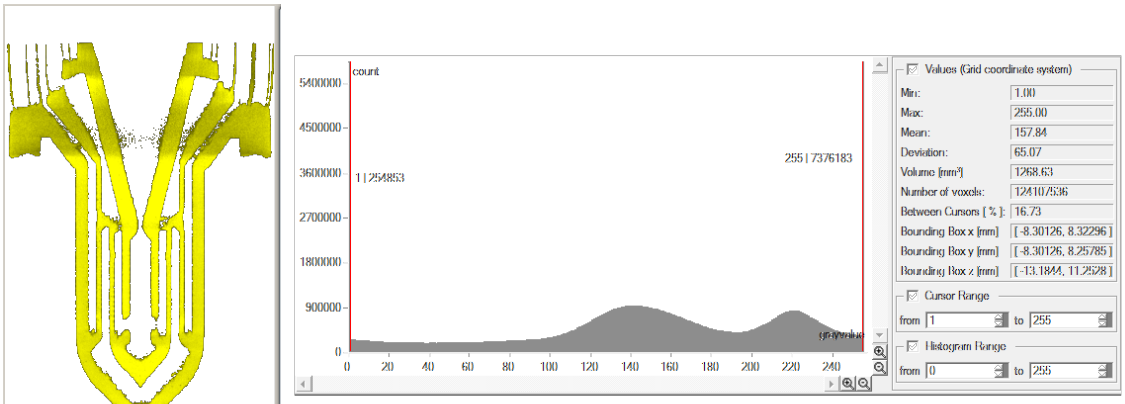

(a)

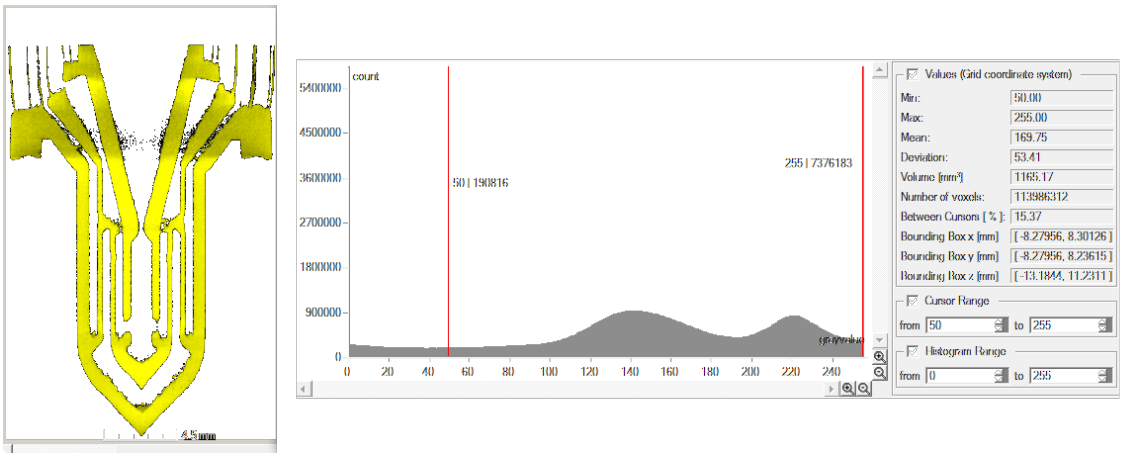

(b)

Fig. 2.45. Total volume evaluation by filtering the voxels' greyscale. Figure (a) takes into account the total greyscale but the black colour while (b) cuts out the voxels with grey less and equal to 50.

Fig. 2.46 shows the central section view parallel to the right plane. The top end of the figure shows less brightness. This occurs since more material is present in that region, which lowers X-ray penetration. Fig. 2.47 shows the downstream region of the component where the supporting material pattern is visible. The supporting material has a minimum measured thickness of about 100 μm (as measured optically in Section 2.2.2.2). Fig. 2.48 and Fig. 2.49 show a visual comparison between the CAD model and the CT scan 3-D dataset of two sections where the mini-channels are located. These show one of the most critical parts of the design, that is, the small flow passages that allow the propellant to recirculate through the concentric heat exchanger. Fig. 2.50 is the detailed view of a top section corresponding to the nozzle throat, which has a design diameter of 420 μm. From this visual inspection, the throat size appears slightly smaller, which was expected from the visual inspection on the nozzles reported in Section 2.2.2.4.

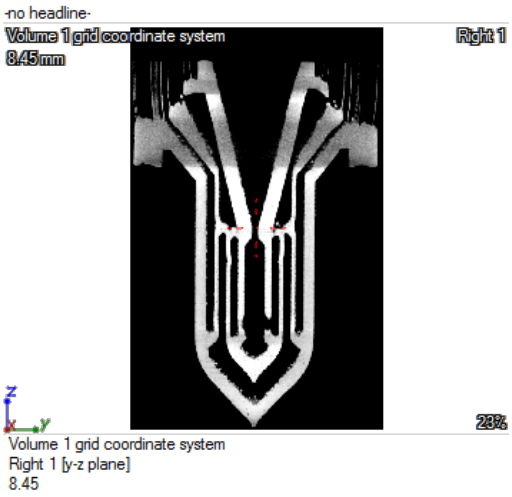

Fig. 2.46. 3-D reconstruction of AM-25. Section parallel to the right plane at X = 8.45 mm.

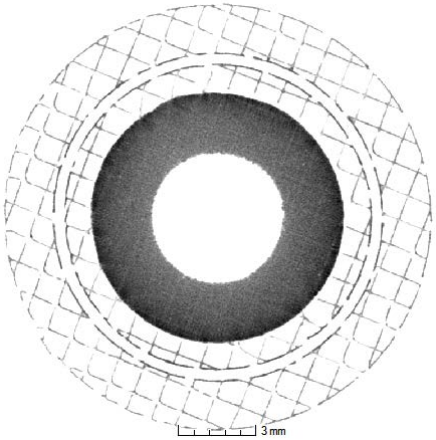

Fig. 2.47. Bottom view of the component showing the supporting grid of about 100 μm thick walls. Y = 22.86 mm.

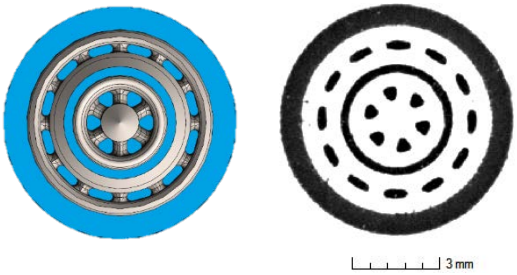

Fig. 2.48. Visual comparison of the section corresponding to the bottom flow passages (elbow end). CAD model highlighted in blue the section plane (left) and CT section (right).

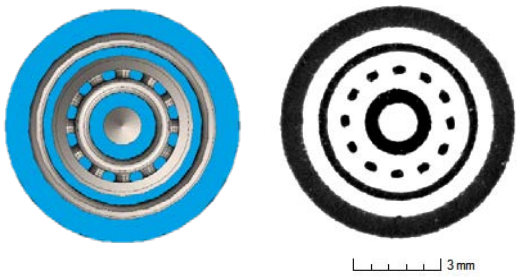

Fig. 2.49. Visual comparison of the section corresponding to the top flow passages (nozzle end). CAD model highlighted in blue the section plane (left) and CT section (right).

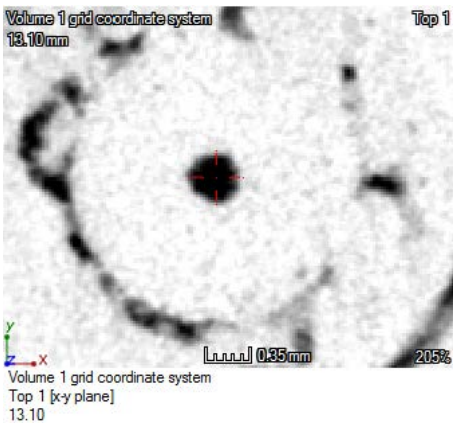

Fig. 2.50. Magnification of a CT section, *Y* = 13.10 mm, showing the nozzle throat hole (nominal diameter = 420 µm).

Fig. 2.51 is a set of images of the reconstructed 3-D domain of AM-25; (1) shows the thin-walled grid-shaped supporting material, and (2) and (3) show the main failure of this prototype thruster. In particular, a short circuit occurs all around the inner and second channels. This might be due to an excessively steep angle of the wall surrounding the mini-channels. Another cause could be the disproportionately small gap between the cylinders. The other views show a generally good and acceptable realisation of both the tubular elements and the mini-channels. The elbows present a very irregular surface on their bottom part, but this is not a major issue for the realisation of the recirculating flow path.

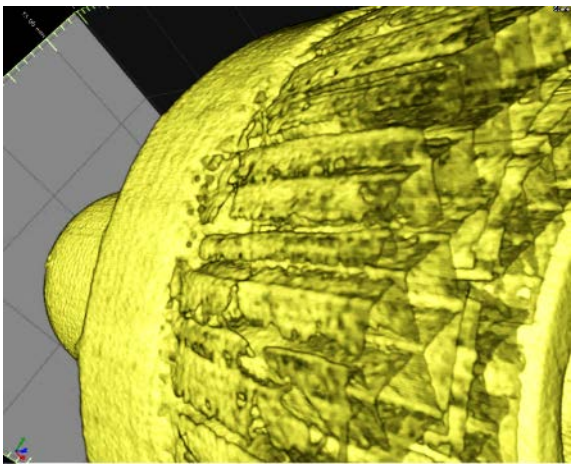

(1) Supporting material detail view.

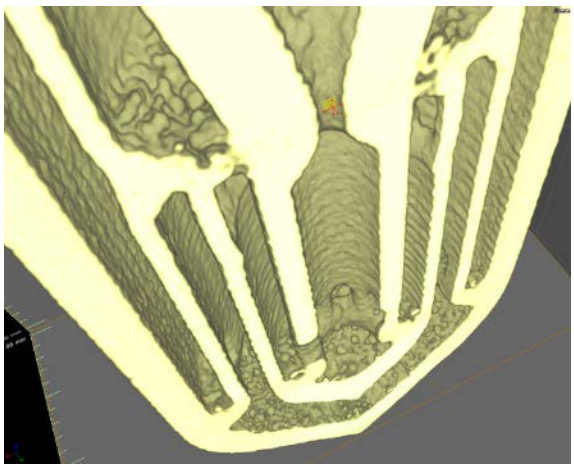

(2) Section view showing the recirculating-flow heat exchanger geometry.

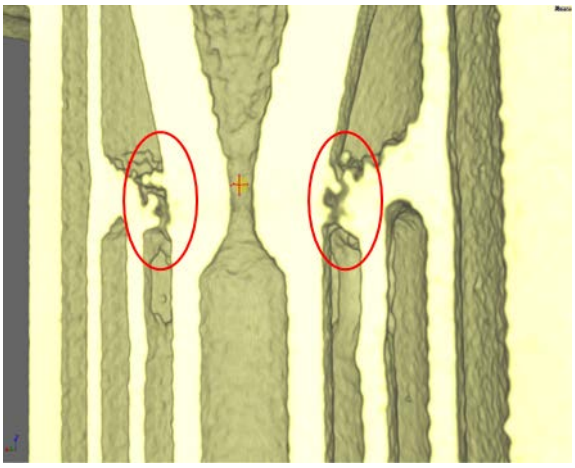

(3) Nozzle region, section plane on the component centre line to show the nozzle geometry. Circled in red is the collapsed material from the outer to the inner wall.

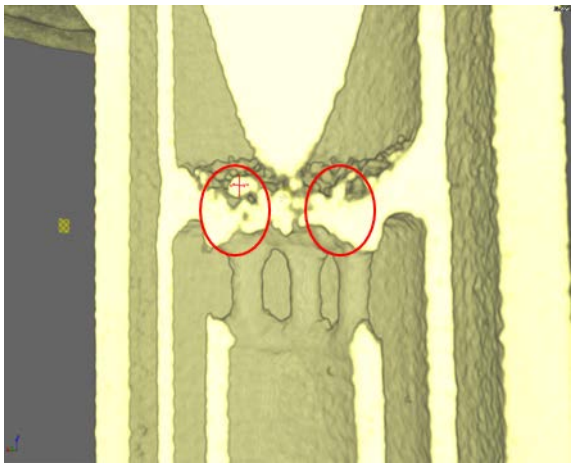

(4) Nozzle region, section plane beyond the component centre line to show the flow passages. Circled in red is the clear melted region connecting the inner wall with the two outer walls.

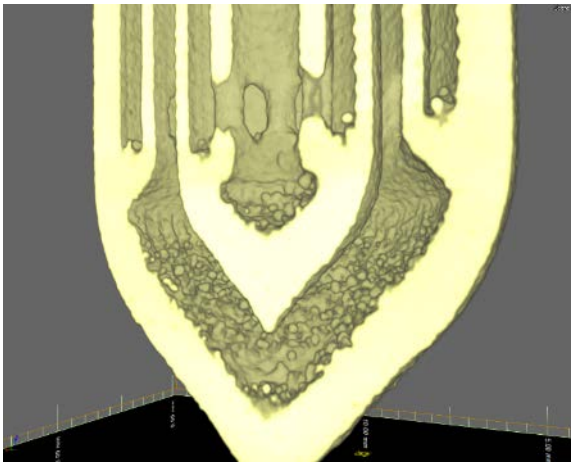

(5) Elbow-end flow passages.

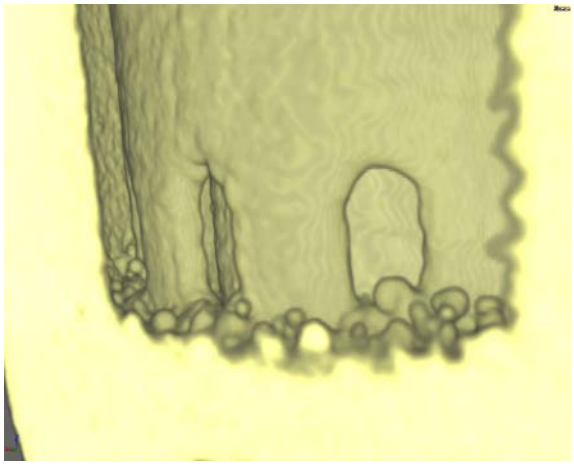

(6) Elbow-end flow passages detail.

Fig. 2.51. Some images of the CT 3-D reconstruction of the component AM-25.

2.3.1.3 Nominal-to-Actual Comparison

A nominal-to-actual comparison between the CAD geometry and the 3-D surface extracted from the CT dataset is performed with GOM Inspector V8 (free version). Fig. 2.52 shows an overview of the overlaid CAD and 3-D surface-mesh geometries of the component AM-25, where the highlighted connector regions will be individually analysed. While Fig. 2.53 shows the maximum deviation of the actual geometry from the nominal, Table 2.8 shows the deviation of a best-fitting cylinder of an actual tubular surface compared to the nominal ones. The actual cylindrical surfaces have been calculated using a Gaussian best-fit method and using about 99.7% of all points (3σ). The measuring point outliers are excluded from the calculation. The resulting absolute deviation reaches a maximum of 49 µm. Nevertheless, the deviation of the walls is always negative, highlighting a general trend for the cylinder to enlarge. Therefore, the actual thickness is only 26 µm higher for cylinders 2 and 3, 6 µm larger for cylinder 1 and 24 µm smaller for cylinder 4, with an uncertainty of ±22 µm (Table 2.7).

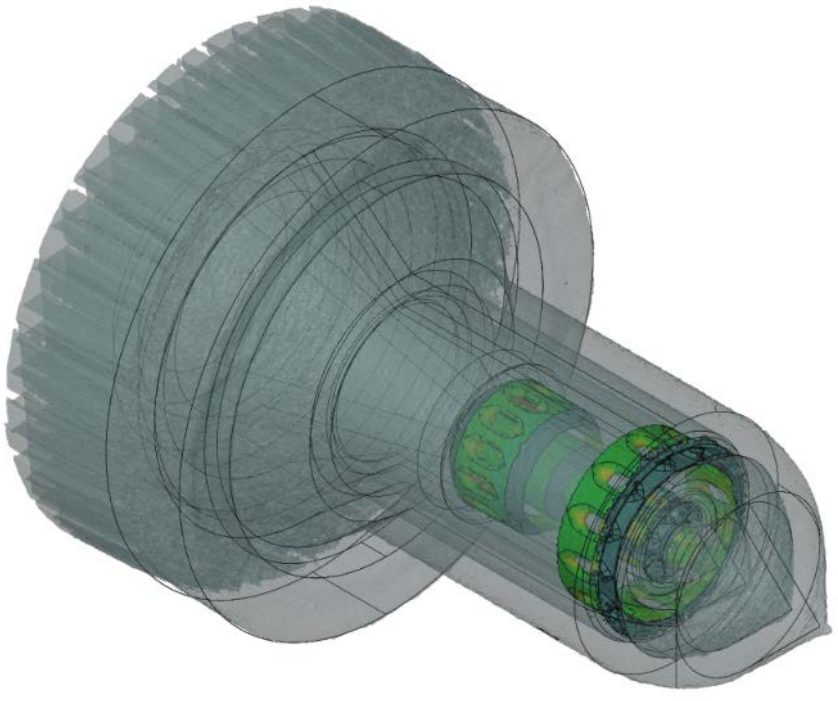

Fig. 2.52. AM-25 nominal-to-actual comparison overview, with highlighted connecting channels.

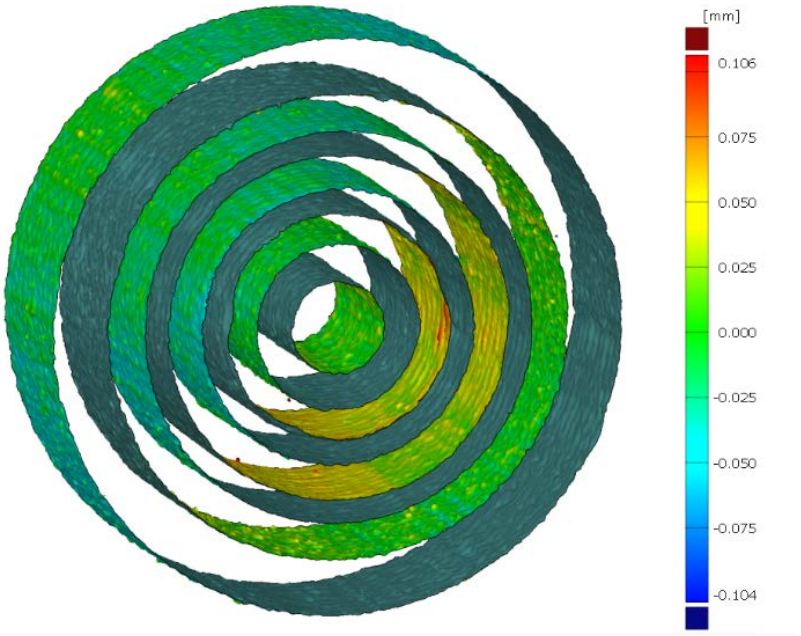

Fig. 2.53. Nominal-to-actual geometry comparison of the heat exchanger wall region.

Table 2.8. Deviation of the actual radius of each cylinder element with respect to the nominal radius.

Radius of	Nominal, mm	Actual, mm	Deviation, mm
Cylinder 1 in	0.664	0.648	-0.016
Cylinder 1 out	1.164	1.154	-0.010
Cylinder 2 in	1.664	1.616	-0.049
Cylinder 2 out	1.964	1.942	-0.023
Cylinder 3 in	2.464	2.418	-0.046
Cylinder 3 out	2.764	2.744	-0.020
Cylinder 4 in	3.264	3.258	-0.006
Cylinder 4 out	4.064	4.034	-0.030

Fig. 2.54 shows the critical parts of the component AM-25 which are analysed in detail in this section. From left to right: nozzle, mini-channel section of cylinder 2, the mini-channel section of cylinder 1 (inner element) and the mini-channel section of cylinder 4 (outer element). Each cylinder has equally distributed mini-channels. The number of fluidic channels on cylinders 1, 2 and 3 is 6, 12 and 12, respectively. This feature makes the component axial symmetric for sectors of π/3 radians.

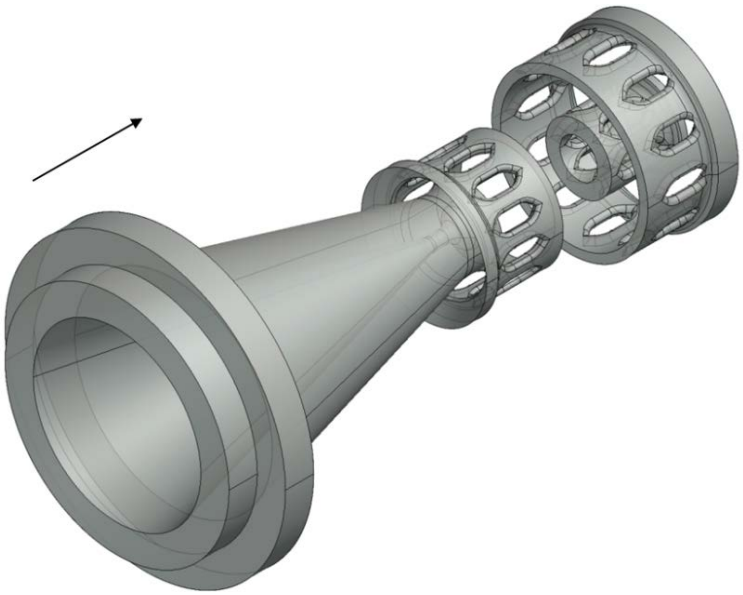

Fig. 2.54. CAD overview of the main parts of the component analysed. The print direction is shown.

Each region of interest has been isolated for a surface comparison between the nominal geometry of the CAD model and the actual geometry of the CT scan (Fig. 2.55). The previous analysis on the wall thickness shows a good agreement with the design values. The green colour shows a zero deviation of the actual over the nominal geometry. The printed component shows very good accuracy of micro-fluidic channels (Fig. 2.55). Slight modifications on the next design aim to limit the granular formation close to them, especially for the cylinder close to the elbows region (cylinders 1 and 2). In the nozzle throat region, part of the material that shorts cylinder 1 and cylinder 3 is visible. At the exit section of the nozzle, part of the supporting material used in the printing process is also visible, which is meant to be removed for the assembly phase to match components. Fig. 2.56 shows two orthogonal section planes of the nominal-to-actual comparison Fig. 2.57 shows a detailed view of the section comparison in the nozzle region. Unwanted material connects cylinder 1 and cylinder 3 to create a short circuit of the heat exchanger electrical resistance, which represents the only manufacturing failure of component AM-25.

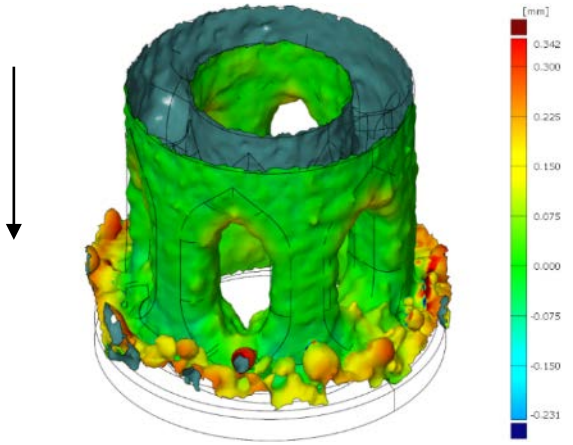

(a) Actual surface of channels located in cylinder 1.

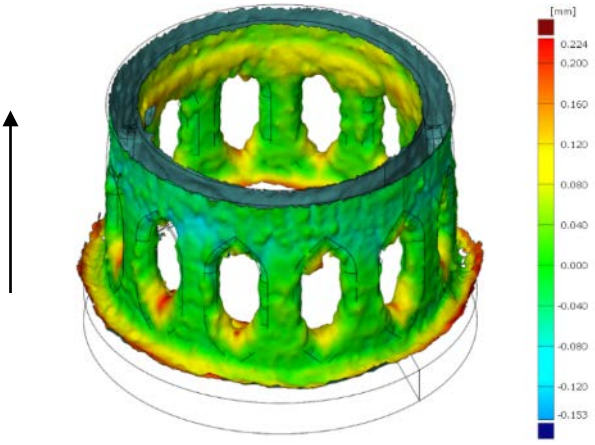

(b) Actual surface of channels located in cylinder 2.

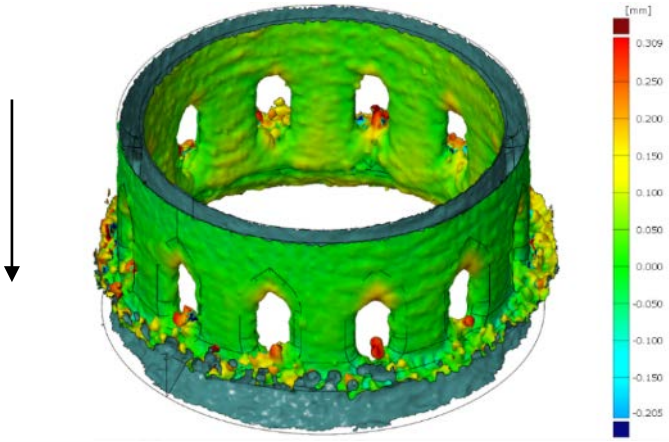

(c) Actual surface of channels located in cylinder 3.

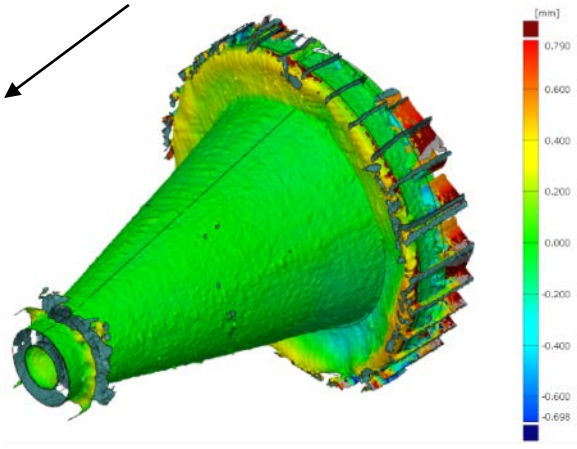

(d) Actual surface of the nozzle element. In the throat region, it is the visible part of the material that shorts cylinder 1 and cylinder 2. At the exit section of the nozzle is the visible part of the supporting material used in the printing process.

Fig. 2.55. Surface comparison of the main parts of component AM-25. The print direction is shown for each part. The actual surface of component AM-25 is obtained by meshing the material surface detected from the CT volume data.

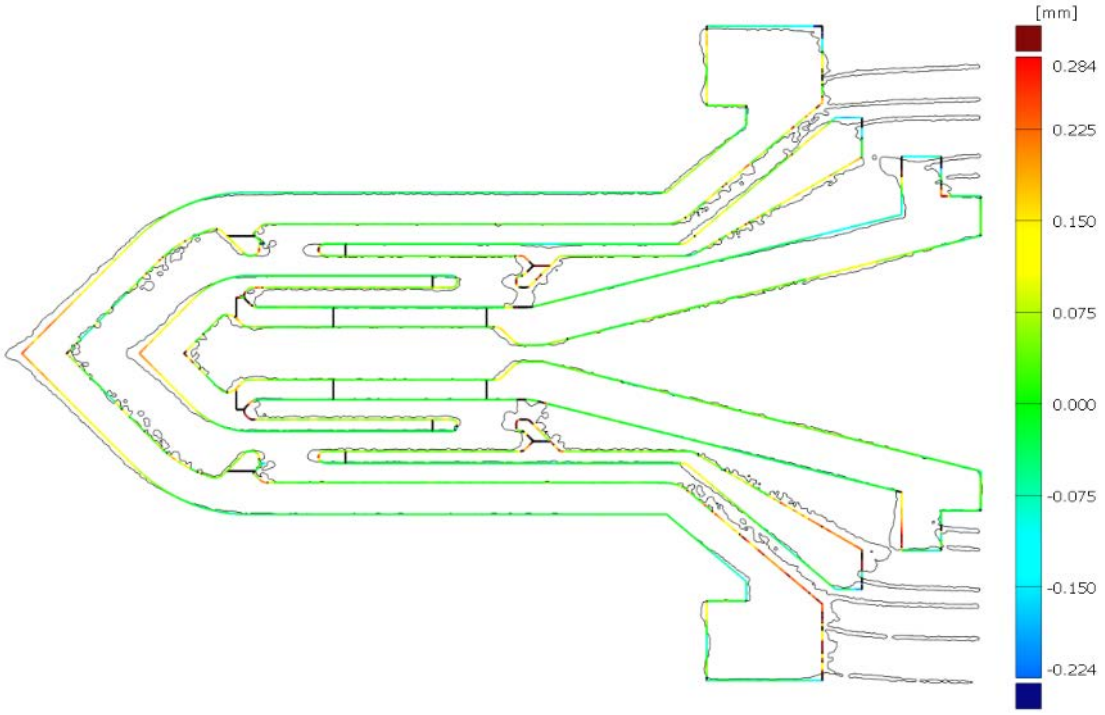

(a)

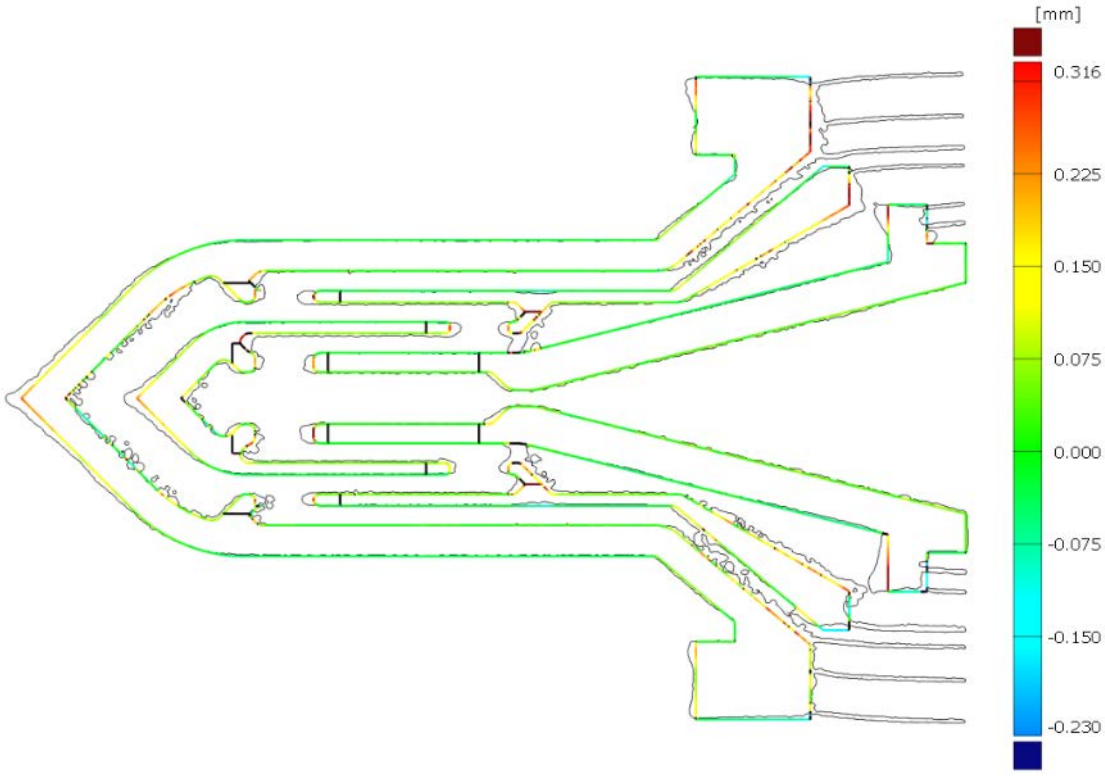

(b)

Fig. 2.56. Longitudinal-section comparison showing the short circuit created by connecting material in the nozzle region. Sections (a) and (b) are orthogonal to each other.

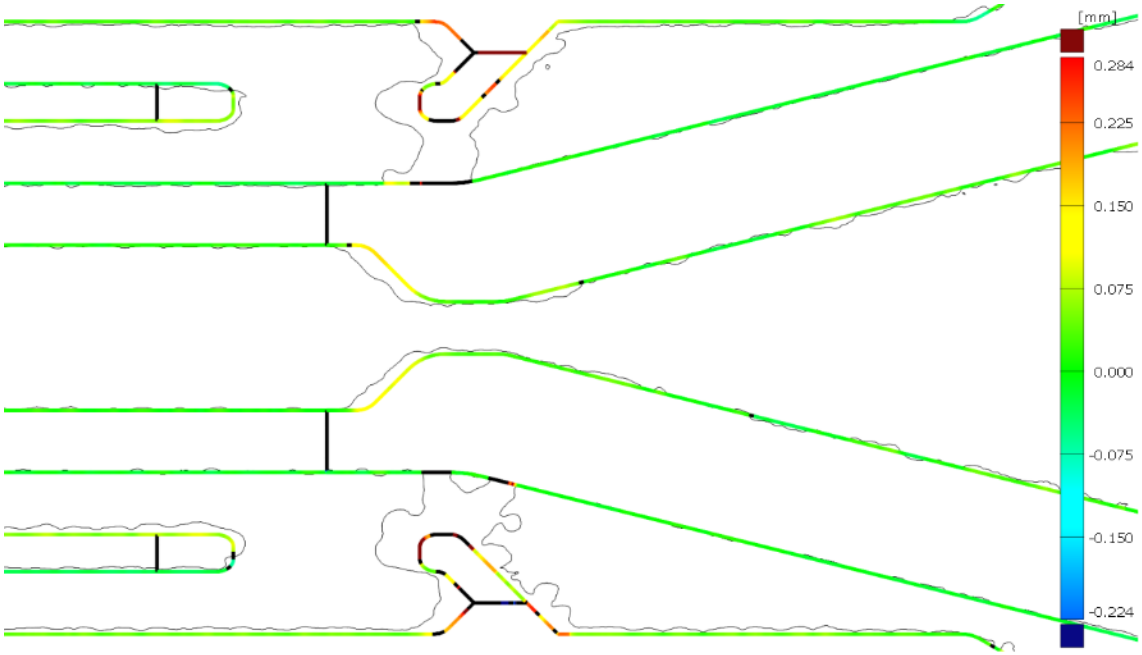

Fig. 2.57. Detailed view of the section comparison in the nozzle region. Unwanted material connects cylinder 1 and cylinder 3 to create a short circuit of the heat exchanger electrical resistance.

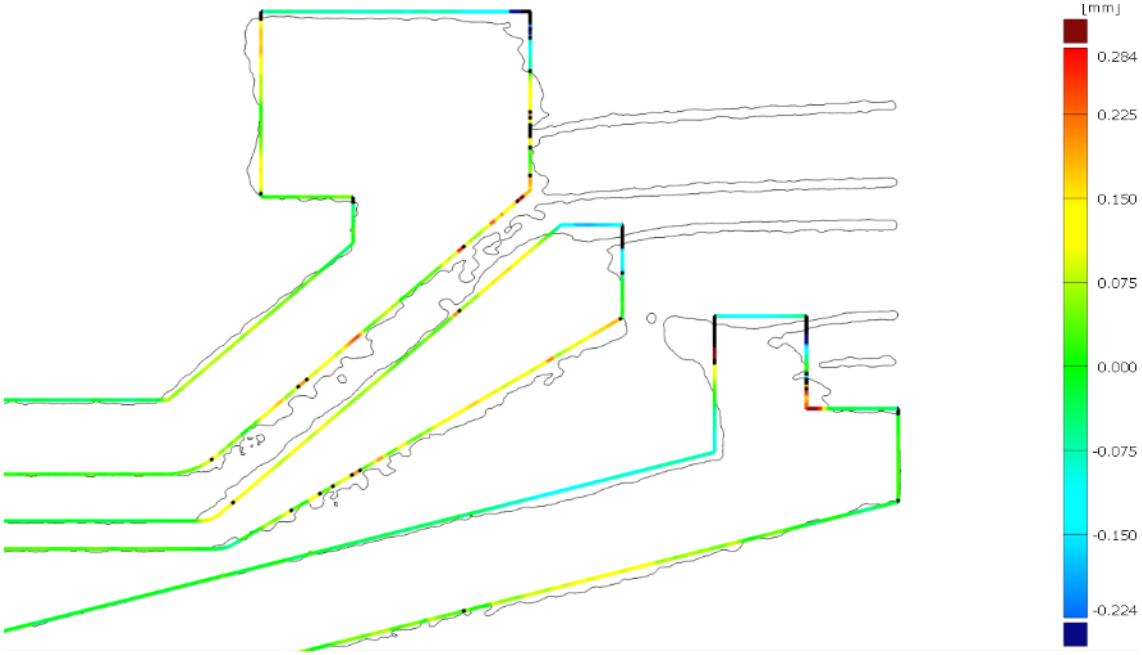

Fig. 2.58. Detailed view of the section comparison in the region of the concentric cones.

Fig. 2.58 shows the region where support material has been added to build a suspended part on the printer base plate. Because the presence of support material leads to very rough and irregular bottom surfaces, its use should be avoided especially in regions where accuracy is important. For this reason, in the next iterations of the thruster, the support material will not be used anymore, but the

component suspended parts will be elongated to reach the base plate as a solid element. Therefore, the excess material will be removed with conventional machining. Finally, the actual throat diameter measured with a cylinder obtained through a Gaussian best-fit method is of 0.395 mm, with σ = 0.01466 mm and a residual of 0.01309 mm, which is close but smaller than the nominal value of the throat of 0.42 mm. This result is in agreement with the optical inspection on the test nozzles (Section 2.2.2.4).

2.3.2 HE Design Iteration 1

The thinner a heat exchanger wall is, the greater the resistive dissipation, therefore thin-wall geometries are preferred. The wall thickness and heat exchanger tests determined that the limit of the SLM with the Concept Laser M2 in terms of achievable cylindrical wall thickness is at 0.15 mm. For this reason, HT_v1 implements a wall thickness of 0.15 mm, in particular for the two intermediate cylinders (2-3). With respect to the previous design, HE_v0, the solid walls are now extended to the print base plate to avoid the accuracy issues discussed in Section 2.3.1.3.

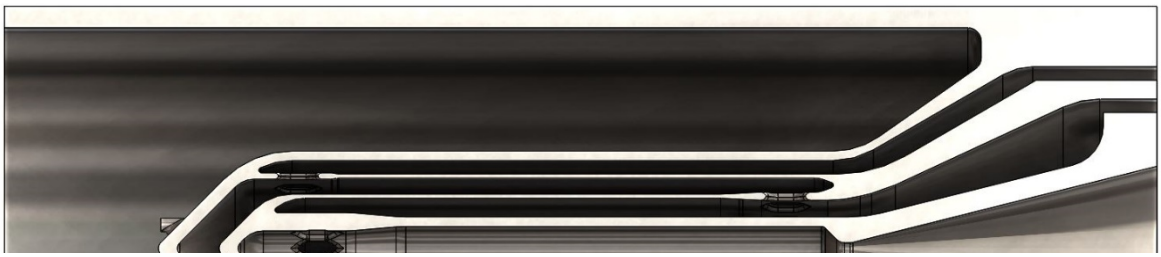

Fig. 2.59. CAD model top section-view of HE_v1.

2.3.2.1 Design Variations: Enlargement of Interconnects

The baseline design of the connectors for this iteration is given by HE_v0.2. Additional changes are made, in particular, the junctions between each cylinder pair are modified, the maximum printing angle is decreased to 20° where possible, all sharp angles have been smoothened and, finally, the fluidic channels section is modified. The restricted sections of material in correspondence of the flow mini-channels must have an equal or lower resistivity of the corresponding cylinder so that there is no concentration of power dissipation, which could ultimately cause component failure In fact, even though the joule heating of each cylinder is different, it has been evaluated critical to keep the resistivity as constant as possible along the cylinders, avoiding heat concentration in the connectors, which are subjected to thermal stress. Therefore, in this new design, the section area of each cylinder

is kept constant also in the flow channels section. As a result, in correspondence to the fluidic mini-channels, the thickness is increased as shown in Fig. 2.60.

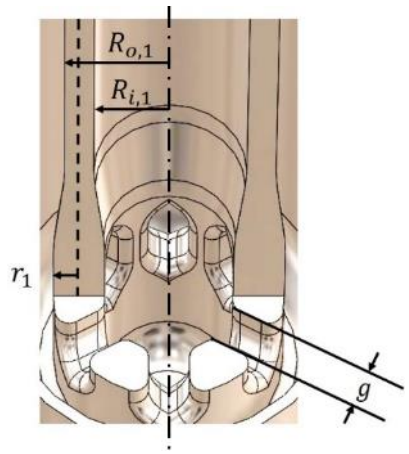

Fig. 2.60. Double-cut section of cylinder 1 showing the parameters used for connector thickening.

With reference to Fig. 2.60, the dimensioning is performed through Eq.(2.2) to Eq.(2.5), where N is the number of connectors or the number of mini-channels, k is the cylinder number, g = 0.5 mm is the mini-channel width, $R_{i,k}$ and $R_{o,k}$ are respectively the inner and outer radiuses of the cylinder k, $R_{ci,k}$ and $R_{co,k}$ are respectively the inner and outer radiuses of the connectors, and r is the half-width of the connectors. Eq.(2.3) is an approximation because the second term on the right-hand side approximates a circular trapezoid to a rectangle. This assumption has been used since it leads to a negligible error while simplifying the expression.

$$A_{t,k} = \pi(R_{o,k}^2 - R_{i,k}^2) \tag{2.2}$$

$$A_{c,k} \approx \pi(R_{co,k}^2 - R_{ci,k}^2) - g(R_{co,k} - R_{ci,k})N_k \tag{2.3}$$

$$R_{co,k} = \frac{R_{o,k} + R_{i,k}}{2} + r \tag{2.4}$$

$$R_{ci,k} = \frac{R_{o,k} + R_{i,k}}{2} - r \tag{2.5}$$

Combining the above equations, Eq.(2.6) is obtained. The half-width r_k has been computed in Excel and used in a design table for Solidworks.

$$r_k = \frac{\pi(R_{o,k}^2 - R_{i,k}^2)}{2\left[\pi(R_{o,k} + R_{i,k}) - gN_k\right]} \tag{2.6}$$

The main purpose of this design was to solve the short-circuit issue presented in the previous AM-25. It has been shown that steep angles, equal or above 45°, increase surface roughness and facilitate the formation of a conglomerate that could short-circuit the thin walls. Therefore, in this new design, instead of forming cylinders 2 and 3 from a thin wall, they are supported by a thick wall (Fig. 2.61-a). Moreover, the concentric conical elements have here the same open-angle, limiting any rough wall formation by eliminating angle gradient. Finally, the gap between the cones is increased to 800 µm from the previous 500 µm.

(a) (b)

Fig. 2.61. New design concept of AM-29/30 showing the thickening of the mini-channel sections.

2.3.2.2 Inspection

Fig. 2.62 shows the nominal-to-actual comparison on the section in the region of the nozzle. The short-circuit issue was not solved with the changes in this iteration. However, overall, the surface finish of the cones has improved by lowering the overture angle.

Hypothesis for the nozzle-end failure

The change in section possibly prevents the heat from escaping that part of the component during the layer melting. Therefore, it is supposed that heat collects during the printing of the highlighted section, eventually increasing the temperature to the point of partially melting the border particles, which would constitute the beginning of the failure. Since the powder layer thickness is about 30 µm (which corresponds to the x_{50} of the particle size), this condition lasts for several layers until the section of the component changes significantly. It is important to highlight that this hypothesis refers to the section area of the entire component. Especially, since the power per unit area, exerted by the laser, and the scan speed are constant, an overall decrease in section area can lead to heat concentration.

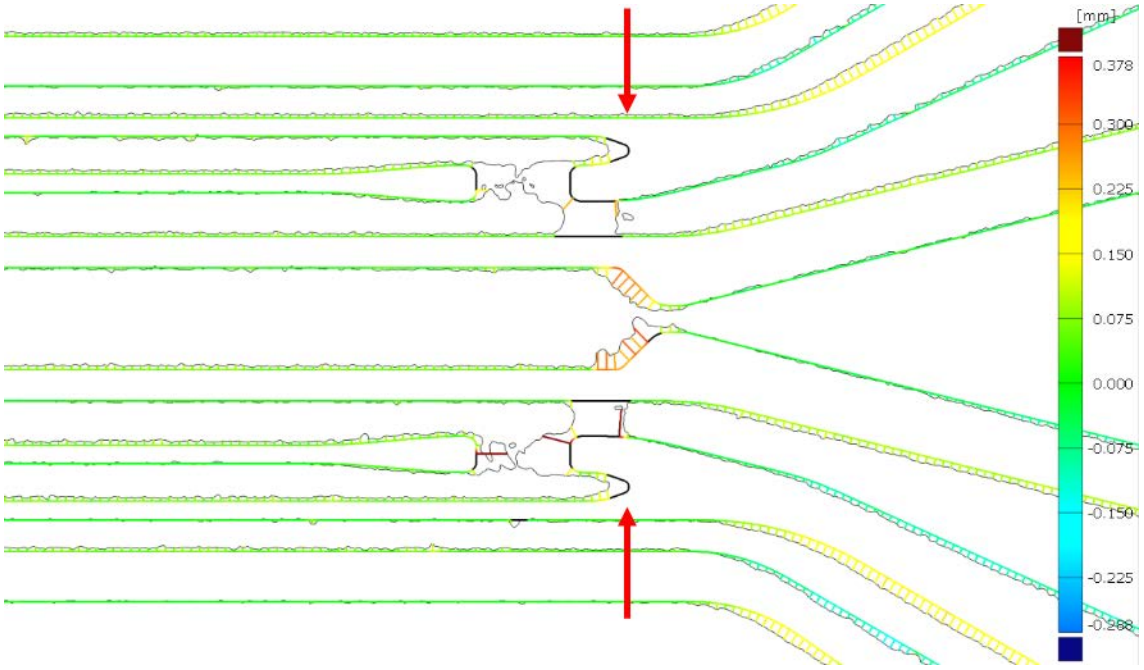

Fig. 2.62. Section nominal-to-actual comparison in the nozzle region of HE_v1.

2.3.3 HE Design Iteration 2

Fig. 2.63 shows the two variations implemented in this HE iteration. The first one (HE_v2.1) implements the same mini-channels geometry of the previous iteration, while in the second variation (HE_v2.2) the height of the channels is maximised towards the elbows and the nozzle respectively. Fig. 2.63 shows an overview of the two variations.

2.3.3.1 Design Variations: Thickness of Cylinders

The last and main issue to solve is still the short-circuit in the throat region. With the design of HE_v2, a wall thickness of 150 μm has been proven. In this iteration, the gaps are increased to 1 mm, 0.8 mm and 0.6 mm, from the inner to the outer cylinder. Also, while HE_v2.1 maintains the same mini-channels design of HE_v1, in HE_v2.2 the height of those is increased. In particular, Fig. 2.64 shows the full extension of the mini-channels up to the nozzle wall, while the height of the mini-channels in the elbow region is increased from 1.5 mm (used in both HE_v0 and HE_v1 designs) to 2.21 mm. Table 2.9 summarises the main geometrical parameters, where several small bit identifiers were printed to visually distinguish the variations. With the thickening of the mini-channels introduced with HE_v1, the effective gap between the wall is reduced in that region and it is dependant of the wall thickness. In addition, as a result of the geometrical parametrisation, the distance between the elbows varies with the thickness of the walls.

Fig. 2.63. CAD model top section-view of HE_v2.1 (top) and HE_v2.2 (bottom).

Table 2.9. Cylinder wall thickness of HE_v2 variations for failure analysis.

Bit	Thickness of cylinder #, μm				Effective gap 1-2	Elbow distance
	1	2	3	4	μm	mm
[2,5]	500	300	300	500	0.86	2.26
[3,6]	400	200	200	400	0.89	2.05
[4,7]	350	150	150	350	0.91	1.91

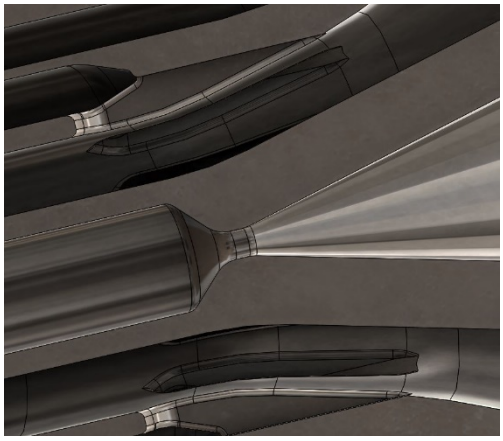

Fig. 2.64. Detail of the extend mini-channels of HE_v2.2 between cylinders 2-3.

2.3.3.2 Inspection with Radiographs

Fig. 2.65 shows a half-section radiograph for each component, arranged per increasing thickness from left to right. In correspondence of each mini-channels regions, a tick or cross mark indicates whether the print was successful or not. The failure occurs in regions where there features with overhanging surfaces. Where the concentric cylinders are built vertically or with shallow angles, gaps as small as 314 μm have been manufactured with no issues (AM-00). The two main failures here described are located in two critical regions. The first one (gap between cylinders 1-2) appears where the mini-channels close up into a pinnacle with a build angle of 45°. As demonstrated before (AM-01), above a build angel of about 40°, the bottom face's surface becomes very irregular, eventually presenting protuberances with an excess length as high as 400 μm.

The best-built component is HE_v2.2, which has the lower thickness and implements the extended mini-channels as described above. As a result, this is the only component that does not propagate the unwanted sintering of material in the next layers of printing. Fig. 2.66 shows a significant difference in the mini-channels design. In particular, in HE_v2.2 the upper part of the channels (1) is lowered and the splitting of the thick wall into cylinders 2-3 is raised (2). As a result, the reduction of section starts at a lower height with respect to the nozzle throat and more importantly, the section of material in correspondence to the mini-channels is larger (3). It is speculated that the larger section area contributed to a lower heat concentration and avoided the sintering of the surrounding particles. It is interesting to notice that, for the two thicker versions of HE_v2.2, the failure in this region started at the closure of the mini-channels (1), beyond the nozzle throat. It is believed that this is caused by the smaller effective gap between cylinders 1-2 (see Table 2.9), which decreased nominally

of only 20 μm and 50 μm, respectively. In addition, the failure appears to be activated by the decrease in accuracy resulting from the 45° build angle used to close the mini-channels (see Fig. 2.55-b for reference). In summary, the failure seems to be triggered by:

- the heat concentration resulting from the decrease of the section of material;
- the gap distance between cylinders;
- the inaccuracy generated by the overhanging features.

Finally, the elbows not failing are those with greater separation. As for the nozzle-end mini-channels, this failure seems to be triggered by the low quality of the overhanging surface with a 45° build angle and caused by the heat concentration in combination with the gap distance.

To assess whether the grey areas observed in the radiographs were solid sintered material or trapped loose powder, all 6 components were sectioned using EDM wire cutting. The visual inspection confirmed that the dark grey areas were sintered material, while lighter grey areas corresponded to loose powder that came off during the cutting. With reference to Fig. 2.67, it can be noted that HE_v2.1 presents unwanted sintered material before and after the mini-channels (1). It is believed that the lower initial failure occurs because of the reduced material section caused by the nozzle converging cone, which increases the heat concentration. The sintering of unwanted material stops at the mini-channels section possibly because the cylinders are built purely vertically at this stage. The last failure starts at the top pinnacle of the mini-channels as previously discussed. This latter issue is still present in HE_v2.2 when the thickness increases (2), and consequently when the effective gap between cylinders 1-2 decreases. Finally, it is interesting to observe that the unwanted sintering of material stops when cylinder 1 increases in thickness in the mini-channel area (3). This suggests that the decrease of heat concentration due to the increase of section area is dominant with respect to the decrease in gap distance between cylinders 1-2.

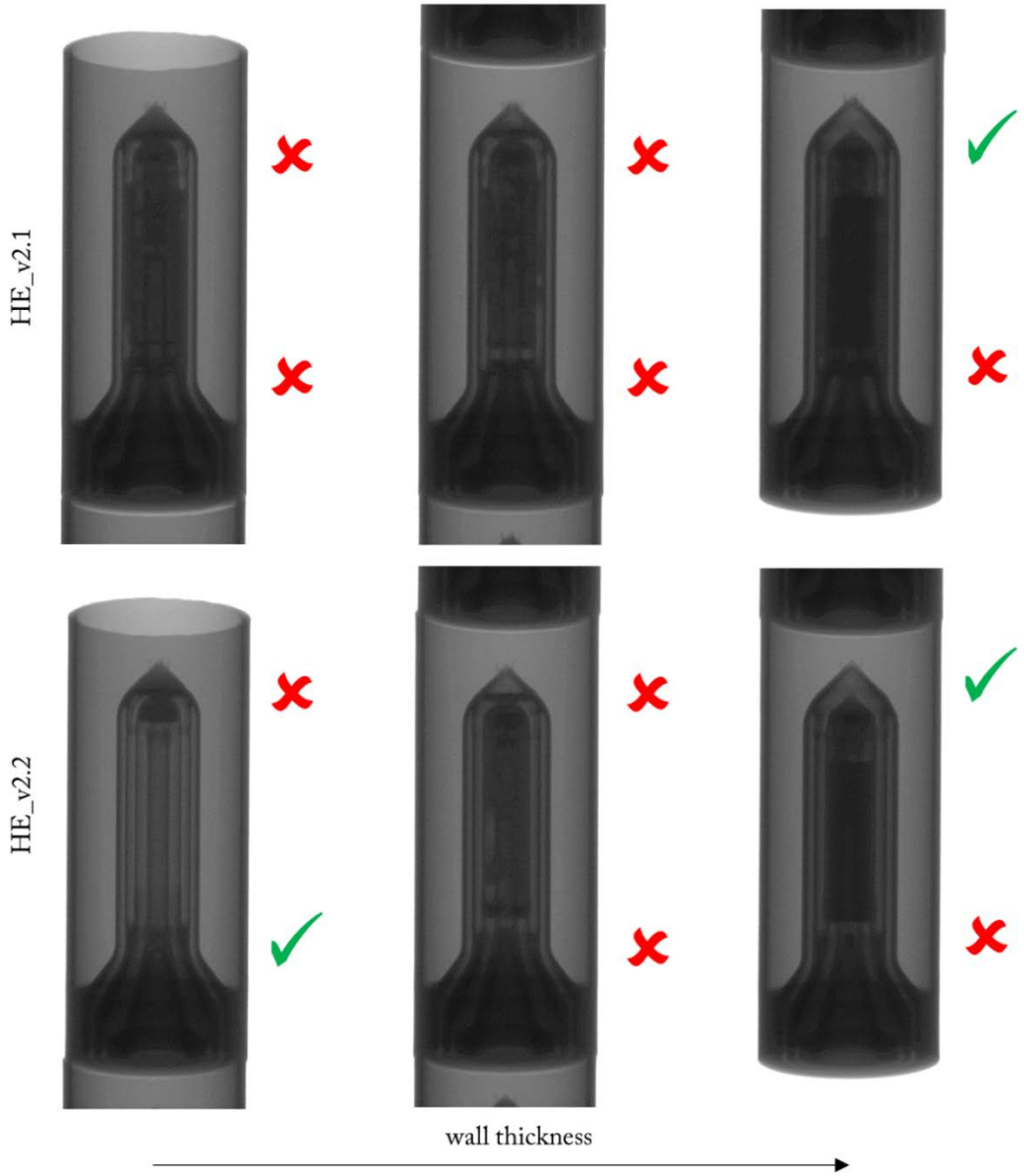

Fig. 2.65. Overview of the HE_v2 radiograms highlighting two different failures at the top and bottom of the heat exchanger.

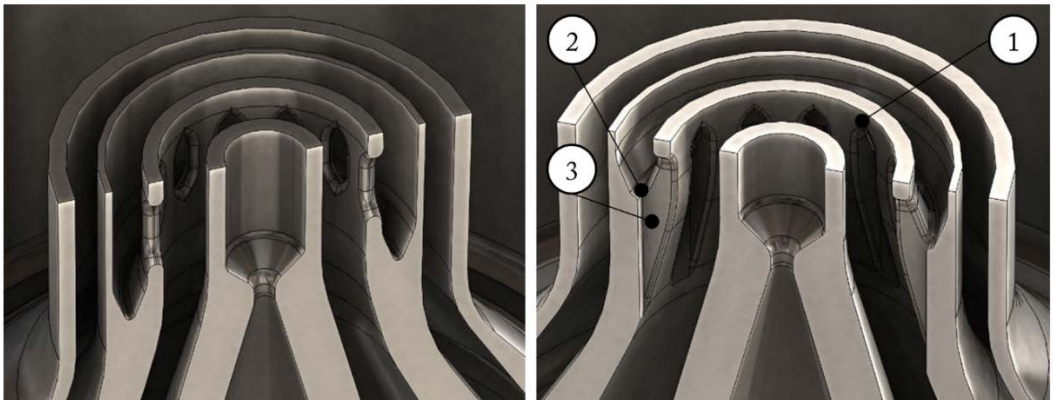

Fig. 2.66. Differences between mini-channels on cylinder 2 for HE_v2.1 (left) and HE_v2.2 (right).

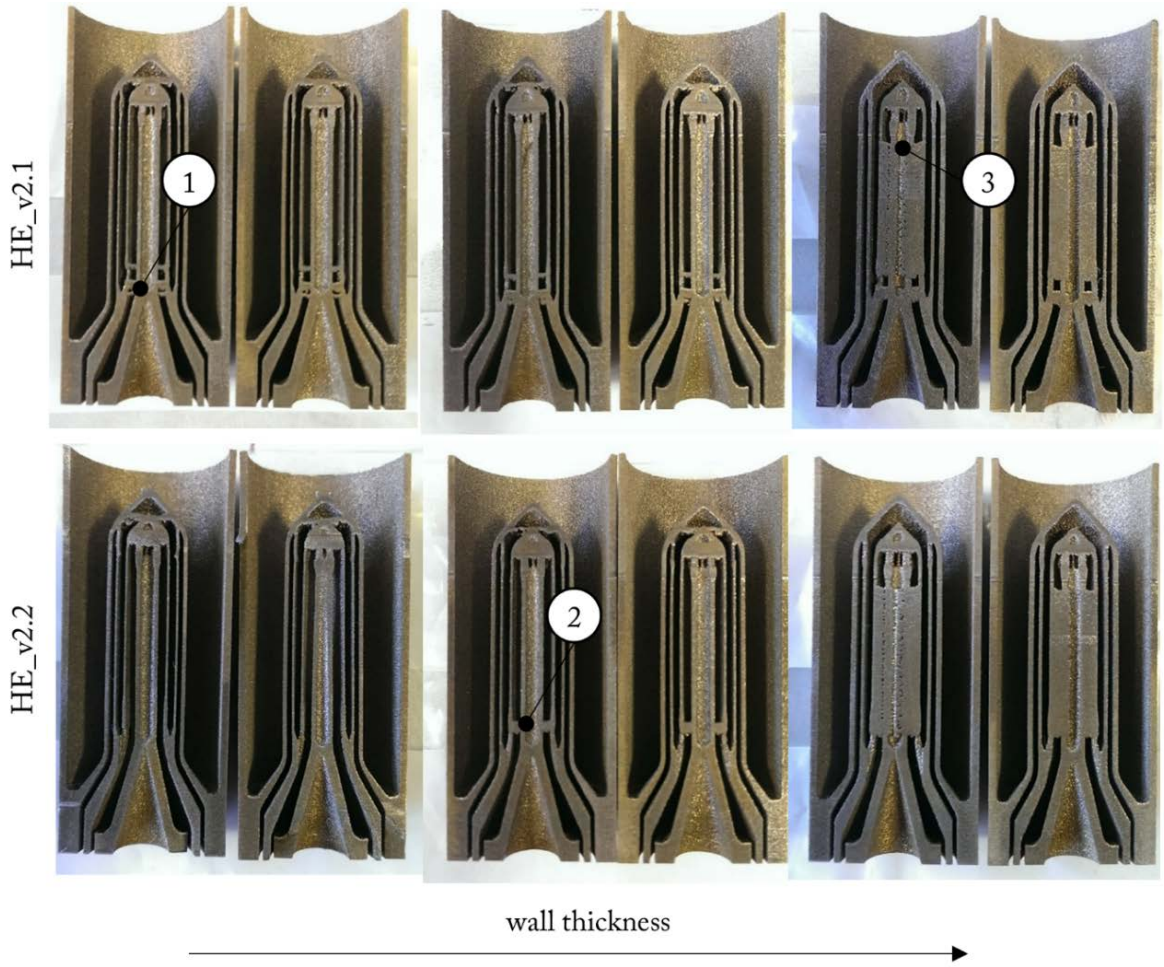

Fig. 2.67. Overview of the HE_v2 sectioned components.

2.3.4 HE Design Iteration 3

Fig. 2.68 shows an overview of the design of the last iterationHE_v3. The nozzle-end geometry is preserved from the previous iteration that was printed successfully with the lower thickness. In the direction of solving the elbow-end failure, the distance between the elbows has been increased to a slightly higher distance with respect to the successful built in the previous iteration. Finally, the fluidic mini-channels of cylinders 1 and 3 are further lengthened up to the elbow wall (Fig. 2.69).

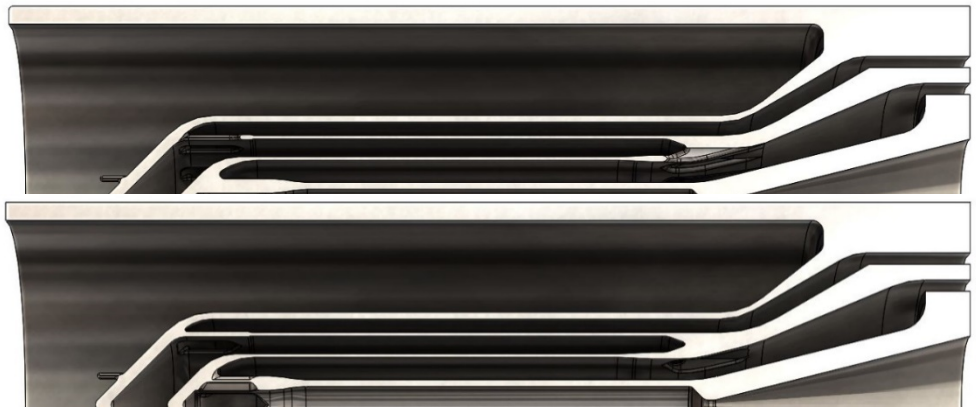

Fig. 2.68. CAD model top section-view of HE_v3.1 (top) and HE_v3.2 (bottom).

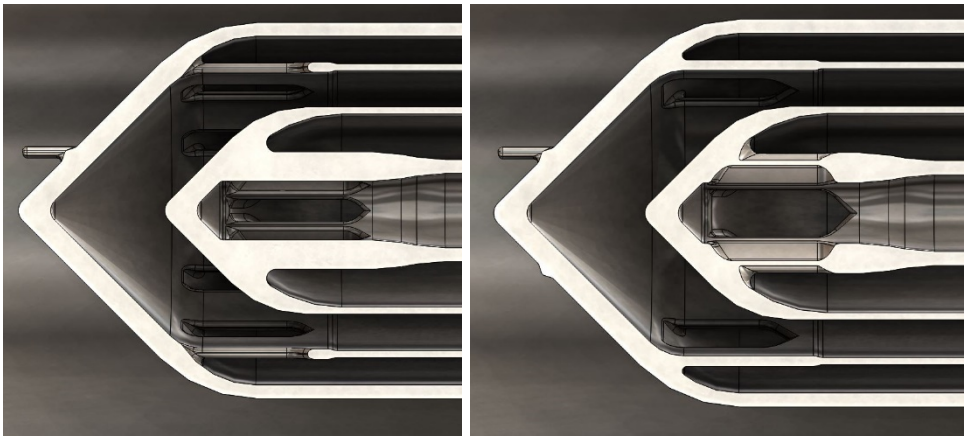

Fig. 2.69. Fluidic mini-channels in the elbow region for HE_v3.1 (left) and HE_v3.2 (right).

2.3.4.1 Variations: Gap between Cylinders

The only difference between the two variations lies in the number of mini-channels, which is halved in HE_v3.2, resulting in 3, 6 and 6 mini-channels for cylinder 1 to 3 respectively. As a consequence, the width of the channels in HE_v3.2 is doubled, going from 0.5 mm to 1 mm.

2.3.4.2 Inspection of HE_v3

Both the variations of the third HE iteration were successfully printed. This was initially confirmed by the resistance measurement in laboratory environment taken with a milli-ohm meter, which gave 27 mΩ for all the 6 printed HE. Fig. 2.70 provides an half-section view of the reconstructed CT volume. No further dimensional analysis was taken.

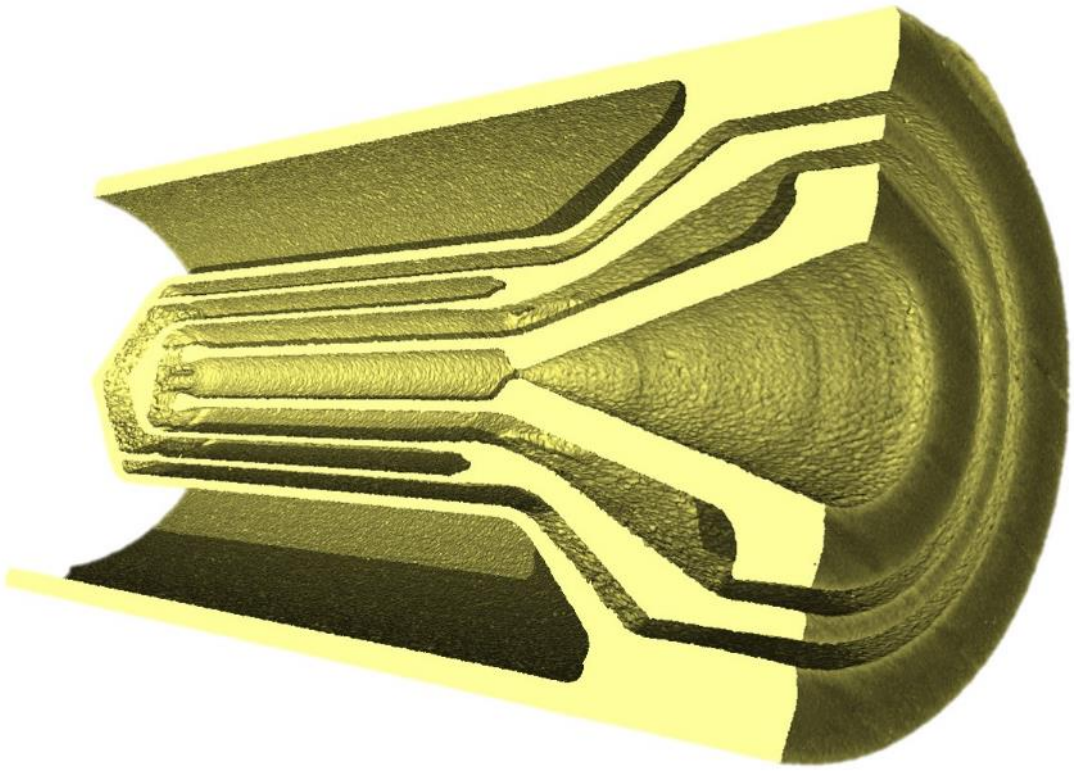

Fig. 2.70. Half-section view of the CT volume of HE v3.2, showing a successful build of the heat exchanger.

2.3.4.3 Resistance Check of HE_v3

A test was conducted to measure the HE_v3.1 electrical resistance between ambient temperature to about 1,100 K. A reference 316L SS wire of length L = 1.028 m was looped into the furnace feedthrough while two pieces of length $L/2$ have been TIG welded to each end of the HE. The measured resistance of the HE is calculated as the difference of the resistances of measured with a milli-ohm meter at the HE terminal and the reference wires terminals. Fig. 2.71 shows the experimental results with error bars. A simple 3D simulation was performed to evaluate the accuracy of the modelled materials, in the assumption of a constant HE temperature. The model uncertainty is shown with error bars of magnitude ±5%. The results show a relatively good agreement indicating the model resistivity of the 316 SS is fairly close to the 3D printed 316L SS.

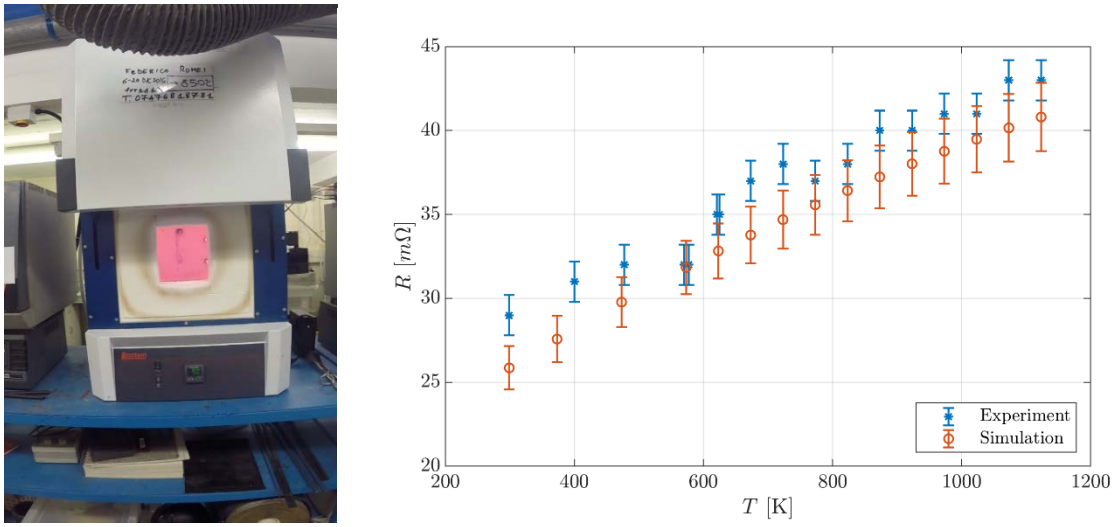

Fig. 2.71. HE_v3.1 inside the furnace at about 850°C (left) and resistance vs temperature with experimental and numerical values.

2.3.4.4 Porosity Assessment of HE_v3

It is known that SLM can produce parts with some porosity. This depends on the processing parameters. All parts were printed with the parameters listed in Table 2.2. A porosity analysis is performed using the software Avizo. In particular, the tool Trainable Weka Segmentation has been used to categorise the solid and void voxels. The training was conducted on manually selected areas where the presence of solid or void was certain. From all detected pores, those equal to or smaller than 4-voxels have been discarded.

Fig. 2.73 depicts the pores in their actual location, highlighting a correlation between the scan speed of the laser and the porosity. In particular, the borders of the 5 mm square islands are clearly visible. The scan speed for the borders is of 1.6 m/s, while for the inside 0.8 m/s. As a result, the borders result more porous than the interior of the square. This effect determines the observed porosity distribution. Despite the stunning effect of the image, the measured porosity with this technique is of only 1.1 %, which means that the part is 98.9% solid. It has to be noted that the detected porosity with this technique filters out the smallest pores, which are not detectable with the scan resolution of 27 μm. This can be argued by observing that the shown histogram resembles the right part of a normal distribution curve.

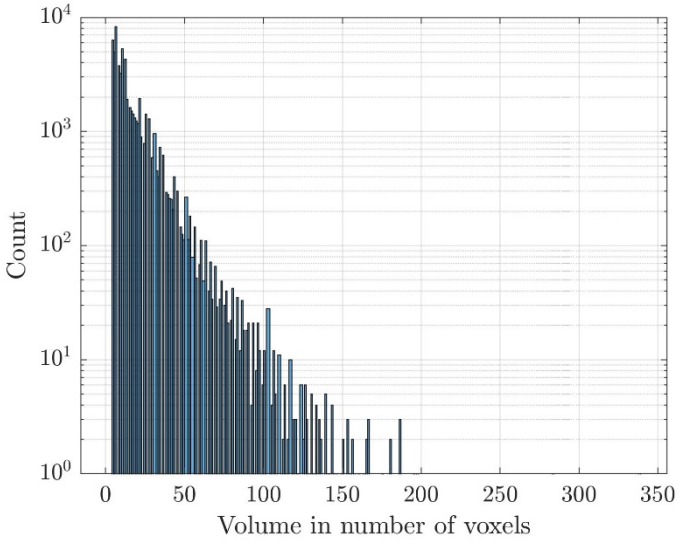

Fig. 2.72. Micro-porosity semi-logarithmic histogram of HE_v3.1 obtained from the CT volume analysis.

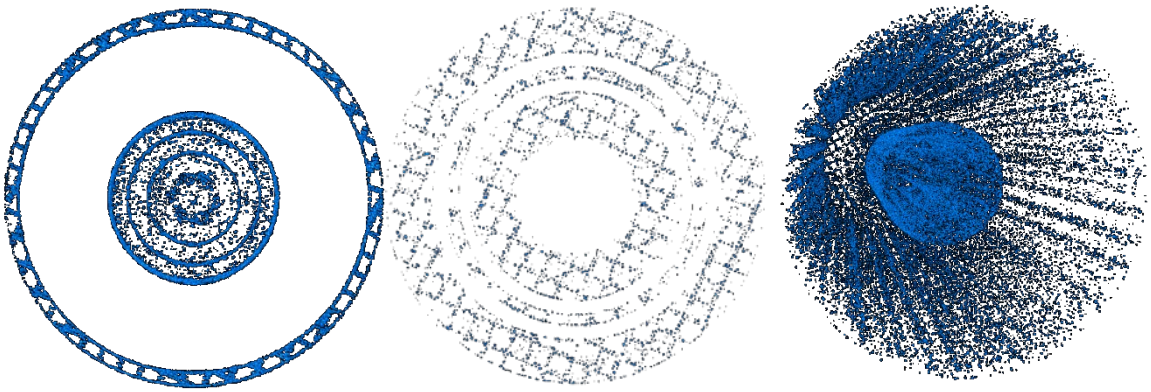

Fig. 2.73. Views of the micro-pores distribution of the HE_v3.1 {1}: view of the top half of the component (left), top view of a 5% length slice at the nozzle end (centre) and overall view of the pores detected with the CT scan (right).

2.3.5 Summary of the HE Iterations

A total number of three iterations has been attempted to successfully produce the heat exchanger design. Fig. 2.74 shows a flowchart of the iterations performed with discarded variations while Table 2.10 reports the main dimensions for each iteration design, where D_{in} is the inner diameter of cylinder 1, t_1 to t_4 are the thicknesses of the fours HE cylinders, g_1 to g_3 the annular gap between cylinders 1-2, 2-3 and 3-4, r_1 to t_3 the thickness of the connectors derived from Eq.(2.6) and *f.c* the number of fluidic mini-channels on cylinders 1,2 and 3 respectively. Below is a summary of the main changes that occurred from one iteration to another:

- **HE v0.1 and v0.2:** Each variation corresponds to a connection method between the concentric cylinders. HE v0.1 was discarded because it produced a major printing failure. With the selection of HE v0.2, the connection method produced a much better result and was selected as a baseline for the next iteration.
- **HE v1**: The overall dimensions of the HE are substantially changed by increasing the length of the cylinders and by producing more shallow angles in the nozzle regions. In this iteration, the fluidic channel sections were thickened to keep a constant section area throughout each cylinder. With this iteration, the two intermediate cylinders are manufactured successfully with a thickness of 0.15 mm, halving the previous value of 0.3 mm. In this design, an increment of the gaps between cylinders has also been implemented.
- **HE v2.1 and v2.2**: Each variation was printed with three increasing thicknesses of the cylinders. HE v2.2 implemented more effectively higher fluidic channels on the nozzle end and was therefore selected as a baseline for the following iteration. In this iteration, the gaps between cylinders were further increased.
- **HE v3.1 and HE v3.2**: Each iteration was printed in three full and three half-section copies to access printing repeatability. HE v3.2 implemented half the number of fluidic channels, which were also 1 mm wide instead of the original 0.5 mm. Both variations implemented higher fluidic channels for the elbow end. They were both successfully printed.

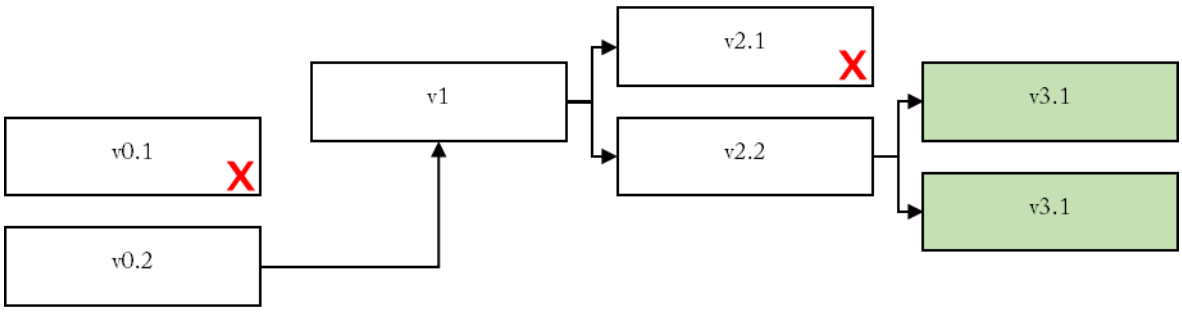

Fig. 2.74. Flow chart of the heat exchanger design iterations. The red cross indicates the discarded variations. Iteration v3.1 was successful.

Table 2.10. Main dimensions corresponding to each heat exchanger iteration with dimensions in mm (f.c. states for fluidic channels).

Iter.	D_{in}	t_1	t_2	t_3	t_4	g_1	g_2	g_3	d_e	r_1	r_2	r_3	f.c.
v0.1	1.33	0.5	0.3	0.3	0.5	0.5	0.5	0.5	1.3	-	-	-	6,6,6
v0.2	1.33	0.5	0.3	0.3	0.5	0.5	0.5	0.5	1.3	-	-	-	6,6,6
v1	1.83	0.35	0.15	0.15	0.35	0.7	0.6	0.5	1.1	0.339	0.148	0.116	6,12,12
v2.1	1.83	0.5	0.3	0.3	0.5	1	0.8	0.6	1.7	0.454	0.282	0.229	6,12,12
	1.83	0.4	0.2	0.2	0.4	1	0.8	0.6	1.5	0.378	0.211	0.161	6,12,12
	1.83	0.35	0.15	0.15	0.35	1	0.8	0.6	1.4	0.339	0.166	0.125	6,12,12
v2.2	1.83	0.5	0.3	0.3	0.5	1	0.8	0.6	1.7	0.454	0.282	0.229	6,12,12
	1.83	0.4	0.2	0.2	0.4	1	0.8	0.6	1.5	0.378	0.211	0.161	6,12,12
	1.83	0.35	0.15	0.15	0.35	1	0.8	0.6	1.4	0.339	0.166	0.125	6,12,12
v3.1	1.83	0.3	0.15	0.15	0.3	1	0.8	0.6	1.768	0.320	0.146	0.111	6,12,12
v3.2	1.83	0.3	0.15	0.15	0.3	1	0.8	0.6	1.768	0.310	0.146	0.111	3,6,6

2.4 Summary

The SLM material verification and process validation exercise have provided one of the most comprehensive studies to date of additive manufacturing for space propulsion applications. A methodical approach to design and characterise the SLM components has been performed, which helps in understanding some very important design and modelling considerations such as the implications of surface roughness and detailed design. Furthermore, additional tests such as EB welding the SLM material and drilling the throat of the printed nozzle were developed to correct some of the shortcomings of the AM process, none of which were unexpected. The highlights of this chapter are:

- The background on metal additive manufacturing with a focus on SLM is shown;
- The typical defect of SLM are discussed, such as stress concentration, porosity, balling, surface quality and overhanging issues;
- Computed tomography NDI is identified as a suitable tool for the HE design iteration process;

- A manufacturing verification process on SLM has been conducted to investigate the printability of the STAR monolithic heat exchanger concept, including the thin cylindrical walls, the nozzle and the elbows;
- SEM shows the morphology of the SLM surfaces, while optical profilometry is used to quantify the surface roughness;
- The surface quality of the representative specimens is verified by optical inspection tools;
- Quantitative nominal-to-actual comparison is performed with computed tomography;
- Fine complex structures with a minimal wall thickness of 150 μm are successfully demonstrated.
- The novel STAR heat exchanger for a spacecraft electrothermal propulsion is produced via SLM in stainless steel 316L;

There are several lessons learned from the metal additive manufacturing investigation reported in this chapter. Some suggestions that can help someone new to the field to design successfully a metal AM part are listed below:

- Know the particle-size distribution of the raw material to infer the as-printed surface roughness of AM parts. In particular, the average surface roughness will be dictated by half-melted particles on net surfaces.
- Think about not accessible parts of the printed component and if the as-printed quality is acceptable, otherwise, rethink the design.
- Conduct a manufacturing investigation of sub-parts if the component is complex. This is useful to isolate local issues and evaluate specific post-manufacturing machining.
- Avoid support material if the facing-down part of the component requires high dimensional accuracy. Support material can, in fact, introduce warping of the component due to limited heat conduction between the melt pool and the print base plate.
- Use extensively fillets, rounded corners and shallow transition in the design. This avoids the concentration of thermal stress in those areas during printing and reduces chances of deformation or crack failure.
- Avoid overhanging of any part and use, instead, a maximum print angle of 45° where possible. Avoid semi-sphere caps oriented in the print direction and use rather cone shape caps.

- Avoid printing small holes with a radius comparable to the laser spot size. The resulting hole will be non-circular, with an irregular contour and in general of a smaller dimension. Guidance holes can be used for post-manufacturing drilling purposes.
- Conduct a literature review and, if necessary, experimental investigation on required joining techniques in the assembly of the component with other parts.
- Do not oversize the component. AM gives the unique advantage to minimise the mass of components with unique design solutions. Rather iterate the design process to minimise the mass from a doable starting point.
- Change one design parameter at a time in the iteration process to address one issue at a time.

3 Design, Manufacturing and Testing of the Prototype Model

Part of this work was published in Acta Astronautica:

Romei, F. and Grubišić, A.N. Validation of an additively manufactured resistojet through experimental and computational analysis. Acta Astronautica, Volume 167, February 2019, Pages 14-22.

This chapter presents the first proof of concept validation of the Super-high Temperature Additive Resistojet (STAR-0). The device contains the innovative multifunctional monolithic heat exchanger, described in Chapter 2 (Section 2.3.4), enabled by SLM metal additive manufacturing processes. The STAR-0 detailed design and construction is described and its performance characterised through a combination of dry-heating and wet-firing tests. This includes verification testing with argon in both cold and hot-firing mode, at a range of electrical power inputs. Thrust measurements range from 9.7 ± 0.16 mN to 29.8 ± 0.16 mN, with a maximum measured specific impulse of 80.11 ± 1.49 s. Thrust performance is measured using a high-precision vertical balance and liquid-metal power transfer terminals to eliminate thermal drift. Highly coupled multi-physics computational models validate the electro-thermal and thermo-fluidic characteristics of the prototype, including a prediction of the maximum propellant stagnation temperature and structural temperature, 649°C and 854°C, respectively.

3.1 Preliminary Considerations

The STAR high-temperature resistojet concept has a target I_{sp} > 80 s, with an overall efficiency of > 60% (Section 1.5.1). The primary novelty of the technology lies in the multifunctional heat

exchanger, which is 3D-printed via SLM. Fig. 3.1 shows the schematics of the Heat Exchanger (HE) component, which consists of a monolithic thin-wall concentric exchanger, which also serves as a resistive heater and regenerative heat recuperator, where the inner cylinder (1) also integrates a converging-diverging nozzle. The gas flows from the outer channel (1) and recirculates around the heat exchanger until it reaches channel (4), which terminates in the nozzle inlet. The iterative design process of the prototype HE manufactured in stainless steel 316L was described in Chapter 2.

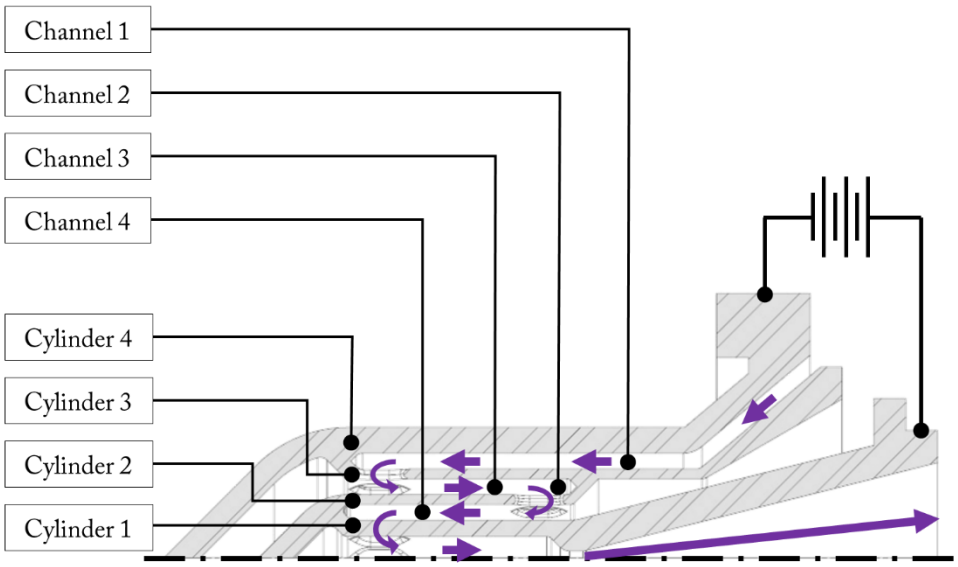

Fig. 3.1. Axial-symmetric schematics of the monolithic STAR heat exchanger concept. The propellant flow path (purple) and the electrical interface are shown.

3.1.1 Preliminary Dimensioning of the Heat Exchanger

The four concentric cylinders are connected in series forming an electrical resistance to which power is applied. The heat is released through Joule heating, $P_e = RI^2$, where each cylinder resistance follows Eq.(3.1), where ρ is the electrical resistivity of the material, L the length of the cylinder and A the cross-sectional area.

$$R = \rho \frac{l}{A} \tag{3.1}$$

For this reason, the lower the cross-sectional area, the higher the resistivity. The manufacturing verification process, described in Chapter 2, showed that a minimal wall thickness of 0.15 mm can be achieved consistently. For this reason, cylinders (2) and (3) have a thickness of 0.15 mm, which maximises their resistivity. At the same time, since cylinder (1) develops the highest temperature, it is also subjected to the greatest thermal stress. For this reason, the thickness of cylinder (1) is set to 0.3 mm. Finally, cylinder (4) creates the outer shell of the HE and gives stiffness to the structure; for this reason, its thickness was also set to 0.3 mm. Another reason for using 0.3 mm for the thicker cylinders is to keep the mass of the HE as low as possible. The gap between each pair of cylinders is also a result of the iterative design process.

The STAR-0 nozzle has the same throat and diverging cone dimensions as the SSTL's resistojet performance comparison. A similar design could suit the LEO M1 mission requirements (Table 1.20) in the perspective of a high-performance thruster to be manufactured in a nickel alloy and able to produce a specific impulse of > 60 s. The computational analysis, described in Chapter 4, shows that this is feasible. In this case, the performance improvement with respect to the current Xe resistojet technology would be +25%. At the same time, the study on the prototype will form the basis of the high-temperature refractory metal applications by highlighting possible design flaws and design improvement for the next development phases. Therefore, the overall length of the heat exchanger was selected such that the overall mass of the thruster was < 250 g. This process took place at the same time of the assembly design development, described later in Section 3.2.1. The resulting average cylinder length is 22 mm.

3.1.2 Nozzle Calculations

In this section, the expected stagnation pressure, flow rate, nozzle efficiency and specific impulse are calculated at the MOT for Xe, the design propellant, and for Ar, the laboratory test propellant. STAR-0 can operate up to 870°C being manufactured in stainless steel 316L. In fact, for this material, this is the maximum temperature for intermittent service in air (no vacuum data available), while for continuous service it can operate up to 925°C [91]. The expected maximum propellant stagnation temperature is 200 degrees less than the maximum structural temperature, as suggested from the simulations in Chapter 4; therefore, it is assumed that MOT = $T_{0,m}$ = 670°C. Calculations are based on the STAR-0 nozzle with A_t = 0.139 mm^2 and using the modelled nozzle efficiency of Eq.(1.23). The conversion of 1 sccm = 7.43583×10^{-4}M_a mg/s is used for the conversion of the mass flow rate, where M_a is the propellant mass in atomic mass units, in particular, M_a(Xe) = 131.30 and

M_a(Ar) = 39.95 (Table 1.1). When calculating the Xe flow rate, a correction factor is taken into account for compressibility at standard temperature and pressure, which changes the mass flow rate by 0.9931468 [2]. For Ar, the viscosity of in μPa·s is calculated using the polynomial function Eq.(1.22) from the COMSOL material library (*Argon [gas]*, where c_0 = 2.823345, c_1 = 7.51229, c_2 = -3.008134, c_3 = 8.881353, c_4 = -1.007569).

Table 3.1 summarises the results at incremental thrust levels. Fig. 3.2 and Fig. 3.3 show the stagnation pressure and efficiency colormaps for Xe and Ar, respectively (same method of Section 1.5.2.3). The values listed in the table are all located at the top edge of each graph, which provides the maximum attainable performance for each propellant in the current assumptions.

Table 3.1. Nozzle performance of STAR-0 at MOT calculated at increasing thrust levels for Xe (top) and Ar (bottom).

F [mN]	p_0 [ba]	$\dot{m}$ [mg/s]	$\dot{V}$ [sccm]	η_n	I_{sp} [s]
10	0.60	24.55	826	0.80	42.8
20	1.13	46.36	1561	0.78	45.1
30	1.60	65.76	2214	0.76	46.3
40	2.13	87.58	2948	0.75	47.3
50	2.60	106.97	3601	0.75	48.0
F [mN]	p_0 [ba]	$\dot{m}$ [mg/s]	$\dot{V}$ [sccm]	η_n	I_{sp} [s]
10	0.35	14.24	145	0.75	75.4
20	0.62	25.56	260	0.78	79.2
30	0.90	36.87	375	0.81	81.5
40	1.20	49.60	505	0.83	83.4
50	1.48	60.91	620	0.84	84.8

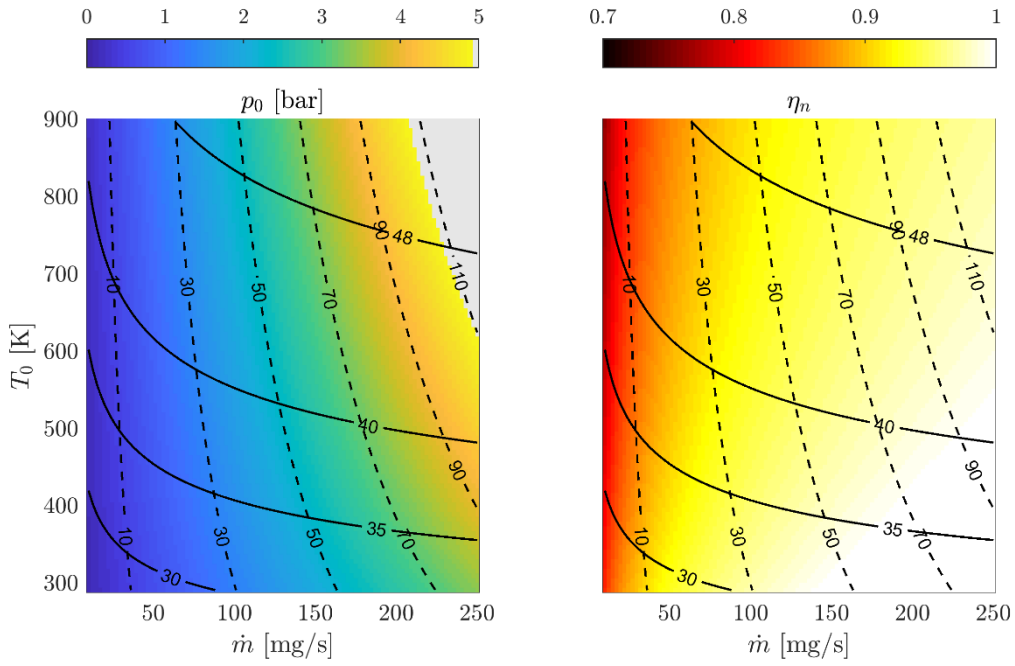

Fig. 3.2. Nozzle stagnation pressure (left) and nozzle efficiency (right) colormaps with overlaid thrust (dashed lines) and specific impulse (solid lines) iso-contours for Xe propellant.

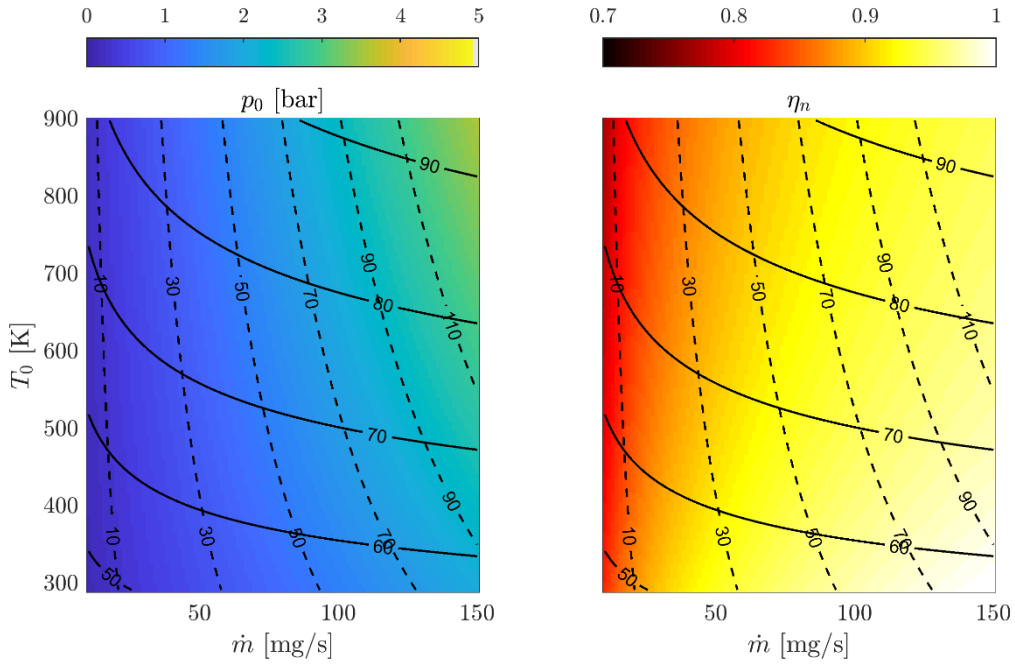

Fig. 3.3. Nozzle stagnation pressure (left) and nozzle efficiency (right) colormaps with overlaid thrust (dashed lines) and specific impulse (solid lines) iso-contours for Ar propellant.

3.1.3 Voltage-Current Range

The total electrical resistance and the resistance breakdown of each cylinder are calculated with Eq.(3.1) on the nominal geometry of the cylinders of HE_v3, corresponding to the last iteration of the design process described in Chapter 2. In particular, the inner cylinder has an internal radius of $r_t\sqrt{\varepsilon_{in}}$ = 0.81 mm, where the throat radius is r_t = 0.21 mm, and the area ratio of the nozzle inlet to the throat is ε_{in} = 15. Each cylinder length is 22.1 mm, 22.78 mm, 22.32 mm and 25.33 mm from cylinder 1 to 4, respectively. The electrical resistance of each cylinder of the HE is calculated interpolating the AINSI 316 resistivity data used in Section 1.5.2.4 (Table 3.2). It is assumed that 100% of the resistance is from the HE and the HE temperature is constant. As most of the resistance is generated by the inner cylinders, this assumption does not lead to a significant error. With this assumption, the resistance portion associated with each cylinder from the innermost is 36%, 32%, 22% and 10%, respectively. The resulting maximum expected resistance is in the region of 40.5 mΩ.

Table 3.2. Expected current-voltage characteristics of STAR-0 up to the MOT.

T_m [°C]	R_1 [mΩ]	R_2 [mΩ]	R_3 [mΩ]	R_4 [mΩ]	R [mΩ]
20	9.25	8.40	5.74	2.58	25.97
200	11.01	9.99	6.83	3.07	30.89
400	12.59	11.42	7.80	3.51	35.32
600	13.65	12.38	8.46	3.80	38.29
870 (MOT)	14.43	13.10	8.95	4.02	40.50

The required electrical power applied to the heater is evaluated with Eq.(3.2), which derives from Eq.(A.7), assuming $P_{0,in} \approx 0$ (cold gas power) and η_{ts} = 60% (total thruster efficiency).

$$P_e = \frac{g_0 F I_{sp}}{2\eta_{ts}} \tag{3.2}$$

It is now possible to estimate the STAR-0 current-voltage characteristics using the values of specific impulse and nozzle efficiency listed in Table 3.1. Table 3.3 shows the expected voltage-current

characteristics deriving from the previously calculated electrical power and resistance. The prototype thruster using Ar propellant is therefore expected to operate at a potential between 0.5 V and 1.2 V and a current between 12.7 A and 29.4 A depending on the objective thrust. The required electrical power to provide 50 mN at the design specific impulse is 19.8 W and 35.1 W for Xe and Ar, respectively.

Table 3.3. Expected voltage-current characteristic of the STAR-0 prototype for the calculated electrical power at the MOT in the assumption of η_{ts} = 0.6.

	Xe			Ar		
F [mN]	P_e [W]	V [V]	I [A]	P_e [W]	V [V]	I [A]
10	3.6	0.38	9.44	6.5	0.51	12.66
20	7.5	0.55	13.65	12.8	0.72	17.80
30	11.3	0.68	16.71	19.6	0.89	22.02
40	15.7	0.80	19.71	27.7	1.06	26.14
50	19.8	0.89	22.10	35.1	1.19	29.43

3.1.4 Power Electronics Discussion

The much lower electrical resistance of the STAR thruster (on the order of 0.01 Ω), when compared to the existing SSTL's T-30 (on the order of 1 Ω), results in a much lower operating voltage, hence, a much higher electrical current. The T-30 heater consists of a commercial filament heater, which operates at an unregulated bus voltage of 28 V to deliver the 30W of power. Therefore, the STAR resistojet requires a Power Conditioning Unit (PCU) to step-down the voltage from the bus 28 V to the range 0-2 V. The STAR PCU might consist of a DC/DC converter, which in commerce has typically a mass on the order of 100 g (e.g., Cosel CDS400480 or Murata DRQ-8/100-L48NB-C). For a space-qualified PCU, the mass can be roughly estimated using Table A.4. Assuming conservatively a mass of 10 kg/kW [20], with 50 W required for the LEO application, the PCU mass is 0.5 kg while for 500 W required for the GEO application using up to two thrusters at a time, the PCU mass is 10 kg. With reference to Section 1.5.2, the PCU mass over the propellant mass saving introduced using the STAR concept as opposed to traditional Xe resistojets is 10% and 23%,

respectively. Therefore, the benefit of using the high-temperature resistojet is still important. It has to be noted that PCU selection and development is not part of this work, but it will be necessary to investigate it in the prospect of producing an engineering model of the thruster.

3.2 STAR-0 Preliminary Assembly Design

3.2.1 Assembly Design Process

The design of the prototype model was iteratively progressed towards the final STAR-0 design depicted in Fig. 3.4 (d). The starting point was mainly based on the design reference, the J3 thruster, found in [46]. The main difference introduced by the novel STAR design is the fact that the heat exchanger is now a single monolithic element manufactured via SLM. Below is a summary of the key points of each design iteration with the main changes introduced at each step:

a) This is the first sketch of the assembly and design at the beginning of the research without any result yet on the additive manufacturing verification. This sketch does not include the fluidic interface. It was initially thought to integrate the nozzle with the external envelope of the thruster, which would have been jointed with the monolithic heat exchanger (1).

b) The nozzle is now integrated into the heat exchanger (1), which is welded on two different inflow cylinders (2 and 3). Ceramics are used to stop the flow to circulate from the inflow envelope to the nozzle wall (4) and to support the radiation shielding (5). The radiation shielding is both wrapping the heat exchanger (6) and shielding the heat at the back of the thruster with radiation shielding disks (7). The inflow is entering the back part of the thruster with an angle to give a swirl (8, not shown in the figure). The back of the thruster is sealed with a ceramic part (9).

c) There are two main differences with respect to the previous design. The first one is that now the heat exchanger integrates the inner inflow cylinder (1). The second one is that the inflow is moved from a radial to a centreline access. This is performed by introducing a new 3D printed element, the thruster inflow part (2), which diverges the flow from a pipe to an annular section. This part was also designed for SLM production (Table 2.3, AM-28). The seal of the pressurised heat exchanger is performed with two ceramic parts (3 and 4) at the back of the thruster.

d) This is the final iteration and incorporates two main changes with respect to the previous one. Firstly, a single ceramic gasket is now placed between the thruster inflow and the heat

exchanger (1). The gasket is compressed with six M3 fasteners. The second major change is that the mechanical support is now moved away from the hot thruster body by elongating and thickening the inflow stem (2). In addition, thermal spacers are introduced to further reduce heat conduction through the support (3). The manufacturing assembly uses the two EB welds, prepared in the manufacturing verification discussed in Section 2.2.4, designed to weld the HE to the Thruster Inflow (4) and the HE to the Thruster Casing (5).

It can also be noted that the heat exchanger design changed during the assembly design process according to the iterative SLM production described in Section 2.3. The final iteration of the assembly design (d) involved the implementation of a thermal insulation package as well as radiation shielding. However, these two elements were removed during the prototype development to simplify as much as possible the assembly during the performance testing. The technical drawings exploded view of the assembly is attached in Appendix E (9).

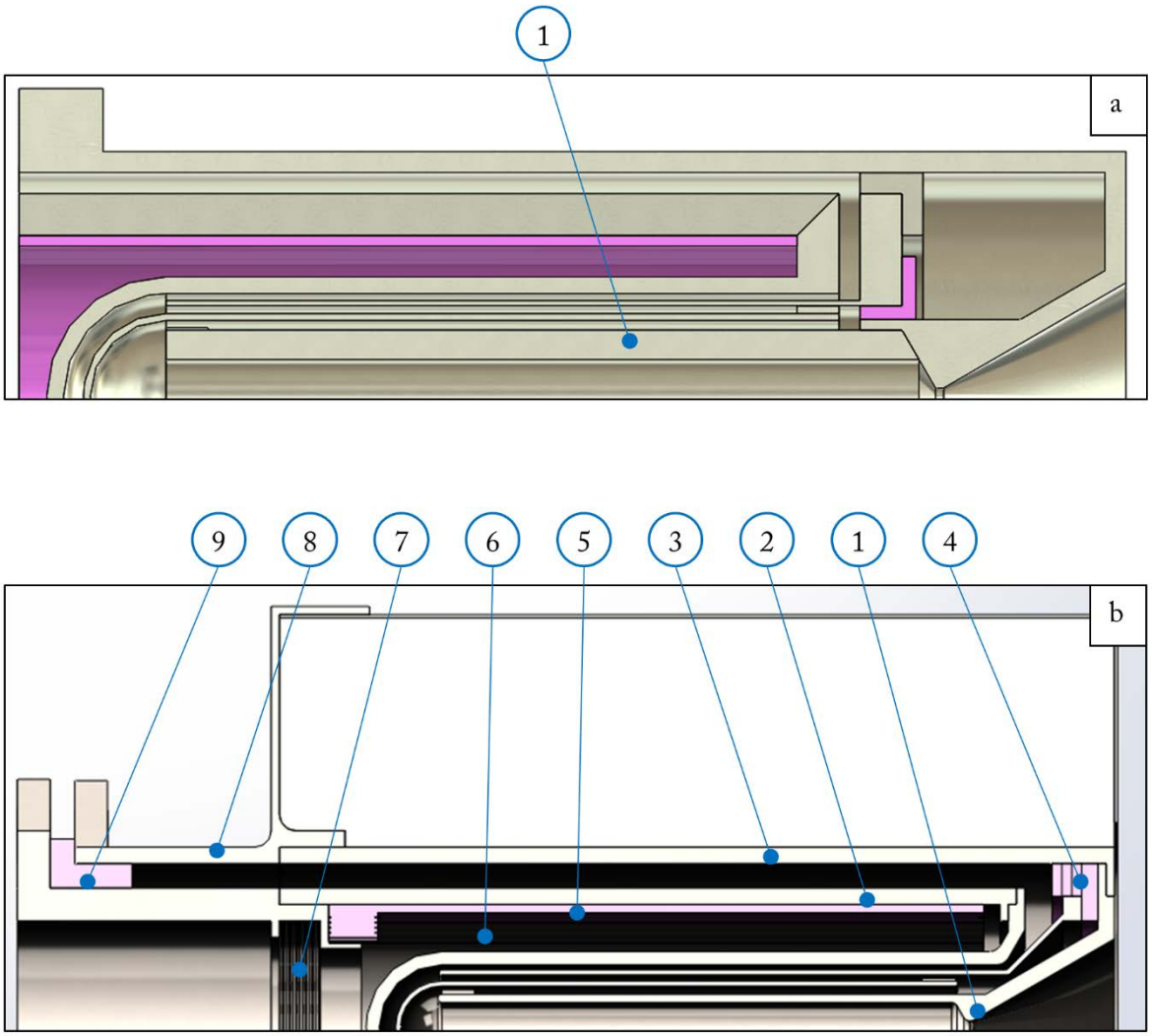

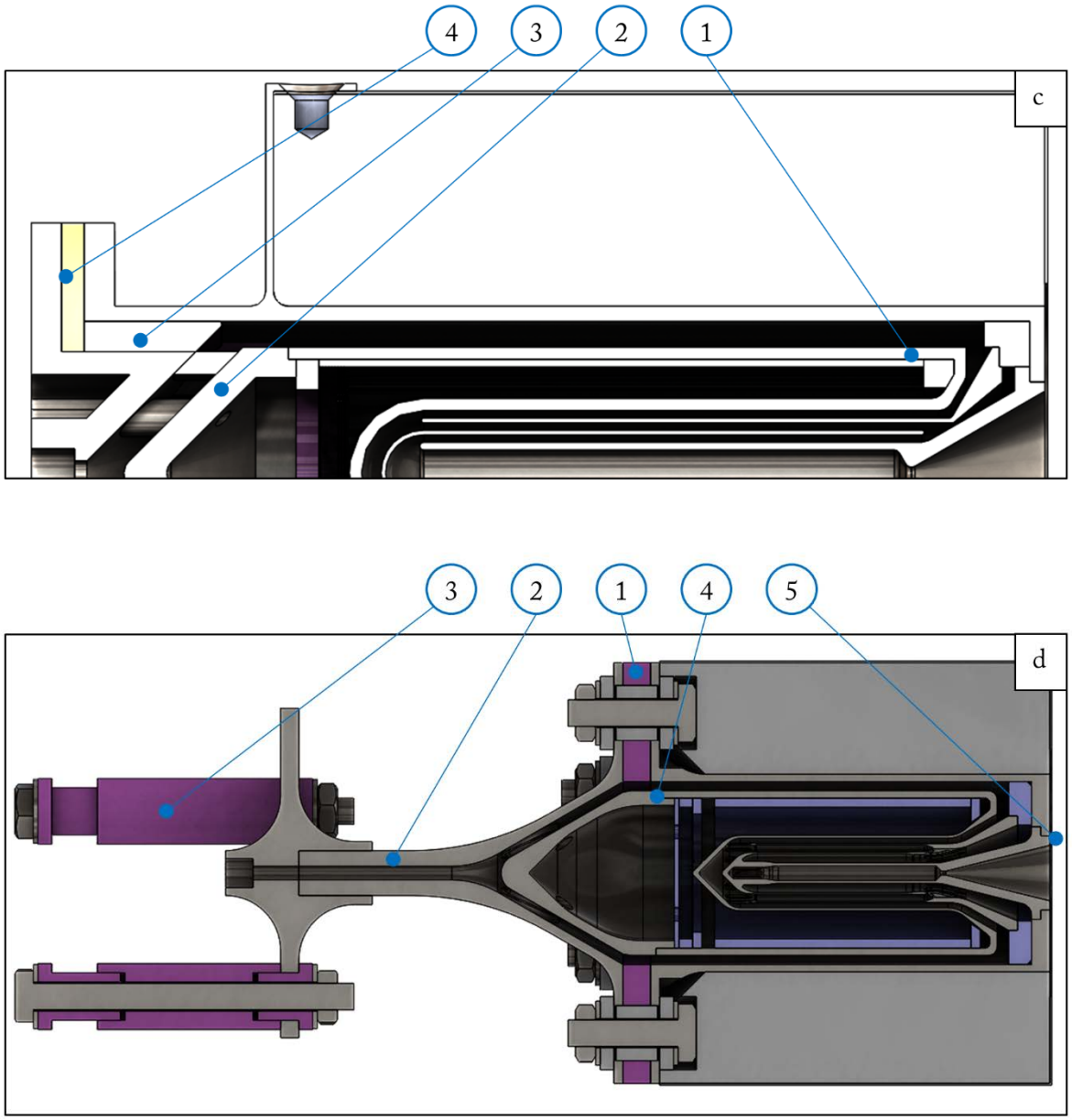

Fig. 3.4. Design iteration that led to the STAR-0 detailed design shown in figure (d). Ceramic components are in purple and blue.

3.2.2 Selection of Ceramics

Ceramic materials achieve both electrical insulation of the heater and withstanding the high temperature generated in the pressurised chamber. Ceramics tend to be excellent electric insulators, having high dielectric strength. Ceramics can be divided into two main categories, of which the most common materials are listed:

- **Machinable ceramics**: Duratec, Macor, Shapal (machinable aluminium nitride ceramic) and hexagonal boron nitride;
- **Non-machinable ceramics**: alumina (aluminium oxide), aluminium nitride, boron carbide, silicon carbide, silicon nitride and zirconia (zirconium oxide).

The ceramics in the first category do not require post-heat treatment and can be machined with ordinary metalworking tools. They are generally a good choice for prototyping a part before moving to harder materials. In general, they possess poorer mechanical properties with respect to non-machinable ceramics, but they are cheaper even for small-quantity orders. The main difference between Shapal and both Macor and Duratec is that the former has superior mechanical properties. Therefore, in many applications where mechanical loads are relatively low, Macor is a common choice. Boron nitride has poorer mechanical properties; however, it is used in applications where the operating temperatures are much higher. The ceramics of the second category, once fired, can only be machined using diamond grinding methods or other advanced machining processes. Their mechanical and thermal properties are superior with respect to machinable ceramics, and if large quantities and very high performance are required, they can be more cost-effective.

In Section 1.4.3.2 it was shown how resistojets in past applications used boron nitride for the highest-temperature thrusters and alumina or magnesia for lower-temperature applications. However, boron nitride costs on the order of 100 £/cm^3 or more, while Duratec costs approximately 0.05–0.10 £/cm^3, Macor is on the order of 1 £/cm^3, Shapal on the order of 5–25 £/cm^3 and Alumina on the order of 20 £/cm^3 [92]. For this reason, boron nitride was excluded from the materials for the prototype implementation. The ceramics selected for the prototype manufacturing were Macor and Shapal, the latter for the highest temperature components. At a later stage, Alumina was selected for the washers because of its superior compressive strength. Table 3.4 summarises the main mechanical properties of the materials selected and used for the STAR-0 fabrication.

Table 3.4. Main properties of the selected ceramics for the prototype assembly [92].

Property	Units	Macor	Alumina	Shapal
Max use temperature	°C	800	1,750	1,900*
Thermal conductivity at 20°C	W/(mK)	1.5	28	92
Specific heat	J/(kgK)	790	880	790
Density	g/cm^3	2.52	3.9	2.88
Coefficient of expansion	10^{-6} K^{-1}	12.6	8.4	5
		(25 - 300°C)	(20 - 100°C)	(800°C)
Flexural strength	MPa	94	250	300
Compressive strength	MPa	345	2,500	100
Modulus of elasticity	GPa	66.9	350	-
Poisson's ratio	°C	0.29	0.22	0.31

* in non-oxidising atmosphere, otherwise 1,000°C in air

3.2.3 Modal Analysis of the STAR-0 Assembly

A simple modal analysis was conducted to envisage the natural frequency and modes of vibration of STAR-0. Fig. 3.5 shows the modes of vibration resulting from the eigenfrequency analysis conducted in COMSOL using the SM physics (Appendix B.1). This is a purely structural study, and all contacts between surfaces are assumed ideal. Mode 1 (243.41 Hz) and mode 2 (243.55 Hz) are due to the bending of the thruster inflow stem on two orthogonal directions. Mode 3 (676.63 Hz) is due to the twisting of the thruster body around the inflow stem. Mode 4 (2250.4 Hz), Mode 5 (2254.6 Hz) and Mode 6 (2552.2 Hz) are due to the deformation of the outer cylinder of the HE. The design passed the structural check because the first mode of vibration is well above a typical launcher requirement of > 100 Hz.

3.3 Detailed Assembly Design and Manufacturing

Two identical assemblies were built and tested, namely STAR-0-A and STAR-0-B. The design details of the prototype and the manufacturing description are reported in this section.

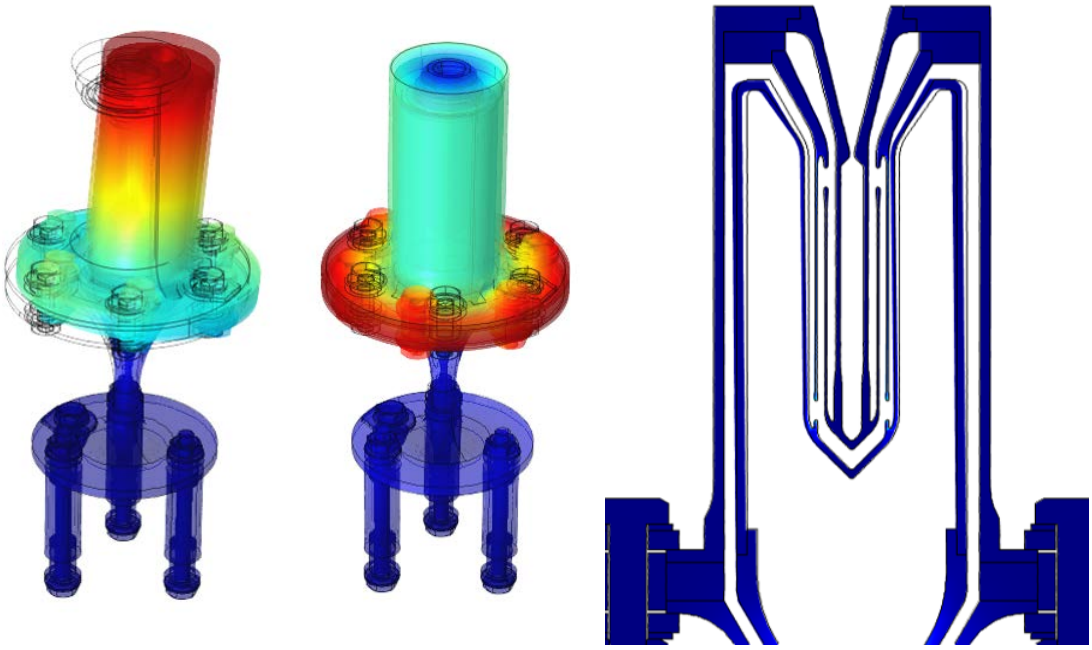

Fig. 3.5. Modal analysis results on STAR-0 assembly: modes 1–2 (left), mode 3 (centre) and mode 4–6 (right).

3.3.1 Detailed Design

Fig. 3.6 depicts the STAR-0 design and shows a radiograph of the STAR-0-B assembly while Table 3.5 lists the key components with respective material, manufacturing processes, quantity in the assembly and nominal mass and volume. The alumina is 99.7% pure, while the ring tab terminals are made in nickel-plated copper. Custom ceramics parts have been produced by Precision Ceramics. The total mass of the assembly, including fasteners, is approximately 150 g. The technical drawings of the assembly and each part can be found in Appendix E.

The cold propellant enters the thruster through the supply pipe, passing through the thruster inflow component and following an annular path, which envelopes the thruster body with relatively cold propellant up to a nozzle spacer. The latter blocks the path of the propellant and ensures that the majority of the flow moves towards channel (1) while maintaining electrical isolation between the walls. The propellant continues flowing through the four regenerative recuperation channels, finally arriving at a converging-diverging nozzle. A ceramic collar serves both leak tightness and electric isolation. Electrical power is supplied through positive and negative ring tab terminals positioned at the casing and the support, respectively, with the current flowing through the metallic body. The STAR-0 has four concentric cylinders with a nominal thickness of 300 μm, 150 μm, 150 μm and 300 μm, where the innermost cylinder is 22 mm long. The design of the connectors and micro-fluidic

channels, allowing the movement of flow between cylinders, are reported in Section 2.3.1. The gaps between the cylinders make three annular channels measured from the innermost as 0.6 mm, 0.8 mm and 1 mm, respectively. The nozzle has a nominal throat diameter of 0.42 mm, a half-angle divergence of 14°, and inlet and outlet area ratios with respect to the throat of 15 and 211, respectively.

The assembly drawings (Appendix E, 10), made in Solidworks, show three section details views of the mechanical interfaces. Section A depicts the half-section cut view of the assembly, including the thermal insulation and radiation shielding ceramic supports, which were ultimately not implemented in the prototype. Detail B shows the support of the thruster through M3×35 bolts, which are embedded with a ceramic thermal spacer assembly. It is also shown the 3.2 mm dia. access for the inflow pipe. Detail C shows the gasket fastener assembly, while detail D shows the same assembly where the positive ring tab terminal is placed. The latter is in contact with the Thruster Casing, while the negative ring tab terminal is positioned on the Thruster Support (Section A).

3.3.2 Manufacturing of the Parts

The SLM components, HE and Thruster Inflow, are printed on a Concept Laser M2 Cusing SLM machine, as described in Chapter 4. Fig. 3.7 shows the print plate no.3 (Table 2.3) with the second iteration heat exchangers and with the Thruster Inflow components immediately after printing and still welded on the print plate, and one HE cut off the print plate, showing the nozzle end. The components are cut from the build plate by electro-discharge machining (EDM) wire-cut. The excess powder of the as-printed components is removed through ultrasonic cleaning, with the components immersed in IPA in a glass beaker placed in water (Fig. 3.8). The cleaning process was performed several times in sessions of 5 minutes with the components turned upside-down each time until no excess powder was observed.

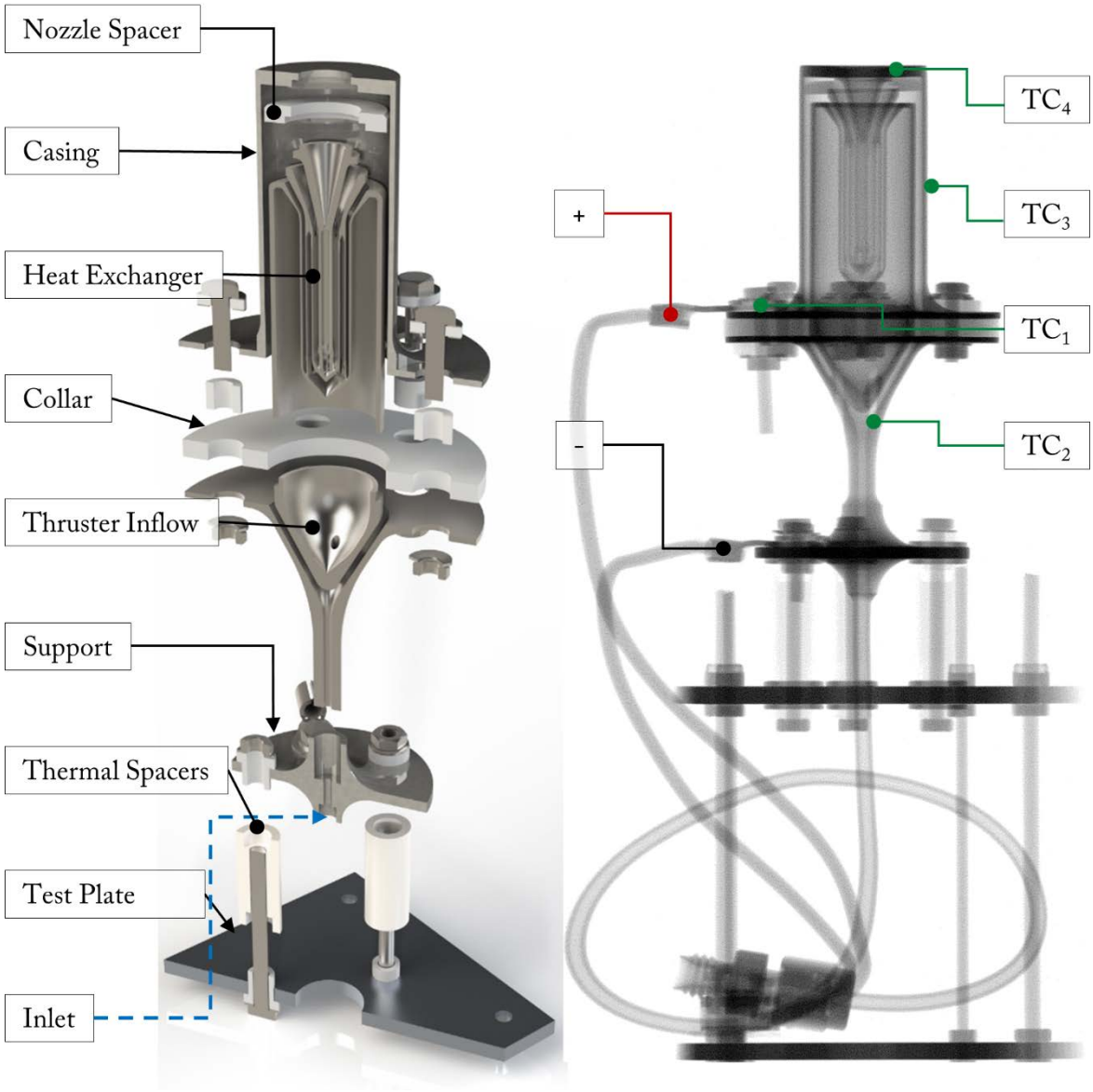

Fig. 3.6. Half-section exploded view of STAR-0 (left) and scatter-free radiograph of the STAR-0-B assembly with thermocouples and ring terminal positions (right).

Table 3.5. Main components of the STAR-0 resistojet (* only one version used per assembly).

File Name	Material	Manufacturing	Qty per assembly	Mass [g]	Volume [cmm]
Heat Exchanger	SS 316L	SLM + CNC	1	20.33	2,541.5
Thruster Inflow	SS 316L	SLM + CNC	1	25.92	3,240.1
Thruster Casing	SS 316L	CNC	1	33.67	4,208.9
Thruster Support	SS 316L	CNC	1	20.3	2,537.7
Nozzle Spacer	Shapal	CNC	1	0.54	532.8
Collar	Macor	custom made	1*	10.60	4,205.8
Support Sleeve	Macor	custom made	3	4.34	574.3
Support Washer Bottom	Macor	custom made	3	1.12	148.0
Support Washer Top	Macor	custom made	3	0.82	108.4
Insulating Sleeve	Macor	custom made	6	0.56	91.0
Insulating Washer	Macor	custom made	11*	0.06	63.3
Insulating Washer v2	Alumina	custom made	11*	0.25	63.3
M3 Nut	SS 316	off-the-shelf	10	3.3	41.3
M3x35 Bolt	SS 316	off-the-shelf	3	6.76	281.5
M3x11 Bolt	SS 316	off-the-shelf	6	5.94	123.8
M3 Steel Washer	SS 316	off-the-shelf	20	2.44	15.2
M3x7 Bolt (Terminal -)	SS 316	off-the-shelf	1	0.78	97.5
Tab Terminal	Ni-Cu	off-the-shelf	2	0.72	45.3

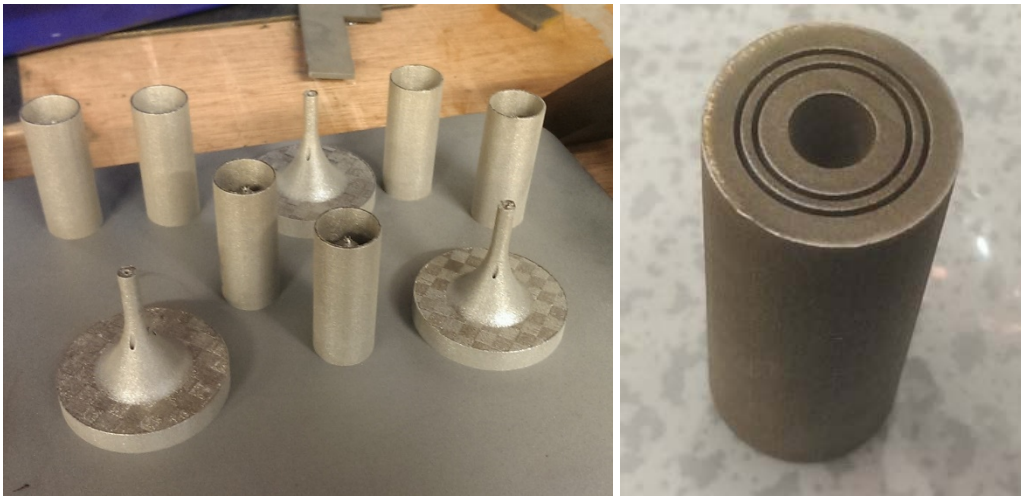

Fig. 3.7. Thruster and thruster inflow as-printed components (print no.3) on the Concept Laser M2 Cusing base plate (left) and as-printed HE_v2 (right).

Fig. 3.8. Ultrasonic cleaning of the HE components (left) and removed powder (right).

Both the heat exchanger and the thruster inflow require minimal CNC post-manufacturing on a lathe. A small jig was designed to support each HE outer cylinder for subsequent cuts, to prevent stressing of the connecting regions between the thin walls. With reference to the jig technical drawings (Appendix E, 25-28), the as-printed HE (Fig. 3.7, right) is placed on the lathe, and the top part of the outer cylinder is removed to expose the nozzle through CUT 1. The intermediate cylinder is fixed on the lathe through jig 1 and CUT 2 is performed. Finally, jig 2 is used to perform CUT 3 and CUT 4, which form the 0.5 mm shoulder on the nozzle end that couples with the thruster casing. Fig. 3.9 depicts the jig parts (left) and the final result on the heat exchanger and the thruster inflow. The nozzle is drilled to obtain the nominal throat diameter, because of the issues highlighted in Section 2.2.2.4. The HE components have been placed on the lathe with the support of jig 2 and the nozzle drilled at the maximum machine speed of 2,000 rpm with a 0.42 mm dia. HSS drill bit (Fig. 3.10, left). To ensure the nozzle centreline alignment, a dial has been used to ensure that the nozzle maximum displacement at the exit section is within ± 0.04 mm. The second thruster inflow (AM-28{2}) was printed with a major defect due to a failure in the powder deposition process occurred during printing no.2. Therefore, this part was used as a test-bed for the post-manufacturing process (Fig. 3.10, right). The machined parts, thruster casing and thruster support are shown in Fig. 3.11 (drawings in Appendix E, 29-30).

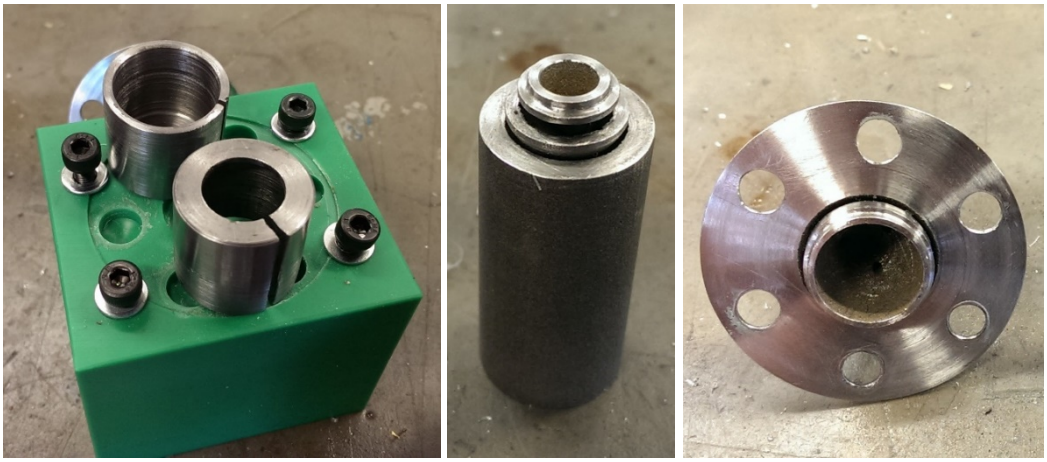

Fig. 3.9. Jig for post-manufacturing of the heat exchanger (left), machined HE_v1_part1 (AM-29, centre) and machined thruster inflow (AM-28, right).

Fig. 3.10. Technicians at EDMC while drilling the AM-01 throat (left) and with the Thruster Casing on the CNC lathe (right).

Fig. 3.11. Machined components at the EDMC: Thruster Casing (left) and Thruster Support (right).

3.3.3 Fit Assembly Notes

A fit assembly procedure served to adjust any interference or misalignment between the components. Fig. 3.13 shows the highlights of the procedure. In general, because of the particularly high surface roughness of the 3D-printed components, surfaces can interfere when coupled. Consequently, holes are slightly smaller (as demonstrated for the nozzle throat), and in general, tolerances are affected by the half-melted particles covering every printed surface (Section 2.2.3). The machined Thruster Inflow (TI) and the HE component are designed for interference fit to then perform the first EB weld of the assembly. However, the HE internal diameter is slightly smaller for the above-mentioned reason (1). Therefore, the internal surface of the HE corresponding to the attachment with TI has been slightly smoothened at the lathe (2, 3). The two components now fit properly (3). Therefore, to the TI-HE sub-assembly are added both the Collar (4) and the Thruster Casing (TC). However, the TC top is excessively out of the nozzle plane, which could affect the EB weld result (5). Therefore, the flange of TC has been skimmed off slightly to reduce this distance to a minimum (6-7). Since, initially, the tolerances on the M3 holes did not match perfectly, the six aligned holes are enlarged manually with an M3 drill bit to fit the ceramic sleeves correctly (8). Fasteners have been manually placed confirming the holes' alignment. The same fit assembly procedure is applied to the two assemblies. Fig. 3.12 shows the fit assembly final check before EB welding on the STAR-0-A.

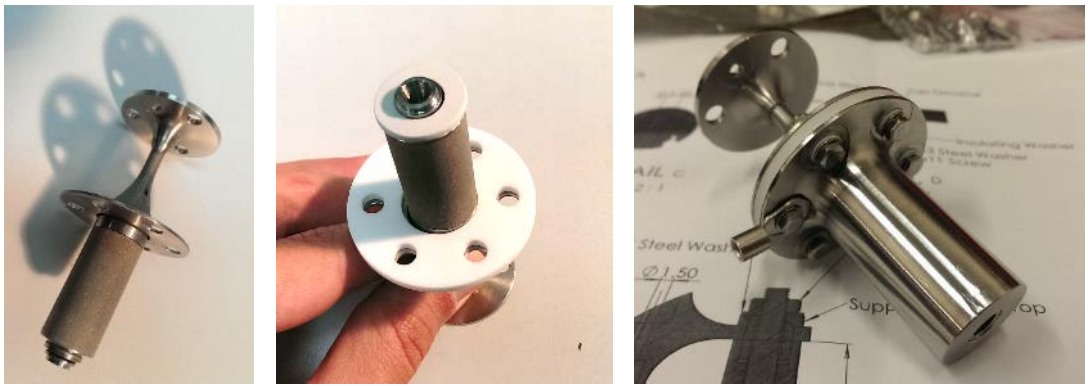

Fig. 3.12. STAR-0-A fit assembly steps to establish tolerances before EB welding.

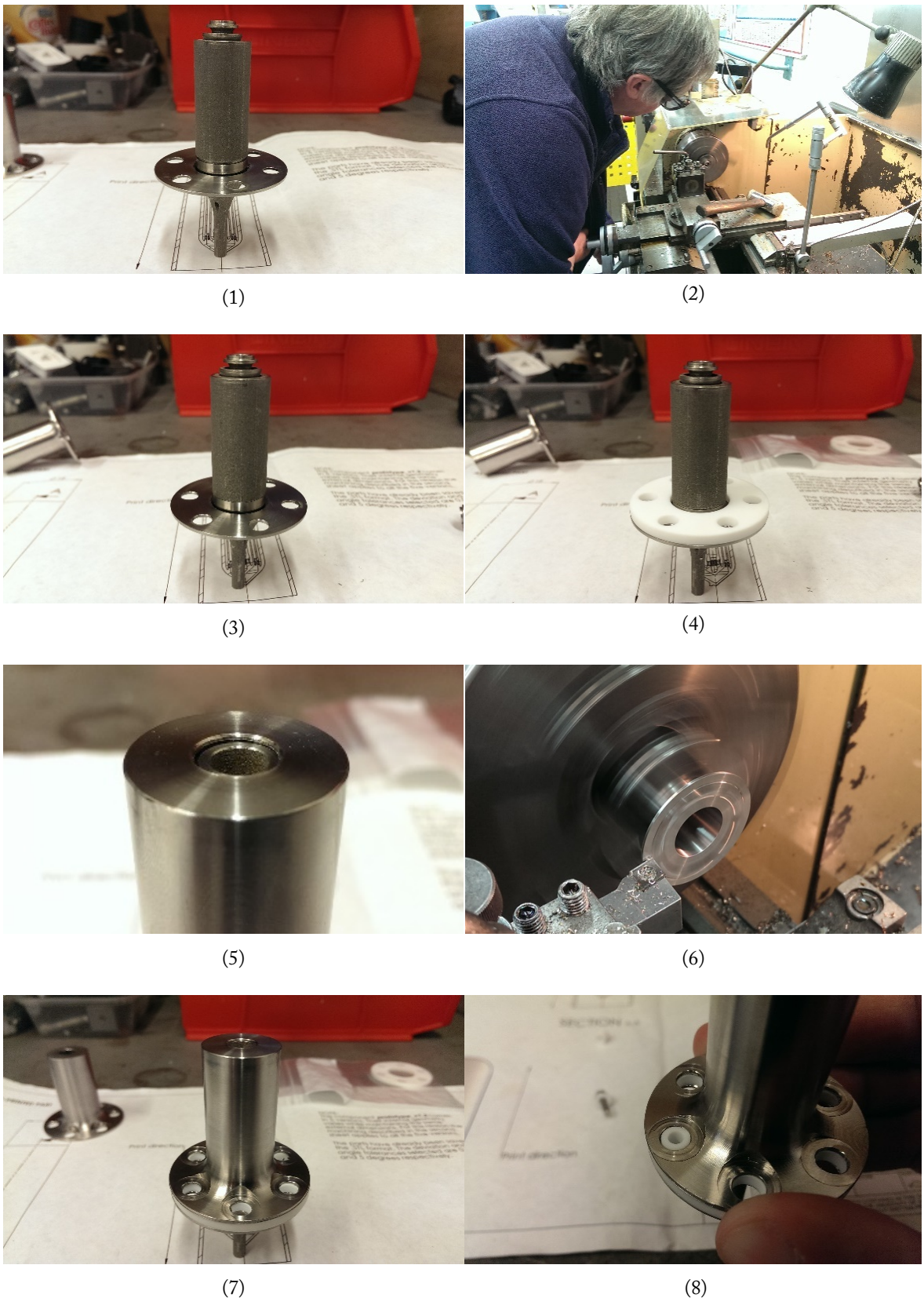

(1) (2)

(3) (4)

(5) (6)

(7) (8)

Fig. 3.13. Fit-assembly adjustments.

3.3.4 Construction of the Proof of Concept Thrusters

An assembly involves two EB welds, EB weld 1 to join heat exchanger–thruster inflow (Fig. 3.14-a) and EB weld 2, to join heat exchanger–thruster casing (Fig. 3.14-d). The EB welds ensure both electrical continuity and hermetic sealing. Fig. 3.14 shows the mounting procedure followed to perform EB weld 1 and 2 in sequence. The EB welds parameters were firstly developed by TWI Ltd and applied to the first assembly (STAR-0-A), while the second set of EB welds on STAR-0-B was produced by Ravenscourt Engineering Ltd using the same processing parameters. Once EB weld 1 is performed, the collar (b) and the nozzle spacer (c) can be inserted from the top of the assembly, then the thruster casing is positioned and the set of six fasteners tightened a quarter past hand-tight. Finally, EB weld 2 is performed. Also, two fusion TIG welds were performed at the EDMC workshop to join TI with to the Thruster Support, and the latter to a 1/8 in. SS propellant supply pipe. Both the EB and TIG welds details are reported in Section 2.2.4.

3.4 Test Setup and Computational Models

A total of two thrusters was produced (Fig. 3.15), STAR-0-A and STAR-0-B, which are nominally identical. STAR-0-A was subjected to a first preliminary wet-firing test campaign, which presented two major issues, in particular, a significant propellant leak and a thermal drift in the thrust measurement. This is discussed in Section 3.5. Subsequently, the same assembly was employed in a dry-firing test reported in Section 3.6.3. The second thruster, STAR-0-B, is subjected to wet-firing performance tests (Section3.6.2), where the propellant leak and thrust measurement drift issues were resolved. All wet tests are performed with argon propellant. The 3D and 2D computational models used for performance verification are also introduced such that they can be later used to gain insight into the performance data.

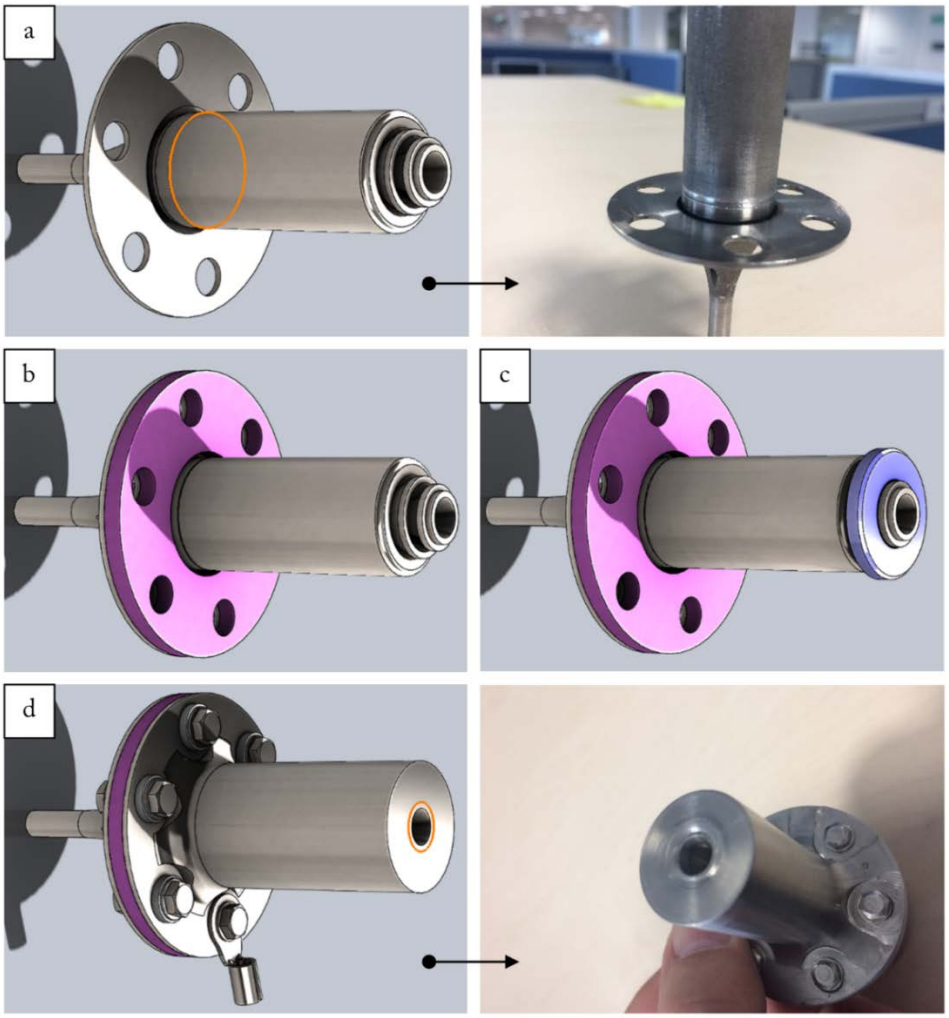

Fig. 3.14. CAD view and results of EB Weld 1 (a) and EB Weld 2 (d), with intermediate assembly passages.

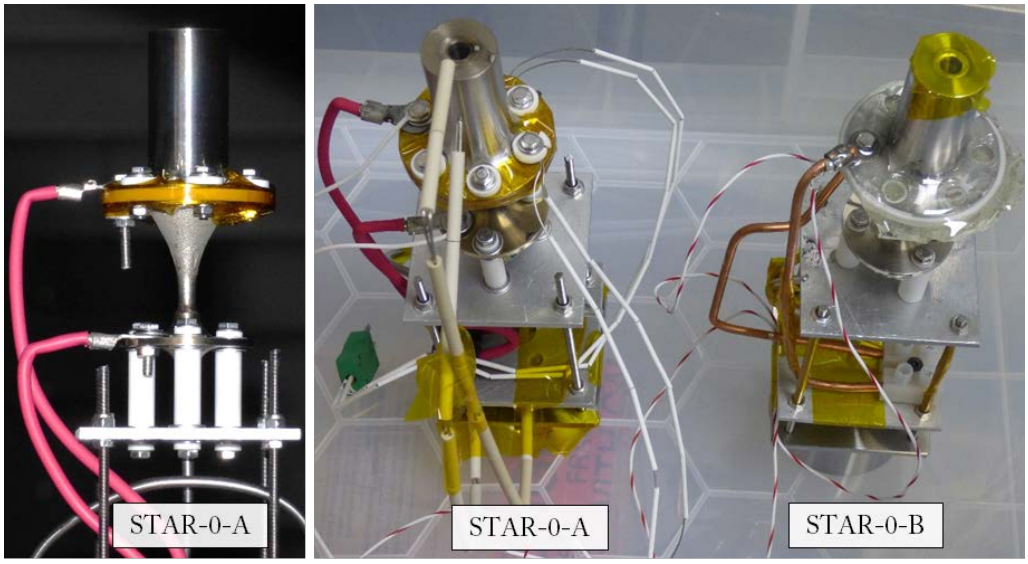

Fig. 3.15. STAR-0-A for the preliminary tests (left), STAR-0-A for the dry-firing tests (centre) and STAR-0-B for the wet-firing tests (right).

3.4.1 Facility

The tests presented in this paper were conducted at the David Fearn Electric Propulsion Laboratory at the University of Southampton (Fig. 3.16). The cryogenic vacuum facility is composed of a 4 m long by 2 m diameter main test chamber and an additional loading chamber separated by a 50 cm gate valve. The pumping equipment consists of two cryopumps, three turbomolecular pumps and two backing pumps. The facility can reach an ultimate vacuum of < 9×10^{-8} mbar with operation < 5.0×10^{-5} mbar with < 28 sccm xenon (~2.8 mg/s). The effective pumping speed with Xe at 5×10^{-5} mbar is 26,664 l/s. The breakdown of the pumping speed of each piece of equipment is shown in Table 3.6 [93].

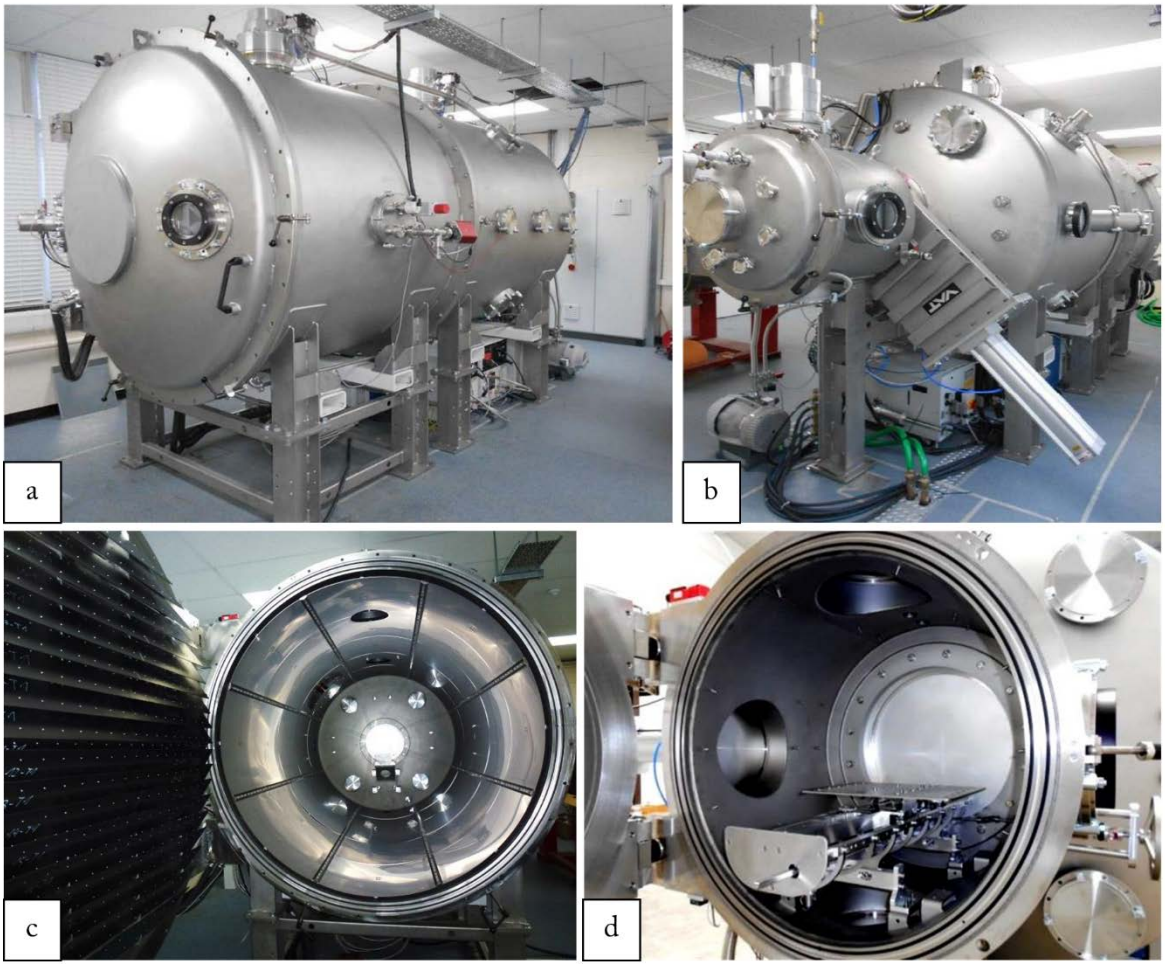

Fig. 3.16. University of Southampton David Fearn Electric Propulsion Laboratory. Main chamber overview (a), hatch and gate valve (b), main chamber access (c) and hatch interior with transversing carriage (d).

Table 3.6. Pumping speed breakdown of the test facility.

Pump	[l/s]
LV 140 C	2,417
XDS35i 583	583
Leybold MAG W 700 iP	590
2 x Leybold MAG W 2200 iP	4,200
2 x COOLPOWER 140 T	20,000
Nominal pumping speed (l/s)	27,790
Effective Xe pumping speed at 5×10^{-5} mbar	26,664

The test setup used for the wet performance evaluation of the STAR-0-B prototype is shown in Fig. 3.17. The 1/8 in. SS inflow pipe and the electrical terminals are fixed on a second aluminium interface plate below the thruster. Argon is supplied to the thruster via a 1/8 in. PFA flexible pipe, which is fixed to a levelled aluminium interface on the opposite end of the thruster to keep any flexural force on the balance to a minimum. Thrust is measured with a Mettler Toledo WMS404C-L/01 weighing module, with the resistojet mounted vertically. Before each test, an in-air adjustment routine was performed using the APW-Link software. This involves compensation in two measurement points, the zero point (no weight) and a test mass of 300 g, consisting of a single E2 calibration weight. The balance was then used for the vacuum tests without performing further calibration. The error on the thrust measurement is based on the manufacturer datasheet in a worst-case scenario, using the limit values rather than the nominal accuracy. In particular, it is calculated as the sum of the repeatability (0.1 mg), linearity deviation (0.4 mg), eccentric load deviation (1 mg), sensitivity offset (2 mg), sensitivity temperature drift (0.00015%/°C×R_{nt}) and sensitivity stability (0.00025%/°C×R_{nt}×20°C), where R_{nt} = 400 g is the maximum net weight and a = 1 the year from last calibration. The resulting uncertainty is of ± 0.16 mN. It must be stressed that the proposed measured uncertainty does not include the effect of vacuum, of the stiffness of the 1/8 in. PFA propellant pipe, of the environmental vibration disturbances and of the interaction between the melted Ga and the copper rods. However, after each one of the wet firing tests the thrust measurement recovered within the readability of the instrument. For these reasons, the thrust balance uncertainty can differ from the proposed value. Future work will aim to perform in-situ measurements with calibration weights to evaluate experimentally the total accuracy of the system.

During an initial test discussed in Section 3.5, hot-fire measurements experienced a significant thermal drift, attributed to the thermal expansion of the thruster terminal wires. A drift-free thrust measurement system was then developed. The electrical terminal consists of two SS baths, each one equipped with a 10 W cartridge heater (Fig. 3.18, left). Each bath contains approximately 8 g of gallium, which is maintained in liquid state (Fig. 3.18, centre) by heating to 35°C with a hysteresis cycle of ± 0.5°C. Two 1/8 in. copper rods are connected to the thruster's positive and negative terminals and positioned in the liquid Ga. During hot-fire operation, the terminal rods are unconstrained under thermal expansion and do not influence thrust measurement (see technical drawings in Appendix E, 31-35).

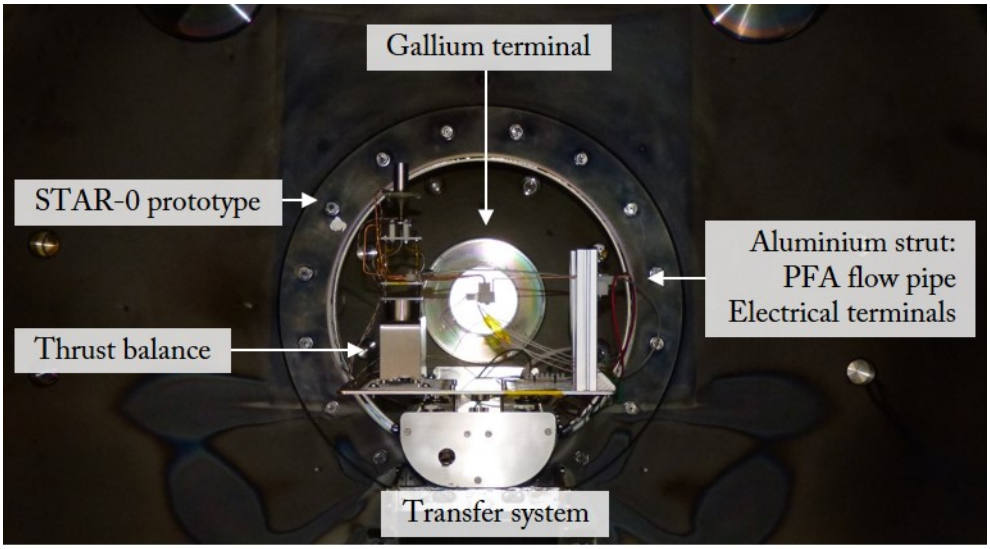

Fig. 3.17. STAR-0-B test rig located into the main test chamber via the transfer system.

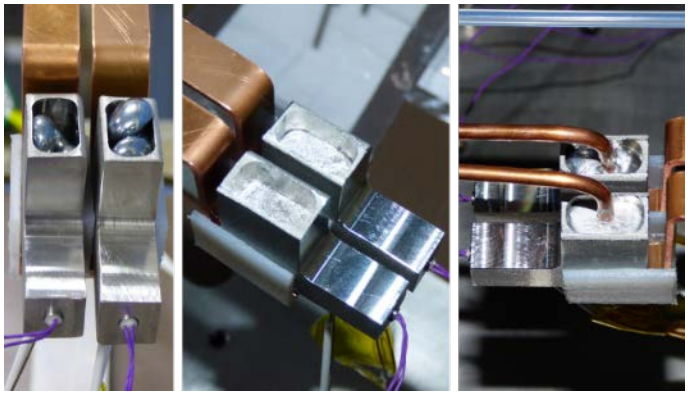

Fig. 3.18. Gallium electrical terminal overview: intact gallium shots at ambient temperature (left), melted gallium (centre) and resistojet terminals submerged into the liquid metal (right).

3.4.2 Test Instrumentation

Table 3.7 lists the equipment used for the tests, as well as the manufacturer, type of measurement, range, nominal accuracy and measurement accuracy of each instrument. A Bronkhorst-based Fluidic Ground Support Equipment (FGSE) provides either flow rate or pressure-controlled argon supply to the thruster (Fig. 3.20-c, drawings 36-41 in Appendix E). The Mass Flow Controller (MFC), that can operate up to 3 ln/min with Xe, and a forward Pressure Controller (PC), that can operate at 4 bar maximum, are connected in series, with the pressure controller fully opened and used to read out the pressure at controlled mass flow rates. The FGSE was designed and built within this research project and the MFC and PC sized to accommodate the HTR tests. In addition, two lower flow rate MFCs (40 sccm maximum with Xe) were mounted to accommodate tests of other EP devices (including the microwave electrothermal [94] and GIT thrusters developed in the context of the IMPULSE project at the University of Southampton). The two controllers are connected to an E-8501-R-20 digital readout and control unit. A high-current power supply, the controller unit of the FGSE, the DAQ system, the thrust balance and the oscilloscope are all connected to a workstation as shown in Fig. 3.19 and controlled using a LabVIEW interface, which uses the respective VISA drivers. In addition to data acquisition, the interface is used to control the Mass Flow Controller (MFC) and Pressure Controller (PC), the power supply output and the heaters used for the Ga terminal, as well as to write the reset and calibration commands to the thrust balance. Fig. 3.20 provides an overview of the test equipment and Fig. 3.21 detail views on the instruments installed in the rack system.

The high-current power supply provides current-limited DC power to the resistojet terminals. Two 10 AWG wires with 105 copper strands connect the power supply to two different KF flanged feedthroughs with a single copper conductor of 2.4 mm diameter. A NI cDAQ-9188XT (Fig. 3.20-a) with a NI 9213 thermocouple module and a NI 9264 analogue output module is used the read the thermocouple values and to control the heaters of the Ga terminal. Each heater of the Ga terminal is activated with an Omega SSR240 solid-state relay (Fig. 3.20-b), which is controlled via analogue outputs from the DAQ. The thrust balance is connected from the feedthrough to a terminal block (Fig. 3.20-d), which supplies 30 Vdc and the communication interface. An oscilloscope was used to measure the voltage at the thruster terminals, *V*, at the feedthrough via a 250 MHz passive probe. Finally, a four-wire milli-Ohm meter was used to check the resistojet's cold resistance at ambient conditions.

Table 3.7. Summary of instrumentation used for the tests with measurement accuracy.

Instrument	Sym.	Range used	Manufacturer	Type	Accuracy
Thrust balance	F	0 – 400 g	Mattler Toledo	WMS404C	0.1 mg readability
MFC	$\dot{m}$	0.06 – 3 ln/min (Xe)	Bronkhorst	F-201CV-5K0	±0.5% RD plus ±0.1% FS
PC	p_{PC}	0.12 – 6 bar (g)	Bronkhorst	P-602CV-21KA	±0.5% FS
Power supply	V_{ps}	0 – 31.5V	Kikusui	PWX1500L	±(0.5% of set + 0.05% of rating)
	I	0 – 157.5 A			±(0.5 % of set + 0.1 % of rating)
Oscilloscope	V_{ts}	1 V, 2.5 V, 5 V	LeCroy	Wavesurfer 3024	±(1.0% of offset value + 3% FS + 1 mV)
DAQ TCs mod.	TC_{1-4}	-260 – 1260°C	National Instrument	NI 9213	±0.25°C
Ohm-meter	R	1 mΩ – 1.999 Ω 0 – 1.4 V	Rhopoint Components Ltd	M210	±(0.1% of range + 1 mΩ zero offset)

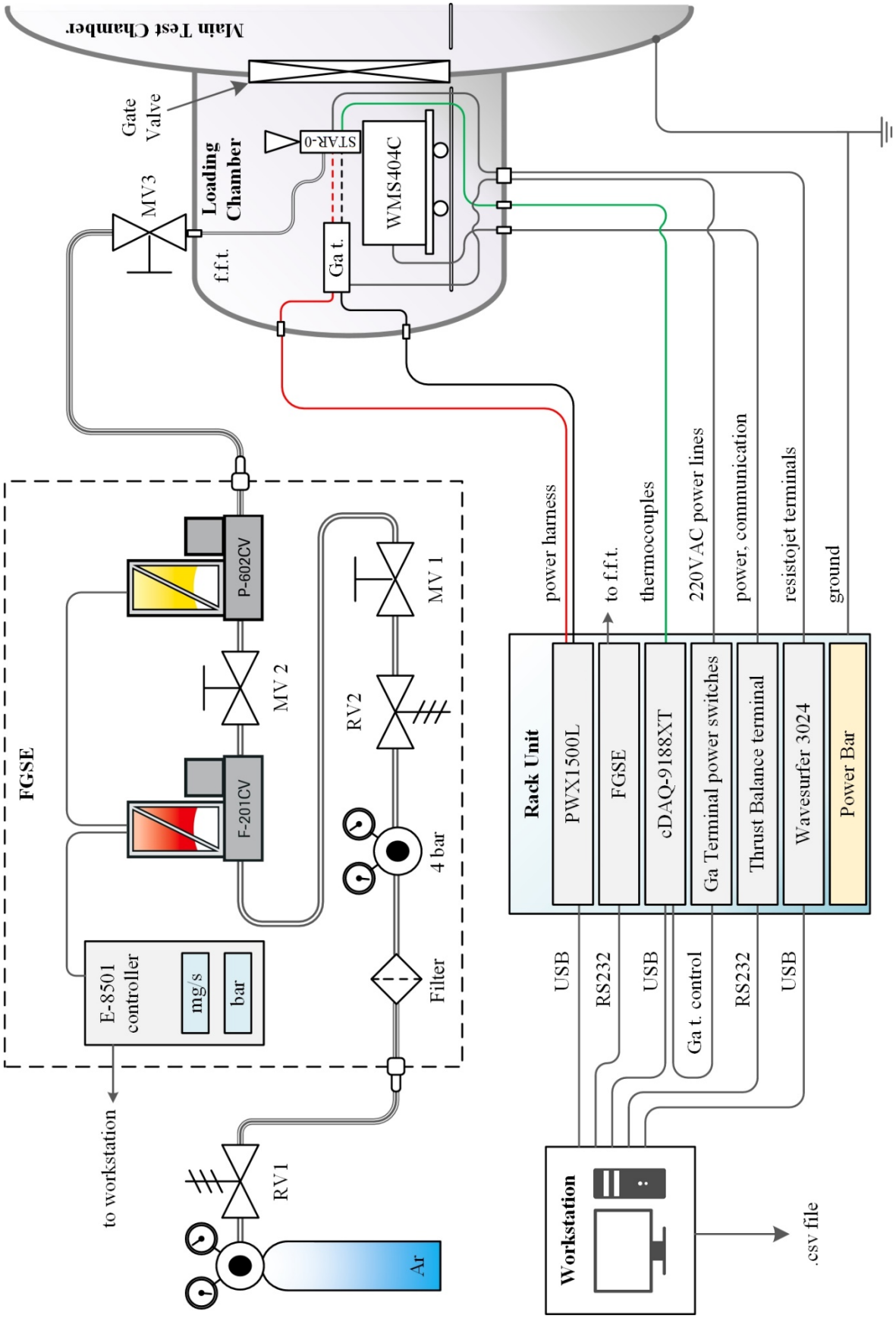

Fig. 3.19. Schematics of the test setup.

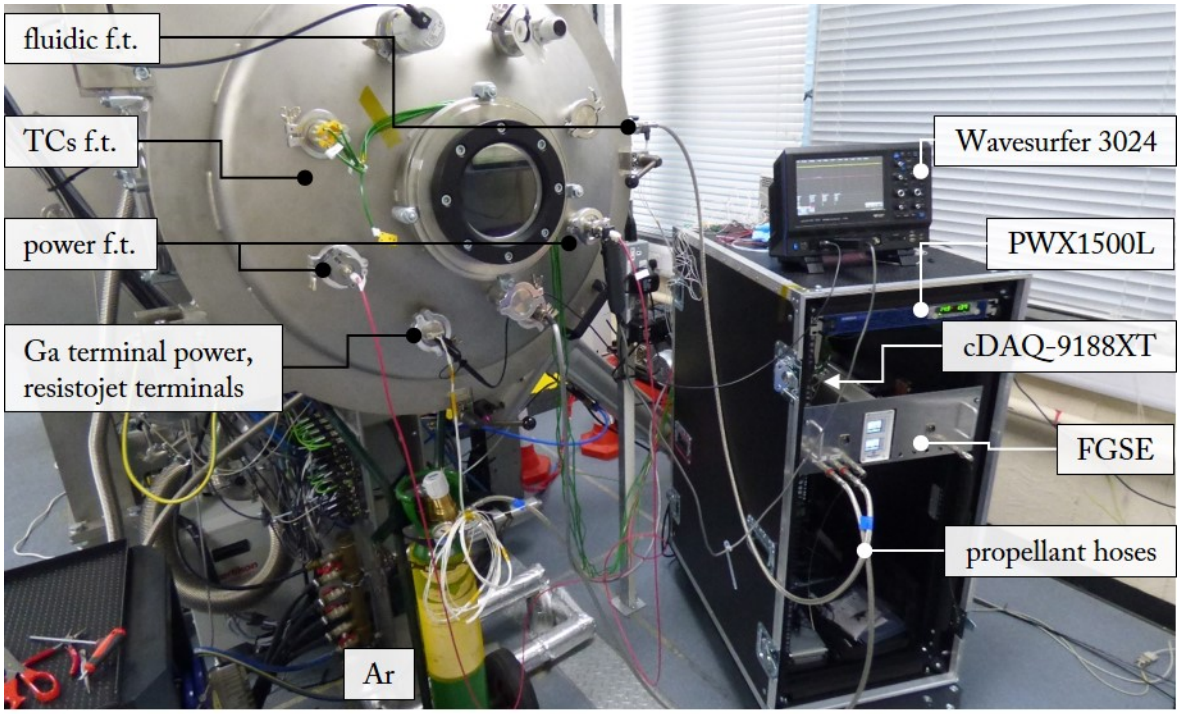

Fig. 3.20. Overview of the test equipment.

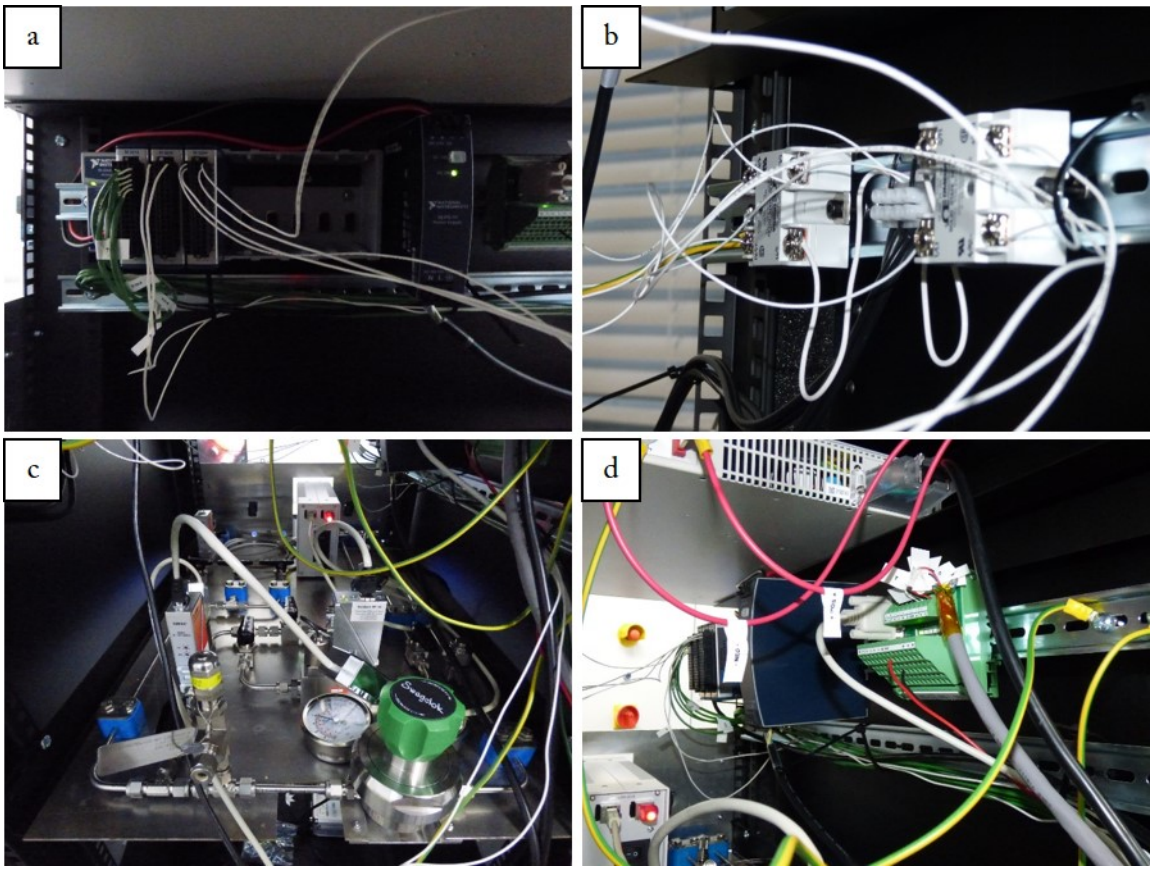

Fig. 3.21. Internal view of the rack system: cDAQ-9188XT (a), Ga terminal power switches (b), FGSE (c) and green terminal block of the thrust balance (d).

3.4.3 Software Selection

To perform a multiphysics study on the thruster assembly, a multiphysics software package that includes electrical, thermal and fluidic modelling capabilities, and with the possibility of conducting parametric and time-dependant studies is required. There are several commercial multiphysics software of this kind, each one having very similar capabilities, including Ansys, Autodesk and Solidworks packages. There are also open source multiphysics software like Elmer, OOFEM, Kratos, with medium/good support documentation [95]. Other open-source packages are mainly CFD oriented, including Salome and OpenFoam. For the multi-disciplinary nature of this research, commercial software with comprehensive capabilities (materials library, mesh discretisation, advanced FEM methods, optimisation tools) and user-friendly interface was selected. At an early stage of the research, COMSOL was used because it covers all the functionalities necessary for the investigation in the HTR design.

The principal reason why COMSOL Multiphysics® has been selected as the numerical modelling software for the resistojet analysis is that it allows for multiphysics and complex-geometry simulations, either of 2D or 3D components. It is important to note that all the mechanisms above are highly coupled, and therefore, no single physics software package would be capable of evaluating the true steady-state solution of a particular design. COMSOL modelling adopts an unparalleled design approach using simultaneous multiphysics modules for rapid and accurate design evaluation. In addition, powerful optimisation algorithms can be used as a design tool that promotes risk reduction in the construction of the HTR prototype.

COMSOL is currently widely used in all research areas. For example, in [96], the authors used this software to study how the throat size of a *de Laval* nozzle effects a supersonic molecular beam. Through these simulations, they have been able to find an optimum throat diameter to maximise the efficiency of the injection. COMSOL has also been used in a number of studies involving heat transfer; for example, Ahmadi et al. [97] successfully compared a stationary model of natural convection of interrupted vertical walls with experimental results, eventually suggesting design modifications to improve it. Podichetty et al. [98] also successfully compared simulations and experiments of a viscous-heating problem involving high-viscosity substances.

COMSOL is also being used in the electric propulsion context. Several studies have used this software to deepen the understanding of some technologies or to optimise their design. For example, Renaud et al. [99] used it to design a Wien filter, a diagnostic tool used to determine the positive ion

velocity in the beam of electric thrusters for SC. Several studies focusing on COMSOL have been discussed in the most recent International Electric Propulsion Conference, with applications on the hollow cathodes modelling [100], on field reversed configuration plasmoids [101], on the ignition erosion mechanism of heatless hollow cathodes [102], on helicon plasma sources [103] and more. Finally, COMSOL Multiphysics v5.0 has been named the 2014 Product of the Year by readers of NASA Tech Briefs.

For all these reasons, COMSOL Multiphysics has been selected to study and design the HTR subject of this research project (Chapters 3 and 4). In Appendix C, some preliminary studies conducted to develop the necessary knowledge of the software and to assess its capabilities are presented and discussed.

3.4.4 Summary of the Validation Studies

A series of validation studies relevant to the HTR development have been produced and reported in Appendix C. In summary, the main results are:

- In Section C.1.1, a study on low-Reynolds number nozzles conducted by Kim (1994) have been replicated successfully using COMSOL, therefore validating the software and the adopted methodology for this particular problem;
- In Section C.1.2, the nozzle behaviour of the SSTL's T50 resistojet has been investigated. A CFD-optimisation study was used to match the experimental measurements of specific impulse, thrust and nozzle surface temperature based on a given inlet propellant pressure and temperature from experimental measurements. The model agrees with the experiments within 3.3% in the mass flow rate, with an average of 0.74% over the 24 cases analysed. The validated multiphysics computational model gives the solution of the fully coupled compressible Navier-Stokes equations and heat transfer in both the gas and the nozzle wall domains. In the full solution, the nozzle radiation-to-ambient loss, the inlet gas temperature of the gas and the Mach number iso-contours were analysed;
- In Section C.2, the J3 resistojet, which is one of the main references for the STAR thruster design development, has been modelled to replicate a set of experimental data available from literature. The relative error of the model against the experimental values is as high as 20% for some of the parameters, and it averaged 7.1% for the T-14 case study, while it averaged 6% for the design point evaluation. This validation exercise was expected to produce results

with a relatively low level of agreement due to the lack of information, such as some relevant thruster dimensions and other uncertainty on the materials properties. However, this exercise provided results in a relatively good agreement with the supplied data and put the basis for the modelling of the STAR thruster, discussed in this chapter. Part of this study have been presented at the 7th European Conference for Aeronautics and Space Sciences (EUCASS, 2017) [104].

3.4.5 Computational Models

A 3D sector-symmetric electrothermal model developed in COMSOL Multiphysics is used to evaluate the performance of the resistojet discussed in Section 3.6 and serves as a validated model for future design iterations. The computed 3D sector is 1/6th of the total geometry; therefore, the current applied to the terminal boundary condition (BC) is 1/6th of the experimental value. The materials, 316L (labelled [solid, polished]) and Macor (labelled [solid]), are selected from the materials library while the thermal properties of Shapal are added manually from datasheets. The resistivity of 316L is extrapolated from 873 K to 1,300 K using an interpolating function. The surface emissivity of the SLM 316L is initially fixed to 0.6. A computational grid convergence was performed as a function of a refinement parameter, *f*. The selected parameter value for simulations is $f = 3$ (corresponding to 63,822 elements), which produces a solution with a relative error $< 10^{-3}$ with respect to $f = 10$ (198,667 elements). BCs of symmetry are applied to the sector-side boundaries for the heat as $\boldsymbol{n} \cdot \boldsymbol{q} = 0$, where $\boldsymbol{n}$ is the unit vector normal to the surface and $\boldsymbol{q}$ the heat flux, and for the surface-to-surface radiation. An electric insulation BC is applied to the same boundaries as $\boldsymbol{n} \cdot \boldsymbol{J} = 0$, where $\boldsymbol{J}$ is the current density. In the model, we assume that all thermal contacts are ideal. The radiograph depicts that the nozzle spacer is not in full contact with the top part of the casing as in the design (Fig. 3.6). The difference in simulation results is large between the two cases of assuming full contact and of introducing a gap between the two components. As highlighted in Table 3.8, the root-mean-square error (RMS), calculated on the relative errors of the measured quantities, is larger when assuming that the nozzle spacer is in ideal contact with the casing. With a gap of 0.5 mm, the RMS error decreases from 0.267 to 0.167. The solution has also been found particularly sensitive to the assumptions on the emissivity of the SLM surfaces where ε_1 is the emissivity of 316L SS found in [105] and ε_2 the emissivity of polished 316 SS found in [106]. With the third-row assumptions, the RMS error reaches a value of 0.097, which is considered sufficient for discussion of the model results.

Several additional factors can influence the solution, including the unknown thermal properties of the SLM material, for which the standard properties have been used. For example, it has been shown that there is a correlation between surface roughness and emissivity, but this is expected to be within ± 5% change as discussed in [107]. In addition, the porosity of the SLM components can produce a higher electrical resistivity [108]. Moreover, the two EB welds could also produce a thermal contact resistance and a change in the heat fluxes between the components. Despite the modest agreement of the model with the experimental measurements, the solution reveals an insight into the temperature distribution inside the heat exchanger, highlighting the location of maximum structural temperature and the increase in temperature inside the channels. The overall agreement of the simulation with experiments expressed as the RMS is < 10%.

In addition to the 3-D model, a 2-D axial-symmetric model described in [109] is used to evaluate the electrothermal-fluidic characteristic of the STAR-0-B prototype and is presented in the discussion. The parametrised geometry has been modified to reflect the prototype geometry, and the assumptions described in the last row of Table 3.8 are also used. The RMS total errors on the five selected variables are 0.121 and 0.097 for the 2D and 3D models, respectively. For this reason, the 2-D model can be used confidently for the evaluation of the electrothermal-fluidic solution of the thruster.

Table 3.8. Simulation over experimental error with different assumptions.

Assumptions			Results					
Geometry	ε_{SLM}	ε_{CNC}	$\tilde{T}_1$	$\tilde{T}_2$	$\tilde{T}_3$	$\tilde{T}_4$	$\tilde{R}_{ts}$	RMS err.
Spacer with contact	0.6	ε_1	0.55	1.32	1.02	1.20	1.08	0.267
Spacer with gap	0.6	ε_1	0.80	0.84	0.93	0.75	0.91	0.167
Spacer with gap	ε_2	ε_1	0.99	0.97	1.19	0.95	0.92	0.097

3.5 Preliminary Tests on STAR-0-A

Before testing, a crack was observed on the Macor collar, which should form a hermetic seal. From visual inspection, it was not possible to determine whether the crack developed through the entire

component (Fig. 3.22, left). During tests, the thruster performed below expectation, and a leak test was performed, confirming that a leak was located in the collar. After the test campaign, the resistojet assembly was inspected with a scatter-free radiograph using a 450 kV source and a Collimated Linear Detector Array (CLDA) with four minutes of exposure in the mid-plane of the collar. The scan (Fig. 3.22, right) highlighted that the crack breached the hermetic seal where the cold annular inflow was located (indicated by a red arrow). This is believed to be the main source of the observed gas leak. Furthermore, the scan shows a second crack in the collar, which could also have contributed to the leak (top right). Possible causes include the excessive torque of 0.6 Nm on the six M3 fasteners or handling during one of the preparation/assembly phases. Macor was selected for the breadboard model due to advantageous machinability and cost, but ceramics with much higher compressible strength are available (e.g. Alumina) and should be considered for future test assemblies.

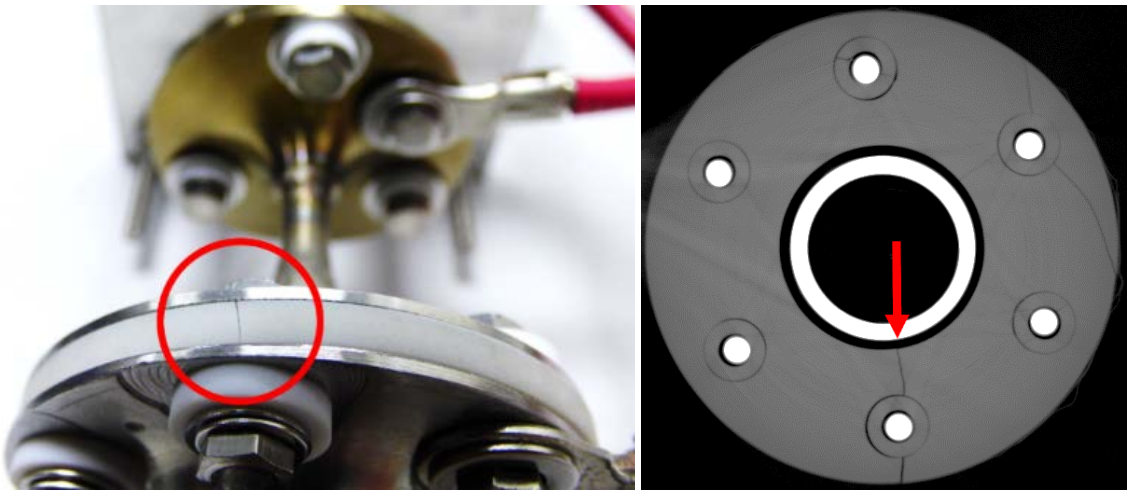

Fig. 3.22. Photo showing a crack that developed in the ceramic collar.

3.5.1 Test Setup

Fig. 3.23 shows the test setup of STAR-0-A in the chamber hatch with fluidic and electrical thruster connections to the lateral support jig. The balance reading was checked with calibrated weights composed of four masses of 20 g, 10 g and 2×2 g, respectively, giving 34.018 g total. The balance measured a force of 333.6 mN ± 0.98 mN based on stainless steel E2 class calibration weight precision, confirming the absence of any stiffness due to the connections. The measured weight was monitored for a relatively long period to establish accuracy.

The cold resistance from the resistojet terminals was 30 mΩ while at the feedthroughs the total measured resistance was 53 mΩ due to the added resistance of the terminals' harness, with the positive terminal harness at 12 mΩ and the negative terminal harness at 10.5 mΩ. The wire used for the connections is 10 AWG copper wire, with 105 strands, resulting in approximately 3.2 mΩ/m. The electrical connection between the thruster and support jig is achieved with a PVC 24A rated cable (green-yellow in Fig. 3.23). The measurement drift at ambient temperature in air was within the balance readability (± 0.1 mN) and the same negligible drift was observed during the cold-gas tests in vacuum. However, thermal drift was observed during heated operation because of the thermal expansion of the electrical supply lines, discussed later.

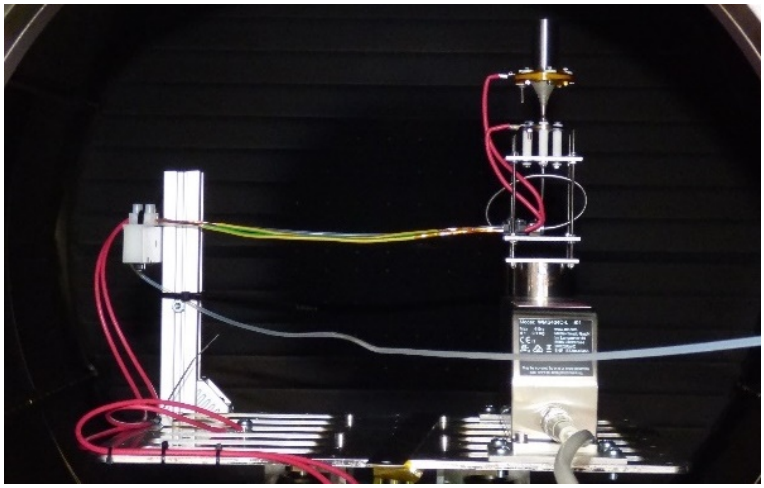

Fig. 3.23. Preliminary tests setup for the STAR-0-A wet-firing tests.

3.5.2 Methodology

The resistojet was tested with five different constant volumetric flow rates, and the heater was switched on in current-limited mode at different electrical currents. Flow rates were selected to produce a theoretical thrust from 10 mN to 50 mN. However, the previously discussed leak issue must be considered for the specific impulse (ISP) evaluation. This can be approximated considering that in cold mode, the specific impulse with Ar must be approximately 50.6 s, assuming a propellant stagnation temperature of 20°C with a nozzle efficiency of 90%. This means that the loss in flow rate is proportional to the loss of thrust under cold conditions. Therefore, the ISP has been estimated from the direct thrust measurement using Eq.(A.5), since calculating ISP from the measured value

at the mass flow controller (MFC) would not be representative of the real flow rate reaching the converging-diverging nozzle. The test procedure consisted of the following steps:

1. Pump down to vacuum chamber pressure of 1.8E-6 mbar with cryogenic pumps indicating a temperature < 20 K;
2. Operate at constant mass flow rate and reach a stable thrust level while the chamber pressure reaches an equilibrium value;
3. If in hot-gas mode, apply power in a current-limited (CC) mode for the amount of time necessary to reach a maximum test thrust;
4. Switch off the electrical power, then the gas flow to assess baseline drift.

3.5.3 Results and Discussion

The maximum hot test thrust was conservatively selected as 150% of the cold-gas case. An increase in thrust at constant mass flow rate corresponds to an increase in specific impulse, hence propellant stagnation temperature. From Eq.(1.9), the expected average nozzle inlet stagnation temperature would be $T_0 \approx 400^{\circ}$C, for a corresponding I_{sp} = 75.9 s, using the leak correction. Table 3.9 shows the measured data for the five flow rates, which theoretically, without a gas leak, should have provided a thrust from 10 mN to 50 mN, respectively. Cold-gas tests 1, 5, 8, 10 and 11 provide a measured thrust of 74% to 57.6% of the expected value if no leak occurred.

Fig. 3.24 shows the typical response of thrust after the heater is switched on after reaching constant thrust with a cold flow for Test 3 and Test 4. In both cases, the thrust is plotted along with the measured pressure at the flow controller exit and with a subplot of the voltage-time heater characteristic measured at the power supply terminals. At the time the heater is switched on, thrust immediately increases, approaching almost a linear gradient as the heat exchanger increases in temperature. This shows that, at that specific flow rate, the heat exchanger was continuing to heat at a rapid rate before the imposed thrust limit was reached, indicating that at this power, the temperature, and thus ISP of the device, could increase significantly. However, this would eventually exceed the material temperature limits of the current heat exchanger while the purpose of this test is for concept validation and basic characterization. Although not observable in the graphs, the measured pressure increases by about 6%–8% due to increasing stagnation temperature.

While a thrust measurement drift was not observed in the cold-gas tests, in the hot cases, a significant drift was present as the device was switched off and the flow rate was stopped. This is visible in both

cases shown in Fig. 3.24. The thrust measurement did eventually return to zero after tens of minutes. This behaviour suggests that the terminal cables connecting the thruster to the support jig are subjected to thermal expansion during hot mode and influence the balance generating the described drift. The voltage-time characteristic of the heater without propellant shows that the voltage-time gradient is only slightly higher with respect to the flowing cases, highlighting that the STAR-0 thruster can be safely pre-warmed up to reach the desired ISP in less time.

Table 3.9. Performance data of STAR-0-A in vacuum with starting pressure of 1.8E-6 mbar and T_{BG} = 20 K.

Test #	MFC* [ln/min]	p_{BG} [mbar]	F [mN]	I_{sp}† [s]	I [A]	t_b‡ [s]
1	0.678	2.4E-4	7.4	50.6	0	NA
2	0.678	2.4E-4	11.1	75.9	15	240
3	0.678	2.4E-4	11.1	75.9	20	130
4	0.678	2.4E-4	11.1	75.9	25	83
5	1.356	6.0E-4	13.5	50.6	0	NA
6	1.356	6.0E-4	16	60.0	15	119
7	1.356	6.0E-4	16	60.0	20	79
8	2.032	9.5E-4	18.8	50.6	0	NA
9	2.032	9.5E-4	20.5	55.2	20	78
10	2.710	1.1E-3	23.9	50.6	0	NA
11	3.388	1.3E-3	28.8	50.6	0	NA

* Measured with the MFC, therefore not accounting for the gas leak.

† Estimated ISP taking into account of the propellant leak.

‡ Heater ON after cold-gas thrust peak reached.

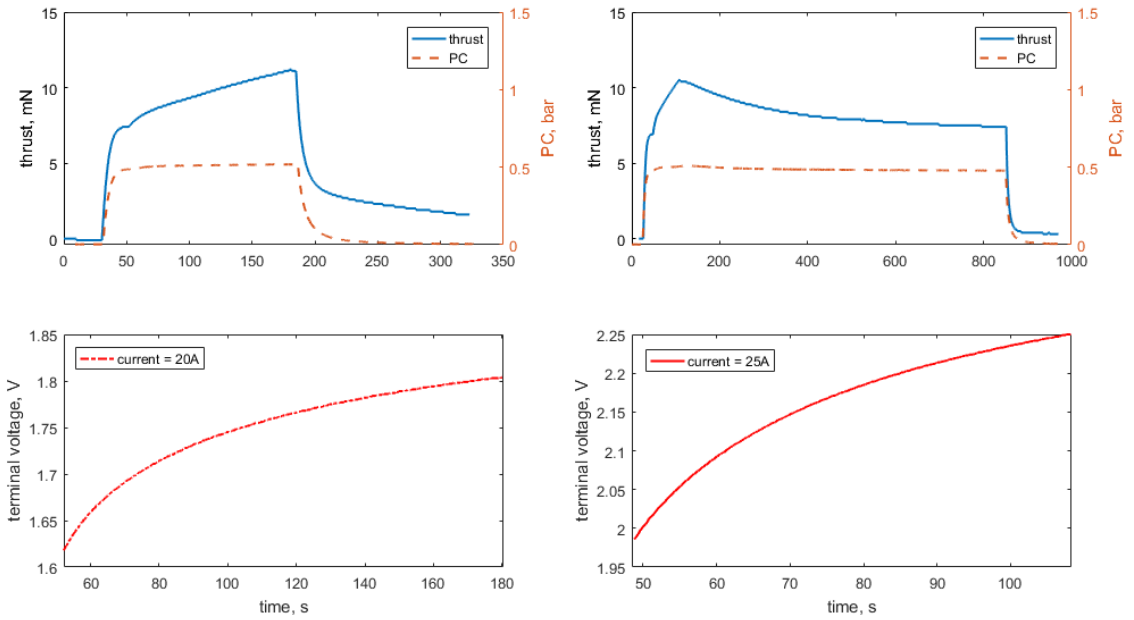

Fig. 3.24. Effect of the gas heating to the thrust profile and the operating voltage at a flow rate of 0.678 ln/min with 20 A and 25 A of constant current. Test 3 (left) and Test 4 (right) are shown.

3.6 Final Tests on STAR-0-A and STAR-0-B

3.6.1 Test Methodology

The two identical prototypes, STAR-0-A and STAR-0-B, are tested in two different ways. The first is used to evaluate the electrothermal dry characteristics over a long heating time. The second prototype is used for evaluating the wet performance of the thruster, deriving the maximum ISP for a range of electrical currents and with two different flow rates of Ar gas. The direct measurements taken in the test campaign were the following: thrust, F; mass flow rate, $\dot{m}$; pressure measured at the pressure controller, p_{PC}; voltage and current at the power supply, V_{ps} and I, respectively; voltage at the resistojet terminals, V; and temperatures, T_j. The mass flow controller was calibrated for Xe, therefore a conversion factor x was used to derive the Ar flow rate in accordance to the Bronkhorst conversion data for the specific MFC [110], where $\dot{m}(\mathrm{Ar}) = x\dot{m}(\mathrm{Xe})$. In particular, at the two test mass flow rates M1 and M2, $x = 0.3164$ and $x = 0.3222$, respectively. The uncertainty of the direct measurement is calculated using the manufactures datasheet shown in Table 3.7.

The STAR-0-A prototype is subjected to a range of electrical input currents without propellant flow. Four temperatures, TC_1 to TC_4, are measured at selected points of the thruster body through k-type

thermocouples as shown in Fig. 3.6. With reference to Fig. 3.19, the dry test only makes use of the electrical test setup. In particular, neither the gallium terminal nor the thrust balance is used. The dry tests are performed in the loading chamber and vacuum conditions. At the lower-current case, the oscilloscope is set to 100 mV/div (± 0.5 V of range), while for the remaining three tests, it is set to 500 mV/div (± 2.5 V of range). The voltage measurement is time-averaged over four sweeps, with a sweep being a 100 ms time window at 100 kS/s. The heating time is 2,500 s in all four cases. The junctions of TC_1 and TC_2 are electrically insulated from the resistojet body using Kapton tape. TC_3 and TC_4 are spot-welded to the respective reference points.

Wet tests on STAR-0-B are performed at a constant volumetric flow rate using Ar gas. Measurements taken in hot-gas tests include thrust, the forward pressure at the PC and the mass flow rate of Ar at the MFC. In addition, the resistojet terminal voltage was measured via an oscilloscope. For tests M1-1 to M1-3 and M2-1 to M2-3, the measurement was set to 100 mV/div (± 0.5 V of range) with an offset of 300 mV. For the remaining tests, the measurement was set 200 mV/div (± 1 V of range) with an offset of 0.2 V. The voltage measurement was time-averaged over four sweeps, with a sweep being a 100 ms time window at 100 kS/s. Tests are performed in the main test chamber at a base pressure of 2×10^{-6} mbar with cryopumps. The testing method consisted of the following process steps:

1. The current is set to 3 A, which corresponds to a negligible power dissipation of 0.3 W while permitting the monitoring of the electrical resistance;
2. The MFC is commanded to the desired mass flow rate;
3. When the thrust reaches a steady value in cold mode and the chamber base pressure stabilises, the thruster is switched to the hot-fire mode by increasing the electrical current to the prescribed setpoint;
4. After a given time, the current is decreased to 3 A, and then the flow controller is closed.

The STAR-0-B prototype was tested with two flow rates corresponding to cases M1 and M2, respectively, and the heater was switched on in current-limited mode at four increasing electrical currents. The electrical currents were selected to achieve a maximum expected power input of 10 W, 15 W, 20 W and 25 W, assuming a final hot resistance of 41 m Ω.

It has to be mentioned that STAR-0-B was produced to solve a leak issue encountered with STAR-0-A (discussed in Section 3.5), by increasing the torque on the six M3 fasteners of the gasket before performing EB weld 2. However, the leak was still large, therefore the metallic flanges and the gasket

were covered with a commercial epoxy resin (Gorilla Epoxy) as shown in Fig. 3.15 (right). This one has a relatively low operating temperature (in the region of 100°C) but resisted without leaking for the whole range of tests.

3.6.2 Wet-firing Test Results

Table 3.10 shows the summary of results of the wet tests in the two cases, M1 and M2, where the parameters are evaluated at the maximum thrust level achieved with the electrothermal enhancement in the heating time t_b for each case. Direct measurements are indicated with a dash, while the formula used to calculate the derived parameters is shown in the reference column. Fig. 3.25 depicts the transient of the thrust for the test cases analysed.

From the direct measurements listed in Table 3.7, the derived parameters of interest are the specific impulse, $I_{sp,}$ given by Eq.(3.3); the electrical power, P_e; the total thruster power input, P_{ts}; and the thruster efficiency, η_{ts}, given by Eq.(3.4). $P_{0,in} = c_p T_{0,in}$ is the inlet thermal energy of the cold gas, and $P_0 = c_p T_0$ is the stagnation energy of the gas at the nozzle inlet.

$$I_{sp} = \frac{F}{\dot{m} g_0} \tag{3.3}$$

$$\eta_{ts} = \eta_h \eta_n = \frac{P_0}{P_{ts}} \frac{P_j}{P_0} = \frac{\text{kinetic power}}{\text{total inlet power}} = \frac{F^2 / 2\dot{m}}{P_{0,in} + P_e} \tag{3.4}$$

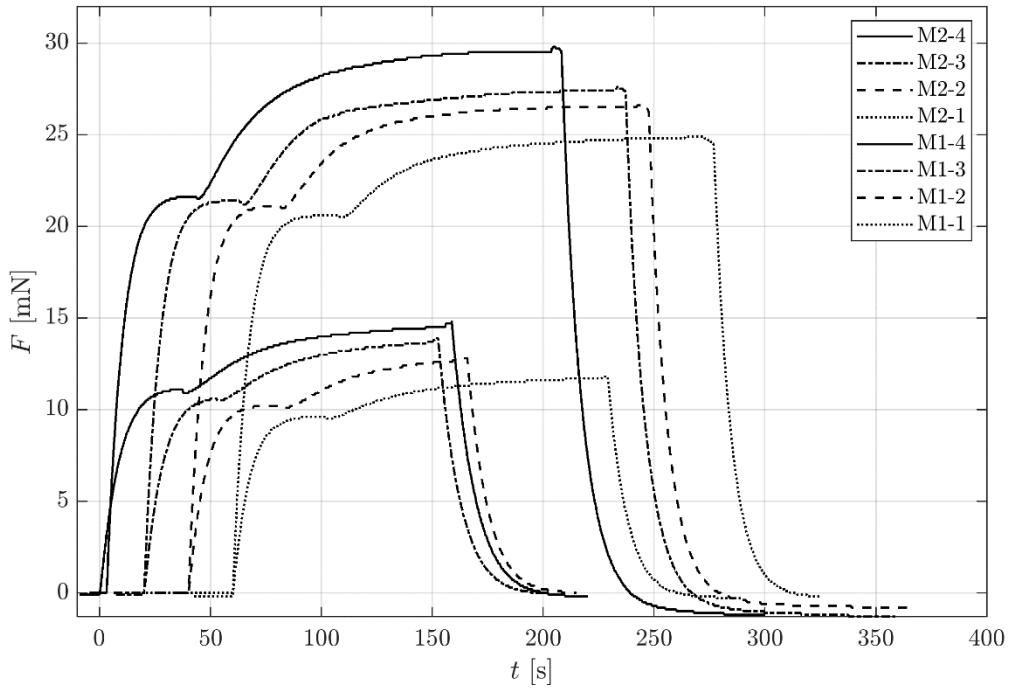

Fig. 3.25. Thrust transient of the M1 and M2 test series. Each start front of the same test currents is separated by 20 seconds for presentation clarity.

The relative uncertainties of the derived parameters, expressed with a δx divided by the absolute value of x, are calculated assuming that the quantities analysed have uncorrelated and random errors. Eq.(3.5) to Eq.(3.7) represent the relative error of the specific impulse, electric power, thrust resistance and thruster's total efficiency. The error on the total thruster power input is estimated with Eq.(3.8), where the stagnation power at the resistojet inlet $P_{0,in}$ (Table 2.5) is calculated in the assumption of $T_{0,in}$ = 20 ± 10 °C. It can be noted that the uncertainty on the thrust measurement is lower than the provided readability. This was caused by erroneously not setting the reading to full precision.

$$\frac{\delta I_{sp}}{\left|I_{sp}\right|} = \sqrt{\left(\frac{\delta \dot{m}}{\dot{m}}\right)^2 + \left(\frac{\delta F}{F}\right)^2} \tag{3.5}$$

$$\frac{\delta P_e}{\left|P_e\right|} = \frac{\delta R}{\left|R\right|} = \sqrt{\left(\frac{\delta V}{V}\right)^2 + \left(\frac{\delta I}{I}\right)^2} \tag{3.6}$$

$$\frac{\delta \eta_{ts}}{\left|\eta_{ts}\right|} = \sqrt{2\left(\frac{\delta F}{F}\right)^2 + \left(\frac{\delta \dot{m}}{\dot{m}}\right)^2 + \left(\frac{\delta P_{ts}}{P_{ts}}\right)^2} \tag{3.7}$$

$$\delta P_{ts} = \sqrt{(\delta P_e)^2 + (\delta P_0)^2} \tag{3.8}$$

3.6.3 Dry-firing Performance

The cold resistance measured at the thruster terminals at ambient conditions with the four-wire Ohm-meter was 30 ± 3 mΩ pre- and post-test. The corresponding model resistance is 27.6 mΩ. Fig. 3.26 depicts the temperature measurements (solid lines) and the simulated values (markers) in the test time window of 2,500 s at the four test currents. The simulated electrical resistance results are underestimated by up to 17.9% at the beginning of the simulations' heat-up cycle for the lower-current case while agreement improves up to 7.8% at 2,500 s for the highest current case. All temperatures agree within ±5% in the steady state except for TC_3, which shows an error of +19.4% at steady state in the 21.1 A test current. It has to be noted that the error is larger for the lower-current cases and, in general, decreases with time. Therefore, the model compares better with the experiments at higher temperatures. This suggests that misjudgements of any assumption play a less significant role in steady-state electro-thermal equilibrium. The dry tests also guarantee that the epoxy resin, used for the wet firing tests on the ceramic gasket, operates below its maximum operational temperature of 80°C. In particular, TC_2 measures a temperature of 36°C after 200 s at the maximum test current (I = 23.6 A), which is well within the maximum firing time.

The model results are used here for further discussion. Table 3.11 lists the maximum temperature of the thruster, T_m, and the maximum temperature evaluated in the three regions connecting each pair of cylinders at 2,500 s (the subscript indicates the cylinder labels as shown in Fig. 3.1). The evolution of these temperatures is also plotted over the firing time in Fig. 3.27. These regions are subjected to significant thermal stress due to the differential expansion of the cylinders caused by large thermal gradients. In addition, the maximum temperature of 316L for intermittent service is 870°C in air (no vacuum data available), and 925°C for continuous service. Thermal cycles exceeding these temperatures influence cracking and spalling. The simulations suggest that above 18 A of current, the connecting material between cylinders 1 and 2 could be prone to cracking during thermal cycling. The time for the heat exchanger to reach a temperature of 870°C is 146 s and 60 s for I = 21.1 A and 23.6 A, respectively. This overheating process is therefore likely to be the cause of the prototype STAR-0 thermal cycling failure described in [111] at test currents of 20 A and 25 A.

Table 3.10. Summary of M1 and M2 tests with quantities evaluated at the maximum measured thrust. The background pressure p_{BG} for M1 was of 8.5E-4 mbar, while for M2 was 1.3E-3 mbar.

Sym.	Unit	Ref.	Test number									
			M1-0	M1-1	M1-2	M1-3	M1-4	M2-0	M2-1	M2-2	M2-3	M2-4
$\dot{m}$	mg/s	-	18.84 ± 0.28					38.44 ± 0.38				
F^*	mN	-	9.7	11.8	12.8	13.9	14.8	20.3	24.9	26.6	27.6	29.8
I_{sp}	s	Eq.(3.3)	52.21 ±1.17	63.87 ±1.30	69.29 ±1.36	75.24 ±1.43	80.11 ±1.49	53.86 ±0.68	66.06 ±0.78	70.57 ±0.82	73.22 ±0.84	79.06 ±0.89
P_e	W	$V \cdot I$	0.300 ±0.060	8.129 ±0.310	12.751 ±0.389	17.880 ±0.731	23.560 ±0.8260	0.300 ±0.060	7.943 ±0.309	12.422 ±0.387	17.335 ±0.730	22.648 ±0.823
η_{ts}	%	Eq. (3.4)	77.4 ±3.7	33.4 ±1.2	27.7 ±0.9	24.6 ±1.0	21.9 ±0.8	85.5 ±3.3	58.0 ±1.5	50.0 ±1.2	42.5 ±1.4	40.4 ±1.3
R	mΩ	$V \,/\, I$	33.3 ±6.6	36.5 ±1.4	38.0 ±1.2	40.1 ±1.6	42.3 ±1.5	33.3 ±6.6	35.6 ±1.4	37.0 ±1.2	38.9 ±1.6	40.6 ±1.5
V	V	-	0.100 ±0.019	0.545 ±0.019	0.696 ±0.019	0.847 ±0.033	0.998 ±0.033	0.100 ±0.019	0.532 ±0.019	0.678 ±0.019	0.821 ±0.033	0.959 ±0.033
I	A	-	3.000 ±0.173	14.924 ±0.232	18.318 ±0.249	21.112 ±0.263	23.610 ±0.276	3.000 ±0.173	14.930 ±0.232	18.321 ±0.249	21.115 ±0.263	23.616 ±0.276
P_{ts}	W	$P_{0,in} + P_e$	3.227 ±0.124	11.056 ±0.310	15.678 ±0.389	20.807 ±0.731	26.488 ±0.833	6.272 ±0.220	13.915 ±0.309	18.394 ±0.387	23.308 ±0.730	28.620 ±0.823
p_{PC} †	bar	-	0.65	0.81	0.87	0.94	1.01	1.28	1.55	1.65	1.71	1.85
t_h	s	-	0	123.9	78.9	97.3	118.4	0	160.7	160.4	167.8	159.6

* Uncertainty of ± 0.16 mN

† Uncertainty of ± 0.02 bar

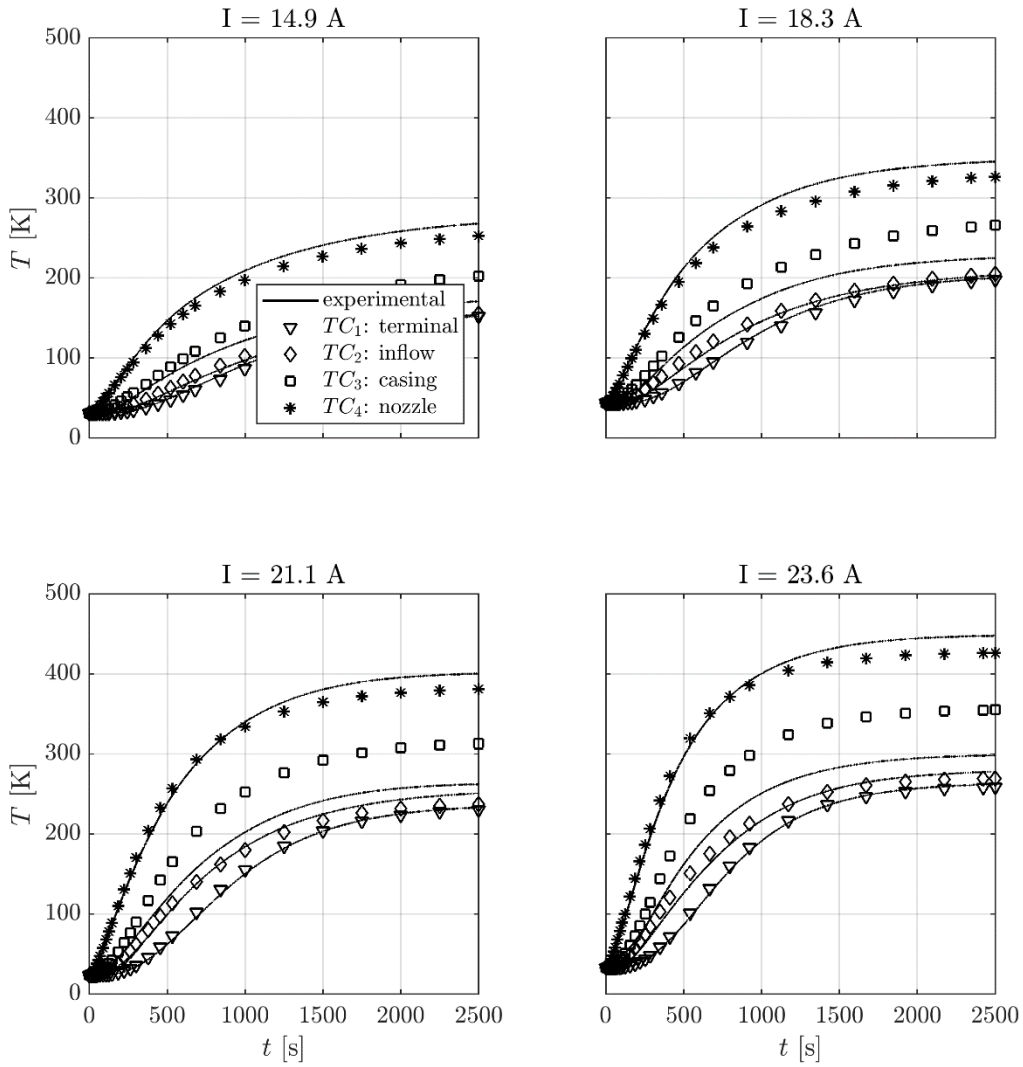

Fig. 3.26. Dry tests: experimental temperatures (solid lines) and 3-D sector-symmetric simulation results (markers).

3.6.4 Wet-firing Performance

The cold-firing stagnation pressure at the nozzle inlet can be estimated using an assumption of choked flow in Eq.(3.9), where R is the specific gas constant, γ the ratio of specific heats, A_t the throat area and T_0 the stagnation temperature at the nozzle inlet, which is assumed to be at 300 K. The thrust is calculated using Eq.(3.11), where v_e, p_e and A_e are the velocity, the static pressure and the area at the nozzle exit, respectively, while p_{vc} is the measured vacuum chamber pressure. The Mach number at the exit is evaluated by calculating the zero of Eq.(3.10), resulting in M = 11.6.

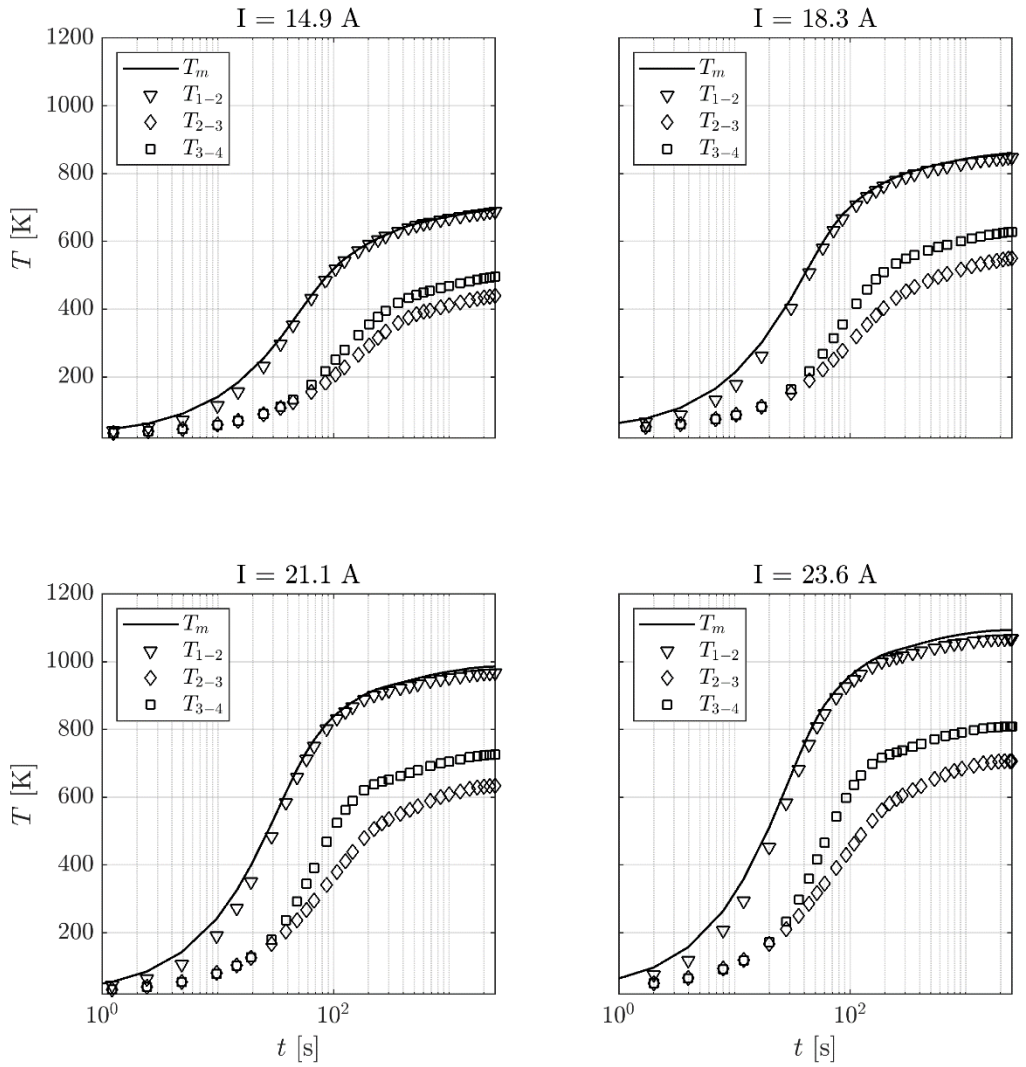

Fig. 3.27. Time-dependant model prediction of the maximum structural temperature and temperature of the connectors in the four test cases.

Table 3.11. Dry-test model results at t = 2,500 s: maximum structural temperature, T_m, and maximum temperature in the connectors regions.

I [A]	T_{m} [°C]	T_{1-2} [°C]	T_{2-3} [°C]	T_{3-4} [°C]
14.9	694.4	687.4	439.8	495.7
18.3	861.0	847.7	549.7	628.1
21.1	985.7	966.2	633.9	726.0
23.6	1093.5	1067.5	707.2	808.5

$$p_t = \frac{\dot{m}\sqrt{T_0}}{A_t}\sqrt{\frac{R}{\gamma}}\left(\frac{\gamma+1}{2}\right)^{\frac{\gamma+1}{2(\gamma-1)}} \tag{3.9}$$

$$f(M) = \frac{(\gamma+1)}{2}^{-\frac{\gamma+1}{2(\gamma-1)}}\frac{(1+\frac{\gamma-1}{2}M^2)^{\frac{\gamma+1}{2(\gamma-1)}}}{M} - \frac{A_e}{A_t} \tag{3.10}$$

$$F = \dot{m}v_e + (p_e - p_{vc})A_e \tag{3.11}$$

As expected, there is a linear relationship between chamber pressure and measured thrust for the cold-gas case. The comparison agrees well with the 1-D isentropic assumptions described above, where the relative error between the 1-D isentropic calculation and the experiments is +7.7% at the lowest mass flow rate, decreasing to -0.13% at the highest mass flow rate (Fig. 3.28). This suggests that the nozzle behaves as expected, that the manufacturing accuracy is acceptable and that the drilling of the throat to nominal diameter is particularly sufficient to produce good nozzle geometry [112].

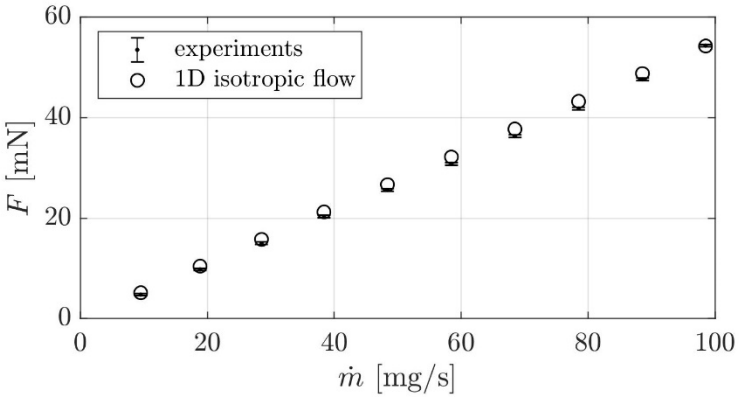

Fig. 3.28. Thrust exerted by the STAR-0-B prototype in cold gas mode at increasing mass flow rate of Ar.

In the 1-D isentropic flow (i.f.) assumption, the calculated cold-specific impulse is 56 s. The STAR-0-B prototype performed as expected in cold gas, proving that the nozzle geometry is close to the nominal design and that the tested assembly is leak-tight. It should be noted that the efficiency of the thruster in the cold-gas case is 77% for M1-0 and 86% for M2-0. This relatively low efficiency is likely because the thruster body is at approximately 20°C while the ambient temperature achieved with the cryogenic pumps is much lower. Therefore, the radiation of the thruster to the ambient was

significant. This is confirmed by the simulations, which for the M1-0 case determine a radiation loss of 0.765 W, which corresponds to 23.7% of the total power input and compares well to the efficiency loss (column M1-0 of Table 3.10).

The pressure drop, p_d, between the PC and the thruster inlet is estimated firstly by the stagnation pressure at the nozzle inlet in cold gas using a gradient-free optimisation method, identifying the stagnation pressure that fits the measured thrust better. This is performed assuming that the inlet temperature is 300 K. The results for M1-0 are p_0 = 0.478 bar and F = 9.67 mN. Secondly, a simulation on the heat exchanger determines that the pressure drop between the nozzle and the thruster inlet is only 3 mbar for M1-0. Therefore, the pressure drop between the PC and the thruster inlet can be calculated as $p_d = p_{PC} - p_{0,in}$ = 0.169 mbar. The calculated pressure drop is constant for all M1 cases, in the assumption that the temperature of the pipe segment between the PC and the thruster remains constant at 300 K.

We further analyse the test case M1-4, where the thruster showed the maximum specific impulse. The time-dependent 2-D axial-symmetric model of the heat exchanger uses the pressure $p_{0,ts}(t) = p_{PC}(t) - p_d$ as the inlet BC and the experimental mass flow rate as the outlet BC. The nozzle is evaluated in a separate simulation using the stagnation conditions, and the nozzle wall temperature profile is evaluated at the last time step of the heat exchanger simulation. Table 3.12 shows a summary of the results, where the simulated-to-experimental relative error is +0.97% for F, -4.88% for $\dot{m}$ and -9.42% for R_{ts}. It has to be noted that in M1-4, the nozzle behaves far from the ideal case. In particular, as a result from the relatively high stagnation temperature and of the relatively low stagnation pressure on the nozzle, a dominant viscous effect determines a thick boundary layer at the nozzle diverging section with a resulting inefficiency of gas expansion (Fig. 3.29, right). A Reynolds number below 6,000 calculated at the throat indicates that viscous effects may be relevant [5,68]. In this test case, Re_t = 1021 and the efficiency of the nozzle results in only 73.6%. For this reason, it is a requirement for the STAR thruster that the nozzle at the design point operates at $Re_t \geq 6{,}000$; otherwise, the potential increase in performance due to the extreme stagnation temperature vanishes in an inefficient expansion of the gas. It also can be noted that the maximum simulated exit Mach number is below the isentropic ideal case. From Eq.(3.4), the calculated heater efficiency is 29.8%.

Table 3.12. Main simulation results for M1-4 at t_b = 118.4 s.

p_0 [bar]	T_0 [°C]	T_m [°C]	Re_t [-]	M_e [-]	η_n [%]
0.826	649	854	1021	7.88	73.6

Fig. 3.29 (left) shows the iso-thermal surface plot of M1-4 at the last time step, highlighting the maximum gas temperature, T_0, and the maximum structural temperature, T_m. The latter is located at the back of cylinder 1 and in the region of the connectors between cylinder 1 and 2. The difference between the maximum structural and gas temperatures is 205°C, which is in line with the values anticipated in [109] for the STAR design using high-temperature materials. Finally, it can be noted that T_m is below the 870°C intermittent usage limit for 316L, indicating that at this condition, the thruster cannot operate for more than two minutes continuously and that a duty cycle must be applied for continuous operation as described in [109].

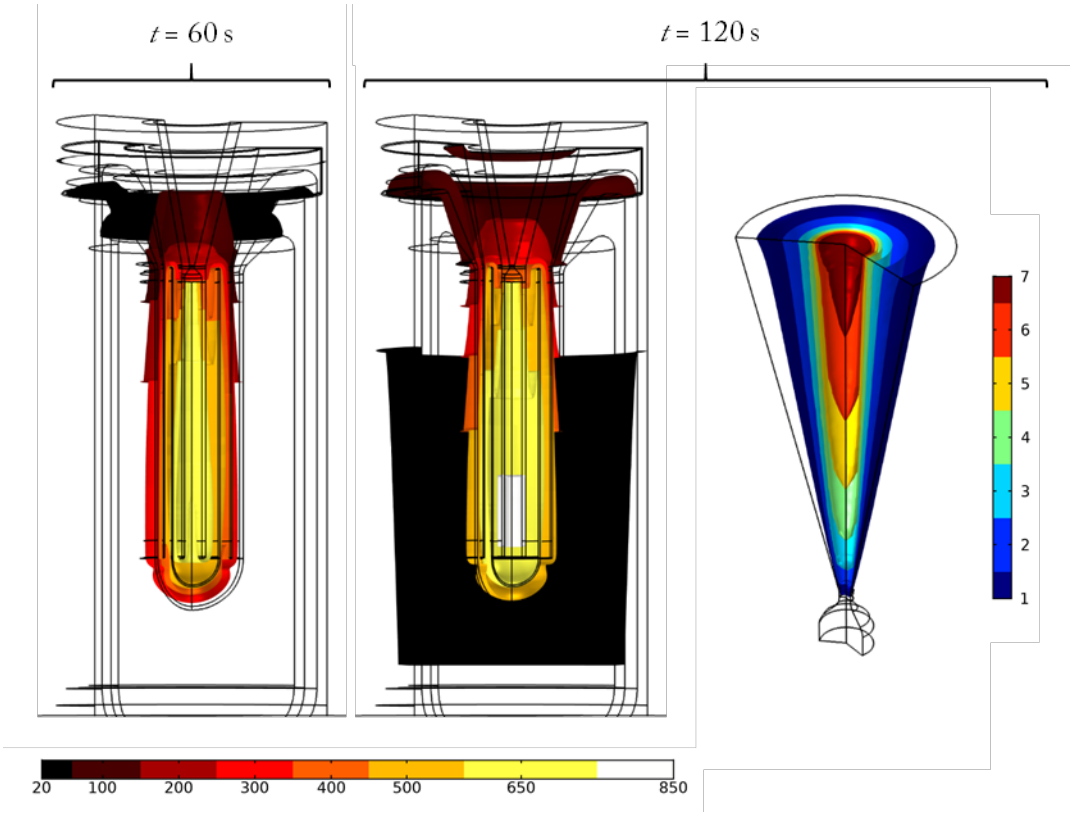

Fig. 3.29. Iso-thermal plot of the test case M1-4 at t_b = 60 s and 120 s highlighting the maximum gas (650° C) and structural (850°C) temperatures (left) and iso-Mach plot of the nozzle at t_b = 120 s (right).

3.7 Summary

In this chapter, it is shown the first validation of a proof-of-concept prototype for the Super-high Temperature Additive Resistojet (STAR) containing an innovative multifunctional monolithic heat exchanger, enabled by selective metal laser melting manufacturing processes. The STAR-0 prototype performed as expected both electrically and thermally and produced a maximum propellant temperature comparable to the state-of-the-art resistojets, hence validating the operational concept. A 316L stainless-steel printed thruster was characterised through a combination of dry-heating and wet-firing tests. This includes verification testing with argon in both cold and hot-firing modes, at a range of electrical power inputs. Thrust measurements ranged from 9.7 ± 0.16 mN to 29.8 ± 0.16 mN, with a maximum measured specific impulse with Ar of 80.11 ± 1.49 s.

Multiphysics models provided insight into the temperature distribution inside the heat exchanger, in particular indicating the maximum expected structural and stagnation temperatures, which were 854°C and 649°C respectively. The degree of agreement of data with the transient simulations provides confidence of the further exploratory simulation discussed in Chapter 5, where STAR has been evaluated with xenon propellant and candidate heat exchanger materials. In conclusion, the first STAR prototype performed as expected and builds the basis for the next phases of the research project, such as to develop an engineering model using refractory metals and nickel alloys. The highlights of this chapter are:

- The STAR thruster cannot be operated directly at the bus voltage but a PCU must be selected for its operation;
- The assembly design process led to a proof of concept thruster formed by four main metallic components: the heat exchanger, the thruster inflow, the thruster casing and the support disk. The first two components are produced by SLM;
- The STAR-0 assembly involved two EB welds and two TIG welds;
- Two identical assemblies have been produced, named STAR-0-A and STAR-0-B. It was decided to use the minimum components necessary to perform testing, such as only the collar and nozzle spacer in addition to the four metallic components. Therefore, the radiation shielding with respective ceramics and the insulation package have not been implemented;
- STAR-0-A has been used in a preliminary test campaign, which encountered two main issues:
    - The collar presented a crack, which determined a propellant leak during testing;

  - The testing showed significant drift in the thrust measurement because of the thermal expansion of the electric harness;
- STAR-0-A has been used for dry-firing tests to achieve quasi-thermal equilibrium and explore the electrothermal characteristics of the thruster;
- STAR-0-B presented also the leak issue at the ceramic collar. This was solved using epoxy resin, which ensured leak tightness during the whole wet-firing tests;
- The proof of concept thruster worked as expected and multiphysics simulations have been validated with a good level of accuracy, giving confidence in the high-temperature exploratory simulations conducted in Chapter 4.

4 Numerical Study of the Super-high Temperature Additive Resistojet Concept

Part of this work was published in:

Romei, F. and Grubišić, A.N. Numerical Study of a Novel Monolithic Heat Exchanger for Electrothermal Space Propulsion. Acta Astronautica, Volume 159, June 2019, Pages 8-16.

The work shown here has been conducted in parallel with the SLM manufacturing verification reported in Chapter 2. The synergy between the manufacturing verification process and the multi-physics numerical investigation conveyed here allowed to produce the prototype heat exchanger of the STAR thruster in three design iterations. While there is a significant design gap between the first and the second iteration, the next two iterations involved small changes necessary to overcome the manufacturing limitations and partially unknown issues deriving from the SLM process. The recirculating flow concept was initially applied to resistojets in the 1960s, where the manufacturing and design constraints were dictated by CVD technology in combination with the EB weld to realise the small connections between the tubular elements. Meanwhile, in this project, a novel SLM heat exchanger, which integrates the nozzle and the four resistance cylindrical elements, is manufactured via SLM in a single element. In this chapter, a multi-physics model is used to investigate the feasibility of the HTR performance goals.

4.1 Preliminary Considerations

4.1.1 Broad Mission Requirements

The thruster requirements are defined by the two mission scenarios, which would benefit from the STAR thruster described in Section 1.5.1.2. Table 4.1 shows the main broad requirements relevant

to the numerical investigation, such as the maximum expected operating pressure (MEOP), the thrust range, the average electrical power and the start-up duration, which is the maximum allowable time in which the thruster shall reach steady-state operation in full working temperature. In this analysis and with reference to Section 1.5.2.4, Inconel has been selected for the small LEO platform scenario because of its compatibility with power requirements while providing reasonable specific impulse improvement with respect to the currently available Xe resistojets. Ta and Re are selected instead for the GEO platform scenario. The three thrusters are named STAR-Inc, Star-Ta and STAR-Re, respectively, while the two mission scenarios M1 and M2 respectively.

Table 4.1. Resistojet requirements for two selected missions with the Xe propellant.

Parameter	Small LEO platform (M1)	M2: GEO platform (M2)
MEOP, bar	4	4
Thrust range, mN	20 – 50	50 – 500
Average power, W	< 50	< 500
Start-up duration, s	< 60	< 60

4.1.2 Methodology

The methodology of investigation is summarised in Fig. 4.1. The dimensioning of the thruster for the three cases in analysis (STAR-Inc, STAR-Ta and STAR-Re) begins with the dimensioning of the nozzle throat. Firstly, 1-D equations are used in step 1 to provide the throat radius and an initial estimate of the Reynolds number at the throat, which determines the flow regime within the nozzle. The throat radius is an input for CFD optimisation (step 2), which determines the optimum diverging nozzle angle, α_{opt}, maximising the specific impulse for a given stagnation condition. In this step, the nozzle efficiency, η_n, is calculated and serves as a baseline for the specific impulse determination in the following steps. The obtained nozzle geometry provides a computed mass flow rate, which is used for the following simulations of the full thruster. In step 3, the influence of the thermal insulation and the radiation shielding is discussed. Additionally, a stationary solver is used to define the electrical current necessary to reach the MOT of the respective materials (step 4). In step 5, a time-dependent study is used to depict the heating time of the thruster at constant current.

Finally, a heating cycle example is shown for STAR-Inc. The multi-physics simulations are made with COMSOL Multiphysics 5.3 (Build: 260).

4.2 Nozzle Study

4.2.1 Nozzle Dimensioning

In this section, the nozzle is dimensioned to meet the requirements of maximum thrust at the MEOP of 4 bar (Table 4.1). At the same time, the nozzle diverging angle is optimised to maximise the specific impulse at given stagnation conditions. Firstly, the mass flow rate is estimated using Eq.(A.5) with the specific impulse calculated at the MOT of each respective material (Table 1.23) and using the required thrust for each mission with a 5% margin. In the assumptions of a 1-D de Laval nozzle, adiabatic wall and constant specific heat expansion, the mass flow rate through the nozzle can be expressed by imposing the mass flow choked condition (Mach = 1), which leads to Eq.(1.7). This relation is used to calculate the throat radius at the given stagnation condition. The Reynolds number is evaluated at the throat to evaluate the flow regime using Eq.(1.20), where the dynamic viscosity of Xe is expressed as a fourth-order polynomial valid up to 3,000 K, Eq.(1.22).

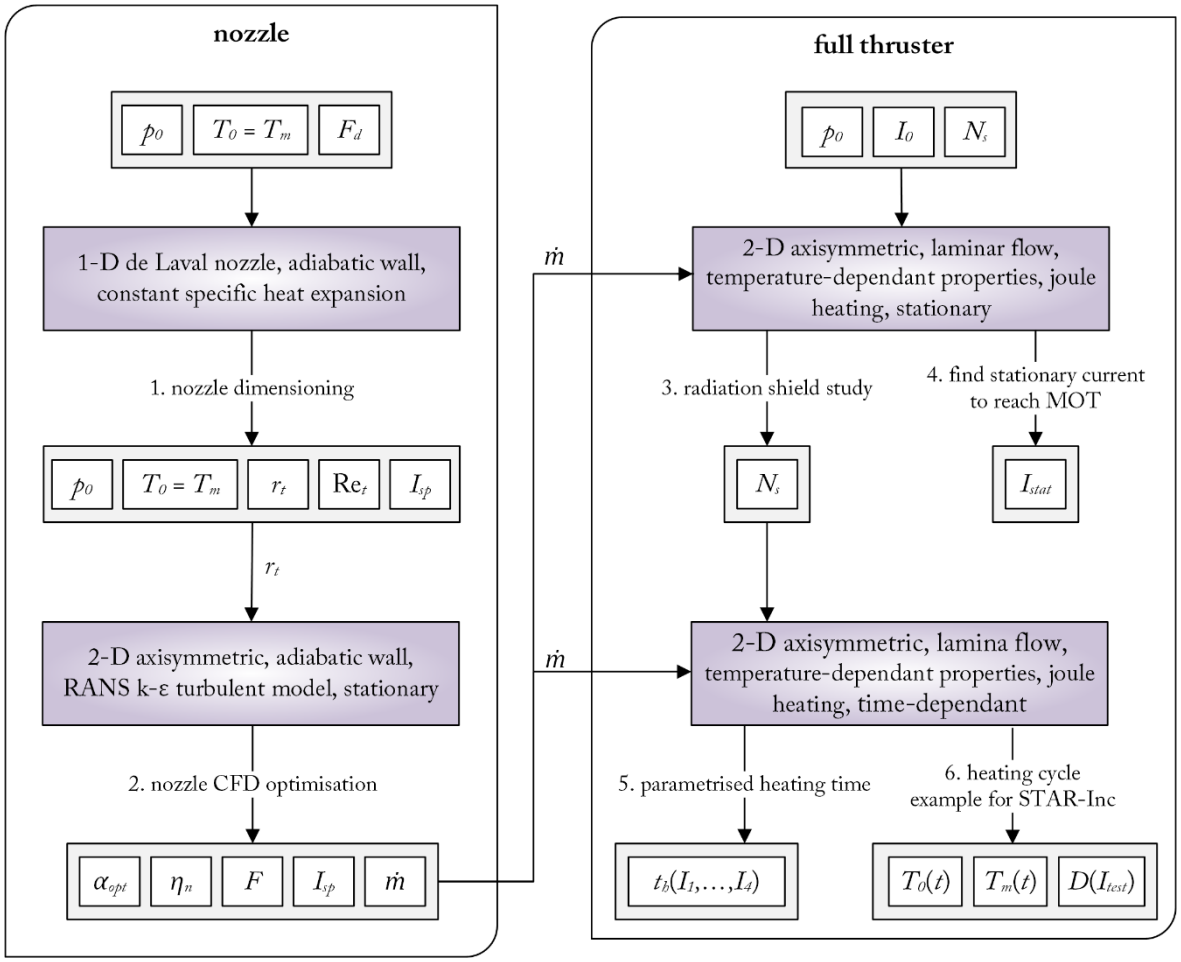

Fig. 4.1. Study steps performed on the three cases under examination.

Fig. 4.2 shows the design regions corresponding to the two missions M1 and M2, where the calculated throat radius guarantee a working pressure corresponding to the MEOP at the maximum thrust level. While a smaller throat would not generate sufficient thrust at the MEOP, a larger throat would decrease the Reynolds number. The dashed iso-Reynolds lines indicate the turbulent–laminar transition for a pipe flow (Re = 2100–4000). As discussed in Section 1.5.2.3, resistojets usually generate a relatively low thrust level and are designed to operate at low chamber pressures with small throat dimensions. Therefore, the Reynolds number can be low and the viscous losses significant. This effect can be mitigated by shortening the nozzle and increasing the divergence angle [65]. For Reynolds numbers below the transition zone, the viscous effect becomes relevant and can significantly lower the nozzle efficiency [66,70]. This has been proven experimentally for different nozzle shapes [68]. For this reason, an HTR using Ta, Re or W is not desirable for M1, as the resulting Reynolds number falls in the laminar region over the whole range of thrust (20–50 mN). This issue is not present for M2. Therefore, the analysis is restricted to STAR-Inc on the M1 LEO requirements and STAR-Ta and STAR-Re on the M2 GEO requirements.

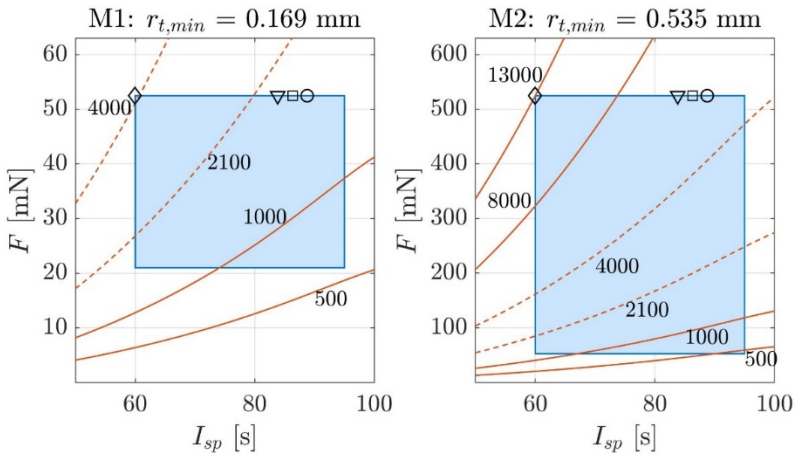

Fig. 4.2. Flow regime estimation with the design box (in blue) in the (Isp, F) plane for the two missions M1 (left) and M2 (right). Iso-Reynolds lines indicate the nozzle flow regime, where the dashed-delimited area corresponds to the laminar-turbulent transition. Markers locate the maximum specific impulse attainable using Inconel 718 (diamond), Ta (triangle), Re (square) and W (circle).

4.2.2 CFD Optimisation Method

The nozzle has a fixed inlet-to-throat area ratio of 10 and a fixed outlet-to-throat area ratio of 200. The internal geometry is smoothed with fillets of the same radius as the throat. The converging half-angle is 45° while the diverging half-angle, α, is the parameter to optimise. The selection of α is a trade-off between the influence of viscosity on the nozzle wall and the divergence of the flow. A CFD optimisation coupled method is performed to determine the optimum diverging angle, given the stagnation conditions, which maximises the specific impulse. The model solves full Navier-Stokes (N-S) equations of compressible flow, assuming a 2-D axisymmetric geometry and an adiabatic wall. The compressible N-S equations in the vectorial form are conservation of mass, Eq.(4.1), momentum, Eq.(4.2), and of energy, Eq.(4.3). These equations correspond to Eq.(B.14), Eq.(B.15) and Eq.(B.13) in the stationary case.

$$\nabla \cdot (\rho \cdot \mathbf{u}) = 0 \tag{4.1}$$

$$\rho(\mathbf{u} \cdot \nabla)\mathbf{u} = \nabla \cdot [-p\mathbf{I} + \mu(\nabla\mathbf{u} + (\nabla\mathbf{u})^T) - 2 \,/\, 3\mu(\nabla \cdot \mathbf{u})\mathbf{I}] + \mathbf{F} \tag{4.2}$$

$$\rho C_p(\mathbf{u} \cdot \nabla)T = \nabla \cdot (k\nabla T) + Q + Q_{vh} + W_p \tag{4.3}$$

where **u** is the velocity vector, Q_{vh} is the viscous heat (the heat irreversibly generated from work by viscous friction in a fluid), W_p is the pressure work, Q contains the heat source and F is the volume force. In this case, $Q = 0$ and $\mathbf{F} = \mathbf{0}$. The High Mach Number Flow (HMNF) interface is used assuming turbulent flow, which is modelled with the standard k – ε model and the built-in Kays-Crawford heat transport turbulence model [113]. At the inlet, stagnation pressure and temperature, as well as turbulence variables are defined. For a fully developed pipe flow, the turbulence intensity, I_T, and the turbulence length scale, L_T, are expressed by Eq.(4.4) and (4.5) respectively, where D_h represents the hydraulic diameter of the nozzle inlet. At the outlet, the boundary condition is defined as static pressure $p = 0$ bar.

$$I_T = 0.16\,\mathrm{Re}_{D_h}^{-1/8} \tag{4.4}$$

$$L_T = 0.038 D_h \tag{4.5}$$

A gradient-free Nelder-Mead optimisation solver (Appendix B) is used to maximise the objective function, J, which is equal to the specific impulse calculated with Eq.(A.5), where the mass flow rate and the thrust are defined at the nozzle exit plane through Eq.(4.6) and Eq.(4.7), respectively, where p and T are the static temperature and pressure, and u and w are the radial and axial components of the velocity **u**, respectively.

$$\dot{m} = \int_0^{2\pi}\int_0^{r_e} \rho w dr d\vartheta \tag{4.6}$$

$$F = \int_0^{2\pi}\int_0^{r_e} (\rho w^2 + p) dr d\vartheta \tag{4.7}$$

4.2.3 Grid Independent Study

A structured computational mesh is parametrised as a function of a refinement parameter f, which is used for the mesh convergence analysis. Fig. 4.3 depicts the relative error of selected variables, measured at the exit plane of the nozzle, as a function of f. Both the number of radial elements and the number of axial elements are proportional to f. The discretisation is refined close to the nozzle wall, that is, where the boundary layer is located. In particular, the radial elements have a ratio of 5

(ratio between the first and last radial length) with arithmetic progression. The number of quadrilateral elements is 185 when f = 1, 4450 when f = 5 and 17,700 when f = 10 (Fig. 4.4). The refinement parameter selected is f = 5, which corresponds to a relative error with respect to the finest solution below 0.5% for mass flow rate and thrust calculated as integral at the exit plane (Eq.(4.6) and (4.7), respectively). The relative error for T, p, u and w, calculated as average at the exit plane, falls below 5%.

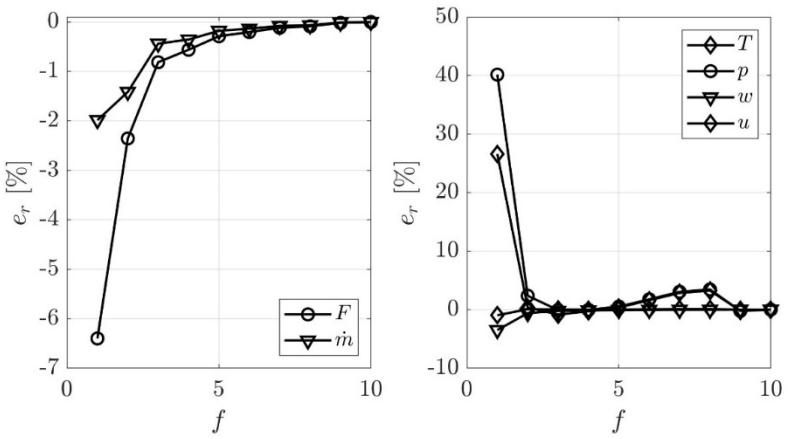

Fig. 4.3. Relative error of variables measured at the exit plane of the nozzle as a function of the mesh refinement parameter.

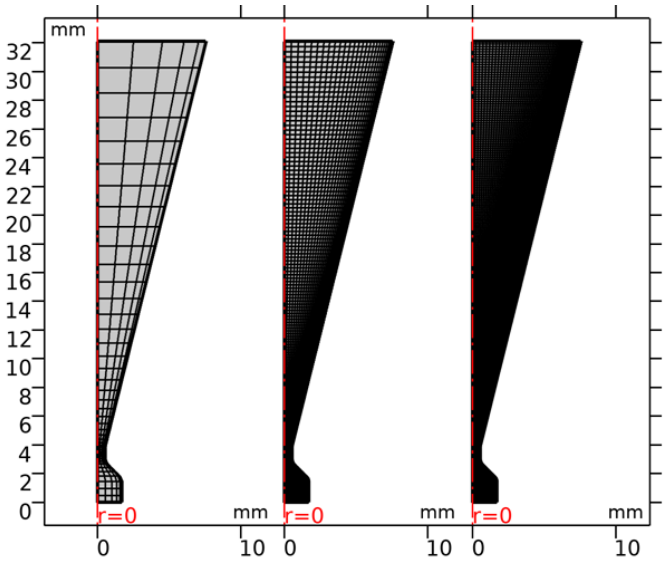

Fig. 4.4. Mesh grid of the nozzle domain for f = 1, 5 and 10 (left to right).

4.2.4 Results

Table 4.2 shows the optimisation results in terms of nozzle efficiency, defined as the ratio between the computed and the theoretical specific impulse, where the latter is given by Eq.(1.9). Table 4.2 summarises the results of the optimisation process in terms of the nozzle's optimum diverging angle, α_{opt}; theoretical mass flow rate from Eq.(1.7); computed mass flow rate, thrust and specific impulse; and Reynolds number evaluated at the throat using Eq.(1.20), with average temperature and dynamic viscosity. It can be noted that the optimum angles are similar. This is not surprising since it is strongly dependent on the Reynolds numbers, which are also similar as previously discussed. The calculation of the thrust using Eq.(4.7), hence specific impulse, is valid if the pressure term is sufficiently small when compared to the total thrust. If the pressure term is significant, the nozzle operates in a strong under-expanded mode. In this case, the streamlines at the exit of the nozzle are subjected to greater divergence loss, which results in a lower specific impulse. This effect cannot be evaluated with the geometrical assumption of the current model of a truncated nozzle at the exit. All three cases analysed are within the model validity since the pressure term represents approximately 0.5% of the total thrust, which means that 99.5% of thrust is due to momentum.

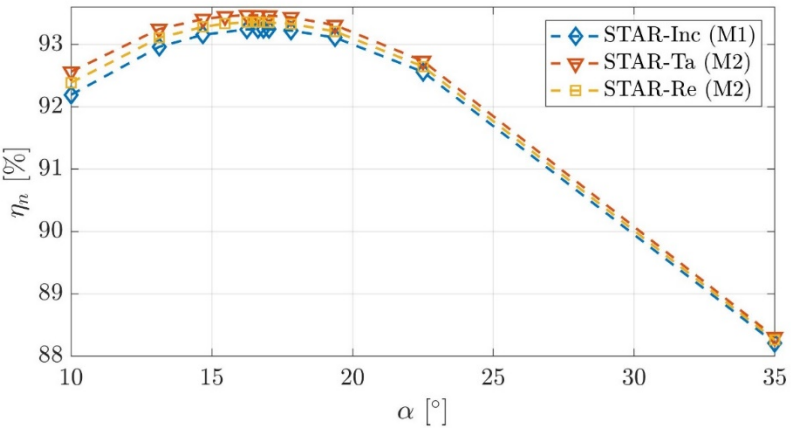

Fig. 4.5. Specific impulse optimisation for the three cases in analysis as a function of the diverging angle of the nozzle.

Table 4.2. Nozzle optimisation results for the three thrusters in analysis.

Parameter	STAR-Inc (M1)	STAR-Ta (M2)	STAR-Re (M2)
T_0 , K	1,350	2,640	2,800
r_t , mm	0.169	0.535	0.535
$\dot{m}_{est}$, mg/s	89.3	638.7	620.1
$\dot{m}$, mg/s	86.55	620.7	602.65
F , mN	52.8	530.5	529.8
I_{sp} , s	62.2	87.1	89.6
η_n , %	93.3	93.5	93.4
α_{opt} , °	16.64	16.25	16.45
Re_t	4,028	5,734	5,349

If compared with the 1-D analysis conducted Section 1.5.2.3, where the nozzle efficiency was extrapolated from experimental data found in the literature for a 15° half-angle nozzle with unheated N_2 and H_2 propellant (Fig. 1.22), the CFD results seem in good agreement, with a calculated efficiency on the higher end of the interpolating curve (Fig. 4.6).

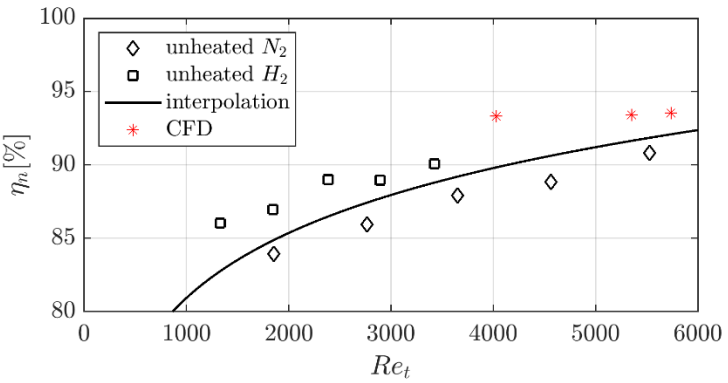

Fig. 4.6. Comparison between experimental data on low Reynolds number nozzles (Fig. 1.22**) and current CFD analysis.**

4.2.5 Examples of CFD optimisation

4.2.5.1 SSTL T-30 Nozzle

In Appendix C.1.2, the results of a validation CFD study on the SSTL T-30 nozzle are summarised. The study shows that, at the highest power, hence stagnation temperature, and lowest flow rate, the nozzle operates with lower efficiency and that the diverging half-angle can be optimised. The CFD-optimisation coupling allows an accurate estimate of the optimum nozzle geometry capable of maximising the thrust, hence I_{sp}, for given supply pressure and temperature at the inlet of the nozzle. The T-30 Xe resistojet (described in Section 0) operates at a wide range of pressures, resulting in most cases in a turbulent flow, which is characterised by a boundary layer with a typical dimension of 1% of the free-stream flow region. Consequently, the resulting Mach number at the nozzle exit can be considered entirely supersonic. Therefore, in the turbulent flow cases, the viscous losses are negligible compared with the divergence losses. Instead, for the laminar flow regime, a large subsonic region exists at the exit of the nozzle, extending approximately 10% into the radius of the nozzle. Among the 24 cases analysed, the one with the lowest Re_t (65 W of power input and 1 bar of inlet pressure) has been optimised in thrust to evaluate improvement using this optimisation strategy.

The CFD-optimisation coupling method described in the previous section has been used. Fig. 4.7 shows the Mach number iso-contours for two different nozzle angles with the same area ratio. On the left, the initial T50 nozzle with α = 14° is represented while on the right the optimised nozzle is represented. As seen in the figure, the flow rapidly becomes supersonic, and the viscous layers along the nozzle walls are very thick. The subsonic flow percentage of exit radius is 25.4% for α = 14°, 28.2% for α = 26.7° and 26.5% for the optimised nozzle, having for α_{opt} = 27.4°. Even if the subsonic region of the first nozzle is slightly smaller than that of the optimised angle, the former has a larger zone where the Mach number is below 3. Therefore, the 27.4° nozzle is shown to minimise the viscous effect. Additionally, it optimises the thrust developed for the given inlet pressure and temperature as a result of the trade-off with the divergence losses.

The results show an improvement in the performance of about 2% in I_{sp} for the optimised 27.4° nozzle, increasing the specific impulse from 54 s to 55.07 s, and a thrust improvement of about 2.5%. Performing the same optimisation study for a high-Reynolds turbulent flow case, for instance, 30 W of power and 2 bar of inlet pressure, the result is α_{opt} = 15.5° with a specific impulse improvement of only 10 ms.

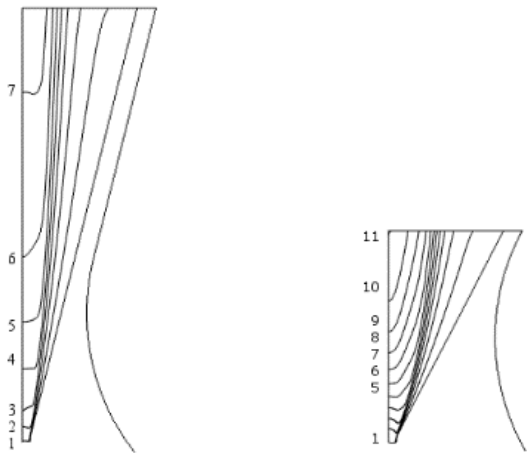

Fig. 4.7. Mach number contours for initial (α = 14°) and optimised (α = 27.4°) nozzles.

4.2.5.2 HTR Nozzle at low-Reynolds Regime

In this section, the optimisation of the HTR nozzle in low-Reynolds regime is discussed. In this example, the nozzle throat diameter and the exit-to-throat area ratio are the same as for the T-30 thruster, such as d_t = 0.42 mm and ε_{out} = 196. The nozzle inlet-to-throat area ratio is ε_{out} = 10. Fig. 4.8 (left) shows the boundary conditions applied to the nozzle; in particular, the nozzle wall is made of *tantalum [solid]*, from the COMSOL material library. A diffuse surface BC is applied to the diverging internal section of the nozzle. A temperature BC is applied to the solid inlet surface, T_n = 3,100 K, to simulate the HTR structural temperature. The value of emissivity used in the simulation is ε = 0.296 (*tantalum [solid]*). The inlet stagnation pressure is set to 5 bar, while the outlet static pressure is set to 0 bar.

The resulting optimal half-angle α_{opt} = 45.7° gives a thrust of 86 mN, a mass flow rate of 97.14 mg/s for a specific impulse of 90 s with Re_t = 2,103. Table 4.3, shows a breakdown of the resulting input and output power contributions calculated as integrals of the computational solution. The nozzle efficiency calculated by dividing the axial kinetic power by the hot-gas power input result of η_n = 79%. Compared to the nozzle efficiency curve from literature (Fig. 1.22), this result collocates on the lower end of the curve. The nozzle efficiency loss terms are of the same magnitude in this analysis (calculated using the equations in Table 1.4). This simulation also suggests that the thermal radiation from the HTR nozzle is a significant thermal loss term.

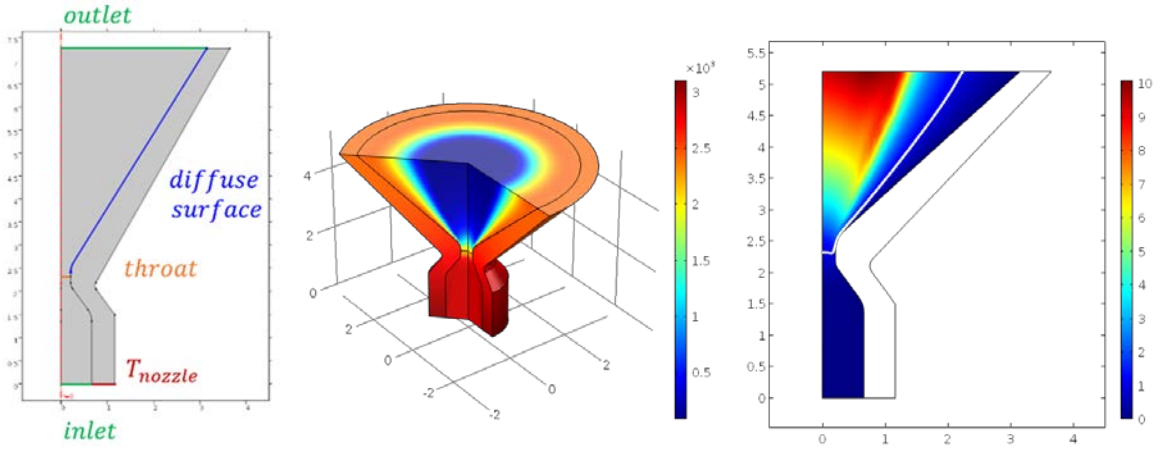

Fig. 4.8. Nozzle boundary conditions and throat section highlighted (left), static temperature solution with optimised diverging section half-angle (centre) and Mach number colour map (right). The white line (M = 1) delimits the subsonic region.

Table 4.3. Power balance of the optimal solution of the HTR nozzle (units in W).

IN	Hot-gas power	44.583
OUT	Axial kinetic power	35.254
	Radial kinetic power	4.518
	Incomplete expansion	5.262
	Radiation to space	27.579

4.3 Multi-physics Study of the STAR Thruster

In this section, the STAR thruster is modelled to evaluate the electrothermal and fluidic characteristics of the whole heat exchanger in the three cases of STAR-Inc, STAR-Ta and STAR-Re.

4.3.1 Geometry and Assumptions

The STAR high-temperature resistojet computational geometry is shown in Fig. 4.9. The propellant enters from the rear of the thruster (inlet) and flows through the annular outer shell of the body. At the point of the nozzle spacer, the flow is directed into the inner heat exchanger, composed of four thin wall cylinders. To increase thermal efficiency, heat transfer is minimised from the high-power-density inner four walls to the outer shell of the thruster, which ultimately radiates heat to space. The

STAR design, therefore, includes a vacuum jacket to insulate the inner heat exchanger. Furthermore, the design includes an optional radiative heat shield, made of thin foils, placed in a vacuum jacket to minimise the radiative heat transfer from the inner to the outer part of the heat exchanger. Also, a thermal insulator further lowers the casing temperature to minimise the radiation to space. The casing is surrounded with a thin metal foil with low emissivity. The influence of the radiation shielding and the thermal insulation is discussed in Section 4.3.3.1.

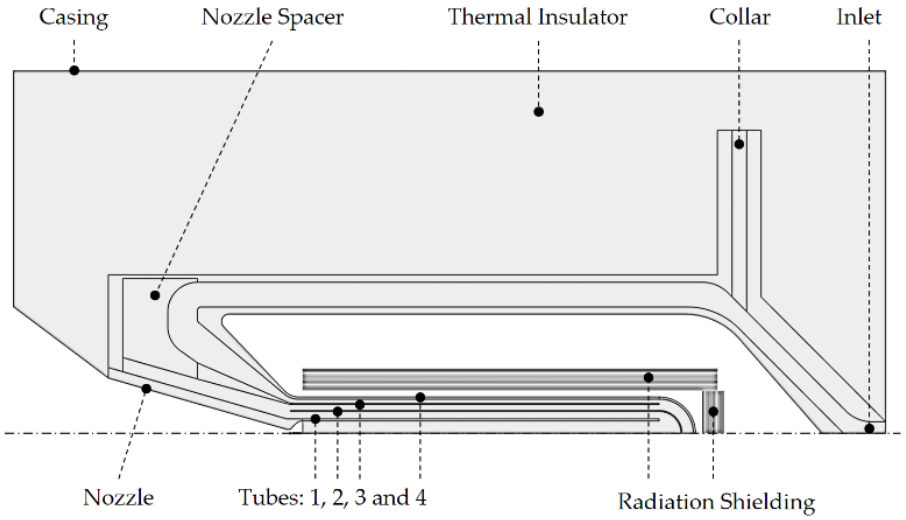

Fig. 4.9. 2-D axial-symmetric geometry of the STAR thruster.

Fig. 4.9 shows the parametrised 2-D axisymmetric geometry developed in COMSOL. The insulation package external diameter is automatically derived as `(length + nozzle_L + depth)/2`, where `nozzle_L` is the nozzle axial length. This way, the insulation package keeps a 1:1 length–height ratio. In all simulations, the four cylinders of the heat exchanger have a thickness of 300 µm, 150 µm, 150 µm and 300 µm, respectively. This feature size is achievable with SLM and has been validated with the successful fabrication of the STAR-0 prototype in both 316L and in pure Ta (as part of the NSTP-3 RADICAL project). The length of the four cylinders is set to twice the nozzle length, which follows from the nozzle dimensioning (Section 4.2.4). The resulting cylinder length is 15.5 mm for the STAR-Inc thruster and 49 mm for the STAR-Ta and Re thrusters. The vacuum gap width is set to 1.5 times the nozzle outlet radius. The diameter of the thermal insulation is approximately equal to the full length of the thruster. The tungsten foil radiation shielding is 30 µm thick and wrapped within the vacuum jacket at a distance of 1 mm from the inner heat exchanger walls and 0.2 mm between each layer.

A specific material is applied to each domain shown in Fig. 4.9. Where not indicated otherwise, these materials are available within the current version of the software. *Xenon [gas]* is used with modified dynamic viscosity and thermal conductivity (sourced from [114]) to extend their validity to 3,000 K. *Inconel 718 [solid, full hardened]*, *tantalum [solid]* and *rhenium [solid, annealed]* are used for the metal parts. *Tungsten [solid, Ho et al.]* is used for the radiation shielding foils and the casing external boundaries. In the case of STAR-Inc, the selected thermal insulator material is Promalight – 1200 [51], while for the other two thrusters is Denka Alcen [115]. The former is rated 1,200˚C made from an opacified blend of filament-reinforced pyrogenic Al_2O_3, while the latter is rated 1,600˚C, composed of polycrystalline wool fibre with Al_2O_3 (80%) and SiO_2 (20%).

For the thruster simulations, the nozzle flow is not solved. It is assumed that the heat transfer between the flow in the nozzle expansion area and the thruster body is negligible. Therefore, Eq. (4.2) to (4.3) are solved for weakly compressible flow; as such, the density is evaluated at a reference pressure, $p_{ref} = p_0$, and is temperature-dependent. The flow regime is assumed laminar for all the following simulations. Joule heating is modelled using the Electrical Currents (EC) interface, which is coupled with the HT interface to evaluate the heat source Q in Eq.(4.3). A constant current boundary condition is applied at one end of each cylinder while at the other end the grounding boundary condition is applied. At the inlet boundary, the mass flow rate is set resulting from the nozzle simulations (given in Table 4.2), while at the outlet boundary, the stagnation pressure is defined, p_0 = 4 bar.

Surface-to-ambient radiation is applied over the whole exterior of the thruster, such as on the casing and the nozzle boundaries. For the nozzle surface, radiation to space assumes a constant emissivity of 0.3 for Inconel. Surface-to-surface radiation is applied to the internal walls of the heat exchanger, assuming a constant emissivity of 0.6, which corresponds to the emissivity of the as-printed component.

4.3.2 Grid Independent Study

Computational grid convergence is conducted on the STAR-Ta thruster without shielding or thermal insulation. A free-triangular computation mesh is parametrised as a function of a refinement parameter *f*, which is used for the mesh convergence analysis. Fig. 4.10 depicts the relative error of selected variables, measured at inlet and outlet of the heat exchanger, as a function of *f*. The discretisation is physics-controlled and corresponds to an extremely coarse mesh when f = 1 and to

an extremely fine mesh when f = 10. The total number of elements is 11,121 when f = 1 and 63,938 when f = 10 (Fig. 4.11). The selected mesh refinement parameter is f = 6, which guarantees e relative error to the finest computational grid of the selected variables within ±2%.

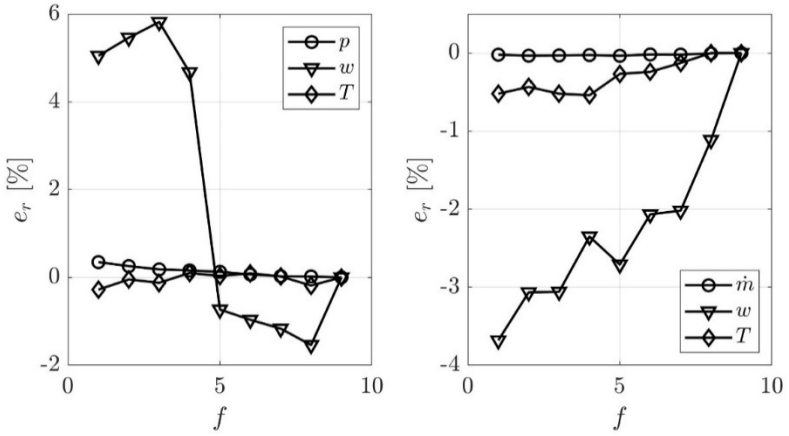

Fig. 4.10. Relative error calculated at the inlet (left) and the outlet (right) of the heat exchanger.

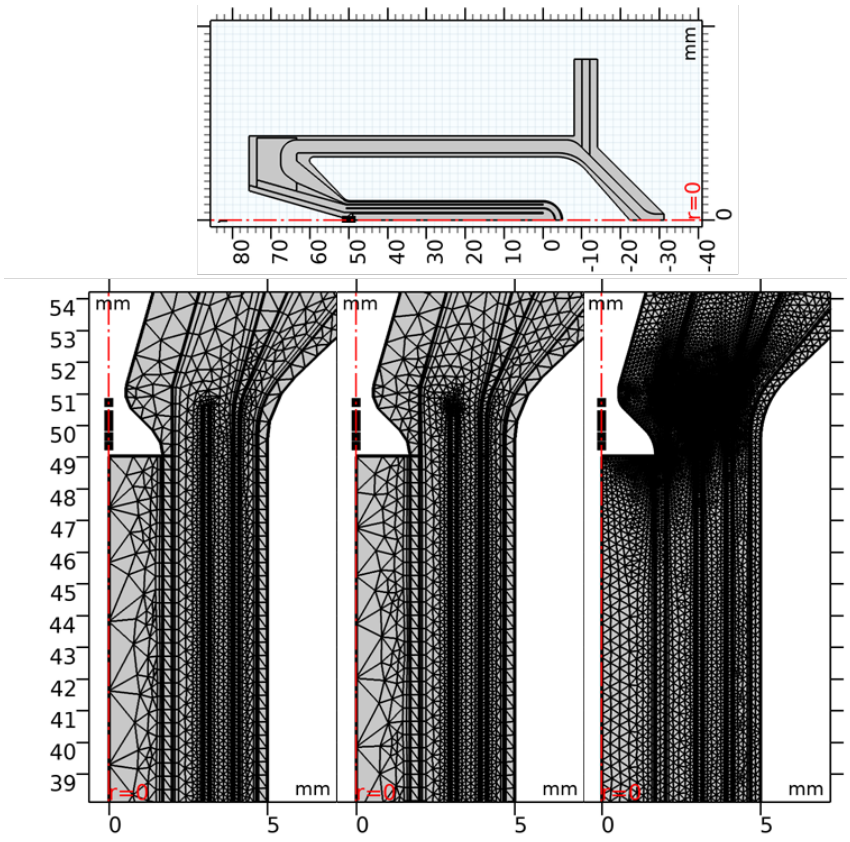

Fig. 4.11. Full thruster 2D axisymmetric domain (top) and particular of the mesh grid in the nozzle region for f = 1, 5 and 10 (left to right).

4.3.3 Stationary Analysis of the STAR Configurations

4.3.3.1 Insulation and Radiation Shielding Study

Stationary analysis of the model is used to quantify the effect of the thermal insulation and the radiation shielding. Three test currents, obtained by trial and error and able to heat the thruster to nearly the MOT, have been used in this analysis. Fig. 4.12 shows the STAR-Ta temperature distribution, depicting a significant increase in gas temperature before the nozzle when including both the thermal insulation and the radiation shielding. Table 4.4 shows in detail the maximum temperatures achieved for both the structure, T_m, and for Xe at the nozzle inlet, T_0, for different amounts of radiation shield foils, N_s, where *shi* and *ins* indicate the presence (= 1) or absence (= 0) of the radiation shielding and the insulator, respectively.

The results show that STAR-Inc benefits significantly from thermal insulation, providing a peak temperature increase of approximately 200 K, while negligible improvement is observed when radiation shielding is included. On the other hand, STAR-Ta and STAR-Re benefit significantly from both the radiation shielding and from the thermal insulator because of significantly higher operating temperatures. When combined, they provide a greater increase in peak operating temperature than the sum of the two single cases. A radiation shielding is more effective at higher temperatures when the thermal insulator is used.

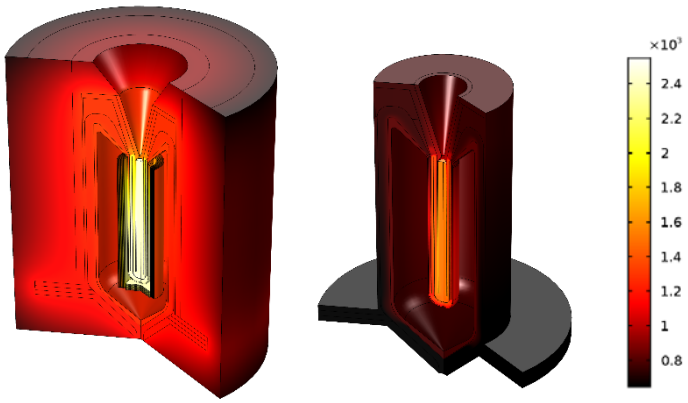

Fig. 4.12. Temperature stationary solution of STAR-Ta, at a test current of 77 A, showing the increase of maximum temperature when including both thermal insulation and radiation shielding located in the vacuum jacket.

Table 4.4. Summary of the thermal insulation and radiation shielding parametrisation study. "Shi" and "ins" indicate presence of the radiation shielding and thermal insulation, respectively. T_m, T_0 and N_s are the maximum structural temperature, the nozzle inlet stagnation temperature and the number of foil for the shielding, respectively. Finally, I_{test} is the test current at which the parametric study is performed in each case.

Thruster	Var.	shi = 0 ins = 0	shi = 0 ins = 1	shi = 1 ins = 0	shi = 1 ins = 0	shi = 1 ins = 1	shi = 1 ins = 1
STAR-In $I_{test} = 18A$	T_m	1,152	1,371	1,166	1,166	1,395	1,395
	T_0	1,014	1,274	1,030	1,030	1,299	1,300
	N_s	-	-	5	10	5	10
STAR-Ta $I_{test} = 75A$	T_m	1,670	1,940	2,146	2,149	2,550	2,566
	T_0	1,528	1,842	1,992	1,995	2,429	2,444
	N_s	-	-	15	30	15	30
STAR-Re $I_{test} = 70A$	T_m	1,668	1,872	2,068	2,069	2,324	2,331
	T_0	1,544	1,773	1,940	1,941	2,211	2,217
	N_s	-	-	15	30	15	30

From the table above, radiation shielding is considered fundamental for STAR-Ta and STAR-Re thrusters while for STAR-Inc this can be eliminated, reducing the complexity of the assembly. The next series of studies are based on these selected configurations. For both extreme-temperature thrusters, the selected number of radiation shielding foils is 15 since the further increase in gas temperature using 30 foils is negligible and does not justify the additional weight and assembly complexity required.

4.3.3.2 Stationary Current Optimisation

The required electrical current necessary to heat the thruster to the maximum structural temperature is obtained with a multi-physics optimisation study. This uses the Nelder-Meads gradient-free algorithm, with the objective function expressed in Eq.(4.8) to be minimised, with an optimality tolerance of 0.01. The control parameter is the electrical current, with lower and upper bounds of 90% and 110% of the respective test currents used in Section 4.3.3.1. This study is fundamental to evaluate the ultimate stagnation temperature achievable, thus the maximum attainable specific impulse. The stationary current, I_{stat}, and other parameters are listed in Table 4.5. Eq.(1.11) is used to evaluate heat exchanger efficiency, including η_h, expressed as the ratio of the stagnation gas power calculated at the inlet of the nozzle, P_0, and the total input power into the thruster, P_{ts}. The latter is

the sum of the electrical power, P_e, and the stagnation power associated to the inlet gas, $P_{0,in}$. It has to be noted that the inlet gas temperature is not fixed as a boundary condition. In particular, no boundary conditions are applied at the back of the thruster. With this assumption, the thruster is perfectly isolated from the spacecraft whereas in reality some heat would be transferred to the spacecraft by conduction through mechanical interfaces.

$$J = (T_m \ / \ \mathrm{MOT} - 1)^2 \times 10^3 \tag{4.8}$$

Table 4.5. Summary of main thruster parameters in the stationary case when T_m = MOT.

Parameter	STAR-Inc (M1)	STAR-Ta (M2)	STAR-Re (M2)
η_h [%]	66.5	62.2	59.0
T_0 [K]	1,252.9	2,424.6	2,618.5
P_e [W]	13.3	277.6	310.8
I_{stat} [A]	17.6	77.0	75.5
$T_{0,in}$ [K]	944	1212	1282

4.3.4 Time-dependent Analysis

4.3.4.1 Time to Operational Temperature

While I_{stat} is the current necessary to maintain thermal equilibrium in the thruster, the time necessary to reach such a condition can be long. The time necessary to reach the operating temperature is determined with a time-dependent simulation of the thruster ignition at four increasing current levels, beginning from I_{stat}. The stationary solution of the thruster in cold state is used as an initial solution for the time-dependent solver. The current increases to the test value after 1 s and reaches the maximum value in 0.1 s. A stop condition, set into the time-dependent solver, ends each simulation when the maximum structural temperature, T_m, reaches the MOT.

Fig. 4.13 shows the resulting temperature increase over time for STAR-Inc. Because of the peculiar quasi-constant resistivity of Inconel (Fig. 1.26), the electrical power is almost constant in time at each current level analysed, and it corresponds to 13 W (at 120 s), 25.3 W, 37.3 W and 49.3 W, respectively. It can be noted that with I_{stat}, the objective of reaching the MOT of Inconel is still far

from achieved after 120 s of power application. In all the other three cases, the objective is reached within the start-up requirement of 60 s.

Fig. 4.14 shows the temperature rising for STAR-Ta and STAR-Re. For the former, the electrical power evaluated at the last time step for each current is 158.6 W at 120 s, 349.6 W at 120 s, 438.4 W at 55.3 s and 512.4 W at 35.1 s. For the latter, the electrical power evaluated at the last time step for each current is 270.2 W at 120 s, 348.4 W at 120 s, 421 W at 108.2 s and 477.8 W at 51.1 s. In general, at lower currents, Re can heat faster than Ta because of its higher electrical resistivity at low temperature.

4.3.4.2 Heating Cycle Example for STAR-Inc

The STAR thruster is characterised by a relatively low electrical resistance, requiring high currents at low voltage. A possible means of power control consists of a duty cycle in current limited mode. In the previous section, it is demonstrated that the minimal current to heat the thruster to its MOT, I_{stat}, determines a heating time on the order of hours. This is not compatible with the mission requirements shown in section 1.5. Consequently, higher current, hence power, is necessary to reach the MOT within the anticipated heating time requirements. Once the operating temperature is reached, the heater must then switch off. Therefore, a pulse width operation is necessary to maintain the objective temperature, and a duty cycle is determined.

In the following example, STAR-Inc is subjected to a pulsed width heating cycle with two test currents corresponding to about 25 W (I = 24.4 A) and 50 W (I = 34.2 A). A domain probe evaluates the maximum structural temperature, T_m. The heater switches on when the measured temperature falls below 90% of MOT and switches off when MOT is reached. Fig. 4.15 depicts the first 30 seconds of the simulation, showing the structural maximum temperature, the maximum stagnation temperature and the electrical current. The resulting duty cycles are D = 89% for P_e = 25 W and D = 42% for P_e = 50 W, which corresponds to an average power of 22.3 W and 21 W, respectively. In the first case, the peak stagnation temperature rises from 1,146 K to 1,149 K while in the second case from 1,108 K to 1,150 K during the two minutes of simulation. In the stationary case, corresponding to a continuous application of I_{stat}, the stagnation temperature reaches 1,253 K. The selection of the power control depends uniquely on the PPU constraints, which is not subject to this work.

4.3.5 Results of the Numerical Study on the Three Test Cases

The heat exchanger efficiency combined with the nozzle efficiency provides the total thruster efficiency, η_{ts}, as shown by Eq.(4.9). Table 4.6 compares the specific impulse, total thruster efficiency, electric power and difference between the maximum structural and the stagnation temperatures, ΔT, calculated in the time-dependent and the stationary cases. The time-dependent cases correspond to the maximum currents evaluated for each thruster in Section 4.3.4.1, where t_h is the heating time necessary to reach the MOT.

$$\eta_{ts} = \eta_h \eta_n \tag{4.9}$$

Table 4.6. Comparison of performance immediately after ignition and the maximum performance achievable corresponding to the stationary solution.

Parameter	STAR-Inc		STAR-Ta		STAR-Re	
	$t_h = 8.2$ s	$t \to \infty$	$t_h = 35.1$ s	$t \to \infty$	$t_h = 51.1$ s	$t \to \infty$
I_{sp} [s]	56.4	59.9	83.5	85.0	86.7	87.7
η_{ts} [%]	26.8%	62.0%	41.3%	58.2%	45.9%	55.1%
P_e [W]	49.4	13.3	512.4	277.6	477.8	310.8
ΔT [K]	239.8	95.6	206.8	131.5	183.5	91.5

Some design and operation guidelines can be drawn from the numerical study here described. The first thing to dimension is the nozzle, which shall provide the objective performance thrust and specific impulse. To maximise its efficiency, the supply pressure shall be the highest possible, which maximises the throat the Reynolds number. The throat shall be then dimensioned to provide the required thrust at the expected propellant stagnation temperature. The dimension of the nozzle imposes a minimum thruster size, which should be optimised for the given propellant flow rate. This optimisation step has not been performed here but should be done through a geometrical parametric study of the thruster. This process has to be performed with the knowledge of the manufacturing capabilities. Multiphysics simulations shall be used to guide the selection and dimensioning of a thermal insulation package and/or of a radiation shielding. The numerical analysis shall also be used to infer the expected dry and wet electrothermal performance of the thruster and therefore draw preliminary pre-heating and either steady-state or pulsed performance test procedures. Due to the

number of uncertainties in the electrothermal and fluidic multiphysics modelling, experimental validation should be performed as soon as possible in the thruster development stage. An extensive experimental campaign shall be conducted if possible and models shall be validated to be then used for further design investigations.

Because of the high electrical currents involved, the proposed heater is likely to operate at constant limited current. Depending on the pre-heating time requirements, a specific current should be selected to reach the maximum operational temperature before starting the propellant flow for the manoeuvre. Thrusting current can differ greatly from dry pre-heating current due to the heat removed by the propellant through forced convection. Therefore, these shall be selected through a combination of experimental and computational analysis to maximise the thruster performance. Finally, to limit the thermal fatigue of the heater, a constant current should be applied throughout the thrust manoeuvre time, while an on-off power switch shall be avoided. This can be achieved employing a PID control using a feedback signal strongly dependant on the operating temperature. For example, a thermocouple placed in a hot region of the thruster or the electrical resistance of the heater could be employed for this purpose.

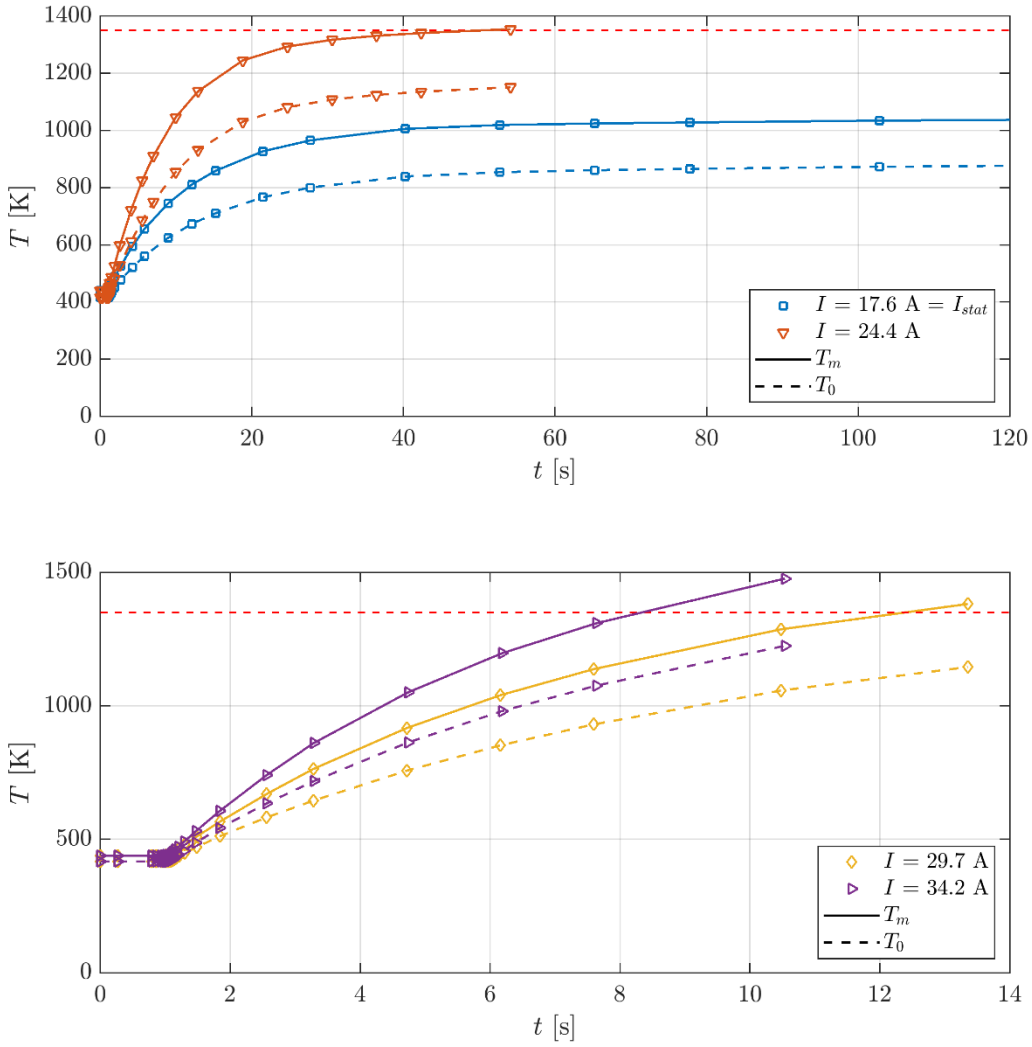

Fig. 4.13. Ignition of STAR-Inc from the cold-gas stationary solution. Maximum structural temperature (solid line) and Xe stagnation temperature at the inlet of the nozzle (dashed line) are shown at four current levels. The MOT of Inconel 718 is represented with a horizontal dashed line.

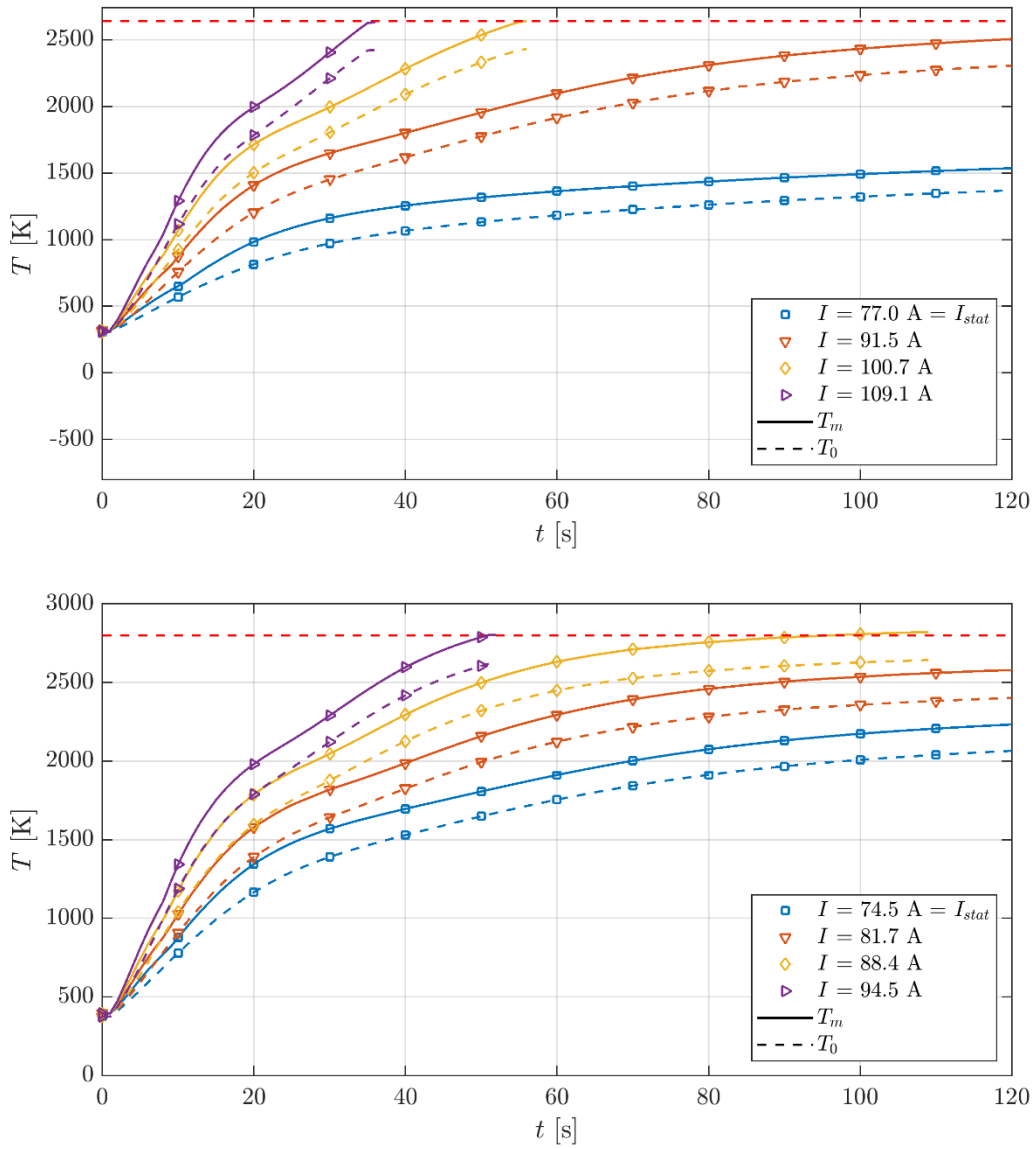

Fig. 4.14. Ignition of STAR-Ta (top) and STAR-Re (bottom) from the cold-gas stationary solution. Maximum structural temperature (solid line) and Xe stagnation temperature at the inlet of the nozzle (dashed line) are shown at four current levels. The MOT of the two materials is represented with a horizontal dashed line.

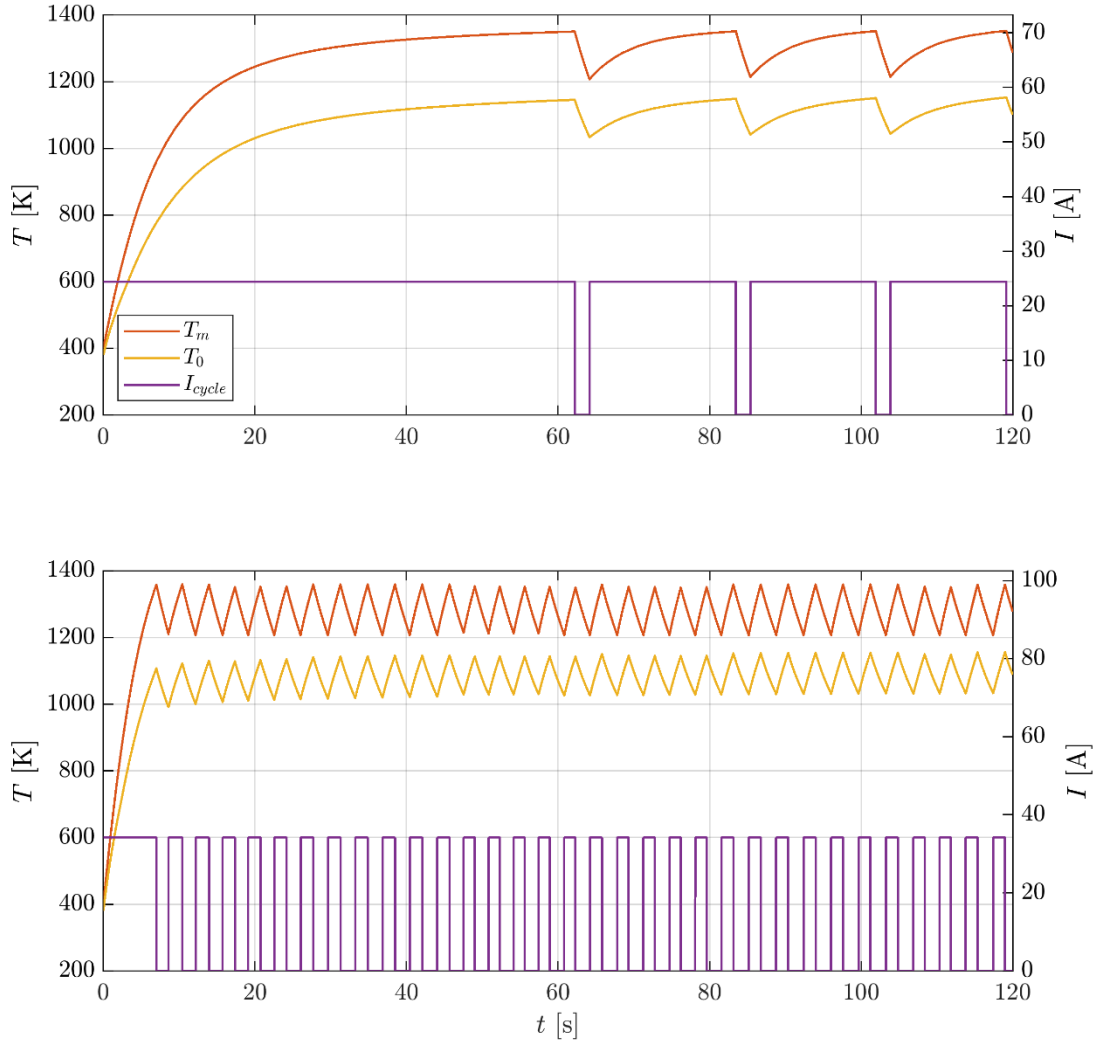

Fig. 4.15. Pulse-width heating cycle of STAR-Inc with two current levels corresponding to approximately 25 W and 50 W of electrical power.

4.4 Summary

In the three cases analysed, the temperature obtainable within one minute is close to the maximum operating temperature evaluated with the stationary solution. In particular, $I_{sp}(t_h)/I_{sp}(\infty)$ results in 94%, 98% and 99% for STAR-Inc, STAR-Ta and STAR-Re, respectively. Therefore, $I_{sp}(\infty)$ could be obtained within minutes using a high-current heat-up, followed by a lower-current firing mode, aimed at maintaining the operational temperature. It has to be noted that the thruster dimensioning, including thermal insulation and radiation shielding selection, was not subjected to an optimisation process. Rather, this study explores the STAR design in the three exploratory cases of interest. A

detailed design of the STAR resistojet should aim to increase stationary thruster efficiency in the region of 60-70%.

Steady-state studies provided the minimum current necessary to reach the operational temperature, or equivalently to maintain the thermal equilibrium over time, while time-dependent studies provided the heating time at increasing current levels. In all cases, the objective temperature is reached within the start-up duration requirement. Finally, a heating cycle example on STAR-Inc shows a possible mode of operation at constant current, which results in a quasi-constant duty cycle.

Conclusions

5

The study and development of a novel high-temperature resistojet design has been presented. This chapter draws the main conclusions from the work discussed in the thesis. A summary of the thesis is provided together with a list of the key findings, the significance of the work, the future work and outlook.

5.1 Novelty of Research

Emerging metal additive manufacturing technology has been identified as a means to enable previously unimaginable designs of resistojets with a significant reduction in parts (see Section 1.5.2). This manufacturing technology also circumvents extremely difficult joining techniques or complex assembly procedures whilst enabling high dimensional accuracy and extensive reductions in time to manufacture and costs. A Selective Laser Melting (SLM) metal printer at the Southampton Engineering Design and Manufacturing Centre (EDMC) represents the current state of the art of this technology and is able to print metal components with a high degree of accuracy; in particular, it is capable of building thin walls on the order of a hundred microns with a high aspect or height-to-thickness ratio (see Chapter 2). These parameters were suitable for a particular flow-recirculating design of the resistojet, which showed the highest performance and efficiency in the literature. In the past, these complex geometries were built with an extreme effort by combining Chemical Vapour Deposition (CVD) technology to build thin-wall tubes and Electron Beam (EB) welding to join them using very small struts designed to transform the recirculating-flow geometry into a resistive element. In this way, the resistive element is coincident with the flow path, simplifying the design and allowing for high thermal efficiency.

The multiphysics simulations performed with the commercial software COMSOL Multiphysics represent a further novelty of the research. This simulation tool permitted the development of a unique multiphysics model where it is possible to couple numerous physical aspects of the resistojet operation. This approach to design is essential given the design freedom brought by SLM but also

due to the highly coupled nature of the physical operating phenomenon. In particular, a DC potential is applied to the electrical heater that is designed to operate at high temperatures, at which radiation is a dominant heat transfer mode. At the same time, heat is removed from the heater through forced convection of the propellant. Moreover, both the heat exchanger materials and the propellant have strongly temperature-dependant properties, resulting in a non-trivial electrothermal dynamics of the thruster. Within COMSOL, this is achieved by coupling Computational Fluid Dynamics (CFD), heat transfer and Joule heating models. CFD simulates the either laminar or turbulent flow of the propellant through the resistojet body, while the heat transfer models (conduction, convection and radiation), are applied to the entire geometry to couple the propellant with the solid parts of the thruster. The heater, which generally consists of a resistive element, is modelled using Joule heating, where temperature-dependant properties of the materials are used to appropriately simulating the voltage-current characteristic of this component. The advantage of using multiphysics modelling is that all the above-mentioned physics can be properly coupled to simulate the thermo-fluidic and electro-mechanical characteristics of the resistojet thruster in a single model. In general, the physics can be coupled in any combination, depending on the study purpose.

Using SLM as the manufacturing technology to build the recirculating-flow heat exchanger resistojet was ambitious, both in terms of the extremely small feature size required and in the uncertain nature of the manufacturing process, as this is still not a mature technology. Additive manufacturing has never been applied to resistojets or, to the authors' knowledge, any other electric propulsion system. Additionally, limited literature is available on metal additive manufacturing in general and on SLM in particular. The project has therefore applied novel non-destructive inspection techniques to SLM-printed parts. The University of Southampton provides a state-of-the-art X-ray Computed Tomography (CT) scanning facility, which has enabled inspection to a micron level of accuracy. This permitted a novel geometric comparison between the nominal CAD geometry and the actual 3D printed SLM X-rayed components.

In conclusion, multiple aspects of novelty of the project are identified by the research and more specifically the realisation and testing of a proof of concept resistojet model. The specific novelties prompted by the research are summarised as follows:

1. The development of multiphysics simulations to design and optimise high-temperature resistojet design;

2. The use of SLM technology to build the complex recirculating-flow resistojet heat exchangers in a monolithic component;
3. Novel non-destructive testing as a means for geometric comparison as applied to SLM components;
4. Experimental characterisation of the first resistojet thruster manufactured with SLM.

5.2 Summary of the Thesis

The work carried out during the PhD and described in the thesis is the result of a multidisciplinary investigation on: multi-physics modelling applied to resistojet; metal additive manufacturing, in particular, Selective Laser Melting (SLM), to enable a novel heat exchanger concept; experimental characterisation of a proof of concept thruster, named STAR-0.

The current state-of-the-art xenon resistojet has shown a specific impulse (ISP) with xenon propellant up to 48 s utilised for small spacecraft below 500 kg. Such performance can result in either propellant mass saving or increased capability with respect to cold-gas thrusters. The primary application for a high-temperature resistojet is primary for propulsion on small satellite platforms with an emerging possibility of utilisation as a secondary propulsion system for all-electric telecommunication satellite platforms, where a complement of thrusters would form a reaction control system (RCS) using xenon as a common propellant in combination with an electric propulsion system. For both these applications, the implementations of a high-temperature Xe resistojet could generate either a propellant mass saving of approximately 40% or an increased delta-V manoeuvre capability of approximately 67%.

To achieve these requirements, high-temperature resistojets have been investigated in literature, concluding that the most successful design utilised in the past for high-temperature applications uses a multi-channel recirculating heat exchanger, which also acts as the electrical heater. This type of design has been called a low-thermal inertia tubular resistojet [116]. The Super-high Temperature Additive Resistojet (STAR) design concept is enabled by SLM, which permits the manufacturing of the novel monolithic HE that incorporates the function of a heater, of a regenerative recirculating heat exchanger, and also integrates the converging-diverging nozzle. SLM metal additive manufacturing is a topic with a relatively recent history of development and, for this reason, a detailed manufacturing verification process has been conducted and presented in Chapter 2, with the objective of enabling the manufacturing of the novel STAR heat exchanger design. A process of dimensional

accuracy and surface quality verification was conducted on more than 80 AM parts, replicating critical parts of the thruster, including the nozzle, thin concentric walls, and the elbows. An iterative design process was conducted on the novel heat exchanger, providing a functional design at the third iteration. This result was enabled by NDT through the use of radiographs or full CT volumetric scans and optical microscopy. The information gathered with these inspection tools allowed the refinement of the design in terms of wall thickness, separation distances between the concentric cylinders and the elaboration of the connecting method between the cylinders. The minimal wall thickness achieved is 0.15 mm, while the fluidic channels for flow recirculation are between 0.5 mm and 1 mm wide. The verification process highlighted that the printed nozzle throat has a lower area and presents an irregular geometry. Therefore, post-manufacturing drilling to the nominal size was set as a requirement.

Two proof of concept thrusters, STAR-0-A and STAR-0-B, have been tested with argon gas and characterised for a range of flow rates and discharge currents (Chapter 3). The preliminary tests on STAR-0-A highlighted two main issues, such as a propellant leak from the ceramic gasket and a drift in the measurement of the thrust due to the thermal expansion of the power harness. Both these issues were then solved and wet-firing tests were successfully performed on STAR-0-B, which produced a maximum thrust of 29.8 ± 0.03 mN and a maximum specific impulse of 80.11 ± 1.22 s. Multiphysics simulations have been validated against the experiments with a maximum error of the measured quantities < 20%.

In Chapter 4, a set of multiphysics studies have been performed to explore the STAR thruster capabilities in two selected missions: M1, where the resistojet would be used as primary propulsion system in small LEO platforms, and M2, where a number of thrusters would be used as RCS of all-electric GEO platforms. Three materials, Inconel 718, pure Ta and pure Re, have been investigated with specific assumptions implemented on the geometry and materials. A preliminary dimensioning of the nozzle at the requirements of the M1 mission immediately highlighted that, at extreme temperatures and low thrust levels, the nozzle would have a low nozzle efficiency. For this reason, STAR-Inc is selected for M1 while the extreme-temperature thrusters, STAR-Ta and STAR-Re, are selected for M2. The multiphysics numerical studies showed that the STAR design can achieve the objective specific impulse of > 80 s with Xe propellant and using Ta or Re for the HE. These two cases implement a W radiation shielding with a number of foils as well as microporous fibrous

ceramics for thermal insulation. A time-dependent study was conducted to evaluate the start-up time necessary to enhance the specific impulse from cold gas to the MOT of the thruster.

5.3 Highlights of the Thesis

The following list summarises the main highlights of the work:

- The high-temperature resistojet is defined such that it provides > 80 s in specific impulse with Xe propellant, with a nozzle efficiency > 90%;
- Low Reynolds number nozzles suffer from high viscous effect, which determines a significant nozzle efficiency loss;
- A high-temperature resistojet with Xe propellant operates at low-Reynolds numbers when the mass flow rate is particularly low and the stagnation temperature particularly high. Therefore, the objective nozzle efficiency of > 90% can be achieved by maximising the stagnation pressure of the thruster and minimising the nozzle throat radius;
- The STAR novel resistojet design is based on the high-temperature resistojet research work conducted between 1966 and 1978 [18,31,34,63,67,116] and introduces SLM to produce a next-generation novel monolithic concept of a multifunctional heater and heat exchanger with integrated nozzle (HE);
- A dedicated SLM manufacturing verification process with stainless steel 316L in combination with non-destructive inspection tools enabled the successful production of the HE component used in the two proof of concept thrusters produced;
- Regarding the novel heat exchanger, one of the finest geometries to date has been produced and applied to space propulsion;
- The detailed design of STAR is composed of only four main components, two of which are produced via SLM. The second SLM component, in addition to the HE, is the inflow component, which distributes the flow from the inlet pipe to the outer annular flow section enveloping the HE;
- Multiphysics studies have been applied to high-temperature versions of the STAR resistojet with Xe propellant to demonstrate that the objective specific impulse of > 80 s is achievable with the HE manufactured in Ta or Re;

- The multiphysics studies with Inconel 718 show that the thruster can produce a specific impulse of 60 s, which represents a substantial improvement with respect to the current resistojet technology;
- The prototypal stainless steel thruster, STAR-0-A, has been fired in dry mode to investigate on the electrothermal equilibrium of the assembly. In this case, the maximum structural temperature foreseen by a 3D sector-symmetric multiphysics model is 1,093°C;
- The wet-firing test campaign with Ar propellant on the prototype stainless steel STAR-0-B shows that the thruster behaved as expected and produces an equivalent performance to the current Xe resistojet technology. According to the simulations, STAR-0-B achieved a stagnation gas temperature of 649°C and a maximum structural temperature of 854°C;
- The test campaign also confirmed that the proof of concept thruster operated, at the test flow rates, at low-Reynolds numbers, determining a nozzle efficiency of only 70%.
- The multiphysics numerical studies have been validated against the experimental results of the prototype test campaign, providing errors on the order of 10% in the time-dependent case and providing useful insight in the electrothermal characteristics of the thruster.

The limitations of the current work are:

- The nozzle dimensioning discussed in section 1.5.2.3 is based on the relation between the throat Reynolds number and the nozzle efficiency obtained by interpolating the experimental data produced by Whalen (1987) [68]. These tests were conducted with unheated N_2 and H_2 propellant. The temperature distribution at the nozzle diverging section is dependant on the stagnation temperature and viscosity of the propellant, thus hot Xe or Ar propellant could produce significantly different results;
- The commercial weight scale used for the thruster vertical thrust measurement is not rated for vacuum and for cryogenic temperatures. Therefore, an in-situ calibration should be performed to validate the linearity of the measurement range and establish the measurement accuracy;
- The current STAR-0 thruster has a design flaw in the ceramic gasket, which was not able to demonstrate leak tightness. The causes could be the flatness of the flanges, the deformation of the flanges under the M3 bolts load or the finishing of the mating surfaces.

5.4 Impact of the Work

Part of the work was published in three peer-reviewed articles, it contributed to an additional article where I am co-author and has been presented at a number of international conferences.

Journal papers:

- Romei, F. and Grubišić, A.N. Validation of an additively manufactured resistojet through experimental and computational analysis. *Acta Astronautica*, Volume 167, February 2020, Pages 14-22. DOI 10.1016/j.actaastro.2019.10.046.
- Robinson, M., Grubišić, A.N., Rempelos, G., Romei, F., Ogunlesi, C., Ahmed, S. Endurance testing of the additively manufactured STAR resistojet. *Materials & Design*, Volume 180, October 2019, 107907. DOI 10.1016/j.matdes.2019.107907.
- Romei, F. and Grubišić, A.N. Numerical Study of a Novel Monolithic Heat Exchanger for Electrothermal Space Propulsion. *Acta Astronautica*, Volume 159, June 2019, Pages 8 – 16. DOI 10.1016/j.actaastro.2019.03.025.
- Romei, F., Grubišić, A. and Gibbon, D. Manufacturing of a High-Temperature Resistojet Heat Exchanger by Selective Laser Melting. *Acta Astronautica*, Volume 138, September 2017, Pages 356 – 368. DOI 10.1016/j.actaastro.2017.05.020.

Conference proceedings:

- Romei, F., Grubišić, A., Gibbon, D., Aimone, P., Dary, F., High Performance Resistojet Thruster: STAR Status Update. *Space Propulsion Conference*, Seville, Spain, 14 - 18 May 2018;
- Robinson, M., Grubišić, A., Romei, F., Ogunlesi, C., Ahmed, S., Aimone, P., Dary, F., Gibbon, D. Environmental Testing and Non-Destructive Inspection of the STAR Additively Manufactured Resistojet. *Space Propulsion Conference*, Seville, Spain, 14 - 18 May 2018;
- Ogunlesi, C., Grubisic, A., Romei, F., Robinson, M., Ahmed, S., Aimone, P., Dary, F., Gibbon, D. Novel Non-Destructive Inspection of the STAR Additively Manufactured Resistojet. *Space Propulsion Conference*, Seville, Spain, 14 - 18 May 2018;
- Romei, F., Grubišić, A. and Gibbon, D. Performance Testing and Evaluation of a High Temperature Xenon Resistojet Prototype Manufactured by Selective Laser Melting, *35th International Electric Propulsion Conference*, Atlanta, Georgia, 8 – 12 October 2017;

- Romei, F., Grubišić, A., Lasagna, D., and Gibbon, D. Multiphysics Model Validation of Resistojets with Concentric Tubular Heat Exchanger. *7th European Conference for Astronautics and Space Science*, Milan, Italy, 3-6 July 2017, DOI:10.13009/EUCASS2017-378;
- Romei, F., Grubišić, A., Gibbon, D. and Lane, O. Selective Laser Melting for Production of a Novel High Temperature Electrothermal Propulsion System. *67th International Astronautical Congress*, Guadalajara, Mexico, 26 - 30 Sep 2016;
- Romei, F., Grubišić, A., Gibbon, D., Lane, O., Hertford, R. and Roberts, G. A Thermo-Fluidic Model for a Low Power Xenon Resistojet. *Joint Conference of 30th ISTS, 34th IEPC and 6th NSAT*, Hyogo, Kobe, Japan, 4 - 10 July 2015.

The work contributed towards three projects funded by the UK government:

- NSTP-4 – National Space Technology Programme – UK Space Agency funding bid – Title: **STAR: Super High Temperature Xenon Resistojet Development of Telecommunication Applications,** total value: £1,044,983, November 2018;
- NSTP-3 – Title: **Refractory Additive Layer Manufacturing for Commercial Space Applications (RADICAL)**, total value: £94,097, December 2016;
- NSTP-2 – Innovate UK funding bid – Title: **High Performance Xenon Resistojet**, total value: £110,311, January 2015.

In addition:

- I am co-inventor with Dr Angelo Grubisic of the patent currently protected by a Provisional Patent Application in respect of a "**High-Temperature Electrothermal Propulsion System**," submitted by HC Starck (HCS) and received by the US Patent Office on 12 May 2017, being allocated EFS ID 29189858 and Application Number 62505169.
- I have been awarded the **Aerospace Speakers' Travel Grant 2017 (Round 2)** from the Royal Aeronautical Society to present a paper at the 7th European Conference for Astronautics and Space Sciences (EUCASS);
- The research initiated with the presented work is currently continuing development by two PhD students who started their activity in 2017.

5.5 Future Work and Outlook

The parametrised multiphysics models developed to investigate the high-temperature version of STAR thruster can be used to further examine additional combinations of materials and geometry. In particular, there are a few modifications and additions that, if introduced, would provide results of interest for the STAR development:

- The possibility of introducing variable thickness of the cylinders, which is within the SLM capabilities, to distribute dissipation more effectively;
- The introduction of the number of recirculation channels as a parameter of investigation;
- The use of reverse engineering by simulating the actual geometry obtained from the CT volumetric scans. This could reduce the geometric uncertainty in the model in the experimental validation;
- An increase in model accuracy through introducing suitable thermal contact modelling and conducting specific tests to obtain a more accurate modelling of parameters to which the model is more sensitive, that are, surface emissivity and electrical resistivity of the SLM material;
- Quantification of the effect of surface roughness in terms of heat transfer and pressure drop, and determine whether it is desirable to reduce it or not;
- Perform a numerical analysis to validate the nozzle efficiency versus throat Reynolds number relation found in literature and extend the study to hot Xe and Ar. If necessary, design a test campaign to evaluate this correlation, specifically for Xe.

The SLM manufacturing investigation conducted in this thesis restricted the sole use of 316L stainless steel as a prototypal material. The development of an engineering model of the thruster requires the use of the either Ta, Re, W or their alloys and, possibly, of a nickel alloy for an intermediate performance application. Besides the presented methodology, the new investigations on those materials can include some additional tasks:

- Investigate thin cylindrical walls in the range of 50–100 μm with controlled porosity, as described in [78], with the aim of maximising the electrical resistance. These walls could be implemented where leak tightness is not essential, that is, cylinders 2 and 3 in the current STAR-0 design. This study requires control of the SLM process parameters, particularly of the scan strategy;

- Investigate a scan strategy that optimises the heat exchanger needs, in particular, which avoids the formation of pores in sensitive regions, such as the connectors, which could reduce the lifetime of the heater;
- Investigate reducing the surface roughness of the internal walls of the heat exchanger using chemical etching.

A prototypal model of the STAR thruster has been tested successfully with the Ar propellant and in dry mode. The STAR-0 prototype produced the expected performance within the limitations of the materials used. However, there is a major design flaw to solve for the future development of the thruster that is the ceramic gasket, which currently leaks propellant. This issue could be addressed in the following ways:

- Increase the metallic flange thickness to avoid their deformation under the M3 fasteners load;
- Alumina could be used for the gasket instead of Macor for its superior compression strength;
- Polish the flanges surfaces to the highest grade possible and design an assembly procedure that preserves their finish;
- The engineering model may not use a gasket with fasteners but rather rely on a weld to ensure the leak tightness. However, this cannot be achieved with the current design because the two flanges are at different potentials. A different approach to the design is therefore necessary.

The most critical component, the monolithic heat exchanger, has already been printed successfully in Ta replicating the HE_v3.1 design [117]. This success and the ongoing development of the STAR project is leading towards the realisation of an engineering model in refractory metal that aims to produce a specific impulse > 80 s with Xe and enable the fully all-electric spacecraft concept.

Appendix A Electric Propulsion Overview

A.1 Electric Propulsion Overview

The primary attraction of electric thrusters with respect to chemical rockets lies in their highly efficient use of propellant. The decrease in propellant mass required for a given spacecraft (SC) mission reflects a gain in useful payload-mass-enabling missions that may otherwise be inaccessible through conventional chemical propulsion systems. The advantage of Electric Propulsion (EP) is offset by low thrust and power limitations. Electric propulsion was first considered for SC applications in the 1950s, but it only started to have a high impact from the 1990s because of the increased availability of electrical power on board.

Before describing the variety of EP technologies available, it is necessary to introduce the equations to describe a fundamental mission requirement, the delta-velocity. This figure corresponds to the increment of velocity that the EP system is required to perform. The flight of a simple rocket, having a simplified centre of gravity and neglecting aerodynamic forces, is described by the vector differential equation of motion [8].

$$m\dot{\mathbf{v}} = \dot{m}\mathbf{c} + \mathbf{F}_g \tag{A.1}$$

$$\mathbf{F} = \dot{m}\mathbf{c} \tag{A.2}$$

$$I = \int_{t_0}^{t_f} F dt \tag{A.3}$$

where the dotted **v** is the acceleration vector of the rocket, $\dot{m}$ is the rate of change of the rocket mass by exhaust of propellant (a negative quantity), **c** is the equivalent exhaust velocity relative to the rocket and F_g is the local gravitational force (null for in-orbit propulsion). The first term at the right-hand side of Eq.(A.1) is identified as the thrust of the rocket, shown in Eq.(A.2), and its integral over the firing time is called the total impulse, shown in Eq.(A.3), where t_0 and t_f are the initial and final firing time of the rocket. For a large total impulse requirement, it is evident that the desired thrust should be achieved by a high exhaust velocity rather than a high ejection rate of propellant mass since

the initial rocket mass would be too large to be practical. Neglecting the gravitational term and assuming a constant equivalent velocity, Eq.(A.1) integrates to the scalar form of Eq.(A.4).

$$\Delta v = c \ln\left(\frac{m_0}{m_0 - \Delta m}\right) = c \ln\left(\frac{m_0}{m_f}\right) \tag{A.4}$$

where m_0 is the initial mass of the rocket, Δm is the mass of propellant used and $m_f = m_0 - \Delta m$ is the final mass of the rocket. Δv represents the magnitude of velocity increment achieved by the ejection of the propellant mass Δm. As a consequence, a particular propulsion system develops a certain increment of velocity depending on its ability to accelerate the exhaust, c, and on the mass ratio of the rocket m_0/m_f. The propellant exhaust velocity, which should be ideally comparable to the mission Δv, is related to the nature of the acceleration of the propellant gas within the rocket. It is directly related to another characteristic performance parameter of a propulsion system, the specific impulse I_{sp}. The latter, is defined as the ratio between the total impulse, Eq.(A.3), and the weight of propellant by sea level.

$$I_{sp} = \frac{\text{total impulse}}{\text{propellant weight}} = \frac{\int_{t_0}^{t_f} F dt}{g_0 \int_{t_0}^{t_f} \dot{m} dt} \overset{\begin{pmatrix} F=const. \\ \dot{m}=const. \end{pmatrix}}{=} \frac{F}{\dot{m} g_0} = \frac{c}{g_0} \tag{A.5}$$

where g_0 is the sea-level gravitational acceleration. On the right-hand side, the thrust and mass flow rate are intended as average values during the considered manoeuvre. In conventional chemical rockets, the thrust is generated by expansion of exhaust products, derived by a combustion process, through a supersonic nozzle (Section 1.4.1.1). Consequently, the attainable exhaust velocity is limited by three main factors:

a) The intrinsic energy available in the chemical reaction to be converted in gas enthalpy;
b) The tolerable heat transfer to the combustion chamber and the nozzle throat;
c) Unrecovered energy deposition into the internal modes of the gas (frozen flow losses) and radiation losses from the exhaust jet.

As opposed to chemical rockets, electric propulsion (EP) relies on electrical power to increase the energy of a gas or plasma, eliminating the limit of input energy into the exhaust or plume. A rigorous definition of EP is given by R. Jahn [8]:

The acceleration of gases for propulsion by electrical heating and/or by electric and magnetic body forces.

Electric propulsion systems are commonly categorised as follows:

Electrothermal propulsion: the propellant gas is heated electrically and then expanded thermodynamically, using a supersonic nozzle as in chemical rockets.

Electrostatic propulsion: the propellant is accelerated by direct application of electric body forces to ionised particles.

Electromagnetic propulsion: an ionised propellant stream is accelerated by interactions of external current driven through the stream. Moderately dense plasmas are high-temperature or non-equilibrium gases, electrically neutral and reasonably good conductors of electricity.

Plasma is the fourth state of matter and consists of heavily ionized matter, usually gaseous, composed of ions, electrons, and neutral atoms or molecules, that has sufficient electrical conductivity to carry substantial current and to react to electric and magnetic body forces [118]. For a mission requiring a specific Δv, the propulsion system must provide an exhaust velocity c of similar order of magnitude. For instance, when $m_0/m_f < e$ (where the constant $e \approx 2.71$), it must be $c > \Delta v$ for the reason of Eq.(A.4). For this reason, for interplanetary missions and high-Δv missions, propulsion systems must provide extremely high exhaust velocities. Specific impulse and exhaust velocity are directly proportional from Eq.(A.5); in particular, it is useful to consider that $10 I_{sp} \approx c$. For the nature of the acceleration principle described above in the list of EP categories, the highest specific impulse is achievable with electrostatic, then electromagnetic, followed by electrothermal propulsions. The principal technologies for each one of these categories is illustrated in Table A.1. A brief description of their functioning principles is explained in the section A.2, while a general overview of the EP technologies is illustrated in the next section.

Table A.1. General classification of electric propulsion technologies.

Electrothermal	Electrostatic	Electromagnetic
Resistojet (including EHT)	Ion Engine (Kaufmann, RF, ECR)	Hall Effect Thruster (HET)
Arcjet	Field-effect Electrostatic (FEEP)	Magnetoplasmadynamic (MPD)
Microwave ECR	Colloidal Ion	Pulsed Plasma Thruster (PPT)
		Inductive Thrusters

A.1.1 General Applications for Electric Propulsion

Before identifying the three general applications where the EP is used, it is necessary to introduce a further equation describing the thrusting time Δt [20]. For a given mission requiring a certain Δv, the mean acceleration is given by $\Delta v/\Delta t = F/m$, where m is the total SC mass and F/m is a mission average value. The total power into the thruster is described as $P_{ts} = Fc/(2\eta_{ts})$, where η_{ts} is the thruster overall efficiency. Recalling the relation between the effective jet velocity and the specific impulse given by Eq.(A.5), the required thrusting time is expressed by Eq.(A.6). This relationship shows two fundamental facts necessary to reduce mission time if required: (1) the importance of a high specific power (P_t/m); (2) the need for a lower specific impulse but using more propellant to keep the Δv constant.

$$\Delta t = \frac{g_0 I_{sp} \Delta v}{2\eta_{ts}(P_{ts} / m)} \tag{A.6}$$

Electric propulsion falls into three main mission categories as illustrated in the following paragraphs.

1. **Station-keeping**

For Geosynchronous Earth Orbits (GEO), the main maintenance manoeuvre is North-South Station Keeping (NSSK). Other manoeuvres can be the alignment of telescopes/antennas or the drag compensation of satellites in Low Earth Orbit (LEO) and medium orbit (MEO). For a typical 350 km LEO orbit, a velocity increment of about 50 m/s per year is required. Several EP systems have accomplished this particular mission, such as resistojets, arcjets, Hall thrusters and ion thrusters.

2. Orbit Raising

This is often performed while overcoming a weak gravitational field, such as orbit rising from a LEO to a higher orbit, even a GEO. Circularising an elliptic orbit may require an increment of 2 km/s. Going from LEO to GEO typically requires a higher increment of 6 km/s. Depending on the manoeuvre time budget described by Eq. (A.6), either a high thrust (chemical or electrothermal hydrazine thrusters) or lower thrust EP system (ion thruster or HET) has been selected.

3. Interplanetary Transfers

Table A.2 shows the Δv needed for some planetary transfer missions with the assumption of an impulsive manoeuvre over minimum propellant semi-ellipse trajectories [8]. The interplanetary mission category requires the highest Δv, in the 10–100 km/s range. The return missions to the Moon, Mars and other planets, comets and asteroids also require a relatively high thrust level and power. A high thrust level is required to mitigate the mission time, Eq.(A.6). As a consequence, the required power increases on the order of 100 kW to accelerate the relatively high propellant flow rates.

Table A.2. Characteristic velocity increments for planetary transfer mission [8].

Mission	Δv [km/s]
Escape from Earth surface (impulsive)	11.2
Escape from 480 km Earth orbit (impulsive)	31.5
Escape from 480 km Earth orbit (gentle spiral)	75.9
Earth surface to Mars surface and return	34
Earth orbit to Mars orbit and return	14
Earth orbit to Venus orbit and return	16
Earth orbit to Mercury orbit and return	31
Earth orbit to Jupiter orbit and return	64
Earth orbit to Saturn orbit and return	110

A.2 Electric Propulsion Technologies

Table A.3 summarises a qualitative overview of the EP technologies not just in terms of performance parameters but also their main advantages and drawbacks. Table A.4 shows instead a quantitative comparison of the main performance parameters, the electrical power required and the typical specific

weight of the thruster and its typical Power Processing Unit (PPU). These tables are used as reference for the following general descriptions of the main EP technologies. In general, an EP subsystem is composed of the following parts:

1. Energy source: solar or nuclear energy;
2. Conversion devices: to transform this energy into electrical form with the proper desired characteristics, in particular AC/DC voltage, frequency, pulse rate and current suitable for the selected EP system;
3. Propellant system: to store, meter, control and deliver the propellant at desired temperature and pressure/flow rate;
4. Thruster: to convert the electric energy into useful kinetic energy of the exhaust. The number of thrusters varies depending on the mission category.

The losses of a global electric propulsion system are related to power conversion (for example, the solar energy is collected by solar arrays with typical efficiencies below 40%), conversion into electric energy suitable for the specific thruster technology and losses in converting the electric energy into propulsive jet energy (thruster efficiency). In electric propulsion, various thruster types have differing efficiencies in converting electrical power into kinetic power useful for thrust. The thruster efficiency η_{ts} is defined as the ratio of the axial component of the kinetic power of the jet P_k, divided by the total input power given by Eq.(A.7). The latter is the sum of the electrical power input P_e, expressed as the sum of all voltage-current products involved into the EP system, and the gas inflow stagnation power, $P_{0,in}$, where for an ideal gas $h = c_p T$.

$$\eta_{ts} = \frac{\text{axial kinetic power of the jet}}{\text{total power input}} = \frac{P_k}{P_e + P_{0,in}} = \frac{g_0 F I_{sp}}{2[\Sigma(VI) + c_p T_{o,in}]} \tag{A.7}$$

The thruster efficiency accounts for all energy losses: unused propellant, divergence of the exhaust with respect to the axial component and heat loss. The specific losses that apply to the resistojet case are discussed further in Section 2.1.1.

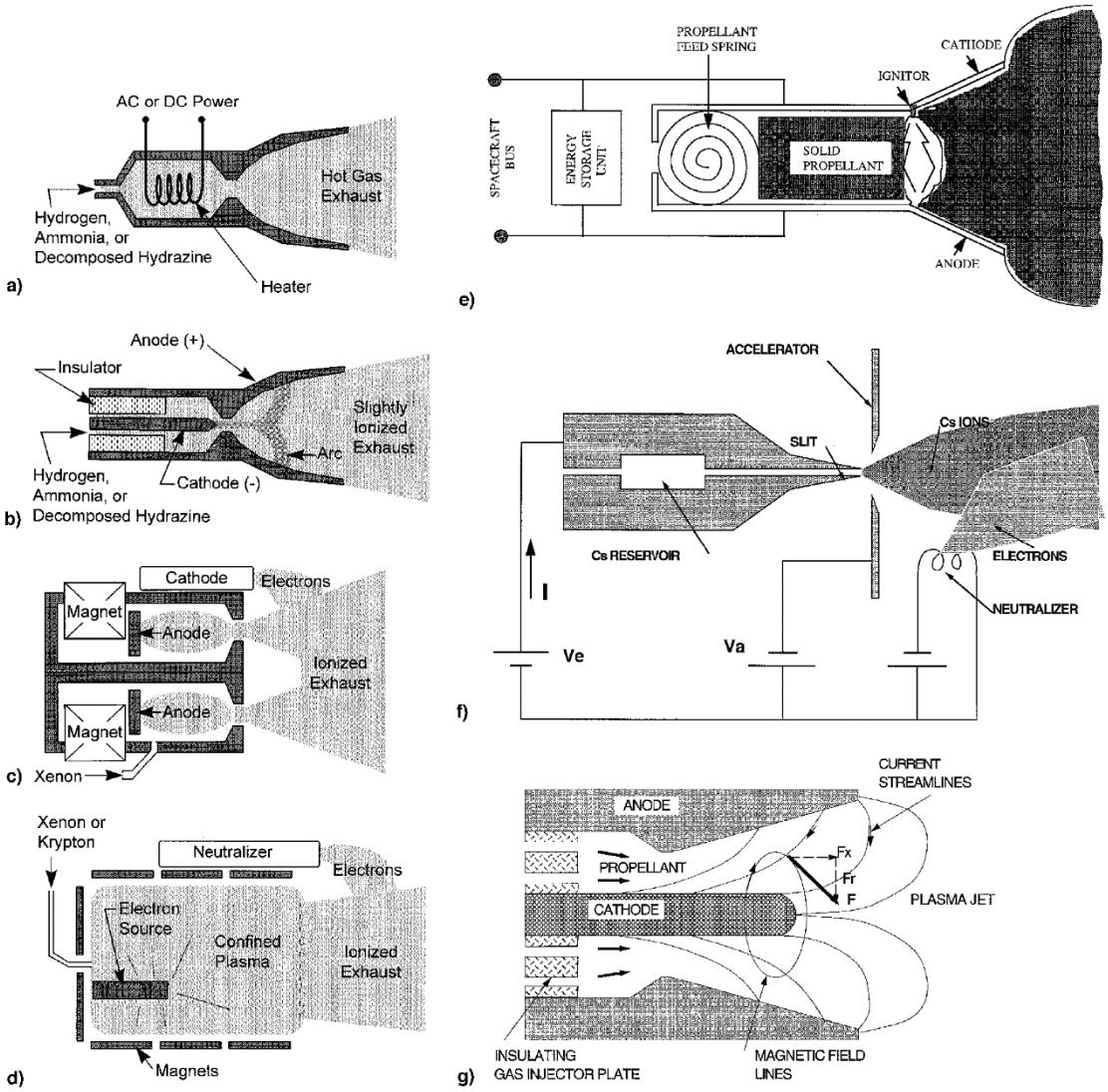

Fig. 5.1. Operating principles and schematics of (a) resistojets, (b) arcjets, (c) Hall thrusters, (d) ion engines, (e) pulsed plasma thrusters, (f) field-effect electrostatic propulsion thrusters, and (g) self-field magneto-plasma-dynamic thrusters [20].

Table A.3. Summary for qualitative comparison of electrical propulsion systems [7].

	Advantages	Disadvantages
Resistojet – electrothermal	Simple device Many propellant (including hydrazine augmentation) Simple power conditioning Relatively high thrust and efficiency Low cost Not ionised plume	Lowest specific impulse Heat loss Gas dissociation Indirect heating of gas Erosion
Arcjet – electrothermal and electromagnetic	Direct heating of gas Low voltage Relatively simple device Relatively high thrust Can use catalytic hydrazine augmentation Inert propellant	Low efficiency Erosion at high power Low specific impulse High current Wiring Heat loss More complex power conditioning
Ion propulsion – electrostatic	High specific impulse High efficiency Inert propellant (Xe)	Complex power conditioning High voltage Single propellant only Low thrust per unit area Heavy power supply
Pulsed Plasma Thruster – electromagnetic	Simple device Low power Solid propellant No gas or liquid feed system No zero-g effects on propellant	Low thrust Teflon reaction products are toxic, may be corrosive or condensable Inefficient
MPD – steady state plasma	Can be relatively simple High specific impulse High thrust per unit area	Difficult to simulate analytically High specific power Heavy power supply
Hall thruster – electromagnetic	Desirable specific impulse range Compact, relatively simple power conditioning Inert propellant (Xe)	Single propellant High beam divergence Erosion

Table A.4. Typical performance, power requirements and specific weights of various types of operational electrical propulsion technologies (data gathered from [7,20] and from the literature review summarised in section 1.4).

Thruster	Prop.	F [mN]	I_{sp} [s]	η_{ts}* [%]	P_e [W]	m_{ts} [kg/kW]	m_{PPU} [kg/kW]
EHT	N_2H_4	200-800	280-310	65-90	350-1500	1-2	1
Arcjet	N_2H_4	200-250	450-600	33-35	300-2000	0.5-0.7	2-3
Resistojet	NH_3	20-200	250-296	80	80-600	-	-
Resistojet	Xe	<50	40-48	65-90	4 - 350	-	-
Hall thruster	Xe	40-200	950-1950	46-60	150-6000	2-3	6-10
Ion engine	Xe, Kr, Ar	10-93	2585-4000	38-75	200-4000	3-6	6-10
Solid PPT	Teflon	0.3	836-1000	0.68-7	1-200	120	110*
MPD - pulsed	Ar, Xe, H_2, Li	1.4-23	600-1150	9.8-16	<430	-	-

*Including capacitors

A.2.1 Electrothermal Thrusters

Resistojets

The resistojet thruster is reviewed and analysed in detail in section 1.4.1. In general, it operates by passing a gaseous propellant through an electrical Heat Exchanger (HE) that raises its stagnation temperature, then the hot gas is expanded and accelerated through a nozzle to generate thrust. The heat exchanger usually does not coincide with the heater element, which can be directly or indirectly in contact with the propellant. The increase in specific impulse is proportional to the square root of the heated gas temperature $T^{1/2}$.

One of the advantages of the resistojet is that it can use nearly any gaseous propellant. Resistojets have typically no special power conditioning except for current surge protection. In case of the heater element failure, operation can, in most cases, continue in cold-gas mode. Because of the relatively low pressure and temperature of the heated propellant, the plume is not ionised and therefore does not introduce SC interaction problems.

Electrothermal Hydrazine Thrusters (EHT)

The EHT is a two-stage device that firstly decomposes liquid hydrazine (N_2H_4) into standard exhaust products of ammonia (NH_3), nitrogen (N_2) and hydrogen (H_2). The second stage, which is essentially a resistojet, resistively heats these gases up to 2,200 K. The heating element is therefore used to increase the enthalpy of the hydrazine decomposition products from the upstream gas generator. Because of the relatively high molecular mass of the exhaust gases (NH_3, N_2 and H_2), and the maximum operating temperature being a limiting factor, EHTs have a specific impulse in the range of 200-300 s. With the aid of the second-stage resistojet, the specific impulse is improved by about 40% without additional heating. Thrust efficiency can easily reach 70%, and thrust levels up to 500 mN have been demonstrated.

These thrusters are in use on GEO communication satellites for station-keeping and orbital manoeuvring. The EHT has represented the most successful application of the resistojet thruster. Other applications are orbit insertion, control and de-orbit of LEO spacecraft.

Arcjets

A simple schematic of an arcjet thruster is shown in Fig. 5.1-b, where the rather simple design does not reflect the complex physical behaviour. An electrical arc is generated between the tip of the central electrode and the anode, which is also forming the thruster's nozzle. The heated gas is accelerated thermodynamically through the nozzle to reach specific impulse as high as 600 s using hydrazine propellant.

The arcjet overcomes the gas temperature limitation of the resistojet by using an electric arc for direct heating of the gas flow, reaching temperatures locally much higher that the surrounding walls. The electrodes must be electrically insulated from each other and have to withstand high temperature and erosion. Although it is ideal to generate a diffused annulus arc, in practice the arc is quite filamentary and tends to directly heat only a portion of the gas stream. A further inefficiency is given by the heating of the gas in the diverging section of the nozzle, where the arc gradually extinguishes, which decreases the gas expansion capability of the nozzle.

The PPU for arcjets is significantly more complex than for resistojets. The discharge voltage is higher than most bus voltages (e.g., 80-120 V), which requires at least a DC-DC conversion. In addition, arcjets have a negative-impedance characteristic, which requires special transient modes at the start-up. In fact, to initialise the breakdown of a vacuum gap, high voltage is initially required. As the

voltage increases, the increase in current becomes more significant, leading to a negative-impedance characteristic [20]. As a result, the PPU can be several times heavier than the thruster itself.

A.2.2 Electrostatic Thrusters

Electrostatic thrusters rely on Coulomb forces to accelerate a propellant composed by non-neutral charged particles [7]. The electric force depends almost exclusively on the positive ions.

Hall Effect Thrusters (HET)

A schematic of a Hall thruster is shown in Fig. 5.1-c. The propellant gas, usually xenon, is injected through the anode into an annular space where it is ionised by counter flowing electrons, which are part of the electrical current injected through an external hollow cathode. The ions are accelerated through the electrostatic field impressed by the negative cathode.

With ion engines, the HET belongs to the class of electrostatic ion accelerators; the main difference lies in the magnetic coils that collect the thrust through their interaction with the electron Hall current, justifying the name. The gas density is typically low enough to ensure near-collision-less ion flow. For this reason, the HET is many times wider than an arcjet of similar power, still being more compact than ion engines.

Their PPU is more complex and heavier than in arcjets (Table A.4), as particular conditioning is necessary to accommodate plasma fluctuations and because coordinated control of magnet current and propellant flow is necessary. Because of their relatively high efficiency at moderately high specific impulse, HETs are found to be optimal in many applications, including NSSK and deployment and orbit control for LEO missions (Martinez-Sanchez and Pollard, 1998).

Gridded Ion Engines

In gridded electrostatic ion accelerators, illustrated schematically in Fig. 5.1-d, ions are produced in a magnetically confined chamber, by either DC discharge or radio-frequency power (RIT), or alternatively by tuned electron cyclotron resonance (ECR ioniser). One side of the chamber is covered by a double grid structure across which the ions are accelerated by a high-voltage electrostatic field.

They typically have a complex set of power supplies and control with resulting high PPU masses (Table A.4). Ion engines are the choice for deep-space missions, requiring high increment of

velocities Δ They are particularly suitable because they can reliably and continuously operate for long periods as orbit transfers require.

A.2.3 Electromagnetic Thrusters

The principle for which thrust is produced in these devices relies on the fact that when a conductor carries a current perpendicular to a magnetic field, a body force is exerted on the conductor in a direction at right angles to both the current and the magnetic field [7]. The two main advantages with respect to the electrostatic propulsion are that (1) the acceleration process of plasma leads to a neutral exhaust beam, which limits the interaction with S/C, and (2) they have a relatively high thrust per unit area, normally between 10 and 100 times that of ion engines.

Appendix B Multiphysics Modelling with COMSOL

B.1 Overview

A resistojet is composed of a heat exchanger (HE) where the temperature of a flowing propellant gas is raised by an electric heater. The hot gas is then accelerated through a supersonic nozzle providing thrust. As in every SC subsystem, an EP thruster must survive the vibration imposed by the launch environment in blast-off phase. Finally, being a high-temperature device, the thermal stress of the thruster must be evaluated in the design phase. As a result, the physics involved are many and strongly coupled. In the following list, the main physics and the reason why they are important to simulate are summarised:

1. **Laminar or turbulent incompressible flow**: the propellant gas flows through the HE channels, where the pressure is almost constant up to the nozzle inlet; depending on the channels size and on the gas pressure and temperature, the regime can be either laminar or turbulent;
2. **Laminar or turbulent compressible flow**: the supersonic nozzle expands the propellant gas to relatively high Mach numbers. Depending on the throat size and on the gas pressure and temperature, the flow regime through the nozzle can be either laminar or turbulent;
3. **Heat transfer**: the propellant is heated while flowing in the HE channels by forced convection. HE walls exchange heat with each other either by surface-to-surface radiation or by conduction. The resistojet is attached to the SC and transfers heat to it by conduction. Finally, the outer surfaces of the resistojet radiate heat to space;
4. **Joule heating**: either DC or AC current is applied to the heater terminals to produce resistive heating and convert electrical to thermal energy.
5. **Solid mechanics:** during the launch phase of the SC, the EP system is subjected to heavy-duty low-frequency vibrations. This represents the higher mechanical stress environment that the EP system must survive. Furthermore, the resistojet is a high-temperature device, and because of the temperature gradient across the engine, thermal stresses must be considered in the design phase.

B.2 Modelling Equations

In COMSOL Multiphysics, there are three main steps to set up a simulation, which also help explain its structure and how it works. They are summarised below:

1. Firstly, the problem *space dimension* is selected: 3D, 2D axisymmetric, 2D, 1D axisymmetric, 1D and even 0D. The geometry can be either created within the software or imported.
2. A series of *interfaces* containing *physics modules* can be added to specific parts, or *domains*, of the geometry analysed.
3. Finally, a *study* type is selected. It can be either stationary, time-dependent or eignefrequency, and, depending on the interface selected, several other specific studies are also applicable.

Once the simulation "skeleton"' is created through these steps, the problem can be defined in detail by applying materials, Initial Conditions (IC) and Boundary Conditions (BC) on the geometry domains and boundaries. In addition, parameters and variables are defined. Therefore, the geometry is discretised in a computational grid using either automatic or custom mesh. Finally, the study is set up, the simulation run and the results post-processed. In the present work, both 2D axisymmetric (Chapter 3 and 4) and 3D sector-symmetric geometries (Chapter 3) have been analysed. The *physics* involved in the HTR studies are contained in the following *module interfaces*:

Single Phase Fluid (SPF) contains the Navier–Stokes and the heat transfer equations. In particular, it solves for conservation of energy, mass and momentum. This module can specialise to both laminar and turbulent flow regimes for subsonic flow.

High Mach Number Flow (HMNF) uses same equations of SPF but specialised for compressible supersonic flow.

Heat Transfer (HT) models the heat transfer in solids by conduction, convection and radiation. The temperature equation defined in the solid domain corresponds to the differential Fourier's law that may contain additional contributions like heat sources. In particular, to model the RJ heater, the additional heat source coincides with the total power dissipation density given by Joule effect, solved by the EC interface.

Electric Current (EC) is used to compute electric field, current and potential distribution in conducting media where inductive effects are negligible. The physics interface solves a current conservation equation based on Ohm's law using the scalar electric potential as the dependent variable.

Solid Mechanics (SM) is based on solving the equations of motion together with a constitutive model for a solid material. Results such as displacements, stresses and strains are computed. This interface has been used to evaluate the natural frequency of the STAR-0 assembly discussed in Section 3.2.3.

The equations contained in the above described interfaces are shown and discussed in the following sections.

B.2.1 Energy Balance

In a heat transfer problem, the total energy is a conserved quantity while the heat is not. Hence, there is both a heat flux and an energy flux that are similar but not identical. When the temperature T is solved in a multiphysics problem, including mass and momentum equations of fluid dynamics for $\mathbf{u}$ and p the total energy flux is conserved and the following equations hold [W] [119]:

$$\frac{d}{dt}\int_{\Omega}\rho E_0 d\omega + \int_{\partial\Omega_{ext}}(\rho\mathbf{u}H_0 - k\nabla T - \boldsymbol{\tau}\mathbf{u} + \mathbf{q}_r)\cdot\mathbf{n}d\sigma = Q_{Int} + W_{Int} \tag{B.1}$$

$$Q_{Int} = \int_{\Omega} Q d\omega + \int_{\Omega_{Int}} Q d\omega + \int_{\partial\Omega_{Int}} Q_r d\omega \tag{B.2}$$

$$W_{Int} = \int_{\Omega} W d\omega \tag{B.3}$$

where Ω is the 2D or 3D domain and $\partial\Omega$ is the edge or surface boundary. Here, Ω_{ext} and Ω_{int} denote the exterior and interior boundaries, respectively. For this equality to be true, the provided velocity field $\mathbf{u}$ and pressure field p must satisfy a mass and a momentum conservation equation such as the Navier-Stokes equations or governing equations of continuum mechanics. The variables and operators used in the above equations are as follows:

- ρ is the fluid density [kg/m^3]
- $E_0 = E + (\mathbf{u}\cdot\mathbf{u})/2$ [J] is the total internal energy, where E is the internal energy
- $\mathbf{u}$ is the velocity vector [m/s]
- $H_0 = H + (\mathbf{u}\cdot\mathbf{u})/2$ [J/kg] is the total enthalpy of the fluid, where H is the enthalpy
- k [W/(mK)] is the thermal conductivity
- $\nabla T = \left(\frac{\partial T}{\partial x}, \frac{\partial T}{\partial y}, \frac{\partial T}{\partial z}\right)$ [K/m] is the temperature (T) gradient

- $\boldsymbol{\tau}$ is the viscous stress tensor [Pa]
- $\mathbf{q}_r$ [Wm^(-2)] is the radiative heat flux
- $\mathbf{n}$ is the unit vector normal to $\partial\Omega_{ext}$
- Q is the heat sources [W/m^{-3}]
- W is the work source [W/m^{-3}]

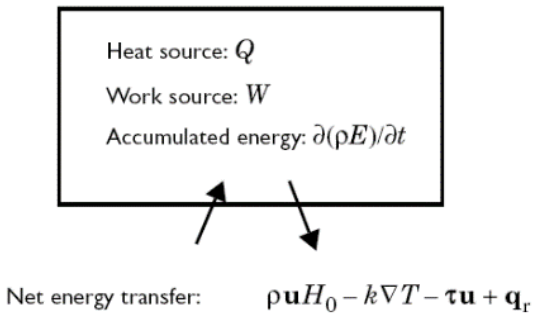

Fig. 5.2. Energy balance diagram (COMSOL, 2015b).

The first term on the left-hand side of Eq.(B.1) is the total accumulated energy rate, which is expressed as the integral of the accumulated energy $\partial(\rho E)/\partial t$ over the domain Ω (see Fig. 5.2). On the right-hand side, Q_{Int} is the total heat source, where in Eq.(B.2) it includes domain sources, interior boundary, edge and point sources, and radiative source at interior boundaries. W_{Int} is the total work source. In COMSOL Multiphysics, Eq.(B.1) corresponds to the following computational equation:

$$\mathrm{dEi0Int} + \mathrm{ntefluxInt} = \mathrm{QInt} + \mathrm{WInt} \tag{B.4}$$

However, in the present work, the models are all studied in the stationary case; therefore, the first term is zero and the energy balance simplifies to:

$$\mathrm{ntefluxInt} = \mathrm{QInt} + \mathrm{WInt} \tag{B.5}$$

B.2.2 Fluid Flow and Heat Transfer

The most general form of the Navier-Stokes equations, including heat transfer, Eq.(B.8), for a single-phase fluid flow, is:

$$\frac{\partial \rho}{\partial t} + \nabla \cdot (\rho \mathbf{u}) = 0 \tag{B.6}$$

$$\rho \frac{\partial \mathbf{u}}{\partial t} + \rho(\mathbf{u} \cdot \nabla)\mathbf{u} = \nabla \cdot [-p\mathbf{I} + \boldsymbol{\tau}] + \mathbf{F} \tag{B.7}$$

$$\rho C_p \left(\frac{\partial T}{\partial t} + (\mathbf{u} \cdot \nabla T) \right) = -(\nabla \cdot \mathbf{q}) + \boldsymbol{\tau} : \mathbf{S} - \frac{T}{\rho} \frac{\partial \rho}{\partial T}\bigg|_p \left(\frac{\partial p}{\partial t} + (\mathbf{u} \cdot \nabla) p \right) + Q \tag{B.8}$$

where $\boldsymbol{S}$ is the strain-rate tensor [s^{-1}] defined as

$$\mathbf{S} = \frac{1}{2}\left[(\nabla \mathbf{u}) + (\nabla \mathbf{u})^T \right] \tag{B.9}$$

The operator ":" represents the product between tensors as:

$$\boldsymbol{\tau} : \mathbf{S} = \sum_n \sum_m \tau_{nm} S_{nm} \tag{B.10}$$

where

- $\mathbf{I}$ is the identity vector
- C_p is the specific heat capacity at constant pressure [J/(kgK)]
- p is pressure [Pa]
- $\mathbf{F}$ is the volume force vector [N/m^3]
- $\mathbf{q}$ is the heat flux vector [W/m^2]

The scalar Eq.(B.6) is the continuity equation or the mass conservation, the vectorial Eq.(B.7) represents conservation of momentum and Eq.(B.8) models the conservation of energy in terms of temperature. The latter is the fundamental law governing the heat transfer for a fluid, known as first law of thermodynamics, referred to the principle of conservation of energy $\Delta E = Q - W$, such that

the change in internal energy is equal to the difference between heat added to the system and the work done by the system. The internal energy is an inconvenient quantity both to measure and to use in simulations. Therefore, the equations are rewritten in terms of temperature T as shown above.

To close the equation system, Eq.(B.6) through Eq.(B.8), constitutive relations are needed. In the present work, the design work fluid of the resistojet is Xe, while in the test phase is Ar. Both these gases are Newtonian fluids, described by Eq.(B.11), where the dynamic viscosity μ depends on the thermodynamic state but not on the velocity field. Other constitutive relations are Fourier's law of heat conduction, Eq.(B.12), and the ideal gas law.

$$\boldsymbol{\tau} = 2\mu\mathbf{S} - \frac{2}{3}\mu(\nabla \cdot \mathbf{u})\mathbf{I} \tag{B.11}$$

$$\mathbf{q} = -k\nabla T \tag{B.12}$$

A material can be generally anisotropic such that its thermodynamic or mechanical properties depend on the direction. In this case, this material's property, for example, thermal conductivity, is represented by a tensor rather than a scalar. In the present work, the materials used are assumed to be isotropic both for mechanical and thermal properties. In microscopic terms, heat conduction takes place through different mechanisms in different media. In a gas, it takes place through collisions of molecules, in liquids through oscillations of each molecule, in metals the heat is carried by electrons, in other solids by molecular motion. Typically, the heat flux is proportional to the temperature gradient as described by the Fourier's law. The second term on the left-hand side of the momentum Eq. (B.8) is the convection term. Convection is the heat dissipation of a solid surface to a fluid, where the flux is described by the heat transfer coefficient and the temperature difference across a fictitious film. Inserting the Fourier's law into this equation and ignoring the viscous dissipation and pressure work, the heat equation simplifies to the computed Eq.(B.13).

$$\rho C_p \frac{\partial T}{\partial t} + \rho C_p \mathbf{u} \cdot \nabla T + \nabla \cdot (-k\nabla T) = Q \tag{B.13}$$

B.2.2.1 High Mach Number Flow (HMNF) Interface

To model the acceleration of the hot gas through the converging-diverging nozzle of the RJ, the high Mach Number Flow (HMNF) interface is used. The HMNF equations in the general time-dependent case are obtained by combining the Navier-Stokes Eq.(B.6) through Eq.(B.8) with the constitutive Eq.(B.11) of Newtonian fluid, the Fourier's law of heat conduction Eq.(B.12) and the ideal gas law. Therefore,

$$\frac{\partial \rho}{\partial t} + \nabla \cdot (\rho \mathbf{u}) = 0 \tag{B.14}$$

$$\rho \frac{\partial \mathbf{u}}{\partial t} + \rho(\mathbf{u} \cdot \nabla)\mathbf{u} = \nabla \cdot \left[-p\mathbf{I} + \mu\left[(\nabla \mathbf{u}) + (\nabla \mathbf{u})^T \right] - \frac{2}{3}\mu(\nabla \cdot \mathbf{u})\mathbf{I} \right] + \mathbf{F} \tag{B.15}$$

where the heat transfer is coupled using Eq.(B.13). The HMNF interface can be used both for laminar and turbulent flow regimes. For the latter case, the Reynolds-averaged Navier-Stokes (RANS) equations, with the standard k - ϵ turbulence model and the Kays-Crawford heat transport turbulence model are used in this work. The heat transport model calculates the Pr_T, and it is considered to be a good approximation for most kinds of turbulent wall-bounded flows, with the exception of the turbulent flow of liquid metals [113]. In general, the Prandtl number is defined as the ratio between the viscous diffusion rate and the thermal diffusion rate. In particular, in the RANS model, the conductive heat flux is defined as:

$$q = -\left(k + k_T\right)\nabla T \tag{B.16}$$

$$k_T = \frac{\mu_T C_p}{\mathrm{Pr}_T} \tag{B.17}$$

where the turbulent dynamic viscosity μ_T is defined by the flow interface, and Pr_T is defined by the heat transport turbulence model (Kays-Crawford).

B.2.2.2 Radiation

Radiation is the third mechanism of heat transfer with conduction and convection. In physics, radiation is described as the transport of heat by photons, which can either be absorbed or reflected by the involved surface. When two surfaces radiate to each other, there is an effect of shading and

reflections between them. This is taken into account into the surface-to-surface radiation node of the COMSOL's heat transfer module.

In general, when incident energy impinges on a surface, it is absorbed, transmitted and reflected following the relation [64]:

$$\alpha + \tau + \rho = 1 \tag{B.18}$$

where τ is the transmissivity, ρ is the reflectivity and α is the absorptivity. For an opaque surface, $\tau = 0$, thererfore $\alpha + \rho = 1$. For a perfect reflector instead, $\rho = 1$. Finally, a black body absorbes all incident energy, resulting $\alpha = 1$. In Fig. 5.3, a point x is located on a surface with temperature T. If the surface is opaque, no radiation is transmitted through the body, which is the case for metals or most solid materials. The incoming radiative flux, called irradiation G, is reflected back depending on the property ρ of the surface. In addition, the surface can emit radiation, and the total outgoing radiation is called radiosity J:

$$J = \rho G + \varepsilon \sigma T^4 \tag{B.19}$$

where the emissivity ε is a dimensionless factor that describes the ability of a surface to radiate energy. Its value lies between 0 and 1, where 1 corresponds to an ideal surface emitting the maximum possible radiative energy. Most opaque bodies also behave as grey bodies, which means emissivity and absorptivity are equal; therefore, in this case,

$$\alpha = \varepsilon = 1 - \rho \tag{B.20}$$

The Surface-to-Ambient Radiation BC is applied on the thruster's case boundaries to account for the radiation loss of the hot surfaces. In the assumption of constant ambient temperature T_{amb}, black body ambient, the irradiation simply becomes $G = \sigma T_{amb}^4$. Therefore, Eq.(B.19) Becomes:

$$q = \varepsilon\sigma(T_{amb}^4 - T^4) \tag{B.21}$$

where σ = 5.670373(21)×10^{-8} [W/(m^{2}K^4)] is the Stefan-Boltzmann constant. In addition, the surface-to-surface radiation BC is used to model the radiation heat exchange between the internal thruster walls. This BC takes into account the mutual irradiation of surfaces, the incoming external sources and the ambient irradiation. The built-in hemicube method is used to evaluate the view factor functions.

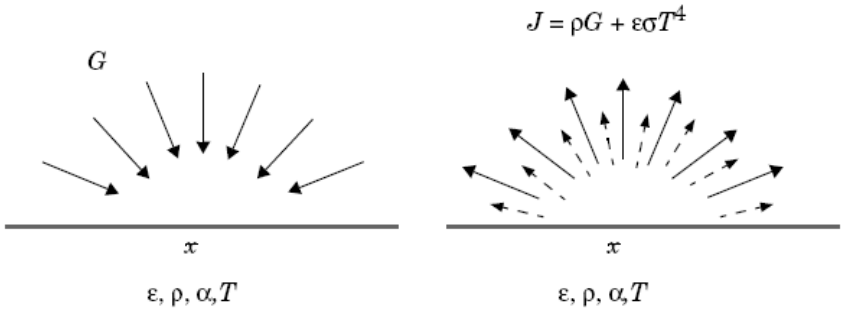

Fig. 5.3. Arriving irradiation (left) and leaving radiosity (right) [119].

B.2.3 Electric Current (EC) Interface

The Electric Current interface (EC) is used to compute Joule heating through the electrostatic equations:

$$\nabla \cdot J = Q_j \tag{B.22}$$

$$J = \sigma E + J_e \tag{B.23}$$

$$E = -\nabla V \tag{B.24}$$

where Eq.(B.22) is the equation of continuity, Eq.(B.23) is the Ohm's law and Eq.(B.24) is the expression of the potential in electrostatics. J_e [Am^{-2}] is the externally generated current density while Q_j [Am^{-3}] is the distributed current source.

Assuming a single resistive element, two boundary conditions are applied on its extremity. They are simply the ground, V= 0 V, and a current or voltage boundary condition on the other terminal. On the remaining part of the domain, the electric insulation equation is applied, $\mathbf{n}\cdot J = 0$, where n is the unit vector normal to the boundaries. The heat source solution Q_0 [Wm^{-3}] of the electrostatic problem is taken as the input to the heat transfer model for the solid domains. Moreover, the EC interface needs to couple the temperature with the flow interface used (for example, HMNF) to evaluate correctly the temperature-dependent quantities such as thermal conductivity, k, and specific heat, C_p. This value is integrated into the heat transfer equation for solids, such as in the purely conductive case (u=0). Therefore, from Eq.(B.8), it results in:

$$\rho C_p \frac{\partial T}{\partial t} = \nabla \cdot \left(k \nabla T \right) + Q_0 \tag{B.25}$$

B.2.4 Optimisation

An optimisation problem is composed of three main elements: (1) the control variables, (2) the objective function and, optionally, (3) the constraints. The optimisation problem consists of finding the maximum or the minimum of the objective function, possibly subjected to a number of constraints. COMSOL allows an optimisation to be performed on a multi-physics problem, which uses one or a combination of the above described interfaces. The most general formulation of an optimisation problem can be written as follows [120]:

$$\min_{\xi} Q\left(\xi\right) \tag{B.26}$$

$$\xi \in C \tag{B.27}$$

$$C = \left\{ \xi : lb \leq G\left(\xi\right) \leq up \right\} \tag{B.28}$$

where ξ is the control variable vector, Q is the objective function (a scalar) and C is the set of constraints vector. In Eq.(B.28) G is a vectorial-valued function where lb and up are the lower and the upper bound of the constraint vector, respectively, which have to be read component-wise. In the case of a single constraint, C, G, and the bounds become scalars.

A multi-physics problem is a PDE, which after discretisation is represented as a system of equations of the form $L(u(\xi),\xi) = 0$, where u is the solution of the problem. Therefore, the objective function is a function of both the PDE solution and of the control variables. The PDE-constrained problem becomes

$$\min_{\xi} Q\left(u\left(\xi\right),\xi\right) \tag{B.29}$$

$$L\left(u\left(\xi\right),\xi\right) = 0 \tag{B.30}$$

$$lb_P \leq P\left(u\left(\xi\right),\xi\right) \leq up_P \tag{B.31}$$

$$lb_\Psi \leq \Psi\left(\xi\right) \leq up_\Psi \tag{B.32}$$

$$lb_b \leq \xi \leq up_b \tag{B.33}$$

In COMSOL, the relation between the PDE solution and the control variables given by Eq.(B.30) is given by the multi-physics problem. Eq.(B.31) through Eq.(B.33) are the three possible set of constraints where the *P*- implicit or performance constraint are the functions of both the PDE solution and the control variables, *Ψ*- explicit or design constraints is the only function of the control variables, and the last equation, such as the control variable bound, represents the direct constraints on the control variables. The reason for dividing the constraint into the above three categories is computational. In fact, being the performance constraint *P* function of the solution u, each evaluation requires an updated solution of the entire multi-physics problem. On the other hand, the design constraints *Ψ* are computed without updating the multi-physics solution. Finally, the control variable bounds are computationally less expensive because they simply limit the optimisation solver to use the control variables. The bounds on *ξ* are often used to improve optimisation stability and efficiency. They can be used when it is known a priori that there is no solution for a range of values or when the solution is known to be in a restricted region of the control variables.

B.2.4.1 Objective Function

In COMSOL Multiphysics, the objective function is given by a sum of terms:

$$Q(u,\xi) = Q_{global}(u,\xi) + Q_{probe}(u,\xi) + \sum_{k=0}^{n} Q_{Int,k}(u,\xi) \tag{B.34}$$

where n is the space dimension of the problem. Q_{global} is the expression of the global variables of the problem. Q_{probe} is an expression defined in a geometrical entity of the problem, which could be either a point, a boundary, a surface or a volume. Finally, $Q_{int,k}$ is an integral objective also defined in a geometric entity.

B.2.4.2 Optimisation Algorithm

COMSOL provides several algorithms to numerically solve the optimisation problem defined in the PDE multi-physics problem. These algorithms are divided into two main categories: gradient-free and gradient-based methods. A gradient-free method does not require the calculation of the derivative of the objective function with respect to the control variables. For this reason, it is suitable for non-smooth objective functions or when it contains noise. Generally, when the control variables define geometrical dimensions, the objective function results are noisy. The reason is that changing the geometry also changes the computational grid (i.e., the mesh). Derivative-free solvers sample the objective function in different points of the control variable space without following a single path toward an optimum as for the gradient-based methods. While this is more expensive computationally, it is also more robust. Moreover, because every evaluation of $Q(u,\xi)$ does not depend directly on the previous one, the computational process can be parallelised.

The gradient-free solvers can be further divided into two groups based either on local or global methods. The former starts from an initial guess and attempts to improve the objective function in a step-by-step manner. Global methods evaluate instead a global map of the design space, refining the evaluation in areas where a global optimum is more likely to exist. For the reasons mentioned above, a gradient-free algorithm has been selected for the optimisation studies presented in this work. In particular, the Nelder-Mead method has been selected to perform geometrical optimisations of the RJ. This method 'walks' towards an improved objective function by iteratively replacing the worst corner of a simplex[*] in the control variable space. The new candidate corner is obtained by transforming the worst vertex through a series of operations about the centroid of the current simplex: reflection, expansion, inside and outside contractions [121].

B.3 Computing on the Iridis Cluster

[*] A simplex is the generalisation of a tetrahedron to arbitrary dimensions.

Some computations were performed on the University of Southampton Iridis supercomputer cluster. The current Iridis 4 is our fourth generation cluster and is one of the largest computational facilities in the UK. Its performance characteristics area as follows:

- 750 compute nodes with dual 2.6 GHz Intel Sandybridge processors;
- Each compute node has 16 CPUs per node with 64 GB of memory;
- 4 high-memory nodes with two 32 cores and 256 GB of RAM;
- 24 Intel Xeon Phi Accelerators;
- login nodes with 16 cores and 125 GB of memory;
- In total 12320 processor-cores providing 250 TFlops peak;
- 1.04 PB of raw storage with Parallel File System;
- InfiniBand network for interprocess communication;
- Moab HPC Suite - advanced workload management system from Adaptive Computing;

With the IRIDIS super- computing cluster, it is possible to employ a number of nodes to compute parametric sweeps in parallel, or to perform simulation with long computing times, where high reliability is required. In particular, the cluster has been used extensively to perform the large parametric sweeps of the validation exercises discussed in Appendix C, for the parametrised STAR geometries discussed Chapter 4, and to overcome memory limitations when performing the 3D simulations discussed in Chapter 3. In general, the SSH script below have been used to submit jobs in batch mode. In addition, many studies were conducted using an i7 Intel workstation with 32 GB of RAM, where the required memory and computational time were compatible.

```
#!/bin/bash

#PBS -l nodes=2:ppn=16
#PBS -l walltime=00:15:00
## #PBS -W x=matchpolicy:=exactnode -l naccesspolicy=singlejob # not used! This is here
for reference

#Change to directory from which job was submitted
cd $PBS_O_WORKDIR

# set number of processors to run on
nprocs=`wc -l $PBS_NODEFILE | awk '{ print $1 }'`

# load comsol module to setup software environment
module load comsol/5.3a
module unload jdk

myhosts="hosts_job_$PBS_JOBID"
cat  $PBS_NODEFILE | uniq > $myhosts
numnodes=`wc -l $myhosts | awk '{ print $1 }'`

comsol -mpirsh rsh -mpifabrics tcp -nn $numnodes -mpd batch -f $myhosts -inputfile
2_half_symmetry_1_no_spacer.mph -outputfile 2_half_symmetry_1_no_spacer_out.mph -tmpdir /
scratch/$USER > 2_half_symmetry_1_no_spacer_info

comsol mpd allexit

rm $myhosts
```

Appendix C Multiphysics Simulations – Validation Studies

The first objective of the research was to validate a methodology of simulating the resistojet thruster and its components, providing results in agreement with previous numerical studies and experimental results.

C.1 Nozzle Study

In this section, the two validation exercises developed in COMSOL Multiphysics to simulate a resistojet nozzle are shown. In particular, in Section C.1.1, simulations are compared and matched with a relevant case study found in literature (Kim, 1994) [65]. In the literature, it is found that the flow field of a resistojet nozzle can be characterised by a thick boundary layer, and subsequently, a large subsonic region could exist near the wall at the nozzle exit area (more details in section 1.5.2.3). In section C.1.2, the nozzle of the SSTL's T50 resistojet is analysed.

C.1.1 Low-Reynolds-number Nozzle

In this section, the results produced by Kim in 1994 [65] on low-Reynolds-number resistojet nozzles have been taken as reference to trim an axisymmetric simulation for validation purposes. The present simulation results are compared with the reference study in which the "Rothe" nozzle is analysed (from the author's name who firstly studied this geometry for low Reynolds numbers). A simulation suing a 2D axisymmetric adiabatic wall is conducted with the same BCs and computational grid of the reference study. The HMNF interface is used in the laminar flow case, with inlet BC of stagnation chamber temperature and pressure of 1,500 K and 0.15 MPa, respectively. The nozzle throat diameter measures 0.84 mm, and the exit area ratio of the nozzle is 82. The nozzle produces 0.12 N of thrust. Further details of the geometry can be found in [65]. Fig. 5.4 shows the geometry of the nozzle and the 240×60 computational grid implemented in COMSOL. In the case of a nozzle, the Reynolds number characteristic length, L, and the characteristic velocity, U, of Eq.(1.20) are

chosen as the diameter, d, and the axial velocity, w, calculated at the throat, in analogy with a pipe flow. A first estimation of Re_t is calculated from the stagnation conditions and the isentropic relations, which gives Re_t = 367. Therefore, the flow is assumed to be laminar, in accordance with Kim (1994), which gives a quite lower Re_t = 270. This value is slightly higher with respect to the present simulation, evaluated using the average quantities at the throat, giving Re_t = 244. The Mach iso-contour images, shown in Fig. 5.5, are very similar. While Kim calculates a maximum centreline Mach number of about 3.9, the present simulation returns a maximum of 3.7, which differs of -5%. Both Fig. 5.6 and Fig. 5.7 show good agreement with the Rothe nozzle experimental data presented in the reference. The second figure displays the density profile near the exit of the nozzle. A good agreement with the reference study is obtained taking a section at 5 mm from the exit (line visible in Fig. 5.4). With reference to this figure, Kim attributes the discrepancy between the simulations and the experimental data to a slip velocity on the walls and to the exit boundary conditions. For the Rothe nozzle examined, the Knudsen number has been plotted (Fig. 5.8) using Eq.(1.21). As it is proportional to the Mach number, it increases along the centreline with a maximum of Kn ≈ 0.1 at the exit. For a better fit with the experimental data, when the flow is rarefied, the slip condition on the wall should be used [122], and as Kn approaches 1, a direct Monte Carlo simulation approach should be used [66].

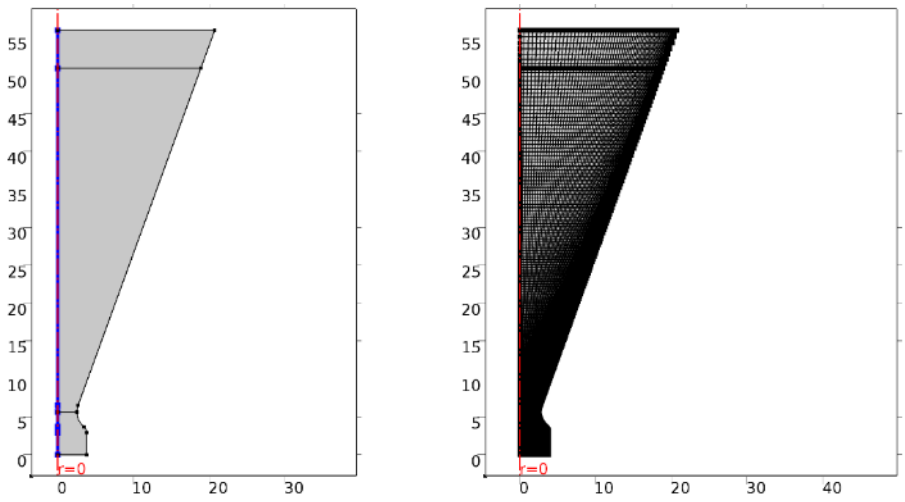

Fig. 5.4. Rothe nozzle geometry build in COMSOL (left) and computational grid according to Kim.

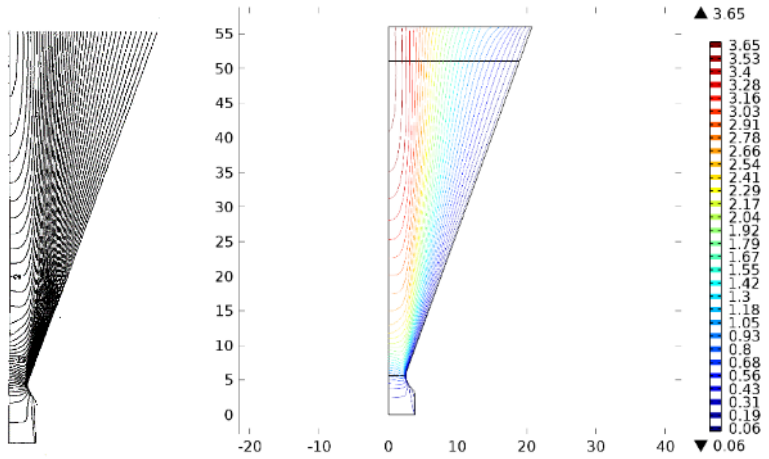

Fig. 5.5. Mach number contour: original study (left) and simulation results (right).

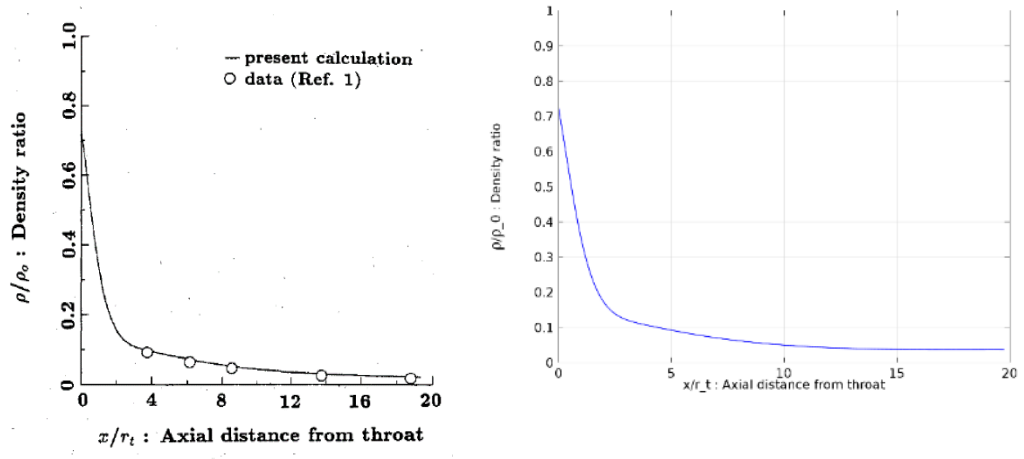

Fig. 5.6. Axial variation of centreline density: original study (left) and simulation results (right).

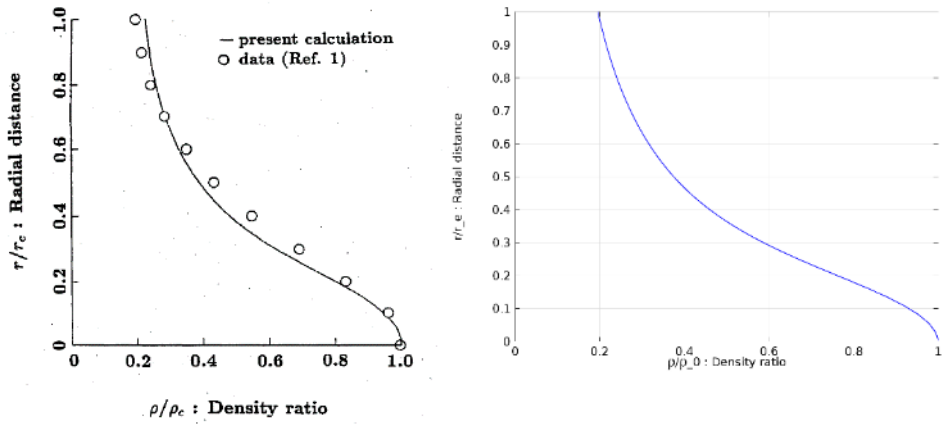

Fig. 5.7. Density profile near the exit of the Rothe nozzle

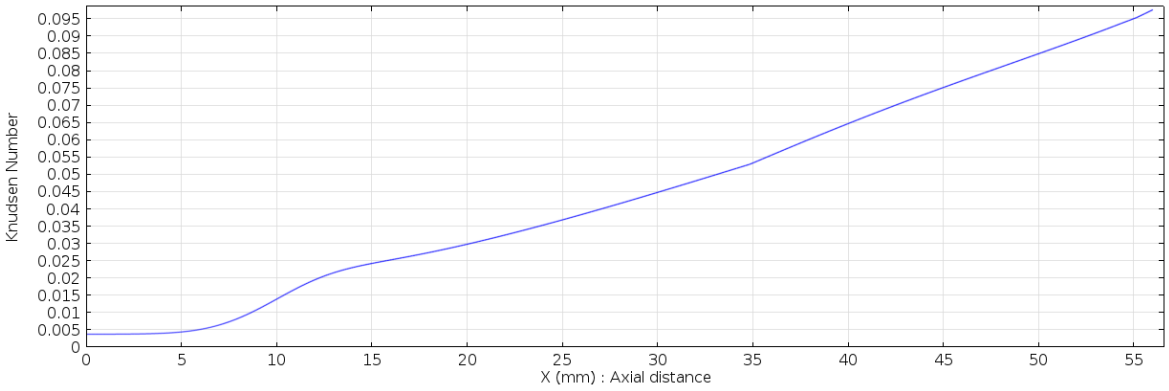

Fig. 5.8. Knudsen number variation along the centreline.

C.1.2 SSTL T50 Nozzle Study

Part of the work discussed in this section was presented at the 34th International Electric Propulsion Conference (IEPC), within the Joint Conference of the 30th International Symposium on Space Technology and Science, in Hyogo, Kobe, Japan, on 4–10 July 2015, with the paper titled *A Thermo-Fluidic Model for a Low Power Xenon Resistojet*.

Fig. 5.9 (right) shows the T50 test setup from thruster performance testing at the ESA Electric Propulsion Laboratory. The xenon supply to the thruster is pressure-regulated with mass flow rate measured via a mass flow rate sensor. A pressure transducer measures the supply pressure upstream of the thruster's heat exchanger. From thruster tests, the pressure drop across the heat exchanger is considered negligible. The measured experimental parameters were propellant mass flow rate, $\dot{m}$; supply pressure, p_s; background pressure, p_{BG}; thruster nozzle temperature, T_n; supply temperature, T_s; and thrust, F [23]. The thruster nozzle temperature, is measured with a k-type thermocouple secured to the exterior of the nozzle (Fig. 5.9, left). The gas temperature inside the nozzle was not directly measured in these tests; however, it has been estimated in previous experiments for butane propellant. These estimations were made with a supply pressure of 2 bar, from a pressure measurement on the pressure-tap shown in the blank-off in Fig. 5.9 (left). In this case, the nozzle inlet stagnation temperature, T_0, was found to be slightly higher than the nozzle temperature, T_N. For example, with a nozzle temperature of 500 K the inlet gas temperature was found to be 516 K.

The current study couples CFD and parametric optimisation to trim the thruster nozzle temperature T_n, and the inlet pressure p_0, to match experimental data to estimate the inlet gas temperature and pressure prior to entry into the nozzle. Mach number and velocity profiles along the axial centreline,

including throughout the nozzle, can then be analysed. IRIDIS 4 has been used compute the 24 cases in parallel, employing between 2 and 4 nodes to compute the parametric sweep (Section B.3). Typically, for the laminar flow simulations, the computational time was of about 20 minutes while for the turbulent flow cases, it took about one hour for each of the 24 cases.

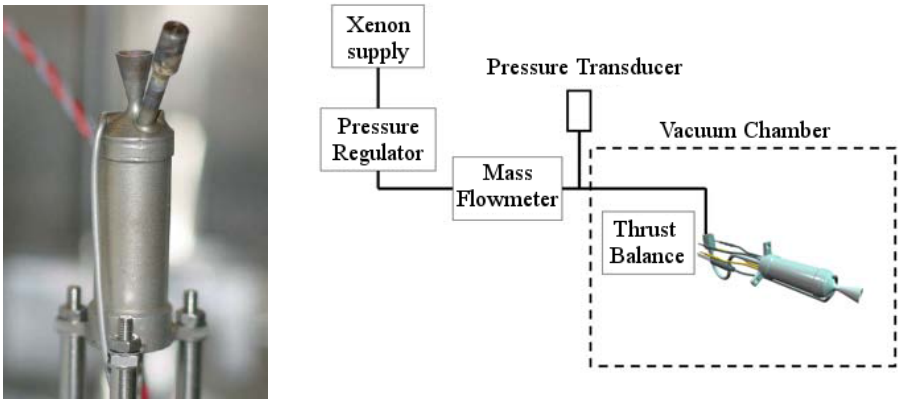

Fig. 5.9. SSTL-T50 resistojet mounted vertically on a thrust balance (left) and test setup for performance measurement (right) at the European Space Agency Electric Propulsion Laboratory.

C.1.2.1 Nozzle Geometry

The T50 resistojet contains a 14° half-angle conical nozzle of 316 grade stainless steel. The expansion corresponds to 211 while the throat-to-inlet area ratio is 661. The throat diameter is 0.42 mm, and the nozzle wall thickness of the diverging section is 1 mm. For the CFD simulations, the selected radius of curvature upstream and downstream of the throat have the same dimension of throat radius and diameter, respectively. The throat is located at z = 6.10 mm, and the total length of the nozzle is 17.80 mm (see Fig. 5.11 left for reference). The available experimental data corresponds to 24 different cases, which are the combinations of different inlet pressure and temperature conditions, corresponding to the power applied to the resistojet heaters. Table C.5 shows the throat Reynolds number evaluated using Eq.(1.20). Re_t has been calculated using the experimental Xe mass flow rate, where it is assumed that $T_0 = T_n$. Hence, for the CFD simulations, the cases (65 W, 1 bar; 50 W, 1 bar; 40 W, 1 bar; 30 W, 1 bar; and 20 W, 1 bar) is solved using the laminar flow model. For the remaining cases, the Reynolds-averaged Navier-Stokes equations (RANS) are used to model the flow.

Table C.5. Reynolds numbers calculated at the nozzle throat for the 24 analysed cases.

P_e [W]	1 bar	2 bar	3 bar	4 bar
65	1,906	4,283	6,845	9,450
50	2,094	4,735	7,434	10,292
40	2,363	4,968	7,967	11,154
30	2,557	5,375	8,546	12,158
20	2,879	6,307	10,215	14,091
10	5,563	9,582	15,180	20,926

C.1.2.2 Multi-physics Model

The thermo-fluidic model of the T50 nozzle is axisymmetric and stationary and uses the HMNF interface, which models a gas flow at low or moderate Reynolds numbers in the compressible case and can model both laminar and turbulent flow. The compressible Navier-Stokes equations in the vectorial form are conservation of mass Eq.(B.14), momentum Eq.(B.15) and energy(B.13). In addition, the Heat Transfer in Solids' interface is used to model the nozzle wall heat transfer by conduction and radiation including both surface-to-surface and surface-to-ambient radiation. For the turbulence case, the standard k - ϵ model is used, with the built-in Kays-Crawford heat transport turbulence model discussed in Section B.2.2.1. For the Xe gas, both thermal conductivity, k, and dynamic viscosity, μ (Fig. 5.10), are evaluated as cubic spline interpolations from a set of experimental data points given in [114]. These interpolations were found to give a slightly better final result on the simulations with respect to the built-in polynomial functions of temperature. Accurate material properties were applied for the 316 grade stainless-steel nozzle, with the thermal conductivity approximated as a linear function of the temperature.

C.1.2.3 Mesh Optimisation

The mesh selected for the nozzle is structured for the Xe gas domain, while it is unstructured for the solid part of the nozzle (Fig. 5.11, left), where only the heat transfer equation is solved. The structured grid is made of a proportional number of axial elements with respect to the number of radial elements, similarly to what shown in Section C.1.1. In the converging and diverging parts of the nozzle, the grid axial spacing evolves to maintain a nearly constant aspect ratio. The solution

accuracy has been studied in a convergence study by varying the number of radial elements. Fig. 5.11 (right) shows how the numerical solution of the model approaches an asymptote as the number of radial elements increases. However, a trade-off between solution accuracy and computational time led to the selection of 40 radial elements as an acceptable value since the model error is less than 1% with respect to the finest grid. The resulting Xe domain computational grid has the size 40 × 200.

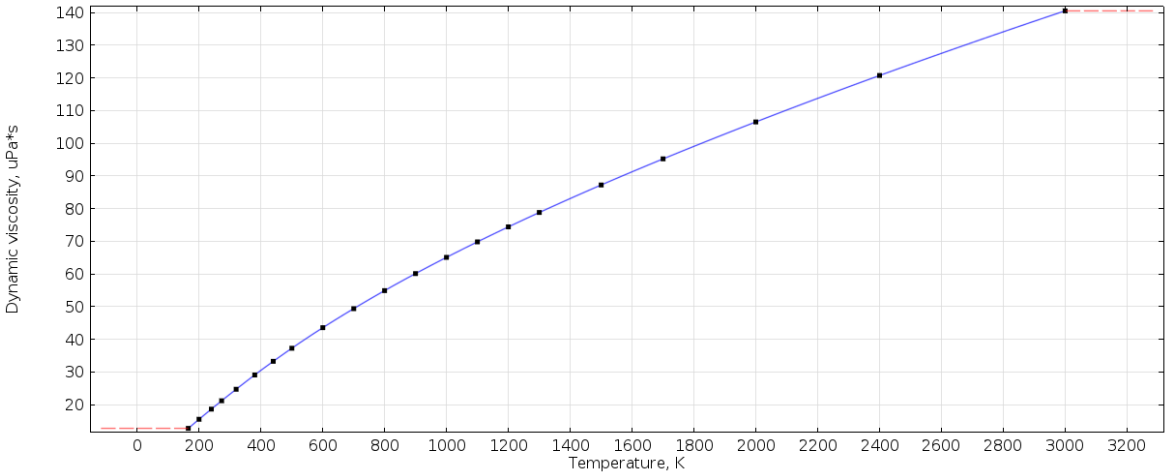

Fig. 5.10. Xenon dynamic viscosity, μPa.

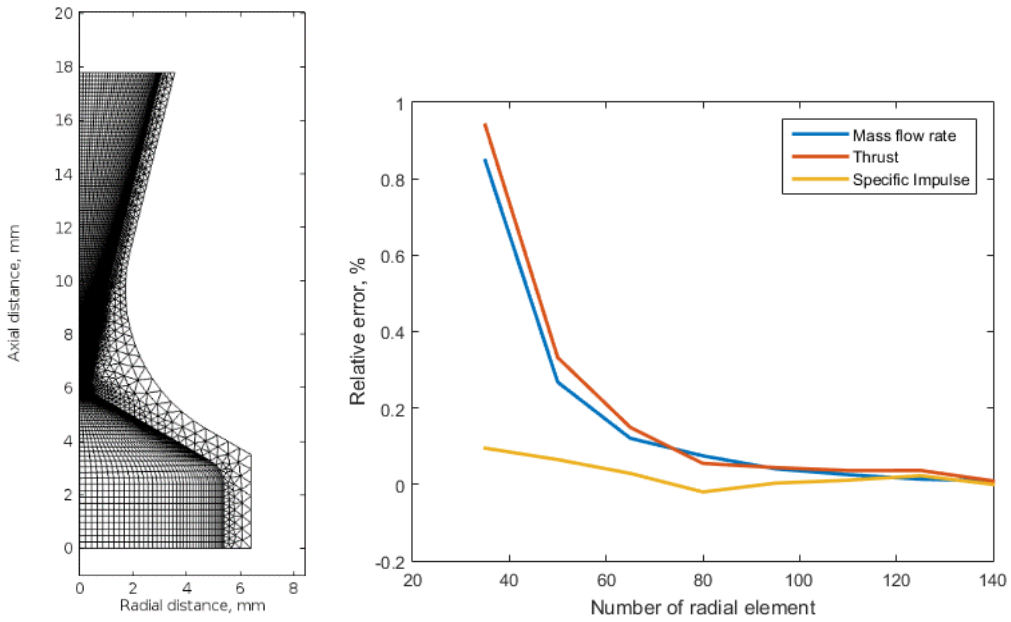

Fig. 5.11. Computational grid for the T50 nozzle (left) and mesh solution accuracy (right).

C.1.2.4 Boundary Conditions

For the laminar flow the no-slip condition, described by Eq.(C.1), is applied on the nozzle internal wall whereas for the turbulence model, the wall functions do apply. The study includes the surface-to-ambient radiation applied on the outer nozzle wall, modelled by Eq.(C.2), where k is the stainless-steel thermal conductivity, $\varepsilon = 0.6$ the surface emissivity (assumption) and $\sigma = 5.6703\times10^{-8}$ W/(m^{2}K^4) is the Stefan-Boltzmann constant. On the assumption that the inlet propellant temperature and the inlet nozzle section are not at the same temperature in equilibrium conditions, a temperature boundary condition is applied to the inlet nozzle wall; its notation is T_{nozzle} (Fig. 5.12).

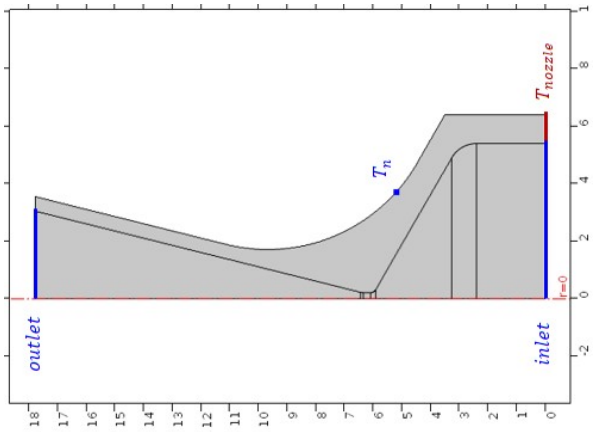

Fig. 5.12. T50 nozzle boundary conditions highlighted.

The inlet condition for the gas is specified in terms of total pressure, total temperature and Mach number. The inlet Mach number, M_0, is evaluated using the equation for an ideal compressible gas in the assumption of isentropic flow (summarised in Section 2.1.1), where A_{in} = 91.6 mm^2 is the nozzle inlet area, p_0 is the inlet total pressure (assuming $p_0 = p_s$), $\gamma = 1.67$ is the ratio of specific heats of Xe, $\underline{R}$ = 63.5 J/(kgK) is the Xe gas constant and T_0 is the inlet total temperature (assuming $T_0 = T_N$). For the turbulence model, the inlet parameters of turbulent intensity, I_T , and turbulence length scale, L_T, are calculated using the equation for a fully developed pipe flow, Eq.(C.3) and Eq.(C.4) respectively [123]. L_T = 0.41 mm while I_T assumes different values depending on the corresponding inlet Reynolds number, Re$_{in}$. The outlet condition of the flow is set as static pressure equal to the experimental background pressure of the vacuum chamber, p_{BG}. It is assumed that the background temperature of the vacuum chamber is near room temperature at T_{BG} = 300 K.

$$\mathbf{u}_{wall} = 0 \tag{C.1}$$

$$\mathbf{n} \cdot (-k \nabla T) = \varepsilon \sigma (T^4 - T_{BG}^4) \tag{C.2}$$

$$I_T = 0.16 \, \mathrm{Re}_{in} \tag{C.3}$$

$$L_T = 0.038 d_h \tag{C.4}$$

C.1.2.5 Optimisation Solver

The built-in Nelder-Mead optimisation solver (Section B.2.4.2) has been used to minimise the objective function, *J*, which is defined by Eq.(C.5),

$$J = (1 - I_{sp} \, / \, \hat{I}_{sp})^2 + (1 - F \, / \, \hat{F})^2 \times 10^6 + (1 - T_n \, / \, \hat{T}_n)^2 \tag{C.5}$$

$$F = 2\pi \int_0^r [\rho w^2 + (p - p_{BG})] r dr \tag{C.6}$$

$$\dot{m} = 2\pi \int_0^r \rho w r dr \tag{C.7}$$

where the terms marked with a hat are the experimental values of specific impulse, thrust and thermocouple temperature, respectively. The minimisation of the objective function *J* corresponds to asking the model to converge to the experimental specific impulse, thrust and nozzle temperature. Eq.(A.5), Eq.(C.6) and Eq.(C.7) show the definitions of specific impulse, thrust and mass flow rate, respectively, defined on the nozzle exit boundary. The solver finds the minimum of the objective function *J*, given the control variables selected: p_0, T_0 and T_{nozzle}. The 10^6 scaling factor on the thrust term serves to give the same weight to 1 mN, 1 K and 1 s. The optimality tolerance has been fixed to 0.01, meaning that the optimisation solver stops iterating when the objective function value at the *j*-th step differs of <1% from the step (*j*-1).

The parameters have been selected since they are coupled principally with a single objective function term. In particular, from the physics point of view, I_{sp} is mainly dependent on T_0, F is mainly dependent on p_0, and T_n is mainly dependent on T_{nozzle}. The convergence of the optimisation solver to the selected optimality tolerance depends strongly on the initial conditions given.

C.1.2.6 Results and Discussion

The optimisation study was made for all 24 experimental cases. The main outputs of the simulation are the space solutions of mass flow rate, temperature, Mach number and nozzle radiation loss. Table

C.6 shows an example of the CFD optimisation iterations. The initial values of inlet pressure and temperature (step 1) have been estimated by optimisation through trial and error.

The mass flow rate, $\dot{m}$, can be used as a model validation parameter. Table C.7 shows the percentage relative error of the mass flow rate with respect to the experimental values, the average inlet static temperature and estimated nozzle radiation-to-ambient loss, calculated for the 24 cases. In the worst case (65 W, 1 bar), the relative mass flow rate error measures 3.3% of on $\dot{m}$ is considered an acceptable value. As a further check on the numerical solution accuracy, the global mass flow rate conservation has been compared in several axial sections along the nozzle length. The mass flow rate conservation error is found to be with 0.5%, which is considered adequate as an engineering estimate. The nozzle inlet total temperature can also be considered an estimate of the outlet heat exchanger gas temperature, as they are coincident in a fully assembled thruster. Fig. 5.13 shows the correlation between the measured temperature at the surface of the nozzle, T_n, and the hot gas entering the nozzle temperature, T_0. Some conclusions on the thruster heat exchanger are deducted from the calculated inlet temperature of the nozzle. From the experiments, the T50 heat exchanger efficiency, η_b defined by Eq.(1.12), is found to improve with the chamber pressure.. However, since mass flow rate is proportional to the inlet pressure, even if the heating efficiency improves with pressure, the final gas temperature, T_0, for higher-pressure cases remains lower. The radiation loss from the nozzle outer surface to the ambient, in the assumption of $\varepsilon = 0.6$, is as expected maximum radiated at the highest test power of 65 W cases. In this cases, the efficiency loss is of about 11%.

Table C.6. Example of optimisation solver iterations (65 W, 1 bar).

Step	p_0 [Pa]	T_0 [K]	T_{nozzle} [K]	T_N [K]	F [mN]	I_{sp} [s]	$\dot{m}$ [mg/s]	J [-]
1	113,985	1,082.250	883.173	858.277	21.138	52.861	40.776	2.390
2	107,985	1,082.250	883.173	858.239	19.906	52.629	38.568	1.927
3	113,985	1,172.250	883.173	866.668	21.065	54.100	39.706	76.066
4	113,985	1,082.250	913.173	882.654	21.094	53.092	40.515	609.579
5	109,985	1,142.250	853.173	839.179	20.314	53.302	38.863	354.716
61	109,107	1,188.671	870.457	858.044	20.069	54.009	37.892	4.300E-03
62	109,270	1,184.804	870.899	857.990	20.105	53.969	37.987	2.560E-04
63	109,337	1,185.652	870.855	858.046	20.118	53.983	38.003	2.180E-03
64	109,207	1,185.794	870.775	857.994	20.092	53.979	37.956	3.278E-04
65	109,270	1,184.804	870.899	857.990	20.105	53.969	37.987	2.560E-04

Table C.7. Mass flow rate relative error, average inlet static temperature and estimated nozzle radiation-to-ambient loss, calculated for the 24 cases (each set of four columns represent the inlet pressure, ranging from 1 to 4 bar).

P_e [W]	$\dot{m}_{err}$ [%]				$\overline{T}_{in}$ [K]				$q_{n,rad}$ [W]			
65	3.262	2.278	1.475	-0.103	1,185	943	864	809	7.5	7.6	7.5	7.3
50	-1.491	0.068	-0.014	0.002	1,065	870	791	733	6.2	6.2	6.0	5.7
40	-3.696	0.050	0.027	-0.017	996	859	797	724	4.9	4.8	4.9	4.5
30	-2.153	0.462	0.167	0.254	947	800	734	676	4.0	4.1	3.9	3.6
20	-0.157	-0.536	0.228	0.306	732	650	580	557	2.6	2.6	2.4	2.3
10	-0.532	-0.223	-0.244	-0.052	492	508	472	483	0.3	0.7	0.7	0.7

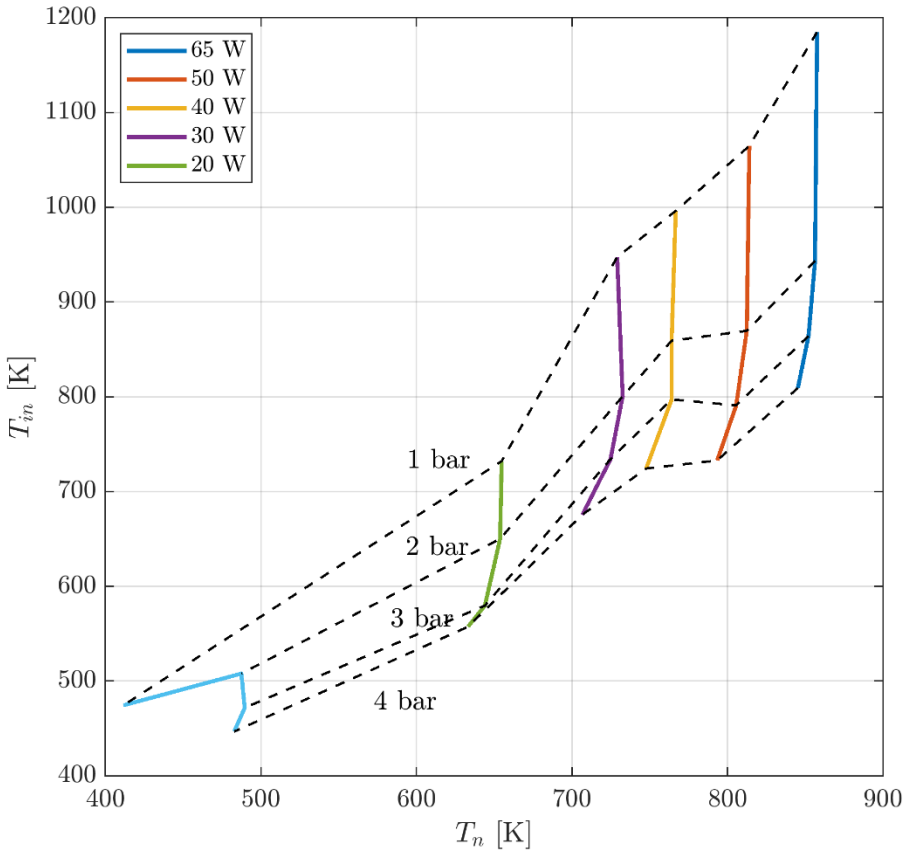

Fig. 5.13. Relation between nozzle temperature T_n (experimental) and inlet gas temperature T_0 (simulation output) for the 24 test cases and supply pressures of the T50 thruster with xenon propellant.

Considering the case with a power input of 30 W, Fig. 5.14 shows the axial variation of the centreline Mach number (the nozzle throat is located at 6.1 mm downstream, and the nozzle exit plane is located at 17.8 mm). It is evident that the 1 bar laminar flow solution provides the lowest exit Mach number among the four cases considered. This is also shown at the exit section of the nozzle. It is clear that a wider portion of the exit radius is subsonic, with the subsonic depth reaching about 2.27 mm into the flow field. For this reason, the nozzle area ratio results reduced, leading to a lower expansion of the gas. The static temperature profiles are shown in Fig. 5.15. Because of the lower level of expansion, the static temperatures for the 1 bar laminar case is found to be higher both at the nozzle exit and the nozzle centreline.

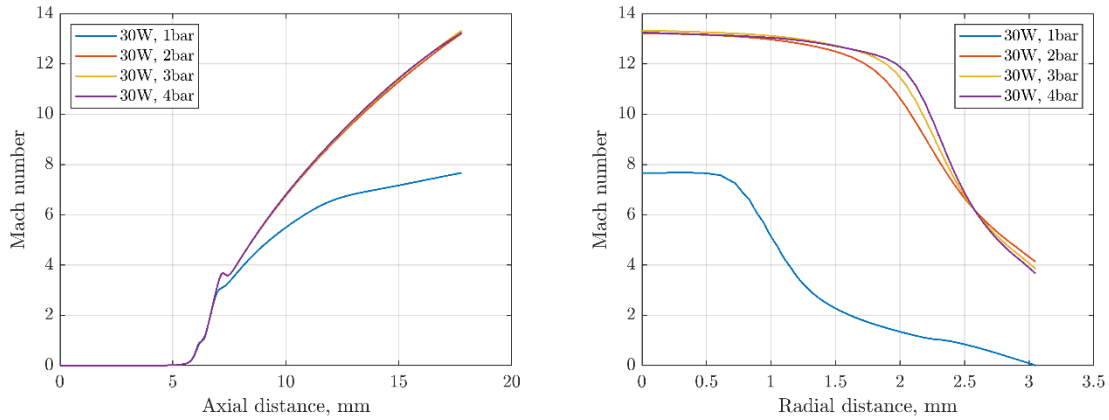

Fig. 5.14. Axial variations of centreline Mach number (left) and Mach number profiles at the nozzle exit plane in the 30 W operative condition at a range of inlet pressures between 1 and 4 bar (right).

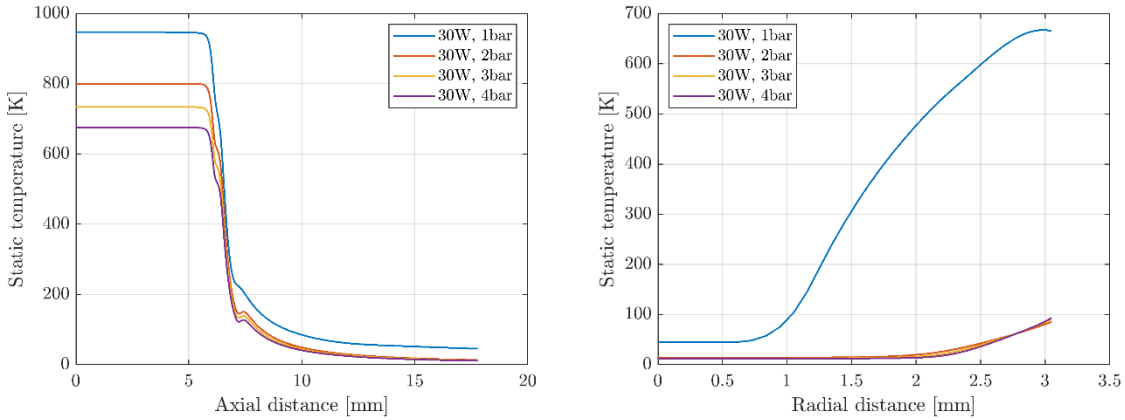

Fig. 5.15. Axial variations of centreline static temperature (left) and exit static temperature profiles at the nozzle exit plane in the 30 W operative condition at a range of inlet pressures between 1 and 4 bar (right).

The Mach number is a non-zero value at the wall for the other cases, where the RANS equations have been used since the wall functions have been implemented as boundary conditions. Wall functions assume that the viscous boundary layer has zero thickness, and the computational wall velocity corresponds to a non-zero analytical solution. This technique is used to save considerable computational cost. Fig. 5.13 shows the T50 nozzle temperature and Mach number solutions plotted in three dimensions for the 30 W case at 1 bar inlet pressure. The temperatures, for both the gas and the solid wall, are shown in four solution slices for the convergent section of the nozzle. The first slice at the bottom shows the constant temperature conditions for the nozzle inlet wall section, T_n = 741 K, and for the xenon gas, T_0 = 947 K. From the Mach number iso-surface profiles at the diverging section, it can be seen that the subsonic portion of the flow at the nozzle exit plane cannot be

considered negligible. The T50 nozzle in low-Reynolds number regime is further analysed in Section 5.2.1.1.

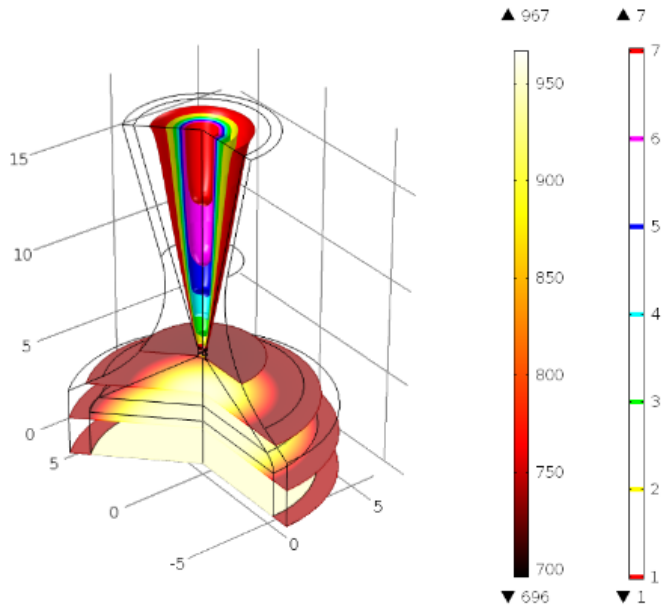

Fig. 5.16. Static temperature in K (for the converging section) and Mach number iso-surface profiles (for the diverging section) for the 30 W case at 1 bar inlet pressure.

C.2 3 kW Hydrogen Resistojet

Part of the work discussed in this section was presented at the 7th European Conference for Aeronautics and Space Sciences (EUCASS 2017), in Milan, Italy, on 3–5 July 2017, with the paper titled *Multiphysics Model Validation of Resistojets with Concentric Tubular Heat Exchanger*.

Donovan et al. (1972) [31] provide detailed information on the J3 3-kW experimental hydrogen resistojet (see Section 2.2.5.1). In particular, they make available a table of measurements and derived data of a test campaign that characterised the thruster at one tenth of the design mass flow rate. Amongst the 14 tests reported, test-14 is taken in analysis, which corresponds to the highest tested electrical power (I = 56.6 A). This paper is of great importance for the present work for two main reasons: (1) it gives a set of experimental data with sufficient thruster design description to set up a great exercise of validation of a complex multi-physics simulation to be used as a baseline for the high-temperature resistojet study; (2) it shows the high-temperature design used as primary reference

for the HTR development. In this section, a multiphysics 2D axisymmetric model of the J3 resistojet is developed and discussed.

C.2.1 Nozzle Evaluation

The simplest way of describing a converging-diverging nozzle is by assuming the following: one-dimension and steady problem, ideal gas, Eq.(1.9), isentropic and compressible flow, Eq.(1.6). The thermodynamic variables ρ, p and T can be evaluated anywhere along the nozzle longitudinal axis. However, the assumptions described above are particularly far from the reality when the nozzle Reynolds number is low. In particular, when the nozzle regime is laminar and the reservoir pressure relatively low, the boundary layer, hence the subsonic region on the nozzle throat and diverging section is extensive. It can reach about one third of the nozzle exit radius as discussed Section C.1.2. In order to correctly evaluate the nozzle, it is necessary to solve the full N-S equations, which are able to model the strong viscous effect on the nozzle wall. In this section, the problem geometry and boundary conditions necessary for an accurate nozzle modelling are shown step by step, by adding complexity to an initial simple adiabatic nozzle model. The HMNF interface is used for the nozzle and for the full thruster models, where the hydrogen gas thermodynamic properties as function of temperature are found in Ref.[124]. The flow regime is assumed laminar in all cases analysed.

C.2.1.1 Computational grid convergence study

The J3 nozzle has a throat diameter of 1.31 mm, an inlet tube diameter of 2.10 mm, a conical diverging section with a half-angle of 18° and an area ratio of 100. A computational grid convergence test is performed on an adiabatic nozzle with the following inlet conditions: T_0 = 302 K, p_0 = 10.6 kPa and an initial inlet Mach number $M_{0,i}$ = 0.19664. The nozzle outlet boundary condition is p_{BG} = 4 Pa, which is the vacuum chamber pressure. The initial Mach number is evaluated with Eq.(C.8), where w_i is the inlet axial velocity and is estimated with Eq.(C.9), where a_i is the inlet speed of sound evaluated at the inlet with Eq.(1.4) , stagnation temperature assumes $T_i = T_0$, A_i is the inlet nozzle area, with r_i = 1.05 mm and $\dot{m}$ = 8.06 mg/s is the experimental mass flow rate. The inlet density ρ_i is evaluated with and the hydrogen gas thermodynamic properties ($\gamma(T)$, $\mu(T)$ and $k(T)$) are found in [124] and implemented in the model.

$$M_{0.i} = w_i \,/\, a_i \tag{C.8}$$

$$w_i = \dot{m} \,/\, (\rho_i A_i) \tag{C.9}$$

The mass flow rate is calculated at the inlet, throat and exit nozzle sections with Eq.(C.7), while the thrust is defined with Eq.(C.6) evaluated at the nozzle exit boundary, with radius R_e, w is the axial component of the velocity. A structured computation mesh is parametrized as function of a refinement parameter f, which is used for the mesh convergence analysis (Fig. 5.17). Both the radial number of elements and the axial number of elements are proportional to f. The radial discretization is divided into two parts (line on the right hand of the nozzle), so that the discretization close to the nozzle wall, i.e. where the boundary layer is located, can be further refined. In particular, the number of radial elements close to the wall is $n_{rw} = 15f$, with an element ratio of 100 (ratio between the first and last radial length) and arithmetic progression. The number of element at the nozzle central part is n_{rc} = 12f. The conical diverging section has n_d = 70f with an element ratio of 7 and arithmetic progression. The other boundaries of the nozzle are similarly discretized to obtain the mesh shown in Fig. 5.17.

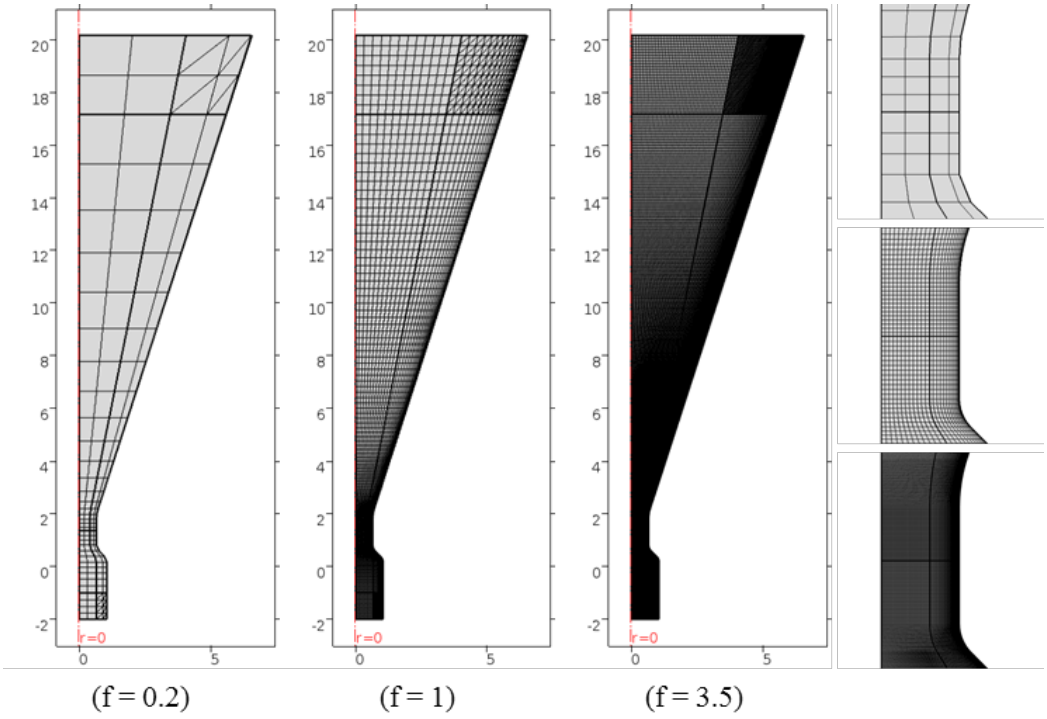

Fig. 5.17. Computational grid of the nozzle geometry as function of the refinement parameter *f*: nozzle overview (left) and throat detail (right). The total number of elements for these cases is 172, 5,088 and 62,072 respectively.

The relative errors are calculated with respect to the finest mesh solutions (f = 3.5). Fig. 5.18 (left) shows the relative errors of mass flow rates calculated at three section of the nozzle: inlet, throat and exit plane. Fig. 5.18 (right) shows the relative error, evaluated at the nozzle exit plane as an average surface integral, of the variables T, static temperature, p, static pressure, w, axial component of the velocity and u, radial component of the velocity. When the refinement factor is the highest (f = 3.5), the average mass flow rate at the three sections is 7.6929 mg/s, while the average values (denoted by an overbar) of the thermodynamic variables calculated at the exit are $\bar{T}_e = 143.26$ K, $\bar{p}_e$ =16.940 Pa, $\bar{w}_e$ =1 823.7 m/s and $\bar{u}_e$ =266.93 m/s. When f = 1, the average relative error of the mass flow rate at the three nozzle sections is $\bar{\epsilon}(\dot{m}) = -0.24\%$, while at the exit section $\epsilon(\bar{T}_e) = -2.10\%$, $\epsilon(\bar{p}_e) = -2.3\%$, $\epsilon(\bar{w}_e) = -0.02\%$ and $\epsilon(\bar{u}_e) = -1.45\%$. It should be noted that the nozzle stagnation condition, derived in the reference, does not provide the expected mass flow rate of 8.06 mg/s. This is attributable to strong viscous effects, which determine a relatively large boundary layer at the throat region and extended to the nozzle diverging section. As a result, there is a smaller 'virtual' throat radius, resulting in a lower mass flow rate.

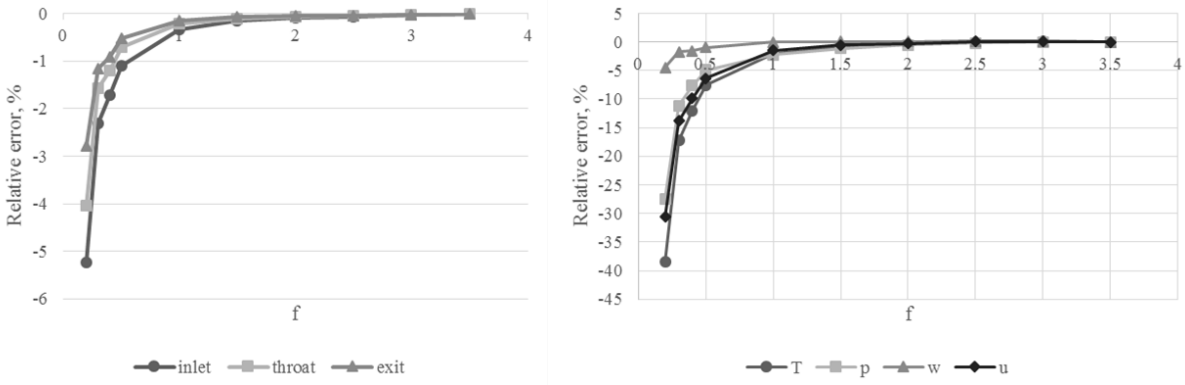

Fig. 5.18. Relative error of mass flow rate (left) and of the average values of T, p, w and u calculated at the nozzle exit (right) as function of the refinement parameter f.

C.2.1.2 Parametric sweep of stagnation conditions

The authors in Ref.[67] estimate analytically both the stagnation pressure and temperature at the inlet of the nozzle. These quantities, $T_{0,i}$ and $p_{0,i}$, are taken as initial input for the model stagnation condition, while the initial inlet Mach number is evaluated as described in section C.2.1.1. The outlet boundary condition is the vacuum chamber pressure, p_{BG}, which is a direct measurement. The computational grid parameter f is set to 1.

A first calculation of thrust and mass flow rate is made assuming an adiabatic nozzle (case a). However, the resulting mass flow rate is underestimated by -6% and -9% with respect to the experimental value of 8.06 mg/s from the first to the last test (Fig. 5.19, right). Since the mass flow rate is directly proportional to the stagnation pressure, a correction factor has been extrapolated from the mass flow rate error and applied to the stagnation pressure for each test condition (case b). The resulting mass flow rate error is less than 2% in each case. Finally, a temperature profile is applied to the nozzle wall (case c) assuming that the wall temperature is equal to the stagnation temperature at the inlet and linearly decreases as function of the axial coordinate, z, to the experimental nozzle temperature, T_n. This assumption largely agrees with the solution of the full thruster (discussed in section C.2.2). The described temperature boundary condition is applied through Eq(C.10), where the nozzle total height H_{nozzle} = 20.159 mm.

$$T_w(z) = T_t + (z+2)\frac{(T_n - T_t)}{(H_{nozzle}+2)} \tag{C.10}$$

Fig. 5.19 shows the resulting thrust and average mass flow rate, for the three different cases (a – c) described above and compared with the experimental values. The experiments provide accurate thrust and mass flow rate measurements. Here, a mass flow rate is obtained reasonably close to the experimental one, therefore the computational thrust can be used to judge the model accuracy. The calculated thrust is overestimated with a relative error with respect to the experiments between 23% to 29%, from the first to the last test.

Fig. 5.20 shows the Reynolds number, defined for a pipe flow in Eq.(1.20), calculated with the average value of viscosity at the respective sections (inlet, throat and nozzle exit). For a pipe flow, the Reynolds upper limit for a laminar flow is 2,100. The exit section exhibits in general the highest Reynolds number because the static temperature rapidly drops along the nozzle diverging section, resulting in a viscosity decrease. As a result, while the flow is guaranteed to remain laminar in a large part of the nozzle, in the diverging section it could be sufficiently high in some cases to determine transition to turbulent.

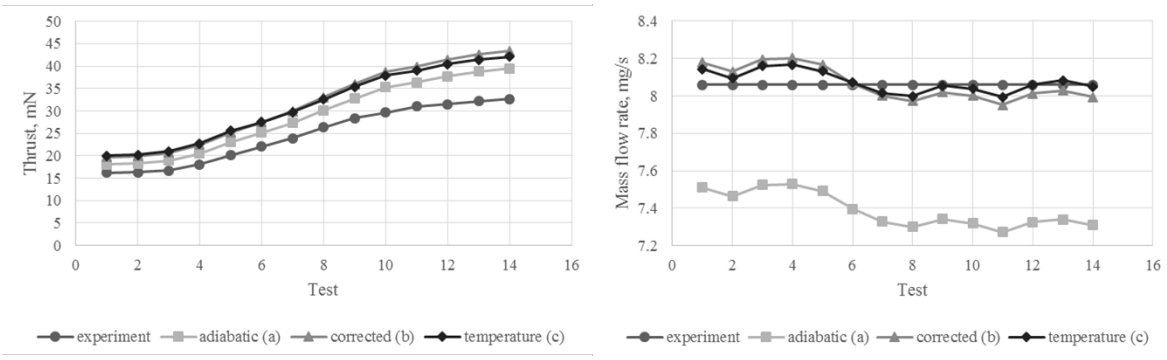

Fig. 5.19. Experimental thrust (left) and mass flow rate (right) compared with simulations results at three different test cases: adiabatic nozzle wall, correction of mass flow rate by changing the stagnation pressure condition and with temperature profile applied to the nozzle wall.

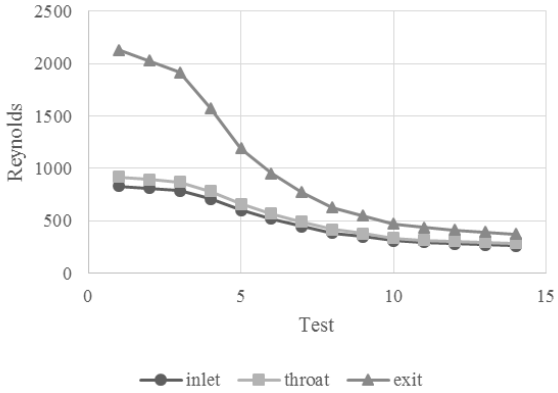

Fig. 5.20. Reynolds number evaluated as at the inlet, throat and exit sections for the 14 experimental points.

C.2.1.3 Vacuum chamber effect

In section C.2.1.2, the calculated thrust resulted largely overestimated. In this section, the influence of the vacuum chamber on the thruster performance is investigated. There is no detailed data regarding the vacuum chamber size utilized in the test campaign, however the following is considered a reasonable approximation: length = 1.125 m, radius = 0.5 m, aperture radius = 210 mm. The thruster is positioned at 100 mm from the bottom part of the chamber domain (Fig. 5.21, left). The J3 thruster is here only modelled as a nozzle with its casing contour. The simulation inlet and outlet conditions are set up as already described. However, several cases have been analyzed to highlight the effect of adding particular boundary condition to the problem: Case 1) the vacuum chamber is adiabatic; Case 2) constant temperature (as from experimental measurements) boundary condition applied to the vacuum chamber wall, T_{cw}; Case 3) temperature boundary condition on the thruster casing top disc, T_{top}, from linear interpolation of the experimental measurements T_n and T_{09} (see Fig.

5.24 for reference), Eq.(C.11); Case 4) additional vacuum chamber outlet boundary at the back of the thruster, in agreement with the experiment set-up; Case 5) inlet boundary condition determined from the solution of the full thruster (shown in section C.2.2), where the stagnation pressure and temperature and velocity profile are developed.

$$T_{top}(r) = T_n + \frac{r - R_{out}}{R_{th} - R_{out}}(T_{09} - T_n) \tag{C.11}$$

In order to evaluate the thrust, Eq.(C.6) can be applied to the nozzle without accounting for the chamber pressure, but adding the contribution of the pressure distribution at the top and bottom of the thruster. In all cases, the inlet condition used is the pressure-corrected condition described in the previous section and the resulting mass flow rate remains approximately constant (Table C.8). In the unrealistic Case 1 (adiabatic vacuum chamber) the average static temperature in the chamber volume is too high and does not corresponds to reality. By applying T_{cw} = 293 K on the chamber wall (Case 2), the thrust evaluation increases by 12%. The effect of adding the top casing temperature profile is minor (Case 3), while in Case 4 the thrust increases of about 4%. Finally, by using temperature and velocity developed profiles from the full thruster model solution as inlet condition (Case 5), the calculated thrust decreases by 1.2%.

Table C.8. Effect of different boundary conditions of Cases (1-5) as thrust relative error with respect to the experimental value F = 32.7 mN (Test-14).

	Case 1	**Case 2**	**Case 3**	**Case 4**	**Case 5**
F [mN]	-27.76%	-18.97%	-18.21%	-14.82%	-15.88%
$\dot{m}$ [mg/s]	8.044	7.994	7.967	8.029	8.042

The calculated pressure on the top disk of the thruster is in general lower than the chamber pressure, contributing negatively to the thrust. In fact, from the standalone nozzle study (section C.2.1.2), where the thrust was overestimated by nearly 30%, this simulation outputs an underestimated thrust between -2.90% to -14.56% from the first to the last test. While the absolute error is reduced, the error direction is changed. Fig. 5.21 shows the chamber geometry and the Mach number scalar field

for Test-1 (cold gas) and Test-14 (I = 56.6 A). The latter is characterized by much lower Mach number at the exit, as well as by a larger divergence of the flow at the exit. In particular, the kinetic power lost in radial divergence, Eq.(C.12), is calculated as 0.97% and 2.01% of the total kinetic power, respectively. The stronger viscous effect in Test-14, determines that the portion of top casing of the thruster with pressure lower than the chamber pressure is wider (Fig. 5.22), leading to a larger negative effect on the calculated thrust.

$$P_{k,r} = 2\pi \int_0^{R_e} \rho w u^2 r dr \tag{C.12}$$

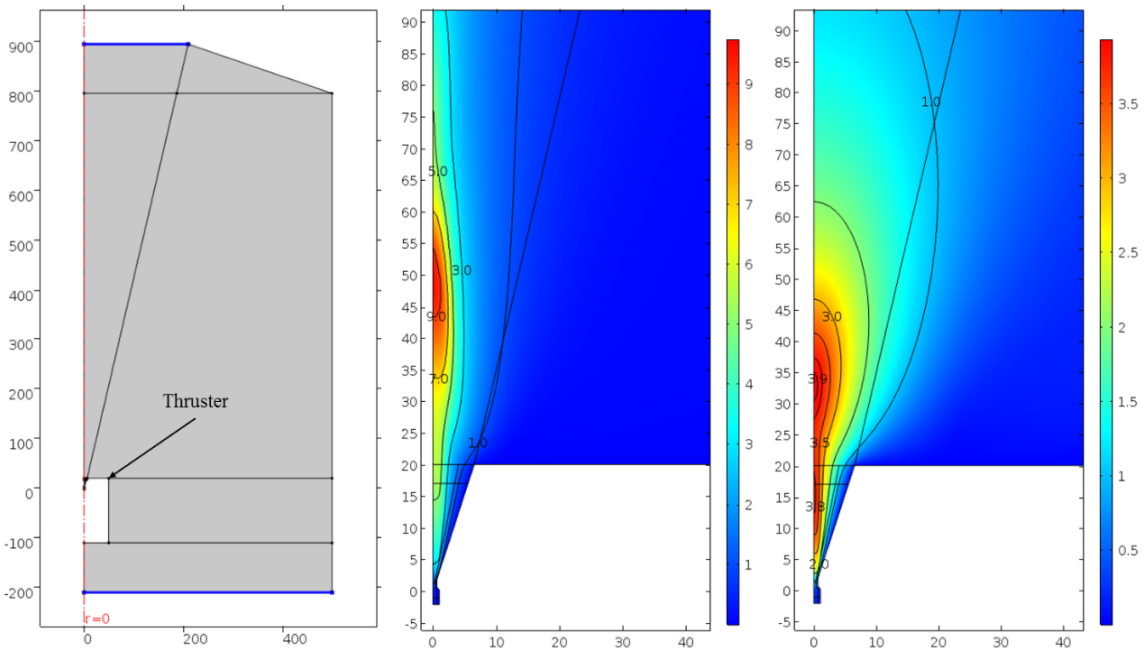

Fig. 5.21. Vacuum chamber geometry with outlet boundaries highlighted (left) and Mach number isocontour near the nozzle: Test-1 (center) and Test-14 (right).

C.2.1.4 Error analysis

A quantitative error analysis of the thrust numerical solution due to uncertainty on selected parameters is here shown. Sensitivity analysis is performed using the adjoint method, available within COMSOL, on the fourteen tests in examination. The objective function selected is the thrust, while the parameters selected, x_i, are composed by three geometrical terms and six thermodynamic terms. The geometrical parameters are the normal displacement of the inlet, d_i, throat, d_t, and diverging

section, d_d, boundaries. Neglecting correlations between these parameters or assuming that these are independent, the error propagation on the thrust is calculated as:

$$\Delta F = \sqrt{\sum_i^n \left(\frac{\partial F}{\partial x_i} \Delta x_i \right)^2} = \sqrt{\sum_i^n \left(\Delta F_i \right)^2} \tag{C.13}$$

where ΔF represents the uncertainty of the computational thrust, and the Δx_i the uncertainty of the selected variables. Since this estimation is based on a linearization of the thrust, it holds for small values of Δx_i.

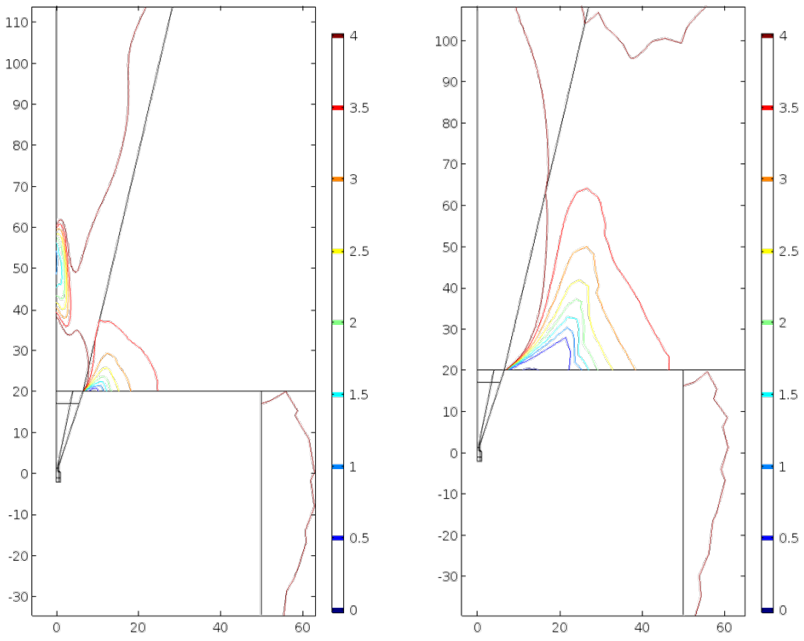

Fig. 5.22. Pressure isocontour for Test-1 (left) and Test-14 (right).

The parameters relative uncertainty $\Delta x_i / x_i$ is kept at 5% for quantities not directly measured in experiments. These are the geometrical displacements and the stagnation condition at the nozzle inlet. The first ones are all set to $\Delta d_i = 42$ μm, which gives a maximum thrust relative uncertainty with respect to geometric variations of 5% among all tests. Whilst the thruster inlet pressure and temperature are directly measured, their values at the nozzle inlet are unknown, therefore their relative uncertainty is set to 5%. For the remaining parameters (T_{09}, T_n, p_c and T_c), the experiment measurement accuracy available is used [31]. The resulting uncertainty of the computed thrust is

shown in Fig. 5.23 in the form of error bars. Table C.9 shows that calculated partial derivatives of thrust with respect to all parameters selected for the last test, where the calculated thrust uncertainty is $\Delta F_{14} = \pm 2.57$ mN. The total thrust uncertainty, $\Delta F/F$, is under 9.5% for all tests.

It has to be noted that the mass flow rate is sensitive to the same list of parameters. In particular, thrust and mass flow rate are proportional, and observing the sensitivity of the mass flow rate with respect to the same parameters, it can be seen that its relative uncertainty is on the same order of magnitude and with same signs. For this reason, the relative error between computational and measured thrust, also reflects a similar error in mass flow rate. It is evident that the solution is highly sensitive to small geometric variation of the nozzle, and, as expected, to the stagnation condition at the nozzle inlet.

Table C.9. List of partial derivatives of thrust with respect to selected variables for the sensitivity analysis (example with Test-14).

	$\frac{\partial F}{\partial d_i}$	$\frac{\partial F}{\partial d_t}$	$\frac{\partial F}{\partial d_d}$	$\frac{\partial F}{\partial T_t}$	$\frac{\partial F}{\partial p_t}$	$\frac{\partial F}{\partial T_{09}}$	$\frac{\partial F}{\partial T_n}$	$\frac{\partial F}{\partial p_c}$	$\frac{\partial F}{\partial T_c}$
	[N/m]	[N/m]	[N/m]	[N/K]	[N/Pa]	[N/K]	[N/m]	[N/Pa]	[N/K]
Value	19.386	39.959	2.07	-5.16×10-6	1.25×10-6	-3.07×10-6	1.71×10-6	-7.72×10-4	-2.72×10-6
ΔF_i [mN]	1.018	1.309	0.678	-3.95×10-1	1.80	-1.15×10-2	8.41×10-3	-1.00×10-2	-3.98×10-2

C.2.1.5 Result and Discussion

The computational thrust diverges from the experiment as the stagnation pressure and temperature increase (from the first to the last test). It is argued that the continuum flow hypothesis loses validity for lower Reynolds numbers, or equally higher Knudsen number. The relative error of the computational thrust with respect to the experiments goes from -2.9% at test 1 to -14.6% in the final test. One possibility is that the no-slip hypothesis on the nozzle diverging section close to the exit is not satisfied, therefore a velocity slip could be present [65]. The effect of a slip flow for a low Reynolds number nozzle is not in itself detrimental, and the resulting skin friction and heat transfer generally decrease, leading to greater expansion [125]. This behavior would agree with the underestimation of thrust for lower Reynolds numbers (Fig. 5.23). Instead of a continuum gas dynamics assumption modelled by full N-S equations, low Reynolds number nozzles could be better modelled by Direct

Simulation Monte Carlo (DSMC) in the molecular gas dynamics assumption [66,122,126]. In conclusion, it is possible that the lower Reynolds number tests solved with N-S have overestimated boundary layer thickness, while DSMC could determine a thinner one and, as a consequence, a higher average Mach number at the exit, hence higher thrust.

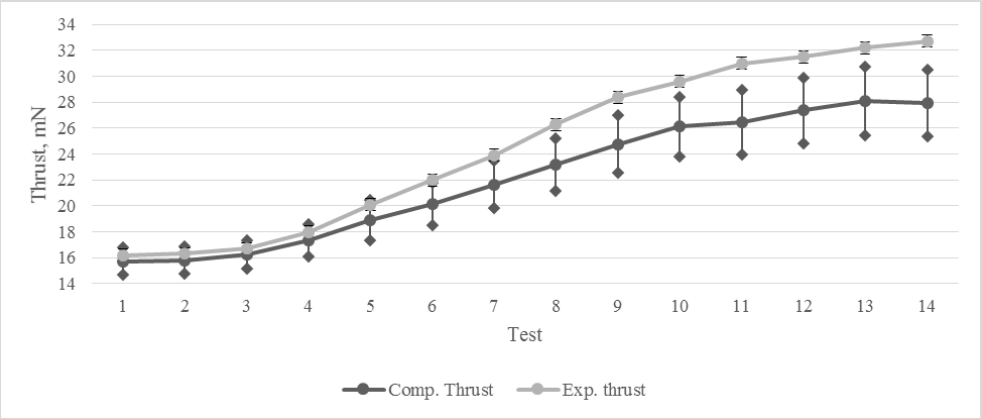

Fig. 5.23. Computed and experimental thrust for the fourteen tests in analysis, with error bars of measurement (from thrust balance measurement accuracy) and model (from sensitivity analysis).

C.2.2 Complete thruster model

Whilst the nozzle model can, within the limits discussed above, predict the thrust for a given inlet stagnation condition ($p_{t,n}$, $T_{t,n}$), the full thruster model could deepen the knowledge of the engine behavior in parts otherwise not accessible for direct measurement. A validation of such model will form the basis for design optimization of the HTR in development. In section C.2.1, the nozzle has been analysed showing a possible limit in the assumption of a continuum flow for the lower Reynolds number regimes analyzed. However, the N-S equations are valid within the heat exchanger, where the subsonic flow determines negligible Knudsen numbers. Since the fluidic solution of the nozzle diverging section only depends on its inlet stagnation conditions, a necessary condition for the full thruster model to be valid, is that the stagnation pressure and temperature solution at nozzle inlet are as expected. The full thruster solution can be compared to experiments through a set of available direct measurements (Fig. 5.24), which include inlet pressure and temperature measured at the propellant inlet tube, (T_i, p_i), electric potential and current at the heater terminals, (V,I), a set of temperatures measured through thermocouples, T_j, and the maximum structural temperature, T_m, measured with an optical pyrometer looking into the nozzle throat.

C.2.2.1 Materials and Geometry

The J3 resistojet thruster is modelled here with its main components, including: concentric tubular heat exchanger, nozzle, thermal insulation package, ceramic electric insulators, low emissivity casing and radiation shield composed by thin low-emissivity foils. Fairly complete information on the materials name and grade and geometry for all of the components of the J3 resistojet can be found in [31,46,63,67]. For the modelling, materials are selected from the COMSOL library apart from the fibrous ceramic insulators of the thermal insulation package, such as Dyna-quartz (innermost insulation block) and Min-K2000 (outer insulation block). The thermal conductivity of these fibrous ceramic insulators are found in [49] and [127] respectively. The stainless steel surface emissivity of the resistojet case is given as temperature independent (ε = 0.08), while the high temperature electric insulators are made of boron nitride (grade HP), with assumed constant thermal conductivity of 28 W/(mK).

As described in Section 2.2.5.1, four heating tubes compose the main heater, while two 2 mm thick tubes form the cold inflow annular flow path of the heat exchanger. The nominal thickness of the four heater tubes from the innermost outwards are: 0.70 mm, 0.165 mm, 0.125 mm and 0.40 mm. It is also known that the struts thickness is 1 mm, the nozzle diverging section thickness is 0.7 mm, the nozzle disk (where the thermocouple T_n is placed) is 1.5 mm thick and the radiation shield foils are 0.025 mm thick. The remaining dimensions have been deduced from a detailed thruster assembly diagram found in xxx. A 2D axisymmetric geometry has been drawn in Solidworks as shown in Fig. 5.24, where the thruster sketch is highlighted and the image used for the reproduction is shown below. The geometry is exported as .DXF and manually optimized for COMSOL computation. The inlet and outlet boundaries and the computational probes utilized to compare the thermocouple measurements are also shown.

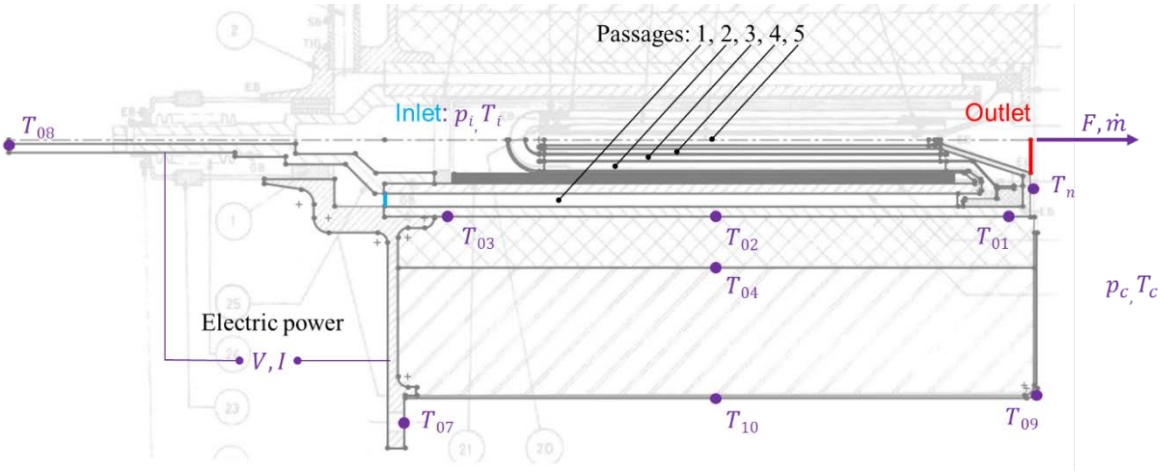

Fig. 5.24. J3 resistojet drawings with direct experimental measurement in purple, inlet and outlet boundary conditions highlighted and numbered concentric tubular heat exchanger annular passages.

C.2.2.2 Problem Definitions and Mesh

In the heat exchanger, and more in general for relatively high stagnation pressures, the continuum flow assumption is always valid, so it is the condition of no slip at the heat exchanger surface xxx. The physics interfaces used within COMSOL for the J3 resistojet simulation are HMNF and Electric Current (EC). The first couples the laminar flow interface, applied to compressible flow, with the heat transfer interface. The second one models the Joule heating within the heater elements. The flow is laminar and the inlet stagnation conditions ($p_{0,i}$, $T_{0,i}$ and $M_{0,i}$) are applied as shown in section C.2.1.1. The outlet boundary condition is imposed on the nozzle exit area, using a hybrid flow (not forcing a supersonic nozzle exit) and setting the static pressure of the vacuum chamber, p_c, in the same way of the single nozzle study. Surface-to-surface radiation is applied on the internal wall boundaries of the whole heat exchanger and nozzle. For the approximation of the form factors, the hemicube method is used with default values. The surface-to-ambient radiation boundaries include the thruster back plate surface and the stainless steel low-emissivity case.

The EC interface is coupled in temperature with the HMNF. The rhenium electrical conductivity is given as a polynomial function of the temperature in the material library. As an initial value, the heat exchanger is at 0 V potential. Because there is only one dependent variable in EC (the potential V), it is sufficient to apply the experimental terminal current I as boundary condition on the four concentric resistive elements independently. The mesh is tailored by refining the flow channels with a structured mesh, while a free triangular mesh is used for the solid domains. The nozzle is meshed as in the section C.2.1.1, as shown in Fig. 5.25 (left). A computational grid

convergence study has not been conducted in this case. Nonetheless, a relatively coarse mesh has been used to investigate on the nonlinear behavior of this multiphysics simulation and the results are accurate in the measure that the mass flow rate is conserved within 1% between the inlet and the outlet boundaries.

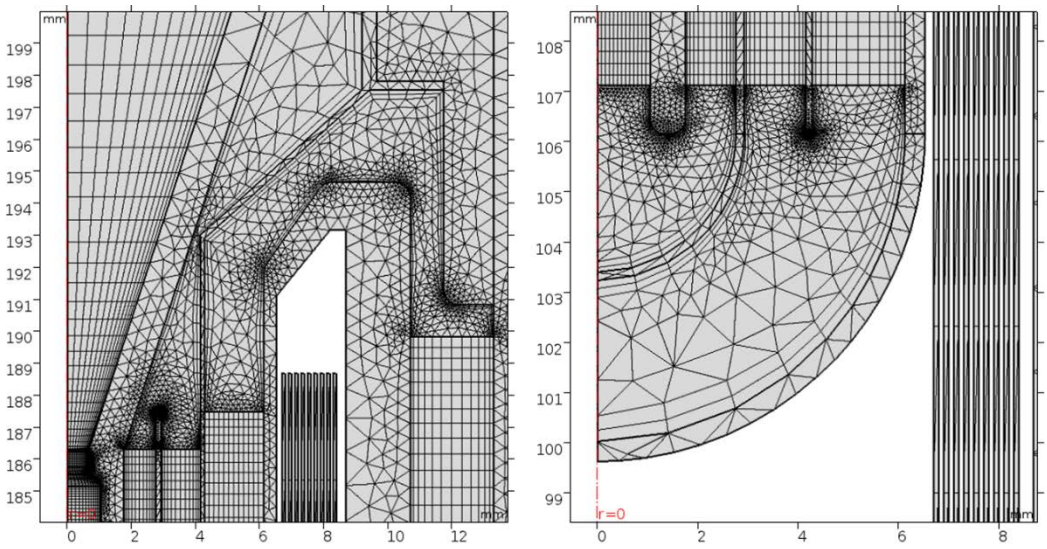

Fig. 5.25. Computational grid of J3 thruster: nozzle region (left) and elbow region (right) (axis units in mm).

C.2.3 Results and Discussion

It this section, the multiphysics simulation results on the Test-14 conditions and at the thruster design point are shown and discussed. Table C.10 shows the relative error of the multiphysics solution with respect to the experimental direct measurements and to the expected stagnation condition at the nozzle inlet, $p_{0,n}$ and $T_{0,n}$. The electrical current is a model input, and its value has been chosen by trial and error to obtain a small relative error of the mass flow rate. The thermocouple computational probes show a good agreement all over the engine, with greater underestimation of the temperatures at the nozzle top disk, T_n, and at the inlet of the thruster, $T_{01} - T_{03}$. The former could derive by an overall underestimation of the temperature at the nozzle inlet, $T_{0,n}$, while the latter could be due to the geometric simplification at the bottom of the thruster. Fig. 5.26 shows the solution of the multiphysics problem as electric potential of the heater in V (left) and the temperature distribution in K for both the fluid and solid domains (right). Table C.11 shows the relative errors of the multiphysics solution of the thruster at its design point as compared with experimental data, where thermocouple measurements are not provided. In this case, the computational electric current is taken equal to experimental one.

Table C.10. Relative error of the solution with respect to experimental values of Test-14.

I	V	P_e	$T_{t,n}$	$p_{t,n}$	$\dot{m}$	T_m	T_n
-7.00%	1.21%	-5.88%	-5.86%	-1.74%	-1.77%	-0.88%	-22.13%
T_{01}	T_{02}	T_{03}	T_{04}	T_{07}	T_{08}	T_{09}	T_{10}
-6.68%	-16.56%	-27.50%	-0.39%	-3.22%	3.91%	-8.57%	0.94%

Table C.11. Relative error of the solution with respect to experimental values at design point (I = 208 A).

V	P_e	R	$T_{t,n}$	$p_{t,n}$	$\dot{m}$	T_m
9.05%	9.29%	9.32%	3.2%	0.77%	-9.64%	-0.6%

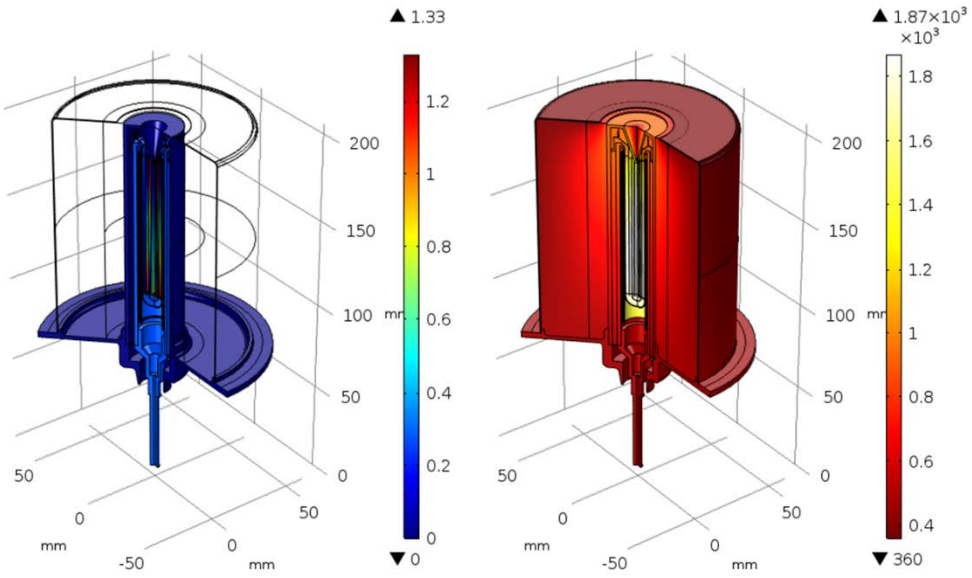

Fig. 5.26. Simulation results on Test-14: heater electric potential in V (left) and thermal solution in K (right) (axis units in mm).

The total thruster efficiency can be calculated using Eq.(1.11), where for Test-14 $P_k = \dot{m}w^2/2 =$ 78.1 W is the axial kinetic power of the jet, $P_e =$ 181.7 W is the total electric power as sum of the voltage-current products of the four heater tubes and $P_{i,p} =$ 43.3 W is the propellant inlet power. When the electric power is zero, this equation can also be used to calculate the efficiency in cold gas mode.

The current simulation determines a total thruster efficiency of 29.8%, taking into consideration the axial kinetic power evaluated with the single nozzle study (Section C.2.1), where the vacuum chamber influence on the thruster body is taken into account. The total efficiency can also be broken down into two parts, the nozzle efficiency, $\eta_n = P_k/P_{0,n}$, and the heat exchanger efficiency, $\eta_h = P_{0,n}/(P_e + P_{i,p})$, where the simulation provides $P_{0,n} = \dot{m}h_{t,n} = 199.2$ W, for resulting efficiencies of $\eta_n = 39.2\%$ and $\eta_h = 88.5\%$ and pressure drop $p_d = p_i - p_{0,n} = 14.552$ kPa.

Fig. 5.27 shows the temperature distribution evaluated at the centerline of the concentric tubular heat exchanger passages up to the nozzle exit, where the static temperature drops (passage 5). The graph highlights the not-ideal behavior of the J3 heat exchanger, which rather should rise the temperature of the propellant monotonically, so that the energy is stored as more internally as possible and thermal losses are reduced to a minimum. Instead, in the Test-14 analyzed the maximum temperature is achieved already after the first recirculation (passage 2), whilst it decreases at the following one (passage 3) to increase again at the next one (passage 4). As Fig. 5.26 shows, the heat exchanger develops a higher temperature at the back end of the thruster, where $T_m = 1{,}870$ K for Test-14. The temperature distribution at the design mass flow rate shows a better functionality of the J3 engine, however still with a temperature decay in channel 3.

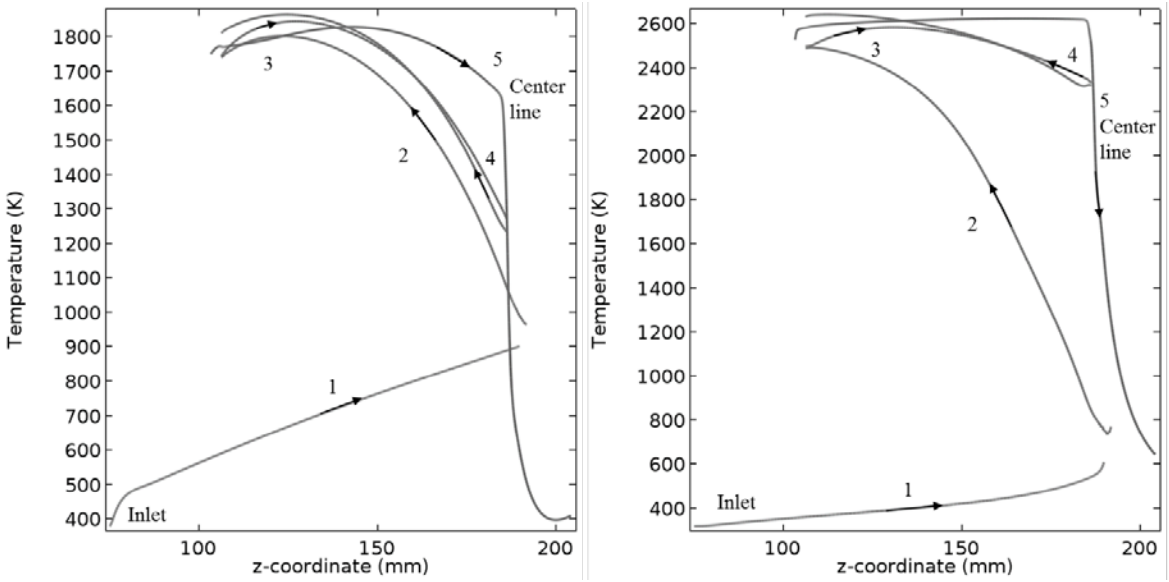

Fig. 5.27. Temperature distribution at the center lines of the heat exchanger passages (numbered): Test-14 (left) and J3 at design point (right).

The full thruster simulation here shown agrees fairly well globally. Nevertheless, some temperature probes suggest that either some physical or geometrical assumptions must be reevaluated for better agreement. It has to be noted that the problem of non-linearity makes the solution very sensitive to the geometry. As an example, the mass flow rate is determined by the stagnation enthalpy at the inlet of the nozzle), which stems from the pressure drop across the heat exchanger. The pressure drop depends on the hydraulic diameters of the heat exchanger annular channels and the local electric power dissipation of the heater tubes depends on their section area. Unfortunately, the annular gaps between the tubular elements are unknown. Future work within the J3 thruster study could include a global parametrization of the thruster geometry within certain tolerances to investigate on a broader sensitivity analysis. The results on the J3 thruster also indicates that the concentric tubular heat exchanger design could be optimized in terms of power dissipation. In particular, the heater tubes thickness could vary along the flow path to enable heat transfer optimization.

Appendix D Technical Drawings

In this Appendix, the most relevant technical drawings to this work are reported. The attached drawings are not to scale (original pdf files are available in the dataset). In summary, the drawings package includes (drawings number in square brackets):

- AM manufactured components with title corresponding to the SolidWorks filename (see Table 4.3) [1-8, 11-12];
- STAR-0 assembly exploded view and details [9-10];
- Custom ceramics components of the STAR-0 assembly [13-24];
- Post-manufacturing instructions and final dimensions of the AM Heat Exchanger and Thruster Inflow components [25-28];
- CNC machined components of the STAR-0 assembly [29-30];
- Design of the Ga power terminal [31-35];
- Design of the FGSE [36-41].

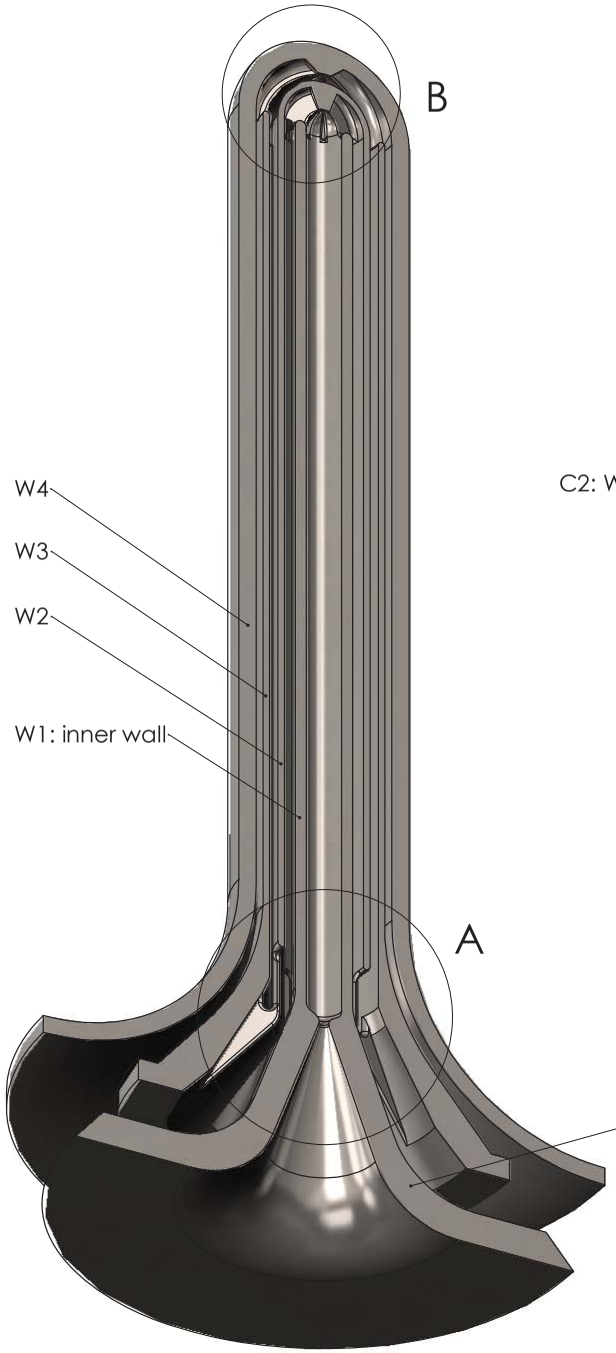

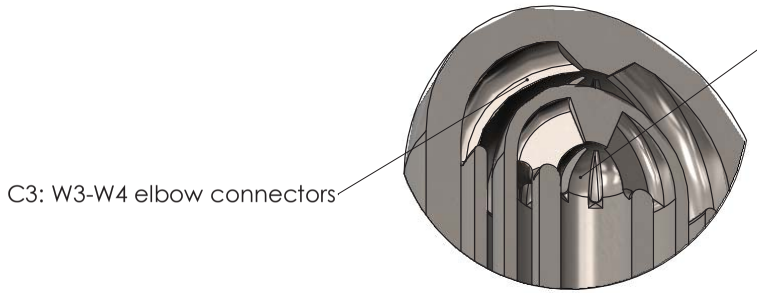

DETAIL B
SCALE 10 : 1

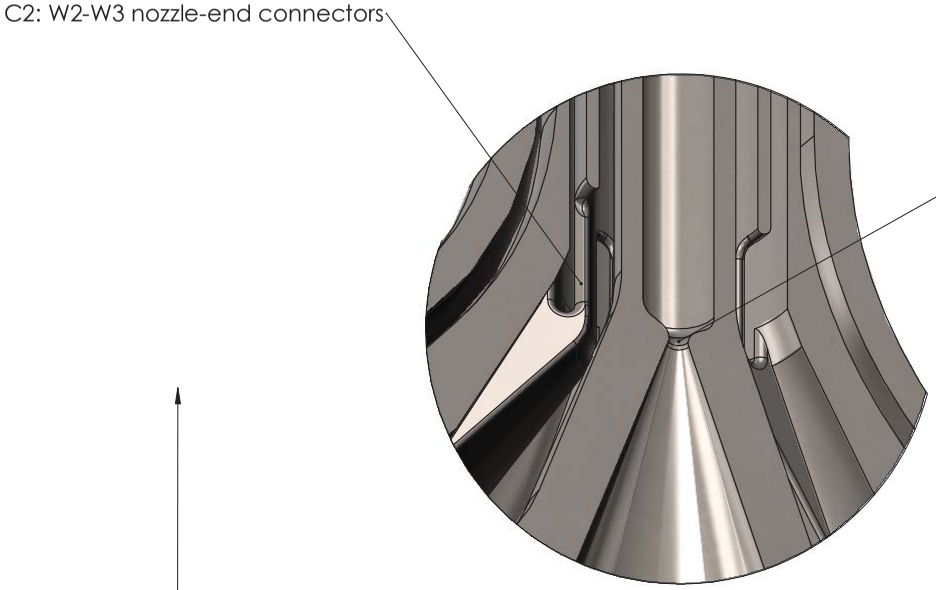

DETAIL A
SCALE 10 : 1

Printing direction

DO NOT SCALE		DRAWN AND DESIGNED BY: F Romei		TOLERANCES UNLESS OTHERWISE STATED: LINEAR X = +/- 0.20, XX = +/- 0.10, XXX = +/- 0.05; ANGULAR +/- 0.50; ALL DIMENSIONS IN mm UNLESS OTHERWISE STATED	UNIVERSITY OF Southampton, Faculty of Engineering and the Environment
A3		APPROVED BY: GT Roberts			
EDMC JOB No: 1	DEPARTMENT: Astronautics	DATE: 22/07/2015	SCALE: 5:1		TITLE: full_heat_exchanger
PROJECT: VHTR	SUPERVISORS: AN Grubisic, GT Roberts	MATERIAL: Stainless Steel	TEXTURE	SURFACE FINISH: ALL OVER UNLESS OTHERWISE STATED	
REMOVE ALL SHARP EDGES		THE INFORMATION CONTAINED IN THIS DOCUMENT IS THE PROPERTY OF THE UNIVERSITY OF SOUTHAMPTON DO NOT COPY WITHOUT WRITTEN PERMISSION.		SHEET: 1 of 2	No OFF / ASSEMBLY NUMBER / DRAWING NUMBER: 1 of 7 / REVISION: 1
IF IN DOUBT PLEASE ASK					

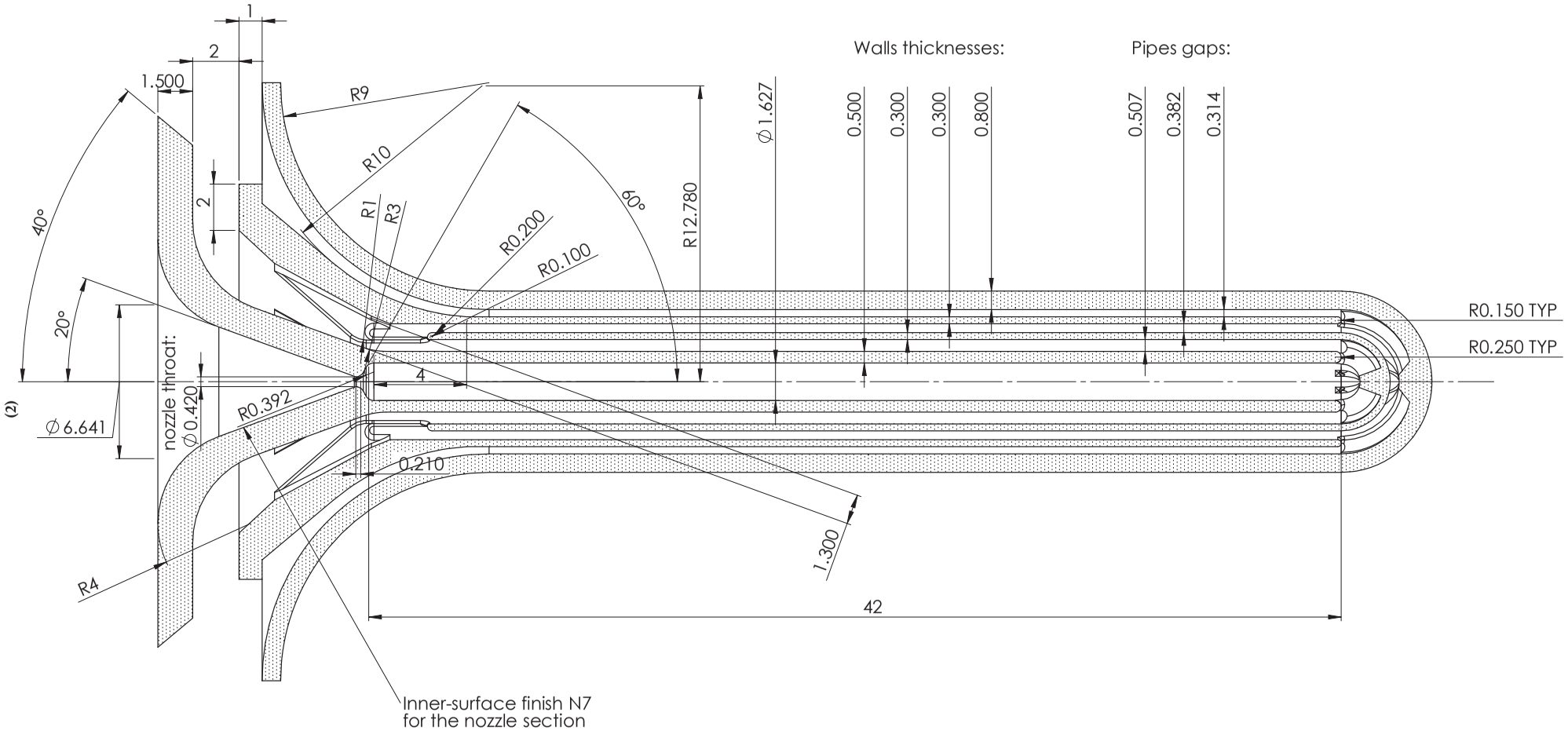

DO NOT SCALE		DRAWN AND DESIGNED BY: F Romei		TOLERANCES UNLESS OTHERWISE STATED: LINEAR X = +/- 0.20, XX = +/- 0.10, XXX = +/- 0.05; ANGULAR +/- 0.50; ALL DIMENSIONS IN mm UNLESS OTHERWISE STATED	UNIVERSITY OF Southampton, Faculty of Engineering and the Environment
A3		APPROVED BY: GT Roberts			
EDMC JOB No: 1	DEPARTMENT: Astronautics	DATE: 22/07/2015	SCALE: 6:1		TITLE: full_heat_exchanger
PROJECT: VHTR	SUPERVISORS: AN Grubisic, GT Roberts	MATERIAL: Stainless Steel	TEXTURE	SURFACE FINISH: ALL OVER UNLESS OTHERWISE STATED	
REMOVE ALL SHARP EDGES		THE INFORMATION CONTAINED IN THIS DOCUMENT IS THE PROPERTY OF THE UNIVERSITY OF SOUTHAMPTON DO NOT COPY WITHOUT WRITTEN PERMISSION.		SHEET: 2 of 2	No OFF	ASSEMBLY NUMBER	DRAWING NUMBER: 1 of 7	REVISION: 1
IF IN DOUBT PLEASE ASK					

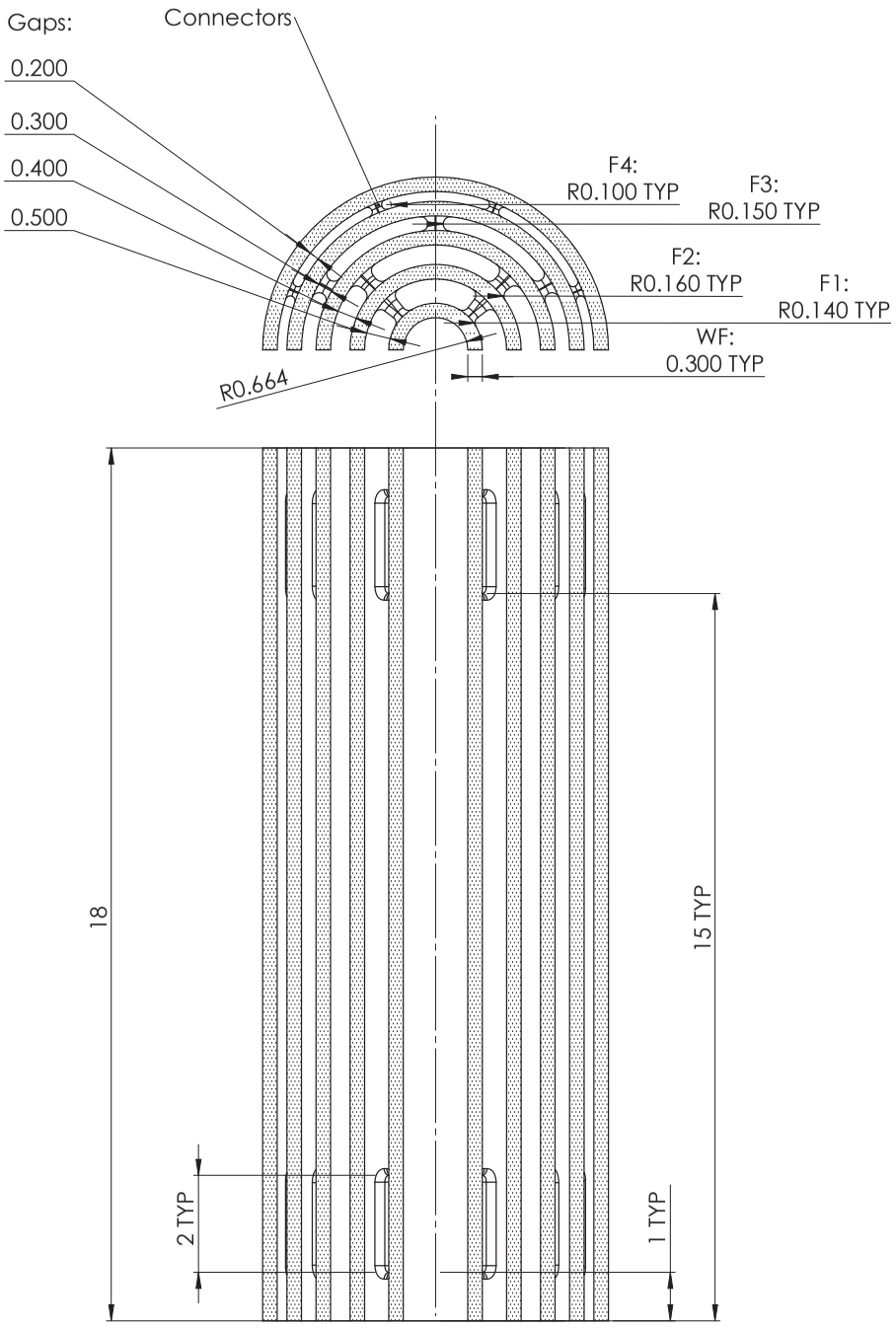

file	WF	F1	F2	F3	F4
walls_and_connectors_300u	0.300	0.140	0.160	0.150	0.100
walls_and_connectors_200u	0.200	0.120	0.140	0.140	0.090
walls_and_connectors_100u	0.100	0.100	0.130	0.120	0.080
walls_and_connectors_80u	0.080	0.100	0.120	0.110	0.070
walls_and_connectors_50u	0.050	0.100	0.120	0.110	0.070

(3)

DO NOT SCALE		DRAWN AND DESIGNED BY: F Romei		TOLERANCES UNLESS OTHERWISE STATED: LINEAR X = +/- 0.20, XX = +/- 0.10, XXX = +/- 0.05; ANGULAR +/- 0.50; ALL DIMENSIONS IN mm UNLESS OTHERWISE STATED	UNIVERSITY OF Southampton, Faculty of Engineering and the Environment
A3		APPROVED BY: GT Roberts			
EDMC JOB No: 1	DEPARTMENT: Astronautics	DATE: 22/07/2015	SCALE: 10:1		TITLE: walls_and_connectors_300u
PROJECT: VHTR	SUPERVISORS: AN Grubisic, GT Roberts	MATERIAL: Stainless Steel	TEXTURE	SURFACE FINISH: ALL OVER UNLESS OTHERWISE STATED	
REMOVE ALL SHARP EDGES		THE INFORMATION CONTAINED IN THIS DOCUMENT IS THE PROPERTY OF THE UNIVERSITY OF SOUTHAMPTON DO NOT COPY WITHOUT WRITTEN PERMISSION.		SHEET: 1 of 1	No OFF / ASSEMBLY NUMBER / DRAWING NUMBER: 2 of 7 / REVISION: 1
IF IN DOUBT PLEASE ASK					

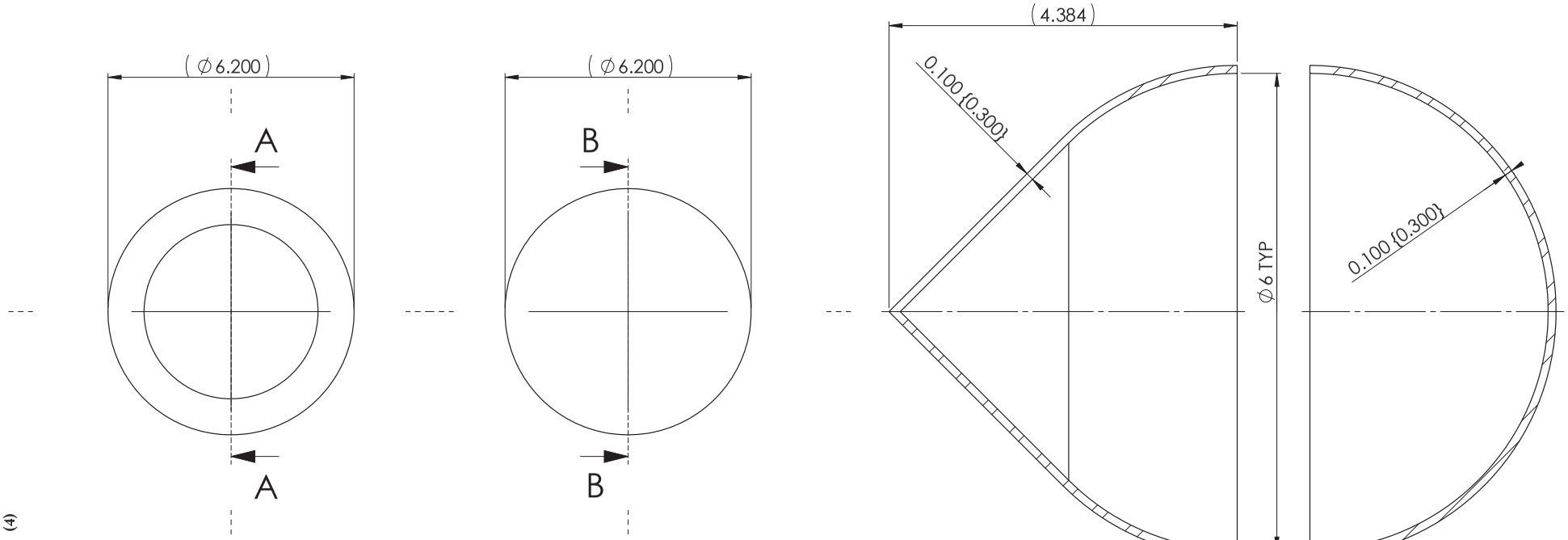

SECTION A-A
SCALE 20 : 1

SECTION B-B
SCALE 20 : 1

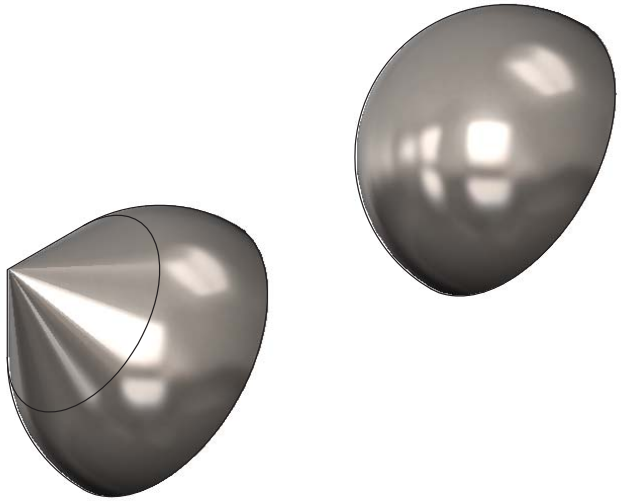

NOTE:
"elbow_300u.SLDPRT" has same dimansions but a bigger wall thickness marked in curly brakets {.}

DO NOT SCALE		DRAWN AND DESIGNED BY: F Romei		TOLERANCES UNLESS OTHERWISE STATED: LINEAR X = +/- 0.20, XX = +/- 0.10, XXX = +/- 0.05; ANGULAR +/- 0.50; ALL DIMENSIONS IN mm UNLESS OTHERWISE STATED	UNIVERSITY OF Southampton, Faculty of Engineering and the Environment
A3		APPROVED BY: GT Roberts			
EDMC JOB No: 1	DEPARTMENT: Astronautics	DATE: 22/07/2015	SCALE: 10:1		TITLE: elbows_100u
PROJECT: VHTR	SUPERVISORS: AN Grubisic, GT Roberts	MATERIAL: Stainless Steel	TEXTURE	SURFACE FINISH: ALL OVER UNLESS OTHERWISE STATED	
REMOVE ALL SHARP EDGES		THE INFORMATION CONTAINED IN THIS DOCUMENT IS THE PROPERTY OF THE UNIVERSITY OF SOUTHAMPTON. DO NOT COPY WITHOUT WRITTEN PERMISSION.		SHEET: 1 of 1	No OFF / ASSEMBLY NUMBER / DRAWING NUMBER: 3 of 7 / REVISION: 1
IF IN DOUBT PLEASE ASK					

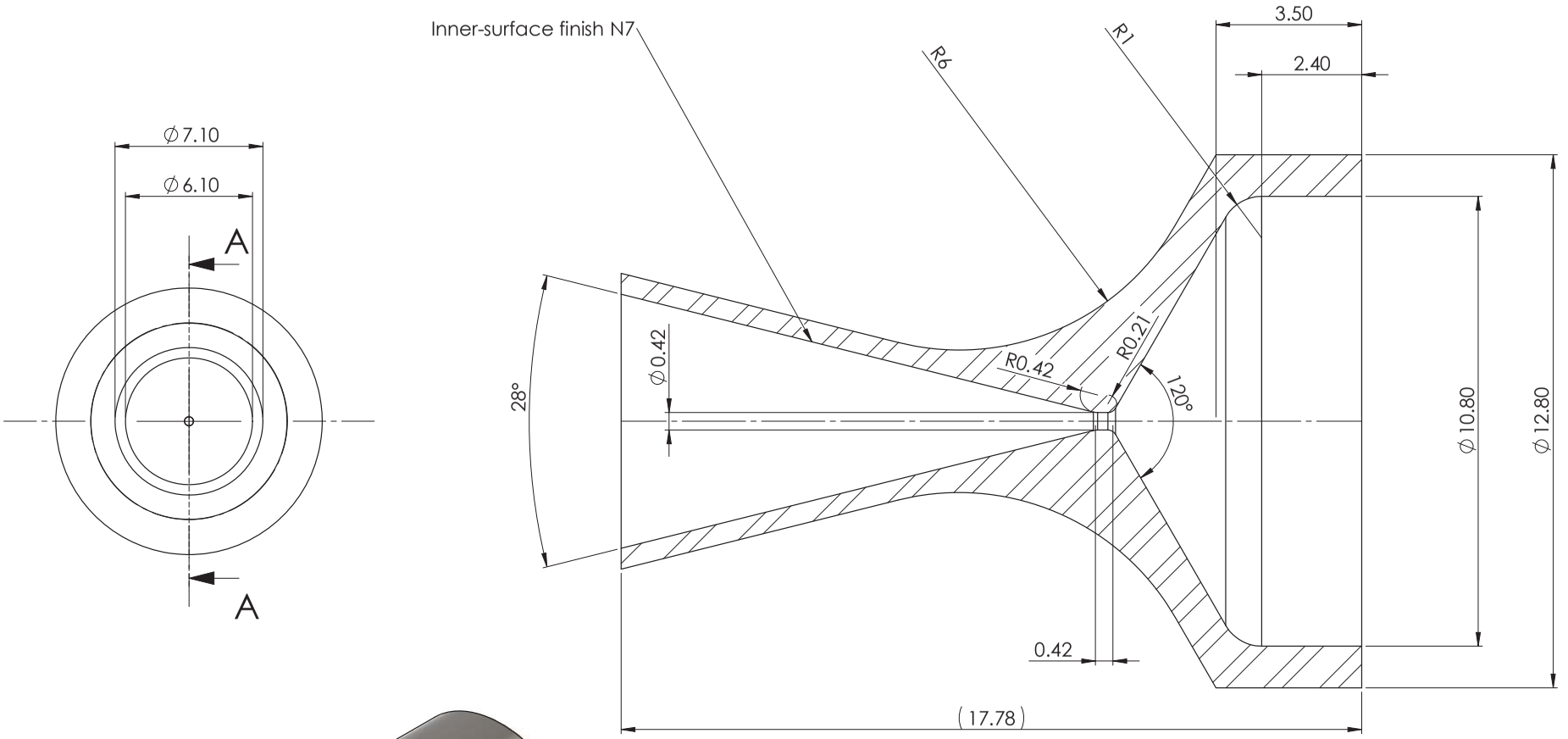

SECTION A-A

SCALE 10 : 1

DO NOT SCALE		DRAWN AND DESIGNED BY F Romei		TOLERANCES UNLESS OTHERWISE STATED LINEAR X = +/- 0.20 XX = +/- 0.10 XXX = +/- 0.05 ANGULAR +/- 0.50 ALL DIMENSIONS IN mm UNLESS OTHERWISE STATED	UNIVERSITY OF Southampton Faculty of Engineering and the Environment
A3		APPROVED BY GT Roberts			TITLE nozzle_T50
EDMC JOB No 1	DEPARTMENT Astronautics	DATE 22/07/2015	SCALE 5:1		
PROJECT VHTR	SUPERVISORS AN Grubisic GT Roberts	MATERIAL Stainless Steel	TEXTURE	SURFACE FINISH ALL OVER UNLESS OTHERWISE STATED	
REMOVE ALL SHARP EDGES		THE INFORMATION CONTAINED IN THIS DOCUMENT IS THE PROPERTY OF THE UNIVERSITY OF SOUTHAMPTON DO NOT COPY WITHOUT WRITTEN PERMISSION.		SHEET 1 of 1	No OFF / ASSEMBLY NUMBER / DRAWING NUMBER 4 of 7 / REVISION 1
IF IN DOUBT PLEASE ASK					

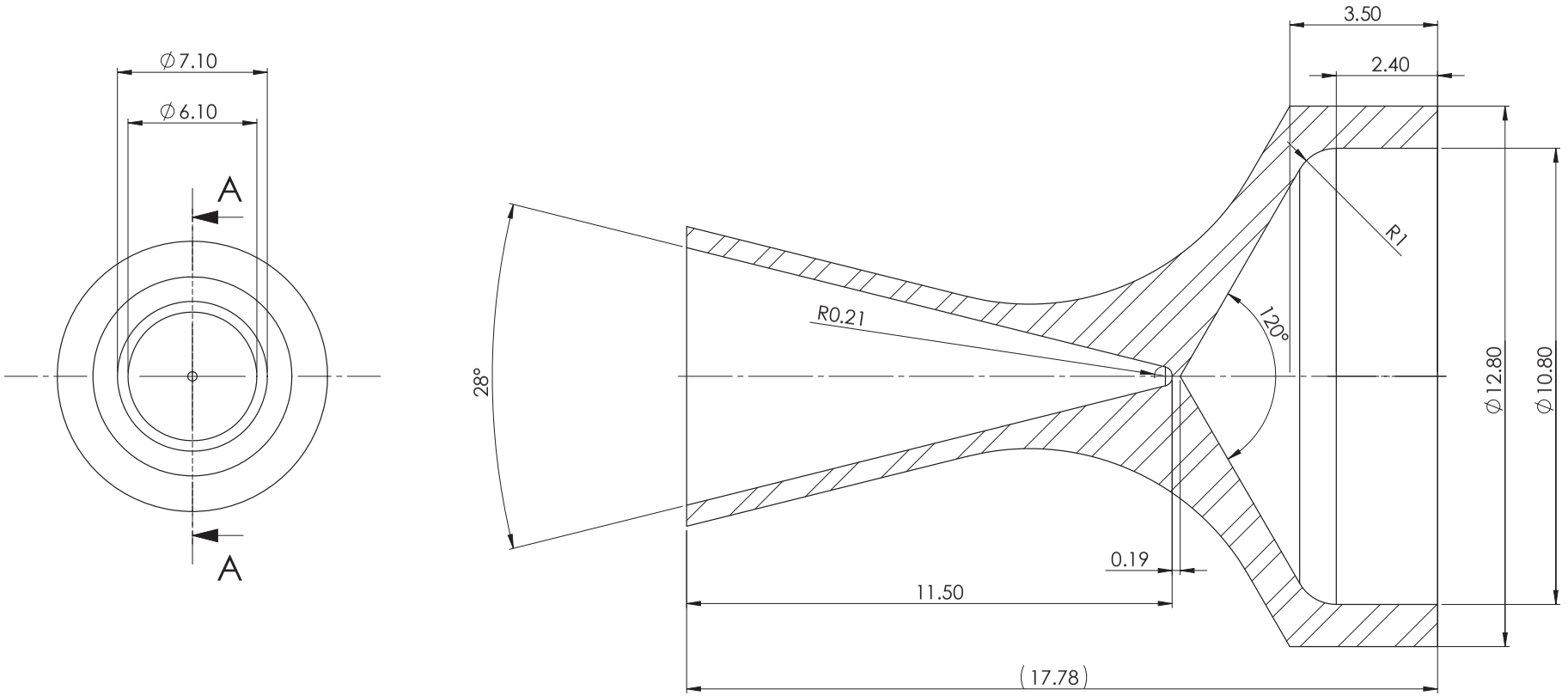

(6)

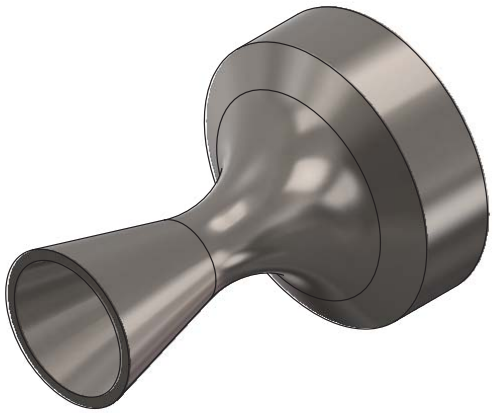

SECTION A-A

SCALE 10 : 1

DO NOT SCALE		DRAWN AND DESIGNED BY: F Romei		TOLERANCES UNLESS OTHERWISE STATED: LINEAR X = +/- 0.20, XX = +/- 0.10, XXX = +/- 0.05; ANGULAR +/- 0.50; ALL DIMENSIONS IN mm UNLESS OTHERWISE STATED	UNIVERSITY OF Southampton, Faculty of Engineering and the Environment
A3		APPROVED BY: GT Roberts			
EDMC JOB No: 1	DEPARTMENT: Astronautics	DATE: 22/07/2015	SCALE: 5:1		TITLE: nozzle_T50_full
PROJECT: VHTR	SUPERVISORS: AN Grubisic, GT Roberts	MATERIAL: Stainless Steel	TEXTURE	SURFACE FINISH: ALL OVER UNLESS OTHERWISE STATED	
REMOVE ALL SHARP EDGES		THE INFORMATION CONTAINED IN THIS DOCUMENT IS THE PROPERTY OF THE UNIVERSITY OF SOUTHAMPTON DO NOT COPY WITHOUT WRITTEN PERMISSION.		SHEET: 1 of 1	No OFF / ASSEMBLY NUMBER / DRAWING NUMBER: 5 of 7 / REVISION: 1
IF IN DOUBT PLEASE ASK					

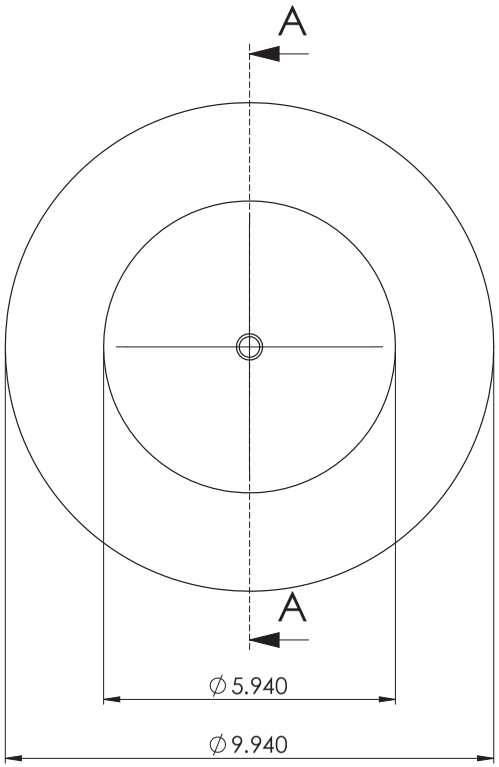

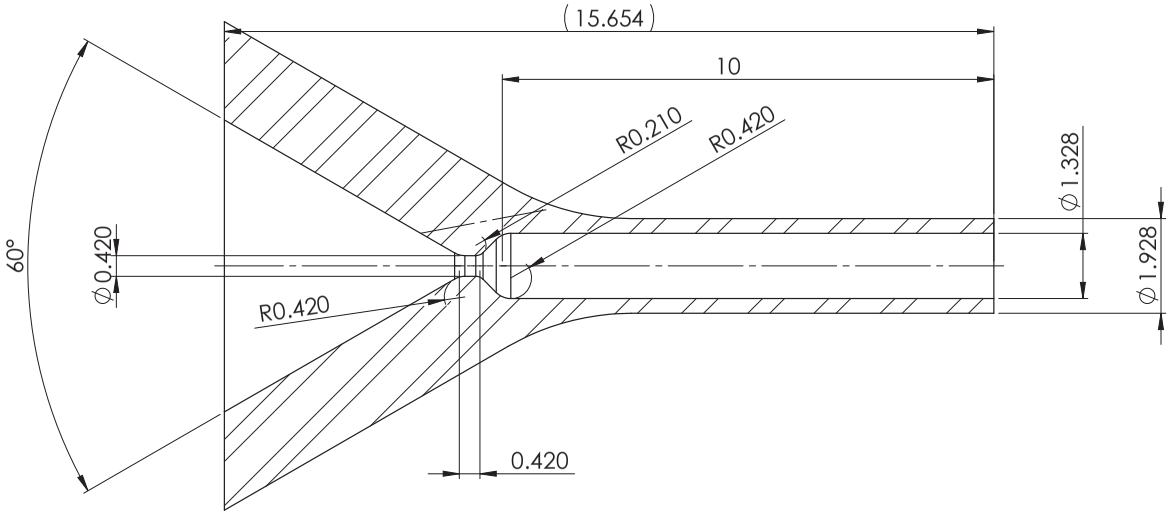

SECTION A-A

DO NOT SCALE		DRAWN AND DESIGNED BY: F Romei		TOLERANCES UNLESS OTHERWISE STATED: LINEAR X = +/- 0.20, XX = +/- 0.10, XXX = +/- 0.05; ANGULAR +/- 0.50; ALL DIMENSIONS IN mm UNLESS OTHERWISE STATED	UNIVERSITY OF Southampton, Faculty of Engineering and the Environment
A3		APPROVED BY: GT Roberts			
EDMC JOB No: 1	DEPARTMENT: Astronautics	DATE: 22/07/2015	SCALE: 10:1		TITLE: nozzle_30deg
PROJECT: VHTR	SUPERVISORS: AN Grubisic, GT Roberts	MATERIAL: Stainless Steel	TEXTURE	SURFACE FINISH: ALL OVER UNLESS OTHERWISE STATED	
REMOVE ALL SHARP EDGES		THE INFORMATION CONTAINED IN THIS DOCUMENT IS THE PROPERTY OF THE UNIVERSITY OF SOUTHAMPTON DO NOT COPY WITHOUT WRITTEN PERMISSION.		SHEET: 1 of 1	No OFF / ASSEMBLY NUMBER / DRAWING NUMBER: 6 of 7 / REVISION: 1
IF IN DOUBT PLEASE ASK					

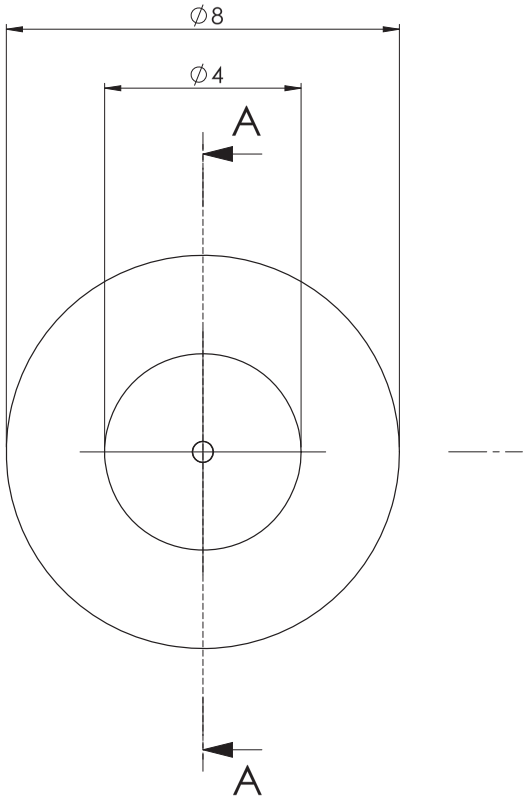

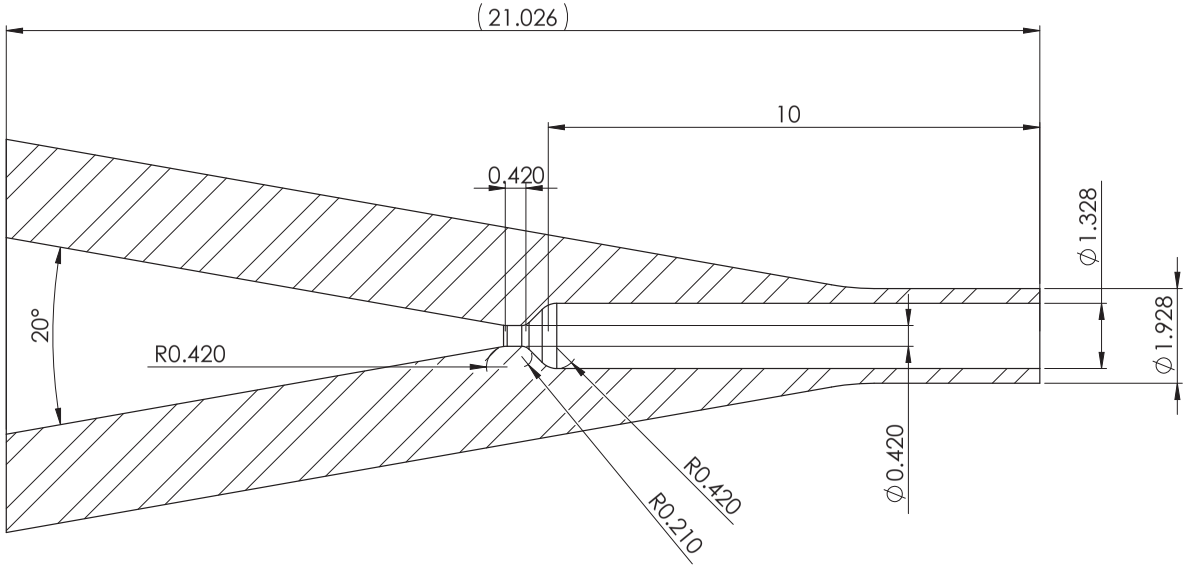

SECTION A-A

SCALE 10 : 1

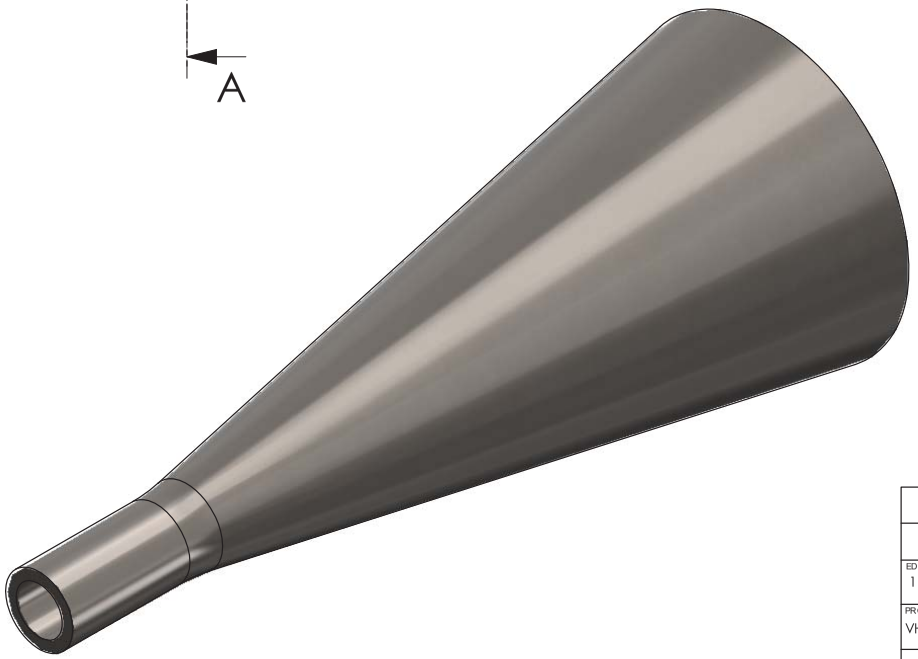

(8)

DO NOT SCALE		DRAWN AND DESIGNED BY: F Romei		TOLERANCES UNLESS OTHERWISE STATED: LINEAR X = +/- 0.20, XX = +/- 0.10, XXX = +/- 0.05; ANGULAR +/- 0.50; ALL DIMENSIONS IN mm UNLESS OTHERWISE STATED	UNIVERSITY OF Southampton, Faculty of Engineering and the Environment
A3		APPROVED BY: GT Roberts			
EDMC JOB No: 1	DEPARTMENT: Astronautics	DATE: 22/07/2015	SCALE: 10:1		TITLE: nozzle_10deg
PROJECT: VHTR	SUPERVISORS: AN Grubisic, GT Roberts	MATERIAL: Stainless Steel	TEXTURE	SURFACE FINISH: ALL OVER UNLESS OTHERWISE STATED	
REMOVE ALL SHARP EDGES		THE INFORMATION CONTAINED IN THIS DOCUMENT IS THE PROPERTY OF THE UNIVERSITY OF SOUTHAMPTON DO NOT COPY WITHOUT WRITTEN PERMISSION.			SHEET: 1 of 1 | No OFF | ASSEMBLY NUMBER | DRAWING NUMBER: 7 of 7 | REVISION: 1
IF IN DOUBT PLEASE ASK					

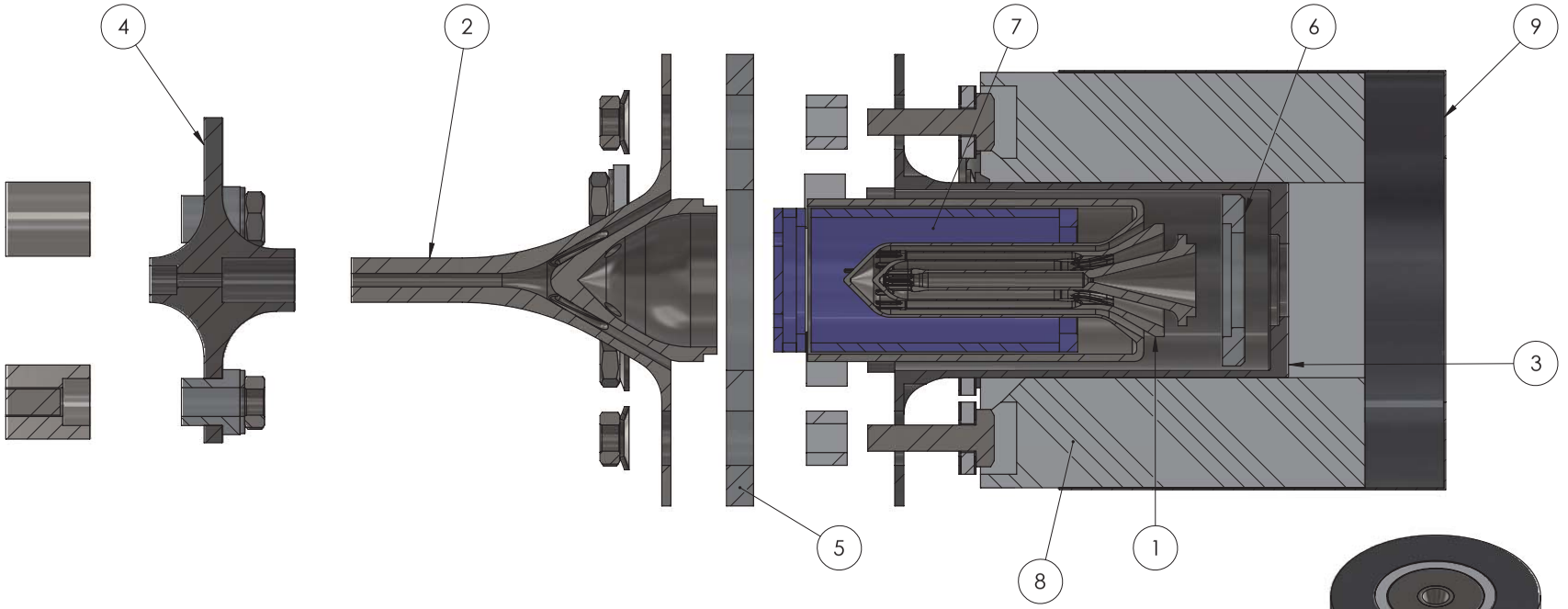

VHTR manufacturing at EDMC				
Item #	Name	Material	Manufacturer	Notes
1	Heat Exchanger	316L	EDMC	AM Metal Printer + lathe post manufacturing
2	Thruster Inflow	316L	EDMC	AM Metal Printer + lathe post manufacturing
3	Thruster Casing	316L	EDMC	CNC machining
4	Thruster Support	316L	EDMC	CNC machining
5	Collar	Alumina	-	-
6	Nozzle Spacer	Shapal	-	-
7	Radiation Shielding Assembly	Shapal	-	-
8	Insulation Package	Porous Ceramic	-	-
9	Thruster Casing	Metal Foil	-	-

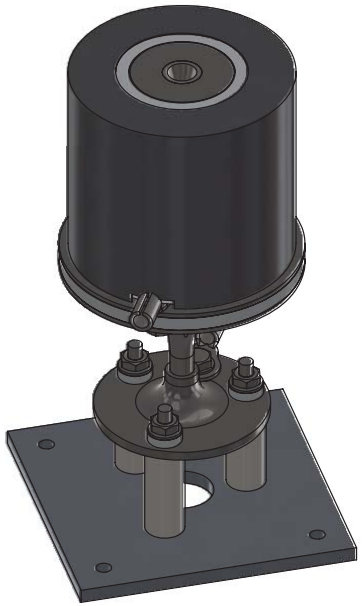

(9)

DO NOT SCALE | A3 | DRAWN AND DESIGNED BY: F Romei | APPROVED BY: AN Grubisic | TOLERANCES UNLESS OTHERWISE STATED: LINEAR X = +/- 0.20, XX = +/- 0.10, XXX = +/- 0.05; ANGULAR +/- 0.50; ALL DIMENSIONS IN mm UNLESS OTHERWISE STATED

JOB No | DEPARTMENT: Astronautics | DATE: 07/11/2017 | SCALE: 2:1

PROJECT: VHTR | SUPERVISORS: AN Grubisic | MATERIAL: 316L | TEXTURE | SURFACE FINISH: ALL OVER UNLESS OTHERWISE STATED

REMOVE ALL SHARP EDGES | IF IN DOUBT PLEASE ASK

UNIVERSITY OF Southampton
Faculty of Engineering and the Environment

TITLE: VHTR assembly

SHEET	No OFF	ASSEMBLY NUMBER	DRAWING NUMBER	REVISION
1 of 3			1 of 1	1

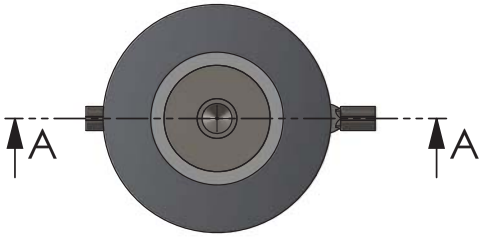

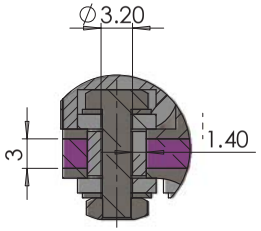

DETAIL C
SCALE 2 : 1

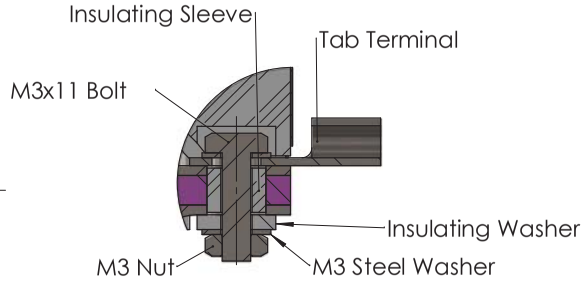

DETAIL D
SCALE 2 : 1

HE_v3 23-09-16

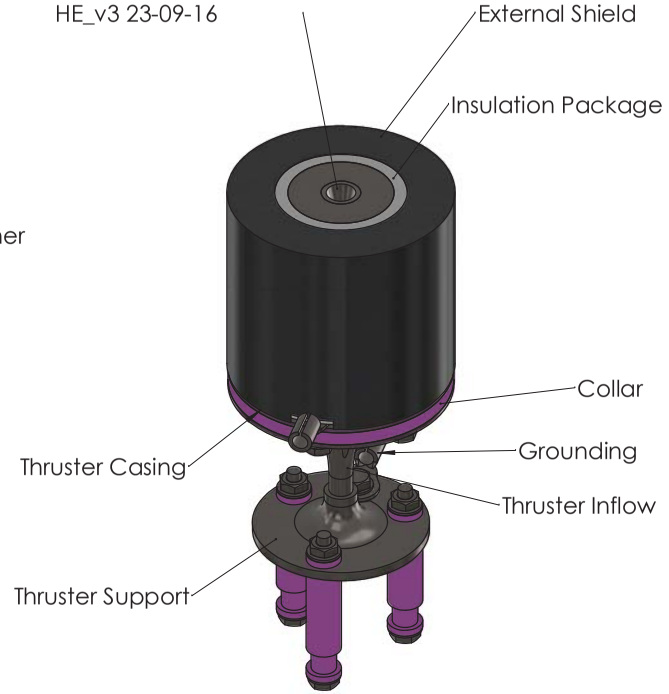

(10)

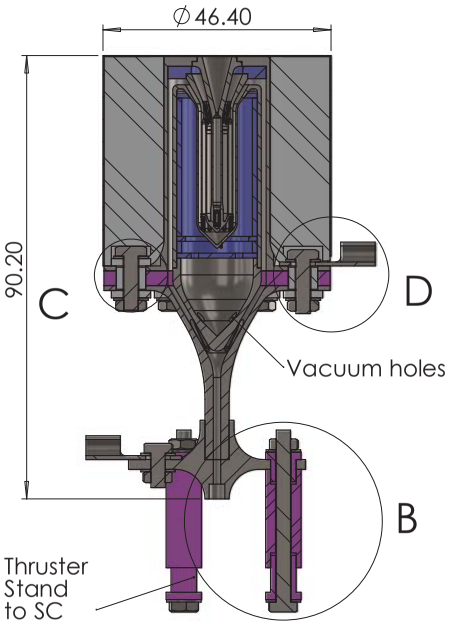

SECTION A-A

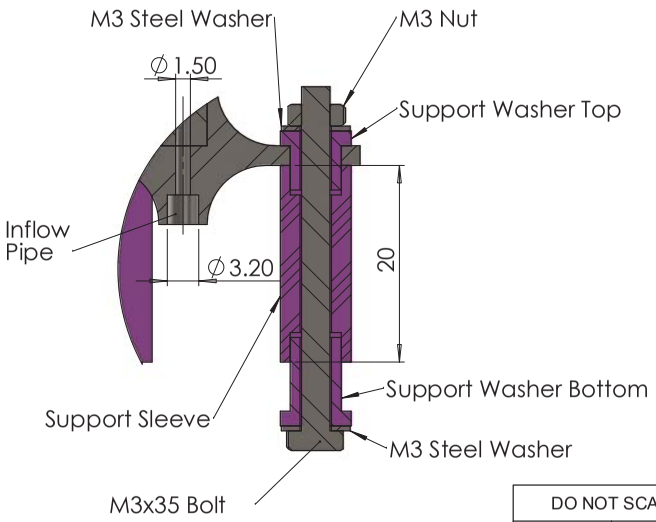

DETAIL B
SCALE 2 : 1

DO NOT SCALE		DRAWN AND DESIGNED BY: F Romei		TOLERANCES UNLESS OTHERWISE STATED: LINEAR X = +/- 0.20, XX = +/- 0.10, XXX = +/- 0.05; ANGULAR +/- 0.50	UNIVERSITY OF Southampton
A3		APPROVED BY: AN Grubisic			Faculty of Engineering and the Environment
EDMC JOB No: 3	DEPARTMENT: VHTR	DATE: 24/10/2016	SCALE: 1:1	ALL DIMENSIONS IN mm UNLESS OTHERWISE STATED	TITLE: STAR-0 assembly REV02 v2 - details
PROJECT: VHTR	SUPERVISORS: AN Grubisic, GT Roberts	MATERIAL	TEXTURE	SURFACE FINISH: ALL OVER UNLESS OTHERWISE STATED	
REMOVE ALL SHARP EDGES		THE INFORMATION CONTAINED IN THIS DOCUMENT IS THE PROPERTY OF THE UNIVERSITY OF SOUTHAMPTON DO NOT COPY WITHOUT WRITTEN PERMISSION.		SHEET: 2 of 2	No OFF	ASSEMBLY NUMBER	DRAWING NUMBER: 1 of 1	REVISION: 2
IF IN DOUBT PLEASE ASK					

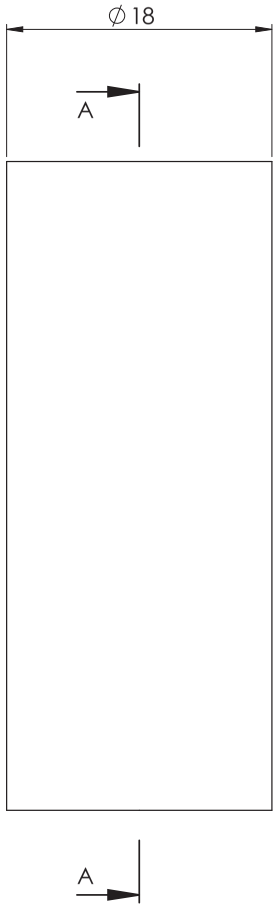

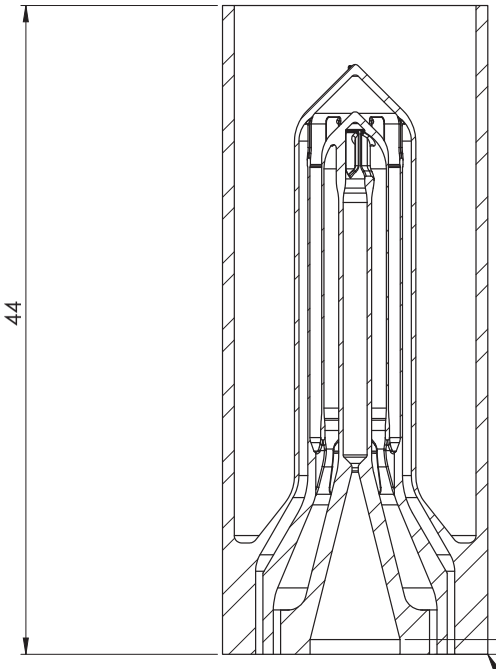

SECTION A-A

NOTE: EDM wire cut to be performed at 1mm from print base plate

DO NOT SCALE		DRAWN AND DESIGNED BY: FRomei		TOLERANCES UNLESS OTHERWISE STATED: LINEAR X = +/- 0.20, XX = +/- 0.10, XXX = +/- 0.05; ANGULAR +/- 0.50; ALL DIMENSIONS IN mm UNLESS OTHERWISE STATED	UNIVERSITY OF Southampton
A3		APPROVED BY: AN Grubisic			Faculty of Engineering and the Environment
JOB No	DEPARTMENT: Astronautics	DATE: 30/10/2017	SCALE: 3:1		TITLE: Heat Exchanger (v3.1 and v3.2)
PROJECT: VHTR	SUPERVISORS: AN Grubisic	MATERIAL: 316L SLM	TEXTURE	SURFACE FINISH: ALL OVER UNLESS OTHERWISE STATED	
REMOVE ALL SHARP EDGES		THE INFORMATION CONTAINED IN THIS DOCUMENT IS THE PROPERTY OF THE UNIVERSITY OF SOUTHAMPTON DO NOT COPY WITHOUT WRITTEN PERMISSION.		SHEET: 1 of 2 / No OFF: 6 / ASSEMBLY NUMBER / DRAWING NUMBER: 1 of 1	REVISION: 1
IF IN DOUBT PLEASE ASK					

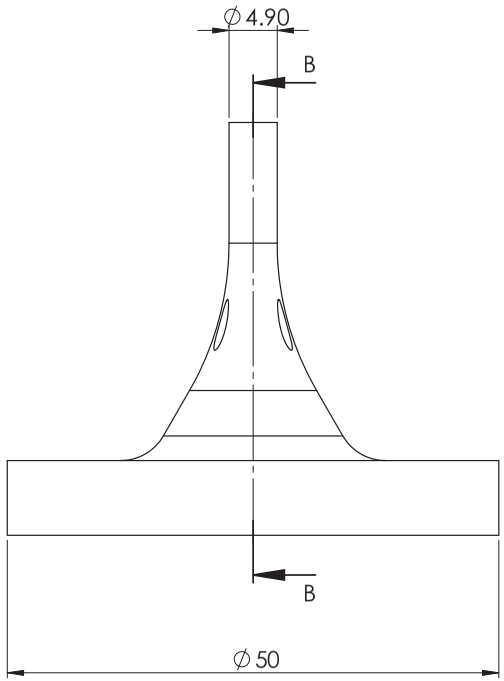

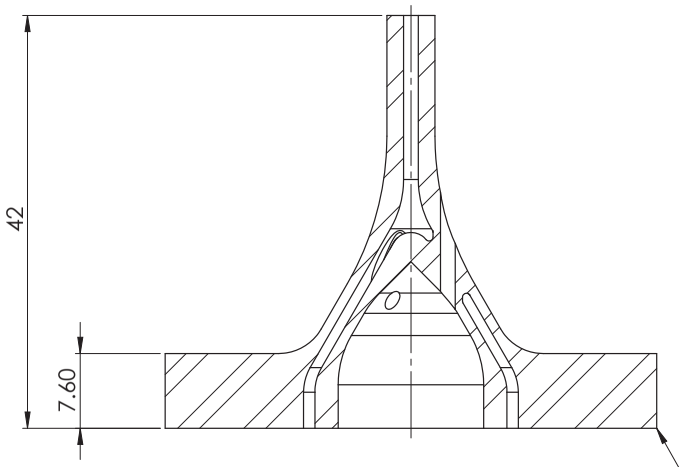

SECTION B-B

NOTE: EDM wire cut to be performed at 1mm from print base plate

(12)

Print Direction

DO NOT SCALE		DRAWN AND DESIGNED BY FRomei		TOLERANCES UNLESS OTHERWISE STATED	UNIVERSITY OF Southampton
A3		APPROVED BY AN Grubisic		LINEAR X = +/- 0.20, XX = +/- 0.10, XXX = +/- 0.05; ANGULAR +/- 0.50; ALL DIMENSIONS IN mm UNLESS OTHERWISE STATED	Faculty of Engineering and the Environment
JOB No	DEPARTMENT Astronautics	DATE 30/10/2017	SCALE 2:1		TITLE Thruster Inflow
PROJECT VHTR	SUPERVISORS AN Grubisic	MATERIAL 316L SLM	TEXTURE	SURFACE FINISH ALL OVER UNLESS OTHERWISE STATED	
REMOVE ALL SHARP EDGES		THE INFORMATION CONTAINED IN THIS DOCUMENT IS THE PROPERTY OF THE UNIVERSITY OF SOUTHAMPTON DO NOT COPY WITHOUT WRITTEN PERMISSION.		SHEET 2 of 2	No OFF 6	ASSEMBLY NUMBER	DRAWING NUMBER 1 of 1	REVISION 1
IF IN DOUBT PLEASE ASK					

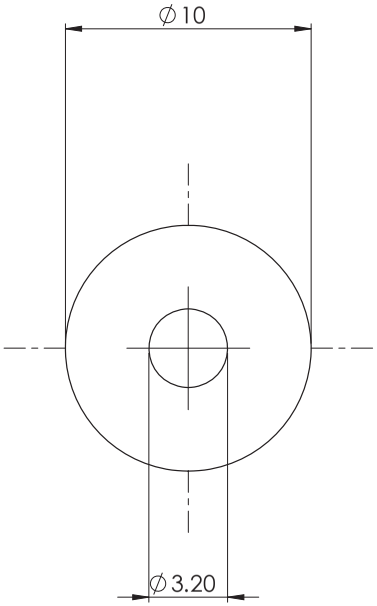

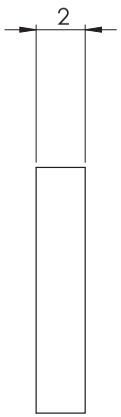

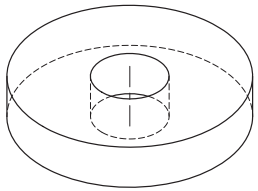

(13)

DO NOT SCALE		DRAWN AND DESIGNED BY F Romei		TOLERANCES UNLESS OTHERWISE STATED	UNIVERSITY OF Southampton
A3		APPROVED BY AN Grubisic		LINEAR X = +/- 0.20 XX = +/- 0.10 XXX = +/- 0.05 ANGULAR +/- 0.50	Faculty of Engineering and the Environment
JOB No	DEPARTMENT Astronautics	DATE 07/11/2017	SCALE 5:1	ALL DIMENSIONS IN mm UNLESS OTHERWISE STATED	TITLE Washer
PROJECT VHTR	SUPERVISORS AN Grubisic	MATERIAL Alumina 99.7%	TEXTURE	SURFACE FINISH ALL OVER UNLESS OTHERWISE STATED	
REMOVE ALL SHARP EDGES		THE INFORMATION CONTAINED IN THIS DOCUMENT IS THE PROPERTY OF THE UNIVERSITY OF SOUTHAMPTON DO NOT COPY WITHOUT WRITTEN PERMISSION.		SHEET 1 of 11	No OFF 16	ASSEMBLY NUMBER	DRAWING NUMBER 1 of 1	REVISION 4
IF IN DOUBT PLEASE ASK					

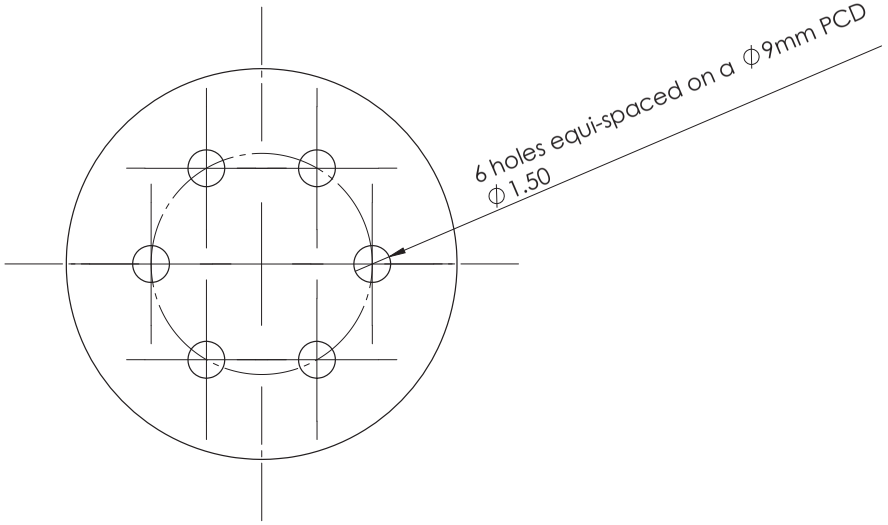

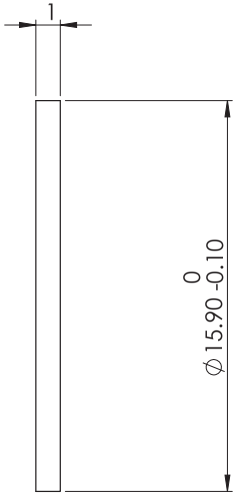

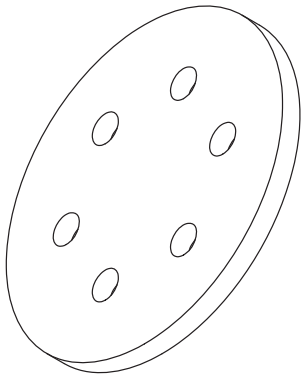

(14)

DO NOT SCALE		DRAWN AND DESIGNED BY: F Romei		TOLERANCES UNLESS OTHERWISE STATED: LINEAR .X = +/-0.20, .XX = +/- 0.10, .XXX = +/-0.05; ANGULAR +/-0.50; ALL DIMENSIONS IN mm UNLESS OTHERWISE STATED	UNIVERSITY OF Southampton Faculty of Engineering and the Environment
A3		APPROVED BY: AN Grubisic			
JOB No	DEPARTMENT: Astronautics	DATE: 07/11/2017	SCALE: 5:1		TITLE: Disk Bottom Insulator
PROJECT: VHTR	SUPERVISORS: AN Grubisic	MATERIAL: Shapal	TEXTURE	SURFACE FINISH: ALL OVER UNLESS OTHERWISE STATED	
REMOVE ALL SHARP EDGES IF IN DOUBT PLEASE ASK		THE INFORMATION CONTAINED IN THIS DOCUMENT IS THE PROPERTY OF THE UNIVERSITY OF SOUTHAMPTON DO NOT COPY WITHOUT WRITTEN PERMISSION.			

SHEET	No OFF	ASSEMBLY NUMBER	DRAWING NUMBER	REVISION
2 of 11	3		1 of 1	4

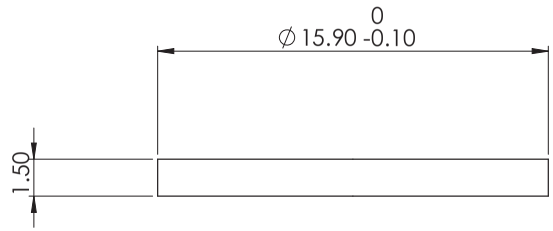

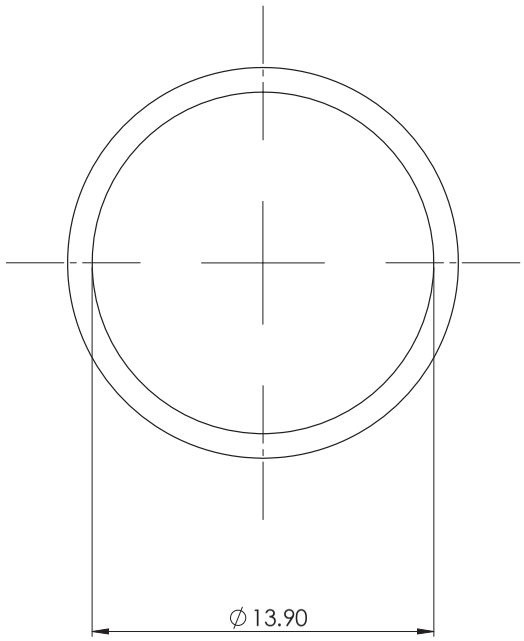

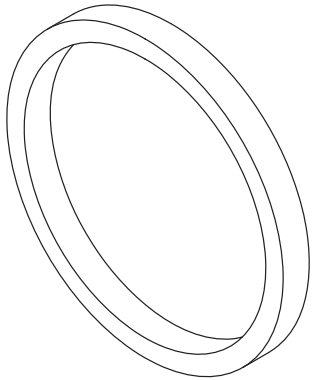

(15)

DO NOT SCALE		DRAWN AND DESIGNED BY F Romei		TOLERANCES UNLESS OTHERWISE STATED LINEAR X = +/- 0.20 XX = +/- 0.10 XXX = +/- 0.05 ANGULAR +/- 0.50 ALL DIMENSIONS IN mm UNLESS OTHERWISE STATED	UNIVERSITY OF Southampton Faculty of Engineering and the Environment
A3		APPROVED BY AN Grubisic			TITLE: Disk Pipe Insulator
JOB No	DEPARTMENT Astronautics	DATE 07/11/2017	SCALE 5:1		
PROJECT VHTR	SUPERVISORS AN Grubisic	MATERIAL Shapal	TEXTURE	SURFACE FINISH ALL OVER UNLESS OTHERWISE STATED	
REMOVE ALL SHARP EDGES IF IN DOUBT PLEASE ASK		THE INFORMATION CONTAINED IN THIS DOCUMENT IS THE PROPERTY OF THE UNIVERSITY OF SOUTHAMPTON DO NOT COPY WITHOUT WRITTEN PERMISSION.			SHEET 3 of 11 | No OFF 3 | ASSEMBLY NUMBER | DRAWING NUMBER 1 of 1 | REVISION 4

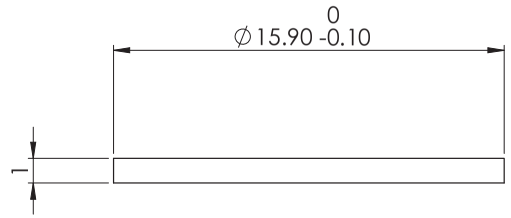

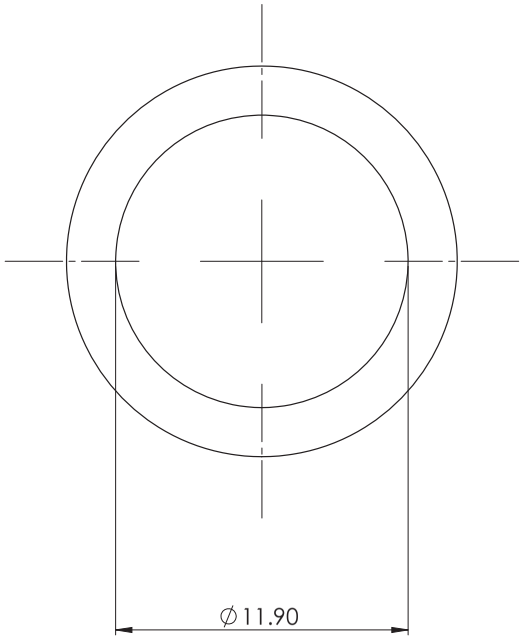

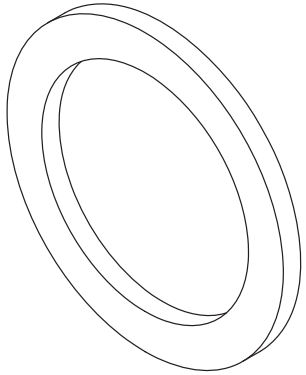

(16)

DO NOT SCALE		DRAWN AND DESIGNED BY: F Romei		TOLERANCES UNLESS OTHERWISE STATED: LINEAR X = +/- 0.20, XX = +/- 0.10, XXX = +/- 0.05; ANGULAR +/- 0.50; ALL DIMENSIONS IN mm UNLESS OTHERWISE STATED	UNIVERSITY OF Southampton
A3		APPROVED BY: AN Grubisic			Faculty of Engineering and the Environment
JOB No	DEPARTMENT: Astronautics	DATE: 07/11/2017	SCALE: 5:1		TITLE: Disk Top Insulator
PROJECT: VHTR	SUPERVISORS: AN Grubisic	MATERIAL: Shapal	TEXTURE	SURFACE FINISH: ALL OVER UNLESS OTHERWISE STATED	
REMOVE ALL SHARP EDGES		THE INFORMATION CONTAINED IN THIS DOCUMENT IS THE PROPERTY OF THE UNIVERSITY OF SOUTHAMPTON DO NOT COPY WITHOUT WRITTEN PERMISSION.		SHEET: 4 of 11	No OFF: 3 / ASSEMBLY NUMBER / DRAWING NUMBER: 1 of 1 / REVISION: 4
IF IN DOUBT PLEASE ASK					

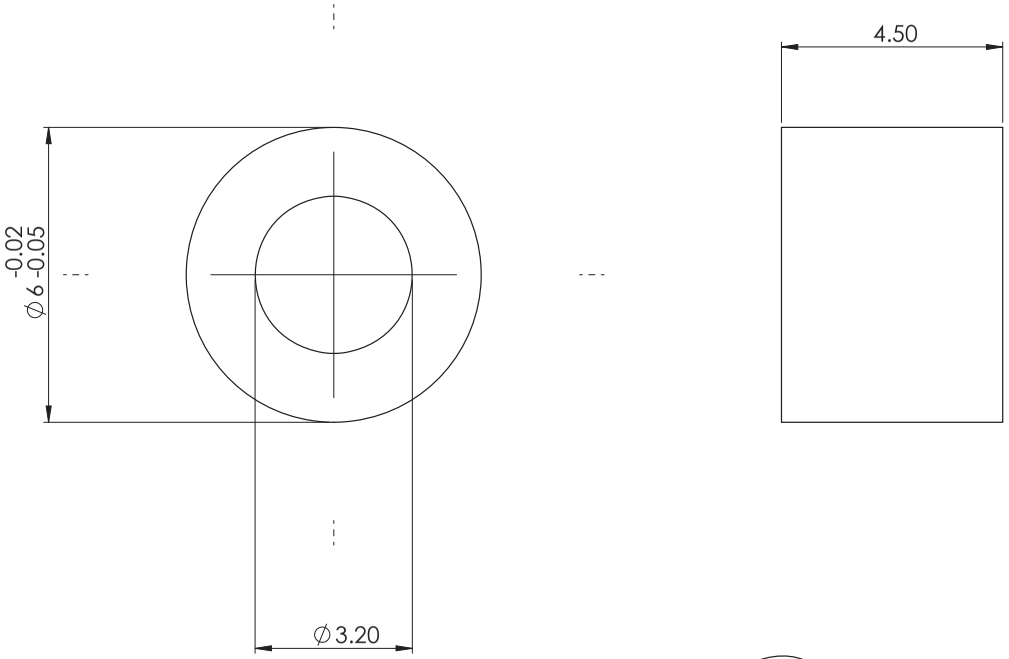

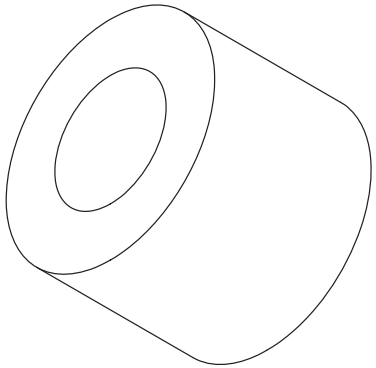

(17)

DO NOT SCALE		DRAWN AND DESIGNED BY: F Romei		TOLERANCES UNLESS OTHERWISE STATED: LINEAR X = +/- 0.20, XX = +/- 0.10, XXX = +/- 0.05; ANGULAR +/- 0.50; ALL DIMENSIONS IN mm UNLESS OTHERWISE STATED	UNIVERSITY OF Southampton
A3		APPROVED BY: AN Grubisic			Faculty of Engineering and the Environment
JOB No	DEPARTMENT: Astronautics	DATE: 07/11/2017	SCALE: 10:1		TITLE: Insulating Sleeve
PROJECT: VHTR	SUPERVISORS: AN Grubisic	MATERIAL: Macor	TEXTURE	SURFACE FINISH: ALL OVER UNLESS OTHERWISE STATED	
REMOVE ALL SHARP EDGES		THE INFORMATION CONTAINED IN THIS DOCUMENT IS THE PROPERTY OF THE UNIVERSITY OF SOUTHAMPTON DO NOT COPY WITHOUT WRITTEN PERMISSION.		SHEET: 5 of 11	No OFF: 18 / ASSEMBLY NUMBER / DRAWING NUMBER: 1 of 1 / REVISION: 4
IF IN DOUBT PLEASE ASK					

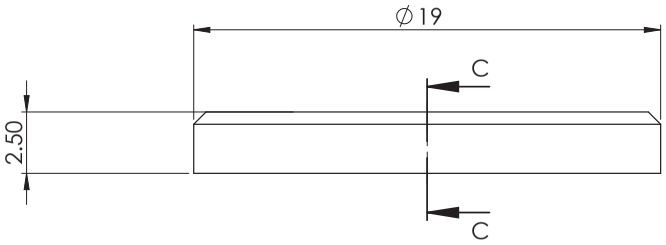

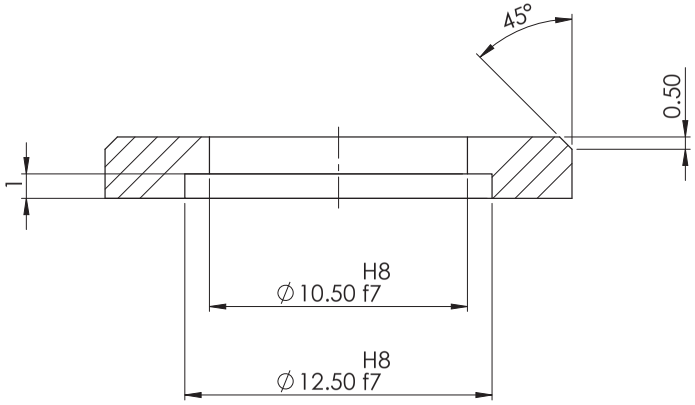

SECTION C-C

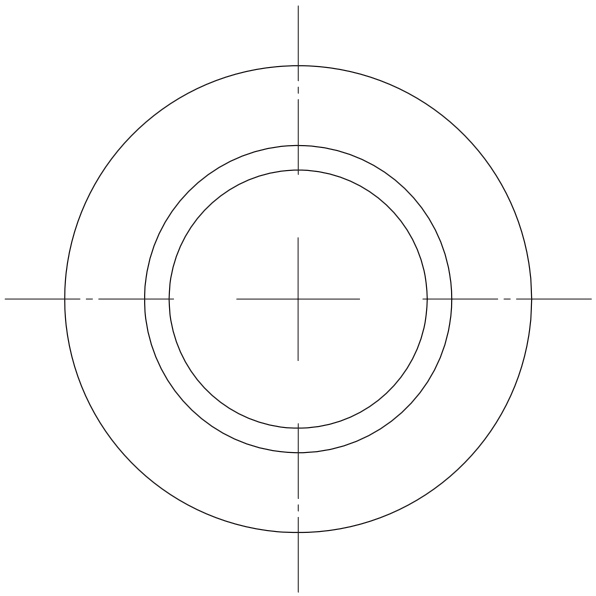

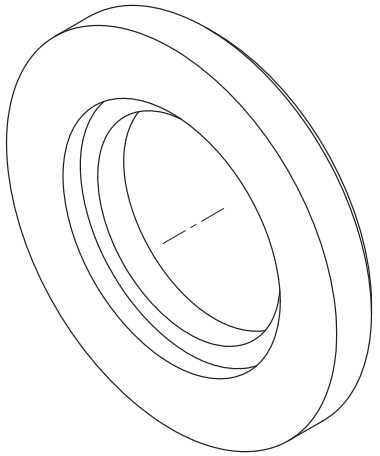

(18)

DO NOT SCALE		DRAWN AND DESIGNED BY: F Romei		TOLERANCES UNLESS OTHERWISE STATED: LINEAR X = +/- 0.20, XX = +/- 0.10, XXX = +/- 0.05; ANGULAR +/- 0.50; ALL DIMENSIONS IN mm UNLESS OTHERWISE STATED	UNIVERSITY OF Southampton
A3		APPROVED BY: AN Grubisic			Faculty of Engineering and the Environment
JOB No	DEPARTMENT: Astronautics	DATE: 07/11/2017	SCALE: 5:1		TITLE: Nozzle Spacer
PROJECT: VHTR	SUPERVISORS: AN Grubisic	MATERIAL: Shapal	TEXTURE	SURFACE FINISH: ALL OVER UNLESS OTHERWISE STATED	
REMOVE ALL SHARP EDGES		THE INFORMATION CONTAINED IN THIS DOCUMENT IS THE PROPERTY OF THE UNIVERSITY OF SOUTHAMPTON DO NOT COPY WITHOUT WRITTEN PERMISSION.		SHEET: 6 of 11	No OFF: 3 / ASSEMBLY NUMBER / DRAWING NUMBER: 1 of 1 / REVISION: 4
IF IN DOUBT PLEASE ASK					

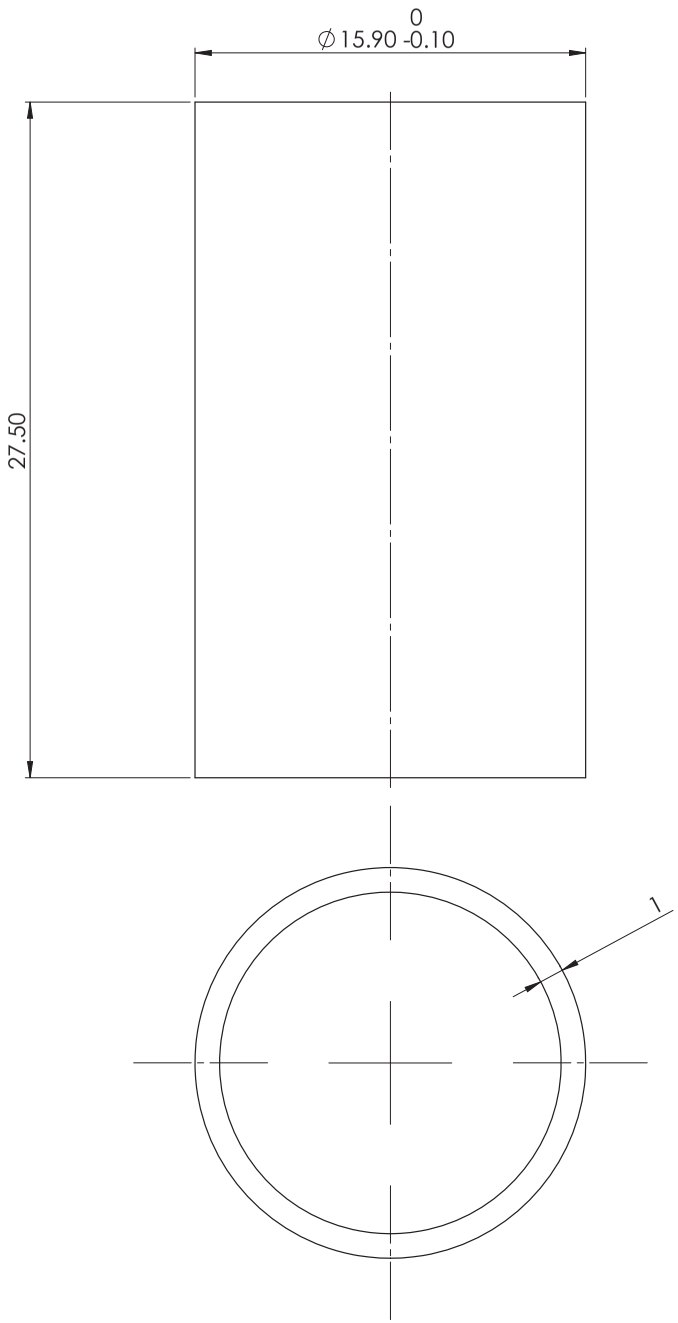

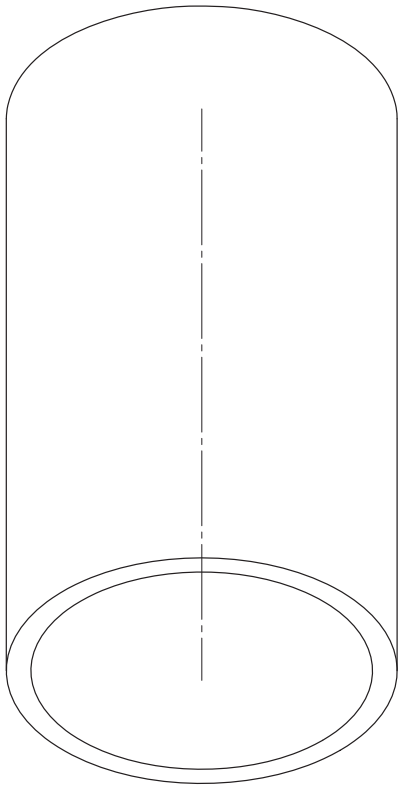

(19)

DO NOT SCALE		DRAWN AND DESIGNED BY: F Romei		TOLERANCES UNLESS OTHERWISE STATED: LINEAR X = +/- 0.20, XX = +/- 0.10, XXX = +/- 0.05; ANGULAR +/- 0.50; ALL DIMENSIONS IN mm UNLESS OTHERWISE STATED	UNIVERSITY OF Southampton
A3		APPROVED BY: AN Grubisic			Faculty of Engineering and the Environment
JOB No	DEPARTMENT: Astronautics	DATE: 07/11/2017	SCALE: 5:1		TITLE: Pipe Insulator
PROJECT: VHTR	SUPERVISORS: AN Grubisic	MATERIAL: Shapal	TEXTURE	SURFACE FINISH: ALL OVER UNLESS OTHERWISE STATED	
REMOVE ALL SHARP EDGES		THE INFORMATION CONTAINED IN THIS DOCUMENT IS THE PROPERTY OF THE UNIVERSITY OF SOUTHAMPTON DO NOT COPY WITHOUT WRITTEN PERMISSION.		SHEET: 7 of 11	No OFF: 3 / ASSEMBLY NUMBER / DRAWING NUMBER: 1 of 1 / REVISION: 4
IF IN DOUBT PLEASE ASK					

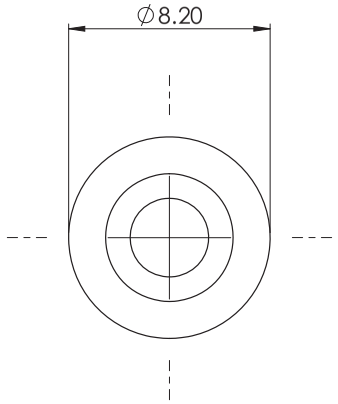

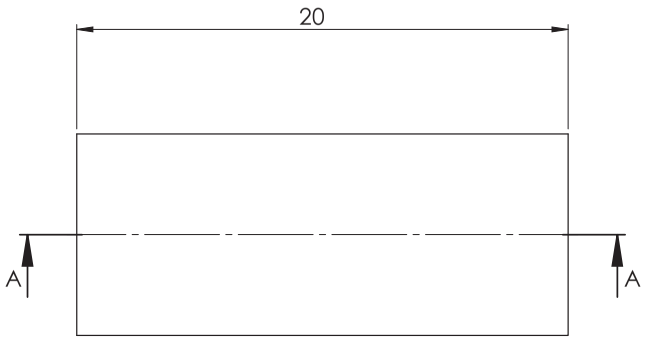

(20)

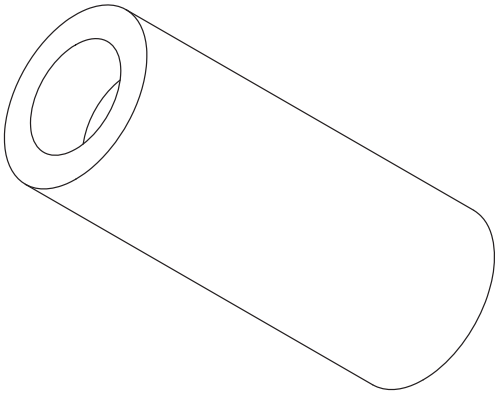

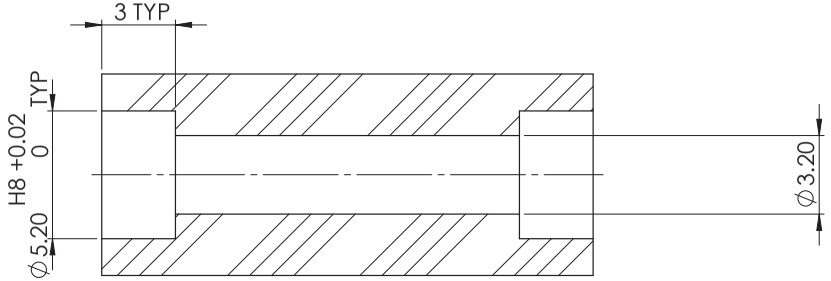

SECTION A-A

DO NOT SCALE		DRAWN AND DESIGNED BY: F Romei		TOLERANCES UNLESS OTHERWISE STATED: LINEAR X = +/- 0.20, XX = +/- 0.10, XXX = +/- 0.05; ANGULAR +/- 0.50; ALL DIMENSIONS IN mm UNLESS OTHERWISE STATED	UNIVERSITY OF Southampton	
A3		APPROVED BY: AN Grubisic			Faculty of Engineering and the Environment	
JOB No	DEPARTMENT: Astronautics	DATE: 07/11/2017	SCALE: 5:1		TITLE: Support Sleeve	
PROJECT: VHTR	SUPERVISORS: AN Grubisic	MATERIAL: Macor	TEXTURE	SURFACE FINISH: ALL OVER UNLESS OTHERWISE STATED		
REMOVE ALL SHARP EDGES / IF IN DOUBT PLEASE ASK		THE INFORMATION CONTAINED IN THIS DOCUMENT IS THE PROPERTY OF THE UNIVERSITY OF SOUTHAMPTON DO NOT COPY WITHOUT WRITTEN PERMISSION.			SHEET: 8 of 11	No OFF: 6 / ASSEMBLY NUMBER / DRAWING NUMBER: 1 of 1 / REVISION: 4

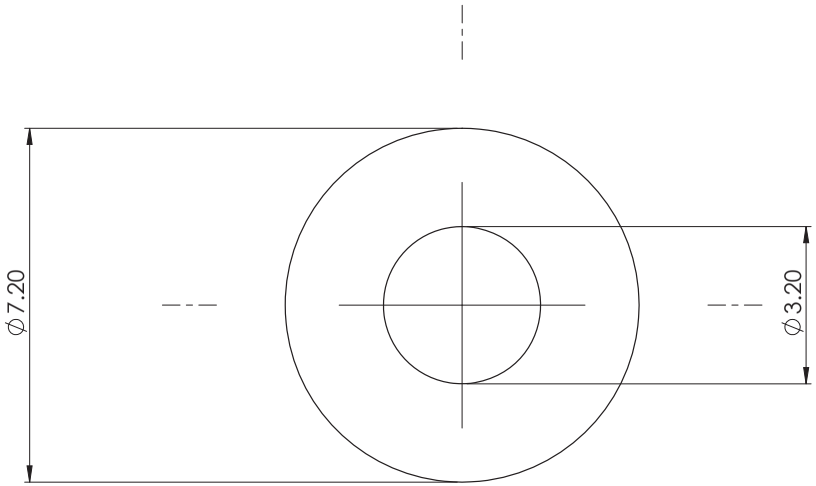

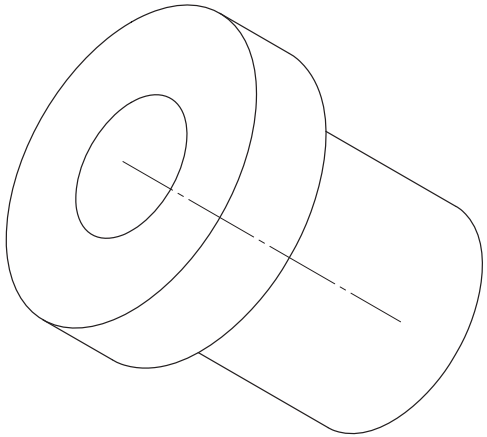

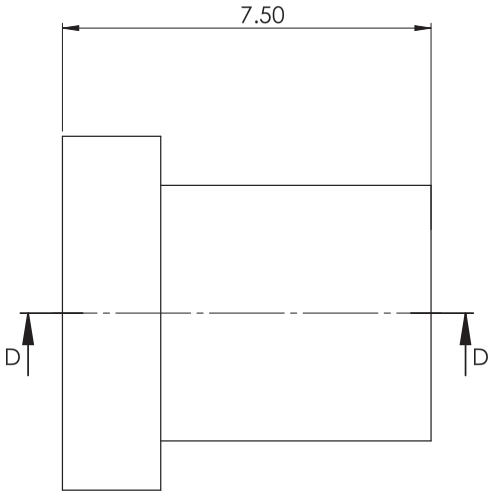

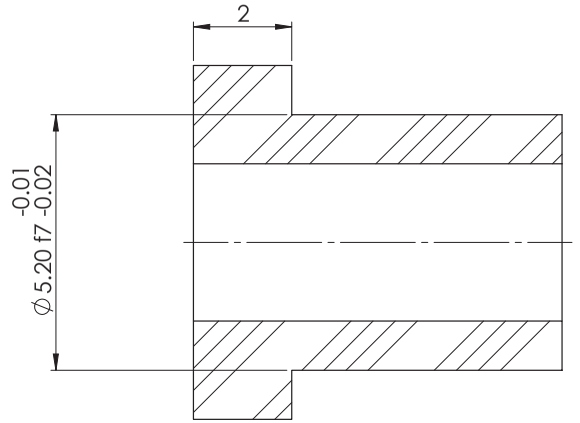

SECTION D-D

(21)

DO NOT SCALE		DRAWN AND DESIGNED BY: F Romei		TOLERANCES UNLESS OTHERWISE STATED: LINEAR X = +/- 0.20, XX = +/- 0.10, XXX = +/- 0.05; ANGULAR +/- 0.50; ALL DIMENSIONS IN mm UNLESS OTHERWISE STATED	UNIVERSITY OF Southampton, Faculty of Engineering and the Environment
A3		APPROVED BY: AN Grubisic			
JOB No	DEPARTMENT: Astronautics	DATE: 07/11/2017	SCALE: 10:1		TITLE: Support Washer Bottom
PROJECT: VHTR	SUPERVISORS: AN Grubisic	MATERIAL: Macor	TEXTURE	SURFACE FINISH: ALL OVER UNLESS OTHERWISE STATED	
REMOVE ALL SHARP EDGES		THE INFORMATION CONTAINED IN THIS DOCUMENT IS THE PROPERTY OF THE UNIVERSITY OF SOUTHAMPTON DO NOT COPY WITHOUT WRITTEN PERMISSION.		SHEET: 9 of 11	No OFF: 6 / ASSEMBLY NUMBER / DRAWING NUMBER: 1 of 1 / REVISION: 4
IF IN DOUBT PLEASE ASK					

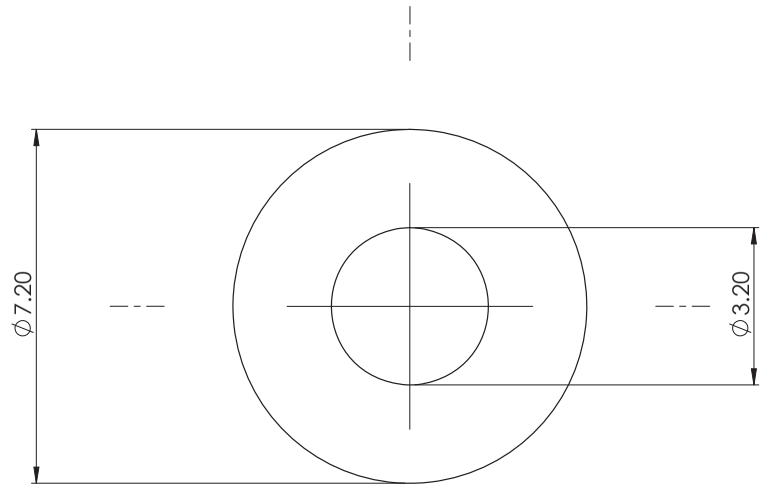

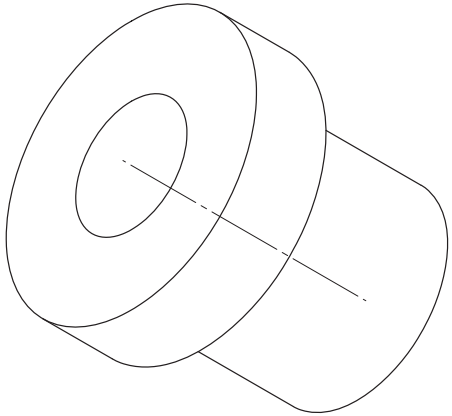

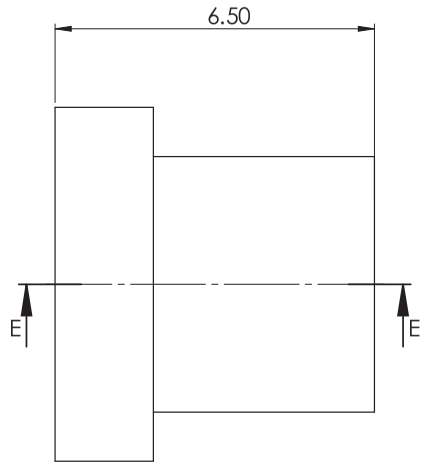

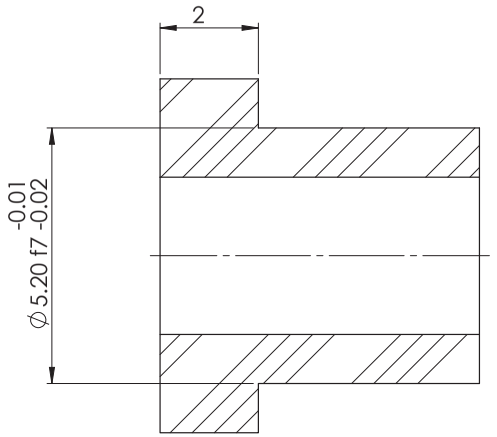

SECTION E-E

(22)

DO NOT SCALE		DRAWN AND DESIGNED BY: F Romei		TOLERANCES UNLESS OTHERWISE STATED: LINEAR X = +/- 0.20, XX = +/- 0.10, XXX = +/- 0.05; ANGULAR +/- 0.50; ALL DIMENSIONS IN mm UNLESS OTHERWISE STATED	UNIVERSITY OF Southampton, Faculty of Engineering and the Environment
A3		APPROVED BY: AN Grubisic			
JOB No	DEPARTMENT: Astronautics	DATE: 07/11/2017	SCALE: 10:1		TITLE: Support Washer Top
PROJECT: VHTR	SUPERVISORS: AN Grubisic	MATERIAL: Macor	TEXTURE	SURFACE FINISH: ALL OVER UNLESS OTHERWISE STATED	
REMOVE ALL SHARP EDGES / IF IN DOUBT PLEASE ASK		THE INFORMATION CONTAINED IN THIS DOCUMENT IS THE PROPERTY OF THE UNIVERSITY OF SOUTHAMPTON DO NOT COPY WITHOUT WRITTEN PERMISSION.		SHEET: 10 of 11 / No OFF: 6 / ASSEMBLY NUMBER / DRAWING NUMBER: 1 of 1	REVISION: 4

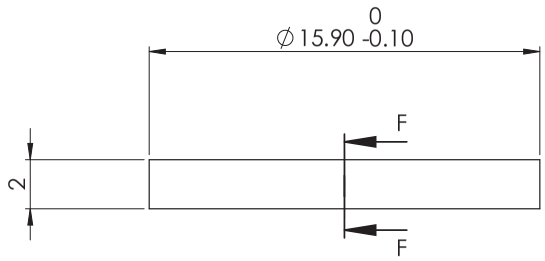

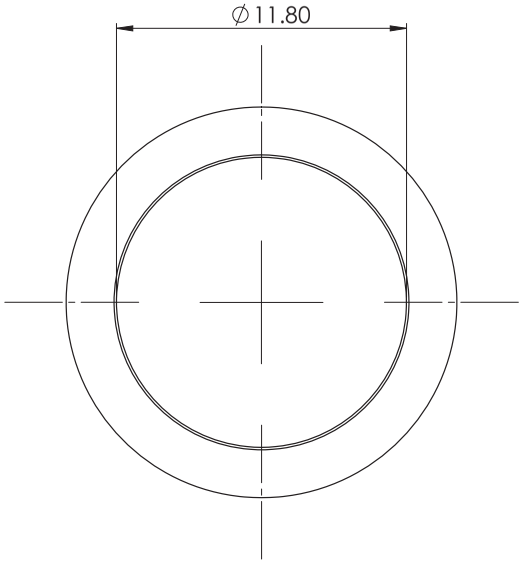

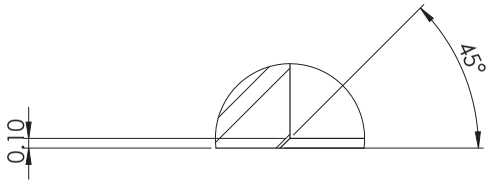

DETAIL G
SCALE 20 : 1

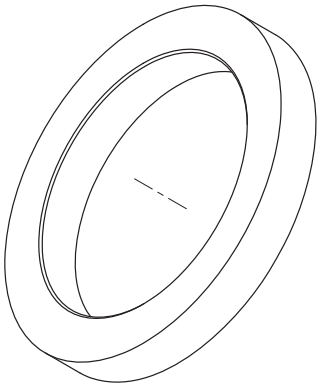

(23)

DO NOT SCALE		DRAWN AND DESIGNED BY: F Romei		TOLERANCES UNLESS OTHERWISE STATED: LINEAR X = +/- 0.20, XX = +/- 0.10, XXX = +/- 0.05; ANGULAR +/- 0.50; ALL DIMENSIONS IN mm UNLESS OTHERWISE STATED	UNIVERSITY OF Southampton, Faculty of Engineering and the Environment
A3		APPROVED BY: AN Grubisic			
JOB No	DEPARTMENT: Astronautics	DATE: 07/11/2017	SCALE: 5:1		TITLE: Top Insulator Ring
PROJECT: VHTR	SUPERVISORS: AN Grubisic	MATERIAL: Shapal	TEXTURE	SURFACE FINISH: ALL OVER UNLESS OTHERWISE STATED	
REMOVE ALL SHARP EDGES		THE INFORMATION CONTAINED IN THIS DOCUMENT IS THE PROPERTY OF THE UNIVERSITY OF SOUTHAMPTON DO NOT COPY WITHOUT WRITTEN PERMISSION.		SHEET: 11 of 11	No OFF: 3 / ASSEMBLY NUMBER / DRAWING NUMBER: 1 of 1 / REVISION: 4
IF IN DOUBT PLEASE ASK					

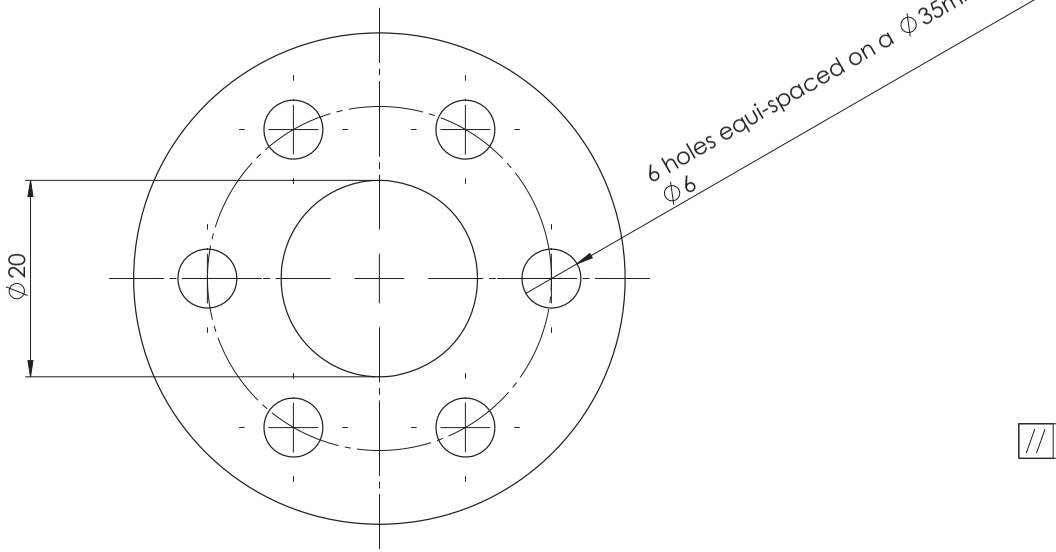

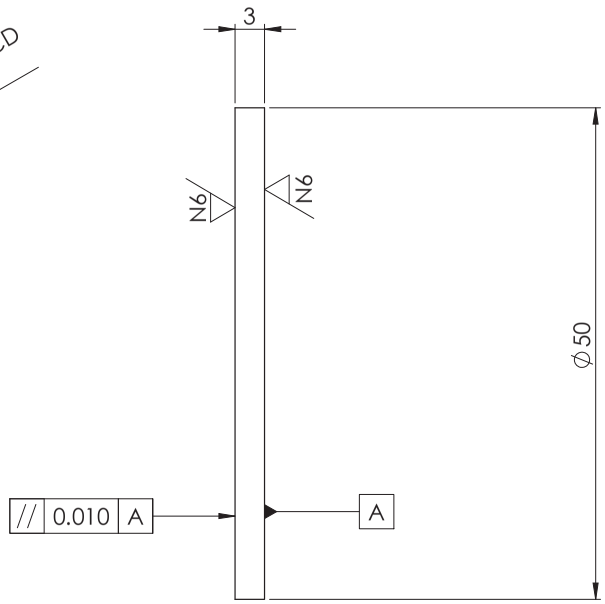

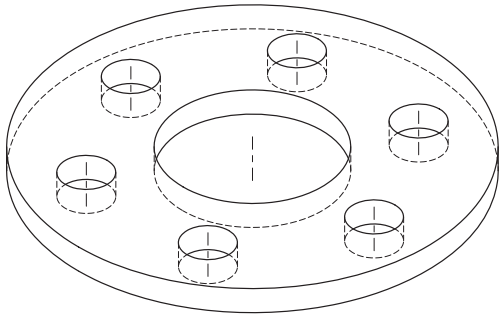

(24)

DO NOT SCALE		DRAWN AND DESIGNED BY F Romei		TOLERANCES UNLESS OTHERWISE STATED	UNIVERSITY OF Southampton
A3		APPROVED BY AN Grubisic		LINEAR X = +/- 0.20 XX = +/- 0.10 XXX = +/- 0.05 ANGULAR +/- 0.50 ALL DIMENSIONS IN mm UNLESS OTHERWISE STATED	Faculty of Engineering and the Environment
JOB No -	DEPARTMENT Astronautics	DATE 20/10/2017	SCALE 2:1		TITLE Collar
PROJECT VHTR	SUPERVISORS AN Grubisic	MATERIAL Aluymina 99.7%	TEXTURE	SURFACE FINISH ALL OVER UNLESS OTHERWISE STATED	
REMOVE ALL SHARP EDGES		THE INFORMATION CONTAINED IN THIS DOCUMENT IS THE PROPERTY OF THE UNIVERSITY OF SOUTHAMPTON DO NOT COPY WITHOUT WRITTEN PERMISSION.			
IF IN DOUBT PLEASE ASK					

SHEET	No OFF	ASSEMBLY NUMBER	DRAWING NUMBER	REVISION
1 of 1	4		1 of 1	3

As-printed (section view)

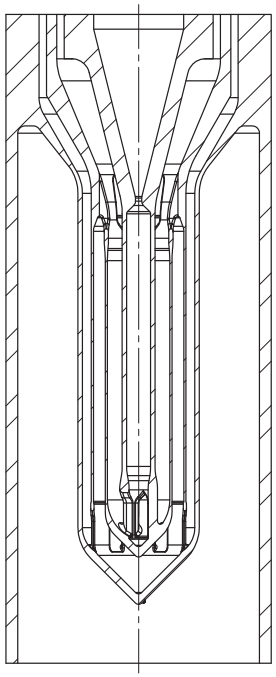

Final component (section view)

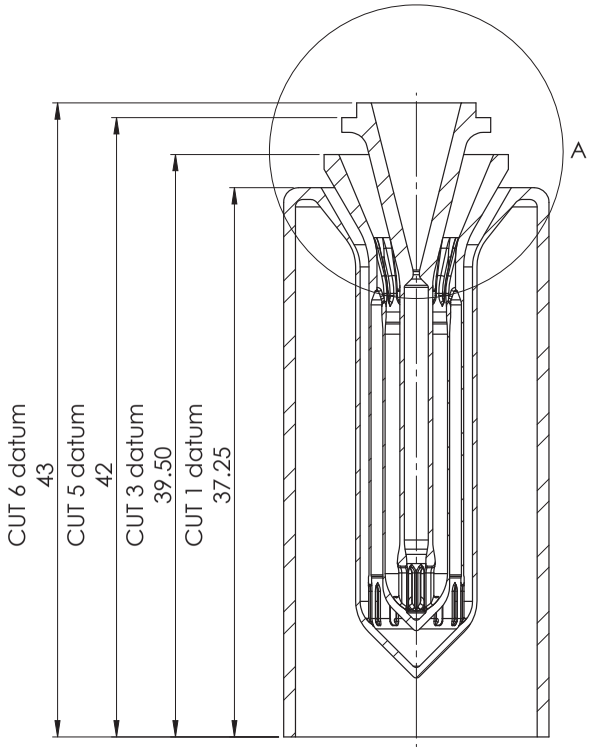

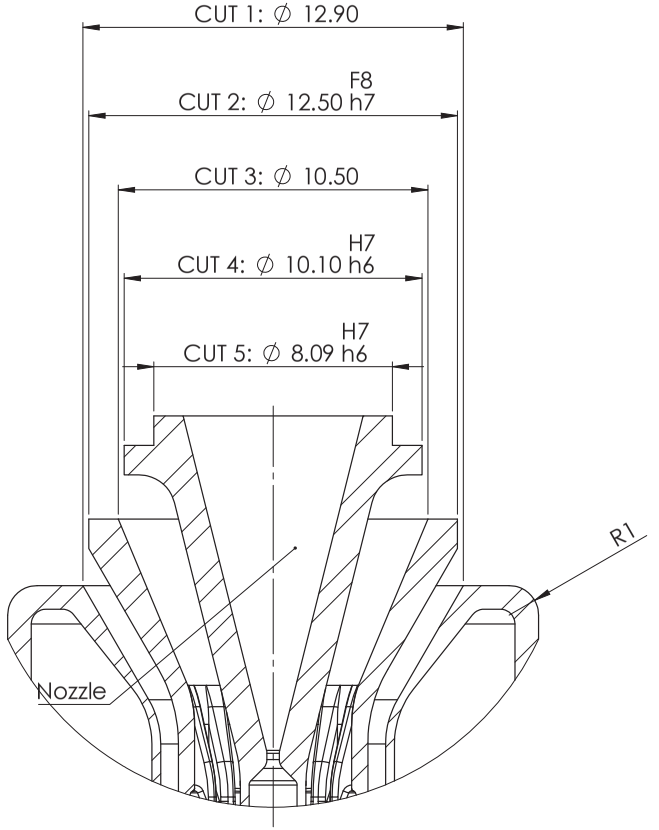

DETAIL A
SCALE 6 : 1

(25)

NOTES:
- the as-printed Heat Exchangers are manufactured in job 772270
- use suggested jig for performing this job
- all cuts are performed on the nozzle end

Suggested machining steps:
1. Polish down the bottom cilindrical surface;
2. CUT 1 (with the datum provided and up to the CUT 1 dia.);
3. Radius R1;
4. CUT 2 to obtain the required close running fit with a ceramic component.
5. CUT 3 up to the specified dia. to avoid contact with the internal nozzle;
6. CUT 4and CUT 5 to obtain the specified tolerance to couple the nozzle with the Thruster Casing component;
7. CUT 6 to obtain the nominal Heat Exchanger length;
8. Manual nozzle sirface polishing on lathe (using jig for CUT 3), details to be further discussed with technician
9. Nozzle throat drilling with 0.42mm drill bit (using jig for CUT 3)

DO NOT SCALE		DRAWN AND DESIGNED BY: F Romei		TOLERANCES UNLESS OTHERWISE STATED: LINEAR X = +/- 0.20, XX = +/- 0.10, XXX = +/- 0.05; ANGULAR +/- 0.50; ALL DIMENSIONS IN mm UNLESS OTHERWISE STATED	UNIVERSITY OF Southampton, Faculty of Engineering and the Environment
A3		APPROVED BY: AN Grubisic			
JOB No	DEPARTMENT: Astronautics	DATE: 07/11/2017	SCALE: 3:1		TITLE: Heat Exchanger post-man.
PROJECT: VHTR	SUPERVISORS: AN Grubisic	MATERIAL: 316L	TEXTURE	SURFACE FINISH: ALL OVER UNLESS OTHERWISE STATED	
REMOVE ALL SHARP EDGES		THE INFORMATION CONTAINED IN THIS DOCUMENT IS THE PROPERTY OF THE UNIVERSITY OF SOUTHAMPTON DO NOT COPY WITHOUT WRITTEN PERMISSION.		SHEET: 2 of 5	No OFF: 6 / ASSEMBLY NUMBER / DRAWING NUMBER: 1 of 1 / REVISION: 1
IF IN DOUBT PLEASE ASK					

CUT 1 + radius R1 (section view)

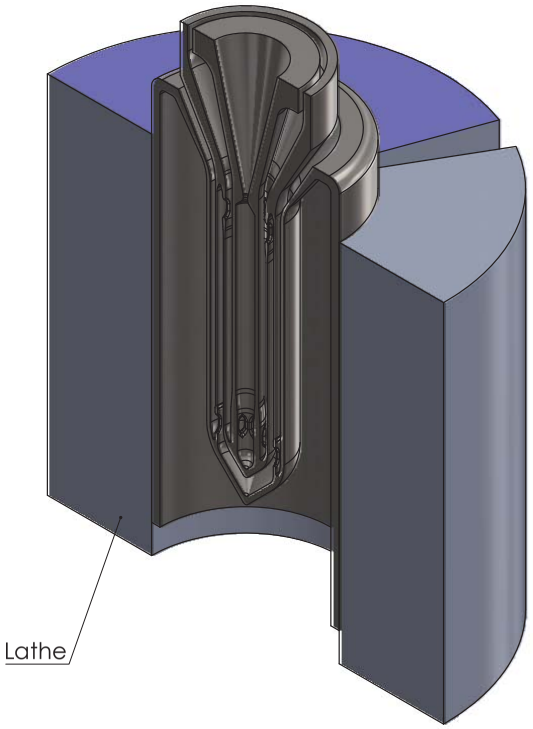

CUT 2

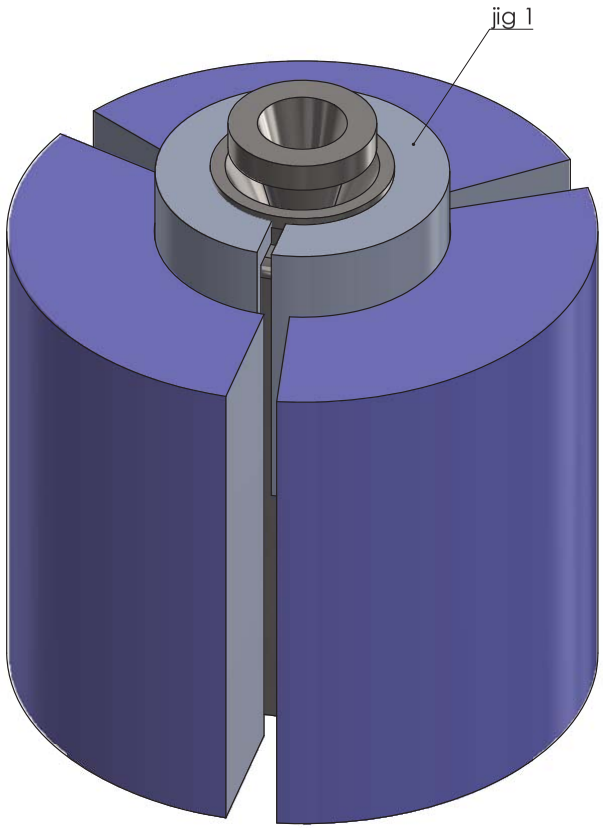

CUT 3 + CUT 4 + nozzle polishing + throat drilling

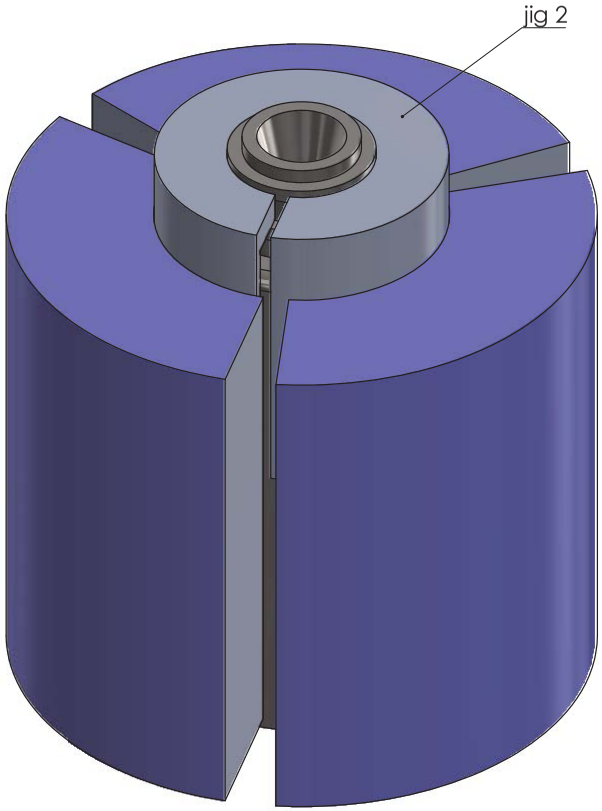

(26)

DO NOT SCALE		DRAWN AND DESIGNED BY F Romei		TOLERANCES UNLESS OTHERWISE STATED	UNIVERSITY OF Southampton
A3		APPROVED BY AN Grubisic		LINEAR X = +/- 0.20, XX = +/- 0.10, XXX = +/- 0.05; ANGULAR +/- 0.50	Faculty of Engineering and the Environment
JOB No	DEPARTMENT Astronautics	DATE 07/11/2017	SCALE 3:1	ALL DIMENSIONS IN mm UNLESS OTHERWISE STATED	TITLE: Suggested jig for HE post-man
PROJECT VHTR	SUPERVISORS AN Grubisic	MATERIAL 316L	TEXTURE	SURFACE FINISH ALL OVER UNLESS OTHERWISE STATED	
REMOVE ALL SHARP EDGES		THE INFORMATION CONTAINED IN THIS DOCUMENT IS THE PROPERTY OF THE UNIVERSITY OF SOUTHAMPTON DO NOT COPY WITHOUT WRITTEN PERMISSION.		SHEET 3 of 5	No OFF 6	ASSEMBLY NUMBER	DRAWING NUMBER 1 of 1	REVISION 1
IF IN DOUBT PLEASE ASK					

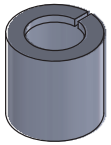

jig 1

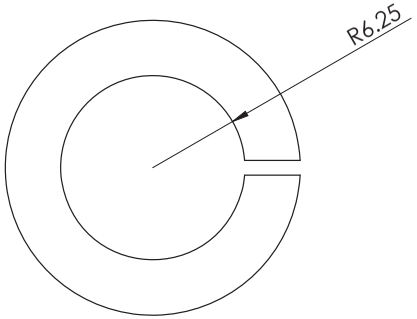

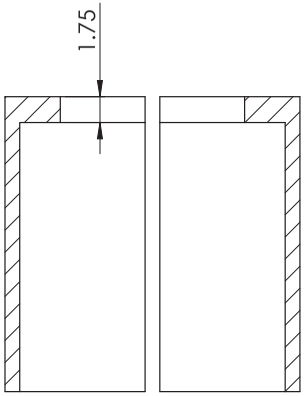

SECTION B-B

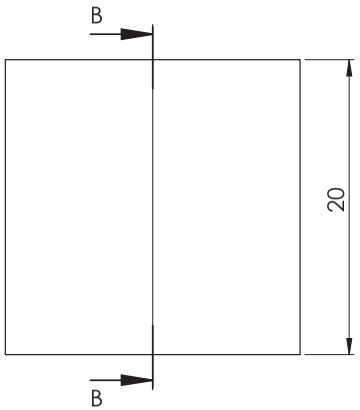

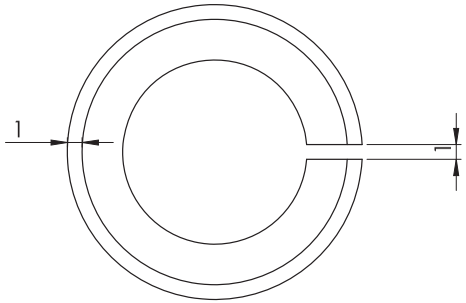

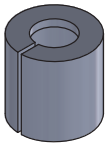

jig 2

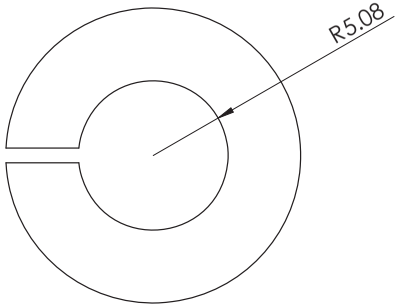

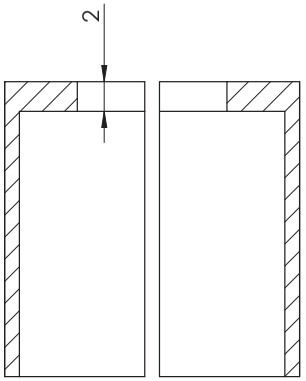

SECTION C-C

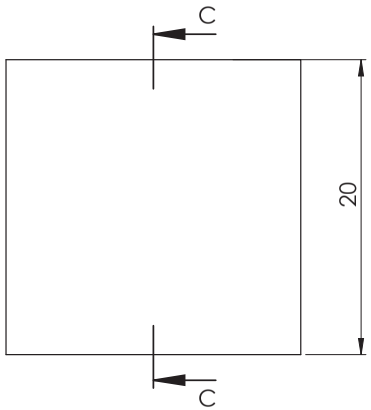

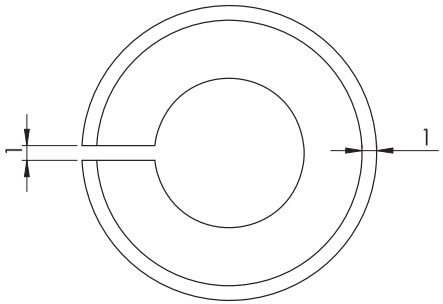

(27)

DO NOT SCALE		DRAWN AND DESIGNED BY: F Romei		TOLERANCES UNLESS OTHERWISE STATED: LINEAR X = +/- 0.20, XX = +/- 0.10, XXX = +/- 0.05; ANGULAR +/- 0.50; ALL DIMENSIONS IN mm UNLESS OTHERWISE STATED	UNIVERSITY OF Southampton, Faculty of Engineering and the Environment
A3		APPROVED BY: AN Grubisic			
JOB No	DEPARTMENT: Astronautics	DATE: 07/11/2017	SCALE: 3:1		TITLE: Suggested jig dimensions
PROJECT: VHTR	SUPERVISORS: AN Grubisic	MATERIAL: 316L	TEXTURE	SURFACE FINISH: ALL OVER UNLESS OTHERWISE STATED	
REMOVE ALL SHARP EDGES		THE INFORMATION CONTAINED IN THIS DOCUMENT IS THE PROPERTY OF THE UNIVERSITY OF SOUTHAMPTON DO NOT COPY WITHOUT WRITTEN PERMISSION.		SHEET: 4 of 5	No OFF: 6 / ASSEMBLY NUMBER / DRAWING NUMBER: 1 of 1 / REVISION: 1
IF IN DOUBT PLEASE ASK					

As-printed

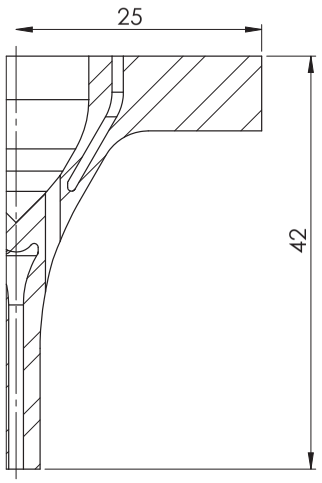

Final component

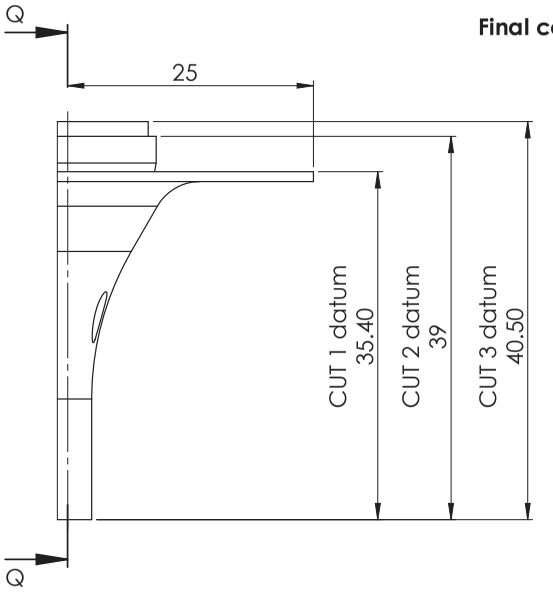

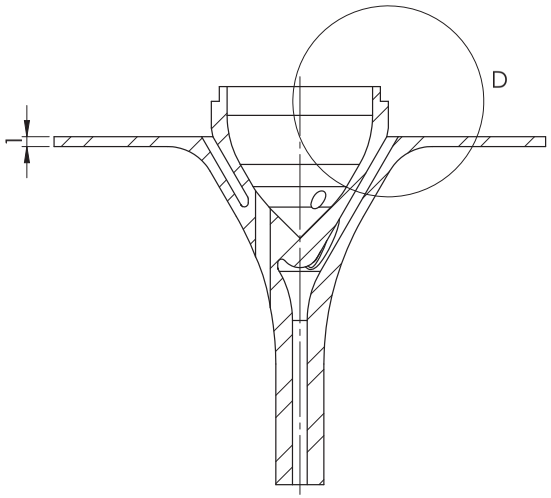

(28)

NOTES:
- the as-printed Thruster Inflows are manufactured in job 772270
- all cuts are performed on the top end

Suggested machining steps:
1. 6 holes machining
2. CUT 1 (with the datum provided and up to the CUT 1 radius)
3. 10° chamfer up to 8.85mm radius at top face of disk
4. CUT 2
5. CUT 3 to obtain the ominal Thruster Inflow length

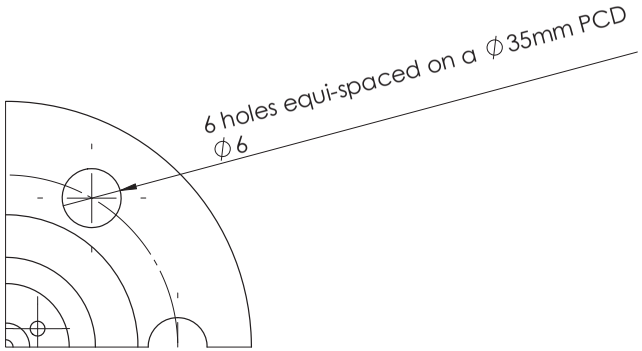

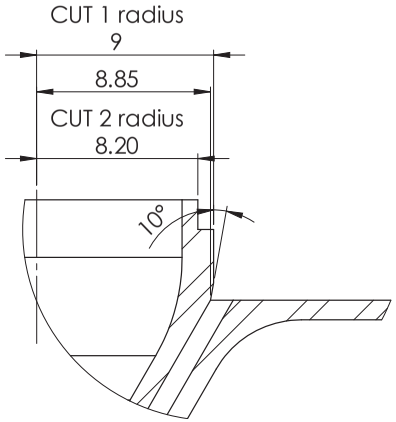

DETAIL D
SCALE 4 : 1

DO NOT SCALE		DRAWN AND DESIGNED BY: F Romei		TOLERANCES UNLESS OTHERWISE STATED: LINEAR X = +/- 0.20, XX = +/- 0.10, XXX = +/- 0.05; ANGULAR +/- 0.50; ALL DIMENSIONS IN mm UNLESS OTHERWISE STATED	UNIVERSITY OF Southampton
A3		APPROVED BY: AN Grubisic			Faculty of Engineering and the Environment
JOB No	DEPARTMENT: Astronautics	DATE: 07/11/2017	SCALE: 2:1		TITLE: Thruster Inflow post-man.
PROJECT: VHTR	SUPERVISORS: AN Grubisic	MATERIAL: 316L	TEXTURE	SURFACE FINISH: ALL OVER UNLESS OTHERWISE STATED	
REMOVE ALL SHARP EDGES		THE INFORMATION CONTAINED IN THIS DOCUMENT IS THE PROPERTY OF THE UNIVERSITY OF SOUTHAMPTON DO NOT COPY WITHOUT WRITTEN PERMISSION.		SHEET: 5 of 5	No OFF: 6
IF IN DOUBT PLEASE ASK				ASSEMBLY NUMBER	DRAWING NUMBER: 1 of 1
					REVISION: 1

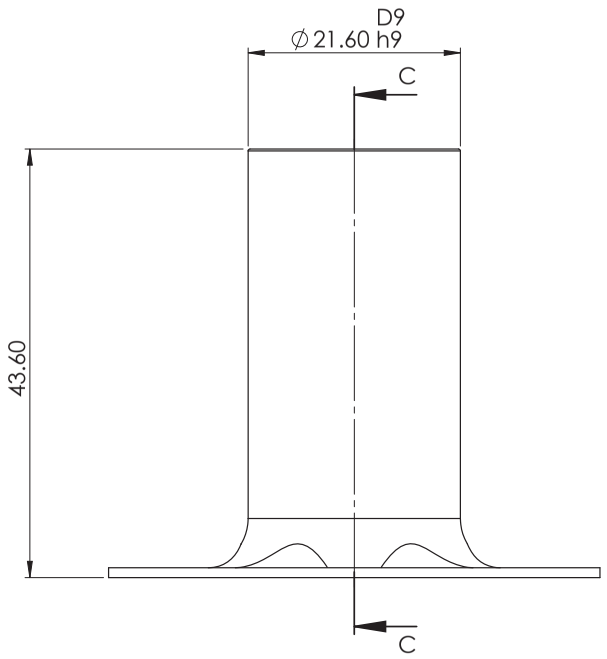

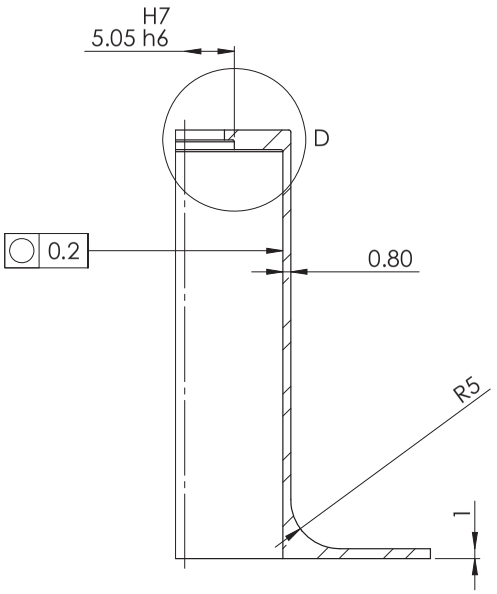

SECTION C-C

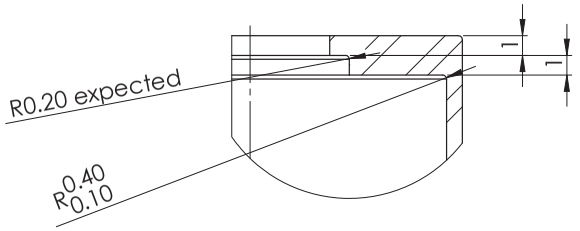

DETAIL D
SCALE 4 : 1

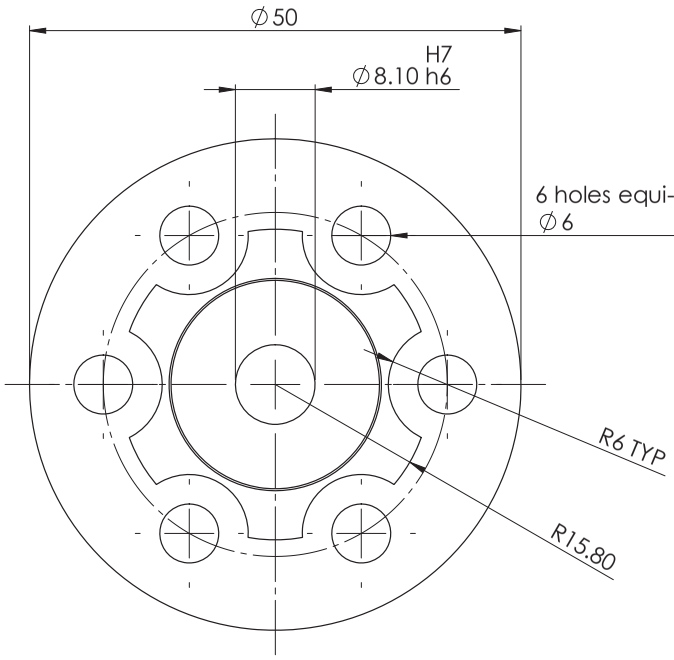

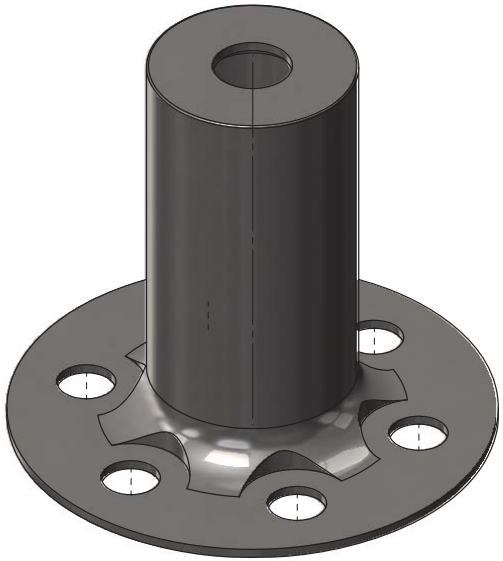

(29)

DO NOT SCALE		DRAWN AND DESIGNED BY: F Romei		TOLERANCES UNLESS OTHERWISE STATED: LINEAR X = +/- 0.20, XX = +/- 0.10, XXX = +/- 0.05; ANGULAR +/- 0.50; ALL DIMENSIONS IN mm UNLESS OTHERWISE STATED	UNIVERSITY OF Southampton Faculty of Engineering and the Environment
A3		APPROVED BY: AN Grubisic			
JOB No	DEPARTMENT: Astronautics	DATE: 07/11/2017	SCALE: 2:1		TITLE: Thruster Casing
PROJECT: VHTR	SUPERVISORS: AN Grubisic	MATERIAL: 316L	TEXTURE	SURFACE FINISH: ALL OVER UNLESS OTHERWISE STATED	
REMOVE ALL SHARP EDGES IF IN DOUBT PLEASE ASK				SHEET: 2 of 3	No OFF: 4 / ASSEMBLY NUMBER / DRAWING NUMBER: 1 of 1 / REVISION: 1

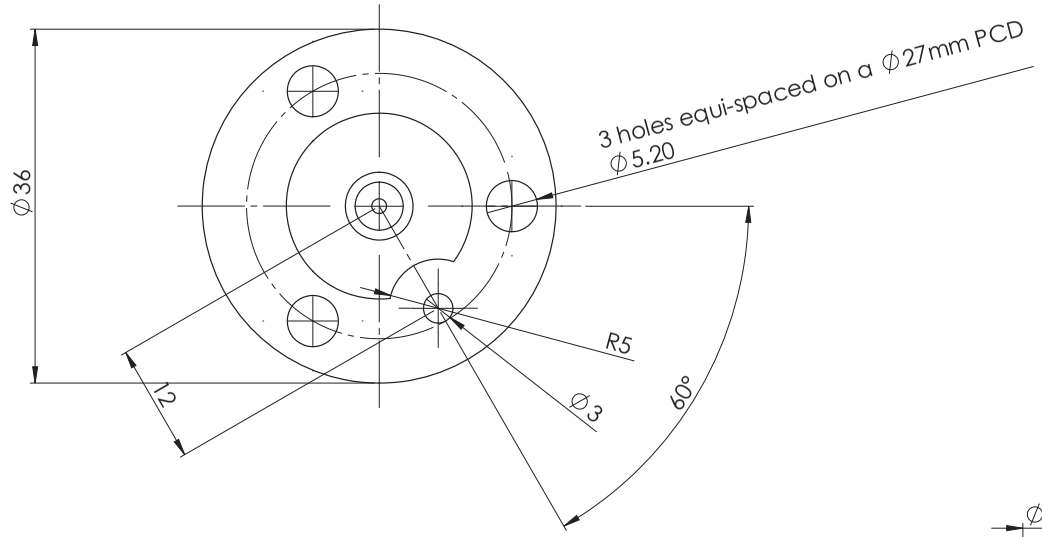

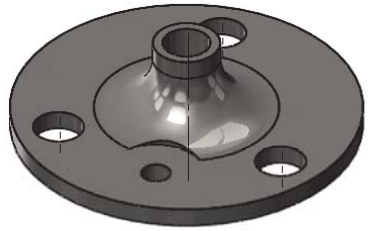

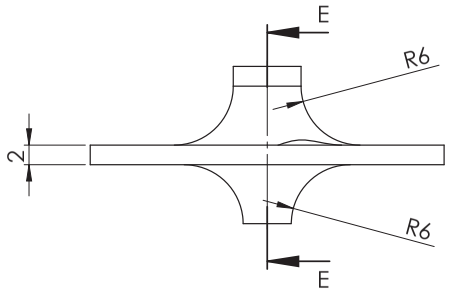

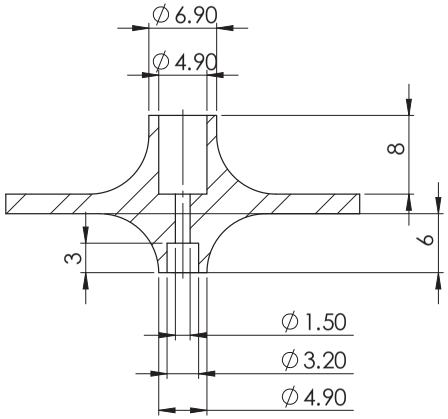

SECTION E-E

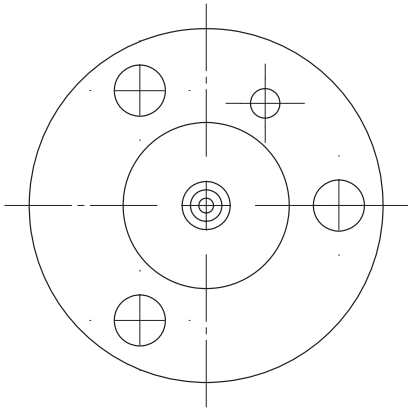

(30)

DO NOT SCALE		DRAWN AND DESIGNED BY: F Romei		TOLERANCES UNLESS OTHERWISE STATED: LINEAR X = +/- 0.20, XX = +/- 0.10, XXX = +/- 0.05; ANGULAR +/- 0.50; ALL DIMENSIONS IN mm UNLESS OTHERWISE STATED	UNIVERSITY OF Southampton
A3		APPROVED BY: AN Grubisic			Faculty of Engineering and the Environment
JOB No	DEPARTMENT: Astronautics	DATE: 07/11/2017	SCALE: 2:1		TITLE: Thruster Support
PROJECT: VHTR	SUPERVISORS: AN Grubisic	MATERIAL: 316L	TEXTURE	SURFACE FINISH: ALL OVER UNLESS OTHERWISE STATED	
REMOVE ALL SHARP EDGES		THE INFORMATION CONTAINED IN THIS DOCUMENT IS THE PROPERTY OF THE UNIVERSITY OF SOUTHAMPTON DO NOT COPY WITHOUT WRITTEN PERMISSION.		SHEET: 3 of 3	No OFF: 4 / ASSEMBLY NUMBER / DRAWING NUMBER: 1 of 1 / REVISION: 1
IF IN DOUBT PLEASE ASK					

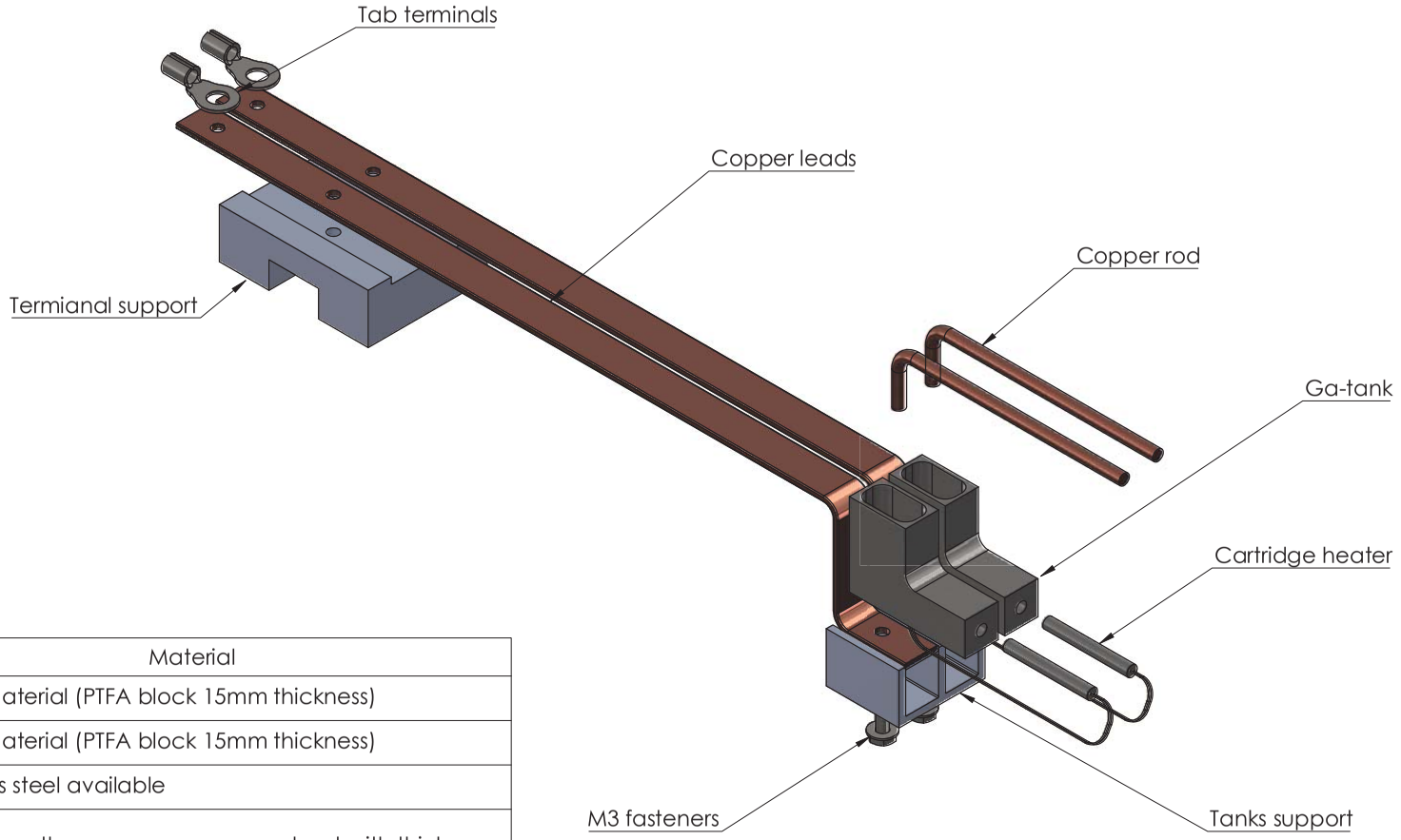

Relevant to this job:

Name	Material
Terminal support	Free issue material (PTFA block 15mm thickness)
Tank support	Free issue material (PTFA block 15mm thickness)
Ga-tank	Any stainless steel available
Copper leads	Please procure the necessary copper sheet with thickness 1.5mm (or 0.06")
Copper rods (only material required)	Please procure copper rods with dia. of 3.175 mm (or 1/8") and total length of 1.22m (48") in pieces not smaller than 203mm each (8")

DO NOT SCALE		DRAWN AND DESIGNED BY F Romei		TOLERANCES UNLESS OTHERWISE STATED	UNIVERSITY OF Southampton
A3		APPROVED BY AN Grubisic		LINEAR X = +/- 0.20, XX = +/- 0.10, XXX = +/- 0.05; ANGULAR +/- 0.50	Faculty of Engineering and the Environment
JOB No	DEPARTMENT Astronautics	DATE 03/11/2017	SCALE 1:1	ALL DIMENSIONS IN mm UNLESS OTHERWISE STATED	TITLE Ga-terminal assembly overview
PROJECT VHTR	SUPERVISORS AN Grubisic	MATERIAL	TEXTURE	SURFACE FINISH ALL OVER UNLESS OTHERWISE STATED	
REMOVE ALL SHARP EDGES				SHEET 1 of 5	No OFF / ASSEMBLY NUMBER / DRAWING NUMBER 1 of 1 / REVISION 1
IF IN DOUBT PLEASE ASK					

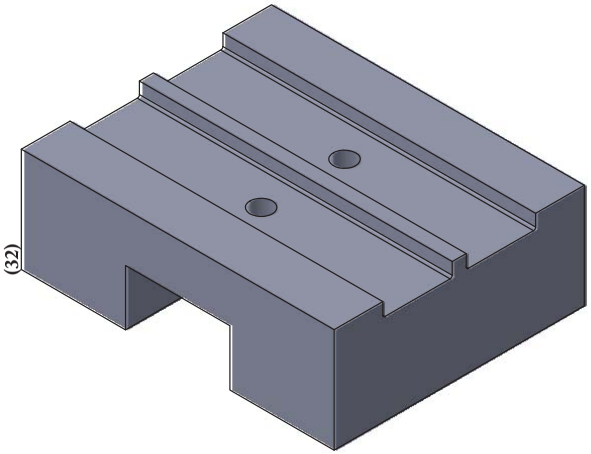

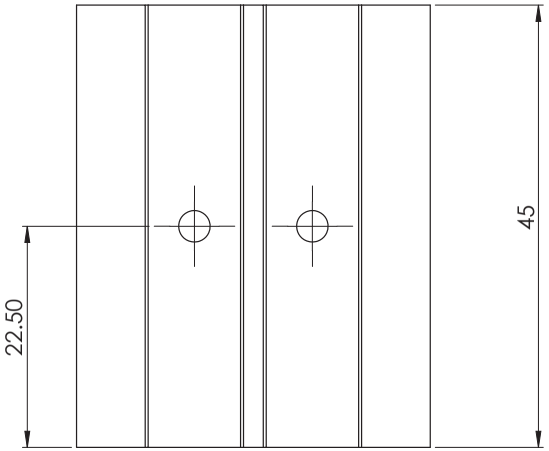

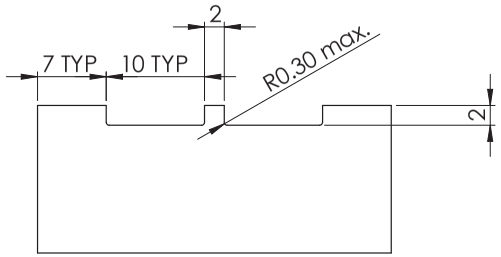

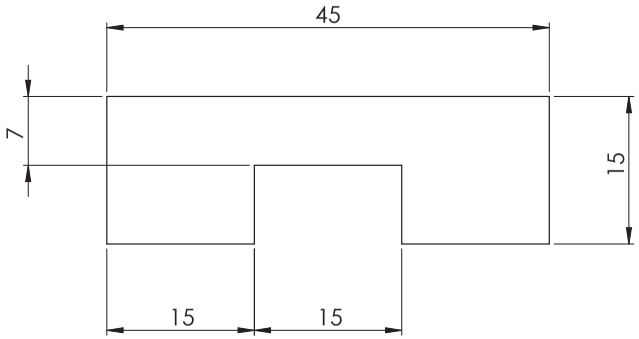

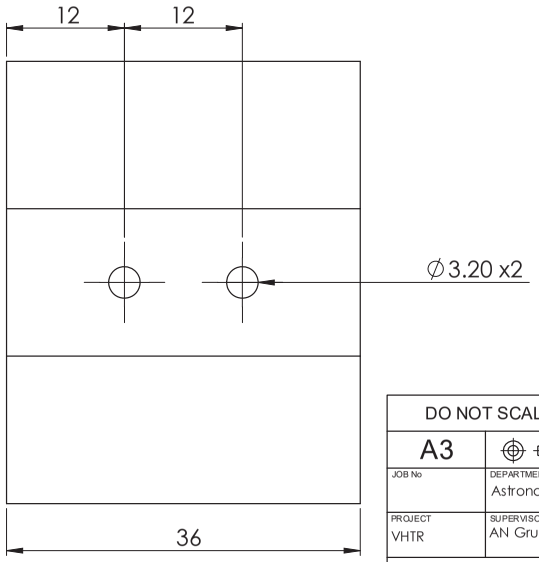

DO NOT SCALE		DRAWN AND DESIGNED BY F Romei		TOLERANCES UNLESS OTHERWISE STATED	UNIVERSITY OF Southampton
A3		APPROVED BY AN Grubisic		LINEAR .X = +/- 0.20 .XX = +/- 0.10 .XXX = +/- 0.05 ANGULAR +/- 0.50	Faculty of Engineering and the Environment
JOB No	DEPARTMENT Astronautics	DATE 03/11/2017	SCALE 2:1	ALL DIMENSIONS IN mm UNLESS OTHERWISE STATED	TITLE Terminal support
PROJECT VHTR	SUPERVISORS AN Grubisic	MATERIAL PTFE	TEXTURE	SURFACE FINISH ALL OVER UNLESS OTHERWISE STATED	
REMOVE ALL SHARP EDGES				SHEET 2 of 5	No OFF 2 / ASSEMBLY NUMBER / DRAWING NUMBER 1 of 1 / REVISION 1
IF IN DOUBT PLEASE ASK					

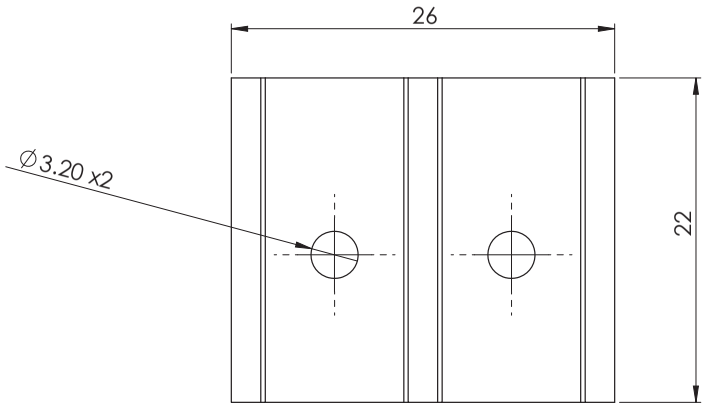

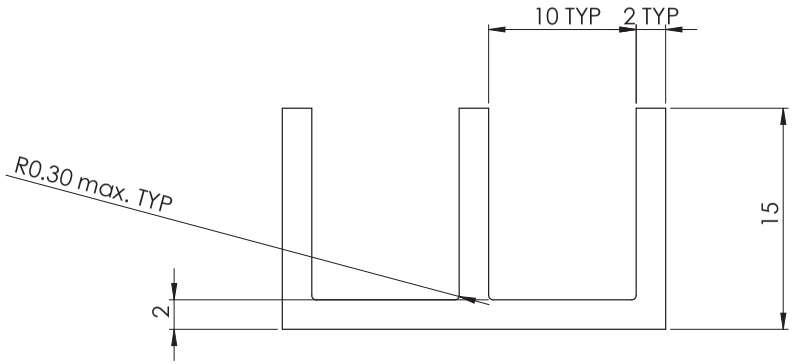

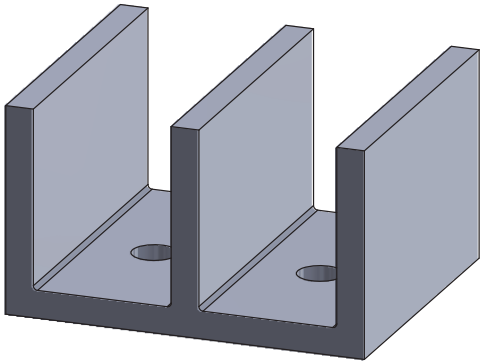

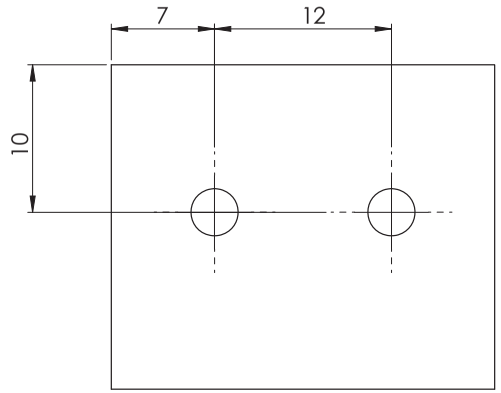

(33)

DO NOT SCALE		DRAWN AND DESIGNED BY: F Romei		TOLERANCES UNLESS OTHERWISE STATED: LINEAR X = +/- 0.20, XX = +/- 0.10, XXX = +/- 0.05; ANGULAR +/- 0.50; ALL DIMENSIONS IN mm UNLESS OTHERWISE STATED	UNIVERSITY OF Southampton
A3		APPROVED BY: AN Grubisic			Faculty of Engineering and the Environment
JOB No	DEPARTMENT: Astronautics	DATE: 03/11/2017	SCALE: 3:1		TITLE: Tanks support
PROJECT: VHTR	SUPERVISORS: AN Grubisic	MATERIAL: PTFE	TEXTURE	SURFACE FINISH: ALL OVER UNLESS OTHERWISE STATED	
REMOVE ALL SHARP EDGES		THE INFORMATION CONTAINED IN THIS DOCUMENT IS THE PROPERTY OF THE UNIVERSITY OF SOUTHAMPTON DO NOT COPY WITHOUT WRITTEN PERMISSION.		SHEET: 3 of 5	No OFF: 2
IF IN DOUBT PLEASE ASK				ASSEMBLY NUMBER	DRAWING NUMBER: 1 of 1
					REVISION: 1

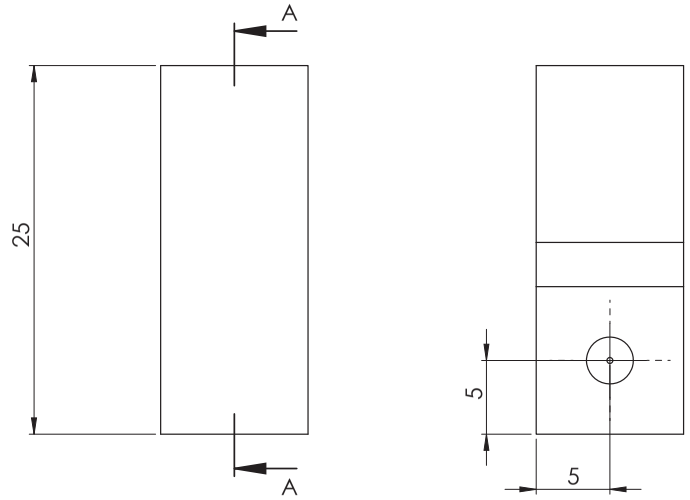

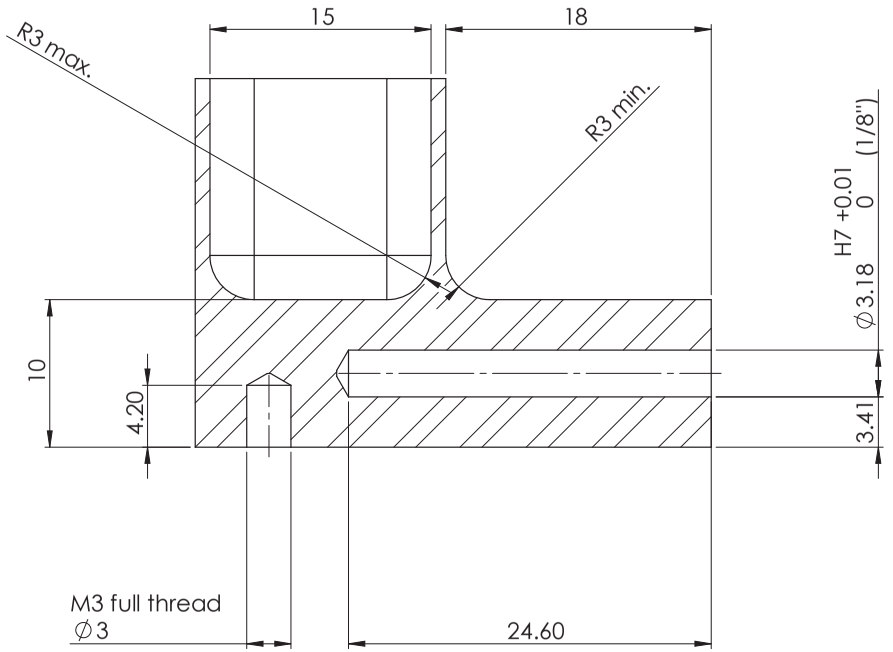

SECTION A-A

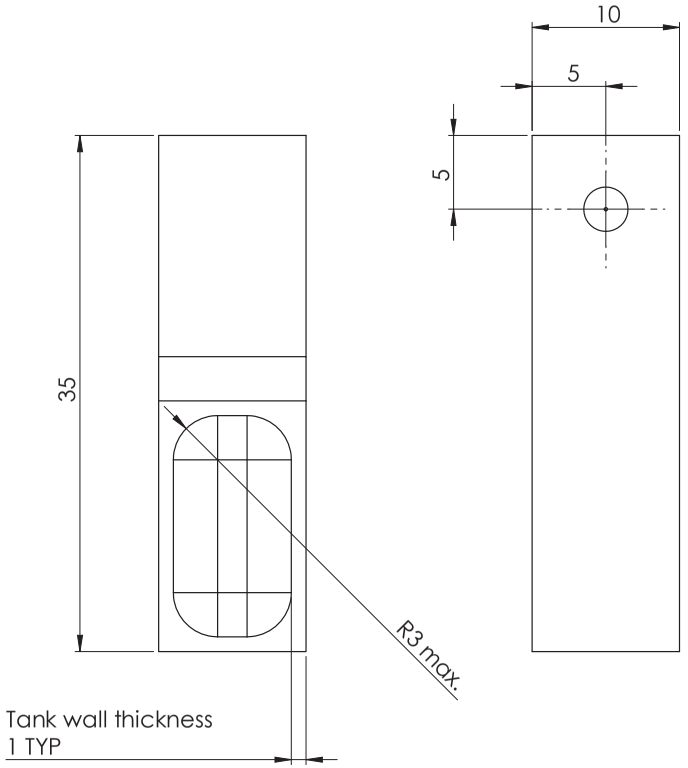

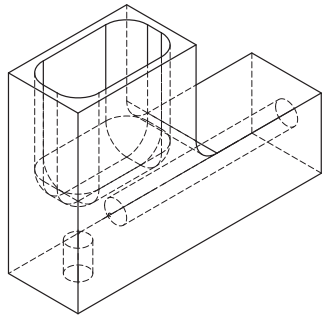

(34)

DO NOT SCALE		DRAWN AND DESIGNED BY F Romei		TOLERANCES UNLESS OTHERWISE STATED	UNIVERSITY OF Southampton
A3		APPROVED BY AN Grubisic		LINEAR X = +/- 0.20, XX = +/- 0.10, XXX = +/- 0.05; ANGULAR +/- 0.50; ALL DIMENSIONS IN mm UNLESS OTHERWISE STATED	Faculty of Engineering and the Environment
JOB No	DEPARTMENT Astronautics	DATE 03/11/2017	SCALE 3:1		TITLE Ga-tank
PROJECT VHTR	SUPERVISORS AN Grubisic	MATERIAL Any SS	TEXTURE	SURFACE FINISH ALL OVER UNLESS OTHERWISE STATED	
REMOVE ALL SHARP EDGES		THE INFORMATION CONTAINED IN THIS DOCUMENT IS THE PROPERTY OF THE UNIVERSITY OF SOUTHAMPTON DO NOT COPY WITHOUT WRITTEN PERMISSION.		SHEET 4 of 5	No OFF 4	ASSEMBLY NUMBER	DRAWING NUMBER 1 of 1	REVISION 1
IF IN DOUBT PLEASE ASK					

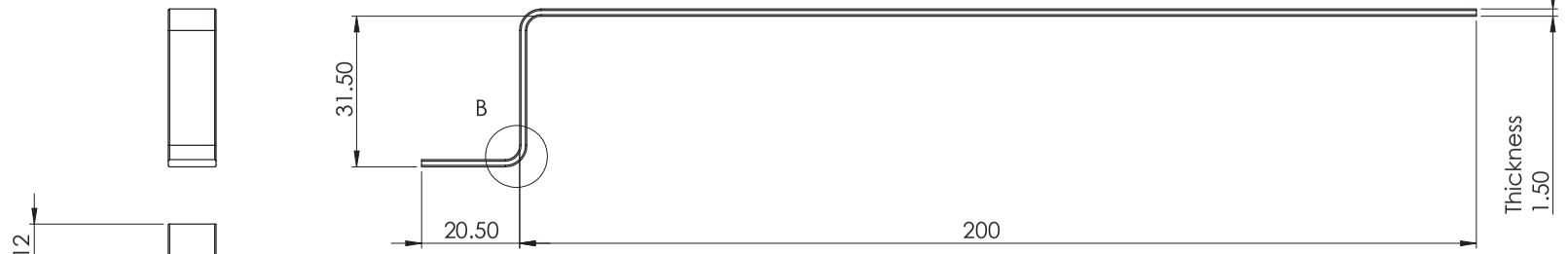

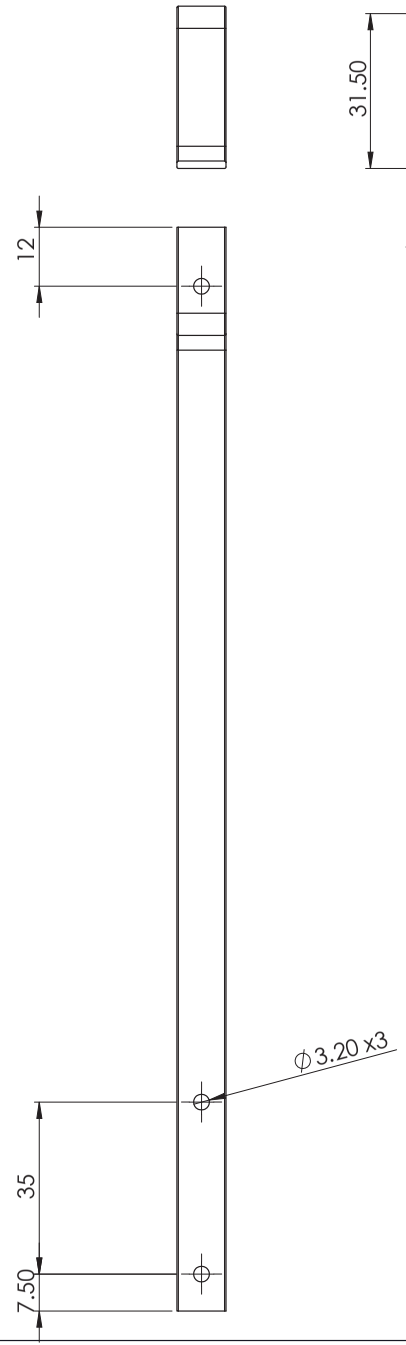

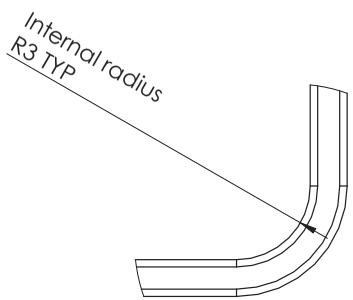

DETAIL B
SCALE 5 : 1

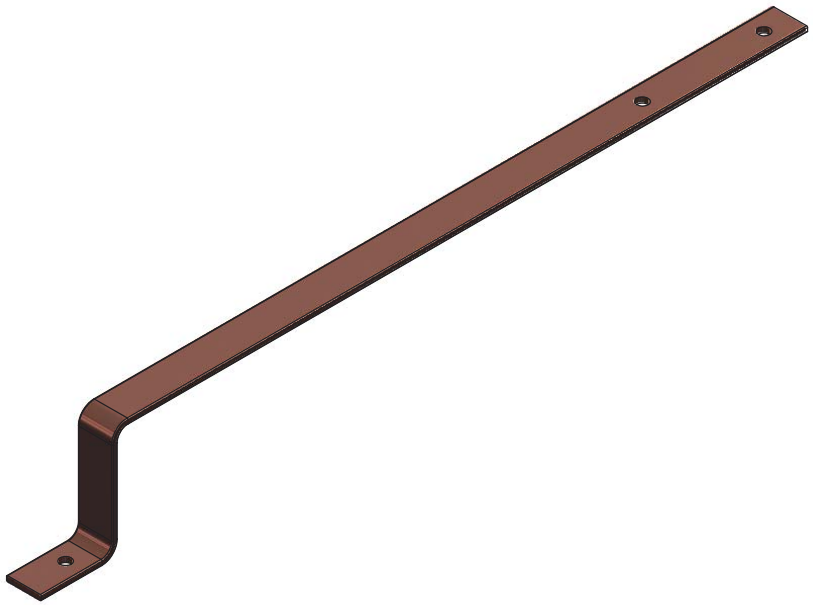

(35)

DO NOT SCALE		DRAWN AND DESIGNED BY: F Romei		TOLERANCES UNLESS OTHERWISE STATED: LINEAR X = +/- 0.20, XX = +/- 0.10, XXX = +/- 0.05; ANGULAR +/- 0.50; ALL DIMENSIONS IN mm UNLESS OTHERWISE STATED	UNIVERSITY OF Southampton, Faculty of Engineering and the Environment
A3		APPROVED BY: AN Grubisic			
JOB No	DEPARTMENT: Astronautics	DATE: 03/11/2017	SCALE: 1:1		TITLE: Copper lead
PROJECT: VHTR	SUPERVISORS: AN Grubisic	MATERIAL: Copper	TEXTURE	SURFACE FINISH: ALL OVER UNLESS OTHERWISE STATED	
REMOVE ALL SHARP EDGES		THE INFORMATION CONTAINED IN THIS DOCUMENT IS THE PROPERTY OF THE UNIVERSITY OF SOUTHAMPTON DO NOT COPY WITHOUT WRITTEN PERMISSION.		SHEET: 5 of 5	No OFF: 4 / ASSEMBLY NUMBER / DRAWING NUMBER: 1 of 1 / REVISION: 1
IF IN DOUBT PLEASE ASK					

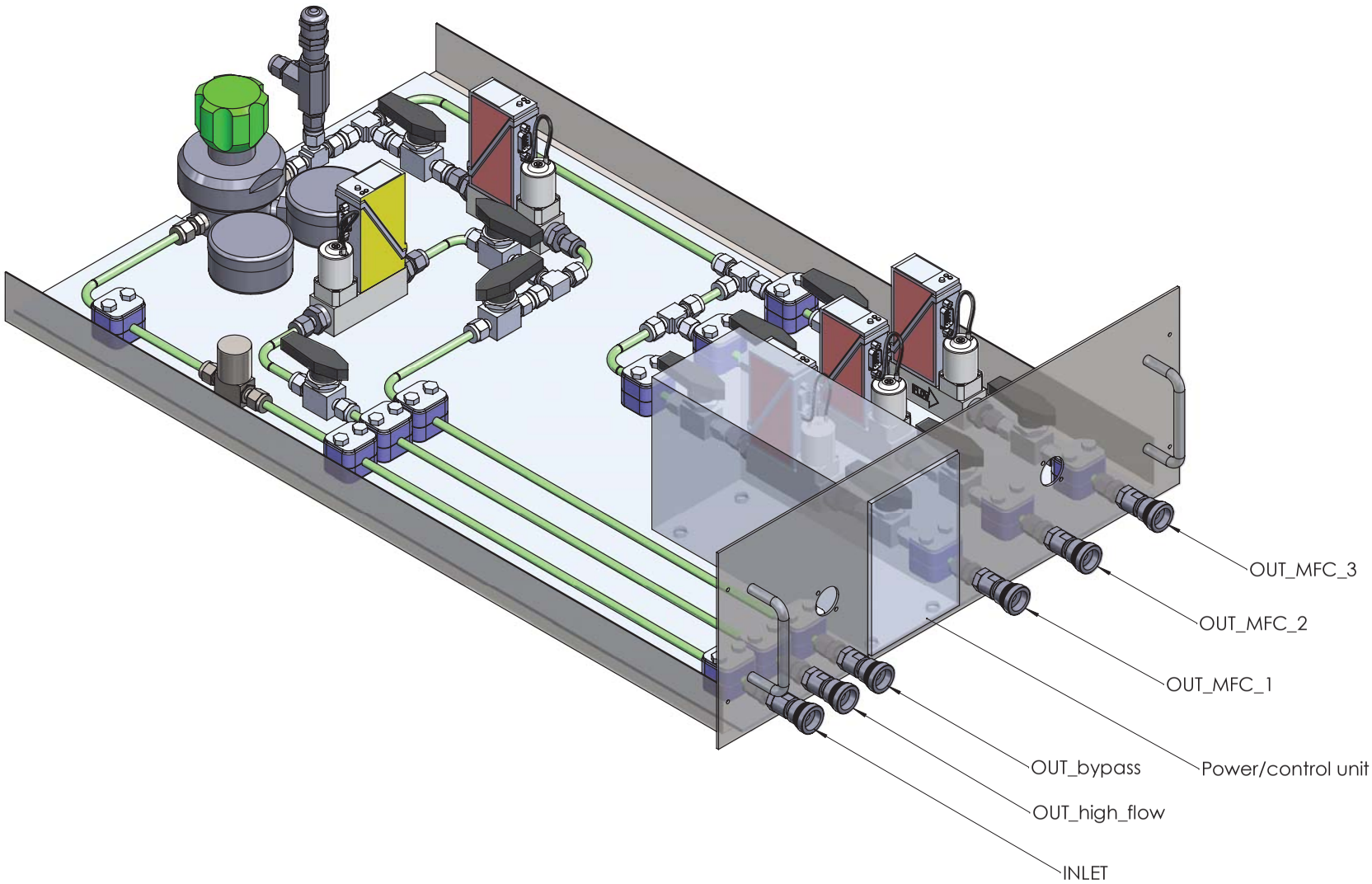

DO NOT SCALE		DRAWN AND DESIGNED BY: FRomei		TOLERANCES UNLESS OTHERWISE STATED: LINEAR X = +/- 0.20, XX = +/- 0.10, XXX = +/- 0.05; ANGULAR +/- 0.50; ALL DIMENSIONS IN mm UNLESS OTHERWISE STATED	UNIVERSITY OF Southampton — Faculty of Engineering and the Environment
A3		APPROVED BY: AN Grubisic			
JOB No	DEPARTMENT: Astronautics	DATE: 25/04/2017	SCALE: 1:3		TITLE: Flow System overview
PROJECT: Flow System	SUPERVISORS: AN Grubisic	MATERIAL	TEXTURE	SURFACE FINISH: ALL OVER UNLESS OTHERWISE STATED	
REMOVE ALL SHARP EDGES / IF IN DOUBT PLEASE ASK		THE INFORMATION CONTAINED IN THIS DOCUMENT IS THE PROPERTY OF THE UNIVERSITY OF SOUTHAMPTON DO NOT COPY WITHOUT WRITTEN PERMISSION.			

SHEET	No OFF	ASSEMBLY NUMBER	DRAWING NUMBER	REVISION
2 of 2			1 of 1	2

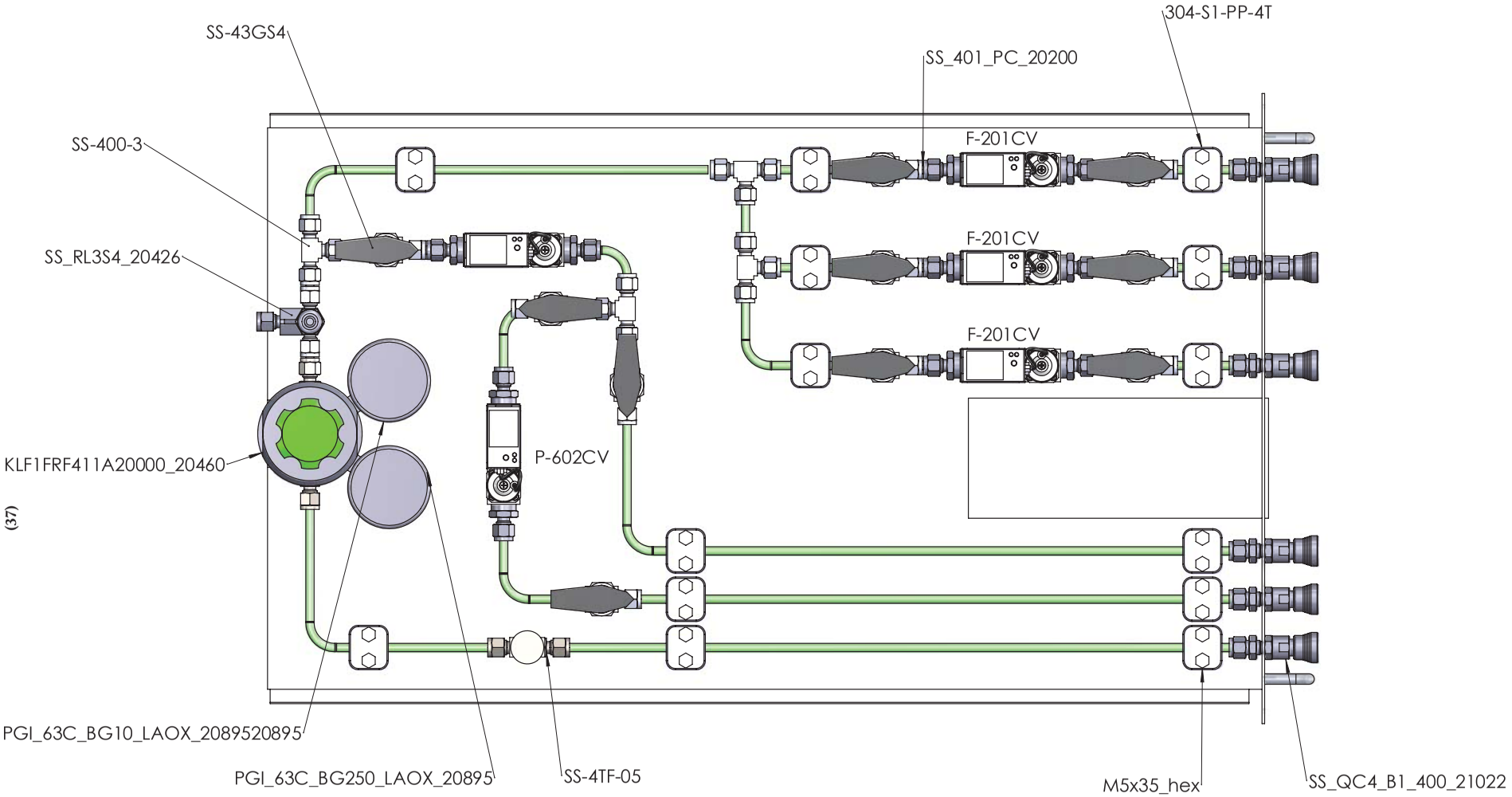

DO NOT SCALE		DRAWN AND DESIGNED BY FRomei		TOLERANCES UNLESS OTHERWISE STATED	UNIVERSITY OF Southampton
A3		APPROVED BY AN Grubisic		LINEAR X = +/- 0.20, XX = +/- 0.10, XXX = +/- 0.05; ANGULAR +/- 0.50; ALL DIMENSIONS IN mm UNLESS OTHERWISE STATED	Faculty of Engineering and the Environment
JOB No	DEPARTMENT Astronautics	DATE 25/04/2017	SCALE 1:3		TITLE Main components
PROJECT Flow System	SUPERVISORS AN Grubisic	MATERIAL	TEXTURE	SURFACE FINISH ✓ ALL OVER UNLESS OTHERWISE STATED	
REMOVE ALL SHARP EDGES / IF IN DOUBT PLEASE ASK		THE INFORMATION CONTAINED IN THIS DOCUMENT IS THE PROPERTY OF THE UNIVERSITY OF SOUTHAMPTON DO NOT COPY WITHOUT WRITTEN PERMISSION.		SHEET 1 of 2	No OFF / ASSEMBLY NUMBER / DRAWING NUMBER 1 of 1 / REVISION 2

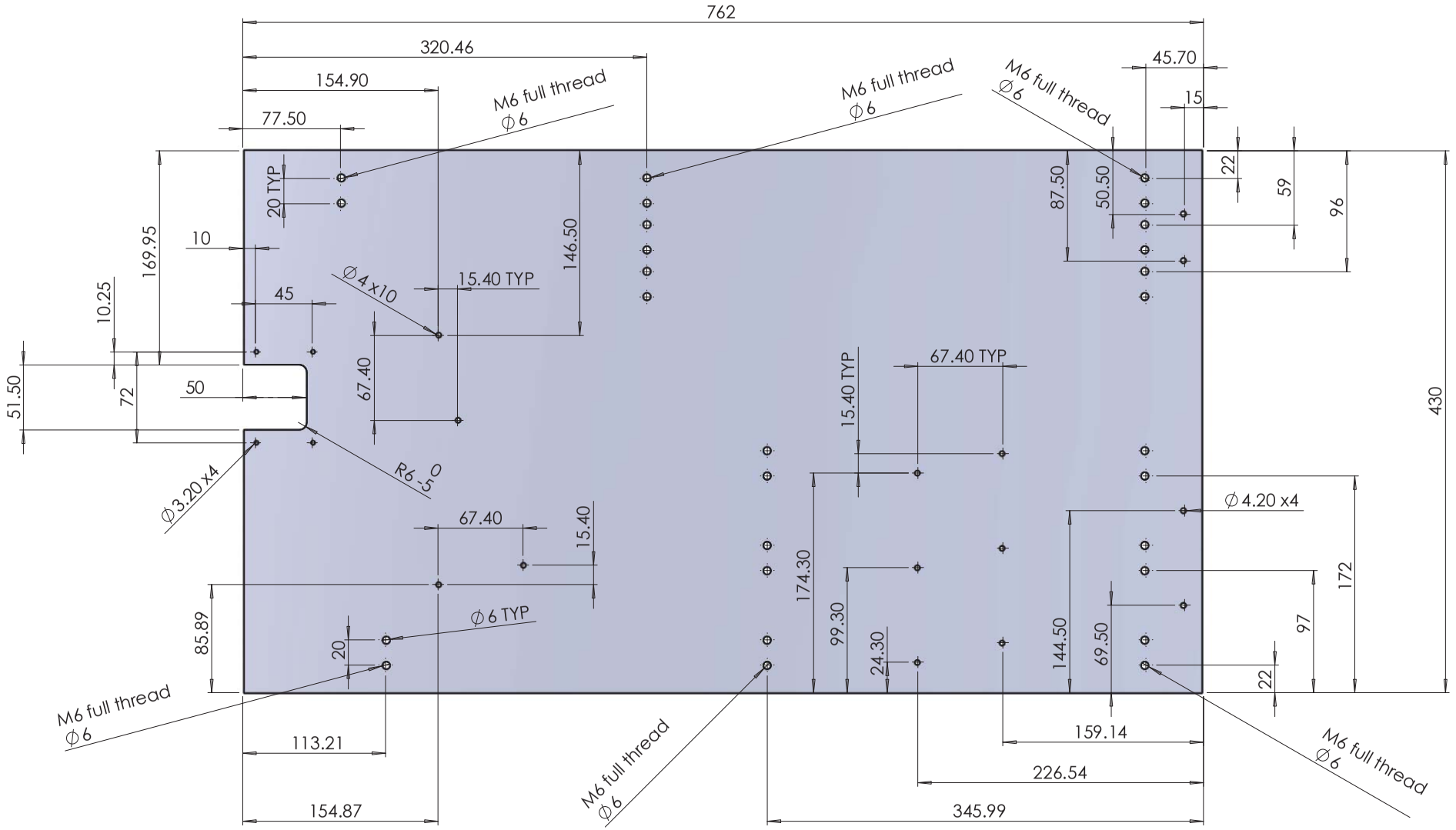

(38)

Thickness required = 3mm
Holes summary:

- M6 full thread x6
- 6mm x 22
- 4mm x 10
- 3.2mm x4

DO NOT SCALE		DRAWN AND DESIGNED BY: FRomei		TOLERANCES UNLESS OTHERWISE STATED: LINEAR X = +/- 0.20, XX = +/- 0.10, XXX = +/- 0.05; ANGULAR +/- 0.50; ALL DIMENSIONS IN mm UNLESS OTHERWISE STATED	UNIVERSITY OF Southampton, Faculty of Engineering and the Environment
A3		APPROVED BY: AN Grubisic			
JOB No: TWI-0	DEPARTMENT: Astronautics	DATE: 16/08/2017	SCALE: 1:3		TITLE: Rack plate
PROJECT: Flow System	SUPERVISORS: AN Grubisic, GT Roberts	MATERIAL: Steel	TEXTURE	SURFACE FINISH: ALL OVER UNLESS OTHERWISE STATED	
REMOVE ALL SHARP EDGES		THE INFORMATION CONTAINED IN THIS DOCUMENT IS THE PROPERTY OF THE UNIVERSITY OF SOUTHAMPTON DO NOT COPY WITHOUT WRITTEN PERMISSION.		SHEET: 2 of 5	No OFF: 1
IF IN DOUBT PLEASE ASK				ASSEMBLY NUMBER	DRAWING NUMBER: 1 of 1
					REVISION: 2

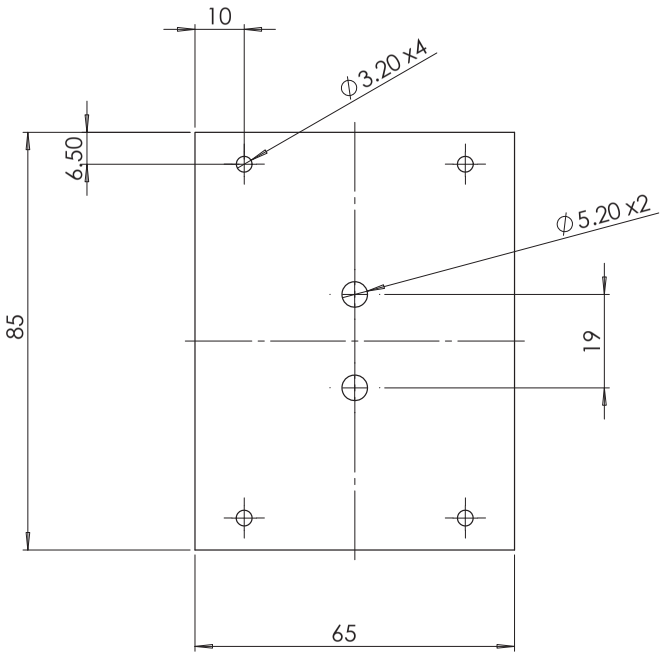

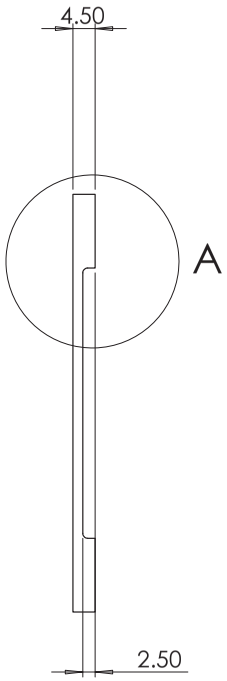

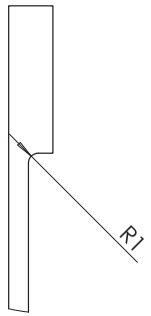

DETAIL A

SCALE 2 : 1

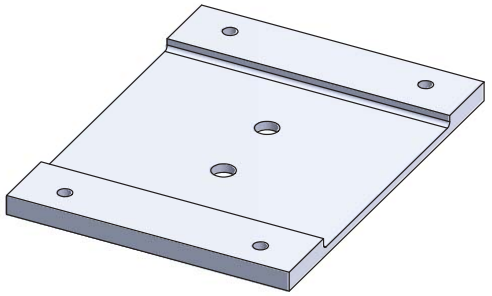

(39)

DO NOT SCALE		DRAWN AND DESIGNED BY FRomei		TOLERANCES UNLESS OTHERWISE STATED	UNIVERSITY OF Southampton
A3		APPROVED BY AN Grubisic		LINEAR X = +/- 0.20, XX = +/- 0.10, XXX = +/- 0.05; ANGULAR +/- 0.50; ALL DIMENSIONS IN mm UNLESS OTHERWISE STATED	Faculty of Engineering and the Environment
JOB No TWI-0	DEPARTMENT Astronautics	DATE 16/08/2017	SCALE 1:1		TITLE Regulator plate
PROJECT Flow System	SUPERVISORS AN Grubisic, GT Roberts	MATERIAL Steel	TEXTURE	SURFACE FINISH ALL OVER UNLESS OTHERWISE STATED	
REMOVE ALL SHARP EDGES				SHEET 3 of 5	No OFF 1	ASSEMBLY NUMBER	DRAWING NUMBER 1 of 1	REVISION 2
IF IN DOUBT PLEASE ASK					

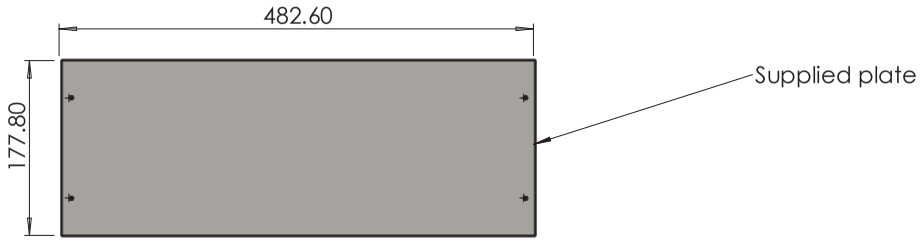

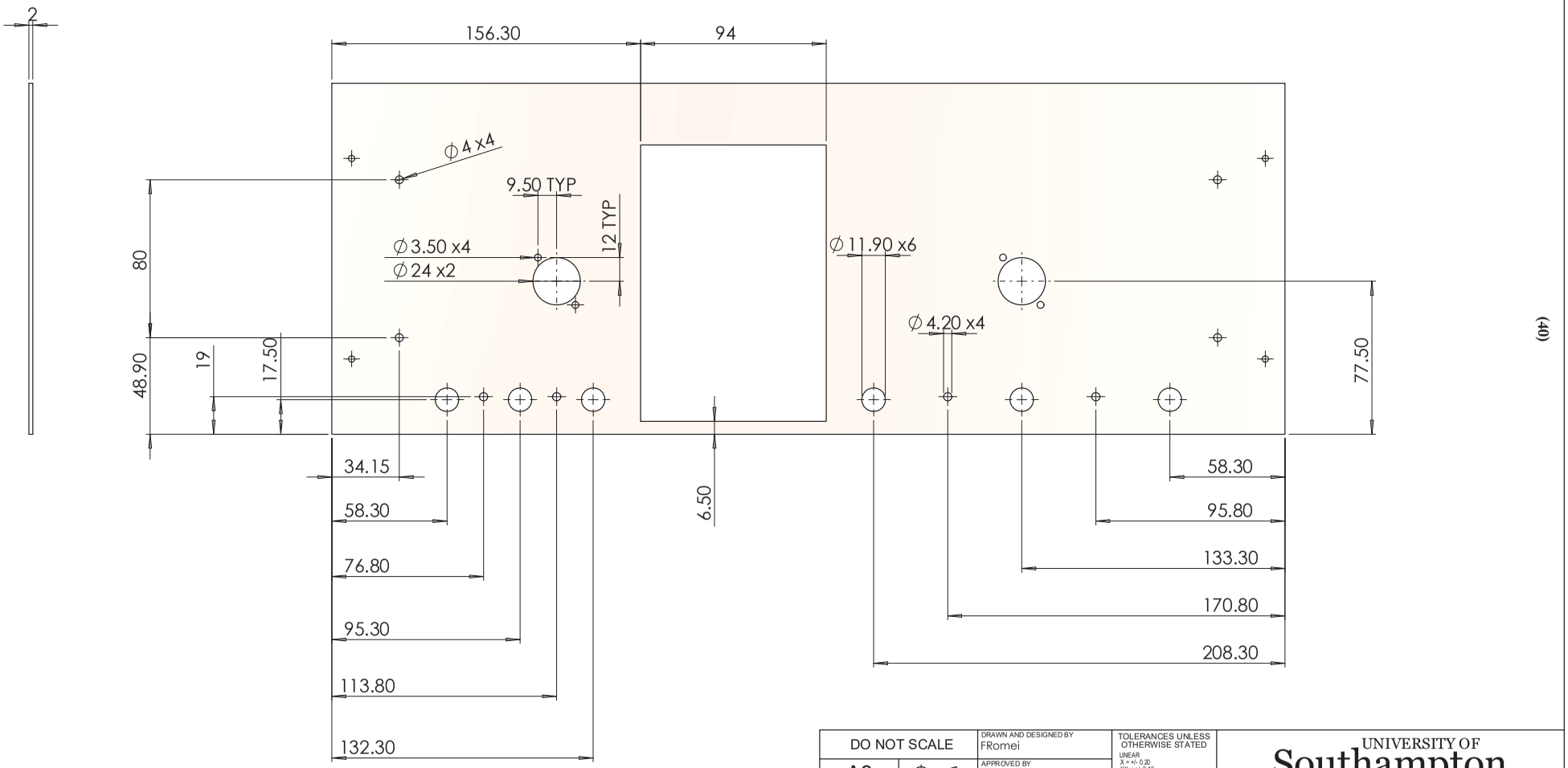

(40)

DO NOT SCALE		DRAWN AND DESIGNED BY: FRomei		TOLERANCES UNLESS OTHERWISE STATED: LINEAR X = +/- 0.20, XX = +/- 0.10, XXX = +/- 0.05; ANGULAR +/- 0.50; ALL DIMENSIONS IN mm UNLESS OTHERWISE STATED	UNIVERSITY OF Southampton, Faculty of Engineering and the Environment
A3		APPROVED BY: AN Grubisic			
JOB No: TWI-0	DEPARTMENT: Astronautics	DATE: 16/08/2017	SCALE: 1:2		TITLE: Front panel
PROJECT: Flow System	SUPERVISORS: AN Grubisic, GT Roberts	MATERIAL: Steel	TEXTURE	SURFACE FINISH: ALL OVER UNLESS OTHERWISE STATED	
REMOVE ALL SHARP EDGES		THE INFORMATION CONTAINED IN THIS DOCUMENT IS THE PROPERTY OF THE UNIVERSITY OF SOUTHAMPTON DO NOT COPY WITHOUT WRITTEN PERMISSION.		SHEET: 4 of 5	No OFF: 1	ASSEMBLY NUMBER	DRAWING NUMBER: 1 of 1	REVISION: 2
IF IN DOUBT PLEASE ASK					

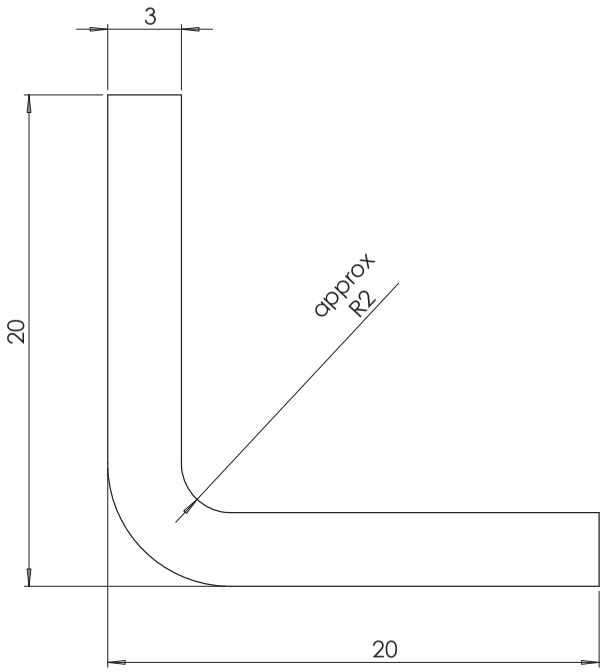

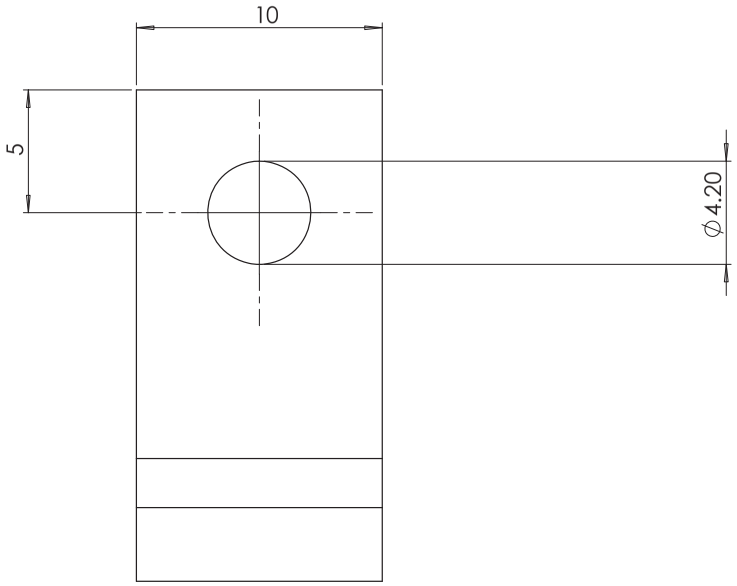

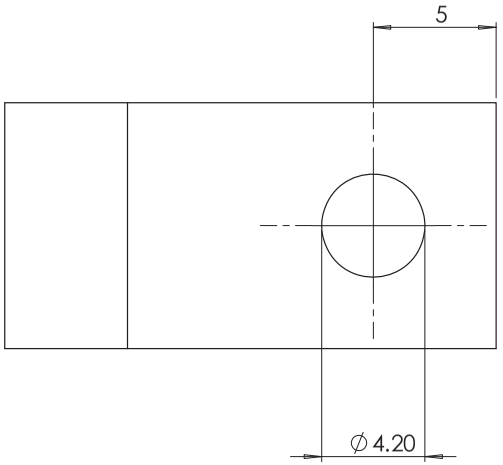

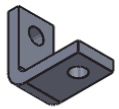

(41)

DO NOT SCALE		DRAWN AND DESIGNED BY FRomei		TOLERANCES UNLESS OTHERWISE STATED	UNIVERSITY OF Southampton
A3		APPROVED BY AN Grubisic		LINEAR X = +/- 0.20 XX = +/- 0.10 XXX = +/- 0.05 ANGULAR +/- 0.50 ALL DIMENSIONS IN mm UNLESS OTHERWISE STATED	Faculty of Engineering and the Environment
JOB No TWI-0	DEPARTMENT Astronautics	DATE 16/08/2017	SCALE 5:1		TITLE Joint
PROJECT Flow System	SUPERVISORS AN Grubisic GT Roberts	MATERIAL steel	TEXTURE	SURFACE FINISH ALL OVER UNLESS OTHERWISE STATED	
REMOVE ALL SHARP EDGES		THE INFORMATION CONTAINED IN THIS DOCUMENT IS THE PROPERTY OF THE UNIVERSITY OF SOUTHAMPTON DO NOT COPY WITHOUT WRITTEN PERMISSION.		SHEET 5 of 5	No OFF 6	ASSEMBLY NUMBER	DRAWING NUMBER 1 of 1	REVISION 2
IF IN DOUBT PLEASE ASK					

Appendix E Dataset Description

This dataset is a collection of .txt files, each one containing the data supporting the most important figures. A README file with supporting information is included. Below, a summary of txt files supporting the following figures:

- Fig.3.10-i, where i = 1 (Inconel 718); i = 2 (AISI 316); i = 3 (Re); i = 4 (Ta); i = 5 (W);
- Fig.5.3-i, where i = 1 (Inconel 718); i = 2 (Ta); i = 3 (Re);
- Fig.5.9-I#;
- Fig.5.10-top-I#;
- Fig.5.10-bottom-I#;
- Fig.5.11-i, where i = 1 (top subfigure); i = 2 (bottom subfigure);
- Fig.6.24.

In addition, the dataset contains the following:

- Dry 3D sector-symmetric simulations results including the following parameters (used as filename):
    - time: t#_s;
    - temperatures: T1#_terminal, T2#_inflow, T3#_casing, T4#_nozzle, T#_max, T#_12, T#_23, T#_34.
- Dry_tests.txt, where the variables included are:
    - time: t#;
    - current: I#;
    - thermocouples: TC1#_terminal, TC2#_inflow,TC3#_casing,TC4#_nozzle;
    - PSU voltage: Vpsu#;
    - Thruster voltage: Vts#.

The symbol # indicates the test current case, where i = 1 corresponds to I = 17.6A; i = 2 corresponds to I = 24.4A; i = 3 corresponds to I = 29.7A; i = 4 corresponds to I = 34.2A. The simulations data are provided at the actual time steps taken by the solver.

The dataset also includes the original technical drawings listed in Appendix D.

References

[1] R.S. Jankovsky, J.M. Sankovic, S. Oleson, Performance of a FAKEL K10K Resistojet, 33rd Jt. Propuls. Conf. Exhib. (1997) 14.

[2] J. Gonzalez, ESA Electric Propulsion Activities, (2011) 1–19.

[3] M. Leomanni, A. Garulli, A. Giannitrapani, F. Scortecci, An MPC-based attitude control system for all-electric spacecraft with on/off actuators, in: Proc. IEEE Conf. Decis. Control, 2013. doi:10.1109/CDC.2013.6760650.

[4] A.N. Grubisic, S.B. Gabriel, Assessment of the T5 and T6 Hollow Cathodes as Reaction Control Thrusters, J. Propuls. Power. 32 (2016) 810–820. doi:10.2514/1.B35556.

[5] F. Romei, A. Grubisic, D. Gibbon, O. Lane, R.A. Hertford, G. Roberts, A Thermo-fluidic Model for a Low Power Xenon Resistojet, in: Jt. Conf. 30th ISTS, 34th IEPC 6th NSAT, Hyogo-Kobe, Japan, Kobe, Japan, 2015: p. 15. https://eprints.soton.ac.uk/401468/.

[6] D. Gibbon, I. Coxhill, M. Drube, The design , Build Test and In-Orbit Performance of the Giove-A Propulsion System Dave Gibbon , Ian Coxhill , Mick Drube, 5th Int. Spacecr. Propuls. Conf. (2008) 1–9.

[7] G.P. Sutton, O. Biblarz, Rocket Propulsion Elements, 2001.

[8] R.G. Jahn, Physics of electric propulsion, Courier Corporation, 2006.

[9] R.L. Sackheim, R. Rosenthal, Electric Propulsion: the Next Real Breakthrough in Space Transportation, in: Int. Electr. Propuls. Conf., Seattle, WA, USA, 1993.

[10] J. Szabo, M. Robin, S. Paintal, B. Pote, V. Hruby, C. Freeman, Iodine Propellant Space Propulsion, 33rd Int. Electr. Propuls. Conf. (2013).

[11] K.A. Polzin, J.F. Seixal, S.L. Mauro, A.O. Burt, A. Martinez, A.K. Martin, The iodine Satellite (iSat) Propellant Feed System - Design and Development, 35th Int. Electr. Propuls. Conf. (2017) IEPC-2017-11.

[12] D. Krejci, P. Lozano, Space Propulsion Technology for Small Spacecraft, Proc. IEEE. (2018). doi:10.1109/JPROC.2017.2778747.

[13] K. Lemmer, Propulsion for CubeSats, Acta Astronaut. 134 (2017) 231–243. doi:10.1016/J.ACTAASTRO.2017.01.048.

[14] K.A. Polzin, S.R. Peeples, J.F. Seixal, S.L. Mauro, B.L. Lewis, G.A. Jerman, D.H. Calvert,

J. Dankanich, H. Kamhawi, T.A. Hickman, J. Szabo, B. Pote, L. Lee, Propulsion System Development for the Iodine Satellite (iSAT) Demonstration Mission, Jt. Conf. 30th Int. Symp. Sp. Technol. Sci. 34th Int. Electr. Propuls. Conf. 6th Nano-Satellite Symp. (2015) 1–14.

[15] Starlink website, (n.d.). https://www.starlink.com/ (accessed October 17, 2019).

[16] I. Coxhill, D. Gibbon, A Xenon Resistojet Propulsion System for Microsatellites, 41st AIAA/ASME/SAE/ASEE Jt. Propuls. Conf. & Exhib. 44 (2005) 1–10. doi:10.2514/6.2005-4260.

[17] V. Zakirov, M. Sweeting, T. Lawrence, J. Sellers, Nitrous oxide as a rocket propellant, Acta Astronaut. 48 (2001) 353–362. doi:10.1016/S0094-5765(01)00047-9.

[18] R.J. Page, C.R. Halbach, R.A.S. J, T.M. Corporation, V. Nuys, 3-kw Concentric Tubular Resistojet Performance, 3 (1966) 1669–1674. doi:10.1016/j.rifk.2012.02.004.

[19] D. Lev, R.M. Myers, K.M. Lemmer, J. Kolbeck, H. Koizumi, K. Polzin, The technological and commercial expansion of electric propulsion, Acta Astronaut. 159 (2019) 213–227. doi:10.1016/J.ACTAASTRO.2019.03.058.

[20] M. Martinez-Sanchez, J.E. Pollard, Spacecraft Electric Propulsion-An Overview, J. Propuls. Power. 14 (1998) 688–699. doi:10.2514/2.5331.

[21] Universitat Stuttgart - resistojets overview, (2019). https://www.irs.uni-stuttgart.de/forschung/elektrische_raumfahrtantriebe/triebwerke/elektrotherm-tw/widerstandsbeheizte-tw/index.html (accessed April 1, 2019).

[22] A. Passaro, A. Bulit, Development and Test of XR-150, a New High-Thrust 100 W Resistojet, in: 33rd Int. Electr. Propuls. Conf., The George Washington University, USA, 2013.

[23] D. Nicolini, D. Robertson, E. Chesta, G. Saccoccia, D. Gibbon, A. Baker, Xenon resistojets as secondary propulsion on ep spacecrafts and performance results of resistojets using xenon ∗, Power. (2003) 17–21.

[24] K.T. Chojnacki, R. Reinicke, Xenon Resistojet Design and Development, in: Int. Electr. Propuls. Conf., Kitakyushu, Japan, 1999.

[25] C.T.J. Lawrence, Research into Resistojet Rockets for Small Satellite Applications, University of Surrey, Guilford, Surrey, UK, 1998.

[26] W. Berry, C. Bartoli, A. Trippi, The ESA Policy and Programme for the Development of Electric Propulsion, in: IEPC-88-001, Noordwijk, The Netherlands, 1988.

[27] A.J. Louviere, R.E. Jones, W.E. Morren, J.S. Sovey, Water-Propellant Resistojets for Man-Tended Platforms, in: NASA Tech. Memo. 100110, 1987. http://www.openpsychodynamic.com/?page_id=32.

[28] Rocketdyne, Electric Propulsion Overview, (n.d.). http://www.rocket.com/ (accessed April 1, 2016).

[29] W.E. Morren, M. V Whalen, J.S. Sovey, Performance and Endurance Tests of a Multipropellant Resistojet for Space Station Auxiliary Propulsion., 1986. doi:doi:10.2514/6.1986-1435.

[30] R. GRABBI, C. MURCH, High performance electrothermal hydrazine thruster /HiPEHT/ development, in: 2013. doi:10.2514/6.1976-656.

[31] J. Donovan, W. Lord, P. Sherwood, Fabrication and preliminary testing of a 3kW hydrogen resistojet, 9th Electr. Propuls. Conf. (1972) 0–15. doi:10.2514/6.1972-449.

[32] C.R. Halbach, R.Y. Yoshida, Development of a Biowaste Resistojet, J. Spacecr. Rockets. 8 (1971) 273–277. doi:10.2514/3.30259.

[33] W. LUND, T. PUGMIRE, ATS-III resistojet thruster system performance, 4th Propuls. Jt. Spec. Conf. 6 (1968) 790–794. doi:doi:10.2514/6.1968-553.

[34] R.J. Page, R.A. Short, Ten-Millipoimd Resistojet Performance, Eng. Notes. 5 (1968) 857–858. doi:10.2514/3.29372.

[35] R.N. Gibson, T.A. Cygnarowicz, Design and Performance of a Thermal Storage Resistojet, in: AI AA Electr. Propuls. Plasmadynamics Conf., Colorado Springs, Colorado, 1967: pp. 686–689. doi:10.2514/3.29331.

[36] W.A. Hoskins, R.J. Cassady, O. Morgan, R.M. Myers, F. Wilson, D.Q. King, K. de Grys, 30 Years of Electric Propulsion Flight Experience at Aerojet Rocketdyne, in: Proc. 33rd Int. Electr. Propuls. Conf., 2013: p. IEPC-439.

[37] M. V. Whalen, Space Station Resistojets: The Compatibility of Disperson-Strengthened Platinum with Candidate Propellants, Platin. Met. Rev. 32 (1988) 2–10.

[38] G. Haag, M. Sweeting, Low Cost Propulsion Development for Small Satellites at the Surrey Space Centre, in: 13 Th AIAA/USU Conf. Small Satell., 1993: pp. 1–10. http://www.smallsat.org/proceedings/13/tech-xii/ts-xii-2.pdf.

[39] J.J. Sellers, T.J. Lawrence, M. Paul, Results of Low-Cost Propulsion System Research for Small Satellite Application, in: Embed. Syst. Appl., 2013: pp. 203–230. doi:10.1007/978-1-4757-2574-2_15.

[40] D. Gibbon, C. Underwood, M. Sweeting, R. Amri, Cost effective propulsion systems for small satellites using butane propellant, in: Acta Astronaut., 2002. doi:10.1016/S0094-5765(02)00074-7.

[41] A.M. Baker, A. Da Silva Curiel, J. Schaffner, M. Sweeting, "you can get there from here": Advanced low cost propulsion concepts for small satellites beyond LEO, Acta Astronaut. 57 (2005) 288–301. doi:10.1016/J.ACTAASTRO.2005.03.046.

[42] M. Leomanni, A. Garulli, A. Giannitrapani, F. Scortecci, Propulsion options for very low Earth orbit microsatellites, Acta Astronaut. (2017). doi:10.1016/j.actaastro.2016.11.001.

[43] D. Gibbon, A. Baker, I. Coxhill, P. Sir, M. Sweeting, The Development of a Family of Resistojet Thruster Propulsion Systems for Small Spacecraft, Small Satell. Conf. (2003).

[44] D. Gibbon, UKSA STAR Project Kick-off SSTL Input, n.d.

[45] G. Cifali, S. Gregucci, T. Andreussi, M. Andrenucci, Resistojet Thrusters for Auxiliary Propulsion of Full Electric Platforms, in: 35th Int. Electr. Propuls. Conf., 2017.

[46] P.J. Sherwood, Construction of a High Performance Resistojet for Satellite Propulsion., (1978). http://www.dtic.mil/docs/citations/ADA064236.

[47] American Elements Website, (n.d.). https://www.americanelements.com (accessed April 1, 2016).

[48] J.F. Justin, a. Jankowiak, A.J. J.F.Justin, Ultra High Temperature Ceramics: Densification, Properties and Thermal Stability, Aerosp. Lab J. 8 (2011) 1–11. http://www.aerospacelab-journal.org/sites/www.aerospacelab-journal.org/files/AL3-08.pdf.

[49] E.J. Rolinski, T.L. Sweeney, Thermal Conductivity of Fibrous Silica, J. Chem. Eng. Data. 13 (1968) 203–206. doi:10.1021/je60037a018.

[50] J. Sun, Z. Hu, J. Li, H. Zhang, C. Sun, Thermal and mechanical properties of fibrous zirconia ceramics with ultra-high porosity, Ceram. Int. 40 (2014) 11787–11793. doi:10.1016/j.ceramint.2014.04.008.

[51] T. Batteries, PROMALIGHT ® High temperature microporous insulation board, (n.d.) 22–23.

[52] S. Mazouffre, Electric propulsion for satellites and spacecraft: Established technologies and novel approaches, Plasma Sources Sci. Technol. (2016). doi:10.1088/0963-0252/25/3/033002.

[53] D. Gibbon, O. Lane, C. Ward, S. Satellite, T. Limited, T. House, Tech Note 1 - VHTR System Requirement and Architechtural Design Document, (2015).

[54] J. Gonzalez del Amo, European Space Agency (ESA) Electric Propulsion Activities, in: 34th Int. Electr. Propuls. Conf., 2017.

[55] C. Boniface, J.-M. Charbonnier, L. Lefebvre, V. Leroi, T. Lienart, An overview of electric propulsion activities at CNES, in: 35th Int. Electr. Propul Sion Conf., Georgia Institute of Technology, Atlanta, Georgia, USA, 2017.

[56] P. Zentgraf, S. Berge, C. Chasset, H. Filippi, E. Gottzein, I. Gutiérrez-Cañas, M. Hartrampf, P.A. Krauss, C. Kuehl, B. Lübke-Ossenbeck, M. Mittnacht, O. Montenbruck, C. Müller, P.R. Boldo, A. Truffi, Preparing the GPS-experiment for the Small GEO mission, Adv. Astronaut. Sci. 137 (2010) 185–202.

[57] OHB System AG, (n.d.). https://www.ohb.de (accessed June 2, 2019).

[58] H. Lubberstedt, A. Schneider, M. Peukert, Electric Propulsion Aplpications in the SmallGEO Product Line, in: Dtsch. Luft- Und Raumfahrtkongress, 2014.

[59] J.-M. Autric, P. Escourrou, I. Laine, Telecom Spacecraft mission design: Electric Orbit Raising for Airbus communications satellites, in: SpaceOps Conf., American Institute of Aeronautics and Astronautics, 2018. doi:10.2514/6.2018-2601.

[60] First Spacebus NEO Service Module Assembled, (2019). https://www.esa.int/.

[61] Lockheed Martin LM2100, (n.d.). https://www.lockheedmartin.com.

[62] F. Guarducci, EP Technologies Development at Mars Space Ltd - Hollow Cathodes, Resistojets, GIE & PPTs, in: Epic Work., 2018. http://epic-src.eu/workshop2018presentations/.

[63] R.J. Page, R.A. Short, Design of High-performance Resistojets for Advanced Spacecraft, in: 9th Aerosp. Sci. Meet., 1971.

[64] W.S. Janna, Engineering Heat Transfer, Third Edition, CRC Press, 2011. doi:10.1201/9781439883143.

[65] S.C. Kim, Calculations of low-Reynolds-number resistojet nozzles, J. Spacecr. Rockets. 31 (1994) 259–264. doi:10.2514/3.26431.

[66] A.D. Ketsdever, M.T. Clabough, S.F. Gimelshein, A.A. Alexeenko, Experimental and Numerical Determination of Micropropulsion Device Efficiencies at Low Reynolds Numbers, AIAA J. 43 (2005) 633–641. doi:10.2514/1.10284.

[67] A.J. Donovan, W.T. Lord, Performance Testing of a 3-kW Hydrogen Resitojet, 1973.

[68] M. V Whalen, Low Reynolds Number Nozzle Flow Study, in: NASA Tech. Memo., 1987.

[69] D. Zelesnik, M.M. Micci, L.N. Long, Direct simulation Monte Carlo model of Low Reynolds number nozzle flows, J. Propuls. Power. 10 (1994) 546–553. doi:10.2514/3.23807.

[70] M.M. Hussaini, J.J. Korte, Investigation of Low-Reynolds-Number Rocket Nozzle Design Using PNS-Based Optimization Procedure, (1996).

[71] WebPlotDigitizer, (n.d.). https://apps.automeris.io/wpd/ (accessed April 1, 2019).

[72] M. Range, C. Temperature, Inconel-alloy-718, (n.d.).

[73] C.Y. Ho, T.K. Chu, Electrical resistivity and thermal conductivity of nine selected AISI stainless steels - Center for Information and Numerical Data Analysis and Synthesis, Distribution. (1977) 15. doi:10.1017/S0954579414000510.

[74] P.D. Desal, H.M. Chu, H.M. James, C.Y. Ho, Electrical Resistivity of Selected Elements, J. Phys. Chem. Ref. Data. 13 (1984) 1069–1096.

[75] W.E. Frazier, Metal additive manufacturing: A review, J. Mater. Eng. Perform. 23 (2014) 1917–1928. doi:10.1007/s11665-014-0958-z.

[76] M. Mani, B. Lane, A. Donmez, S. Feng, S. Moylan, R. Fesperman, Measurement Science Needs for Real-time Control of Additive Manufacturing Powder Bed Fusion Processes, 2015. doi:http://dx.doi.org/10.6028/NIST.IR.8036.

[77] E. Yasa, J. Kruth, Application of Laser Re-Melting on Selective Laser Melting Parts, Adv. Prod. Eng. Manag. 6 (2011) 259–270.

[78] E. Abele, H.A. Stoffregen, M. Kniepkamp, S. Lang, M. Hampe, Selective laser melting for manufacturing of thin-walled porous elements, J. Mater. Process. Technol. 215 (2015) 114–122. doi:10.1016/j.jmatprotec.2014.07.017.

[79] BSLL, Building Success Layer by Layer, (2016). www.3trpd.co.uk (accessed April 1, 2016).

[80] EOS, EOS GmbH Electro Optical System, (2016). www.3trpd.co.uk (accessed April 1, 2016).

[81] AKSTEEL, Datasheet: 316/316L Stainless Steel, 2019.

[82] L. Thijs, M.L. Montero Sistiaga, R. Wauthle, Q. Xie, J.P. Kruth, J. Van Humbeeck, Strong morphological and crystallographic texture and resulting yield strength anisotropy in selective laser melted tantalum, Acta Mater. 61 (2013) 4657–4668. doi:10.1016/j.actamat.2013.04.036.

[83] 3ders, Philips' Smit Röntgen introduces pure tungsten components made by laser sintering, (n.d.). https://www.3ders.org.

[84] 3DPrint.com, Philips Brand, Smit Röntgen Revolutionizes the Metal Additive

Manufacturing Industry by 3D Printing Pure Tungsten Parts, (n.d.). https://3dprint.com/13540/smit-rontgen-3d-printing-tungsten/ (accessed September 1, 2014).

[85] O.O. Manual, M2 Cusing, Concept Laser. (2014). http://www.concept-laser.de/en/industry/automotive/machines.html.

[86] B. Zhang, Y. Li, Q. Bai, Defect Formation Mechanisms in Selective Laser Melting: A Review, Chinese J. Mech. Eng. 30 (2017) 515–527. doi:10.1007/s10033-017-0121-5.

[87] J.-P. Kruth, S. Dadbakhsh, B. Vrancken, K. Kempen, J. Vleugels, J. Van Humbeeck, Additive Manufacturing of Metals via Selective Laser Melting Process Aspects and Material Developments, Addit. Manuf. Innov. Adv. Appl. (2016) 69–99. doi:10.1201/b19360-4.

[88] C. Laser, CL20ES (1.4404) Powder Delivery note, (2015).

[89] J.A. Slotwinski, E.J. Garboczi, K.M. Hebenstreit, Porosity Measurements and Analysis for Metal Additive Manufacturing Process Control, J. Res. Natl. Inst. Stand. Technol. 119 (2014) 494. doi:10.6028/jres.119.019.

[90] NASA Marshall Capabilities, (2014). www.nasa.gov/marshallcapabilities (accessed December 1, 2014).

[91] Design Guidelines for the Selection and Use of Stainless Steel, n.d. http://www.ssina.com/composition/temperature.html (accessed February 18, 2019).

[92] Precision-Ceramics, (2019). http://www.precision-ceramics.co.uk/materials/ (accessed May 1, 2016).

[93] A.N. Grubišić, University of Southampton David Fearn Electric Propulsion Laboratory Specification, 2019.

[94] D. Staab, A. Frey, A. Garbayo, L. Shadbolt, A. Grubisic, D. Hoffman, F. Romei, D. Faircloth, S. Lawrie, XMET: A Xenon Electrothermal Thruster using additive manufacturing, (2018). https://eprints.soton.ac.uk/420213/ (accessed June 3, 2019).

[95] Ö. Babur, V. Smilauer, T. Verhoeff, M. van den Brand, A Survey of Open Source Multiphysics Frameworks in Engineering, Procedia Comput. Sci. 51 (2015) 1088–1097. doi:10.1016/J.PROCS.2015.05.273.

[96] X. He, X. Feng, M. Zhong, F. Gou, S. Deng, Y. Zhao, The influence of Laval nozzle throat size on supersonic molecular beam injection, J. Mod. Transp. 22 (2014) 118–121. doi:10.1007/s40534-014-0041-3.

[97] M. Ahmadi, G. Mostafavi, M. Bahrami, Natural Convection From Interrupted Vertical

Walls, 136 (2014) 1–8. doi:10.1115/1.4028369.

[98] J.T. Podichetty, M. Waliul Islam, D. Van, G.L. Foutch, A.H. Johannes, Viscous heating analysis of simulant feces by computational fluid dynamics and experimentation, J. Water, Sanit. Hyg. Dev. 4 (2014) 62. doi:10.2166/washdev.2013.070.

[99] D. Renaud, D. Gerst, S. Mazouffre, A. Aanesland, E × B probe measurements in molecular and electronegative plasmas, Rev. Sci. Instrum. (2015). doi:10.1063/1.4937604.

[100] S.B. Gabriel, COMSOL Modelling of Hollow Cathodes, 35th Int. Electr. Propuls. Conf. (2017) 1–12. https://iepc2017.org/sites/default/files/speaker-papers/iepc-2017-487final.pdf.

[101] X.F. Sun, Y.H. Jia, T.P. Zhang, J.J. Chen, The Study of the RMF effect on the Performance of Field Reversed Configuration Thruster, Iepc. (2017).

[102] Z. Ning, H. Zhang, L. OU-Yang, D.-R. Yu, The Ignition Erosion Mechanism of Heatless Hollow Cathode, 35th Int. Electr. Propuls. Conf. (2017) IEPC-2017-70.

[103] X. Wen, T. Zhang, Y. Jia, C. Wu, N. Guo, X. Sun, Magnetohydrodynamics simulation of plasma processes in a helicon plasma source for a MW-level electromagnetic thruster at LIP, (2017) 1–7.

[104] F. Romei, A. Grubisic, D. Lasagna, D. Gibbon, Multiphysics Model Validation of Resistojets with Concentric Tubular Heat Exchanger, in: 7th Eur. Conf. Aeronaut. Sp. Sci. (EUCASS 2017), Milan, Italy, 2017. doi:10.13009/EUCASS2017-378.

[105] T.S. Hunnewell, K.L. Walton, S. Sharma, T.K. Ghosh, R. V. Tompson, D.S. Viswanath, S.K. Loyalka, Total hemispherical emissivity of SS 316L with simulated very high temperature reactor surface conditions, Nucl. Technol. (2017). doi:10.1080/00295450.2017.1311120.

[106] Emissivity Table, Calex Electron. Ltd. (2019).

[107] P. Wang, Z. Xie, H. Meng, Z. Hu, Effects of the temperature and roughness on the metal emissivity, in: 27th Chinese Control Decis. Conf. (2015 CCDC), IEEE, 2015: pp. 6197–6200. doi:10.1109/CCDC.2015.7161926.

[108] K.A. Ibrahim, B. Wu, N.P. Brandon, Electrical conductivity and porosity in stainless steel 316L scaffolds for electrochemical devices fabricated using selective laser sintering, Mater. Des. 106 (2016) 51–59. doi:10.1016/J.MATDES.2016.05.096.

[109] F. Romei, A. Grubisic, Numerical study of a novel monolithic heat exchanger for electrothermal space propulsion, Acta Astronaut. 159 (2019) 8–16. doi:10.1016/J.ACTAASTRO.2019.03.025.

[110] Bronkhorst, FLUIDAT® web page, (2018).

[111] M. Robinson, A. Grubisic, F. Romei, C. Ogunlesi, S. Ahmed, P. Aimone, F. Dary, D. Gibbon, Endurance Testing of the STAR Additively Manufactured Resistojet, in: Sp. Propuls. Conf., Seville, Spain, 2018. https://eprints.soton.ac.uk/417912/.

[112] F. Romei, A.N. Grubišić, D. Gibbon, Manufacturing of a High-Temperature Resistojet Heat Exchanger by Selective Laser Melting, Acta Astronaut. 138 (2017) 356–368. doi:10.1016/j.actaastro.2017.05.020.

[113] COMSOL Multiphysics, CFD Module, in: User's Guid., 5.3a, 2017.

[114] E. Bich, J. Millat, E. Vogel, The viscosity and thermal conductivity of pure monatomic gases from their normal boiling point up to 5000 K in the limit of zero density and at 0.101325 MPa, J. Phys. Chem. Ref. Data. 19 (1990) 1289–1305. doi:10.1063/1.555846.

[115] Denka Alcen Bulk Datasheet, (n.d.). http://www.morganthermalceramics.com (accessed August 1, 2016).

[116] G.R. Enos, T.K. Pugmire, R. Shaw, Applied Resistojet Technology, J. Spacecr. Rockets. 8 (1971) 63–68. doi:10.1016/j.bjps.2014.05.057.

[117] C. Ogunlesi, A. Grubisic, F. Romei, M. Robinson David, S. Ahmed, P. Aimone, F. Dary, D. Gibbon, M. Curtis Rouse, Novel non-destructive inspection of the STAR additively manufactured resistojet, in: Sp. Propuls. Conf., 2018. https://eprints.soton.ac.uk/417166/.

[118] R.G. Jahn, E.Y. Choueiri, Electric Propulsion, 3rd ed., Elsevier, 2001.

[119] COMSOL Multiphysics, Heat Transfer Module, in: User's Guid., 5.3a, 2017.

[120] COMSOL Multiphysics, Optimization Module, in: User's Guid., 5.3a, 2017.

[121] L.M. Rios, N. V. Sahinidis, Derivative-free optimization: A review of algorithms and comparison of software implementations, J. Glob. Optim. 56 (2013) 1247–1293. doi:10.1007/s10898-012-9951-y.

[122] C. Chung, S.C. Kim, R.M. Stubbs, K.J. De Witt, Low-Density Nozzle Flow by the Direct of Propulsion and, J. Propuls. Power. 11 (1995) 64–70.

[123] Standard k-epsilon Model, (n.d.). https://www.cfd-online.com (accessed January 1, 2019).

[124] R.D. McCarty, J. Fors, H.M. Roder, Selected Properties Hydrogen (Engineering Design Data), National Bureau of Standards, 1981.

[125] I. Edwards, A theoretical Study of the Performance of Resistojet Nozzles, University of Southampton, 1972.

[126] A.A. Alexeenko, D.A. Levin, S.F. Gimelshein, R.J. Collins, B.D. Reed, Numerical Modeling of Axisymmetric and Three-Dimensional Flows in Microelectromechanical Systems Nozzles, AIAA J. 40 (2002) 897–904. doi:10.2514/2.1726.

[127] MatWeb, Thermal Ceramics Min-K 2000 Data Recorder Molded Min-K Insulation, (n.d.). http://www.matweb.com (accessed January 1, 2017).